

MOLECULAR MANGANESE COMPOUNDS AS SINGLE-MOLECULE MAGNETS:  
A MOLECULAR APPROACH TO NANOSCALE MAGNETS

By

NICOLE E. CHAKOV

A DISSERTATION PRESENTED TO THE GRADUATE SCHOOL  
OF THE UNIVERSITY OF FLORIDA IN PARTIAL FULFILLMENT  
OF THE REQUIREMENTS FOR THE DEGREE OF  
DOCTOR OF PHILOSOPHY

UNIVERSITY OF FLORIDA

2005

Copyright 2005

by

Nicole E. Chakov

I dedicate this document to my family, for their love and unending support of me as I pursue my career goals.

## ACKNOWLEDGMENTS

First and foremost, I would like to thank my research advisor, Professor George Christou, for the opportunity to pursue my goal of earning a doctoral degree in chemistry in his research group. His guidance, unwavering support and constant encouragement during my time as a member of his group have been invaluable, allowing me to draw on my own creativity to achieve my research potential. I would also like to thank my other committee members, Dr. Daniel Talham, Dr. David Powell, Dr. McElwee-White and Dr. Stephen Hill, for their insightful comments and words of encouragement.

I would like to take this opportunity to thank the many research scientists with whom I have worked during my doctoral studies. These collaborators include Dr. Wolfgang Wernsdorfer, who provided essential single crystal measurements on numerous compounds below 1.8 K using his unique micro-SQUID apparatus. I also express my sincerest gratitude to the crystallographers, who worked diligently to solve numerous challenging crystal structures. These include Dr. Khalil Abboud and his staff at UFCXC, Dr. Arnie Rheingold and Dr. Lev Zahkarov at the University of Southern California at San Diego, as well as Dr. Maren Pink and the IUMSC staff. Special appreciation is also given to Dr. Grégory Chabboussant, Dr. Hans Güdel, Dr. Reto Basler and Andreas Sieber for their INS measurements on three  $Mn_{12}$  samples and to Dr. Monica Soler for her involvement in the synthetic portion of this project. Additionally, my genuine gratitude goes to Dr. Stephen Hill, Dr. Rachel Edwards and Dr. Konstantin Petukhov in the UF Physics Department for their HFEPR measurements, which generated such excitement in

the area of single-molecule magnetism. Their patience and understanding as they taught me the fundamentals, from understanding a HFEPR experiment to interpreting the terms in a spin Hamiltonian of a SMM, were exceptional. I also thank Dr. Andrew Kent and Dr. Enrique del Barco in the Physics Department at New York University for their magnetization measurements. The initial interest of Dr. Kent in the study of a high symmetry  $Mn_{12}$  complex has resulted in a better understanding of the magnetic behavior exhibited by a “model”  $Mn_{12}$  complex – a much debated topic for researchers in the SMM area. Lastly, I would like to thank Dr. Naresh Dalal, Andrew Harter and Dr. Randy Achey for  $^{55}Mn$  NMR measurements on single crystals of two  $Mn_{12}$  clusters, a study that was the first of its kind on a SMM.

The friendships that I made both in Gainesville and Bloomington were an integral part of this journey for me, providing me with a special support network. I would like to express my appreciation to the entire Christou group, past and present, for their thoughtful discussions, companionship and for helping me to grow as a chemist. To Gosia, I am especially grateful for her sincere friendship, for always cheering me up and for all the moments we spent together talking, laughing and celebrating.

Finally, and most importantly, I would like to express my sincerest gratitude to my family, my mother, father, grandmother and sister, who have always been there for me in every way. Their encouragement, pride and unwavering confidence in me throughout my pursuit of my doctoral degree have been invaluable. I am forever grateful for their love and support, for the understanding ear with which they listen and for their enduring belief in me.

## TABLE OF CONTENTS

	<u>page</u>
ACKNOWLEDGMENTS .....	iv
LIST OF TABLES .....	x
LIST OF FIGURES .....	xiv
ABBREVIATIONS .....	xxii
ABSTRACT .....	xxiii
CHAPTER	
1 GENERAL INTRODUCTION.....	1
2 SINGLE-MOLECULE MAGNETS. A Mn <sub>12</sub> COMPLEX WITH MIXED CARBOXYLATE-SULFONATE LIGATION: [Mn <sub>12</sub> O <sub>12</sub> (O <sub>2</sub> CMe) <sub>8</sub> (O <sub>3</sub> SPh) <sub>8</sub> (H <sub>2</sub> O) <sub>4</sub> ] .....	17
2.1 Introduction.....	17
2.2 Results and Discussion .....	19
2.2.1 Syntheses.....	19
2.2.2 Description of Structures .....	22
2.2.2.1 X-ray crystal structure of [Mn <sub>12</sub> O <sub>12</sub> (O <sub>2</sub> CMe) <sub>8</sub> (O <sub>3</sub> SPh) <sub>8</sub> (H <sub>2</sub> O) <sub>4</sub> ] ( <b>2</b> ) .....	22
2.2.2.2 X-ray crystal structure of [Mn <sub>4</sub> O <sub>4</sub> (O <sub>2</sub> PPh <sub>2</sub> ) <sub>6</sub> ] ( <b>5</b> ).....	28
2.2.3 Magnetochemistry of Complexes <b>2</b> and <b>3</b> .....	34
2.2.3.1 DC studies.....	34
2.2.3.2 AC studies.....	37
2.2.3.3 Relaxation studies .....	39
2.2.3.4 Hysteresis studies below 1.8 K.....	42
2.2.4 Magnetochemistry of Complex <b>5</b> .....	43
2.3 Conclusions.....	45
2.4 Experimental.....	46
2.4.1 Syntheses.....	46
2.4.2 X-ray Crystallography .....	48

3	NOVEL MIXED-VALENCE Mn <sup>III</sup> /Mn <sup>IV</sup> CLUSTERS FROM THE USE OF BENZENESELENINATE LIGANDS: [Mn <sub>7</sub> O <sub>8</sub> (O <sub>2</sub> CMe)(O <sub>2</sub> SePh) <sub>8</sub> (H <sub>2</sub> O)] AND [Mn <sub>7</sub> O <sub>8</sub> (O <sub>2</sub> SePh) <sub>9</sub> (H <sub>2</sub> O)].....	51
3.1	Introduction.....	51
3.2	Results and Discussion .....	53
3.2.1	Syntheses.....	53
3.2.2	Description of Structures .....	55
3.2.2.1	X-ray crystal structure of [Mn <sub>7</sub> O <sub>8</sub> (O <sub>2</sub> CMe)(O <sub>2</sub> SePh) <sub>8</sub> (H <sub>2</sub> O)] ( <b>6</b> ).....	55
3.2.2.2	X-ray crystal structure of [Mn <sub>7</sub> O <sub>8</sub> (O <sub>2</sub> SePh) <sub>9</sub> (H <sub>2</sub> O)] ( <b>7</b> ).....	60
3.2.3	Magnetochemistry of Complexes <b>6</b> and <b>7</b> .....	63
3.2.3.1	DC studies.....	63
3.2.3.2	AC studies.....	66
3.2.3.3	Hysteresis studies below 1.8 K.....	68
3.2.3.4	Origin of the relaxation barrier .....	71
3.3	Conclusions.....	74
3.4	Experimental.....	75
3.4.1	Syntheses.....	75
3.4.2	X-ray Crystallography .....	76
4	AN INVESTIGATION OF THE REACTIVITY OF Mn <sub>12</sub> COMPLEXES WITH DIMETHYLARSINIC ACID: NEW Mn <sub>4</sub> CUBANE COMPLEXES AND Mn <sub>16</sub> SINGLE-MOLECULE MAGNETS .....	79
4.1	Introduction.....	79
4.2	Results and Discussion .....	81
4.2.1	Syntheses.....	81
4.2.2	Description of Structures .....	85
4.2.2.1	X-ray crystal structure of [Mn <sub>4</sub> O <sub>4</sub> (O <sub>2</sub> AsMe <sub>2</sub> ) <sub>6</sub> ] ( <b>9</b> ) .....	85
4.2.2.2	X-ray crystal structure of {[Mn <sub>4</sub> O <sub>4</sub> (O <sub>2</sub> AsMe <sub>2</sub> ) <sub>6</sub> ](NO <sub>3</sub> )} <sub>2</sub> ( <b>10</b> ).....	89
4.2.2.3	X-ray crystal structure of [Mn <sub>16</sub> O <sub>8</sub> Ca <sub>4</sub> (O <sub>2</sub> CPh) <sub>8</sub> (O <sub>2</sub> AsMe <sub>2</sub> ) <sub>28</sub> (NO <sub>3</sub> ) <sub>4</sub> ] ( <b>11</b> ).....	92
4.2.2.4	X-ray crystal structure of [Mn <sub>16</sub> O <sub>8</sub> Sr <sub>4</sub> (O <sub>2</sub> CPh) <sub>16</sub> (O <sub>2</sub> AsMe <sub>2</sub> ) <sub>24</sub> ] ( <b>12</b> ).....	98
4.2.3	Magnetochemistry of Complexes <b>9</b> and <b>10</b> .....	103
4.2.4	Magnetochemistry of Complexes <b>11</b> and <b>12</b> .....	109
4.2.4.1	DC studies.....	109
4.2.4.2	AC studies.....	112
4.2.4.3	Hysteresis studies below 1.8 K.....	114
4.3	Conclusions.....	116
4.4	Experimental.....	118
4.4.1	Syntheses.....	118
4.4.2	X-ray Crystallography .....	120

5	NEW POLYNUCLEAR Mn CLUSTERS FROM THE USE OF THE HYDROPHOBIC CARBOXYLATE LIGAND 2,2-DIMETHYLBUTYRATE .....	125
5.1	Introduction.....	125
5.2	Results and Discussion .....	127
5.2.1	Syntheses.....	127
5.2.2	Electrochemistry .....	130
5.2.3	Description of Structures .....	134
5.2.3.1	X-ray crystal structure of [Mn <sub>12</sub> O <sub>12</sub> (O <sub>2</sub> CPe <sup>f</sup> ) <sub>16</sub> (MeOH) <sub>4</sub> ] ( <b>15</b> ) .....	134
5.2.3.2	X-ray crystal structure of [Mn <sub>6</sub> O <sub>2</sub> (O <sub>2</sub> CH <sub>2</sub> )(O <sub>2</sub> CPe <sup>f</sup> ) <sub>11</sub> (HO <sub>2</sub> CPe <sup>f</sup> ) <sub>2</sub> (O <sub>2</sub> CMe)] ( <b>16</b> )....	139
5.2.3.3	X-ray crystal structure of [Mn <sub>9</sub> O <sub>6</sub> (OH)(CO <sub>3</sub> )(O <sub>2</sub> CPe <sup>f</sup> ) <sub>12</sub> (H <sub>2</sub> O) <sub>2</sub> ] ( <b>17</b> ) .....	143
5.2.3.4	X-ray crystal structure of [Mn <sub>4</sub> O <sub>2</sub> (O <sub>2</sub> CPe <sup>f</sup> ) <sub>6</sub> (bpy) <sub>2</sub> ] ( <b>18</b> ) .....	146
5.2.4	Magnetochemistry of Complexes <b>15 - 19</b> .....	149
5.2.4.1	DC studies of <b>15</b> .....	149
5.2.4.2	AC studies of <b>15</b> .....	151
5.2.4.3	DC and AC susceptibility studies of complexes <b>16 - 19</b> .....	154
5.3	Conclusions.....	158
5.4	Experimental.....	160
5.4.1	Syntheses.....	160
5.4.2	X-ray Crystallography .....	163
6	SINGLE-MOLECULE MAGNETS: STRUCTURAL CHARACTERIZATION, MAGNETIC PROPERTIES AND <sup>19</sup> F NMR SPECTROSCOPY OF A Mn <sub>12</sub> FAMILY SPANNING THREE OXIDATION LEVELS.....	165
6.1	Introduction.....	165
6.2	Results and Discussion .....	167
6.2.1	Syntheses and Electrochemistry .....	167
6.2.2	Description of Structures .....	171
6.2.2.1	X-ray crystal structure of [Mn <sub>12</sub> O <sub>12</sub> (O <sub>2</sub> CC <sub>6</sub> F <sub>5</sub> ) <sub>16</sub> (H <sub>2</sub> O) <sub>4</sub> ] ( <b>20</b> ).....	171
6.2.2.2	X-ray crystal structure of (NMe <sub>4</sub> )[Mn <sub>12</sub> O <sub>12</sub> (O <sub>2</sub> CC <sub>6</sub> F <sub>5</sub> ) <sub>16</sub> (H <sub>2</sub> O) <sub>4</sub> ] ( <b>21</b> ) .....	176
6.2.2.3	X-ray crystal structure of (NMe <sub>4</sub> ) <sub>2</sub> [Mn <sub>12</sub> O <sub>12</sub> (O <sub>2</sub> CC <sub>6</sub> F <sub>5</sub> ) <sub>16</sub> (H <sub>2</sub> O) <sub>4</sub> ] ( <b>22</b> ) .....	178
6.2.3	<sup>19</sup> F Nuclear Magnetic Resonance Spectroscopy .....	180
6.2.4	Inelastic Neutron Scattering Spectroscopy .....	185
6.2.5	Magnetochemistry of Complexes <b>20 - 22</b> .....	192
6.2.5.1	DC studies.....	192
6.2.5.2	AC studies.....	198

	6.2.5.3 Relaxation studies using AC and DC data.....	204
	6.2.5.4 Variable-frequency AC susceptibility studies .....	209
	6.2.5.5 Hysteresis studies below 1.8 K.....	213
	6.3 Conclusions.....	216
	6.4 Experimental.....	217
	6.4.1 Syntheses.....	217
	6.4.2 X-ray Crystallography .....	220
7	EFFECT OF SYMMETRY ON MAGNETIC BEHAVIOR: A STUDY OF THE HIGH-SYMMETRY Mn <sub>12</sub> SINGLE-MOLECULE MAGNET [Mn <sub>12</sub> O <sub>12</sub> (O <sub>2</sub> CCH <sub>2</sub> Br) <sub>16</sub> (H <sub>2</sub> O) <sub>4</sub> ].....	224
	7.1 Introduction.....	224
	7.2 Results and Discussion .....	233
	7.2.1 Synthesis .....	233
	7.2.2 Electrochemistry .....	233
	7.2.3 X-Ray Crystal Structure of [Mn <sub>12</sub> O <sub>12</sub> (O <sub>2</sub> CCH <sub>2</sub> Br) <sub>16</sub> (H <sub>2</sub> O) <sub>4</sub> ] ( <b>26</b> )..	236
	7.2.4 <sup>1</sup> H Nuclear Magnetic Resonance Spectroscopy.....	243
	7.2.5 Single Crystal <sup>55</sup> Mn Nuclear Magnetic Resonance Spectroscopy..	247
	7.2.6 Magnetochemistry of Complex <b>26</b> .....	257
	7.2.6.1 DC studies.....	257
	7.2.6.2 AC studies.....	260
	7.2.6.3 Relaxation studies using AC and DC data.....	265
	7.2.6.4 Hysteresis studies below 1.8 K.....	267
	7.2.7 Single Crystal High-Frequency Electron Paramagnetic Resonance .....	268
	7.3 Conclusions.....	282
	7.4 Experimental.....	283
	7.4.1 Synthesis .....	283
	7.4.2 X-ray Crystallography .....	284
8	GENERAL CONCLUSIONS.....	286
APPENDIX		
A	BOND DISTANCES AND ANGLES.....	295
B	LIST OF COMPOUNDS.....	349
C	PHYSICAL MEASUREMENTS .....	351
	LIST OF REFERENCES.....	355
	BIOGRAPHICAL SKETCH .....	371

## LIST OF TABLES

<u>Table</u>	<u>page</u>
2-1	[Mn <sub>12</sub> O <sub>12</sub> (O <sub>2</sub> CR) <sub>16</sub> (H <sub>2</sub> O) <sub>4</sub> ] derivatives, together with pK <sub>a</sub> values of the conjugate acid of the carboxylate ligand ..... 19
2-2	Crystallographic data for [Mn <sub>12</sub> O <sub>12</sub> (O <sub>2</sub> CMe) <sub>8</sub> (O <sub>3</sub> SPh) <sub>8</sub> (H <sub>2</sub> O) <sub>4</sub> ]·4CH <sub>2</sub> Cl <sub>2</sub> ..... 23
2-3	Bond valence sum calculations for <b>2</b> ·4CH <sub>2</sub> Cl <sub>2</sub> ..... 26
2-4	Bond valence sum calculations for selected oxygen atoms in <b>2</b> ·4CH <sub>2</sub> Cl <sub>2</sub> ..... 26
2-5	Comparison of selected bond distances (Å) and angles (°) for [Mn <sub>12</sub> O <sub>12</sub> (O <sub>2</sub> CMe) <sub>16</sub> (H <sub>2</sub> O) <sub>4</sub> ]·2MeCO <sub>2</sub> H·4H <sub>2</sub> O ( <b>1</b> ), [Mn <sub>12</sub> O <sub>12</sub> (O <sub>2</sub> CMe) <sub>8</sub> (O <sub>3</sub> SPh) <sub>8</sub> (H <sub>2</sub> O) <sub>4</sub> ] ( <b>2</b> ) and [Mn <sub>12</sub> O <sub>12</sub> (O <sub>2</sub> CMe) <sub>8</sub> (O <sub>2</sub> PPh <sub>2</sub> ) <sub>8</sub> (H <sub>2</sub> O) <sub>4</sub> ] ( <b>4</b> ) ..... 29
2-6	Crystallographic data for [Mn <sub>4</sub> O <sub>4</sub> (O <sub>2</sub> PPh <sub>2</sub> ) <sub>6</sub> ] ..... 30
2-7	Bond valence sum calculations for <b>5</b> ..... 33
2-8	Bond valence sum calculations for selected oxygen atoms in <b>5</b> ..... 33
3-1	Crystallographic data for [Mn <sub>7</sub> O <sub>8</sub> (O <sub>2</sub> CMe)(O <sub>2</sub> SePh) <sub>8</sub> (H <sub>2</sub> O)]·6MeCN and [Mn <sub>7</sub> O <sub>8</sub> (O <sub>2</sub> SePh) <sub>9</sub> (H <sub>2</sub> O)]·2CH <sub>2</sub> Cl <sub>2</sub> ..... 57
3-2	Bond valence sum calculations for <b>6</b> ·6MeCN and <b>7</b> ·2CH <sub>2</sub> Cl <sub>2</sub> ..... 59
3-3	Bond valence sum calculations for selected oxygen atoms in <b>6</b> ·6MeCN and <b>7</b> ·2CH <sub>2</sub> Cl <sub>2</sub> ..... 59
3-4	Comparison of selected bond distances (Å) and angles (°) for [Mn <sub>7</sub> O <sub>8</sub> (O <sub>2</sub> CMe)(O <sub>2</sub> SePh) <sub>8</sub> (H <sub>2</sub> O)] ( <b>6</b> ) and [Mn <sub>7</sub> O <sub>8</sub> (O <sub>2</sub> SePh) <sub>9</sub> (H <sub>2</sub> O)] ( <b>7</b> ) ..... 62
4-1	Crystallographic data for [Mn <sub>4</sub> O <sub>4</sub> (O <sub>2</sub> AsMe <sub>2</sub> ) <sub>6</sub> ]·5H <sub>2</sub> O·C <sub>5</sub> H <sub>12</sub> and { [Mn <sub>4</sub> O <sub>4</sub> (O <sub>2</sub> AsMe <sub>2</sub> ) <sub>6</sub> ](NO <sub>3</sub> ) } <sub>2</sub> ·½MeCN·12H <sub>2</sub> O ..... 88
4-2	Bond valence sum calculations for <b>9</b> ·5H <sub>2</sub> O·C <sub>5</sub> H <sub>12</sub> and <b>10</b> ·½MeCN·12H <sub>2</sub> O ..... 88
4-3	Bond valence sum calculations for selected oxygen atoms in <b>9</b> ·5H <sub>2</sub> O·C <sub>5</sub> H <sub>12</sub> and <b>10</b> ·½MeCN·12H <sub>2</sub> O ..... 89

4-4	Comparison of selected bond distances (Å) and angles (°) for [Mn <sub>4</sub> O <sub>4</sub> (O <sub>2</sub> AsMe <sub>2</sub> ) <sub>6</sub> ] ( <b>9</b> ) and {[Mn <sub>4</sub> O <sub>4</sub> (O <sub>2</sub> AsMe <sub>2</sub> ) <sub>6</sub> ](NO <sub>3</sub> ) <sub>2</sub> } <sub>2</sub> ( <b>10</b> ).....	91
4-5	Comparison of selected bite distances (Å) for MeCO <sub>2</sub> <sup>-</sup> , PhSO <sub>3</sub> <sup>-</sup> , Ph <sub>2</sub> PO <sub>2</sub> <sup>-</sup> , PhSeO <sub>2</sub> <sup>-</sup> and Me <sub>2</sub> AsO <sub>2</sub> <sup>-</sup> ligands in <b>1, 2, 4, 5, 6, 7, 9</b> and <b>10</b> .....	92
4-6	Crystallographic data for [Mn <sub>16</sub> O <sub>8</sub> Ca <sub>4</sub> (O <sub>2</sub> CPh) <sub>8</sub> (O <sub>2</sub> AsMe <sub>2</sub> ) <sub>28</sub> (NO <sub>3</sub> ) <sub>4</sub> ]·32MeCN and [Mn <sub>16</sub> O <sub>8</sub> Sr <sub>4</sub> (O <sub>2</sub> CPh) <sub>16</sub> (O <sub>2</sub> AsMe <sub>2</sub> ) <sub>24</sub> ]·16MeCN .....	94
4-7	Bond valence sum calculations for <b>11</b> ·32MeCN and <b>12</b> ·16MeCN .....	96
4-8	Bond valence sum calculations for selected oxygen atoms in <b>11</b> ·32MeCN and <b>12</b> ·16MeCN .....	96
4-9	Comparison of selected bond distances (Å) and angles (°) for <b>11</b> ·32MeCN and <b>12</b> ·16MeCN .....	102
4-10	Distribution of spin states for <b>9</b> .....	104
4-11	Spin states of <b>9</b> in the  S <sub>T</sub> , S <sub>A</sub> , S <sub>B</sub> > format ordered as a function of energy .....	107
4-12	Selected Mn···O···Mn angles (°) of <b>9</b> .....	107
5-1	Anodic / cathodic peak current ratios at the indicated scan rates for the -0.07 V and -0.21 V reduction waves of <b>13</b> and <b>15</b> .....	134
5-2	Crystallographic data for [Mn <sub>12</sub> O <sub>12</sub> (O <sub>2</sub> CPe <sup>t</sup> ) <sub>16</sub> (MeOH) <sub>4</sub> ]·2MeCN, [Mn <sub>6</sub> O <sub>2</sub> (O <sub>2</sub> CH <sub>2</sub> )(O <sub>2</sub> CPe <sup>t</sup> ) <sub>11</sub> (HO <sub>2</sub> CPe <sup>t</sup> ) <sub>2</sub> (O <sub>2</sub> CMe)]·½CH <sub>2</sub> Cl <sub>2</sub> , [Mn <sub>9</sub> O <sub>6</sub> (OH)(CO <sub>3</sub> )(O <sub>2</sub> CPe <sup>t</sup> ) <sub>12</sub> (H <sub>2</sub> O) <sub>2</sub> ]·H <sub>2</sub> O·HO <sub>2</sub> CPe <sup>t</sup> and [Mn <sub>4</sub> O <sub>2</sub> (O <sub>2</sub> CPe <sup>t</sup> ) <sub>6</sub> (bpy) <sub>2</sub> ]·2H <sub>2</sub> O .....	136
5-3	Bond valence sum calculations for <b>15</b> ·2MeCN.....	137
5-4	Bond valence sum calculations for selected oxygen atoms in <b>15</b> ·2MeCN .....	138
5-5	Bond valence sum calculations for <b>16</b> ·½CH <sub>2</sub> Cl <sub>2</sub> .....	141
5-6	Bond valence sum calculations for selected oxygen atoms in <b>16</b> ·½CH <sub>2</sub> Cl <sub>2</sub> .....	142
5-7	Bond valence sum calculations for <b>17</b> ·H <sub>2</sub> O·HO <sub>2</sub> CPe <sup>t</sup> .....	146
5-8	Bond valence sum calculations for selected oxygen atoms in <b>17</b> ·H <sub>2</sub> O·HO <sub>2</sub> CPe <sup>t</sup> ...	146
5-9	Bond valence sum calculations for <b>18</b> ·2H <sub>2</sub> O .....	148
5-10	Bond valence sum calculations for selected oxygen atoms in <b>18</b> ·2H <sub>2</sub> O .....	148
6-1	Anodic / cathodic peak current ratios at the indicated scan rates for the 0.64 V and 0.30 V reduction waves of <b>20</b> .....	171

6-2	Crystallographic data for $[\text{Mn}_{12}\text{O}_{12}(\text{O}_2\text{CC}_6\text{F}_5)_{16}(\text{H}_2\text{O})_4]\cdot 3\text{CH}_2\text{Cl}_2$ , (NMe <sub>4</sub> )[Mn <sub>12</sub> O <sub>12</sub> (O <sub>2</sub> CC <sub>6</sub> F <sub>5</sub> ) <sub>16</sub> (H <sub>2</sub> O) <sub>4</sub> ] $\cdot 4.5\text{CH}_2\text{Cl}_2\cdot \frac{1}{2}\text{H}_2\text{O}$ , and (NMe <sub>4</sub> ) <sub>2</sub> [Mn <sub>12</sub> O <sub>12</sub> (O <sub>2</sub> CC <sub>6</sub> F <sub>5</sub> ) <sub>16</sub> (H <sub>2</sub> O) <sub>4</sub> ] $\cdot 6\text{C}_7\text{H}_8$ .....	174
6-3	Bond valence sum calculations for <b>20</b> $\cdot 3\text{CH}_2\text{Cl}_2$ , <b>21</b> $\cdot 4.5\text{CH}_2\text{Cl}_2\cdot \frac{1}{2}\text{H}_2\text{O}$ , and <b>22</b> $\cdot 6\text{C}_7\text{H}_8$ .....	175
6-4	Bond valence sum calculations for selected oxygen atoms in <b>20</b> $\cdot 3\text{CH}_2\text{Cl}_2$ , <b>21</b> $\cdot 4.5\text{CH}_2\text{Cl}_2\cdot \frac{1}{2}\text{H}_2\text{O}$ , and <b>22</b> $\cdot 6\text{C}_7\text{H}_8$ .....	175
6-5	Interatomic distances (Å) of Mn(11) in <b>20</b> .....	176
6-6	Selected interatomic distances (Å) and angles (°) for [Mn <sub>12</sub> O <sub>12</sub> (O <sub>2</sub> CC <sub>6</sub> F <sub>5</sub> ) <sub>16</sub> (H <sub>2</sub> O) <sub>4</sub> ] ( <b>20</b> ), (NMe <sub>4</sub> )[Mn <sub>12</sub> O <sub>12</sub> (O <sub>2</sub> CC <sub>6</sub> F <sub>5</sub> ) <sub>16</sub> (H <sub>2</sub> O) <sub>4</sub> ] ( <b>21</b> ), and (NMe <sub>4</sub> ) <sub>2</sub> [Mn <sub>12</sub> O <sub>12</sub> (O <sub>2</sub> CC <sub>6</sub> F <sub>5</sub> ) <sub>16</sub> (H <sub>2</sub> O) <sub>4</sub> ] ( <b>22</b> ).....	181
6-7	Solution <sup>19</sup> F NMR spectral data for <b>20-22</b> .....	184
6-8	Experimental and calculated energies and relative intensities of the INS transitions of isomers <b>a</b> and <b>b</b> in [Mn <sub>12</sub> O <sub>12</sub> (O <sub>2</sub> CC <sub>6</sub> F <sub>5</sub> ) <sub>16</sub> (D <sub>2</sub> O) <sub>4</sub> ] ( <b>23</b> ) .....	188
6-9	Zero-field splitting parameters D and B <sub>4</sub> <sup>0</sup> (in cm <sup>-1</sup> ) for <b>23-25</b> .....	190
6-10	M/Nμ <sub>B</sub> vs H/T fitting parameters for <b>20-22</b> .....	194
6-11	Arrhenius parameters for wet and dried samples of <b>20-22</b> .....	203
6-12	Fitting parameters of the m' and m'' AC susceptibility vs frequency data for <b>20-22</b> .....	212
7-1	Debye-Waller thermal parameters for atoms of MeCO <sub>2</sub> <sup>-</sup> ligands in <b>1</b> .....	231
7-2	Crystallographic data for [Mn <sub>12</sub> O <sub>12</sub> (O <sub>2</sub> CCH <sub>2</sub> Br) <sub>16</sub> (H <sub>2</sub> O) <sub>4</sub> ] $\cdot 4\text{CH}_2\text{Cl}_2$ .....	237
7-3	Bond valence sum calculations for <b>26</b> $\cdot 4\text{CH}_2\text{Cl}_2$ .....	240
7-4	Bond valence sum calculations for selected oxygen atoms in <b>26</b> $\cdot 4\text{CH}_2\text{Cl}_2$ .....	240
7-5	Comparison of selected interatomic distances (Å) and angles (°) for [Mn <sub>12</sub> O <sub>12</sub> (O <sub>2</sub> CMe) <sub>16</sub> (H <sub>2</sub> O) <sub>4</sub> ] $\cdot 2\text{MeCO}_2\text{H}\cdot 4\text{H}_2\text{O}$ ( <b>1</b> ) and [Mn <sub>12</sub> O <sub>12</sub> (O <sub>2</sub> CCH <sub>2</sub> Br) <sub>16</sub> (H <sub>2</sub> O) <sub>4</sub> ] ( <b>26</b> ).....	242
7-6	Solution <sup>1</sup> H NMR spectral data for <b>1</b> and <b>26</b> .....	244
7-7	Comparison of parameters obtained from <sup>55</sup> Mn NMR spectra of an aligned powder and single crystal of <b>26</b> .....	252
8-1	Comparison of selected bite distances (Å) for MeCO <sub>2</sub> <sup>-</sup> , PhSO <sub>3</sub> <sup>-</sup> , Ph <sub>2</sub> PO <sub>2</sub> <sup>-</sup> , PhSeO <sub>2</sub> <sup>-</sup> and Me <sub>2</sub> AsO <sub>2</sub> <sup>-</sup> ligands in <b>1, 2, 4, 5, 6, 7, 9</b> and <b>10</b> .....	289

A-1	Selected interatomic distances (Å) and angles (°) for [Mn <sub>12</sub> O <sub>12</sub> (O <sub>2</sub> CMe) <sub>8</sub> (O <sub>3</sub> SPh) <sub>8</sub> (H <sub>2</sub> O) <sub>4</sub> ] $\cdot$ 4CH <sub>2</sub> Cl <sub>2</sub> .....	295
A-2	Selected interatomic distances (Å) and angles (°) for [Mn <sub>4</sub> O <sub>4</sub> (O <sub>2</sub> PPh <sub>2</sub> ) <sub>6</sub> ]	300
A-3	Selected interatomic distances (Å) and angles (°) for [Mn <sub>7</sub> O <sub>8</sub> (O <sub>2</sub> CMe)(O <sub>2</sub> SePh) <sub>8</sub> (H <sub>2</sub> O)] $\cdot$ 6MeCN .....	303
A-4	Selected interatomic distances (Å) and angles (°) for [Mn <sub>7</sub> O <sub>8</sub> (O <sub>2</sub> SePh) <sub>9</sub> (H <sub>2</sub> O)] $\cdot$ 2CH <sub>2</sub> Cl <sub>2</sub> .....	307
A-5	Selected interatomic distances (Å) and angles (°) for [Mn <sub>4</sub> O <sub>4</sub> (O <sub>2</sub> AsMe <sub>2</sub> ) <sub>6</sub> ] $\cdot$ 5H <sub>2</sub> O $\cdot$ C <sub>5</sub> H <sub>12</sub> .....	309
A-6	Selected interatomic distances (Å) and angles (°) for {[Mn <sub>4</sub> O <sub>4</sub> (O <sub>2</sub> AsMe <sub>2</sub> ) <sub>6</sub> ](NO <sub>3</sub> ) <sub>2</sub> } $\cdot$ $\frac{1}{2}$ MeCN $\cdot$ 12H <sub>2</sub> O .....	312
A-7	Selected interatomic distances (Å) and angles (°) for [Mn <sub>16</sub> O <sub>8</sub> Ca <sub>4</sub> (O <sub>2</sub> CPh) <sub>8</sub> (O <sub>2</sub> AsMe <sub>2</sub> ) <sub>28</sub> (NO <sub>3</sub> ) <sub>4</sub> ] $\cdot$ 32MeCN .....	317
A-8	Selected interatomic distances (Å) and angles (°) for [Mn <sub>16</sub> O <sub>8</sub> Sr <sub>4</sub> (O <sub>2</sub> CPh) <sub>16</sub> (O <sub>2</sub> AsMe <sub>2</sub> ) <sub>24</sub> ] $\cdot$ 16MeCN .....	319
A-9	Selected interatomic distances (Å) and angles (°) for [Mn <sub>12</sub> O <sub>12</sub> (O <sub>2</sub> CPe <sup>t</sup> ) <sub>16</sub> (MeOH) <sub>4</sub> ] $\cdot$ 2MeCN .....	323
A-10	Selected interatomic distances (Å) and angles (°) for [Mn <sub>6</sub> O <sub>2</sub> (O <sub>2</sub> CH <sub>2</sub> )(O <sub>2</sub> CPe <sup>t</sup> ) <sub>11</sub> (HO <sub>2</sub> CPe <sup>t</sup> ) <sub>2</sub> (O <sub>2</sub> CMe)] $\cdot$ $\frac{1}{2}$ CH <sub>2</sub> Cl <sub>2</sub> .....	329
A-11	Selected interatomic distances (Å) and angles (°) for [Mn <sub>9</sub> O <sub>6</sub> (OH)(CO <sub>3</sub> )(O <sub>2</sub> CPe <sup>t</sup> ) <sub>12</sub> (H <sub>2</sub> O) <sub>2</sub> ] $\cdot$ H <sub>2</sub> O $\cdot$ HO <sub>2</sub> CPe <sup>t</sup> .....	331
A-12	Selected interatomic distances (Å) and angles (°) for [Mn <sub>4</sub> O <sub>2</sub> (O <sub>2</sub> CPe <sup>t</sup> ) <sub>6</sub> (bpy) <sub>2</sub> ] $\cdot$ 2H <sub>2</sub> O .....	333
A-13	Selected interatomic distances (Å) and angles (°) for [Mn <sub>12</sub> O <sub>12</sub> (O <sub>2</sub> CC <sub>6</sub> F <sub>5</sub> ) <sub>16</sub> (H <sub>2</sub> O) <sub>4</sub> ] $\cdot$ 3CH <sub>2</sub> Cl <sub>2</sub> .....	334
A-14	Selected interatomic distances (Å) and angles (°) for (NMe <sub>4</sub> )[Mn <sub>12</sub> O <sub>12</sub> (O <sub>2</sub> CC <sub>6</sub> F <sub>5</sub> ) <sub>16</sub> (H <sub>2</sub> O) <sub>4</sub> ] $\cdot$ 4.5CH <sub>2</sub> Cl <sub>2</sub> $\cdot$ $\frac{1}{2}$ H <sub>2</sub> O .....	339
A-15	Selected interatomic distances (Å) and angles (°) for (NMe <sub>4</sub> ) <sub>2</sub> [Mn <sub>12</sub> O <sub>12</sub> (O <sub>2</sub> CC <sub>6</sub> F <sub>5</sub> ) <sub>16</sub> (H <sub>2</sub> O) <sub>4</sub> ] $\cdot$ 6C <sub>7</sub> H <sub>8</sub> .....	344
A-16	Selected interatomic distances (Å) and angles (°) for [Mn <sub>12</sub> O <sub>12</sub> (O <sub>2</sub> CCH <sub>2</sub> Br) <sub>16</sub> (H <sub>2</sub> O) <sub>4</sub> ] $\cdot$ 4CH <sub>2</sub> Cl <sub>2</sub> .....	347

## LIST OF FIGURES

<u>Figure</u>	<u>page</u>
1-1 Representations of magnetic dipole arrangements in (i) paramagnetic, (ii) ferromagnetic, (iii) antiferromagnetic, and (iv) ferrimagnetic materials .....	3
1-2 Typical hysteresis loop of a magnet .....	4
1-3 ORTEP representation showing (a) the $[\text{Mn}_{12}\text{O}_{12}]^{16+}$ core and (b) the $[\text{Mn}_{12}\text{O}_{12}(\text{O}_2\text{CMe})_{16}(\text{H}_2\text{O})_4]$ complex with peripheral ligation .....	8
1-4 Simplified representation of the exchange interactions in the $[\text{Mn}_4^{\text{IV}}\text{Mn}_8^{\text{III}}(\mu_3\text{-O})_{12}]^{16+}$ core of <b>1</b> .....	9
1-5 ORTEP representation of the $[\text{Mn}_{12}\text{O}_{48}]$ core of a typical $\text{Mn}_{12}$ complex showing the relative disposition of the JT elongation axes .....	10
1-6 Representative plots of the potential energy versus (a) the orientation of the $m_s$ vector ( $\theta$ ) along the $z$ axis and (b) the $m_s$ sublevel for a typical $\text{Mn}_{12}$ complex .....	11
1-7 In-phase and out-of-phase AC susceptibility signals for a dried, microcrystalline sample of $[\text{Mn}_{12}\text{O}_{12}(\text{O}_2\text{CR})_{16}(\text{H}_2\text{O})_4]$ .....	12
1-8 Magnetization hysteresis loops for a typical $\text{Mn}_{12}$ complex .....	13
1-9 Representation of the change in energy of $m_s$ sublevels as a function of applied magnetic field.....	15
2-1 ORTEP representation of $[\text{Mn}_{12}\text{O}_{12}(\text{O}_2\text{CMe})_8(\text{O}_3\text{SPh})_8(\text{H}_2\text{O})_4]$ ( <b>2</b> ) .....	24
2-2 ORTEP representation of $[\text{Mn}_{12}\text{O}_{12}(\text{O}_2\text{CMe})_8(\text{O}_3\text{SPh})_8(\text{H}_2\text{O})_4]$ ( <b>2</b> ) showing the relative disposition of the JT elongation axes .....	25
2-3 ORTEP representation of $[\text{Mn}_4\text{O}_4(\text{O}_2\text{PPh}_2)_6]$ ( <b>5</b> ).....	31
2-4 ORTEP representation of the packing of <b>5</b> .....	31
2-5 Plot of $\chi_M T$ vs $T$ for dried, microcrystalline samples of (a) <b>2</b> · $\text{C}_6\text{H}_{14}$ and (b) <b>3</b> · $0.2\text{C}_6\text{H}_{14}$ .....	34
2-6 Plot of $M/N\mu_B$ vs $H/T$ for dried, microcrystalline samples of (a) <b>2</b> · $\text{C}_6\text{H}_{14}$ and (b) <b>3</b> · $0.2\text{C}_6\text{H}_{14}$ .....	36

2-7	Contour plot of the error surface for the D vs g fit for (a) $2 \cdot C_6H_{14}$ and (b) $3 \cdot 0.2C_6H_{14}$ .....	37
2-8	Plot of the in-phase and out-of-phase AC susceptibility signals vs $T$ for dried, microcrystalline samples of (a) $2 \cdot C_6H_{14}$ and (b) $3 \cdot 0.2C_6H_{14}$ .....	38
2-9	Plot of the natural logarithm of relaxation rate vs $1/T$ for (a) $2 \cdot C_6H_{14}$ and (b) $3 \cdot 0.2C_6H_{14}$ using $\chi_M''$ versus $T$ data .....	40
2-10	Relaxation time vs $T$ studies for a single crystal of $2 \cdot 4CH_2Cl_2$ . (a) Plot of magnetization vs time decay. (b) Arrhenius plot generated using AC $\chi_M''$ data and DC magnetization decay data.....	41
2-11	Magnetization hysteresis loops for a single crystal of $2 \cdot 4CH_2Cl_2$ .....	42
2-12	Plot of $\chi_M T$ vs $T$ for a dried, microcrystalline sample of $5 \cdot 2H_2O$ .....	44
2-13	Plot of the in-phase and out-of-phase AC susceptibility signals vs $T$ for a dried, microcrystalline sample of $5 \cdot 2H_2O$ .....	45
3-1	ORTEP representation of $[Mn_7O_8(O_2CMe)(O_2SePh)_8(H_2O)]$ ( <b>6</b> ).....	56
3-2	ORTEP representations of (a) the $[Mn_7O_8]^{9+}$ core of <b>6</b> and (b) the relative disposition of the elongation axes .....	58
3-3	ORTEP representation of the packing of <b>6</b> along the $a$ axis of the crystal .....	60
3-4	ORTEP representation of $[Mn_7O_8(O_2SePh)_9(H_2O)]$ ( <b>7</b> ).....	61
3-5	Plot of $\chi_M T$ vs $T$ for dried, microcrystalline samples of $6 \cdot 2H_2O \cdot \frac{1}{2}MeCN$ ( $\blacktriangle$ ) and $7 \cdot 2H_2O$ ( $\bullet$ ).....	63
3-6	Plot of $M/N\mu_B$ vs $H/T$ for a dried microcrystalline sample of $6 \cdot 2H_2O \cdot \frac{1}{2}MeCN$ .....	64
3-7	Plot of $\chi_M' T$ vs $T$ for $6 \cdot 2H_2O \cdot \frac{1}{2}MeCN$ in the 2.0-10.0 K range from AC and DC susceptibility measurements.....	66
3-8	Plot of the in-phase and out-of-phase AC susceptibility signals for a dried, microcrystalline sample of $6 \cdot 2H_2O \cdot \frac{1}{2}MeCN$ .....	67
3-9	Magnetization hysteresis loops for a single crystal of $6 \cdot 6MeCN$ .....	69
3-10	Curie-Weiss plot for $6 \cdot 2H_2O \cdot \frac{1}{2}MeCN$ .....	70
3-11	Relaxation time vs $T$ studies for a single crystal of $6 \cdot 6MeCN$ . (a) Magnetization vs time decay plots. (b) Arrhenius plot generated using the resulting relaxation time vs $T$ data .....	71
4-1	ORTEP representation of $[Mn_4O_4(O_2AsMe_2)_6]$ ( <b>9</b> ) .....	86

4-2	ORTEP representation of the cation of $\{[\text{Mn}_4\text{O}_4(\text{O}_2\text{AsMe}_2)_6](\text{NO}_3)\}_2$ ( <b>10</b> ).....	90
4-3	ORTEP representation of $[\text{Mn}_{16}\text{O}_8\text{Ca}_4(\text{O}_2\text{CPh})_8(\text{O}_2\text{AsMe}_2)_{28}(\text{NO}_3)_4]$ ( <b>11</b> ).....	93
4-4	ORTEP representation of <b>11</b> showing the crystallographic $D_2$ symmetry .....	94
4-5	ORTEP representation of the asymmetric unit of $[\text{Mn}_{16}\text{O}_8\text{Ca}_4(\text{O}_2\text{CPh})_8(\text{O}_2\text{AsMe}_2)_{28}(\text{NO}_3)_4]$ ( <b>11</b> ) .....	95
4-6	Schematic representation of the eight chelating and/or bridging modes in <b>11</b> .....	97
4-7	ORTEP representation of $[\text{Mn}_{16}\text{O}_8\text{Sr}_4(\text{O}_2\text{CPh})_{16}(\text{O}_2\text{AsMe}_2)_{24}]$ ( <b>12</b> ) .....	98
4-8	ORTEP representation of the asymmetric unit of $[\text{Mn}_{16}\text{O}_8\text{Sr}_4(\text{O}_2\text{CPh})_{16}(\text{O}_2\text{AsMe}_2)_{24}]$ ( <b>12</b> ) .....	99
4-9	ORTEP representation of the side-view of <b>12</b> .....	100
4-10	Schematic representation of the nine chelating and/or bridging modes in <b>12</b> .....	101
4-11	Representation of the pairwise exchange interactions $J$ , $J'$ and $J''$ between numbered Mn ions of <b>9</b> .....	104
4-12	Plot of $\chi_{\text{M}}T$ vs $T$ for a dried, microcrystalline sample of <b>9</b> ·H <sub>2</sub> O.....	105
4-13	Ordering of the spin states of <b>9</b> .....	106
4-14	Plot of the in-phase and out-of-phase AC susceptibility signals vs $T$ for a dried, microcrystalline sample of <b>9</b> ·H <sub>2</sub> O .....	108
4-15	Plot of $\chi_{\text{M}}T$ vs $T$ for dried, microcrystalline samples of (a) <b>11</b> ·2MeCN and (b) <b>12</b> .....	110
4-16	Plot of the in-phase and out-of-phase AC susceptibility signals vs $T$ for a dried, microcrystalline sample of <b>11</b> ·2MeCN .....	113
4-17	Magnetization hysteresis loops for a single crystal of <b>11</b> ·32MeCN.....	114
5-1	Cyclic voltammogram and differential pulse voltammogram for (a) <b>15</b> and (b) <b>13</b> in CH <sub>2</sub> Cl <sub>2</sub> .....	132
5-2	Scan rate dependence of oxidation wave at -0.07 V of <b>13</b> . (a) Cyclic voltammogram at the indicated scan rates. (b) Plot of cathodic and anodic peak current dependence vs $v^{1/2}$ .....	133
5-3	Scan rate dependence of oxidation wave at -0.21 V of <b>15</b> . (a) Cyclic voltammogram at the indicated scan rates. (b) Plot of cathodic and anodic peak current dependence vs $v^{1/2}$ .....	133

5-4	ORTEP representation of $[\text{Mn}_{12}\text{O}_{12}(\text{O}_2\text{CPe}^f)_{16}(\text{MeOH})_4]$ ( <b>15</b> ) .....	135
5-5	ORTEP representation of the $[\text{Mn}_{12}\text{O}_{44}(\text{MeOH})_4]$ core of complex <b>15</b> , emphasizing the relative disposition of the JT elongation axes .....	137
5-6	Space-filling diagram of complex <b>15</b> including all non-hydrogen atoms .....	139
5-7	ORTEP representation of $[\text{Mn}_6\text{O}_2(\text{O}_2\text{CH}_2)(\text{O}_2\text{CPe}^f)_{11}(\text{HO}_2\text{CPe}^f)_2(\text{O}_2\text{CMe})]$ ( <b>16</b> ) .....	140
5-8	ORTEP representation of the $[\text{Mn}_6\text{O}_{30}\text{CH}_2]$ core of <b>16</b> , emphasizing the relative disposition of the JT elongation axes .....	142
5-9	ORTEP representation of $[\text{Mn}_9\text{O}_6(\text{OH})(\text{CO}_3)(\text{O}_2\text{CPe}^f)_{12}(\text{H}_2\text{O})_2]$ ( <b>17</b> ) .....	143
5-10	ORTEP representations of (a) the $[\text{Mn}_9\text{O}_6(\text{OH})(\text{CO}_3)]^{12+}$ core of <b>17</b> and (b) the relative dispositions of the elongation axes .....	144
5-11	ORTEP representation of $[\text{Mn}_4\text{O}_2(\text{O}_2\text{CPe}^f)_6(\text{bpy})_2]$ ( <b>18</b> ) .....	147
5-12	Plot of $\chi_M T$ vs $T$ for a dried, microcrystalline sample of <b>15</b> ·2CH <sub>2</sub> Cl <sub>2</sub> .....	149
5-13	Determination of ground state spin of <b>15</b> ·2CH <sub>2</sub> Cl <sub>2</sub> . (a) Plot of $M/N\mu_B$ vs $H/T$ for a dried, microcrystalline sample. (b) Error surface for the $D$ vs $g$ fit .....	150
5-14	Plot of the in-phase and out-of-phase AC susceptibility signals vs $T$ for a dried, microcrystalline sample of <b>15</b> ·2CH <sub>2</sub> Cl <sub>2</sub> .....	152
5-15	Plot of the natural logarithm of relaxation rate vs $1/T$ for a dried, microcrystalline sample of <b>15</b> ·2CH <sub>2</sub> Cl <sub>2</sub> using AC $\chi_M''$ data .....	154
5-16	Plot of $\chi_M T$ vs $T$ for a dried, microcrystalline sample of <b>16</b> ·½CH <sub>2</sub> Cl <sub>2</sub> ·4H <sub>2</sub> O .....	155
5-17	Determination of ground state spin of <b>17</b> ·HO <sub>2</sub> CPe <sup>f</sup> . (a) Plot of $\chi_M T$ vs $T$ for a dried, microcrystalline sample. (b) Plot of $\chi_M' T$ vs $T$ in the 2.0-30.0 K range from AC and DC susceptibility measurements .....	157
5-18	Determination of ground state spin of <b>19</b> ·½MeNO <sub>2</sub> . (a) Plot of $\chi_M T$ vs $T$ for a dried, microcrystalline sample. (b) Plot of $\chi_M' T$ vs $T$ in the 2.0-30.0 K range from AC and DC susceptibility measurements .....	157
5-19	Determination of ground state spin of <b>18</b> ·2H <sub>2</sub> O. (a) Plot of $\chi_M T$ vs $T$ for a dried, microcrystalline sample. (b) Plot of $\chi_M' T$ vs $T$ in the 2.0-30.0 K range from AC and DC susceptibility measurements .....	158
6-1	Cyclic voltammogram and differential pulse voltammogram of <b>20</b> in CH <sub>2</sub> Cl <sub>2</sub> .....	169
6-2	Scan rate dependence of reduction waves of <b>20</b> . (a) Cyclic voltammogram with corresponding plot of cathodic and anodic peak current dependence vs $v^{1/2}$ for (b) 0.64 V reduction wave and (c) 0.30 V reduction wave .....	170

6-3	ORTEP representation of $[\text{Mn}_{12}\text{O}_{12}(\text{O}_2\text{CC}_6\text{F}_5)_{16}(\text{H}_2\text{O})_4]$ ( <b>20</b> ) .....	172
6-4	ORTEP representation of the anion of $(\text{NMe}_4)[\text{Mn}_{12}\text{O}_{12}(\text{O}_2\text{CC}_6\text{F}_5)_{16}(\text{H}_2\text{O})_4]$ ( <b>21</b> ).....	177
6-5	Packing diagram for <b>21</b> , emphasizing intermolecular $\pi$ -stacking of carboxylate aromatic rings .....	178
6-6	ORTEP representation of the anion of $(\text{NMe}_4)_2[\text{Mn}_{12}\text{O}_{12}(\text{O}_2\text{CC}_6\text{F}_5)_{16}(\text{H}_2\text{O})_4]$ ( <b>22</b> ) .....	179
6-7	$^{19}\text{F}$ NMR (282 MHz) spectra at $\sim 23$ °C in $\text{CD}_2\text{Cl}_2$ of <b>20-22</b> .....	182
6-8	Neutron energy loss side INS spectrum of <b>23-25</b> .....	186
6-9	Neutron energy loss side INS spectrum of (a) <b>23</b> at 20 K and (b) <b>24</b> at 9.9 K .....	186
6-10	Energy level diagram for <b>23</b> calculated using the determined INS parameters .....	189
6-11	Plot of $\chi_M T$ versus $T$ for dried, microcrystalline samples of (a) <b>20</b> , (b) <b>21</b> and (c) <b>22</b> $\cdot 2.5\text{C}_7\text{H}_8$ .....	193
6-12	Plot of $M/N\mu_B$ versus $H/T$ for dried, microcrystalline samples of (a) <b>20</b> , (b) <b>21</b> and (c) <b>22</b> $\cdot 2.5\text{C}_7\text{H}_8$ .....	195
6-13	Contour plot of the error surface for the $D$ vs $g$ fit for (a) <b>20</b> , (b) <b>21</b> and (c) <b>22</b> $\cdot 2.5\text{C}_7\text{H}_8$ .....	196
6-14	$\chi_M' T$ vs $T$ plots for vacuum-dried $[\text{Mn}_{12}]$ complex <b>20</b> , $[\text{Mn}_{12}]^-$ complex <b>21</b> , and $[\text{Mn}_{12}]^{2-}$ complex <b>22</b> $\cdot 2.5\text{C}_7\text{H}_8$ .....	199
6-15	$\chi_M''$ vs $T$ plots for vacuum-dried $[\text{Mn}_{12}]$ complex <b>20</b> , $[\text{Mn}_{12}]^-$ complex <b>21</b> , and $[\text{Mn}_{12}]^{2-}$ complex <b>22</b> $\cdot 2.5\text{C}_7\text{H}_8$ .....	201
6-16	$m''$ vs $T$ plots for wet crystals of $[\text{Mn}_{12}]$ complex <b>20</b> , $[\text{Mn}_{12}]^-$ complex <b>21</b> , and $[\text{Mn}_{12}]^{2-}$ complex <b>22</b> .....	202
6-17	Plots of relaxation time vs $1/T$ for wet crystals of complexes <b>20 - 22</b> using AC $\chi_M''$ data.....	205
6-18	Relaxation time vs $T$ studies for a single crystal of <b>20</b> $\cdot 3\text{CH}_2\text{Cl}_2$ . (a) Magnetization vs time decay plots. (b) Arrhenius plot generated using AC $\chi_M''$ and DC decay data.....	206
6-19	Relaxation time vs $T$ studies for the slower-relaxing species of <b>21</b> $\cdot 4.5\text{CH}_2\text{Cl}_2 \cdot \frac{1}{2}\text{H}_2\text{O}$ . (a) Magnetization vs time decay plots. (b) Arrhenius plot generated using AC $\chi_M''$ and DC decay data .....	207

6-20	Relaxation time vs $T$ studies for the faster-relaxing species of <b>21</b> ·4.5CH <sub>2</sub> Cl <sub>2</sub> ·½H <sub>2</sub> O. (a) Magnetization vs time decay plots. (b) Arrhenius plot generated using DC decay data .....	207
6-21	Relaxation time vs $T$ studies for a single crystal of <b>22</b> ·6C <sub>7</sub> H <sub>8</sub> . (a) Magnetization vs time decay plots. (b) Arrhenius plot generated using AC $\chi_M''$ and DC decay data .....	208
6-22	Argand plot of $m'$ vs $m''$ for wet crystals of (a) <b>20</b> ·3CH <sub>2</sub> Cl <sub>2</sub> at 4.0 K, (b) <b>21</b> ·4.5CH <sub>2</sub> Cl <sub>2</sub> ·½H <sub>2</sub> O at 3.4 K and (c) <b>22</b> ·6C <sub>7</sub> H <sub>8</sub> at 2.2 K.....	210
6-23	Plot of (a) the in-phase and (b) the out-of-phase AC magnetic susceptibility vs frequency at 4.0 K for <b>20</b> ·3CH <sub>2</sub> Cl <sub>2</sub> .....	211
6-24	Plot of (a) the in-phase and (b) the out-of-phase AC magnetic susceptibility vs frequency at 3.4 K for <b>21</b> ·4.5CH <sub>2</sub> Cl <sub>2</sub> ·½H <sub>2</sub> O .....	211
6-25	Plot of (a) the in-phase and (b) the out-of-phase AC magnetic susceptibility vs frequency at 2.2 K for <b>22</b> ·6C <sub>7</sub> H <sub>8</sub> .....	212
6-26	Magnetization hysteresis loops for a single crystal of <b>20</b> ·3CH <sub>2</sub> Cl <sub>2</sub> .....	214
6-27	Temperature dependence of the magnetization hysteresis loops for a single crystal of <b>21</b> ·4.5CH <sub>2</sub> Cl <sub>2</sub> ·½H <sub>2</sub> O.....	215
6-28	Scan rate dependence of the magnetization hysteresis loops for a single crystal of <b>21</b> ·4.5CH <sub>2</sub> Cl <sub>2</sub> ·½H <sub>2</sub> O .....	215
6-29	Magnetization hysteresis loops for a single crystal of <b>22</b> ·6C <sub>7</sub> H <sub>8</sub> .....	216
7-1	Representations of the structure of <b>1</b> . (a) Photograph of seven crystals and (b) packing diagram showing the orientation of molecules of <b>1</b> relative to each other .....	225
7-2	Magnetization hysteresis loops for a single crystal of <b>1</b> at the indicated transverse field sweep rate at 0.04 K.....	226
7-3	Edge dislocation along the $y$ axis with the extra plane $y, z$ inserted at $z > 0$ .....	228
7-4	ORTEP representation of the two-fold disorder of the MeCO <sub>2</sub> H solvent molecules of crystallization in <b>1</b> .....	229
7-5	ORTEP representation of the hydrogen-bonding interaction between an MeCO <sub>2</sub> H molecule of crystallization and an MeCO <sub>2</sub> <sup>-</sup> ligand bridging Mn <sup>III</sup> Mn <sup>III</sup> pairs in <b>1</b> .....	230

7-6	ORTEP representation of (a) $[\text{Mn}_{12}\text{O}_{12}(\text{O}_2\text{CMe})_{16}(\text{H}_2\text{O})_4]$ with $\text{MeCO}_2\text{H}$ solvent molecules and (b) $[\text{Mn}_{12}\text{O}_{12}(\text{O}_2\text{CCH}_2\text{Br})_{16}(\text{H}_2\text{O})_4]$ with $\text{CH}_2\text{Cl}_2$ solvent molecules.....	230
7-7	ORTEP representation of the coordination sphere of Mn(2) and Mn(3) of <b>1</b> .....	231
7-8	Depiction of the six isomers of <b>1</b> that differ in the number of hydrogen-bonded $\text{MeCO}_2\text{H}$ molecules of crystallization.....	232
7-9	Cyclic voltammogram and differential pulse voltammogram for <b>26</b> in $\text{CH}_2\text{Cl}_2$ ....	235
7-10	Scan rate dependence of the reduction waves of <b>26</b> . (a) Cyclic voltammogram with corresponding plot of cathodic and anodic peak current dependence vs $v^{1/2}$ for (b) 0.57 V reduction wave and (c) 0.21 V reduction wave.....	236
7-11	ORTEP representation of $[\text{Mn}_{12}\text{O}_{12}(\text{O}_2\text{CCH}_2\text{Br})_{16}(\text{H}_2\text{O})_4]$ ( <b>26</b> ).....	238
7-12	Seven different geometric isomers of $\text{Mn}_{12}$ SMMs .....	239
7-13	ORTEP representation of the anisotropy axes of Mn(1) and Mn(2) in <b>26</b> .....	241
7-14	ORTEP representation of the packing of <b>26</b> .....	242
7-15	$^1\text{H}$ NMR (300 MHz) spectrum at $\sim 23$ °C in $\text{CD}_2\text{Cl}_2$ of <b>26</b> .....	243
7-16	ORTEP representation of the fluxional process between the water ligand and the axial carboxylate bridging a $\text{Mn}^{\text{III}}\text{Mn}^{\text{III}}$ pair in a typical $\text{Mn}_{12}$ molecule.....	244
7-17	ORTEP representation of $[\text{Mn}_{12}\text{O}_{12}(\text{O}_2\text{CCH}_2\text{Br})_{16}(\text{H}_2\text{O})_4]$ ( <b>26</b> ) showing the $D_{2d}$ symmetry typical of a $\text{Mn}_{12}$ molecule in solution.....	245
7-18	Array of inversion recovery data of <b>26</b> in $\text{CD}_2\text{Cl}_2$ at 23 °C.....	246
7-19	$^1\text{H}$ NMR (300 MHz) spectrum at $\sim 23$ °C in $\text{CD}_3\text{CN}$ of <b>1</b> .....	246
7-20	Comparison of zero-field $^{55}\text{Mn}$ NMR spectra of (a) an aligned dried, microcrystalline sample of <b>26</b> , (b) a single crystal of <b>26</b> $\cdot 4\text{CH}_2\text{Cl}_2$ and (c) a single crystal of <b>1</b> .....	249
7-21	ORTEP representation of <b>26</b> , emphasizing the three crystallographically independent Mn ions within the cluster .....	250
7-22	Angular dependence of $^{55}\text{Mn}$ NMR in the <i>ab</i> plane of a single crystal of <b>26</b> $\cdot 4\text{CH}_2\text{Cl}_2$ .....	254
7-23	Angular dependence of $^{55}\text{Mn}$ NMR in the <i>ac</i> plane of a single crystal of <b>26</b> $\cdot 4\text{CH}_2\text{Cl}_2$ .....	255

7-24	Temperature dependence of the $^{55}\text{Mn}$ NMR spectrum of a single crystal of $\mathbf{26}\cdot 4\text{CH}_2\text{Cl}_2$ at the indicated temperatures.....	256
7-25	Plot of $\chi_M T$ vs $T$ for a dried, microcrystalline sample of $\mathbf{26}$ .....	257
7-26	Determination of the ground state spin of $\mathbf{26}$ . (a) Plot of $M/N\mu_B$ versus $H/T$ for a dried, microcrystalline sample. (b) Error surface for the $D$ vs $g$ fit.....	259
7-27	Plot of the in-phase and out-of-phase AC susceptibility signals vs $T$ for a dried, microcrystalline sample of $\mathbf{26}$ .....	261
7-28	Plot of the out-of-phase AC susceptibility signals vs $T$ for dried, microcrystalline $\mathbf{26}$ and for wet crystals of $\mathbf{26}\cdot 4\text{CH}_2\text{Cl}_2$ .....	262
7-29	Plots of (a) $m'$ and (b) $m''$ vs frequency for wet crystals of $\mathbf{26}\cdot 4\text{CH}_2\text{Cl}_2$ .....	264
7-30	Argand plot of $m'$ vs $m''$ of wet crystals of $\mathbf{26}\cdot 4\text{CH}_2\text{Cl}_2$ at 4.6 K.....	265
7-31	Relaxation time vs $T$ studies on a single crystal of $\mathbf{26}\cdot 4\text{CH}_2\text{Cl}_2$ . (a) Magnetization vs time decay plots in zero field. (b) Plot of relaxation time vs $1/T$ for $\mathbf{26}$ using AC $\chi_M''$ and DC decay data.....	267
7-32	Magnetization hysteresis loops for a single crystal of $\mathbf{26}\cdot 4\text{CH}_2\text{Cl}_2$ .....	268
7-33	Plot of HF EPR peak positions deduced from easy-axis measurements.....	271
7-34	Plot of the frequency of the $m_s$ sublevels of the $S = 10$ ground state of $\mathbf{26}$ versus applied magnetic field.....	271
7-35	Contour plot of the angle-dependent EPR spectra.....	272
7-36	Comparison of hard plane EPR spectra of $\mathbf{26}\cdot 4\text{CH}_2\text{Cl}_2$ measured under different conditions.....	273
7-37	Angle dependence of the EPR spectrum of $\mathbf{26}\cdot 4\text{CH}_2\text{Cl}_2$ .....	274
7-38	Fits to eq 7-12 for the frequency dependence of the hard plane spectra for the $S = 10$ state and for the $S = 9$ state of $\mathbf{26}$ .....	275
7-39	Comparison of EPR spectrum of $\mathbf{26}\cdot 4\text{CH}_2\text{Cl}_2$ with simulated spectrum.....	277
7-40	Angle dependence of several of the most important resonances.....	277
7-41	EPR spectra for a single crystal of $\mathbf{26}\cdot 4\text{CH}_2\text{Cl}_2$ measured at (a) different temperatures at 51.5 GHz and (b) different frequencies.....	278
7-42	Determination of relative energy of $S = 9$ excited state. (a) Temperature dependence of the area of the $\alpha_9$ and $\beta_9$ resonances. (b) Schematic for the energy levels of both the $S = 10$ and $S = 9$ states in zero magnetic field.....	279

## ABBREVIATIONS

Bu'	tertiary butyl
BVS	bond valence sum
CF	crystal field
CH <sub>2</sub> Cl <sub>2</sub>	dichloromethane
CV	cyclic voltammogram
DFT	density functional theory
DPV	differential pulse voltammogram
Et	ethyl
Fc (Fc <sup>+</sup> )	ferrocene (ferrocenium)
G	gauss
fwhm	full-width at half maximum
HFEPR	high-frequency electron paramagnetic resonance
INS	inelastic neutron scattering
IR	infrared
JT	Jahn-Teller
Me	methyl
MeCN	acetonitrile
MeOH	methanol
NMR	nuclear magnetic resonance
ORTEP	Oak Ridge thermal ellipsoid plotting program
Pe'	tertiary pentyl
Ph	phenyl
PS II	photosystem II
QTM	quantum tunneling of magnetization
SCM	single-chain magnet
sp	square pyramidal
SQUID	superconducting quantum interference device
T	tesla
tbp	trigonal bipyramidal
THF	tetrahydrofuran
TIP	temperature-independent paramagnetism
WOC	water-oxidizing complex
ZFS	zero-field splitting

Abstract of Dissertation Presented to the Graduate School  
of the University of Florida in Partial Fulfillment of the  
Requirements for the Degree of Doctor of Philosophy

MOLECULAR MANGANESE COMPOUNDS AS SINGLE-MOLECULE MAGNETS:  
A MOLECULAR APPROACH TO NANOSCALE MAGNETS

By

Nicole E. Chakov

August 2005

Chair: George Christou  
Major Department: Chemistry

The primary reason for the current interest in high nuclearity manganese carboxylate clusters is the study of single-molecule magnets (SMMs), or molecular nanomagnets. A SMM possesses a significant energy barrier to relaxation of its magnetization vector and, consequently, exhibits out-of-phase AC susceptibility signals and magnetization hysteresis loops, both properties characteristic of a superparamagnet-like particle. Hence, SMMs function as monodisperse, nanoscale magnetic particles below their blocking temperature and have potential applications for high density information storage as well as qubits in quantum computers. The SMMs with the largest energy barriers to date are the  $[\text{Mn}_{12}\text{O}_{12}(\text{O}_2\text{CR})_{16}(\text{H}_2\text{O})_4]$  ( $\text{Mn}_{12}$ ) family. However, the isolation of a SMM that behaves as a magnet at technologically relevant temperatures continues to elude researchers despite (i) the preparation of numerous novel 3d metal carboxylate clusters possessing different topologies and (ii) the expansion of existing families of SMMs with new derivatives. Such an approach is essential both for the

correlation of structural features with magnetic properties and for the design of a rational synthetic method for improved SMMs. Progress toward this end has already resulted in the isolation of a number of SMMs.

With this same goal in mind, a variety of synthetic strategies have been developed to access new  $Mn_{12}$  derivatives as well as other polynuclear  $Mn_x$  complexes. Such approaches include (i) ligand substitution reactions of  $Mn_{12}$  complexes to derivatize them with non-carboxylate ligands; (ii) introduction of a bulky carboxylate ligand to destabilize the  $Mn_{12}$  complex and allow access to other new polynuclear Mn clusters; and (iii) chemical reduction of a  $Mn_{12}$  derivative to facilitate a thorough study of a  $Mn_{12}$  family spanning three oxidation levels. Yet another strategy involves single crystal measurements of  $Mn_{12}$  SMMs by previously unemployed techniques, specifically  $^{55}Mn$  nuclear magnetic resonance, to directly probe the magnetic structure and individual metal ions in these clusters. Each of the complexes isolated as a result of this investigation has been characterized by spectroscopic, electrochemical and magnetochemical techniques. These studies provide useful insight into the influence of small modifications, including variation of the peripheral ligation or oxidation level, on both the isolated product and the magnetic behavior of a  $Mn_{12}$  species.

## CHAPTER 1 GENERAL INTRODUCTION

From the ancient times to the modern era, the discovery and subsequent utilization of magnetic materials have been central to significant technological advancements that have dramatically affected civilization and humankind.<sup>1</sup> Beginning with the Greeks, who first recognized that the mixed-valent iron oxide, magnetite, attracts elemental iron, the magnetic properties of materials have long been pursued for technological progress. Approximately two thousand years ago, the Chinese exploited the magnetic properties of magnetite to build the first magnetic device – the compass. Following this early development, magnets have become essential to every modern society and have found uses in magnetomechanical applications, acoustic instruments, information and telecommunications devices, electrical motors and generators, magnetic shielding as well as numerous others.<sup>1,2</sup> Modern day magnetic materials include magnetic alloys and oxides, particularly ferrites such as  $\text{MgFe}_2\text{O}_4$ , which can function in transformer cores, magnetic recording or information storage devices.<sup>2,3</sup>

The magnetic field associated with a magnetic substance is the result of an electrical charge in motion, specifically the spin and orbital angular momenta of electrons within atoms of a material. While all matter is composed of atoms containing one or more electrons, only a small handful of materials behave as magnets. In most substances, atoms have closed electron shells, i.e., electrons with magnetic fields aligned in opposite directions are paired with each other. Such materials with no magnetic moment are called diamagnets.<sup>4,5</sup> Hence, the crucial element that distinguishes a magnetic substance, or a

paramagnet, from a diamagnet is the existence of a magnetic moment that arises from at least one unpaired electron.

The various types of magnetic materials are grouped according to their response or susceptibility,  $\chi$ , to an applied magnetic field. The electron pairs of a diamagnet interact with an applied field, generating a repulsive field that weakly repels the diamagnet from the applied field; the sign of  $\chi$  is negative. In contrast, a paramagnet is attracted to an applied magnetic field; the sign of  $\chi$  is positive. The strength of the attraction is governed both by the number of unpaired electrons in the material as well as the nature of the interactions of its electron spins.<sup>1,2,6,7</sup> Both the temperature dependence as well as the absolute magnitude of  $\chi$  are measures by which the various types of paramagnetism are distinguished.<sup>7</sup> Simple paramagnetic behavior is observed in substances in which the magnetic moments of unpaired electrons are independent of each other. In the absence of a magnetic field, individual magnetic moments are randomly oriented. As a field is applied, the moments align parallel, albeit weakly, to the field; this alignment is opposed by the randomizing effect of thermal energy (Figure 1-1). The susceptibility of these materials is inversely proportional to temperature as defined by the Curie Law ( $\chi = C/T$ ), where  $C$  is the Curie constant.<sup>4-8</sup> There are other paramagnetic materials however that display a temperature dependence unlike that of a simple paramagnet. In these substances, the magnetic moments of the unpaired spins are not independent, but rather interact with each other, either in a cooperative manner when there is a parallel alignment of the magnetic moments or in a non-cooperative way when there is an overall anti-parallel alignment of magnetic moments. The former describes ferromagnetic behavior while the latter is associated with an antiferromagnetic or ferrimagnetic response;

antiferromagnetism refers to a complete canceling of magnetic moments while ferrimagnetism corresponds to the situation in which magnetic moments align in an antiparallel fashion but a non-zero magnetization results.<sup>1,2,4,7,8</sup> Examples of ferromagnets include iron, cobalt, nickel and several rare earth metals and their alloys while magnetite,  $\text{Fe}_3\text{O}_4$ , is a ferrimagnet.<sup>4</sup>

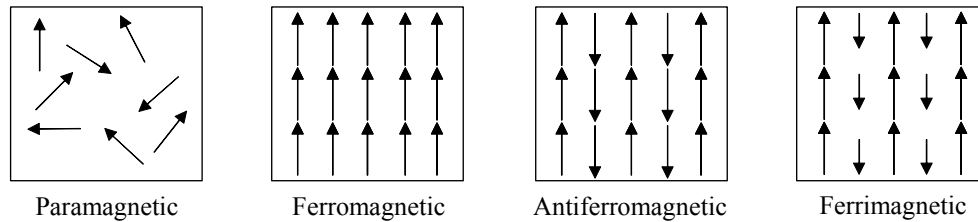


Figure 1-1. Representations of magnetic dipole arrangements in (i) paramagnetic, (ii) ferromagnetic, (iii) antiferromagnetic, and (iv) ferrimagnetic materials.

At all temperatures, ferro-, antiferro- and ferrimagnets are composed of domains, or tiny regions in which all the spins are aligned parallel. The transition from independent to cooperative behavior in these materials is associated with a critical temperature,  $T_c$ . Above  $T_c$ , there is enough thermal energy to cause a random alignment of each domain with respect to its neighbor, maximizing the entropy while minimizing the magnetization of the system. The application of a strong magnetic field induces the alignment of all of the domains with the field and hence, with each other, imparting a net magnetization to the material. As alignment occurs, the interaction of spins becomes strong enough to overcome dipole interactions and entropy considerations that maintain the random alignment of the domains.<sup>6,8</sup> When a magnetic field is applied and then removed at a temperature below  $T_c$ , the magnetization induced by the field does not entirely disappear, and in some cases can remain equal to the field-induced magnetization. This is in contrast to the behavior observed for paramagnetic systems in which the spins immediately

randomly reorient following removal of the field. For suppression of the remnant magnetization, a coercive field in the opposite direction is applied, inducing the realignment of the spins in the opposite direction and resulting in a hysteresis loop (Figure 1-2). For information storage, a small coercive field with a relatively rectangular-shaped hysteresis loop is crucial so that the two magnetic orientations of the spin can represent zero and one in the binary digital system used by current technology.<sup>4,7,8</sup> The requirement for information storage is that the system remains at a temperature at which the material exhibits hysteresis while the removal of the stored information involves heating to a temperature above  $T_c$ .<sup>8</sup>

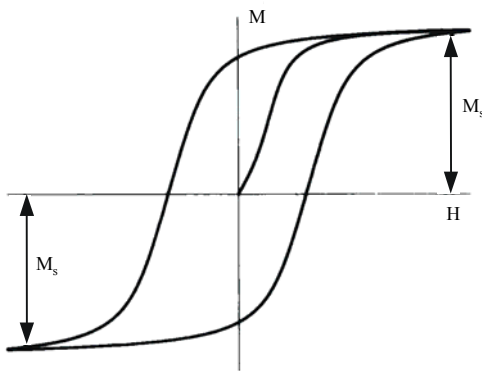


Figure 1-2. Typical hysteresis loop of a magnet, where M is magnetization, H is the applied magnetic field and  $M_s$  is the saturation value of the magnetization.

Economic studies estimate that the information storage area of the nanomagnetic market generated \$3.4 billion in revenues in 2003 and is expected to reach \$4.07 billion in 2004.<sup>9</sup> Considering the economic impact of this technology as well as the projected continual importance of magnets for storage devices as well as in other areas (average annual growth rate of 22.6%),<sup>9</sup> much research is being devoted towards the discovery and development of new, improved magnetic materials. The overwhelming trend of this research is towards miniaturization of magnetic storage media; the first hard disk drive, “RAMAC” introduced by IBM in 1957 had a storage capacity of only 2000 bits in<sup>-2</sup> while

storage density reached approximately  $10 \text{ Gbits in}^{-2}$  in 2000 – an increase by a factor of five million.<sup>10</sup> Because of the need for the storage of greater quantities of digital information on smaller surfaces areas, the development of magnetic particles of nanoscale dimensions is a necessity. Progress towards this end involves the use of smaller materials of nanoscale dimensions that behave as “permanent” magnets with functional temperatures in the practical range for technological use.

One approach towards this end involves the fragmentation of bulk ferromagnets or ferrimagnets such as ferro-spinels. For example, crystals of magnetite can be broken down such that each fragment is smaller in size than a single domain (20-200 nm); these nanoscale magnetic particles are known as superparamagnets. The magnetic moments within one superparamagnetic particle are ferrimagnetically aligned due to short range order. Alignment of the superparamagnets is induced by the application of a magnetic field, resulting in a remnant magnetization.<sup>12,13</sup> The reversal of the magnetization direction of a single domain requires an energy to overcome the crystal field anisotropy. Hence, slow magnetization relaxation is not related to domain formation as with a traditional ferromagnet, but rather involves an energy barrier that arises in part from the magnetic anisotropy associated with the shape of the particles. Giving no control in size versus properties and a non-uniform response to an applied field, the major drawback with this approach involves the wide distribution of particle sizes that result from fragmentation.<sup>11</sup> Recently, new fragmentation techniques based on scanning tunneling microscopy and biomineralization have been devised as a method of improvement of the non-uniform particle size obstacle.<sup>12,13</sup>

Yet another strategy currently being explored in detail is the development of new magnets using molecules as building blocks. Such materials, called molecule-based magnets, have the potential to demonstrate characteristics that are unattainable by the conventional metal/intermetallics and metal-oxide magnets used currently. These properties include low-temperature processability, high magnetic susceptibilities, high solubility, compatibility with polymers for composites, biocompatibility, transparency, semiconducting and insulating properties, high remnant magnetizations, as well as several other desirable characteristics.<sup>1,14</sup> Paramagnetic organic or inorganic molecules with a large number of unpaired electrons are typically used as the building blocks for the preparation of these molecule-based magnets, which rely on long-range intermolecular interactions to account for their magnetic behavior. Reported in 1967, the first molecule-based magnet,  $[\text{Fe}(\text{dtc})_2\text{Cl}]$ , where dtc = diethyldithiocarbamate, was found to have an  $S = 3/2$  ground state with ferromagnetic ordering at 2.46 K.<sup>8,15</sup> Subsequently, there was very little published activity in the area until 1987 when Miller and co-workers reported a molecular ferromagnet composed of alternating stacks of metallocenium donor cations ( $\text{D}^+$ ) and organic radical acceptor anions ( $\text{A}^-$ ), each with a single unpaired electron. For the complex  $[\text{Fe}(\text{C}_5\text{Me}_5)_2]^+$ , where  $\text{D}^+$  is the decamethylferrocenium cation and  $\text{A}^-$  is the tetracyanoethylene anion,  $[\text{TCNE}]^-$ , the ordering temperature was found to be 4.8 K.<sup>16,17</sup> From these studies, it was determined that the position of adjacent chains relative to one another had a significant effect on the bulk magnetic properties of the material.

In order to gain more insight on the effect of chain arrangement on magnetic properties, Kahn and co-workers prepared compounds containing ferromagnetic chains of  $\text{Cu}^{\text{II}}$ -bridge- $\text{Mn}^{\text{II}}$  moieties.<sup>18</sup> Antiferromagnetic coupling was observed between the

chains of  $\text{Mn}^{\text{II}}\text{Cu}^{\text{II}}(\text{pba})(\text{H}_2\text{O})_3$ , where pba = 1,3-propylenebis(oxamate). By changing the ligand only very slightly, contrasting data were observed as the compound,  $\text{Mn}^{\text{II}}\text{Cu}^{\text{II}}(\text{pbaOH})(\text{H}_2\text{O})_3$ , where pbaOH = 2-hydroxy-1,3-propylenebis(oxamate), showed overall ferromagnetic coupling with  $T_c = 4.6 \text{ K}$ .<sup>18</sup> Such studies emphasized the importance of selected bridging groups that aid in the formation of 2D or 3D lattices and facilitate communication between the magnetic centers in the molecular building blocks.

Based on the magnetic data collected from these and other similar molecular-based magnetic compounds, an attractive solution aimed at the improvement of the magnetic properties became apparent – molecules containing several transition metal ions, such as Mn, Fe, V, Ni, and Co, can potentially exhibit behavior similar to that of superparamagnets. Several polynuclear metal complexes that act as nanoscale magnetic particles have been prepared, resulting in the rapid development of an exciting new area of high-spin metal clusters termed single-molecule magnets (SMMs).<sup>19</sup> For numerous reasons, SMMs represent an exciting area, promising several advantages over conventional nanoscale magnetic particles. Such advantages include (i) the preparation of purified compounds by solution methods, resulting in a product with a single, sharply defined size; (ii) possible variation in peripheral carboxylate ligation such that small or bulky, hydrophilic or hydrophobic ligands can be incorporated into the synthesis; (iii) solubility in several organic solvents, providing access to industrial applications; and (iv) the possibility of reaching sub-nanoscale dimensions, resulting in the potential development of even better memory storage devices.<sup>19</sup>

The magnetic behavior of a SMM arises from the combination of a large ground state spin,  $S$ , and a large negative magnetic anisotropy as gauged by the axial zero-field

splitting parameter (ZFS),  $D$ .<sup>11,20</sup> Both in the fields of inorganic and organic chemistry, there is an intense search underway for such potentially useful high-spin molecules. In 1993, it was discovered that this exceptional combination of high-spin ground state and large, negative magnetic anisotropy is displayed by the complex,  $[\text{Mn}_{12}\text{O}_{12}(\text{O}_2\text{CMe})_{16}(\text{H}_2\text{O})_4] \cdot 2\text{MeCO}_2\text{H} \cdot 4\text{H}_2\text{O}$  (**1**), resulting in nanoscale-like magnetic behavior and the subsequent classification of the molecule as a SMM (Figure 1-3).<sup>11,21-23</sup> Probably the most intensely studied SMM,  $[\text{Mn}_{12}\text{O}_{12}(\text{O}_2\text{CMe})_{16}(\text{H}_2\text{O})_4]$  has an  $S = 10$  ground state spin and is only one in a class of well-characterized  $\text{Mn}_{12}$  complexes of the general formula,  $[\text{Mn}_{12}\text{O}_{12}(\text{O}_2\text{CR})_{16}(\text{H}_2\text{O})_4]$ , where  $R = \text{Me}, \text{Et}, \text{Ph}$  as well as numerous other groups.<sup>19</sup>

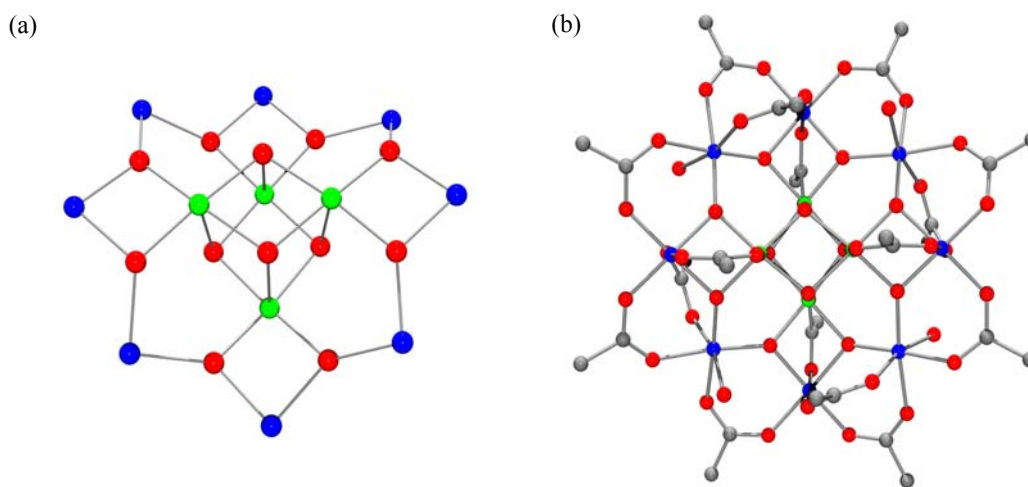


Figure 1-3. ORTEP representation in Pov-Ray format showing (a) the  $[\text{Mn}_{12}\text{O}_{12}]^{16+}$  core and (b) the  $[\text{Mn}_{12}\text{O}_{12}(\text{O}_2\text{CMe})_{16}(\text{H}_2\text{O})_4]$  complex with peripheral ligation.  $\text{Mn}^{\text{IV}}$  green;  $\text{Mn}^{\text{III}}$  blue; O red; C gray.

In these dodecanuclear complexes, a non-planar ring composed of eight alternating  $\text{Mn}^{\text{III}}$  and eight triply bridging oxide ions surrounds a central  $[\text{Mn}_4^{\text{IV}}\text{O}_4]^{8+}$  cubane moiety. Peripheral ligation is provided by sixteen bridging carboxylate ligands and four terminal water molecules. The large ground state spin arises from exchange interactions between

the  $S = 3/2$  spins of the  $\text{Mn}^{\text{IV}}$  ions and the  $S = 2$  spins of the  $\text{Mn}^{\text{III}}$  ions. The magnitude of the various exchange interactions between the magnetic centers in the  $\text{Mn}_{12}$  molecule has recently been determined by the fitting of a Heisenberg spin Hamiltonian to reproduce high-field magnetization data collected on samples of complex **1**.<sup>24</sup> A simplified representation of the  $[\text{Mn}_4^{\text{IV}}\text{Mn}_8^{\text{III}}(\mu_3\text{-O})_{12}]^{16+}$  core shows the four most important exchange pathways: (i)  $J_1$  relates each  $\text{Mn}^{\text{IV}}$  bridged by two  $\mu_3\text{-O}$  ions to a  $\text{Mn}^{\text{III}}$ ; (ii)  $J_2$  relates each  $\text{Mn}^{\text{IV}}$  bridged by one  $\mu_3\text{-O}$  ion to a  $\text{Mn}^{\text{III}}$ ; (iii)  $J_3$  refers to coupling between  $\text{Mn}^{\text{IV}}$  ions and; (iv)  $J_4$  refers to coupling between  $\text{Mn}^{\text{III}}$  ions (Figure 1-4). The determined values of the exchange interactions found in this study are  $J_1 = -119$  K,  $J_2 = -118$  K,  $J_3 = 8$  K and  $J_4 = 23$  K.<sup>24</sup> On the basis of these  $J$  values, the cluster can be approximately described as four  $\text{Mn}^{\text{III}}/\text{Mn}^{\text{IV}}$  dimers with spin  $S = 1/2$  that are ferromagnetically coupled to the four remaining  $\text{Mn}^{\text{III}}$  ions with spin  $S = 2$ , accounting for the  $S = 10$  ground state spin of the molecule.

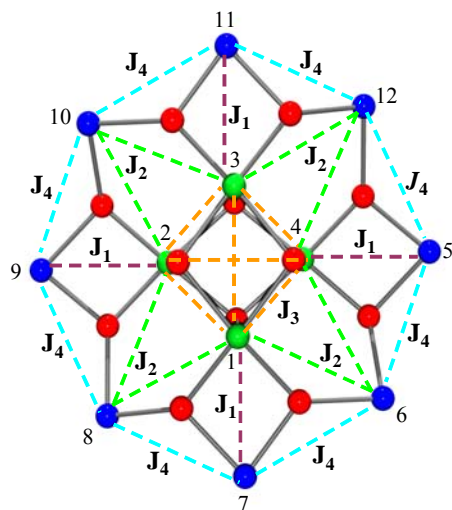


Figure 1-4. Simplified representation of the exchange interactions in the  $[\text{Mn}_4^{\text{IV}}\text{Mn}_8^{\text{III}}(\mu_3\text{-O})_{12}]^{16+}$  core of **1**.  $\text{Mn}^{\text{IV}}$  ions (green) are numbered 1-4;  $\text{Mn}^{\text{III}}$  ions (blue) are numbered 5-12; O red.

Each of the eight  $\text{Mn}^{\text{III}}$  ions on the outer periphery of the complex undergoes a Jahn-Teller (JT) distortion as expected for a high-spin  $d^4$  ion in near-octahedral geometry. The distortion takes place in the form of an elongation of two *trans* bonds. The approximately parallel alignment of the elongation axes of the eight  $\text{Mn}^{\text{III}}$  ions accounts for a high degree of molecular anisotropy; the anisotropy of a cluster is primarily a consequence of the single-ion anisotropies of the constituent ions within the cluster and of the relative orientations of the magnetic axes of these ions with respect to each other (Figure 1-5).

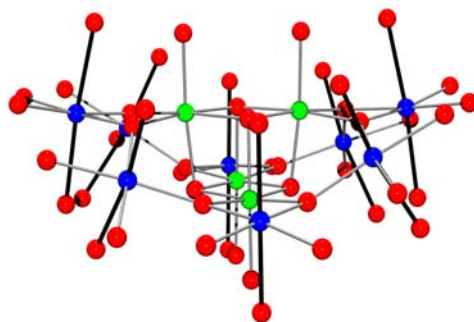


Figure 1-5. ORTEP representation in Pov-Ray format of the  $[\text{Mn}_{12}\text{O}_{48}]$  core of a typical  $[\text{Mn}_{12}\text{O}_{12}(\text{O}_2\text{CR})_{16}(\text{H}_2\text{O})_4]$  complex, showing the relative disposition of the JT elongation axes indicated as solid black bonds.  $\text{Mn}^{\text{IV}}$  green;  $\text{Mn}^{\text{III}}$  blue; O red.

Hence, the magnetic anisotropy of a  $\text{Mn}_{12}$  cluster is primarily of the axial type, with the  $x$  and  $y$  directions approximately equivalent to each other while different from the  $z$  direction. The magnetic moment of an individual  $\text{Mn}_{12}$  molecule preferentially lies in the  $z$  direction, or the easy-axis, of the molecule. A consequence of this Ising type of zero-field splitting is that the  $S = 10$  ground state spin is divided into 21 ( $2S + 1$ ) sublevels, each characterized by a spin projection quantum number,  $m_s$ , where  $-S \leq m_s \leq S$ . The energy of each sublevel is given as  $E(m_s) = m_s^2 D$ , giving rise to a double well potential (Figure 1-6). Because the value of the axial ZFS parameter  $D$  for a SMM is negative

( $-0.50 \text{ cm}^{-1}$  for **1**), the  $m_s = \pm 10$  sublevels lie lowest in energy while the  $m_s = 0$  sublevel lies highest. Consequently, there is a potential energy barrier between the “spin-up” ( $m_s = -10$ ) and “spin-down” ( $m_s = +10$ ) orientations of the magnetic moment.

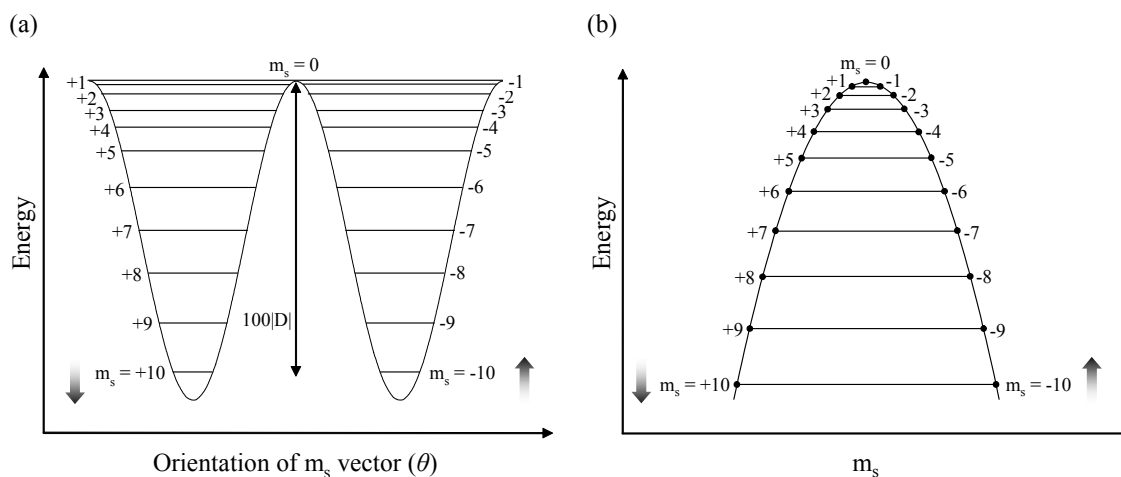


Figure 1-6. Representative plots of the potential energy versus (a) the orientation of the  $m_s$  vector ( $\theta$ ) along the  $z$  axis and (b) the  $m_s$  sublevel for a  $\text{Mn}_{12}$  complex with an  $S = 10$  ground state, experiencing zero-field splitting,  $D\hat{S}_z^2$ .

To reverse the spin of the molecule from along the  $-z$  (spin up) to the  $+z$  (spin down) axis of the molecule, a potential energy barrier,  $U = S^2|D| \approx 72 \text{ K}$  for **1**, must be overcome. For this reason, SMMs exhibit slow magnetization relaxation at low temperatures. Experimental evidence for this behavior is supported by the appearance of frequency-dependent signals ( $\chi_M''$  signals) in out-of-phase AC magnetic susceptibility measurements, as shown in Figure 1-7, and of hysteresis loops in magnetization versus DC field scans.<sup>11</sup> To ensure that the slow magnetization relaxation shown by a SMM is intrinsic to the molecule itself and not to long-range interactions, experiments have been carried out on frozen solutions and on polycrystalline samples embedded in a polymeric matrix in which single molecules are infinitely separated from their neighbors.<sup>25</sup>

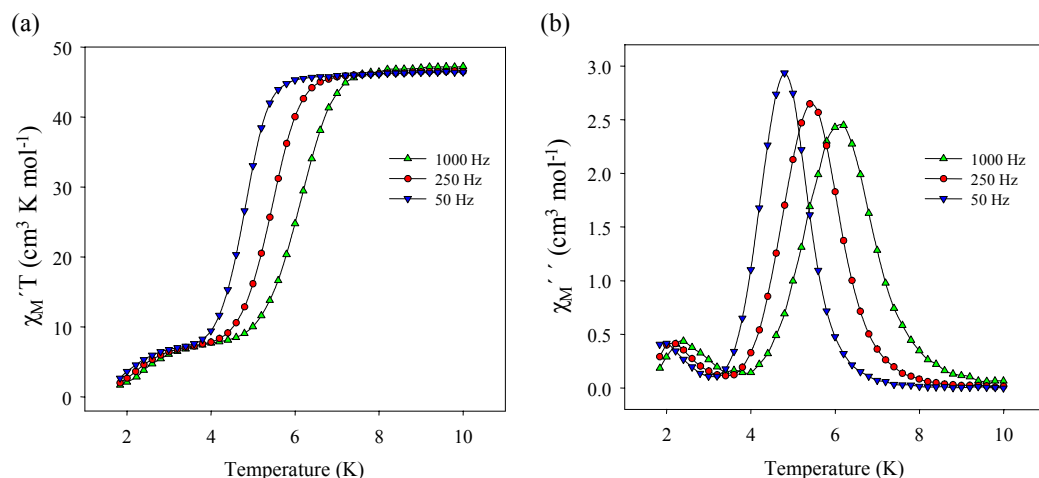


Figure 1-7. In-phase (as  $\chi_M' T$ ) and out-of-phase (as  $\chi_M''$ ) AC susceptibility signals for a dried, microcrystalline sample of  $[\text{Mn}_{12}\text{O}_{12}(\text{O}_2\text{CR})_{16}(\text{H}_2\text{O})_4]$  at the indicated oscillation frequencies.

The splitting of the  $S = 10$  spin into 21 sublevels to give a double well potential in zero applied magnetic field is a consequence of the first term in the Hamiltonian describing the giant spin of an individual  $\text{Mn}_{12}$  molecule (eq 1-1):

$$\hat{H} = D\hat{S}_z^2 + E(\hat{S}_x^2 + \hat{S}_y^2) + \mu_B \vec{H} \cdot \vec{g} \cdot \hat{S} + \hat{O}_4 + \hat{H}' \quad (1-1)$$

where  $D$  is the axial anisotropy constant,  $\hat{S}_z$  is the spin projection operator along the easy-axis of the molecule,  $E$  is the rhombic anisotropy constant,  $\hat{S}_x$  and  $\hat{S}_y$  are the  $x$  and  $y$  projections of the total spin operator  $\hat{S}$ , the third term represents the Zeeman interaction with an applied magnetic field  $H$ ,  $\hat{O}_4$  includes fourth order terms in the crystal field, and  $\hat{H}'$  represents environmental couplings such as hyperfine, dipolar and exchange interactions.<sup>26</sup> In an applied magnetic field, the potential energy barrier becomes asymmetric and the degeneracy of the  $\pm m_s$  sublevels is removed. According to the Zeeman term of the spin Hamiltonian, the  $m_s = -10$  sublevel is stabilized in energy with respect to other  $m_s$  states and, hence, is preferentially populated, giving a net magnetization. As the field is cycled to zero, the  $\pm m_s$  sublevels again become degenerate

in energy as described in Figure 1-6. However, molecules remain trapped in the  $m_s = -10$  sublevel as the magnetization is frozen by the existence of the large energy barrier ( $U = S^2|D|$  for integer spin systems and  $U = (S^2 - 1/4)|D|$  for non-integer spin systems), resulting in very slow magnetization relaxation, i.e., a remnant magnetization. Reversal of the magnetization direction is accomplished by cycling the field first to zero and then to a strong magnitude in the opposite direction, generating a hysteresis loop (Figure 1-8). Hence, the energy barrier that arises from the spin and anisotropy of a SMM imparts a memory effect; molecules in the “spin up” or “spin down” states can represent zero and one for information storage purposes.

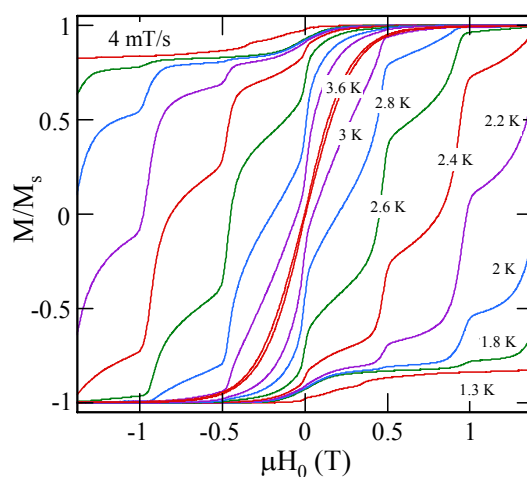


Figure 1-8. Magnetization hysteresis loops for a typical  $[\text{Mn}_{12}\text{O}_{12}(\text{O}_2\text{CR})_{16}(\text{H}_2\text{O})_4]$  complex in the 1.3-3.6 K temperature range at a 4 mT/s field sweep rate.  $M$  is normalized to its saturation value,  $M_s$ .

In contrast to the hysteresis loops of traditional ferri- or ferromagnetic materials, such as those of magnetite or chromium dioxide, respectively, the plots of magnetization versus magnetic field of many SMMs show steps that occur at regular intervals. The observed steps correspond to an increase in the relaxation rate of magnetization that occurs when there is an energy coincidence of  $m_s$  sublevels on the opposite sides of the potential energy barrier (Figure 1-9). For these critical field values,  $H = nD/g\mu_B$ , at which

steps occur, quantum tunneling of the magnetization (QTM) is allowed, resulting in an increase in the relaxation rate of the molecule.<sup>20,27-30</sup> Such predicted, but never before observed behavior was first reported in 1996 for molecules of  $[\text{Mn}_{12}\text{O}_{12}(\text{O}_2\text{CMe})_{16}(\text{H}_2\text{O})_4]\cdot 2\text{MeCO}_2\text{H}\cdot 4\text{H}_2\text{O}$ .<sup>27</sup> Hence, the relaxation of the magnetization of a SMM occurs not just by thermal activation over the energy barrier, but also by quantum tunneling of the magnetization through the energy barrier. A transverse component contained in the Hamiltonian of the molecule must be present to promote tunneling through the energy barrier, however. Such transverse components include second and fourth order transverse anisotropy terms,  $E$  and  $B_4^4$ , that can be provided in three ways: (i) by low-symmetry components of the crystal field; (ii) by a magnetic field provided by magnetic nuclei; and (iii) by a magnetic field provided by neighboring molecules.

This quantum phenomenon is not unique to **1**, but is also exhibited by many other SMMs, including the octanuclear  $\text{Fe}^{\text{III}}$  oxo-hydroxo cluster,  $[\text{Fe}_8\text{O}_2(\text{OH})_{12}(\text{tacn})_6]^{8+}$  (tacn = 1,4,7-triazacyclononane), where ground state tunneling was first observed, i.e., tunneling between the lowest energy  $m_s$  levels.<sup>31</sup> In contrast, quantum tunneling of magnetization in molecules of **1** occurs between  $m_s$  sublevels higher in energy than the lowest lying  $m_s = \pm 10$  states. Here, molecules in the ground state  $m_s = -10$  sublevel are thermally activated to higher lying  $m_s$  sublevels through which tunneling of the magnetization occurs. Relaxation of the magnetization to the  $m_s = +10$  sublevel follows in a process termed thermally-activated quantum tunneling. Although tunneling provides a route for rapid reversal of magnetization and, hence, a less attractive memory storage

device, an investigation into the gap between the quantum and classical understanding of magnetism can be made using these complexes as models.

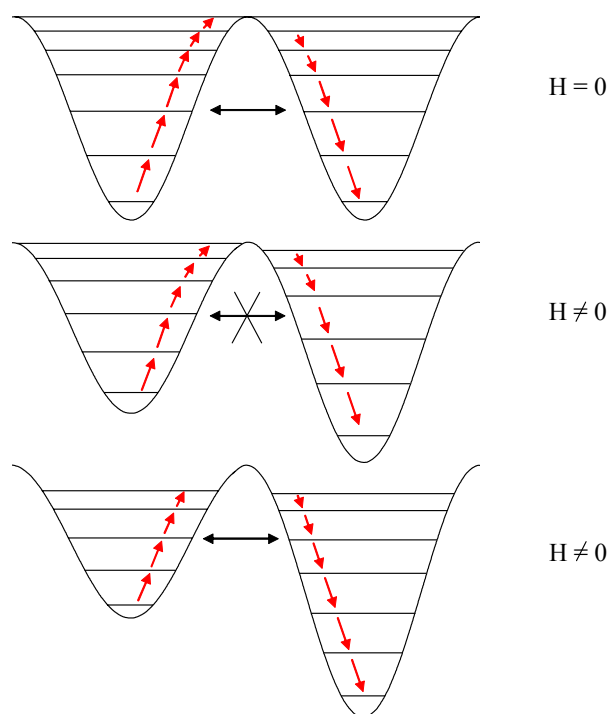


Figure 1-9. Representation of the change in energy of  $m_s$  sublevels as the magnetic field is swept from zero to a non-zero value. Resonant magnetization tunneling occurs when the  $m_s$  sublevels are aligned between the two halves of the diagram.

Due to the strong need for SMMs with even larger  $S$  values and more negative  $D$  values, numerous synthetic strategies aimed at the improvement of these materials have been considered. However, in contrast to the relative ease with which synthetic routes are developed in other fields of chemistry, the preparation of polynuclear metal complexes presents a considerable challenge. One of the primary goals of this research is the development of new synthetic methods aimed at the preparation of new SMMs. Three of the strategies employed towards this goal include (i) ligand substitution reactions of  $Mn_{12}$  complexes to derivatize them with non-carboxylate ligands in a site-specific manner, in order to direct or enhance reactivity at selected sites, and also to distort the geometry of

the  $[\text{Mn}_{12}\text{O}_{12}]^{16+}$  core, thereby changing the magnitudes of the exchange interactions between the Mn centers as well as the spin and magnetic anisotropy of the molecule; (ii) the introduction of a bulky, strongly electron donating carboxylate ligand to reductively destabilize the  $\text{Mn}_{12}$  complex, thereby making it more reactive and more likely to afford new polynuclear Mn clusters which may behave as SMMs; and (iii) the chemical reduction of a neutral  $\text{Mn}_{12}$  derivative to facilitate a thorough study of a family of neutral, one- and two-electron reduced  $\text{Mn}_{12}$  species with identical peripheral ligation using inelastic neutron scattering (INS) as well as other techniques. An additional research aim involves the study of single crystals of high-symmetry  $\text{Mn}_{12}$  single-molecule magnets by previously unemploye techniques, specifically  $^{55}\text{Mn}$  nuclear magnetic resonance, to directly probe the magnetic structure and individual metal ions in the core of these interesting molecules. Such studies provide insight into the necessary pathways to gain access to clusters that behave as single-molecule magnets at more technologically relevant temperatures.

CHAPTER 2  
SINGLE-MOLECULE MAGNETS. A Mn<sub>12</sub> COMPLEX WITH MIXED  
CARBOXYLATE-SULFONATE LIGATION: [Mn<sub>12</sub>O<sub>12</sub>(O<sub>2</sub>CMe)<sub>8</sub>(O<sub>3</sub>SPh)<sub>8</sub>(H<sub>2</sub>O)<sub>4</sub>]

**2.1 Introduction**

One of the primary reasons for the current interest in high nuclearity Mn carboxylate clusters is the study of single-molecule magnets (SMMs). A SMM possesses a significant energy barrier to relaxation (reorientation) of its magnetization vector, owing to a combination of a large ground state spin (*S*) value and a large easy-axis type of magnetoanisotropy (negative axial zero-field splitting parameter, *D*). The upper limit of the energy barrier is given by  $S^2|D|$  or  $(S^2-1/4)|D|$  for integer and non-integer spins, respectively.<sup>13,19,22,23</sup> The SMMs with the largest energy barriers to date are the [Mn<sub>12</sub>O<sub>12</sub>(O<sub>2</sub>CR)<sub>16</sub>(H<sub>2</sub>O)<sub>4</sub>] (Mn<sub>12</sub>) family, and they have thus received a great deal of attention.

Amongst the many studies that we have performed on Mn<sub>12</sub> complexes have been attempts to derivatize them with non-carboxylate ligands in a site-specific manner, in order to direct or enhance reactivity at selected sites and thus make regioselective reactions feasible. Such selectivity would be important for achieving clean and controllable reactivity in a complex containing so many carboxylate groups, and would make more feasible important objectives such as the binding of groups that might enhance the shape anisotropy or magnetic properties of the Mn<sub>12</sub> complexes, and/or facilitate the binding of the latter to surfaces, or to each other to give dimers (or higher aggregates) of Mn<sub>12</sub> species. One objective has been to replace just the eight axial, or just

the eight equatorial carboxylate groups with non-carboxylate ones, and thus obtain a mixed-ligand derivative with the two types of groups in specific positions on the  $\text{Mn}_{12}$  molecule. Unfortunately, our previous attempts have met with limited success, and we have been unable to substitute all axial or all equatorial carboxylate ligands with non-carboxylate groups to date. For example, four (but no more) of the eight axial carboxylate groups could be replaced with  $\text{NO}_3^-$  groups using nitric acid, giving  $[\text{Mn}_{12}\text{O}_{12}(\text{O}_2\text{CCH}_2\text{Bu}^t)_{12}(\text{NO}_3)_4(\text{H}_2\text{O})_4]$ ; <sup>32</sup> additional equivalents of nitric acid caused decomposition. This incorporation of nitrate was a useful step forward but did not fulfill our desire to functionalize all axial sites with non-carboxylate ligands. Similarly, we have been able to replace eight of the carboxylate groups with diphenylphosphinates ( $\text{Ph}_2\text{PO}_2^-$ ) to give  $[\text{Mn}_{12}\text{O}_{12}(\text{O}_2\text{CMe})_8(\text{O}_2\text{PPh}_2)_8(\text{H}_2\text{O})_4]$ , <sup>33</sup> but the steric bulk of the  $\text{Ph}_2\text{PO}_2^-$  groups resulted in them distributing themselves equally between axial and equatorial sites.

However, we have now achieved the above goal by the introduction into all the axial sites of benzenesulfonate groups,  $\text{PhSO}_3^-$ , with retention of the  $\text{Mn}_{12}$  structure and its SMM properties. This also represents the first incorporation of S-based ligands into the  $\text{Mn}_{12}$  SMMs. The synthesis, structure, and magnetic properties of the obtained complex are described. In addition, reactivity studies on this new  $\text{Mn}_{12}$  complex have led to the preparation of a tetranuclear Mn cluster,  $[\text{Mn}_4\text{O}_4(\text{O}_2\text{PPh}_2)_6]$ , possessing a manganese-oxo cubane core  $[\text{Mn}_4\text{O}_4]^{6+}$ . The cluster contains non-carboxylate diphenylphosphinate ligands and maintains the central cubane core of the  $\text{Mn}_{12}$  cluster, but it is not a SMM.

## 2.2 Results and Discussion

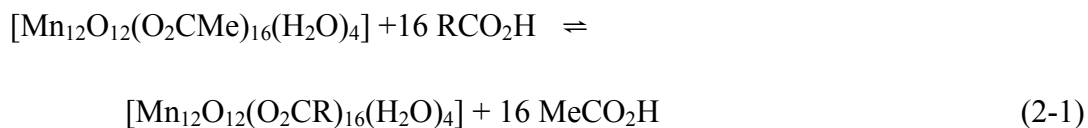
### 2.2.1 Syntheses

Our previous development and use of ligand substitution reactions on readily available complex **1** have allowed us access to  $[\text{Mn}_{12}\text{O}_{12}(\text{O}_2\text{CR})_{16}(\text{H}_2\text{O})_4]$  derivatives with a large variety of substituents (Table 2-1).

Table 2-1.  $[\text{Mn}_{12}\text{O}_{12}(\text{O}_2\text{CR})_{16}(\text{H}_2\text{O})_4]$  derivatives, together with  $\text{pK}_a$  values of the conjugate acid of the carboxylate ligand.

$[\text{Mn}_{12}]$ derivative	$\text{pK}_a^{34-37}$
$[\text{Mn}_{12}\text{O}_{12}(\text{O}_2\text{CEt})_{16}(\text{H}_2\text{O})_3]$	4.87
$[\text{Mn}_{12}\text{O}_{12}(\text{O}_2\text{CPh})_{16}(\text{H}_2\text{O})_4]$	4.20
$[\text{Mn}_{12}\text{O}_{12}(\text{O}_2\text{CCH}_2\text{Cl})_{16}(\text{H}_2\text{O})_4]$	2.86
$[\text{Mn}_{12}\text{O}_{12}(\text{O}_2\text{CCHCl}_2)_{16}(\text{H}_2\text{O})_4]$	1.29
$[\text{Mn}_{12}\text{O}_{12}(\text{O}_2\text{CCH}_2\text{Bu}^t)_{16}(\text{H}_2\text{O})_4]$	5.00
$[\text{Mn}_{12}\text{O}_{12}(\text{O}_2\text{C}^i\text{Pr})_{16}(\text{H}_2\text{O})_4]$	5.03
$[\text{Mn}_{12}\text{O}_{12}(\text{O}_2\text{CC}_6\text{F}_5)_{16}(\text{H}_2\text{O})_4]$	1.48
$[\text{Mn}_{12}\text{O}_{12}(\text{O}_2\text{CCH}_2\text{Br})_{16}(\text{H}_2\text{O})_4]$	2.90
$[\text{Mn}_{12}\text{O}_{12}(\text{O}_2\text{CC}_6\text{H}_4\text{-}i\text{p}^o\text{-OMe})_{16}(\text{H}_2\text{O})_4]$	4.47
$[\text{Mn}_{12}\text{O}_{12}(\text{O}_2\text{CC}_6\text{H}_4\text{-}i\text{p}^o\text{-F})_{16}(\text{H}_2\text{O})_4]$	4.14
$[\text{Mn}_{12}\text{O}_{12}(\text{O}_2\text{CC}_6\text{H}_4\text{-}o\text{-(NO}_2)_2)_{16}(\text{H}_2\text{O})_4]$	2.22
$[\text{Mn}_{12}\text{O}_{12}(\text{O}_2\text{CC}_6\text{H}_4\text{-}i\text{p}^o\text{-(NO}_2)_2)_{16}(\text{H}_2\text{O})_4]$	3.44
$[\text{Mn}_{12}\text{O}_{12}(\text{O}_2\text{CC}_6\text{H}_3\text{-}o\text{-}i\text{p}^o\text{-(NO}_2)_2)_{16}(\text{H}_2\text{O})_4]$	1.42

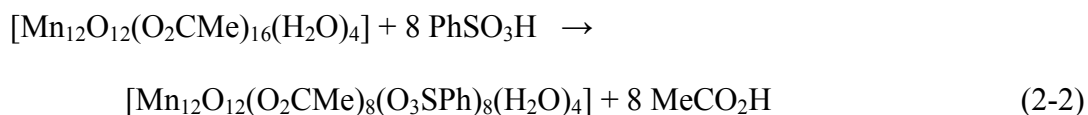
The ligand substitution reaction (eq 2-1) is an equilibrium that must be driven to completion by (i) using a carboxylic acid with a much lower  $\text{pK}_a$  than that of acetic acid (4.76); and/or (ii) using an excess of  $\text{RCO}_2\text{H}$ ; and/or (iii) removing the acetic acid as its toluene azeotrope.



The latter is particularly useful for incorporating carboxylate groups whose conjugate acid has a  $\text{pK}_a$  comparable to, or even higher than that of acetic acid. The substitution reaction has been successfully employed for ligands such as benzoate (and substituted benzoates), and a variety of alkanecarboxylates.<sup>13,38</sup> Of relevance to the present work is

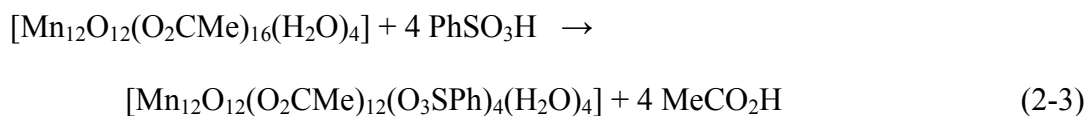
the fact that the substitution procedure has already been extended to non-carboxylate ligands in the successful incorporation of  $\text{Ph}_2\text{PO}_2^-$  groups,<sup>33</sup> as mentioned above.

Thus, the reactions of **1** with another type of organic acid were explored, namely benzenesulfonic acid ( $\text{pK}_a = 2.55$ ). The reaction of complex **1** with eight equivalents of benzenesulfonic acid ( $\text{PhSO}_3\text{H}$ ) in MeCN was followed by several cycles of addition of toluene and its removal under vacuum. Note that since only partial replacement of acetate groups was being sought, excess acid could not be added, and the removal of acetic acid as the toluene azeotrope thus was an essential step to ensure complete reaction. This procedure successfully led to the crystallization and isolation of  $[\text{Mn}_{12}\text{O}_{12}(\text{O}_2\text{CMe})_8(\text{O}_3\text{SPh})_8(\text{H}_2\text{O})_4]$  (**2**) in essentially quantitative (96%) yield (eq 2-2). Recrystallization from  $\text{CH}_2\text{Cl}_2/\text{hexanes}$  gave dark brown crystals of **2**·4 $\text{CH}_2\text{Cl}_2$  suitable for X-ray crystallography.



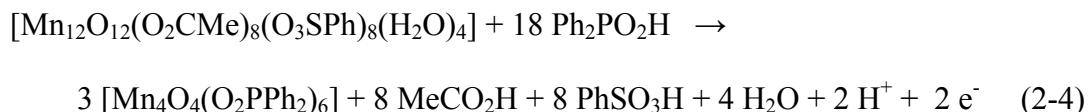
Similarly, the reaction of **1** with four equivalents of  $\text{PhSO}_3\text{H}$  (eq 2-3) led to the formation of  $[\text{Mn}_{12}\text{O}_{12}(\text{O}_2\text{CMe})_{12}(\text{O}_3\text{SPh})_4(\text{H}_2\text{O})_4]$  (**3**), whose identity was established by elemental analysis and spectroscopic comparison with **2**. Reactions of  $\text{PhSO}_3\text{H}$  with other Mn carboxylate complexes, including  $[\text{Mn}_3\text{O}(\text{O}_2\text{CR})_6(\text{py})_3]^{0,+}$  and  $[\text{Mn}_4\text{O}_2(\text{O}_2\text{CPh})_9(\text{H}_2\text{O})]^-$ , have also been carried out, but attempts to crystallographically characterize the products have all been unsuccessful to date. The carboxylate substitution with benzenesulfonate is reversible on treatment of **2** with eight equivalents of  $\text{MeCO}_2\text{H}$  in  $\text{CH}_2\text{Cl}_2$ , supporting the feasibility of using **2** for reactions directed at site-specific

replacement of axial  $\text{PhSO}_3^-$  ligands by some added reagent, taking advantage of the good leaving properties of this group.



Reactions of complex **1** with various non-carboxylic acids, including  $\text{HNO}_3$ ,  $\text{Ph}_2\text{PO}_2\text{H}$  and  $\text{PhSO}_3\text{H}$  have resulted in the partially-substituted  $\text{Mn}_{12}$  complexes,  $[\text{Mn}_{12}\text{O}_{12}(\text{O}_2\text{CCH}_2\text{Bu}^t)_{12}(\text{NO}_3)_4(\text{H}_2\text{O})_4]$ ,<sup>32</sup>  $[\text{Mn}_{12}\text{O}_{12}(\text{O}_2\text{CMe})_8(\text{O}_2\text{PPh}_2)_8(\text{H}_2\text{O})_4]$  (**4**),<sup>33</sup>  $[\text{Mn}_{12}\text{O}_{12}(\text{O}_2\text{CMe})_8(\text{O}_3\text{SPh})_8(\text{H}_2\text{O})_4]$  (**2**) and  $[\text{Mn}_{12}\text{O}_{12}(\text{O}_2\text{CMe})_{12}(\text{O}_3\text{SPh})_4(\text{H}_2\text{O})_4]$  (**3**)<sup>39</sup> as discussed. Despite many attempts, however, reactions aimed at the isolation of a  $\text{Mn}_{12}$  complex with ligation by only non-carboxylate ligands have been ineffective. This is likely due to a combination of effects, including steric hindrance of  $\text{Ph}_2\text{PO}_2^-$  ligands about the  $\text{Mn}_{12}$  cluster and poor solubility of the  $\text{PhSO}_3^-$  ligand in various solvents. Hence, the reaction of **2** with  $\text{Ph}_2\text{PO}_2\text{H}$  was of particular interest; a mixed non-carboxylate ligand strategy might be effective route to obtain a  $\text{Mn}_{12}$  cluster with ligation by at least more than eight non-carboxylate ligands, if not by sixteen such ligands. Thus, complex **2** in MeCN was treated with eight equivalents of  $\text{Ph}_2\text{PO}_2\text{H}$ . Acetic acid was removed from the reaction system by multiple cycles of addition and removal of toluene. After 12 hours, the resulting deep brown solution was separated by filtration from some white powder. The filtrate was evaporated to dryness and crystallization from  $\text{CH}_2\text{Cl}_2$ /toluene gave dark brown crystals of  $[\text{Mn}_4\text{O}_4(\text{O}_2\text{PPh}_2)_6]$  (**5**) in ~50% yield. Accompanying the dark brown crystalline product was some white powder which was subsequently identified by spectroscopic methods as a mixture of the excess ligands, diphenylphosphinic acid and benzenesulfonic acid. The overall transformation of **2** into **5** is summarized in eq 2-4. The

average oxidation state of the starting material is +3.33 while that of the product (**5**) is +3.5. Thus, the formation of complex **5** appears to involve the oxidation of **2** followed by structural rearrangement.



## 2.2.2 Description of Structures

### 2.2.2.1 X-ray crystal structure of $[\text{Mn}_{12}\text{O}_{12}(\text{O}_2\text{CMe})_8(\text{O}_3\text{SPh})_8(\text{H}_2\text{O})_4]$ (**2**)

A labeled ORTEP<sup>40</sup> plot in PovRay format of complex **2** is shown in Figure 2-1, together with a stereoview. The crystallographic data and structure refinement details are collected in Table 2-2, and selected interatomic distances and angles are listed in Table A-1. Complex **2**·4CH<sub>2</sub>Cl<sub>2</sub> crystallizes in the triclinic space group  $P\bar{1}$  with the asymmetric unit consisting of one Mn<sub>12</sub> molecule and four CH<sub>2</sub>Cl<sub>2</sub> molecules of crystallization. The Mn<sub>12</sub> cluster possesses an overall structure similar to that of **1**, with a central [Mn<sup>IV</sup><sub>4</sub>O<sub>4</sub>] cubane held within a non-planar ring of eight Mn<sup>III</sup> ions by eight μ<sub>3</sub>-O<sup>2-</sup> ions (Figure 2-1).

The oxidation levels of the Mn ions were assigned quantitatively on the basis of bond valence sum calculations,<sup>41</sup> indicating a mixed-valence, trapped-valence Mn<sup>III</sup><sub>8</sub>Mn<sup>IV</sup><sub>4</sub> complex (Table 2-3 and 2-4). A bond valence sum (BVS) is an empirical value based on crystallographically determined metal-ligand distances that is routinely used to determine the oxidation level of an atom in a molecule. The valence of the *i*th atom,  $V_i$ , can be defined in terms of the sum of the individual bond valences,  $s_{ij}$ , of the atom *i* with those atoms, *j*, in its coordination sphere (eq 2-5).<sup>42</sup>

$$V_i = \sum_j s_{ij} = \sum_j e^{[(R_0 - R_{ij})/b]} \quad (2-5)$$

The valences of the individual bonds,  $s_{ij}$ , can be calculated from the observed bond length in the crystal structure of a molecule using eq 2-5, where  $R_{ij}$  is the observed bond length,  $R_0$  is the length expected for a bond of unit valence and  $b$  is an experimentally determined constant equal to 0.37. Values of  $R_0$  for Mn-O bonds for  $Mn^{n+}$  ( $n = 2, 3, 4,$  and  $7$ ) are available,<sup>43</sup> allowing the application of this calculation to determine the oxidation states of the Mn centers in our clusters. The calculations can also be extended to include inorganic oxygen atoms and are a useful means of assessing the protonation levels of such atoms in a complex. In addition to transition metal clusters, bond valence sum analysis has been used to determine the oxidation states of metal centers in metalloenzymes<sup>44</sup> and superconductors.<sup>45</sup>

Table 2-2. Crystallographic data for  $[Mn_{12}O_{12}(O_2CMe)_8(O_3SPh)_8(H_2O)_4] \cdot 4CH_2Cl_2$ .

Parameter	$2 \cdot 4CH_2Cl_2$
formula <sup>a</sup>	$C_{68}H_{80}S_8Cl_8Mn_{12}O_{56}$
fw, $g\ mol^{-1}$	2992.76
space group	$P\bar{1}$
a, Å	15.9971(6)
b, Å	16.0923(7)
c, Å	22.0964(9)
$\alpha$ , deg	94.742(2)
$\beta$ , deg	90.307(2)
$\gamma$ , deg	104.262(2)
$V$ , Å <sup>3</sup>	5492.1(4)
$Z$	2
$T$ , °C	-80(2)
radiation, Å <sup>b</sup>	0.71073
$\rho_{calc}$ , $g\ cm^{-3}$	1.810
$\mu$ , $cm^{-1}$	17.69
$R1$ ( $wR2$ ), % <sup>c,d</sup>	3.79 (9.90)

<sup>a</sup> Including solvent molecules. <sup>b</sup> Graphite monochromator. <sup>c</sup>  $R1 = \Sigma||F_o| - |F_c|| / \Sigma|F_o|$ . <sup>d</sup>  $wR2 = [\Sigma[w(F_o^2 - F_c^2)^2] / \Sigma[wF_o^2]^2]^{1/2}$  where  $S = [\Sigma[w(F_o^2 - F_c^2)^2] / (n-p)]^{1/2}$ ,  $w = 1/[\sigma^2(F_o^2) + (mp)^2 + np]$ ,  $p = [\max(F_o^2, 0) + 2F_c^2]/3$ , and  $m$  and  $n$  are constants.

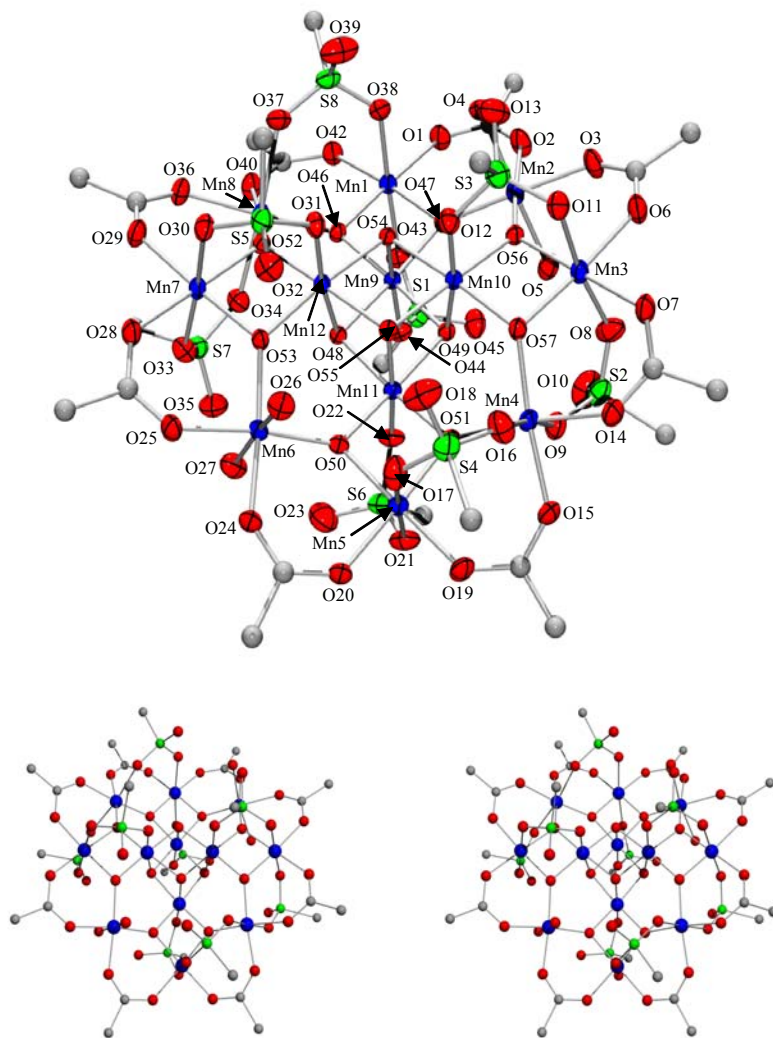


Figure 2-1. ORTEP representation in PovRay format of  $[\text{Mn}_{12}\text{O}_{12}(\text{O}_2\text{CMe})_8(\text{O}_3\text{SPh})_8(\text{H}_2\text{O})_4]$  (**2**) with thermal ellipsoids at the 50% probability level except for the C atoms, together with a stereopair. For clarity, only the *ipso* C atoms of the benzenesulfonate groups are shown. Mn blue; O red; S green; C gray.

The eight  $\text{Mn}^{\text{III}}$  ions separate into two groups of four  $\text{Mn}^{\text{III}}$  ions each. In the first group, each  $\text{Mn}^{\text{III}}$  ion is coordinated to a single  $\text{Mn}^{\text{IV}}$  ion via two oxide bridges [Mn(1), Mn(3), Mn(5), Mn(7)], while in the second group each  $\text{Mn}^{\text{III}}$  ion is coordinated to two  $\text{Mn}^{\text{IV}}$  ions via two oxide bridges [Mn(2), Mn(4), Mn(6), Mn(8)].<sup>29</sup> Four water molecules, eight  $\mu$ -carboxylate and eight  $\mu$ -benzenesulfonate groups complete the peripheral ligation about the  $[\text{Mn}_{12}\text{O}_{12}]$  core of the complex. The eight  $\text{Mn}^{\text{III}}$  centers exhibit a Jahn-Teller

(JT) distortion, as expected for a high-spin  $d^4$  ion in near-octahedral geometry (Figure 2-2). As is almost always the case for  $Mn^{III}$ , the JT distortion in **2** takes the form of an axial elongation of two *trans* bonds. Again as is usually the case, the JT elongation axes avoid the  $Mn-O^{2-}$  bonds, the shortest and strongest in the molecule, and thus the JT axes are all axially disposed, roughly perpendicular to the  $[Mn_{12}O_{12}]$  disk-like core. As a result, there is a near parallel alignment of the eight  $Mn^{III}$  JT elongation axes. This is also the origin of the significant magnetic anisotropy in the  $z$  direction that greatly influences the observed magnetic properties (*vide infra*).

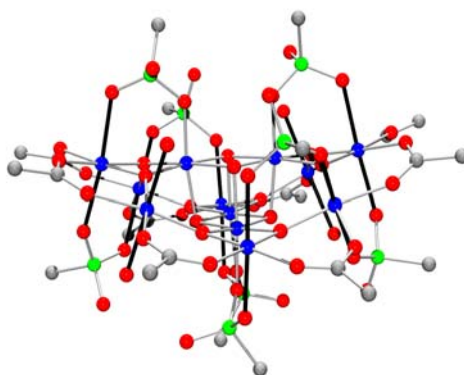


Figure 2-2. ORTEP representation in PovRay format of  $[Mn_{12}O_{12}(O_2CMe)_8(O_3SPh)_8(H_2O)_4]$  (**2**) showing the relative disposition of the Jahn-Teller elongation axes indicated as solid black bonds. For clarity, only the *ipso* C atoms of the benzenesulfonate groups are shown. Mn blue; O red; S green; C gray.

The  $MeCO_2^-$  groups occupy the eight equatorial sites of **2**, while the  $PhSO_3^-$  ligands are located at the eight axial sites above and below the disk-like  $[Mn_{12}O_{12}]$  core. This selectivity in axial vs equatorial binding sites can be rationalized on the basis of the relative basicities of acetate vs benzenesulfonate. The  $pK_a$  value of  $PhSO_3H$  is 2.55 while that of  $MeCO_2H$  is 4.76.<sup>37</sup> The more basic, stronger donor  $MeCO_2^-$  ligands favor occupation of the equatorial sites where shorter, stronger Mn-O bonds can be formed, to the benefit of the overall energy stabilization of the molecule.<sup>46</sup> The less basic  $PhSO_3^-$

ligands thus occupy axial positions where they bridge either Mn<sup>III</sup>Mn<sup>III</sup> or Mn<sup>III</sup>Mn<sup>IV</sup> pairs and thus have one or both of their O atoms on the JT elongation axes. There are twenty axial coordination sites, of which sixteen lie on JT elongation axes, and these bonds are thus lengthened by 0.1-0.2 Å, and thus weakened relative to the equatorial, non- JT elongated Mn-carboxylate bonds. The same rationalization based on relative acid pK<sub>a</sub> values also explained the selective axial vs equatorial disposition in mixed-carboxylate [Mn<sub>12</sub>O<sub>12</sub>(O<sub>2</sub>CR)<sub>8</sub>(O<sub>2</sub>CR')<sub>8</sub>(H<sub>2</sub>O)<sub>4</sub>] complexes.<sup>46</sup>

Table 2-3. Bond valence sum calculations<sup>a</sup> for complex 2·4CH<sub>2</sub>Cl<sub>2</sub>.

Atom	Mn <sup>2+</sup>	Mn <sup>3+</sup>	Mn <sup>4+</sup>
Mn(1)	3.293	<u>3.012</u>	3.162
Mn(2)	3.167	<u>2.897</u>	3.041
Mn(3)	3.232	<u>2.957</u>	3.104
Mn(4)	3.284	<u>3.004</u>	3.154
Mn(5)	3.270	<u>2.991</u>	3.140
Mn(6)	3.191	<u>2.918</u>	3.064
Mn(7)	3.289	<u>3.008</u>	3.158
Mn(8)	3.277	<u>2.997</u>	3.146
Mn(9)	4.261	3.898	<u>4.092</u>
Mn(10)	4.198	3.840	<u>4.032</u>
Mn(11)	4.253	3.890	<u>4.084</u>
Mn(12)	4.169	3.813	<u>4.003</u>

<sup>a</sup> The underlined value is the one closest to the actual charge for which it was calculated. The oxidation state of a particular atom can be taken as the nearest whole number to the underlined value.

Table 2-4. Bond valence sum calculations<sup>a</sup> for selected oxygen atoms in complex 2·4CH<sub>2</sub>Cl<sub>2</sub>.

Atom	V <sub>i</sub>	Assignment	Atom	V <sub>i</sub>	Assignment
O(46)	2.189	O <sup>2-</sup>	O(54)	2.071	O <sup>2-</sup>
O(47)	2.092	O <sup>2-</sup>	O(55)	2.052	O <sup>2-</sup>
O(48)	2.082	O <sup>2-</sup>	O(56)	2.101	O <sup>2-</sup>
O(49)	2.079	O <sup>2-</sup>	O(57)	2.089	O <sup>2-</sup>
O(50)	2.123	O <sup>2-</sup>	O(4)	0.286	H <sub>2</sub> O
O(51)	2.209	O <sup>2-</sup>	O(5)	0.290	H <sub>2</sub> O
O(52)	2.100	O <sup>2-</sup>	O(26)	0.287	H <sub>2</sub> O
O(53)	2.077	O <sup>2-</sup>	O(27)	0.285	H <sub>2</sub> O

<sup>a</sup> The oxygen atoms is O<sup>2-</sup> if V<sub>i</sub> ≈ 2, OH<sup>-</sup> if V<sub>i</sub> ≈ 1, and H<sub>2</sub>O if V<sub>i</sub> ≈ 0.

In all  $[\text{Mn}_{12}\text{O}_{12}(\text{O}_2\text{CR})_{16}(\text{H}_2\text{O})_4]$  complexes studied to date, the four water ligands coordinate only to the four  $\text{Mn}^{\text{III}}$  ions in the second group described above  $[\text{Mn}(2)$ ,  $\text{Mn}(4)$ ,  $\text{Mn}(6)$ ,  $\text{Mn}(8)]$ ,<sup>20</sup> either one water on each Mn, two each on two Mn, or similar. Indeed, complex **2** similarly has two water ligands, O(4) and O(5), on a  $\text{Mn}^{\text{III}}$  ion of the second group  $[\text{Mn}(2)]$ , and two water ligands, O(26) and O(27), on another  $\text{Mn}^{\text{III}}$  ion of the same group  $[\text{Mn}(6)]$ . This *trans* disposition two pairs of  $\text{H}_2\text{O}$  ligands has also been observed for  $[\text{Mn}_{12}\text{O}_{12}(\text{O}_2\text{CPh})_{16}(\text{H}_2\text{O})_4]$ ,  $[\text{Mn}_{12}\text{O}_{12}(\text{O}_2\text{CC}_6\text{H}_4\text{-}p\text{-Cl})_{16}(\text{H}_2\text{O})_4]$  and others.<sup>20,29</sup>

The formation of complex **3** from **1** represents an abstraction of only four carboxylate groups from a  $[\text{Mn}_{12}\text{O}_{12}(\text{O}_2\text{CR})_{16}(\text{H}_2\text{O})_4]$  complex. This has been previously achieved exclusively at the axial ligands bridging the  $\text{Mn}^{\text{III}}\text{Mn}^{\text{III}}$  pairs, where the four bridging carboxylates are the only ones to have both their O atoms on JT elongation sites and thus are the most susceptible to substitution. Both  $[\text{Mn}_{12}\text{O}_{12}(\text{O}_2\text{CR})_{12}(\text{NO}_3)_4(\text{H}_2\text{O})_4]$  ( $\text{R} = \text{CH}_2\text{Bu}'$  and  $\text{Ph}$ )<sup>32</sup> and, subsequently,  $[\text{Mn}_{12}\text{O}_{12}(\text{O}_2\text{CPh})_{12}(\text{O}_2\text{P}(\text{OPh})_2)_4(\text{H}_2\text{O})_4]$ <sup>47</sup> have been crystallographically confirmed to have their non-carboxylate bridging groups at these positions. Thus, although we have not sought the crystal structure of complex **3**, it is very likely that it has the four  $\text{PhSO}_3^-$  groups in axial positions bridging the same  $\text{Mn}^{\text{III}}\text{Mn}^{\text{III}}$  pairs as the  $\text{NO}_3^-$  and  $(\text{PhO})_2\text{PO}_2^-$  derivatives.

Comparison of **2** with the related clusters

$[\text{Mn}_{12}\text{O}_{12}(\text{O}_2\text{CMe})_{16}(\text{H}_2\text{O})_4] \cdot 2\text{MeCO}_2\text{H} \cdot 4\text{H}_2\text{O}$  (**1**) and  $[\text{Mn}_{12}\text{O}_{12}(\text{O}_2\text{CMe})_8(\text{O}_2\text{PPh}_2)_8(\text{H}_2\text{O})_4]$  (**4**) reveals that there is no significant distortion of the  $[\text{Mn}_{12}\text{O}_{12}]^{16+}$  core upon coordination of the non-carboxylate benzenesulfonate groups (Table 2-5). The apparent lack of distortion is in contrast to that seen within the core of **4**

in which the  $\text{Mn}^{\text{III}}\cdots\text{O}^{2-}\cdots\text{Mn}^{\text{III}}$  bond angles differ significantly and the  $\text{Mn}^{\text{III}}\cdots\text{Mn}^{\text{III}}$  bond distances are on average 0.1 Å longer than the corresponding values of **1**. Additional differences are reflected in the linearity of the  $\text{Mn}_4$  units that span the core of the cluster, with **1** and **2** having angles of the type  $\text{Mn}^{\text{III}}\cdots\text{Mn}^{\text{IV}}\cdots\text{Mn}^{\text{IV}}$  equal to almost  $180^\circ$  while the corresponding angle in **4** is only  $\sim 171^\circ$ .<sup>33</sup> The similarity of complexes **1** and **2**, and the difference between them and **4** are likely reflective of the distribution of ligands around the cluster. In **4**, the acetate groups at the four axial  $\text{Mn}^{\text{III}}\text{Mn}^{\text{III}}$  and four of the equatorial  $\text{Mn}^{\text{III}}\text{Mn}^{\text{III}}$  carboxylate sites have been replaced by relatively bulky diphenylphosphinate groups, giving rise to a distortion of the core of the complex from steric effects.

#### 2.2.2.2 X-ray crystal structure of $[\text{Mn}_4\text{O}_4(\text{O}_2\text{PPh}_2)_6]$ (**5**)

A labeled ORTEP<sup>40</sup> plot in PovRay format of complex **5** is shown in Figure 2-3, together with a stereoview. The crystallographic data and structure refinement details are collected in Table 2-6, and selected interatomic distances and angles are listed in Table A-2. Complex **5** crystallizes in the cubic space group  $P2_13$  with four crystallographically independent molecules in the unit cell, each slightly different with respect to the orientation of the phenyl groups of the diphenylphosphinate ligands.<sup>48</sup> The bond distances and angles of the four molecules also vary within a small range. For the sake of brevity, references to specific atoms in the following discussion implicitly include their symmetry-related partners.

Table 2-5. Comparison of selected bond distances (Å) and angles (°) for [Mn<sub>12</sub>O<sub>12</sub>(O<sub>2</sub>CMe)<sub>16</sub>(H<sub>2</sub>O)<sub>4</sub>] $\cdot$ 2MeCO<sub>2</sub>H $\cdot$ 4H<sub>2</sub>O (**1**), [Mn<sub>12</sub>O<sub>12</sub>(O<sub>2</sub>CMe)<sub>8</sub>(O<sub>3</sub>SPh)<sub>8</sub>(H<sub>2</sub>O)<sub>4</sub>] (**2**) and [Mn<sub>12</sub>O<sub>12</sub>(O<sub>2</sub>CMe)<sub>8</sub>(O<sub>2</sub>PPh<sub>2</sub>)<sub>8</sub>(H<sub>2</sub>O)<sub>4</sub>] (**4**).

Parameter <sup>a</sup>	<b>1</b>	<b>2</b>	<b>4</b>
Mn <sup>IV</sup> – O <sub>c</sub> (ax)	1.8954(13)	1.863(2) – 1.876(2)	1.894(2)
Mn <sup>IV</sup> – O <sub>c</sub> (eq)	1.9116(11), 1.9196(10)	1.9157(19) – 1.9393(19)	1.905(2), 1.960(2)
Mn <sup>IV</sup> – O <sub>r</sub>	1.8592(11), 1.8795(11)	1.854(2) – 1.874(2)	1.855(2), 1.862(2)
Mn <sup>IV</sup> – O <sub>ax</sub>	1.9131(13)	1.907(2) – 1.945(2)	1.915(3)
Mn <sup>IIIb</sup> – O <sub>r</sub>	1.8770(11), 1.8983(11)	1.883(2) – 1.909(2)	1.890(2), 1.932(2)
Mn <sup>IIIc</sup> – O <sub>r</sub>	1.8860(11), 1.8964(11)	1.880(2) – 1.910(2)	1.873(2), 1.992(3)
Mn <sup>IIIb</sup> – O <sub>eq</sub>	1.9371(13), 1.9393(12)	1.920(2) – 1.942(2)	1.935(3), 1.963(3)
Mn <sup>IIIc</sup> – O <sub>eq</sub>	1.9655(12), 1.9884(13)	1.929(2) – 1.962(2)	1.910(3), 1.998(3)
Mn <sup>IIIb</sup> – O <sub>ax</sub>	2.111(5) <sup>*</sup> , 2.228(3), 2.2318(13)	2.163(2) – 2.261(2)	2.167(3), 2.195(3)
Mn <sup>IIIc</sup> – O <sub>ax</sub>	2.117(11), 2.151(17) <sup>*</sup>	2.174(2) – 2.190(2)	2.066(3)
Mn <sup>IIIc</sup> – O <sub>w</sub>	2.1735(15)	2.216(2) – 2.222(2)	2.208(3)
Mn <sup>IIIb</sup> ...Mn <sup>IIIc</sup>	3.321, 3.414	3.352 – 3.454	3.410, 3.547
Mn <sup>IV</sup> ...Mn <sup>IV</sup>	2.8166(4), 2.8166(4), 2.9271(4)	2.8054(6) – 2.9478(6)	2.8492(9), 2.9461(10)
Mn <sup>IIIb</sup> ...Mn <sup>IV</sup>	2.7643(3)	2.7905(6) – 2.8016(6)	2.7726(8)
Mn <sup>IIIc</sup> ...Mn <sup>IV</sup>	3.445, 3.448	3.416 – 3.466	3.420, 3.452
O <sub>r</sub> – Mn <sup>IV</sup> – O <sub>r</sub>	84.96(5)	83.27(9) – 84.13(9)	84.90(11)
O <sub>r</sub> – Mn <sup>IIIb</sup> – O <sub>r</sub>	83.95(5)	81.70(9) – 82.74(8)	82.06(10)
O <sub>r</sub> – Mn <sup>IIIc</sup> – O <sub>r</sub>	93.29(5)	94.83(8) – 95.52(9)	95.78(10)
Mn <sup>IIIb</sup> ...Mn <sup>IV</sup> ...Mn <sup>IV</sup>	178.380(14)	175.99(2) – 178.21(2)	171.45(2)

<sup>a</sup> O<sub>c</sub> = cubane O<sup>2-</sup>, O<sub>r</sub> = ring O<sup>2-</sup>, O<sub>ax</sub> = axial carboxylate, O<sub>eq</sub> = equatorial carboxylate, O<sub>w</sub> = water; <sup>b</sup> Mn<sup>IIIb</sup> atoms: Mn(2) in **1**, Mn(1, 3, 5 and 7) in **2**, and Mn(3) in **4**; <sup>c</sup> Mn<sup>IIIc</sup> atoms: Mn(3) in **1**, Mn(2, 4, 6 and 8) in **2**, and Mn(2) in **4**. <sup>\*</sup> Involves the disordered acetate ligand bridging Mn(2) and Mn(3).

The cluster consists of a cubane  $[\text{Mn}_4\text{O}_4]^{6+}$  core in which there is one unique  $[\text{Mn}(2)]$  and three symmetry-related Mn ions  $[\text{Mn}(1)]$  (Figure 2-3). Six diphenylphosphinate ligands that bridge Mn pairs across each of the six  $[\text{Mn}_2\text{O}_2]$  faces complete the coordination sphere of the complex. The unit cell contains sixteen  $\text{Mn}_4$  molecules; eight are located on the cell corners ( $8 \times \frac{1}{8}$ ), twelve are located on cell edges ( $12 \times \frac{1}{4}$ ), six are located on the cell faces ( $6 \times \frac{1}{2}$ ) and seven complete molecules are situated within the cell dimensions. The  $\text{Mn}_4$  molecules in the cubic  $P2_13$  lattice are stacked in columns, with all of the molecules approximately oriented in the same way with respect to the cell axes. There is no evidence of any interaction between molecules in the same column or in different columns (Figure 2-4).

Table 2-6. Crystallographic data for  $[\text{Mn}_4\text{O}_4(\text{O}_2\text{PPh}_2)_6]$  (**5**).

Parameter	<b>5</b>
formula <sup>a</sup>	$\text{C}_{72}\text{H}_{60}\text{P}_6\text{Mn}_4\text{O}_{16}$
fw, $\text{g mol}^{-1}$	1586.83
space group	$P2_13$
a, Å	29.9772(10)
b, Å	29.9772(10)
c, Å	29.9772(10)
$\alpha$ , deg	90
$\beta$ , deg	90
$\gamma$ , deg	90
$V$ , Å <sup>3</sup>	26938.5(16)
Z	16
T, °C	-123(2)
radiation, Å <sup>b</sup>	0.71073
$\rho_{\text{calc}}$ , $\text{g cm}^{-3}$	1.565
$\mu$ , $\text{cm}^{-1}$	9.46
R1 (wR2), % <sup>c,d</sup>	11.20 (20.58)

<sup>a</sup> Including solvent molecules. <sup>b</sup> Graphite monochromator. <sup>c</sup>  $R1 = \Sigma||F_o| - |F_c|| / \Sigma|F_o|$ . <sup>d</sup>  $wR2 = [\Sigma[w(F_o^2 - F_c^2)^2] / \Sigma[wF_o^2]^2]^{1/2}$  where  $S = [\Sigma[w(F_o^2 - F_c^2)^2] / (n-p)]^{1/2}$ ,  $w = 1/[\sigma^2(F_o^2) + (mp)^2 + np]$ ,  $p = [\max(F_o^2, 0) + 2F_c^2]/3$ , and  $m$  and  $n$  are constants.

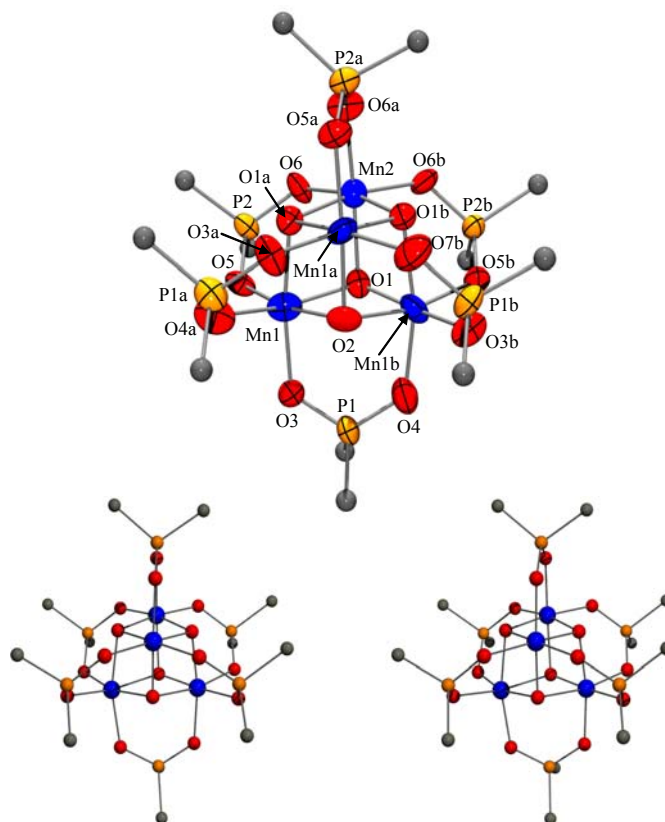


Figure 2-3. ORTEP representation in PovRay format of  $[\text{Mn}_4\text{O}_4(\text{O}_2\text{PPh}_2)_6]$  (**5**) with thermal ellipsoids at the 50% probability level, together with a stereopair. For clarity, only the *ipso* C atoms of the diphenylphosphinate groups are shown. Mn blue; O red; P orange; C gray.

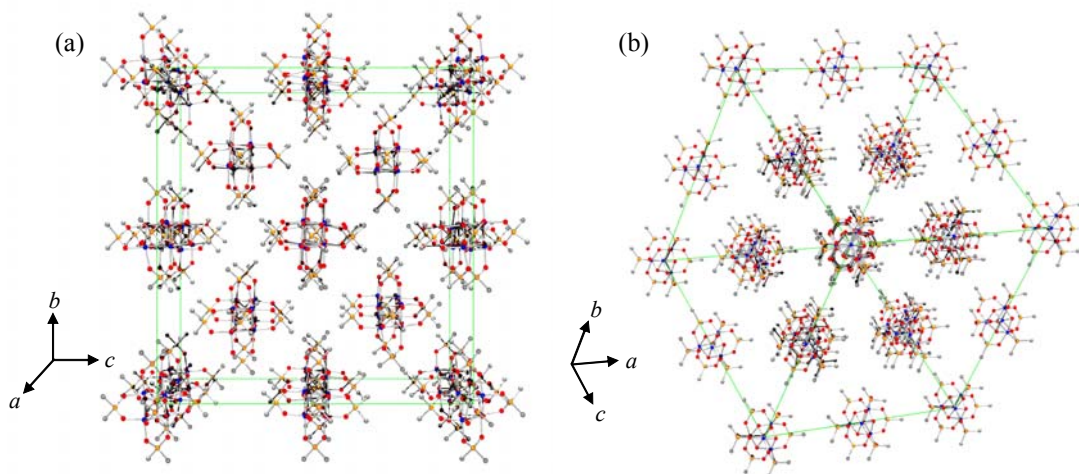


Figure 2-4. ORTEP representation in PovRay format of the packing of complex **5** along (a) one of the faces and (b) a selected  $C_3$  rotation axis of the unit cell. Mn blue; O red; P orange; C gray.

All of the Mn centers are six-coordinate, with near-octahedral geometry. Charge considerations require a mixed-valence  $\text{Mn}^{\text{III}}_2\text{Mn}^{\text{IV}}_2$  system. A bond valence sum<sup>41</sup> analysis to determine the oxidation levels of the Mn centers is not conclusive however. The results of the BVS analyses for the Mn and inorganic O atoms are summarized in Tables 2-7 and 2-8. Similarly, an examination of the bond distances around the Mn centers does not reveal obvious Jahn-Teller (JT) distortion axes on any of the Mn centers as would be expected for a high-spin  $\text{Mn}^{\text{III}}$  ( $d^4$ ) ion in near-octahedral geometry. The absence of such JT elongation axes is in contrast to the related distorted-cubane clusters with  $[\text{Mn}^{\text{III}}_3\text{Mn}^{\text{IV}}(\mu_3\text{-O})_3(\mu_3\text{-X})]^{6+}$  ( $X = \text{Cl}^-, \text{F}^-, \text{Br}^-, \text{N}_3^-, \text{NCO}^-, \text{ or } \text{RCO}_2^-$ ) cores, in which there are clear JT elongation axes of two *trans* bonds on each of the  $\text{Mn}^{\text{III}}$  ions.<sup>12</sup> On average, the JT elongated bond distance in  $[\text{Mn}_{12}\text{O}_{12}(\text{O}_2\text{CMe})_{16}(\text{H}_2\text{O})_4] \cdot 2\text{MeCO}_2\text{H} \cdot 4\text{H}_2\text{O}$  (**1**) and a representative distorted-cubane complex  $[\text{Mn}_4\text{O}_3\text{Cl}_4(\text{O}_2\text{CMe})_3(\text{py})_3]$ , is 2.188 Å and 2.146 Å, respectively, approximately 0.1-0.2 Å longer than similar non-JT elongated bond distances.<sup>49,50</sup> The Mn-O bond distances in **5** are in the range of 1.841(6) – 2.051(7) Å; distinguishable JT elongation or compression axes are not obvious on this basis. Symmetry considerations require that three Mn ions are crystallographically identical with equivalent bond distances and angles, making  $\text{Mn}^{\text{III}}$  ions indistinguishable from  $\text{Mn}^{\text{IV}}$  ions. An electronically delocalized system or a static disorder of trapped-valence  $\text{Mn}^{\text{III}}$  and  $\text{Mn}^{\text{IV}}$  sites can account for this behavior.

Comparison of the Mn···Mn separations across the faces of the cube with related Mn complexes having cubane cores indicates that the distances in **5** most closely resemble those in the central  $[\text{Mn}_4(\mu_3\text{-O})_4]^{16+}$  core of members of the  $\text{Mn}_{12}$  family. Averaged over the four independent molecules of the unit cell, the mean Mn···Mn

distance is 2.928 Å. Similar distances are found in Mn<sub>12</sub> complexes while those in the distorted-cubane Mn<sub>4</sub> complexes are slightly shorter. Unlike **5**, the Mn<sub>12</sub> complexes have no carboxylate-bridged Mn<sub>2</sub> pairs in the cubane core. Comparison of the O<sup>2-</sup>...Mn...O<sup>2-</sup> angles in the cores of complexes **1** and **5** reveals additional similarities. The average O<sup>2-</sup>...Mn...O<sup>2-</sup> angle in **1** is 82.7° while the corresponding angle in **5** is 81.7°. A evaluation of the O...O distances of the carboxylate ligands in **1** with the non-carboxylate ligands in **2** and **5** shows that Ph<sub>2</sub>PO<sub>2</sub><sup>-</sup> groups may be preferred for formation of the cubane complex. The average O...O distances for the bridging ligands acetate, benzenesulfonate, and diphenylphosphinate are 2.24, 2.42, and 2.57 Å, respectively.

Table 2-7. Bond valence sum calculations<sup>a</sup> for complex **5**.

Atom	Mn <sup>2+</sup>	Mn <sup>3+</sup>	Mn <sup>4+</sup>
Mn(1)	3.751	3.431	3.602
Mn(2)	3.553	3.249	3.411
Mn(3)	3.489	3.192	3.351
Mn(4)	4.172	3.816	4.006
Mn(5)	3.891	3.559	3.737
Mn(6)	3.274	2.995	3.144
Mn(7)	3.415	3.123	3.279
Mn(8)	3.887	3.556	3.733

<sup>a</sup> The underlined value is the one closest to the actual charge for which it was calculated. The oxidation state of a particular atom can be taken as the nearest whole number to the underlined value.

Table 2-8. Bond valence sum calculations<sup>a</sup> for selected oxygen atoms in complex **5**.

Atom	$V_i$	Assignment
O(1)	2.189	O <sup>2-</sup>
O(2)	2.092	O <sup>2-</sup>
O(48)	2.082	O <sup>2-</sup>
O(49)	2.079	O <sup>2-</sup>
O(50)	2.123	O <sup>2-</sup>
O(51)	2.209	O <sup>2-</sup>
O(52)	2.100	O <sup>2-</sup>
O(53)	2.077	O <sup>2-</sup>

<sup>a</sup> The oxygen atoms is O<sup>2-</sup> if  $V_i \approx 2$ , OH<sup>-</sup> if  $V_i \approx 1$ , and H<sub>2</sub>O if  $V_i \approx 0$ .

## 2.2.3 Magnetochemistry of Complexes 2 and 3

### 2.2.3.1 DC studies

Solid-state, variable-temperature magnetic susceptibility measurements were performed on vacuum-dried, powdered samples of complexes **2**·C<sub>6</sub>H<sub>14</sub> and **3**·0.2C<sub>6</sub>H<sub>14</sub>, suspended in eicosane to prevent torquing. DC magnetic susceptibility ( $\chi_M$ ) data were collected in the 2.00-300 K range in a 5.0 kG magnetic field (Figure 2-5). The  $\chi_M T$  versus  $T$  behavior is similar to those of previously studied [Mn<sub>12</sub>O<sub>12</sub>(O<sub>2</sub>CR)<sub>16</sub>(H<sub>2</sub>O)<sub>4</sub>] complexes with  $S = 10$  ground states, exhibiting a nearly temperature-independent  $\chi_M T$  value of 21-22 cm<sup>3</sup> K mol<sup>-1</sup> (**2**) and 18-19 cm<sup>3</sup> K mol<sup>-1</sup> (**3**) in the 150-300 K range which then increases rapidly to a maximum value of 45-46 cm<sup>3</sup> K mol<sup>-1</sup> (**2**) and 44-45 cm<sup>3</sup> K mol<sup>-1</sup> (**3**) at ~20 K before decreasing rapidly at lower temperatures. The maximum indicates a large ground state spin ( $S$ ) value, and the low temperature decrease is primarily due to Zeeman and zero-field splitting (ZFS) effects.

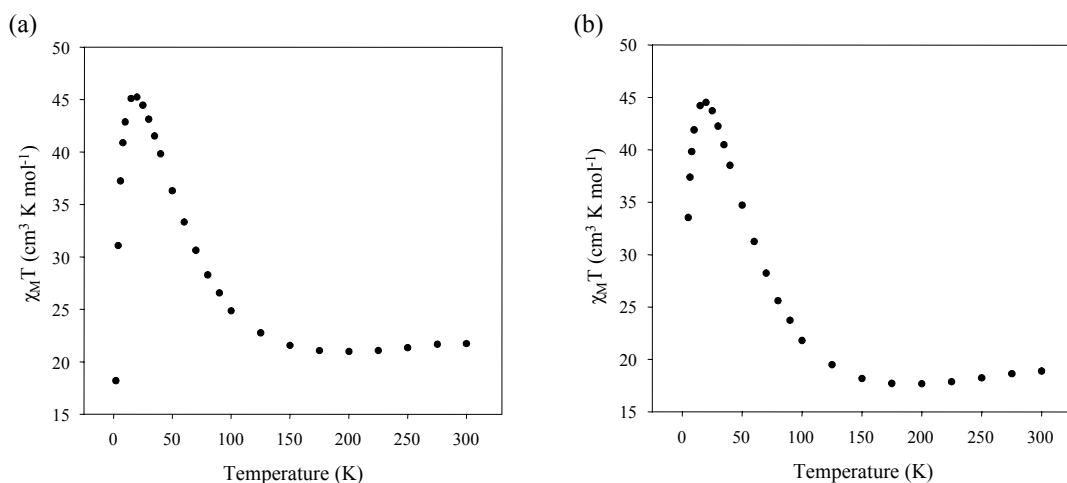


Figure 2-5. Plot of  $\chi_M T$  vs temperature for dried, microcrystalline samples of (a) complex **2**·C<sub>6</sub>H<sub>14</sub> and (b) complex **3**·0.2C<sub>6</sub>H<sub>14</sub> in eicosane.  $\chi_M$  is the DC molar magnetic susceptibility measured in a 5.0 kG field.

A theoretical treatment of the susceptibility data via the Kambe<sup>51</sup> method to determine the individual pairwise Mn<sub>2</sub> exchange interactions was not possible owing to the topological complexity and low symmetry of the Mn<sub>12</sub> core. Instead, the ground state spin of complexes **2** and **3** was determined from magnetization (M) measurements in the 1.80-5.00 K temperature range and 2.0-7.0 T field range, where N is Avogadro's number,  $\mu_B$  is the Bohr magneton, and H is the applied magnetic field. The obtained data are plotted as  $M/N\mu_B$  vs  $H/T$  in Figure 2-6. For a system occupying only the ground state and experiencing no ZFS, the various isofield lines would be superimposed and  $M/N\mu_B$  would saturate at a value of  $gS$ . The non-superposition of the isofield lines Figure 2-6 is indicative of the presence of strong ZFS. The data were fit using the method described elsewhere<sup>49,52</sup> that involves diagonalization of the spin Hamiltonian matrix, assuming only the ground state is occupied at these temperatures and including axial ZFS ( $D\hat{S}_z^2$ ), Zeeman interactions, and a full powder average of the magnetization.<sup>53,54</sup> The obtained fit of the data, shown as solid lines in Figure 2-6, gave  $S = 10$ ,  $g = 1.96$  and  $D \sim -0.34 \text{ cm}^{-1}$  (-0.49 K) for complex **2** and  $S = 10$ ,  $g = 1.78$  and  $D \sim -0.37 \text{ cm}^{-1}$  (-0.53 K) for complex **3**. Thus, complexes **2** and **3** retain the same spin as **1**, with fitting parameters typical for  $[\text{Mn}_{12}\text{O}_{12}(\text{O}_2\text{CR})_{16}(\text{H}_2\text{O})_4]$  clusters. The poorer quality of the fit than is typically found for  $[\text{Mn}_{12}\text{O}_{12}(\text{O}_2\text{CR})_{16}(\text{H}_2\text{O})_4]$  complexes likely results from population of an excited state of each cluster that is lower-lying than normal; thus, the obtained D values must be considered as only a rough approximation.<sup>46</sup> The  $S = 10$  value shows that, as previously seen with the mixed-carboxylate  $[\text{Mn}_{12}\text{O}_{12}(\text{O}_2\text{CR})_8(\text{O}_2\text{CR}')_8(\text{H}_2\text{O})_4]$  clusters, the presence of two types of ligands with distinctly different basicities does not affect the large ground state S value of the Mn<sub>12</sub> complex.<sup>46</sup>

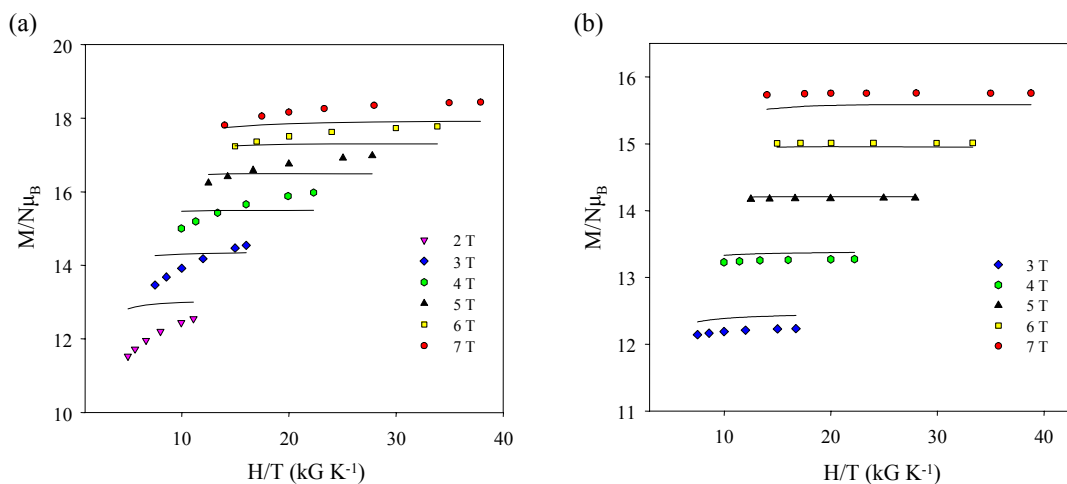


Figure 2-6. Plot of reduced magnetization  $M/N\mu_B$  vs  $H/T$  for dried, microcrystalline samples of (a) complex **2**· $\text{C}_6\text{H}_{14}$  and (b) complex **3**· $0.2\text{C}_6\text{H}_{14}$  in eicosane at the indicated applied fields. The solid lines are the fit of the data; see the text for the fit parameters.

To confirm that the obtained minima were the true global minima and to assess the uncertainty in the obtained  $g$  and  $D$  values, root-mean square  $D$  vs  $g$  error surfaces for the fits were generated with the program GRID,<sup>55</sup> which calculates the relative difference between the experimental  $M/N\mu_B$  data and those calculated for various combinations of  $D$  and  $g$ . This is shown as a contour plot for complexes **2** and **3** in Figure 2-7 for the  $D = -0.10$  to  $-0.70 \text{ cm}^{-1}$  and  $g = 1.7$  to  $2.2$  ranges (**2**) and the  $D = -0.15$  to  $-0.65 \text{ cm}^{-1}$  and  $g = 1.5$  to  $2.05$  ranges (**3**). One very soft fitting minimum for **2** is observed; the contour describes the region of minimum error encompassing  $D \approx -0.24$  to  $-0.49 \text{ cm}^{-1}$  and  $g = 1.70$  to  $2.20$ , giving fitting parameters of  $D = -0.36 \pm 0.12 \text{ cm}^{-1}$  and  $g = 1.95 \pm 0.25$ . Similarly, the region of minimum error for **3** is  $D \approx -0.28$  to  $-0.51 \text{ cm}^{-1}$  and  $g = 1.70$  to  $1.92$ , giving fitting parameters of  $D = -0.39 \pm 0.12 \text{ cm}^{-1}$  and  $g = 1.81 \pm 0.10$ .

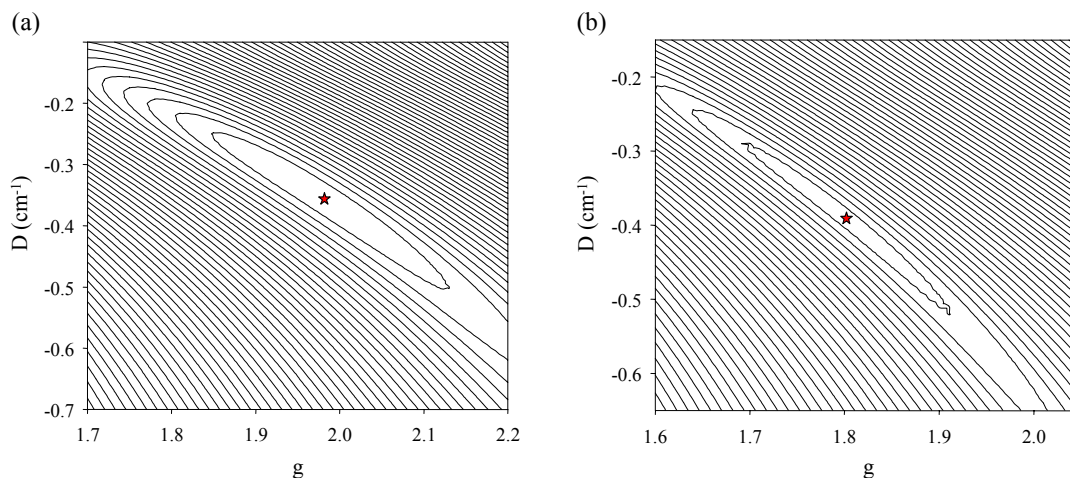


Figure 2-7. Two-dimensional contour plot of the error surface for the  $D$  vs  $g$  fit for (a) complex  $2 \cdot C_6H_{14}$  and (b) complex  $3 \cdot 0.2C_6H_{14}$  in eicosane. The asterisk indicates the the soft minimum.

### 2.2.3.2 AC studies

In an AC susceptibility experiment, a weak field (typically 1 - 5 G) oscillating at a particular frequency ( $\nu$ ) is applied to a sample to probe the dynamics of the magnetization (magnetic moment) relaxation. An out-of-phase AC susceptibility signal ( $\chi_M''$ ) is observed when the rate at which the magnetization of a molecule relaxes is close to the operating frequency of the AC field, and there is a corresponding decrease in the in-phase ( $\chi_M' T$ ) signal. At low enough temperature, where the thermal energy is lower than the barrier for relaxation, the magnetization of the molecule cannot relax fast enough to keep in-phase with the oscillating field. Therefore, the molecule will exhibit a frequency-dependent  $\chi_M''$  signal indicative of slow magnetization relaxation. Frequency-dependent  $\chi_M''$  signals are an important indicator of SMMs.

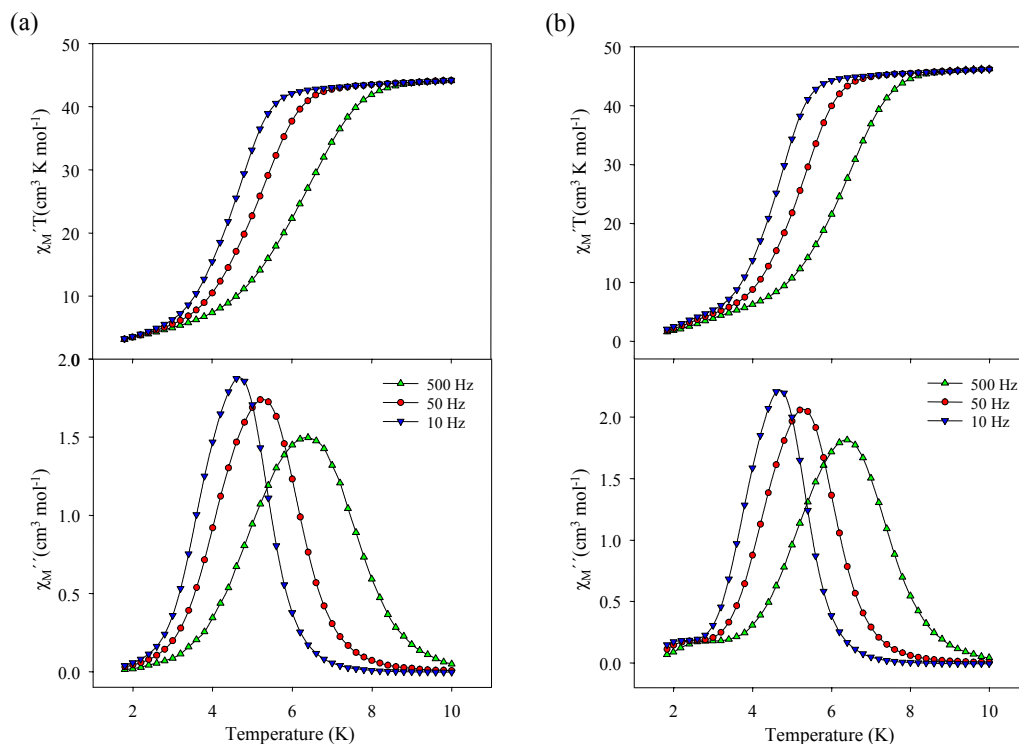


Figure 2-8. Plot of the in-phase (as  $\chi_M'T$ ) and out-of-phase ( $\chi_M''$ ) AC susceptibility signals vs temperature for dried, microcrystalline samples of (a) complex  $2 \cdot C_6H_{14}$  and (b) complex  $3 \cdot 0.2C_6H_{14}$  in eicosane at the indicated oscillation frequencies.

AC susceptibility studies were performed on complexes  $2 \cdot C_6H_{14}$  and  $3 \cdot 0.2C_6H_{14}$  in the 1.80-10.0 K range in a 3.5 G AC field oscillating at frequencies ( $\nu$ ) up to 1488 Hz. The in-phase ( $\chi_M'$ ) signal (as  $\chi_M'T$ ) and out-of-phase ( $\chi_M''$ ) signal are plotted vs temperature in Figure 2-8. Clearly evident are a frequency-dependent decrease in  $\chi_M'T$  at  $T < 10$  K, concomitant with the appearance of a frequency-dependent out-of-phase ( $\chi_M''$ ) signal. These indicate that the magnetization of both **2** and **3** cannot relax fast enough to stay in-phase with the oscillating field, and this is a strong indication that complexes **2** and **3** are single-molecule magnets (SMMs). Note that at each AC oscillation frequency for complex **2** there is only one  $\chi_M''$  peak, and complex **2** does not therefore exhibit JT isomerism. The latter is the presence of an abnormally oriented JT axis, equatorial with respect to the  $Mn_{12}$  disk, that leads to a lower barrier to magnetization relaxation and a

$\chi_M''$  peak at consequently lower temperatures.<sup>56-59</sup> Complex **2** is thus present as exclusively the normal, slower-relaxing JT isomer. This is in contrast to complex **3** where in addition to the frequency-dependent signal in the 4-7 K range, there is also a frequency-dependent out-of-phase signal in the 2-3 K range that corresponds to a faster-relaxing species. Loss of solvent molecules as the material is dried under vacuum likely causes the conversion of a small fraction of slower-relaxing molecules of complex **3** to the faster-relaxing isomer almost certainly by re-orientation of a normally-oriented JT elongation axis to an abnormal position.<sup>56b</sup>

### 2.2.3.3 Relaxation studies

The  $\chi_M''$  versus  $T$  plots were used as a source of kinetic data to calculate the effective energy barrier ( $U_{\text{eff}}$ ) to magnetization relaxation. At a given oscillation frequency ( $\nu$ ), the position of the  $\chi_M''$  peak maximum is the temperature at which the angular frequency ( $\omega = 2\pi\nu$ ) of the oscillating field equals the relaxation rate ( $1/\tau$ , where  $\tau$  is the relaxation time) at which the magnetization vector of a molecule relaxes between one orientation along the easy-axis (the  $z$  axis) to the opposite one. The relaxation rates at a given temperature can thus be obtained from  $\omega = 1/\tau$  at the maxima of the  $\chi_M''$  peaks. The peak maxima were accurately determined by fitting the peaks to a Lorentzian function.

The magnetization relaxation of a SMM obeys the Arrhenius relationship (eq 2-6), the characteristic behavior of a thermally-activated Orbach process,<sup>60</sup> where  $U_{\text{eff}}$  is the effective anisotropy energy barrier,  $k$  is the Boltzmann constant, and  $1/\tau_0$  is the pre-exponential term.

$$(1/\tau) = (1/\tau_0) \exp(-U_{\text{eff}}/kT) \quad (2-6a)$$

$$\ln(1/\tau) = \ln(1/\tau_0) - U_{\text{eff}}/kT \quad (2-6b)$$

The frequency dependence of the  $\chi_M''$  peak for complexes **2** and **3** was determined at eight oscillation frequencies up to 1488 Hz. Plots of  $\ln(1/\tau)$  vs  $1/T$  for **2** and **3** using  $\chi_M''$  versus  $T$  data are separately shown in Figure 2-9, with the least-squares fits to eq 2-6 shown as solid lines. From the slope and intercept, it was determined that  $U_{\text{eff}} = 45.5 \text{ cm}^{-1}$  (65.5 K) and  $1/\tau_0 = 1.1 \times 10^8 \text{ s}^{-1}$  for complex **2**, and  $U_{\text{eff}} = 47.2 \text{ cm}^{-1}$  (67.9 K) and  $1/\tau_0 = 1.6 \times 10^8 \text{ s}^{-1}$  for complex **3**.

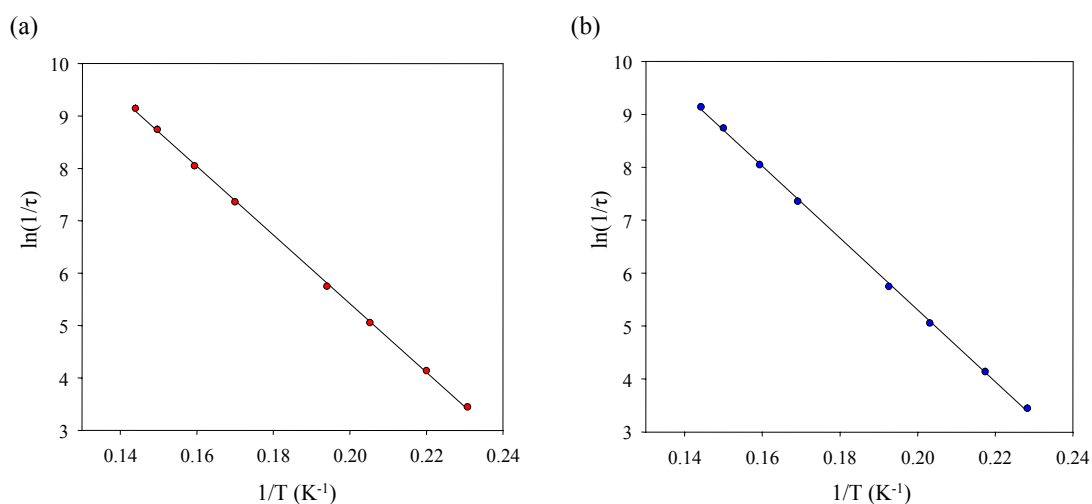


Figure 2-9. Plot of the natural logarithm of relaxation rate,  $\ln(1/\tau)$ , vs inverse temperature for (a) complex **2**· $\text{C}_6\text{H}_{14}$  and (b) complex **3**· $0.2\text{C}_6\text{H}_{14}$  using  $\chi_M''$  versus  $T$  data at different frequencies. The solid line is a fit to the Arrhenius equation; see the text for the fit parameters.

To supplement the AC data and thus provide for a more accurate kinetic analysis, additional relaxation versus temperature data were obtained for **2** at temperatures below 1.8 K, the operating minimum of our SQUID instrument, from DC magnetization decay vs time measurements. These data were obtained on a single crystal of  $2\cdot4\text{CH}_2\text{Cl}_2$  using a micro-SQUID apparatus. First, a large DC field of 1.4 T was applied to the sample at

about 5 K to saturate its magnetization in one direction, and the temperature was then lowered to a chosen value between 0.04 and 2.0 K. When the temperature was stable, the field was swept from 1.4 T to zero at a rate of 0.14 T/s, and then the magnetization in zero field was measured as a function of time. This gave a set of relaxation time ( $\tau$ ) vs  $T$  data, which were combined with the AC data and used to construct an Arrhenius plot of  $\tau$  vs  $1/T$  (Figure 2-10).

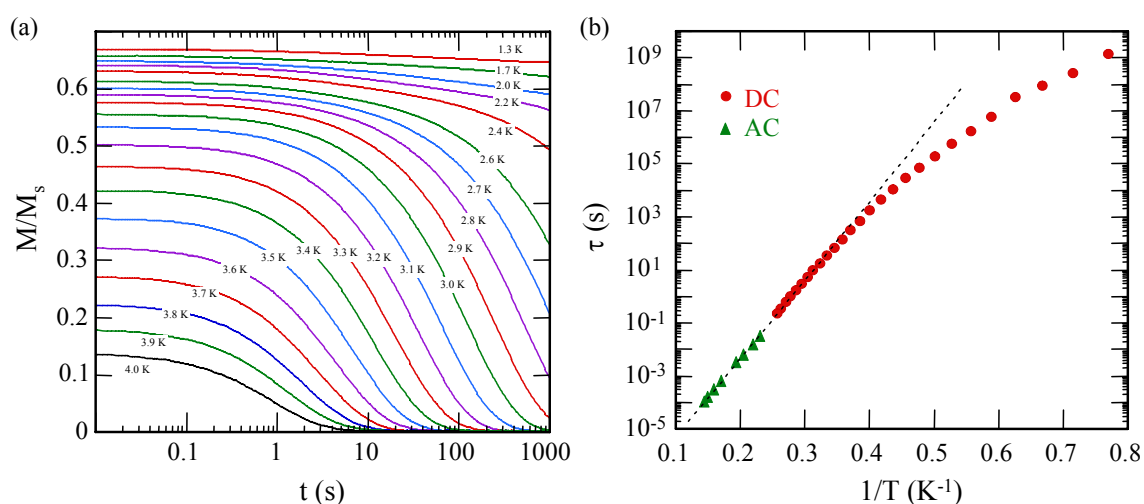


Figure 2-10. Relaxation time vs temperature studies for complex  $2 \cdot 4\text{CH}_2\text{Cl}_2$ . (a) Plot of magnetization vs time decay in zero field. The magnetization is normalized to its saturation value,  $M_s$ . (b) Arrhenius plot using AC  $\chi_M''$  data ( $\blacktriangle$ ) on a microcrystalline sample and DC magnetization decay data ( $\bullet$ ) on a single crystal. The dashed line is the fit of the data in the thermally-activated region to eq 2-6; see the text for the fitting parameters.

The data above 2.5 K ( $1/T = 0.4 \text{ K}^{-1}$ ) were fit to the Arrhenius relationship (eq 2-6), and the fit (dashed line in Figure 2-10b) gave an effective energy barrier ( $U_{\text{eff}}$ ) of 67 K and a pre-exponential factor ( $\tau_0$ ) of  $6.6 \times 10^{-9}$  s. The  $U_{\text{eff}}$  value falls within the normal range  $42\text{-}50 \text{ cm}^{-1}$  (60-72 K) observed previously for several  $[\text{Mn}_{12}\text{O}_{12}(\text{O}_2\text{CR})_{16}(\text{H}_2\text{O})_4]$  complexes.<sup>19,22,23</sup> Below  $\sim 2.5$  K, the  $\tau$  vs  $1/T$  plot of Figure 2-10b deviates from linearity as the thermally-activated relaxation rate diminishes and the relaxation via quantum tunneling through the anisotropy barrier becomes more important. Eventually, at low

enough temperature, the plot would plateau and become temperature-independent, as expected for the relaxation now being only via quantum tunneling as the thermally-activated relaxation rate becomes insignificant.

#### 2.2.3.4 Hysteresis studies below 1.8 K

Since complex **2** is a SMM, it should exhibit hysteresis below its blocking temperature,  $T_B$ , in a magnetization versus DC field plot. Figure 2-11a shows such magnetization vs field scans for  $2 \cdot 4\text{CH}_2\text{Cl}_2$  at different temperatures in the 2.0-4.0 K range and a constant sweep rate of 4 mT/s. Hysteresis loops were indeed observed below 4.0 K, whose coercivities increase with decreasing temperature, as expected for a SMM. The SMM behavior of complex **2** is further emphasized in Figure 2-11b where magnetization vs field scans are shown at 2.5 K for different field sweep rates.

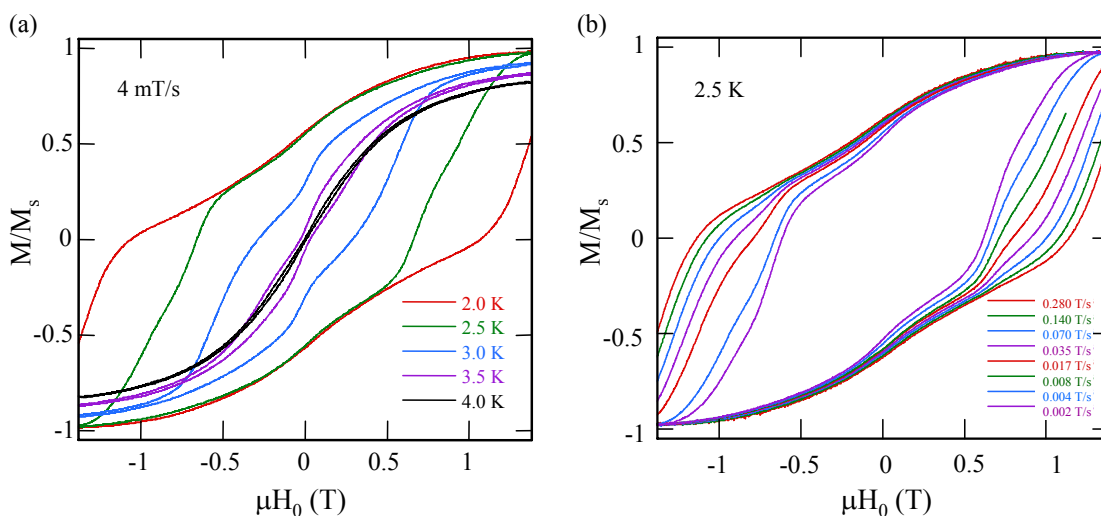


Figure 2-11. Magnetization ( $M$ ) vs magnetic field hysteresis loops for a single crystal of complex  $2 \cdot 4\text{CH}_2\text{Cl}_2$  at (a) the indicated temperatures and fixed sweep rate and (b) the indicated sweeping rates at 2.5 K.  $M$  is normalized to its saturation value,  $M_s$ .

As expected for a SMM, the coercivity of the hysteresis loops at zero field increases with increasing scan rates. The loops are not completely smooth, instead showing the step-like features characteristic of quantum tunneling of the magnetization

(QTM) through the anisotropy barrier. Such steps are a common feature of the hysteresis loops of many types of SMMs.<sup>28</sup> However, the steps in the loops for complex **2** in Figure 2-11 are much less well defined than usual for  $[\text{Mn}_{12}\text{O}_{12}(\text{O}_2\text{CR})_{16}(\text{H}_2\text{O})_4]$  complexes.<sup>61</sup> Instead, they are rather broad and poorly resolved, although clearly present at field positions of zero,  $\sim 0.65$  and  $\sim 1.3$  T. Examination of many crystals gave comparable results, the steps occasionally being almost totally smeared out. Such broadening of QTM steps is not uncommon, particularly in larger SMMs such as  $\text{Mn}_{18}$ <sup>62</sup> and  $\text{Mn}_{30}$ <sup>63</sup> where no sign of a step feature is evident even though the presence of QTM is confirmed from other types of data such as temperature-independent relaxation rates and quantum hole digging. The primary origins of step broadening are weak intermolecular interactions (exchange and dipolar), and a distribution of molecular environments arising from disordered solvent molecules of crystallization, partial solvent loss, ligand disorder, crystal defects, and similar.<sup>62,63</sup> A distribution of molecular environments results in a distribution in D values, and thus a distribution in step positions, which depend upon the D value. As a result, the observed steps are broadened, or even smeared out if the broadening is sufficient. Since intermolecular interactions are likely to be comparable in all  $\text{Mn}_{12}$  complexes and the latter usually give well defined steps, it is likely that the main causes of step broadening in **2** are the other reasons listed above, particularly the disorder in the  $\text{CH}_2\text{Cl}_2$  solvents of crystallization, their partial loss on removing crystals from their mother liquor, and the slight crystal damage that results from the latter.

#### 2.2.4 Magnetochemistry of Complex 5

DC magnetic susceptibility data were collected in the 5.00-300 K range on a powdered microcrystalline sample of  $5 \cdot 2\text{H}_2\text{O}$  restrained in eicosane to prevent torquing. The  $\chi_{\text{M}}T$  per molecule smoothly decreases from  $6.58 \text{ cm}^3 \text{ K mol}^{-1}$  at 300 K to

0.78 cm<sup>3</sup> K mol<sup>-1</sup> at 5 K (Figure 2-12). The value at 300 K is less than 9.75 cm<sup>3</sup> K mol<sup>-1</sup>, the spin-only value expected for a 2Mn<sup>III</sup>, 2Mn<sup>IV</sup> complex with noninteracting metal centers, indicating the presence of appreciable antiferromagnetic interactions between the manganese ions and suggesting a small ground state spin.

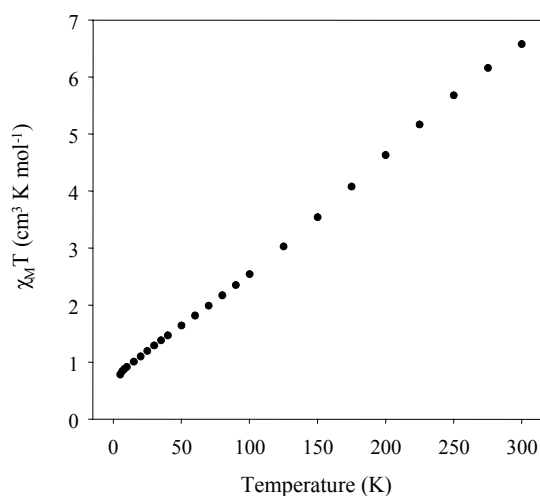


Figure 2-12. Plot of  $\chi_M T$  vs temperature for a dried, microcrystalline sample of complex **5**·2H<sub>2</sub>O in eicosane.  $\chi_M$  is the DC molar magnetic susceptibility measured in a 5.0 kG field.

This was confirmed by AC magnetic susceptibility measurements carried out on a dried, microcrystalline sample of **5**·2H<sub>2</sub>O in a 3.5 G AC field oscillating at 1000 Hz. In Figure 2-13 is shown the in-phase AC susceptibility, plotted as  $\chi_M' T$  versus  $T$ , together with the out-of-phase AC susceptibility ( $\chi_M''$ ), in the 1.8-10 K temperature range to minimize the possibility of populating excited states. The downward sloping  $\chi_M' T$  versus  $T$  plot confirms that depopulation of excited states with greater  $S$  value than the ground state is occurring as the temperature decreases. Extrapolation of the plot to 0 K, where only the ground state will be populated, gives a  $\chi_M' T$  value of  $\sim 0.5$  cm<sup>3</sup> K mol<sup>-1</sup>. This value is approximately that expected for an  $S = 0$  state with  $g = 2$ . Also evident from the AC studies is the lack of an out-of-phase AC susceptibility signal ( $\chi_M''$ ). Such a signal is

indicative of the onset of slow magnetic relaxation and confirms that complex **5** does not function as a single-molecule magnet in accord with the small ground state spin of the molecule.

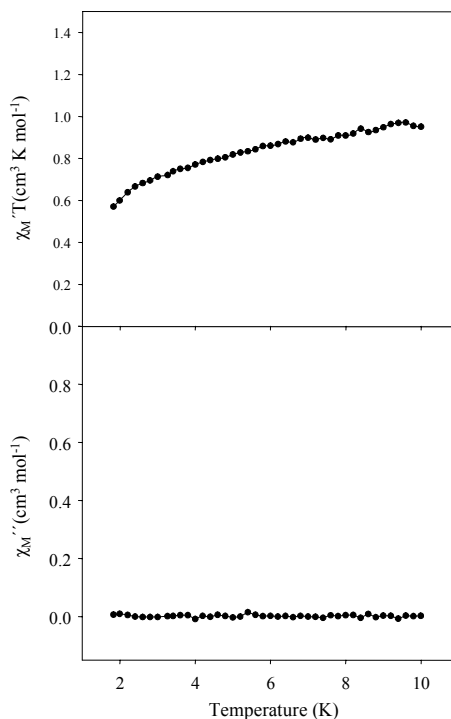


Figure 2-13. Plot of the in-phase (as  $\chi_M' T$ ) and out-of-phase ( $\chi_M''$ ) AC susceptibility signals vs temperature for a dried, microcrystalline sample of complex **5**·2H<sub>2</sub>O in eicosane in a 3.5 G AC field oscillating at 1000 Hz.

### 2.3 Conclusions

Complete derivatization of all the axial sites with non-carboxylate ligands has been achieved for the first time in an Mn<sub>12</sub> complex by replacement of the axial carboxylate ligands of **1** with PhSO<sub>3</sub><sup>-</sup> groups. Incorporation of the non-carboxylate, S-based ligands is driven by the greater acidity of PhSO<sub>3</sub>H over MeCO<sub>2</sub>H, with the less basic PhSO<sub>3</sub><sup>-</sup> ligands occupying axial sites with at least one O atom lying along a Mn<sup>III</sup> JT elongation axis. The resultant mixed-ligand product retains both the high ground state spin value and SMM properties of the parent [Mn<sub>12</sub>O<sub>12</sub>(O<sub>2</sub>CR)<sub>16</sub>(H<sub>2</sub>O)<sub>4</sub>] complexes, with the complex

possessing an  $S = 10$  ground state spin and displaying frequency-dependent peaks in the out-of-phase AC magnetic susceptibility. Complex **2** is also a potential starting point for further chemistry, and reactivity studies on **2** with diphenylphosphinic acid have afforded a clean route for the preparation of a tetranuclear cluster possessing a  $[\text{Mn}_4\text{O}_4]^{6+}$  cubane core. Although **5** does not retain the SMM properties of its parent compound, it provides further insight into the behavior of **2** when treated with additional non-carboxylate ligands. Complex **2** is also the first  $\text{Mn}_{12}$  species with sulfur-containing ligands and thus represents a useful expansion of this family of SMMs. In addition, with the more basic  $\text{MeCO}_2^-$  groups blocking the equatorial sites, regioselective chemistry at the axial positions should now be feasible with a variety of anionic groups. Such reactions are currently under investigation.

## 2.4 Experimental

### 2.4.1 Syntheses

All manipulations were performed under aerobic conditions using chemicals as received, unless otherwise stated.  $[\text{Mn}_{12}\text{O}_{12}(\text{O}_2\text{CMe})_{16}(\text{H}_2\text{O})_4] \cdot 2\text{MeCO}_2\text{H} \cdot 4\text{H}_2\text{O}$  (**1**) was prepared as described elsewhere.<sup>50</sup>

$[\text{Mn}_{12}\text{O}_{12}(\text{O}_2\text{CMe})_8(\text{O}_3\text{SPh})_8(\text{H}_2\text{O})_4]$  (**2**). A solution of complex **1** (1.00 g, 0.49 mmol) in MeCN ( $75 \text{ cm}^3$ ) was treated with  $\text{PhSO}_3\text{H}$  (0.61 g, 3.9 mmol) in MeCN ( $25 \text{ cm}^3$ ). The solution was stirred overnight and the solvent was removed. Toluene ( $25 \text{ cm}^3$ ) was added to the residue, and the solution was evaporated to dryness. The addition and removal of toluene was repeated three more times. The residue was dissolved in  $\text{CH}_2\text{Cl}_2$  ( $50 \text{ cm}^3$ ) and filtered. An equal volume of hexanes was added to the filtrate, and the solution was allowed to stand at room temperature for 4 days. Dark brown crystals of  $\mathbf{2} \cdot 4\text{CH}_2\text{Cl}_2$  were collected by filtration, washed with hexanes, and dried *in vacuo*; yield

~96%. A sample for crystallography was maintained in contact with the mother liquor to prevent the loss of interstitial solvent. Anal. Calcd (found) for  $2 \cdot C_6H_{14}$  ( $C_{70}H_{86}Mn_{12}O_{56}S_8$ ): C, 30.69 (30.72); H, 3.16 (2.99); N, 0.00 (0.13). Selected IR data ( $cm^{-1}$ ): 1506 (s), 1446 (vs), 1245 (m), 1203 (m), 1127 (s), 1037 (m), 1018 (s), 996 (m), 981 (m), 757 (w), 732 (m), 690 (s), 671 (s), 607 (vs), 564 (s).

**[Mn<sub>12</sub>O<sub>12</sub>(O<sub>2</sub>CMe)<sub>12</sub>(O<sub>3</sub>SPh)<sub>4</sub>(H<sub>2</sub>O)<sub>4</sub>] (3)**. A solution of complex **1** (0.50 g, 0.24 mmol) in MeCN (75 cm<sup>3</sup>) was treated with PhSO<sub>3</sub>H (0.15 g, 0.97 mmol) in MeCN (25 cm<sup>3</sup>). The solution was stirred overnight, and the solvent was then removed. Toluene (25 cm<sup>3</sup>) was added to the residue, and the solution was evaporated to dryness. The addition and removal of toluene was repeated three more times. The residue was dissolved in CH<sub>2</sub>Cl<sub>2</sub> (25 cm<sup>3</sup>) and filtered. An equal volume of hexanes was added to the filtrate, and the solution allowed to stand at room temperature for ~ 4 days. Dark brown crystals of **3** were collected by filtration, washed with hexanes, and dried *in vacuo*; yield ~81%. Anal. Calcd (found) for **3** ( $C_{48}H_{64}Mn_{12}O_{52}S_4$ ): C, 25.50 (25.73); H, 2.85 (3.24); N, 0.00 (0.02). Selected IR data ( $cm^{-1}$ ): 1576 (m), 1506 (m), 1447 (vs), 1330 (m), 1192 (s), 1128 (s), 1039 (m), 1019 (s), 997 (m), 761 (w), 731 (m), 673 (vs), 646 (s), 607 (vs).

**[Mn<sub>4</sub>O<sub>4</sub>(O<sub>2</sub>PPh<sub>2</sub>)<sub>6</sub>] (5)**. To a stirred solution of complex **2**·4CH<sub>2</sub>Cl<sub>2</sub> (0.50 g, 0.17 mmol) in CH<sub>2</sub>Cl<sub>2</sub> (50 cm<sup>3</sup>) was added a solution of Ph<sub>2</sub>PO<sub>2</sub>H (0.29 g, 1.3 mmol) in CH<sub>2</sub>Cl<sub>2</sub> (25 cm<sup>3</sup>). The resulting solution was stirred for 12h. The solvent was removed *in vacuo*. Toluene (25 cm<sup>3</sup>) was added to the residue, and the solution was again evaporated to dryness. The addition and removal of toluene was repeated two more times and the residue was redissolved in CH<sub>2</sub>Cl<sub>2</sub> (40 cm<sup>3</sup>) and filtered through Celite. Diffusion of toluene into the CH<sub>2</sub>Cl<sub>2</sub> solution slowly produced dark brown hexagonal crystals, and

these were suitable for X-ray crystallography if maintained in contact with the mother liquor to prevent the loss of interstitial solvent. After three weeks, the crystals were isolated by filtration, washed with toluene, and dried under vacuum; yield ~51%. The dried crystals are hygroscopic. Anal. Calcd (found) for  $5 \cdot 2\text{H}_2\text{O}$  ( $\text{C}_{72}\text{H}_{64}\text{P}_6\text{Mn}_4\text{O}_{18}$ ): C, 53.29 (53.05); H, 3.97 (3.71); N, 0.00 (0.01). Selected IR data (KBr,  $\text{cm}^{-1}$ ): 1481 (s), 1312 (w), 1260 (w), 1184 (m), 1132 (vs), 1106 (s), 1067 (m), 1032 (vs), 986 (vs), 974 (vs), 859 (w), 755 (vs), 732 (vs), 694 (vs), 630 (m), 562 (s), 542 (vs), 524 (s), 513 (s), 485 (s).

#### 2.4.2 X-ray Crystallography

Data were collected using a Siemens SMART PLATFORM equipped with a CCD area detector and a graphite monochromator utilizing  $\text{MoK}_\alpha$  radiation ( $\lambda = 0.71073 \text{ \AA}$ ). A suitable crystal of  $2 \cdot 4\text{CH}_2\text{Cl}_2$  was attached to a glass fiber using silicone grease and transferred to the goniostat where it was cooled to  $-80 \text{ }^\circ\text{C}$  for characterization and data collection. The structure was solved by direct methods (SHELXTL)<sup>64</sup> and standard Fourier techniques. All non-hydrogen atoms were refined anisotropically. Hydrogen atoms were placed in calculated positions and refined with the use of a riding model. Cell parameters were refined using up to 8192 reflections. A full sphere of data (1381 frames) was collected using the  $\omega$ -scan method ( $0.3^\circ$  frame width). The first 50 frames were re-measured at the end of data collection to monitor instrument and crystal stability (maximum correction on I was  $< 1\%$ ). Absorption corrections by integration were applied based on measured indexed crystal faces.

A preliminary search of reciprocal space for  $2 \cdot 4\text{CH}_2\text{Cl}_2$  revealed a set of reflections with no symmetry and no systematic absences. An initial choice of the centrosymmetric

space group  $P\bar{1}$  was confirmed by the subsequent solution and refinement of the structure. The asymmetric unit contains the  $Mn_{12}$  cluster and four  $CH_2Cl_2$  molecules of crystallization. Two of the dichloromethane solvent molecules were disordered. The Cl atoms in one  $CH_2Cl_2$  molecule were disordered over three positions and their site occupancy factors refined to 85:17:8%. The Cl atoms in the remaining disordered  $CH_2Cl_2$  molecule were disordered over two (main) positions and the occupancies refined to 56:44%. A total of 1406 parameters were refined in the final cycle of refinement using 16674 reflections with  $I > 2\sigma(I)$  to yield  $R1$  and  $wR2$  of 3.79% and 9.90%, respectively. The final difference Fourier map was essentially featureless, the largest peak being  $0.813 \text{ e } \text{\AA}^{-3}$  and the deepest hole being  $-0.784 \text{ e } \text{\AA}^{-3}$ .

Data were collected on a Bruker D8 platform goniometer equipped with a SMART APEX CCD area detector and a graphite monochromator utilizing  $MoK_{\alpha}$  radiation ( $\lambda = 0.71073 \text{ \AA}$ ). A suitable single crystal of **5** was mounted on a glass fiber using silicone grease and transferred to the diffractometer where it was cooled to  $-123 \text{ }^{\circ}\text{C}$  for characterization and data collection. The intensity data were collected using the  $\omega$ -scan methods with a scan step  $\Delta\omega = 0.03^{\circ}$ . The first 50 frames were re-measured at the end of data collection to monitor instrument and crystal stability (maximum correction was  $< 1\%$ ). The data were corrected for Lorentz and polarization effects using the Bruker SAINT software and an absorption correction was performed using the SADABS program supplied by Bruker AXS ( $T_{\min}/T_{\max} = 0.804$ ).

The structure was solved by direct methods and standard Fourier techniques, and was refined on  $F^2$  using full-matrix least-squares method (SHELXTL).<sup>64</sup> All non-hydrogen atoms were refined anisotropically. Hydrogen atoms were placed in

calculated positions and refined with the use of a riding model. A total of 1175 parameters were refined in the final cycle of refinement using 21864 [ $R_{\text{int}} = 0.0935$ ] independent reflections with  $I > 2\sigma(I)$  to yield  $R1$  and  $wR2$  of 3.70 and 10.14%, respectively. The final difference Fourier map was reasonably clean, max/min residual electron density are  $+0.99/-1.029 \text{ e } \text{\AA}^{-3}$ . The Flack parameter is 0.05(2), i.e., the found structure is an absolute structure of **5**.

CHAPTER 3  
NOVEL MIXED-VALENCE Mn<sup>III</sup>/Mn<sup>IV</sup> CLUSTERS FROM THE USE OF  
BENZENESELENINATE LIGANDS: [Mn<sub>7</sub>O<sub>8</sub>(O<sub>2</sub>CMe)(O<sub>2</sub>SePh)<sub>8</sub>(H<sub>2</sub>O)] AND  
[Mn<sub>7</sub>O<sub>8</sub>(O<sub>2</sub>SePh)<sub>9</sub>(H<sub>2</sub>O)]

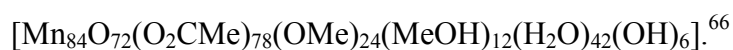
### 3.1 Introduction

There are many motivations for the preparation of new polynuclear Mn clusters, not least of which is the structural beauty that such complexes often display. However, a more practical and major objective is the search for new examples of molecules with significant values of ground state spin, *S*. Indeed, Mn chemistry has proven a fertile source of such species. In cases where *S* is fairly large and there is also a significant magnetoanisotropy of the easy-axis (or Ising) type, as reflected in a negative value of the zero-field splitting (ZFS) parameter *D*, then such molecules will have a significant energy barrier to relaxation of the magnetization vector and will thus function as single-molecule magnets (SMMs). The upper limit of the energy barrier is given by  $S^2|D|$  or  $(S^2-1/4)|D|$  for integer and half-integer *S* values, respectively. Experimental evidence for SMMs is provided by the observation of frequency-dependent, out-of-phase AC susceptibility signals ( $\chi_M''$ ), and by hysteresis loops in magnetization vs DC field scans, both properties characteristic of a superparamagnet-like particle.<sup>21,23</sup> Additionally, several SMMs display step-like features in the hysteresis loops, a consequence of quantum tunneling of the magnetization (QTM).<sup>27,61,65</sup>

The two preparative strategies that have typically been employed previously for the preparation of new SMMs (and new Mn<sub>*x*</sub> clusters in general) are the following: (i) ligand substitution of some or all of the peripheral ligands in preformed compounds with

retention of the core structure;<sup>13,38,46</sup> and (ii) structural transformation of a given  $Mn_x$  core to a new structural type by reaction with some suitably chosen chelate or other reagent.<sup>11</sup>

Of the SMMs known to date, the  $[Mn_{12}O_{12}(O_2CR)_{16}(H_2O)_4]$  family is the most thoroughly studied, exhibiting SMM behavior at the highest temperatures.<sup>13,21-23,38,46</sup> A number of  $Mn_{12}$  derivatives have been prepared through the use of ligand substitution reactions on the parent  $Mn_{12}$  complex ( $R = Me$ ), making possible the tunability of solubility and redox properties of the clusters.<sup>13,38,46</sup>  $Mn_{12}$  compounds are also good starting materials for the preparation of other high nuclearity Mn complexes. They have been used in this capacity to prepare a number of high nuclearity products, and some of these have also proven to be new additions to the SMM family, including the largest Mn carboxylate cluster obtained to date,



As part of this general characterization of the reactivity properties of  $Mn_{12}$  complexes, we have recently been studying the replacement of some or all of the carboxylate ligands with non-carboxylate ones. This has included the replacement of the carboxylate ligands in a site-specific manner, enhancing reactivity at selected sites and making site-specific reactions feasible. Published progress along these lines includes the site-selective replacement of some of the carboxylate groups with nitrate, diphenylphosphinate, and benzenesulfonate anions (by reactions of  $[Mn_{12}O_{12}(O_2CMe)_{16}(H_2O)_4]$  with the corresponding conjugate acids) to give  $[Mn_{12}O_{12}(O_2CCH_2Bu^t)_{12}(NO_3)_4(H_2O)_4]$ ,<sup>32</sup>  $[Mn_{12}O_{12}(O_2CMe)_8(O_2PPh_2)_8(H_2O)_4]$ ,<sup>33</sup> and  $[Mn_{12}O_{12}(O_2CMe)_8(O_3SPh)_8(H_2O)_4]$ ,<sup>39</sup> respectively. In addition, other groups have reported the replacement of four carboxylate groups with diphenylphosphates to give

$[\text{Mn}_{12}\text{O}_{12}(\text{O}_2\text{CPh})_{12}(\text{O}_2\text{P}(\text{OPh})_2)_4(\text{H}_2\text{O})_4]$ .<sup>47</sup> In all of these cases, the  $[\text{Mn}_{12}\text{O}_{12}]^{16+}$  core is retained intact, although occasionally slightly distorted compared with the all-carboxylate parent compound.

The present report is an extension of these studies into a new direction, the reaction of  $[\text{Mn}_{12}\text{O}_{12}(\text{O}_2\text{CMe})_{16}(\text{H}_2\text{O})_4]$  with benzeneseleninic acid ( $\text{PhSeO}_2\text{H}$ ). The latter is significantly different from both  $\text{Ph}_2\text{PO}_2^-$  and  $\text{PhSO}_3^-$  in containing only a three-coordinate central atom; however, it is also unlike carboxylate and nitrate groups in that the Se possesses a stereoactive lone pair. In fact, we have found that the  $\text{PhSeO}_2\text{H}$  causes rupture of the  $[\text{Mn}_{12}\text{O}_{12}]$  core and gives products of an unprecedented structural type containing a  $[\text{Mn}^{\text{III}}_3\text{Mn}^{\text{IV}}_4\text{O}_8]^{9+}$  core. Herein we report the syntheses, single crystal X-ray structures, and magnetic properties of two related examples of this new type of  $\text{Mn}_7$  complex.

## 3.2 Results and Discussion

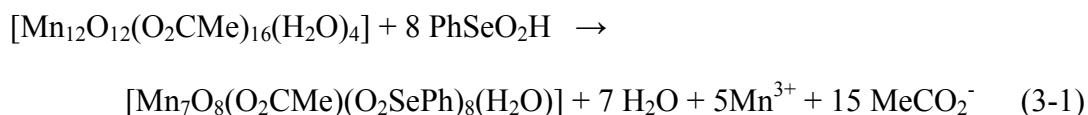
### 3.2.1 Syntheses

Our initial attempts to introduce  $\text{PhSeO}_2^-$  groups into high-nuclearity Mn aggregates involved the reaction of benzeneseleninic acid with several trinuclear and tetranuclear complexes containing the  $[\text{Mn}_3(\mu_3\text{-O})]$  and  $[\text{Mn}_4(\mu_3\text{-O})_2]$  cores, respectively. These were known from previous work to yield magnetically interesting complexes upon reaction with a chelating ligand.<sup>52,62,67-69</sup> However, despite many attempts, such reactions were ineffective, and spectroscopic characterization of the products indicated that no reaction between the Mn complexes and  $\text{PhSeO}_2\text{H}$  had occurred. This is likely due to a combination of effects, including the poor solubility of the ligand in the MeCN solvent and the essentially identical acid dissociation constants of  $\text{PhSeO}_2\text{H}$  ( $\text{pK}_a = 4.79$ ) and

MeCO<sub>2</sub>H (pK<sub>a</sub> = 4.76);<sup>70</sup> a large difference in pK<sub>a</sub> values facilitates substitution of MeCO<sub>2</sub><sup>-</sup> ligands.

We thus turned our attention to reactions of the acid with [Mn<sub>12</sub>O<sub>12</sub>(O<sub>2</sub>CMe)<sub>16</sub>(H<sub>2</sub>O)<sub>4</sub>], thinking that this might allow at least some PhSeO<sub>2</sub><sup>-</sup> groups to be incorporated around the [Mn<sub>12</sub>O<sub>12</sub>] core, as had been found with PhSO<sub>3</sub><sup>-</sup>. Thus, complex **3** in distilled MeCN was treated with eighteen equivalents of PhSeO<sub>2</sub>H, which slowly dissolved. After 12 hours, the resulting deep brown solution was separated by filtration from some brown powder, and from the filtrate was obtained a dark brown crystalline product. It was immediately obvious from the infrared spectrum that the reaction had led to transformation of the [Mn<sub>12</sub>O<sub>12</sub>] core of **1**, and the product was subsequently identified by X-ray crystallography as [Mn<sub>7</sub>O<sub>8</sub>(O<sub>2</sub>CMe)(O<sub>2</sub>SePh)<sub>8</sub>(H<sub>2</sub>O)] (**6**), obtained in ~35% yield.

When the same reaction system was maintained for longer reaction times, the amount of the brown precipitate steadily increased. After 48 hours, the precipitate was collected by filtration and recrystallized from CH<sub>2</sub>Cl<sub>2</sub>/Et<sub>2</sub>O to give crystals of [Mn<sub>7</sub>O<sub>8</sub>(O<sub>2</sub>SePh)<sub>9</sub>(H<sub>2</sub>O)] (**7**) in 40% yield. The overall transformations to give **6** and **7** are summarized in eq 3-1, which has been formulated for product **6**; that for **7** would be very similar.



Charge considerations and inspection of metric parameters indicate **6** and **7** to be mixed-valence 3Mn<sup>III</sup>, 4Mn<sup>IV</sup>, with a trapped-valence situation (*vide infra*). Clearly, the overall conversion of [Mn<sub>12</sub>O<sub>12</sub>(O<sub>2</sub>CMe)<sub>16</sub>(H<sub>2</sub>O)<sub>4</sub>] (8Mn<sup>III</sup>, 4Mn<sup>IV</sup>) into these products

must involve a complicated mechanism involving fragmentation and recombination steps. There are almost certainly other species left in the colored filtrates after the product crystals are collected, and these are likely  $\text{Mn}^{\text{III}}$  acetate species, but we have not explored these further. Since complexes **6** and **7** are so similar, differing only in the identity of one ligand, acetate vs benzeneseleninate, we were fortunate that they have significantly different solubilities in MeCN or their isolation in pure form would not have been possible. Complex **6** is fairly soluble in MeCN whereas **7** is not. Thus, at shorter reaction times we were able to obtain **6** from the filtered reaction solution, whereas at longer reaction times substitution of its remaining acetate by another  $\text{PhSeO}_2^-$  group converts it to **7**, which precipitates from the solution.

### 3.2.2 Description of Structures

#### 3.2.2.1 X-ray crystal structure of $[\text{Mn}_7\text{O}_8(\text{O}_2\text{CMe})(\text{O}_2\text{SePh})_8(\text{H}_2\text{O})]$ (**6**)

A labeled ORTEP<sup>40</sup> plot in PovRay format of complex **6** is shown in Figure 3-1, together with a stereoview. The crystallographic data and structure refinement details are collected in Table 3-1, and selected interatomic distances and angles are listed in Table A-3. The complex crystallizes in the triclinic space group  $P\bar{1}$  with the  $\text{Mn}_7$  molecule in a general position. The structure consists of a  $[\text{Mn}^{\text{III}}_3\text{Mn}^{\text{IV}}_4(\mu_3\text{-O})_5(\mu\text{-O})_3]^{9+}$  core (Figure 3-2a), with the peripheral ligation provided by eight bridging  $\text{PhSeO}_2^-$  ligands, one bridging  $\text{MeCO}_2^-$  ligand, and one terminal  $\text{H}_2\text{O}$  molecule. Bond valence sum (BVS) calculations<sup>41</sup> indicate a mixed-valence, trapped-valence complex; Mn(3), Mn(4), and Mn(5) are  $\text{Mn}^{\text{III}}$ , while the remaining Mn centers Mn(1), Mn(2), Mn(6), and Mn(7) are  $\text{Mn}^{\text{IV}}$  (Table 3-2 and 3-3). Each  $\text{Mn}^{\text{IV}}$  ion is in a distorted octahedral environment. The two outer  $\text{Mn}^{\text{III}}$  ions, Mn(3) and Mn(5), are five-coordinate with square pyramidal geometry ( $\tau = 0.06$  and  $0.07$ , respectively, where  $\tau$  is 0 and 1 for ideal square pyramidal

and trigonal bipyramidal geometries, respectively<sup>71</sup>), while the remaining Mn<sup>III</sup> ion, Mn(4), has a very distorted octahedral geometry.

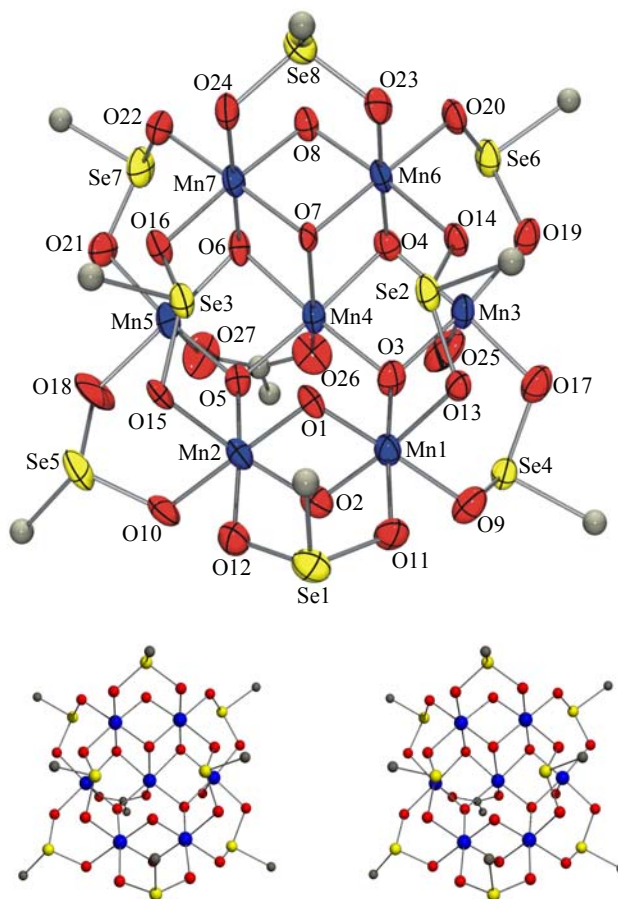


Figure 3-1. ORTEP representation in PovRay format of  $[\text{Mn}_7\text{O}_8(\text{O}_2\text{CMe})(\text{O}_2\text{SePh})_8(\text{H}_2\text{O})]$  (**6**) with thermal ellipsoids at the 50% probability level except for the C atoms, together with a stereopair. For clarity, the hydrogen atoms have been omitted, and only the *ipso* C atoms of the phenyl groups are shown. Mn blue; O red; Se yellow; C gray.

At first glance, the viewpoints of Figures 3-1 and 3-2a suggest that a useful way of describing the core of **6** is as a Mn<sub>6</sub> ring with a seventh Mn in the middle. However, this is not a good description, because the Mn<sub>7</sub> unit is very far from planar. This is emphasized in the side-view of Figure 3-2b. As can be seen, a much better dissection of the core is as a central  $[\text{MnO}_2\text{MnO}_2\text{Mn}]^+$  unit (i.e., 3Mn<sup>III</sup>) to whose bridging oxide ions on each side is attached an  $[\text{MnO}_2\text{Mn}]^{4+}$  unit (2Mn<sup>IV</sup>). The three Mn<sup>III</sup> ions in the central

unit are ligated on one side by the bridging acetate and terminal water groups (O(25) – O(27)), and these Mn<sup>III</sup> ions would thus all be five-coordinate except that one [MnO<sub>2</sub>Mn]<sup>4+</sup> unit swivels about its bridging oxide atoms O(4) and O(6) to bring O(7) within bonding distance of Mn(4), making the latter six-coordinate (Mn(4)-O(7) = 2.278 Å).

Table 3-1. Crystallographic data for [Mn<sub>7</sub>O<sub>8</sub>(O<sub>2</sub>CMe)(O<sub>2</sub>SePh)<sub>8</sub>(H<sub>2</sub>O)]·6MeCN and [Mn<sub>7</sub>O<sub>8</sub>(O<sub>2</sub>SePh)<sub>9</sub>(H<sub>2</sub>O)]·2CH<sub>2</sub>Cl<sub>2</sub>.

Parameter	6·6MeCN	7·2CH <sub>2</sub> Cl <sub>2</sub>
formula <sup>a</sup>	C <sub>62</sub> H <sub>63</sub> Se <sub>8</sub> N <sub>6</sub> Mn <sub>7</sub> O <sub>27</sub>	C <sub>56</sub> H <sub>51</sub> Cl <sub>4</sub> Se <sub>9</sub> Mn <sub>7</sub> O <sub>27</sub>
fw, g mol <sup>-1</sup>	2340.45	2393.02
space group	<i>P</i> $\bar{1}$	<i>P</i> 2 <sub>1</sub> / <i>m</i>
<i>a</i> , Å	10.7432(8)	10.7776(7)
<i>b</i> , Å	15.1584(11)	27.7484(8)
<i>c</i> , Å	24.3955(18)	13.4463(9)
$\alpha$ , deg	99.639(2)	90
$\beta$ , deg	91.197(2)	105.670(2)
$\gamma$ , deg	105.776(2)	90
<i>V</i> , Å <sup>3</sup>	3759.9(5)	3871.8(4)
<i>Z</i>	2	2
<i>T</i> , °C	-100(2)	-100(2)
radiation, Å <sup>b</sup>	0.71073	0.71073
$\rho_{\text{calc}}$ , g cm <sup>-3</sup>	2.067	2.053
$\mu$ , cm <sup>-1</sup>	50.94	55.48
<i>R</i> 1 ( <i>wR</i> 2), % <sup>c,d</sup>	5.91 (14.96)	8.73 (24.55)

<sup>a</sup> Including solvent molecules. <sup>b</sup> Graphite monochromator. <sup>c</sup>  $R1 = \sum ||F_o| - |F_c|| / \sum |F_o|$ . <sup>d</sup>  $wR2 = [\sum [w(F_o^2 - F_c^2)^2] / \sum [wF_o^2]^2]^{1/2}$  where  $S = [\sum [w(F_o^2 - F_c^2)^2] / (n-p)]^{1/2}$ ,  $w = 1/[\sigma^2(F_o^2) + (mp)^2 + np]$ ,  $p = [\max(F_o^2, 0) + 2F_c^2]/3$ , and  $m$  and  $n$  are constants.

Discrete examples of the [Mn( $\mu$ -O)<sub>2</sub>Mn]<sup>4+</sup> core in dinuclear complexes are fairly common.<sup>72</sup> But note that only recently, in the [Mn<sub>8</sub>O<sub>10</sub>(O<sub>2</sub>CMe)<sub>6</sub>(H<sub>2</sub>O)<sub>2</sub>(bpy)<sub>6</sub>]<sup>4+</sup> cation,<sup>73</sup> has the [Mn<sup>IV</sup><sub>2</sub>( $\mu$ -O)( $\mu_3$ -O)]<sup>4+</sup> variant of these units, as found in **6**, been previously observed. Note also that the [MnO<sub>2</sub>Mn]<sup>4+</sup> units can alternatively be described as [MnO<sub>2</sub>(O<sub>2</sub>SePh)Mn]<sup>4+</sup> units since there is also a PhSeO<sub>2</sub><sup>-</sup> bridging them. Thus, they are also very similar to the common dinuclear complexes containing the triply bridged

$[\text{Mn}_2(\mu\text{-O})_2(\mu\text{-O}_2\text{CR})]^{2+,3+}$  core.<sup>74,75</sup> In contrast, the central  $[\text{MnO}_2\text{MnO}_2\text{Mn}]^+$  fragment, containing a linear  $\text{Mn}_3$  unit, has never been seen before in a discrete  $\text{Mn}_3$  complex, although it is a commonly encountered sub-fragment of several higher nuclearity clusters, such as certain  $\text{Mn}_{10}$ ,<sup>76</sup>  $\text{Mn}_{11}$ <sup>77</sup> and  $\text{Mn}_{18}$ <sup>62</sup> species. Overall, the complete  $\text{Mn}_7$  complex possesses  $C_1$  symmetry.

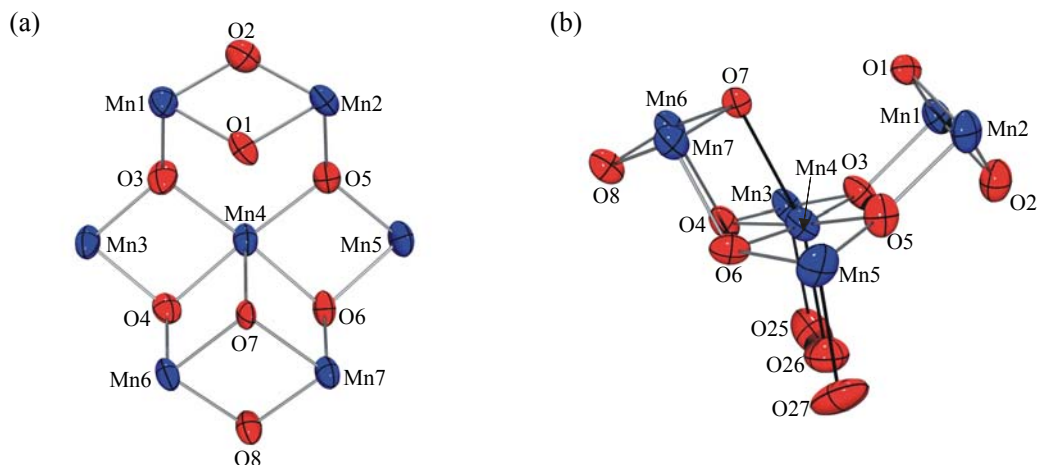


Figure 3-2. ORTEP representations in PovRay format of (a) the  $[\text{Mn}_7\text{O}_8]^{9+}$  core of complex **6** and (b) the relative disposition of the elongation axes, indicated as solid black bonds.

The central  $\text{Mn}^{\text{III}}$  ion, Mn(4), displays a Jahn-Teller (JT) axial elongation, as expected for a high-spin  $\text{Mn}^{\text{III}}$  ( $d^4$ ) ion. Normally, JT elongation axes avoid Mn-oxide bonds, almost always the strongest and shortest in the molecule, but in this case the oxide O(7) cannot in any case approach too closely and the resulting Mn(4)-O(7) distance (2.278(6) Å) is very long for a Mn-oxide bond, even a JT elongated one. The other JT elongated bond is Mn(4)-O(27) (2.180(7) Å). For the two square pyramidal  $\text{Mn}^{\text{III}}$  ions, Mn(3) and Mn(5), their local  $z$  axis is oriented parallel to the JT axis of Mn(4). Thus, the long, apical bonds of the sp geometries (Mn(3)-O(25) = 2.289(8) and Mn(5)-O(27) = 2.172(8) Å) are parallel to the long bonds at Mn(4). In effect, then, there is parallel alignment of the three  $\text{Mn}^{\text{III}}$  distortion axes, which will dominate the magnetic anisotropy

(i.e., the magnitude of the ZFS parameter,  $D$ ) of the complete  $\text{Mn}_7$  molecule. This will be of relevance to the magnetic discussion later.

Table 3-2. Bond valence sum<sup>a</sup> calculations for complexes **6**·6MeCN and **7**·2CH<sub>2</sub>Cl<sub>2</sub>.

Atom	<b>6</b> ·6MeCN			<b>7</b> ·2CH <sub>2</sub> Cl <sub>2</sub>		
	Mn <sup>2+</sup>	Mn <sup>3+</sup>	Mn <sup>4+</sup>	Mn <sup>2+</sup>	Mn <sup>3+</sup>	Mn <sup>4+</sup>
Mn(1)	4.165	3.810	<u>3.999</u>	4.136	3.783	<u>3.972</u>
Mn(2)	4.049	3.704	<u>3.888</u>	3.584	<u>3.278</u>	3.442
Mn(3)	3.108	<u>2.842</u>	2.984	4.141	3.787	<u>3.976</u>
Mn(4)	3.185	<u>2.914</u>	3.059	3.137	<u>2.869</u>	3.012
Mn(5)	3.158	<u>2.888</u>	3.032			
Mn(6)	4.134	3.781	<u>3.969</u>			
Mn(7)	4.182	3.825	<u>4.016</u>			

<sup>a</sup> The underlined value is the one closest to the actual charge for which it was calculated. The oxidation state of a particular atom can be taken as the nearest whole number to the underlined value.

Table 3-3. Bond valence sum calculations<sup>a</sup> for selected oxygen atoms in complexes **6**·6MeCN and **7**·2CH<sub>2</sub>Cl<sub>2</sub>.

<b>6</b> ·6MeCN			<b>7</b> ·2CH <sub>2</sub> Cl <sub>2</sub>		
Atom	$V_i$	Assignment	Atom	$V_i$	Assignment
O(1)	1.850	O <sup>2-</sup>	O(11)	1.761	O <sup>2-</sup>
O(2)	1.647	O <sup>2-</sup>	O(12)	2.049	O <sup>2-</sup>
O(3)	2.024	O <sup>2-</sup>	O(13)	1.994	O <sup>2-</sup>
O(4)	1.976	O <sup>2-</sup>	O(14)	1.876	O <sup>2-</sup>
O(5)	2.091	O <sup>2-</sup>	O(15)	1.617	O <sup>2-</sup>
O(6)	1.977	O <sup>2-</sup>	O(16)	1.911	O <sup>2-</sup>
O(7)	1.856	O <sup>2-</sup>			O <sup>2-</sup>
O(8)	1.726	O <sup>2-</sup>			O <sup>2-</sup>

<sup>a</sup> The oxygen atoms is O<sup>2-</sup> if  $V_i \approx 2$ , OH<sup>-</sup> if  $V_i \approx 1$ , and H<sub>2</sub>O if  $V_i \approx 0$ .

The Se geometry is pyramidal, owing to the presence of a stereochemically active lone pair of electrons. The only previous example of the PhSeO<sub>2</sub><sup>-</sup> group bridging in the manner seen in **6** was the polymer [Ph<sub>3</sub>SnO<sub>2</sub>SePh]<sub>n</sub> in which the PhSeO<sub>2</sub><sup>-</sup> ligand symmetrically bridges two Sn atoms.<sup>78</sup> There is evidence for strong intermolecular Se⋯O interactions in **6** involving Se and oxide O atoms, forming chains along the *a* axis of the crystal (Figure 3-3). The Se(1)⋯O(8) distance (2.749(6) Å) is longer than the sum of the

covalent radii of Se and O (1.89 Å), but much shorter than the sum of their van der Waals radii (3.40 Å). This interaction likely involves O( $p_\pi$ ) to Se( $d_\pi$ ) donation into empty Se d-orbitals. Additionally, the Se(6)-O(11) contact (3.327(6) Å), and perhaps also Se(7)-O(12) (3.643(6) Å), likely contribute to the intermolecular interaction.

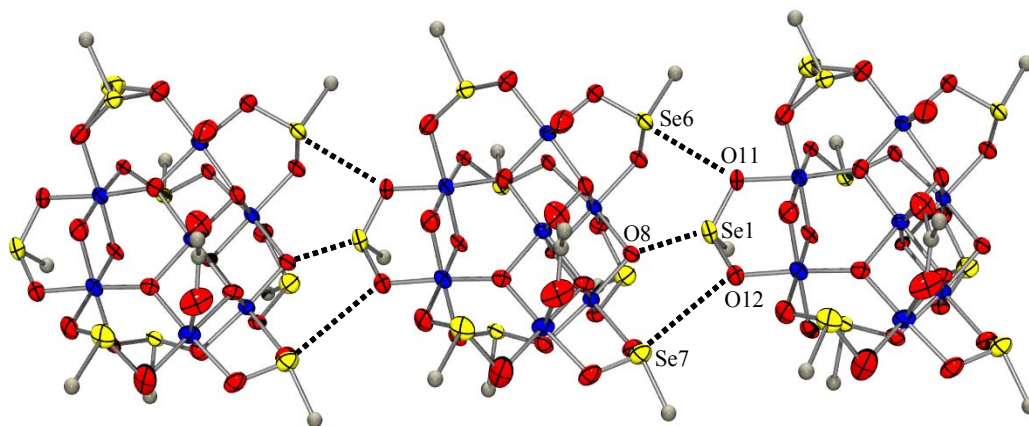


Figure 3-3. ORTEP representation in PovRay format at the 50% probability level of the packing of complex **6** along the *a* axis of the crystal. For clarity, the hydrogen atoms have been omitted, and only the *ipso* C atoms of the phenyl groups are shown.

There is precedent for these types of interactions; there are several examples in the literature of intramolecular Se $\cdots$ O non-bonded interactions, including those in selenoiminoquinones,<sup>79</sup> selenoxocine,<sup>80</sup> and selenazofurin.<sup>81</sup> However, none of these previous examples involve the same kind of seleninate ligands as present in **6**. There are also numerous weak inter-chain contacts apparent in packing diagrams between aromatic rings and/or solvent molecules, but the disorder in these groups discussed in the Experimental Section complicates their clear visualization.

### 3.2.2.2 X-ray crystal structure of [Mn<sub>7</sub>O<sub>8</sub>(O<sub>2</sub>SePh)<sub>9</sub>(H<sub>2</sub>O)] (**7**)

A labeled ORTEP<sup>40</sup> plot in PovRay format of complex **7** is shown in Figure 3-4, together with a stereoview. The crystallographic data and structure refinement details are collected in Table 3-1, and selected interatomic distances and angles are listed in Table

A-4. The complex crystallizes in the monoclinic space group  $P2_1/m$ , with the  $Mn_7$  molecule lying on a mirror plane. For the sake of brevity, references to specific atoms in the following discussion implicitly include their symmetry-related partners. The structure of **7** is very similar to that of **6**, except that the  $MeCO_2^-$  group in the latter has been replaced with a ninth  $PhSeO_2^-$  group.

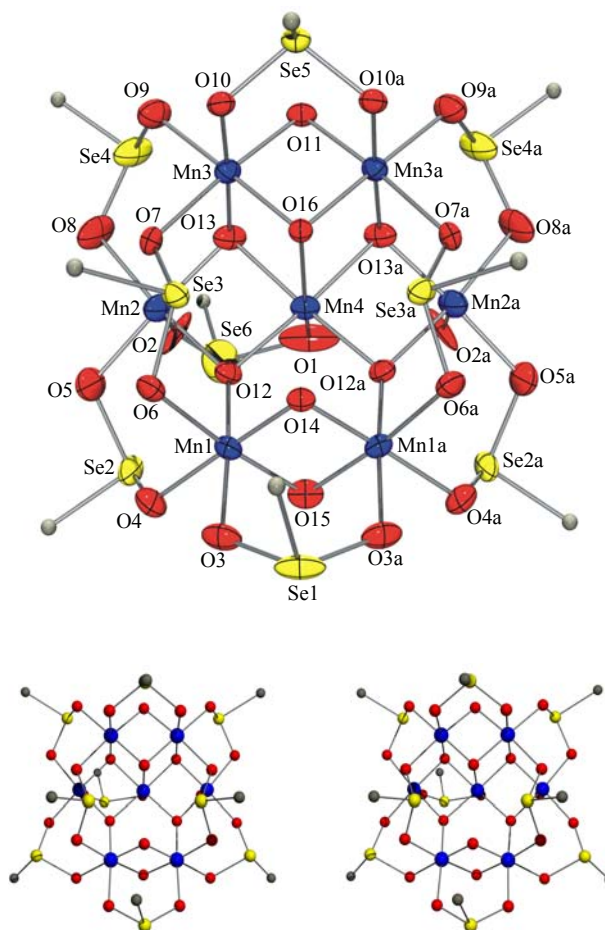


Figure 3-4. ORTEP representation in PovRay format of  $[Mn_7O_8(O_2SePh)_9(H_2O)]$  (**7**) with thermal ellipsoids at the 50% probability level except for the C atoms, together with a stereopair. For clarity, the hydrogen atoms have been omitted, and only the *ipso* C atoms of the phenyl groups are shown. Mn blue; O red; Se yellow; C gray.

Bond valence sum calculations<sup>41</sup> again indicate a  $3Mn^{III}$ ,  $4Mn^{IV}$  trapped-valence situation (Table 3-3). The core has the same structure as that for **6** in Figure 3-2a, with

five-coordinate Mn(2) being square pyramidal ( $\tau = 0.08$ ). The  $\text{PhSeO}_2^-$  for  $\text{MeCO}_2^-$  substitution causes almost insignificant perturbation of the core. The long Mn(4)-O(16) bond (2.276(9) Å) is very similar to that in **6**, and the three  $\text{Mn}^{\text{III}}$  distortion axes are again essentially parallel. As observed with complex **6**, there is a strong intermolecular interaction between Se atoms and oxide O atoms, forming chains along the *a* axis of the crystal, with weak inter-chain contacts. The shortest, strongest contact is  $\text{Se}(1)\cdots\text{O}(11)$  (2.754(6) Å).

Complexes **6** and **7** possess a structure that is quite different from that of any previously characterized  $\text{Mn}_7$  complex. These include  $[\text{Mn}^{\text{II}}_3\text{Mn}^{\text{III}}_4(\text{OMe})_{12}(\text{dbm})_6]$  (dbm<sup>-</sup> is the anion of dibenzoylmethane),<sup>82</sup> the  $[\text{Mn}^{\text{II}}_4\text{Mn}^{\text{III}}_3(\text{OH})_3(\text{hmp})_9\text{Cl}_3]^{3+}$  cation (hmp<sup>-</sup> is the anion of 2-(hydroxymethyl)pyridine),<sup>76,83</sup> and the  $[\text{Mn}^{\text{II}}_4\text{Mn}^{\text{III}}_3(\text{teaH})_3(\text{tea})_3]^{2+}$  cation (teaH<sub>3</sub> = triethanolamine).<sup>84</sup> Table 3-4 shows a comparison of selected Mn-O bond distances and angles for the complexes **6** and **7**. This comparison confirms that the bond distances in the  $[\text{Mn}_7\text{O}_8]^{9+}$  cores are almost superimposable.

Table 3-4. Comparison of selected bond distances (Å) and angles (°) for  $[\text{Mn}_7\text{O}_8(\text{O}_2\text{CMe})(\text{O}_2\text{SePh})_8(\text{H}_2\text{O})]$  (**6**) and  $[\text{Mn}_7\text{O}_8(\text{O}_2\text{SePh})_9(\text{H}_2\text{O})]$  (**7**).

Parameter <sup>a</sup>	<b>6</b>	<b>7</b>
$\text{Mn}^{\text{IV}} - \text{O}$	1.788(6) – 1.852(5)	1.800(6) – 1.845(7)
$\text{Mn}^{\text{III}} - \text{O}$	1.880(6) – 1.944(6)	1.873(8) – 1.963(7)
$\text{Mn}^{\text{IV}} - \text{O}_{\text{carb}}$	1.909(7) – 2.002(6)	1.923(7) – 2.010(8)
$\text{Mn}^{\text{III}} - \text{O}_{\text{carb}}$	1.909(7) – 1.950(6)	1.903(10) – 1.935(8)
$\text{Mn}^{\text{III}} - \text{O}_{\text{elong}}$	2.172(8) – 2.180(7)	2.001(17) – 2.160(12)
$\text{Mn}^{\text{III}} - \text{O}_{\text{w}}$	2.289(8)	2.001(17)
$\text{Mn}^{\text{IV}}\cdots\text{Mn}^{\text{IV}}$	2.722(2) – 2.758(2)	2.740(3) – 2.761(3)
$\text{Mn}^{\text{III}}\cdots\text{Mn}^{\text{III}}$	2.829(2) – 2.856(2)	2.8429(19)
$\text{O} - \text{Mn}^{\text{IV}} - \text{O}$	82.6(2) – 83.7(3)	81.5(3) – 83.1(3)
$\text{Mn}^{\text{III}}\cdots\text{Mn}^{\text{III}}\cdots\text{Mn}^{\text{III}}$	174.10(8)	174.45(12)

<sup>a</sup> O = bridging oxide ion,  $\text{O}_{\text{carb}}$  = bridging  $\text{PhSeO}_2^-$  or  $\text{MeCO}_2^-$  carboxylate,  $\text{O}_{\text{elong}}$  = bridging bridging  $\text{PhSeO}_2^-$  or  $\text{MeCO}_2^-$  carboxylate situated along an  $\text{Mn}^{\text{III}}$  elongation axis,  $\text{O}_{\text{w}}$  = water

### 3.2.3 Magnetochemistry of Complexes 6 and 7

#### 3.2.3.1 DC studies

Variable-temperature DC susceptibility measurements were performed in the 5.0-300 K range on powdered microcrystalline samples of **6**·2H<sub>2</sub>O·½MeCN and **7**·2H<sub>2</sub>O, restrained in eicosane to prevent torquing, in a 5 kG field (Figure 3-5). For complex **6**, the  $\chi_M T$  value of 12.0 cm<sup>3</sup> K mol<sup>-1</sup> at 300 K decreases gradually with decreasing temperature to 3.4 cm<sup>3</sup> K mol<sup>-1</sup> at 5.0 K. For complex **7**, the  $\chi_M T$  value of 12.8 cm<sup>3</sup> K mol<sup>-1</sup> at 300 K decreases gradually to 4.1 cm<sup>3</sup> K mol<sup>-1</sup> at 5.0 K. The spin-only ( $g = 2$ ) value for a molecule composed of non-interacting Mn<sup>III</sup><sub>3</sub>Mn<sup>IV</sup><sub>4</sub> ions is 16.5 cm<sup>3</sup> K mol<sup>-1</sup>. Hence, the molecules appear to have appreciable intramolecular antiferromagnetic interactions.

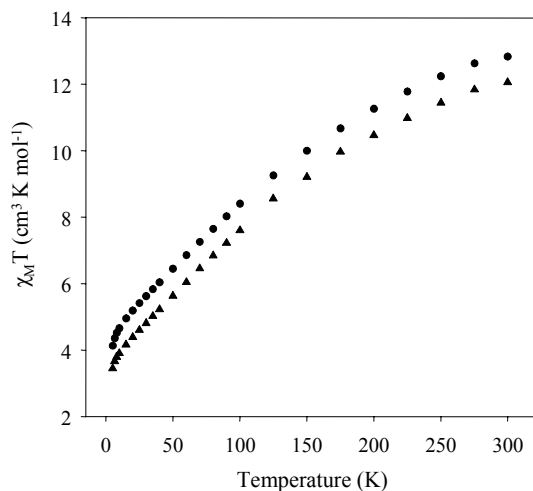


Figure 3-5. Plot of  $\chi_M T$  vs temperature for dried, microcrystalline samples of complex **6**·2H<sub>2</sub>O·½MeCN (▲) and **7**·2H<sub>2</sub>O (●) in eicosane.  $\chi_M$  is the DC molar magnetic susceptibility measured in a 5.0 kG field.

Each complex contains three Mn<sup>III</sup> and four Mn<sup>IV</sup> centers, with total spin (S) values therefore ranging from 0 to 12. The low symmetry and size of the molecules makes very difficult a matrix diagonalization approach, and completely precludes application of the Kambe equivalent operator method<sup>51</sup> to determine the various Mn<sub>2</sub> pairwise exchange

interaction constants ( $J$ ) in the molecule. Efforts were instead concentrated on determining the ground state  $S$  value of the complexes. Thus, magnetization data were collected in the 0.10-70 kG and 1.8-10.0 K field and temperature ranges (Figure 3-6).

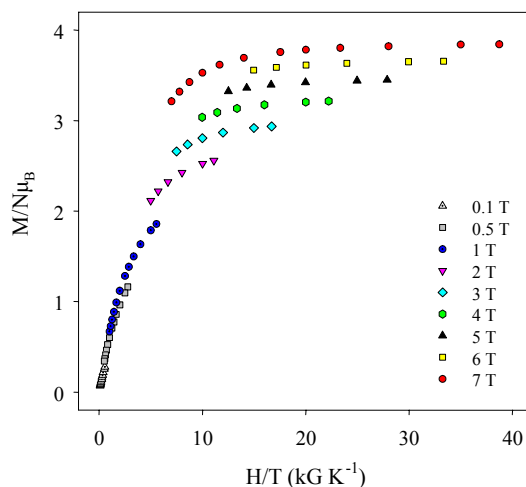


Figure 3-6. Plot of reduced magnetization ( $M/N\mu_B$ ) vs  $H/T$  for a dried microcrystalline sample of  $6 \cdot 2\text{H}_2\text{O} \cdot \frac{1}{2}\text{MeCN}$ ; the DC field value of each of the isofield plots is indicated.

The saturation value in the highest fields is approaching the value of  $\sim 4$  expected for an  $S = 2$  spin. However, it was not possible to obtain a reasonable fit for these data. This is likely due to the intermolecular exchange interactions mediated by the intermolecular  $\text{Se} \cdots \text{O}$  contacts that were detected in the crystal structures and which are not incorporated in the fitting model. In addition, there may be low-lying excited states that are populated even at very low temperatures. The latter is unfortunately a common problem in higher nuclearity clusters, due to a high density of spin states and/or the presence of spin frustration effects. Spin frustration, in its general sense, is the presence of competing antiferromagnetic exchange interactions of comparable magnitude, which can often prevent (frustrate) the antiparallel alignment of all spins. Such spin frustration effects have been previously described in detail.<sup>85,86</sup> The ground state spin value and the energies of low-lying excited states become sensitive to the precise magnitude of the

competing exchange interactions. The triangular arrangement of coupled metal ions, as found in **6** and **7**, is the textbook topology for spin frustration if the couplings are antiferromagnetic, since the spins cannot all be antiparallel to all their neighbors. It is anticipated, based on the properties of dinuclear systems, that all the oxide-bridged  $\text{Mn}^{\text{IV}}\text{Mn}^{\text{IV}}$ ,  $\text{Mn}^{\text{IV}}\text{Mn}^{\text{III}}$  and  $\text{Mn}^{\text{III}}\text{Mn}^{\text{III}}$  pairwise exchange interactions in **6** and **7** will possibly be antiferromagnetic, and thus the presence of spin frustration in this core is expected. The strongest exchange interaction within the molecule is very likely a strong antiferromagnetic coupling within the  $\text{Mn}^{\text{IV}}_2$  units. This  $\text{Mn}^{\text{IV}}_2$  interaction in several dinuclear complexes with the  $[\text{Mn}^{\text{IV}}_2(\mu\text{-O})_2(\mu\text{-O}_2\text{CR})]$  core is in the range from  $-37$  to  $-67\text{ cm}^{-1}$ , depending strongly on the  $\text{Mn}^{\text{IV}}\text{-O-Mn}^{\text{IV}}$  angle,<sup>72a,75</sup> and it is likely that the  $\text{Mn}^{\text{IV}}_2$  interactions in **6** and **7** are of similar magnitude. This is also the magnitude expected for the various  $\text{Mn}^{\text{III}}\text{Mn}^{\text{IV}}$  interactions.<sup>74</sup>

The lowest temperature data in Figure 3-5 and the saturation value of  $M/N\mu_B$  in Figure 3-6 suggest a small ground state spin value of  $S \sim 2$  for **6**·2H<sub>2</sub>O·½MeCN and **7**·2H<sub>2</sub>O, but this is not the safest way to determine the ground state spins because of potential complications from Zeeman effects from the applied DC field. A better way is to measure the AC susceptibility, which does not involve use of a DC field. Such studies were carried out with a 3.5 G AC field oscillating at frequencies up to 1488 Hz. In fact, the AC in-phase susceptibilities ( $\chi_M' T$ ) for the two complexes are essentially superimposable, and turn out to be very similar to the DC susceptibilities ( $\chi_M T$ ). The AC  $\chi_M' T$  and DC  $\chi_M T$  for **6** are compared in Figure 3-7.

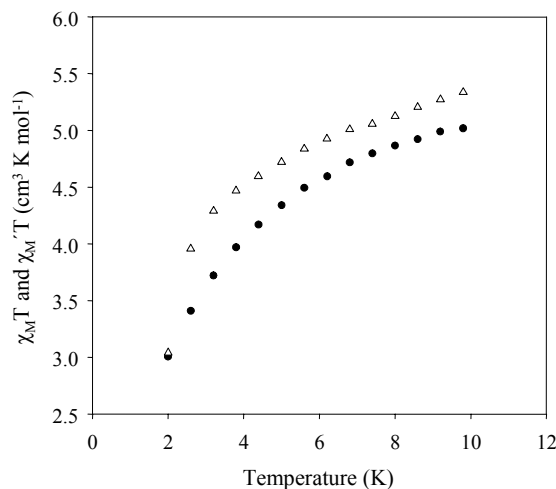


Figure 3-7. Plot of  $\chi_M' T$  vs temperature for complex **6**·2H<sub>2</sub>O·½MeCN in the 2.0-10.0 K range from AC magnetic susceptibility measurements ( $\Delta$ ), and including the DC  $\chi_M T$  data ( $\bullet$ ) from Figure 3-5 for this temperature range. The AC data were measured with a 3.5 G AC field oscillating at 997 Hz.

The strongly sloping  $\chi_M' T$  vs  $T$  plot is strongly indicative of the population of low-lying excited states, since occupation of only the ground state would give an essentially temperature-independent value. Extrapolation suggests the plot is heading to a  $\chi_M T$  value of  $\sim 3 \text{ cm}^3 \text{ K mol}^{-1}$ , the value of an  $S = 2$  state with  $g = 2$ , before a noticeable downturn at the lowest temperatures due to relaxation effects (*vide infra*). We conclude that the ground state spin of **6** and **7** is  $S = 2$ , but that there are several low-lying excited states that are significantly populated even below 10 K. Note that the extrapolation from higher temperatures also avoids complications from weak intermolecular interactions.

### 3.2.3.2 AC studies

With such a small ground state, it seemed unlikely that complexes **6** and **7**, even with significant magnetic anisotropy as a result of their three parallel Mn<sup>III</sup> elongation axes, would possess a significantly large barrier to magnetization relaxation to be SMMs. As a result, we did not expect to see an out-of-phase AC susceptibility signal ( $\chi_M''$ ), an indicator of slow magnetization relaxation. However, with AC oscillation frequencies up

to 997 Hz (Figure 3-8), a frequency-dependent  $\chi_M''$  signal was indeed observed for complex **6**, or rather the tail of a  $\chi_M''$  signal whose peak lies at a temperature significantly below 1.8 K. It is very important to note that similar  $\chi_M''$  signals were seen whether we used crystals kept wet with mother liquor (i.e., **6**·6MeCN) or those that had been filtered and dried (i.e., **6**·2H<sub>2</sub>O·½MeCN), showing that for this compound the drying and consequent change in solvation content has no significant effect on the magnetic properties. Since we did not believe **6** could be a SMM, we instead suspected that this signal might be due to a spin-chain behavior resulting from the intermolecular exchange interactions mediated by the short Se···O contacts observed in the crystal structure. We thus decided to investigate the magnetic properties at lower temperatures.

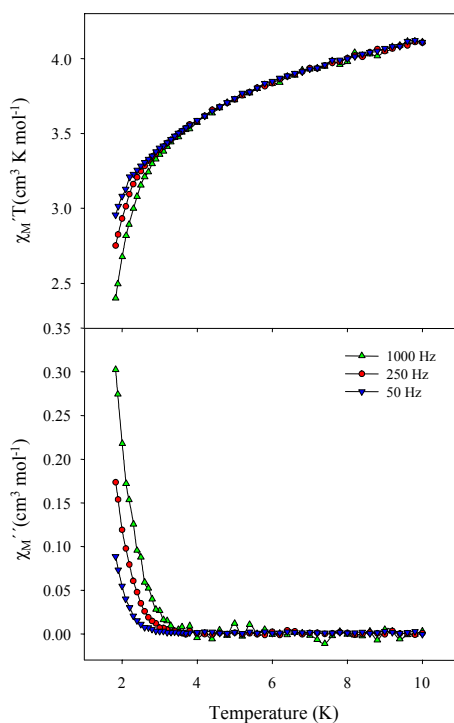


Figure 3-8. In-phase and out-of-phase ( $\chi_M''$ ) AC susceptibility signals for a dried, microcrystalline sample of **6**·2H<sub>2</sub>O·½MeCN at the indicated AC oscillation frequencies.

### 3.2.3.3 Hysteresis studies below 1.8 K

Single-molecule magnets (SMMs) or single-chain magnets (SCMs)<sup>87-91</sup> below their blocking temperature,  $T_B$ , will exhibit hysteresis in their magnetization vs DC field response, the classical property of a magnet. Such studies were therefore performed on a single crystal of **6**·6MeCN using a micro-SQUID apparatus;<sup>92</sup> crystals were kept wet with mother liquor to prevent any damage from loss of solvent. Measurements were performed in the 0.04 to 7.0 K temperature range, using different field sweep rates from 0.008 to 0.56 T/s. The sensitivity and time resolution of a micro-SQUID magnetometer allows the study of very small single crystals in good contact with a thermal bath. The temperature dependence at a fixed sweep rate of 0.07 T/s is shown in Figure 3-9a. Hysteresis loops become evident in the scans at 4 K, but they only have a small coercivity. The latter increases, but only slightly, with decreasing temperature down to 0.5 K, and then is constant down to 0.04 K. In Figure 3-9b is shown the sweep rate dependence of the loops at a constant temperature of 0.04 K. A small decrease in coercivity is observed with decreasing sweep rate, but again the change is only slight. This behavior is not that expected for a SMM, for which one would expect a greater dependence of the coercivity on the temperature and on the sweep rate. Instead we believe that the hysteresis behavior is the consequence of the one-dimensional chain structure of **6** and **7** in the solid state. Thus, complex **6** (and by implication **7**, given its very similar structure) appears to be a new example of the small but growing family of single-chain magnets (SCMs).<sup>93</sup> This implies that the intermolecular interactions mediated by the Se···O contacts are ferromagnetic in nature, leading to a parallel alignment of spins of the interacting Mn<sub>7</sub> units along the chain, a significant barrier (versus thermal energy) to magnetization reversal, and the resulting hysteresis loops.

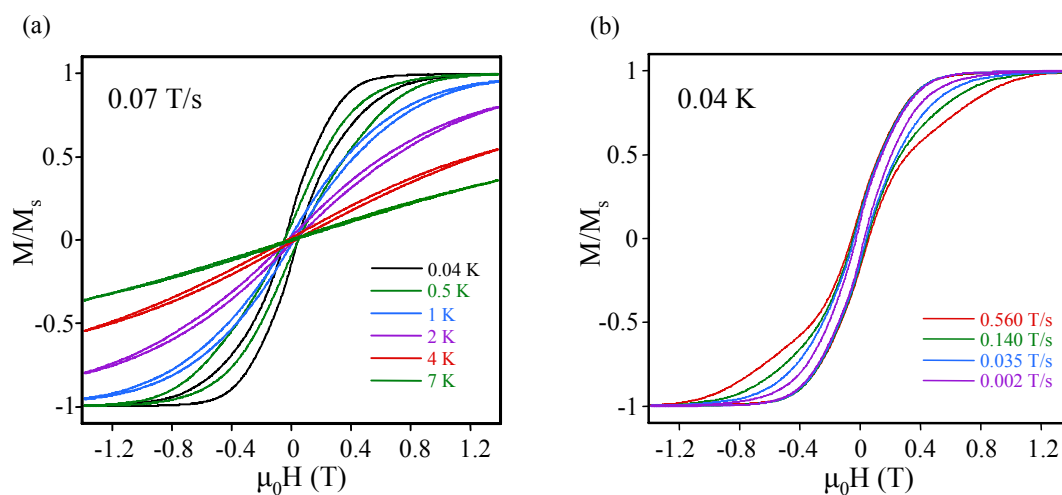


Figure 3-9. Magnetization vs DC field plots for a single crystal of complex **6·6MeCN** at (a) the indicated temperatures and a fixed field sweep rate of 0.07 T/s; and (b) four sweep rates and a fixed temperature of 0.04 K. The magnetization is normalized to its maximum value,  $M_s$ .

However, closer inspection of the loops in Figure 3-9 indicates that this ferromagnetic coupling between molecules within the chains is not sufficient to completely account for the observed hysteresis behavior. Following saturation of the magnetization in one direction with a large field, the reversal of the direction of the magnetization should occur after the field has been swept past zero for a ferromagnetically-coupled chain. However, this is clearly not the case in Figure 3-9; the reversal of the magnetization direction begins before zero field. This feature is characteristic of the presence of antiferromagnetic interactions, and we assign these as being inter-chain interactions mediated by the weak contacts observed in the crystal structure. Similar behavior has been observed in some SMM systems, including  $[\text{CeMn}_8\text{O}_8(\text{O}_2\text{CMe})_{12}(\text{H}_2\text{O})_4]^{94}$  and the  $\text{Fe}_{19}$  SMMs.<sup>95</sup>

Since the hysteresis loops are suggestive of antiferromagnetic inter-chain interactions, we sought additional evidence for their presence, and this was obtained from the Curie-Weiss plot of the lowest temperature DC susceptibility data, shown in

Figure 3-10. The Weiss constant is obtained from the  $x$ -axis intercept, and this is -2.0 K, confirming the weakest interaction in the system to be antiferromagnetic. This is assigned to the inter-chain interaction.

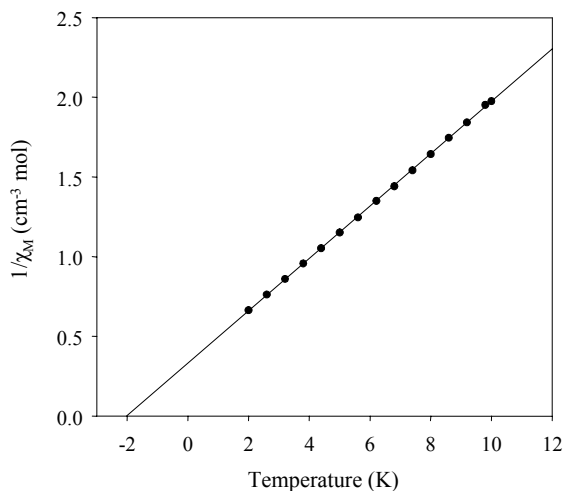


Figure 3-10. Curie-Weiss plot for  $6 \cdot 2\text{H}_2\text{O} \cdot \frac{1}{2}\text{MeCN}$  showing a negative (antiferromagnetic) intercept assigned to inter-chain interactions.

To characterize the system further, we collected magnetization decay data to determine the barrier to magnetization relaxation. The magnetization of the sample was saturated in one direction with a large applied field at 5 K. The temperature was decreased to a chosen value in the 0.04-1.0 K range, the applied field was removed, and the magnetization of the sample was monitored with time. The resulting data are shown in Figure 3-11a. The decay data at each temperature were analyzed to give a set of relaxation time ( $\tau$ ) vs temperature data, which were used to construct the Arrhenius plot of Figure 3-11b, based on the Arrhenius relationship of eq 3-2, where  $\tau_0$  is the pre-exponential factor,  $U_{\text{eff}}$  is the mean effective barrier to relaxation, and  $k$  is the Boltzmann constant.

$$\tau = \tau_0 \exp(U_{\text{eff}}/kT) \quad (3-2)$$

The fit of the thermally-activated region above  $\sim 0.5$  K, shown as the dashed line in Figure 3-11b, gave  $U_{\text{eff}} = 9.87 \text{ cm}^{-1} = 14.2 \text{ K}$  and  $1/\tau_0 = 1.9 \times 10^{-9} \text{ s}^{-1}$ . Below this temperature, the relaxation time levels off and becomes temperature-independent at  $\sim 10^4$  s. This temperature-independence of the relaxation rate is the characteristic signature of quantum tunneling of the magnetization through the anisotropy barrier.

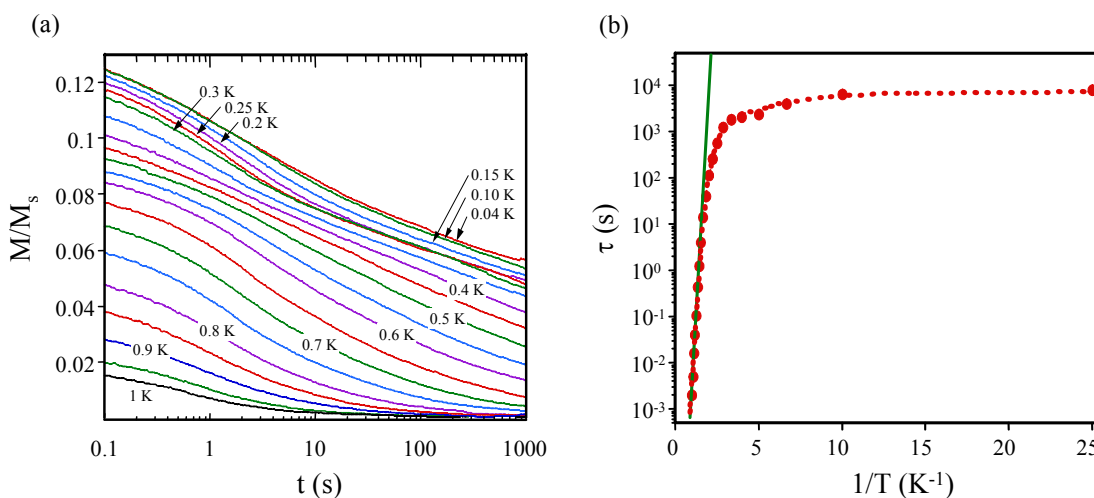


Figure 3-11. Relaxation time vs temperature studies for a single crystal of **6·6MeCN**. (a) Magnetization vs time decay plots at the indicated temperatures. (b) Arrhenius plot using the resulting relaxation time ( $\tau$ ) vs  $T$  data. The dashed line is a fit of the thermally-activated region to the Arrhenius equation. See the text for the fit values.

### 3.2.3.4 Origin of the relaxation barrier

The picture that emerges from the above magnetic analysis of complex **6** is that there is a significant barrier to magnetization relaxation of 14.2 K in this compound. As a result, at low enough temperatures the compound exhibits the characteristic behavior of a magnet, namely magnetization hysteresis. This cannot be rationalized on the basis of single-molecule magnetism, because the spin of the molecule is only  $S = 2$  and this is unlikely to give a significant barrier to magnetization relaxation. The upper limit ( $U$ ) of the latter for an integer spin system is given by  $U = S^2|D|$ , where  $D$  is the axial anisotropy

(zero-field splitting) parameter. Even assuming a value of  $D$  of  $-1.0 \text{ cm}^{-1}$ , which is actually larger (more negative) than typical for  $\text{Mn}_x$  clusters, would still only give a barrier  $U$  of  $4.0 \text{ cm}^{-1}$  ( $5.8 \text{ K}$ ). When one then takes into account that the actual (or effective) barrier ( $U_{\text{eff}}$ ) is usually considerably less than  $U$ , because the magnetization can tunnel through the barrier via higher-lying  $m_s$  levels rather than going over the top, then it becomes impossible to convincingly rationalize the observed effective barrier ( $U_{\text{eff}}$ ) of  $9.87 \text{ cm}^{-1} = 14.2 \text{ K}$  on the basis of the properties of the individual molecules of **6**.

Instead, as we mentioned earlier, we interpret the observed behavior as a result of the one-dimensional chains formed between  $\text{Mn}_7$  molecules, giving a single-chain magnet (SCM). The latter is a relatively new phenomenon in molecular magnetism, but it is nevertheless now well established with several well-documented examples.<sup>87-91</sup> In such a system, the magnetization relaxation barrier and the resulting slow relaxation rates are caused by one-dimensional intermolecular exchange interactions between the constituent spin carriers. Such chains may be either homometallic<sup>90</sup> or heterometallic,<sup>88,91</sup> and can even comprise an alternating metal/organic radical arrangement.<sup>89</sup>

According to Glauber theory for one-dimensional Ising chains,<sup>93</sup> the magnetization relaxation rate follows an Arrhenius law (eq 3-3) with a barrier given by  $8JS^2$  (for the  $-2J\hat{S}_i\hat{S}_j$  convention), where  $S$  is the spin of the repeating unit and  $J$  is the exchange parameter between these units.

$$\tau = \tau_0 \exp(8JS^2/kT) \quad (3-3)$$

If the repeating unit also possesses intrinsic anisotropy and thus a magnetization relaxation barrier of  $U = S^2|D|$ , then there will be two contributions to the total relaxation barrier, that from the anisotropy of the molecular unit and that from the interaction

between these units. This was clearly described in a recent paper by Miyasaka *et al* on a series of related SCMs,<sup>88</sup> and the corresponding Arrhenius relationship for such a system can then be expressed by eq 3-4, where  $\Delta = (8J + |D|)S^2$  is the barrier to magnetization relaxation, or rather its upper limit in the absence of tunneling.

$$\tau = \tau_0 \exp(\Delta/kT) \quad (3-4)$$

The results described in the present work can be rationalized within the framework of the above model. The Mn<sub>7</sub> cluster has a small but nevertheless significant spin of  $S = 2$ , and in the presence of some easy-axis (or Ising) type anisotropy, as expected for axially-elongated Mn<sup>III</sup>, there will be a small barrier to magnetization relaxation. This is insufficient to provide a single-molecule magnet, but the interactions between the Mn<sub>7</sub> units (Figure 3-3) provide an additional contribution to the barrier. As a result, and even allowing for the diminution of the barrier by tunneling effects, there is still a large enough barrier ( $U_{\text{eff}}$ ) of 14.2 K to yield out-of-phase AC susceptibility signals and hysteresis.

The relaxation barrier for complex **6** of 14.2 K is unfortunately rather small compared with other SCMs in the literature, which fall in the 50 – 154 K range.<sup>87-91</sup> In addition, there are noticeable inter-chain interactions, so the best description of **6** is as an SCM with weak inter-chain coupling, in the same way that SMMs with weak intermolecular interactions are also known.<sup>94,95</sup> The important thing is that in these SMMs, and also complex **6**, the intermolecular or inter-chain interactions are weak enough to be considered a perturbation of the SMM or SCM behavior, respectively, rather than strong enough to give a true three-dimensional ordered solid. Clearly the frequency-dependent AC data and the sweep rate and temperature-dependent coercivities in the hysteresis loops rule out **6** as a 3-dimensional magnet. Thus, regardless of its low

anisotropy barrier, it is appropriate to call **6** a SCM. It would also be the first example to consist of a chain of polynuclear metal clusters rather than mononuclear or dinuclear repeating units, and it is also the first to exhibit the temperature-independent relaxation regime in the Arrhenius plot characteristic of quantum tunneling. It thus represents a significant new addition to the SCM family.

### 3.3 Conclusions

The use of benzeneseleninic acid (PhSeO<sub>2</sub>H) in attempted ligand substitution reactions with [Mn<sub>12</sub>O<sub>12</sub>(O<sub>2</sub>CMe)<sub>16</sub>(H<sub>2</sub>O)<sub>4</sub>] (**1**) instead causes a structural change and has afforded two new heptanuclear Mn clusters, [Mn<sub>7</sub>O<sub>8</sub>(O<sub>2</sub>CMe)(O<sub>2</sub>SePh)<sub>8</sub>(H<sub>2</sub>O)] (**6**) and [Mn<sub>7</sub>O<sub>8</sub>(O<sub>2</sub>SePh)<sub>9</sub>(H<sub>2</sub>O)] (**7**), which possess a novel [Mn<sup>III</sup><sub>3</sub>Mn<sup>IV</sup><sub>4</sub>(μ<sub>3</sub>-O)<sub>5</sub>(μ-O)<sub>3</sub>]<sup>9+</sup> core and represent the first examples of transition metal clusters ligated by PhSeO<sub>2</sub><sup>-</sup> groups. Magnetic studies suggest a low ground state spin value of S = 2 and the appearance in the AC susceptibility of out-of-phase signals characteristic of slow magnetization relaxation. Studies down to 0.04 K reveal that these species are not new additions to the growing family of single-molecule magnets (SMMs). Instead, the slow relaxation is caused by single-chain magnetism behavior, with the relaxation barrier arising from a combination of the molecular anisotropy and the exchange interaction between the individual Mn<sub>7</sub> molecules. These complexes are thus interesting for a number of reasons, including aesthetically pleasing structures and their average oxidation state of +3.6, which is unusually high for a high nuclearity Mn cluster. It will be interesting to see in future work whether the PhSeO<sub>2</sub><sup>-</sup> allows access to other high oxidation state species.

Finally, it is important to remember for the future that the observation of the χ<sub>M</sub>'' signals in Figure 2-8 for an ostensibly molecular compound did not presage the observation of the characteristic properties of a SMM. This represents an important

reminder that it is by not safe to take the appearance of  $\chi_M''$  signals as sufficient proof that a SMM has been prepared.

### 3.4 Experimental

#### 3.4.1 Syntheses

All manipulations were performed under aerobic conditions using materials as received, except where otherwise noted.  $[\text{Mn}_{12}\text{O}_{12}(\text{O}_2\text{CMe})_{16}(\text{H}_2\text{O})_4] \cdot 2\text{MeCO}_2\text{H} \cdot 4\text{H}_2\text{O}$  (**1**) was prepared as described elsewhere.<sup>50</sup>

**$[\text{Mn}_7\text{O}_8(\text{O}_2\text{CMe})(\text{O}_2\text{SePh})_8(\text{H}_2\text{O})]$  (**6**).** To a stirred solution of complex **1** (0.50 g, 0.24 mmol) in MeCN (75 cm<sup>3</sup>) was added solid PhSeO<sub>2</sub>H (0.83 g, 4.4 mmol) in portions, and the mixture was stirred for 12h. The deep brown solution containing some brown powder was filtered through Celite. The volume of the filtrate was reduced by half by roto-evaporation, and it was then allowed to evaporate slowly in air. Crystals formed slowly over one week, and these were suitable for X-ray studies if maintained in contact with the mother liquor to prevent the loss of interstitial solvent. After one week, the crystals were isolated by filtration, washed with small volumes of MeCN, and dried under vacuum; yield ~35%. The dried crystals are hygroscopic, and analyze for **6**·2H<sub>2</sub>O·½MeCN. Anal. Calcd (found) for C<sub>51</sub>H<sub>50.5</sub>Se<sub>8</sub>N<sub>0.5</sub>O<sub>29</sub>Mn<sub>7</sub>: C, 28.25 (28.26); H, 2.44 (2.37); N, 0.32 (0.29). Selected IR data (KBr, cm<sup>-1</sup>): 1636 (w), 1542 (m), 1474 (m), 1441 (m), 1419 (m), 1172 (w), 1094 (m), 1063 (m), 1021 (w), 997 (w), 747 (vs), 712 (vs), 686 (vs), 623 (s), 599 (s), 528 (s), 439 (m).

**$[\text{Mn}_7\text{O}_8(\text{O}_2\text{SePh})_9(\text{H}_2\text{O})]$  (**7**).** A solution of complex **1** (0.50 g, 0.24 mmol) in MeCN (75 cm<sup>3</sup>) was treated with solid PhSeO<sub>2</sub>H (0.83 g, 4.4 mmol) in portions. The reaction mixture was stirred for 48h, during which time the amount of a brown precipitate continuously increased. The latter was collected by filtration, re-dissolved in CH<sub>2</sub>Cl<sub>2</sub>

(30 cm<sup>3</sup>) and filtered through Celite. Vapor diffusion of Et<sub>2</sub>O into the CH<sub>2</sub>Cl<sub>2</sub> solution slowly produced crystals, and these were suitable for X-ray crystallography if maintained in contact with the mother liquor to prevent the loss of interstitial solvent. After 2 weeks, crystals were isolated by filtration, washed with Et<sub>2</sub>O, and dried under vacuum; yield 40%. The dried material is hygroscopic, analyzing for 7·2H<sub>2</sub>O. Anal. Calcd (found) for C<sub>54</sub>H<sub>51</sub>Se<sub>9</sub>O<sub>29</sub>Mn<sub>7</sub>: C, 28.71 (28.65); H, 2.28 (2.19); N, 0.00 (0.02). Selected IR data (KBr, cm<sup>-1</sup>): 3054 (w), 1650 (w), 1635 (w), 1576 (w), 1540 (w), 1475 (w), 1441 (m), 1418 (w), 1336 (w), 1176 (w), 1065 (m), 1021 (w), 998 (w), 744 (vs), 709 (vs), 687 (vs), 622 (s), 599 (s), 530 (s).

### 3.4.2 X-ray Crystallography

Data were collected using a Siemens SMART PLATFORM equipped with a CCD area detector and a graphite monochromator utilizing MoK<sub>α</sub> radiation ( $\lambda = 0.71073 \text{ \AA}$ ). Suitable single crystals of 6·6MeCN and 7·2CH<sub>2</sub>Cl<sub>2</sub> were attached to glass fibers using silicone grease and transferred to the goniostat where they were cooled to -100 °C for characterization and data collection. Each structure was solved by direct methods (SHELXTL)<sup>64</sup> and standard Fourier techniques, and was refined using full-matrix least-squares methods. All non-hydrogen atoms were refined anisotropically. Hydrogen atoms were placed in calculated positions and refined with the use of a riding model. Cell parameters were refined using up to 8192 reflections. For each complex, a full sphere of data (1850 frames) was collected using the  $\omega$ -scan method (0.3° frame width). The first 50 frames were re-measured at the end of data collection to monitor instrument and crystal stability (maximum correction on I was < 1%). Absorption corrections by integration were applied based on measured indexed crystal faces.

A preliminary search of reciprocal space for **6**·6MeCN revealed a set of reflections with no symmetry and no systematic absences. An initial choice of the centrosymmetric space group  $P\bar{1}$  was subsequently confirmed by the successful solution of the structure. The asymmetric unit contains the Mn<sub>7</sub> molecule and six disordered MeCN molecules. The solvent molecules could not be modeled properly, and the program SQUEEZE,<sup>96</sup> a part of the PLATON<sup>97</sup> package of crystallographic software, was used to calculate the solvent disorder area and remove its contribution to the overall intensity data. The phenyl rings in two of the PhSeO<sub>2</sub><sup>-</sup> ligands [C(7)-C(12) and C(43)-C(48)] were disordered. Their site occupancy factors were dependently refined to 85:15% and 70:30%, respectively. Atoms of the minor disorder position in each case were refined with isotropic thermal parameters. Both Se(4) and Se(5) were disordered about two (main) positions and the occupancies refined to 76:24% and 51:49%, respectively; the phenyl rings in these ligands were not involved in the disorder. Additionally, the acetate ligand bridging Mn(4)-Mn(5) was disordered about two positions, where the minor disorder position was bridging Mn(3) and Mn(4). This disorder was very minor and could not be modeled; a peak of 1.68 e Å<sup>-3</sup> appears where the acetate central atom [C(49)] should be, but the corresponding methyl peak [C(50)] could not be found and properly refined. A total of 830 parameters were refined in the final cycle of refinement using 33358 reflections with  $I > 2\sigma(I)$  to yield  $R1$  and  $wR2$  of 5.91% and 14.96%, respectively. The final difference Fourier map was essentially featureless, the largest peak being 1.68 e Å<sup>-3</sup> and the deepest hole being -0.78 e Å<sup>-3</sup>.

For complex **7**·2CH<sub>2</sub>Cl<sub>2</sub>, an initial survey of a portion of reciprocal space located a set of reflections with a monoclinic lattice. Analysis of the full data set revealed that the

space group was  $P2_1/m$ . The asymmetric unit contains half of the  $Mn_7$  molecule and one disordered  $CH_2Cl_2$  molecule. The solvent molecule was disordered and could not be modeled properly, so the program SQUEEZE<sup>96</sup> was used to calculate the solvent disorder area and remove its contribution to the overall intensity data. The phenyl rings in two of the  $PhSeO_2^-$  ligands [C(1)-C(6) and C(51)-C(56)] were disordered about the crystallographic mirror plane that bisects the molecule. Their site occupancy factors were fixed at 50%. Additionally, the phenyl rings in two  $PhSeO_2^-$  ligands not centered over the mirror plane [C(31)-C(36) and C(41)-C(46)] were disordered over two sites. Their site occupancy factors were dependently refined to 53:47% and 50:50%, respectively; atoms of minor disorder positions were refined with isotropic thermal parameters. Se(2) and its phenyl ring were disordered about two positions and the occupancies dependently refined to 67:33% and 32:68%, respectively. Finally, Se(6) and its phenyl ring [C(61)-C(66)] bridge Mn(2) and Mn(4) and, because of the mirror symmetry, Mn(4) and Mn(2a). The disorder is with a water molecule. The site occupancy factors were refined to 50%. As a precaution, the structure was also solved and refined in space group  $P2_1$ , the mirror symmetry removed, but the amount of disorder was not changed compared with the structure in space group  $P2_1/m$ . A total of 328 parameters were refined in the final cycle of refinement using 29004 reflections with  $I > 2\sigma(I)$  to yield  $R1$  and  $wR2$  of 8.73% and 24.55%, respectively. The final difference Fourier map was essentially featureless, with the largest peak and deepest hole being 1.704 and -1.540 e  $\text{\AA}^{-3}$ , respectively.

CHAPTER 4  
AN INVESTIGATION OF THE REACTIVITY OF Mn<sub>12</sub> COMPLEXES WITH  
DIMETHYLARSINIC ACID: NEW Mn<sub>4</sub> CUBANE COMPLEXES AND Mn<sub>16</sub>  
SINGLE-MOLECULE MAGNETS

**4.1 Introduction**

The search for new polynuclear 3d transition metal complexes has intensified over recent years largely as a result of the superparamagnetic-like properties exhibited by a number of such clusters.<sup>19,22,23,27</sup> The magnetic behavior results from a combination of high ground state spin (S) and large, negative magnetic anisotropy as gauged by the axial zero-field splitting parameter (D) of a molecule.<sup>12,21-23</sup> Together, these two parameters give rise to an energy barrier (U) for magnetization reversal, the magnitude of which is given by  $S^2|D|$  and  $(S^2-1/4)|D|$  for integer and non-integer spin systems, respectively.<sup>19</sup> The first complex to display such superparamagnetic-like behavior as evidenced by hysteresis loops obtained from magnetization vs DC field studies was [Mn<sub>12</sub>O<sub>12</sub>(O<sub>2</sub>CMe)<sub>16</sub>(H<sub>2</sub>O)<sub>4</sub>] $\cdot$ 2MeCO<sub>2</sub>H $\cdot$ 4H<sub>2</sub>O (**1**).<sup>27</sup> Subsequent studies proved the origin of the magnetic properties to be intrinsic to the molecule, i.e., molecules of **1** are discrete magnetically non-interacting units, and such complexes have been consequently termed single-molecule magnets (SMMs).<sup>25</sup>

Much research has been devoted to the area of single-molecule magnetism, with the principal objective being the preparation of a SMM that behaves as a magnet at technologically relevant temperatures, i.e., at least 77 K (that of liquid N<sub>2</sub>). The goal has been approached primarily by two means: (i) the preparation of novel 3d metal carboxylate clusters possessing differing topologies that may behave as SMMs and (ii)

the addition of new derivatives to already existing families of SMMs so that structural features may be correlated with magnetic properties and ultimately, a rational synthetic method for improved SMMs may be developed. Progress toward this end has resulted in the isolation of a number of SMMs, most of which are Mn clusters.<sup>13,32,33,38,39,46,47,56-59,61-63,66,94,98-114</sup> Several complexes comprising V,<sup>115</sup> Co,<sup>116</sup> Ni<sup>117</sup> and Fe<sup>95,118</sup> also behave as SMMs however. By far, single-molecule magnets composed of Mn centers are the most abundant, and this likely results from the spin associated with the accessible oxidation states of Mn and from the magnetic anisotropy that arises from the presence of Jahn-Teller elongation axes of Mn<sup>III</sup> ions. Some of the most well-studied families of single-molecule magnets include Mn<sub>12</sub>, [Mn<sub>12</sub>]<sup>-</sup> and [Mn<sub>12</sub>]<sup>2-</sup> complexes.<sup>13,38,46,61,100,113</sup>

An important avenue of approach involves the study of the reactivity of SMMs with various ligands, chelating, non-carboxylate and otherwise. With this strategy, a knowledge base of the reactivity properties of various SMMs has been developed and new polynuclear clusters that behave as high-spin molecules and/or SMMs have been accessed. Reported progress along these lines includes the characterization of clusters obtained from the reactions of Mn<sub>12</sub> complexes with non-carboxylate ligands.<sup>32,33,39,47,58,101</sup> Such studies were first reported for nitric acid, where reactions with [Mn<sub>12</sub>O<sub>12</sub>(O<sub>2</sub>CCH<sub>2</sub>Bu<sup>t</sup>)<sub>16</sub>(H<sub>2</sub>O)<sub>4</sub>] with four equivalents of HNO<sub>3</sub> yielded [Mn<sub>12</sub>O<sub>12</sub>(O<sub>2</sub>CCH<sub>2</sub>Bu<sup>t</sup>)<sub>12</sub>(NO<sub>3</sub>)<sub>4</sub>(H<sub>2</sub>O)<sub>4</sub>].<sup>32</sup> Similarly, reactions of diphenylphosphinic acid (Ph<sub>2</sub>PO<sub>2</sub>H) with [Mn<sub>12</sub>O<sub>12</sub>(O<sub>2</sub>CR)<sub>16</sub>(H<sub>2</sub>O)<sub>4</sub>] (R = Me (**1**), Ph (**8**)) gave [Mn<sub>12</sub>O<sub>12</sub>(O<sub>2</sub>CMe)<sub>8</sub>(O<sub>2</sub>PPh<sub>2</sub>)<sub>8</sub>(H<sub>2</sub>O)<sub>4</sub>]<sup>33</sup> and [Mn<sub>12</sub>O<sub>12</sub>(O<sub>2</sub>CPh)<sub>7</sub>(O<sub>2</sub>PPh<sub>2</sub>)<sub>9</sub>(H<sub>2</sub>O)<sub>4</sub>].<sup>58</sup> In each case, the [Mn<sub>12</sub>O<sub>12</sub>]<sup>16+</sup> core was retained with the substitution causing only a slight

distortion. In further work, we and other groups have extended these studies to include reactions with  $(\text{PhO})_2\text{PO}_2\text{H}$ ,<sup>47</sup>  $\text{PhSO}_3\text{H}$ ,<sup>39</sup>  $\text{MeSO}_3\text{H}$ ,<sup>101</sup> and more recently,  $\text{PhSeO}_2\text{H}$ .<sup>119</sup>

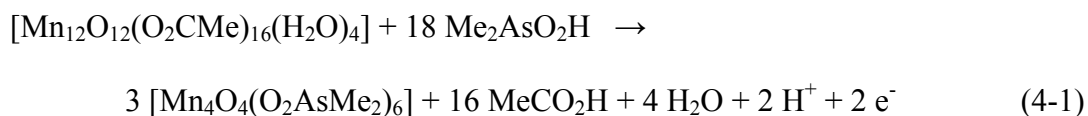
As part of our continuing interest in the reactivity of non-carboxylate ligands with  $[\text{Mn}_{12}\text{O}_{12}(\text{O}_2\text{CMe})_{16}(\text{H}_2\text{O})_4]$ , we decided to shift the focus of our investigation to a previously unexplored reactant, namely dimethylarsinic acid ( $\text{Me}_2\text{AsO}_2\text{H}$ ). The latter is very similar to  $\text{Ph}_2\text{PO}_2\text{H}$ , which was already shown to yield new  $\text{Mn}_{12}$  derivatives upon reaction with either **1** or **8**,<sup>33,58</sup> and a survey of the literature shows that oftentimes, the  $\text{Me}_2\text{AsO}_2^-$  analogue of a complex with ligation by  $\text{Ph}_2\text{PO}_2^-$  can be prepared.<sup>120</sup> However, we were still interesting in exploring this strategy as a potential route to new topologies in Mn chemistry and possibly to new single-molecule magnets. We herein report the syntheses, single crystal X-ray structures and magnetic properties of two  $[\text{Mn}_4\text{O}_4]$  cubane clusters obtained from reactions of  $\text{Me}_2\text{AsO}_2\text{H}$  with  $[\text{Mn}_{12}\text{O}_{12}(\text{O}_2\text{CMe})_{16}(\text{H}_2\text{O})_4]$  and of two related  $\text{Mn}_{16}$  complexes isolated from reactions of  $\text{Me}_2\text{AsO}_2\text{H}$  with  $[\text{Mn}_{12}\text{O}_{12}(\text{O}_2\text{CPh})_{16}(\text{H}_2\text{O})_4]$  (**8**). We show that these  $\text{Mn}_{16}$  complexes are new additions to the family of SMMs.

## 4.2 Results and Discussion

### 4.2.1 Syntheses

As already discussed, various non-carboxylate ligands have previously been found to be useful reactants for the synthesis of new  $\text{Mn}_{12}$  derivatives. Reactions of **1** with either four or eight equivalents of  $\text{Ph}_2\text{PO}_2\text{H}$ ,  $(\text{PhO})_2\text{PO}_2\text{H}$ ,  $\text{PhSO}_3\text{H}$ ,  $\text{MeSO}_3\text{H}$ , and  $\text{HNO}_3$  have afforded a handful of new  $\text{Mn}_{12}$  SMMs<sup>32,33,39,47,58,101</sup> while the use of  $\text{PhSeO}_2\text{H}$  transformed the core of **1** into a new structural type in Mn chemistry that was found to behave as a single-chain magnet (SCM).<sup>119</sup> Thus, the reaction of **1** with  $\text{Me}_2\text{AsO}_2\text{H}$  was of particular interest. A solution of **1** in MeCN was treated with 18 equivalents of

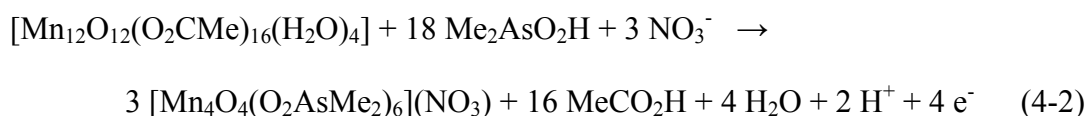
Me<sub>2</sub>AsO<sub>2</sub>H, which immediately dissolved, changing the solution color from dark brown to deep red. After 12 h, several cycles of addition of toluene and its removal under vacuum were completed to facilitate the removal of MeCO<sub>2</sub>H from the reaction solution; the acid dissociation constant of Me<sub>2</sub>AsO<sub>2</sub>H (pK<sub>a</sub> = 6.27)<sup>121</sup> is very high relative to MeCO<sub>2</sub>H (pK<sub>a</sub> = 4.76), i.e., Me<sub>2</sub>AsO<sub>2</sub>H is much less acidic than MeCO<sub>2</sub>H, and hence this was thought to be an essential step to ensure ligand substitution. Extraction of the soluble component of the residue into CH<sub>2</sub>Cl<sub>2</sub> and diffusion of pentane into the resulting solution leads to the formation of a dark red crystalline product. It was immediately obvious from the infrared spectrum of the material that the [Mn<sub>12</sub>O<sub>12</sub>] core of **1** was not retained, and the product was subsequently identified by X-ray crystallography as [Mn<sub>4</sub>O<sub>4</sub>(O<sub>2</sub>AsMe<sub>2</sub>)<sub>6</sub>] (**9**), obtained in ~75% yield. The transformation of **1** into **9** is summarized in eq 4-1. Previous findings have similarly shown that [Mn<sub>4</sub>O<sub>4</sub>(O<sub>2</sub>PPh<sub>2</sub>)<sub>6</sub>] can also be isolated from an attempted ligand substitution reaction of [Mn<sub>12</sub>O<sub>12</sub>(O<sub>2</sub>CMe)<sub>8</sub>(O<sub>3</sub>SPh)<sub>8</sub>(H<sub>2</sub>O)<sub>4</sub>] with Ph<sub>2</sub>PO<sub>2</sub>H,<sup>39</sup> suggesting that such reactions might be an effective route to obtain manganese-oxo complexes possessing a cubane structure.



Subsequent studies showed that complex **9** can be obtained from the same reaction without the repeated addition and removal of toluene, and hence, the substitution of MeCO<sub>2</sub>H need not be driven by the removal as its toluene azeotrope. In an attempt to obtain a structural analogue of **9** with ligation by more biologically relevant carboxylate groups, reactions of **9** with MeCO<sub>2</sub>H, EtCO<sub>2</sub>H, Cl<sub>2</sub>CHCO<sub>2</sub>H and Bu<sup>t</sup>CH<sub>2</sub>CO<sub>2</sub>H were performed. However, despite many attempts, such reactions were ineffective, and

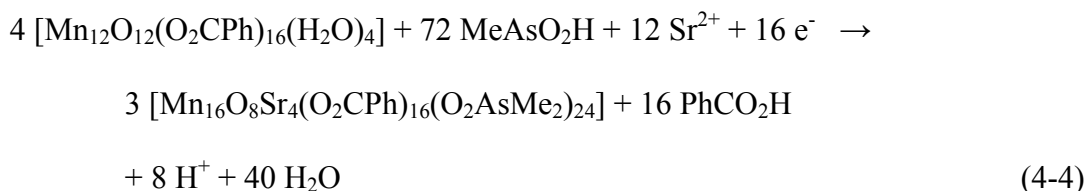
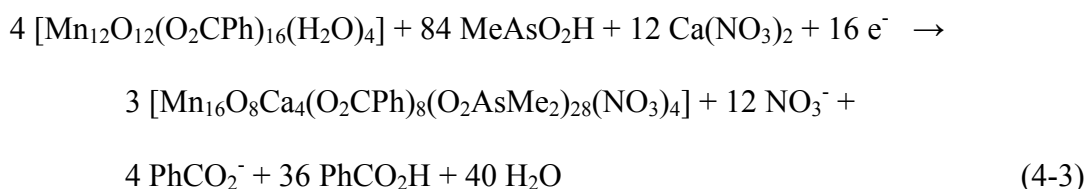
spectroscopic characterization of the products indicated that no reactions between **9** and the various carboxylic acids had occurred. This can likely be attributed to the strong basicity of the  $\text{Me}_2\text{AsO}_2^-$  group coordinated to the Mn centers as reflected in the relatively high  $\text{pK}_a$  value of its conjugate acid ( $\text{pK}_a = 6.27$ ). Similarly, as part of our continuing efforts to obtain a tetranuclear Mn cluster incorporating a  $\text{Ca}^{2+}$  ion, a topology that has potential relevance to the water-oxidizing complex (WOC) found in photosystem II (PS II),<sup>122</sup> we focused our attention on the reaction of **9** with various  $\text{Ca}^{2+}$  salts, including  $\text{Ca}(\text{NO}_3)_2$ ,  $\text{Ca}(\text{O}_2\text{CMe})_2$  and  $\text{Ca}(\text{ClO}_4)_2$ . However, our efforts were again without success, with no reactions occurring. We thought that the addition of  $\text{Ca}^{2+}$  to the reaction *in situ* might be a more effective route towards the incorporation of at least one  $\text{Ca}^{2+}$  ion. Thus, a solution of **1** in a 30:1 mixture of MeCN and MeOH was treated with 18 equivalents of  $\text{Me}_2\text{AsO}_2\text{H}$  and 1.5 equivalents of  $\text{Ca}(\text{NO}_3)_2$ . MeOH was added to the reaction system to aid in the dissolution of  $\text{Ca}(\text{NO}_3)_2$ , which is not readily soluble in MeCN. The solution color changed from dark brown to deep red as observed with **9**, and after 20 min, a small amount of brown powder was separated from the reaction solution by filtration. To the filtrate was added 1,2-dichloroethane and after 2 weeks, dark red crystals of  $\{[\text{Mn}_4\text{O}_4(\text{O}_2\text{AsMe}_2)_6](\text{NO}_3)\}_2$  (**10**) were obtained in ~24% yield. The infrared spectrum of **10** is nearly superimposable with that of **9**, except for a prominent signal that corresponds to a  $\text{NO}_3^-$  anion. Spectroscopic characterization of precipitates isolated from reactions solutions left undisturbed for more than ~2 weeks suggest the formation of Mn oxides. The deep red color of the filtrate following collection of the product crystals suggests that there are almost certainly other species remaining in the solution. We have

not explored these further however. The transformation of **1** into **10** is summarized in eq 4-2.



We extended this work to include reactions of  $\text{Me}_2\text{AsO}_2\text{H}$  with  $[\text{Mn}_{12}\text{O}_{12}(\text{O}_2\text{CPh})_{16}(\text{H}_2\text{O})_4]$  (**8**), thinking that the difference in solubility properties of the  $\text{MeCO}_2^-$  and  $\text{PhCO}_2^-$  ligands might lead to the isolation of a substantially different product; crystallization kinetics and relative solubility as well as numerous other factors are expected to play an important role in the determination of the identity of the isolated product. Hence, treatment of a solution of complex **8** in a 10:3 solvent mixture of MeCN and MeOH with 18 equivalents of  $\text{Me}_2\text{AsO}_2\text{H}$  and 1 equivalent of  $\text{Ca}(\text{NO}_3)_2$  leads to the formation of a deep red solution after ~20 min. Some brown powder was removed from the reaction mixture by filtration, and diffusion of  $\text{Et}_2\text{O}$  into the resulting filtrate leads to the formation of crystalline  $[\text{Mn}_{16}\text{O}_8\text{Ca}_4(\text{O}_2\text{CPh})_8(\text{O}_2\text{AsMe}_2)_{28}(\text{NO}_3)_4]$  (**11**). Similarly, diffusion of  $\text{Et}_2\text{O}$  into the filtrate obtained from the reaction of **8** with 18 equivalents of  $\text{Me}_2\text{AsO}_2\text{H}$  and 1 equivalent of  $\text{Sr}(\text{ClO}_4)_2$  in a 10:1 solvent mixture of MeCN and MeOH yields the related complex  $[\text{Mn}_{16}\text{O}_8\text{Sr}_4(\text{O}_2\text{CPh})_{16}(\text{Me}_2\text{AsO}_2)_{24}]$  (**12**). Although the final yield for both complexes is very low, 5% and 7%, respectively, the preparations are reproducible. The reaction system is unquestionably very complicated, involving the conversion of  $[\text{Mn}_{12}\text{O}_{12}(\text{O}_2\text{CPh})_{16}(\text{H}_2\text{O})_4]$  (**8**) to both **11** and **12** via fragmentation and recombination steps. The poor solubility of **11** and **12** in MeCN is likely an important consideration for the rationalization of the isolation of pure crystalline products although other factors undoubtedly are also important for the preferential crystallization of **11** and

**12.** The transformation of **8** into **11** and **12** is summarized in eq 4-3 and eq 4-4, respectively.



MeOH is required for the isolation of the products and likely functions as a reducing agent, providing the needed electrons to the reaction system; only precipitates were obtained from those reactions carried out in MeCN alone. Spectroscopic analysis of crystalline materials indicates that complexes **11** and **12** are also formed from reactions with EtOH instead of MeOH. The yield and quality of the crystals are strongly affected by the ratio of MeCN and MeOH solvents, with the optimum ratios herein reported.

## 4.2.2 Description of Structures

### 4.2.2.1 X-ray crystal structure of $[\text{Mn}_4\text{O}_4(\text{O}_2\text{AsMe}_2)_6]$ (**9**)

A labeled ORTEP<sup>40</sup> plot in PovRay format of complex **9** is shown in Figure 4-1, together with a stereoview. The crystallographic data and structure refinement details are collected in Table 4-1, and selected interatomic distances and angles are listed in Table A-5. The complex crystallizes in the triclinic space group  $P\bar{1}$  with the  $\text{Mn}_4$  molecule in a general position. The structure consists of a  $[\text{Mn}^{\text{III}}_2\text{Mn}^{\text{IV}}_2(\mu_3\text{-O})_4]^{6+}$  core with the peripheral ligation provided by six bridging  $\text{Me}_2\text{AsO}_2^-$  ligands.

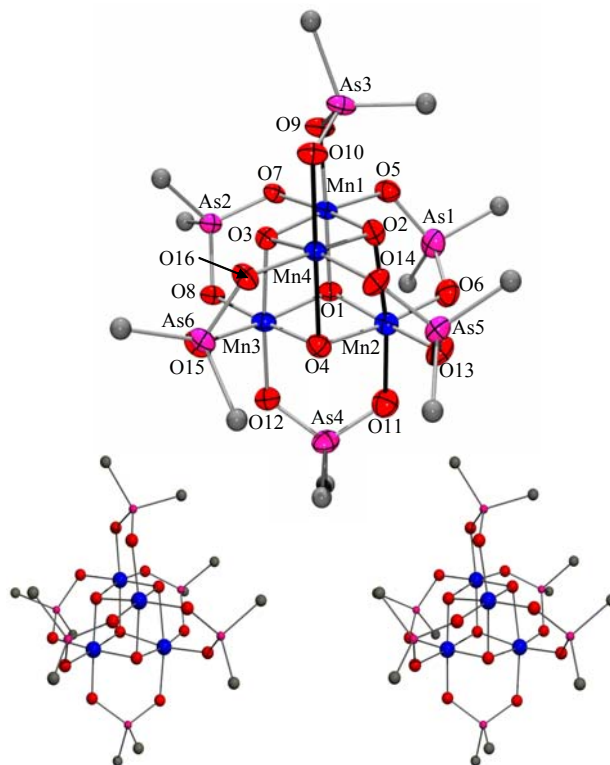


Figure 4-1. ORTEP representation in PovRay format of  $[\text{Mn}_4\text{O}_4(\text{O}_2\text{AsMe}_2)_6]$  (**9**) with thermal ellipsoids at the 50% probability level except for the C atoms, together with a stereopair. Hydrogen atoms have been omitted for clarity. Mn blue; O red; As pink; C gray. The relative dispositions of the JT elongation axes are indicated as solid black bonds.

Assignment of the oxidation states of the metal centers was done qualitatively by charge consideration and also by comparison of the bond distances around the Mn centers. These assignments were confirmed quantitatively by bond valence sum (BVS) calculations,<sup>41</sup> indicating that Mn(1) and Mn(3) are  $\text{Mn}^{\text{IV}}$  while Mn(2) and Mn(4) are  $\text{Mn}^{\text{III}}$  (Table 4-2). All of the Mn centers are six-coordinate, with near-octahedral geometry. A BVS calculation was also carried out for the inorganic O atoms, confirming that the the triply bridging O atoms are all deprotonated (Table 4-3). Both of the octahedral  $\text{Mn}^{\text{III}}$  centers in **9** displays a JT axial elongation of two *trans* bonds as expected for a high-spin  $\text{Mn}^{\text{III}}$  ( $d^4$ ) ion; the elongation axes are oriented along the

O(2)-Mn(2)-O(11) and O(4)-Mn(4)-O(10) bonds. The axial Mn<sup>III</sup>-O bonds lengths are in the range of 2.066(3) – 2.291(3) Å, and are significantly longer than equatorial Mn<sup>III</sup>-O bonds in the range of 1.897(3) – 1.974(3) Å. The Mn<sup>IV</sup> ions, Mn(1) and Mn(3), exhibit shorter Mn-O bond lengths in the range of 1.838(3) – 1.959(3) Å and lack JT elongation axes, consistent with their assignment as Mn<sup>IV</sup>. Normally, the JT elongation axes avoid Mn-oxide bonds, almost always the strongest and shortest in the molecule, but the cubane core of **9** requires that the JT elongation axes of Mn(2) and Mn(4) be situated in an abnormal position containing a core O<sup>2-</sup> ion, O(2) and O(4), respectively. The JT elongation axes are oriented nearly parallel to each other and this alignment will dominate the magnetic anisotropy (i.e., the magnitude of the ZFS parameter, D) of the complete Mn<sub>4</sub> molecule. This will be of relevance to the magnetic discussion later (*vide infra*). Overall, the complete Mn<sub>4</sub> complex does not possess any crystallographic symmetry element although the virtual symmetry is *T<sub>d</sub>*.

There are a handful of other reported examples of Me<sub>2</sub>AsO<sub>2</sub><sup>-</sup> groups symmetrically bridging Fe,<sup>123</sup> Mo<sup>120,124</sup> and W<sup>125</sup> ion pairs in the manner seen in **9**. However, to our knowledge complex **9** is the first example of the use of the Me<sub>2</sub>AsO<sub>2</sub><sup>-</sup> ligand in Mn chemistry. Two other discrete examples of the [Mn<sup>III</sup><sub>2</sub>Mn<sup>IV</sup><sub>2</sub>(μ<sub>3</sub>-O)<sub>4</sub>]<sup>6+</sup> core as found in **9** have been previously observed in the valence-delocalized compound [Mn<sub>4</sub>O<sub>4</sub>(O<sub>2</sub>PPh<sub>2</sub>)<sub>6</sub>]<sup>48</sup> (**5**) and the trapped-valence [Mn<sub>4</sub>O<sub>4</sub>(O<sub>2</sub>P(OPh-*p*-Me)<sub>2</sub>)<sub>6</sub>]<sup>126</sup> complex. Hence, complex **9** is only the second example of a mixed-valence, trapped-valence [Mn<sup>III</sup><sub>2</sub>Mn<sup>IV</sup><sub>2</sub>(μ<sub>3</sub>-O)<sub>4</sub>]<sup>6+</sup> molecule. The only other complexes possessing manganese-oxo cubane cores include the trapped-valence [Mn<sup>III</sup>Mn<sup>IV</sup><sub>3</sub>(μ<sub>3</sub>-O)<sub>4</sub>(O<sub>2</sub>PPh<sub>2</sub>)<sub>6</sub>]<sup>127</sup> and [Mn<sup>III</sup><sub>4</sub>(μ<sub>3</sub>-O)<sub>2</sub>(μ<sub>3</sub>-OMe)<sub>2</sub>(HOMe)(O<sub>2</sub>P(OPh-*p*-Me)<sub>2</sub>)<sub>6</sub>]<sup>126</sup> molecules reported by Dismukes and others and

the distorted cubane clusters of general formula  $[\text{Mn}^{\text{III}}_3\text{Mn}^{\text{IV}}(\mu_3\text{-O})_3(\mu_3\text{-X})]^{6+}$ , where  $\text{X} = \text{Cl}^-, \text{F}^-, \text{Br}^-, \text{N}_3^-, \text{NCO}^-, \text{or RCO}_2^-$ , reported by Christou and coworkers.<sup>12,49,128</sup>

Table 4-1. Crystallographic data for  $[\text{Mn}_4\text{O}_4(\text{O}_2\text{AsMe}_2)_6]\cdot 5\text{H}_2\text{O}\cdot \text{C}_5\text{H}_{12}$  and  $\{[\text{Mn}_4\text{O}_4(\text{O}_2\text{AsMe}_2)_6](\text{NO}_3)\}_2\cdot \frac{1}{2}\text{MeCN}\cdot 12\text{H}_2\text{O}$ .

Parameter	<b>9</b> ·5H <sub>2</sub> O·C <sub>5</sub> H <sub>12</sub>	<b>10</b> ·½MeCN·12H <sub>2</sub> O
formula <sup>a</sup>	C <sub>17</sub> H <sub>58</sub> As <sub>6</sub> Mn <sub>4</sub> O <sub>21</sub>	C <sub>25</sub> H <sub>97.5</sub> As <sub>12</sub> N <sub>2.5</sub> Mn <sub>8</sub> O <sub>50</sub>
fw, g mol <sup>-1</sup>	1267.91	2572.08
space group	$P\bar{1}$	$P\bar{1}$
<i>a</i> , Å	11.7278(7)	14.0401(7)
<i>b</i> , Å	13.7179(8)	14.3205(7)
<i>c</i> , Å	14.0559(9)	21.1805(2)
$\alpha$ , deg	99.8690(10)	103.945(2)
$\beta$ , deg	90.4520(10)	99.819(2)
$\gamma$ , deg	111.7540(10)	94.437(2)
<i>V</i> , Å <sup>3</sup>	2062.9(2)	4041.2(3)
<i>Z</i>	2	2
<i>T</i> , °C	-55(2)	-100(2)
radiation, Å <sup>b</sup>	0.71073	0.71073
$\rho_{\text{calc}}$ , g cm <sup>-3</sup>	2.041	2.114
$\mu$ , cm <sup>-1</sup>	60.41	61.78
<i>R</i> 1 ( <i>wR</i> 2), % <sup>c,d</sup>	3.70 (10.14)	5.15 (12.40)

<sup>a</sup> Including solvent molecules. <sup>b</sup> Graphite monochromator. <sup>c</sup>  $R1 = \sum||F_o| - |F_c|| / \sum|F_o|$ . <sup>d</sup>  $wR2 = [\sum[w(F_o^2 - F_c^2)^2] / \sum[wF_o^2]]^{1/2}$  where  $S = [\sum[w(F_o^2 - F_c^2)^2] / (n-p)]^{1/2}$ ,  $w = 1/[\sigma^2(F_o^2) + (mp)^2 + np]$ ,  $p = [\max(F_o^2, 0) + 2F_c^2]/3$ , and *m* and *n* are constants.

Table 4-2. Bond valence sum<sup>a</sup> calculations for complexes **9**·5H<sub>2</sub>O·C<sub>5</sub>H<sub>12</sub> and **10**·½MeCN·12H<sub>2</sub>O.

Atom	<b>9</b> ·5H <sub>2</sub> O·C <sub>5</sub> H <sub>12</sub>			<b>10</b> ·½MeCN·12H <sub>2</sub> O		
	Mn <sup>2+</sup>	Mn <sup>3+</sup>	Mn <sup>4+</sup>	Mn <sup>2+</sup>	Mn <sup>3+</sup>	Mn <sup>4+</sup>
Mn(1)	4.172	3.816	<u>4.006</u>	3.886	3.554	<u>3.731</u>
Mn(2)	3.476	<u>3.179</u>	3.338	3.665	<u>3.353</u>	3.520
Mn(3)	3.853	3.524	<u>3.700</u>	3.841	3.513	<u>3.688</u>
Mn(4)	3.184	<u>2.913</u>	3.058	4.098	3.748	<u>3.935</u>
Mn(5)				4.136	3.783	<u>3.971</u>
Mn(6)				4.124	3.772	<u>3.960</u>
Mn(7)				3.228	<u>2.952</u>	3.100
Mn(8)				4.177	3.821	<u>4.011</u>

<sup>a</sup> The underlined value is the one closest to the actual charge for which it was calculated. The oxidation state of a particular atom can be taken as the nearest whole number to the underlined value.

Table 4-3. Bond valence sum calculations<sup>a</sup> for selected oxygen atoms in complexes **9**·5H<sub>2</sub>O·C<sub>5</sub>H<sub>12</sub> and **10**·½MeCN·12H<sub>2</sub>O.

<b>9</b> ·5H <sub>2</sub> O·C <sub>5</sub> H <sub>12</sub>			<b>10</b> ·½MeCN·12H <sub>2</sub> O		
Atom	$V_i$	Assignment	Atom	$V_i$	Assignment
O(1)	1.927	O <sup>2-</sup>	O(13)	1.909	O <sup>2-</sup>
O(2)	1.822	O <sup>2-</sup>	O(14)	1.804	O <sup>2-</sup>
O(3)	1.898	O <sup>2-</sup>	O(15)	1.904	O <sup>2-</sup>
O(4)	1.754	O <sup>2-</sup>	O(16)	1.913	O <sup>2-</sup>
			O(29)	1.888	O <sup>2-</sup>
			O(30)	1.921	O <sup>2-</sup>
			O(31)	1.996	O <sup>2-</sup>
			O(32)	1.799	O <sup>2-</sup>

<sup>a</sup> The oxygen atoms is O<sup>2-</sup> if  $V_i \approx 2$ , OH<sup>-</sup> if  $V_i \approx 1$ , and H<sub>2</sub>O if  $V_i \approx 0$ .

#### 4.2.2.2 X-ray crystal structure of {[Mn<sub>4</sub>O<sub>4</sub>(O<sub>2</sub>AsMe<sub>2</sub>)<sub>6</sub>](NO<sub>3</sub>)<sub>2</sub>} (10)

A labeled ORTEP<sup>40</sup> plot in PovRay format of complex **10** is shown in Figure 4-2, together with a stereoview. The crystallographic data and structure refinement details are collected in Table 4-1, and selected interatomic distances and angles are listed in Table A-6. Complex **10**·½MeCN·12H<sub>2</sub>O crystallizes in the triclinic space group  $P\bar{1}$  with two independent Mn<sub>4</sub> anions in general positions. The structure of **10** is very similar to that of **9**, except that the oxidation levels of the Mn ions in the latter (Mn<sup>III</sup><sub>2</sub>Mn<sup>IV</sup><sub>2</sub>) have been changed; **10** contains two [Mn<sup>III</sup>Mn<sup>IV</sup><sub>3</sub>(μ<sub>3</sub>-O)<sub>4</sub>]<sup>7+</sup> molecules each with the peripheral ligation provided by six bridging Me<sub>2</sub>AsO<sub>2</sub><sup>-</sup> ligands. Two nitrate cations serve as counterions. Bond valence sum (BVS) calculations<sup>41</sup> indicate a mixed-valence, trapped-valence complex; Mn(2) and Mn(7) are Mn<sup>III</sup>, while the remaining Mn centers Mn(1), Mn(3), Mn(4), Mn(5), Mn(6) and Mn(8) are Mn<sup>IV</sup> (Table 4-2). Similarly, a BVS calculation carried out to assess the protonation levels of the inorganic O atoms confirms that the triply bridging cubane O atoms are deprotonated (Table 4-3).

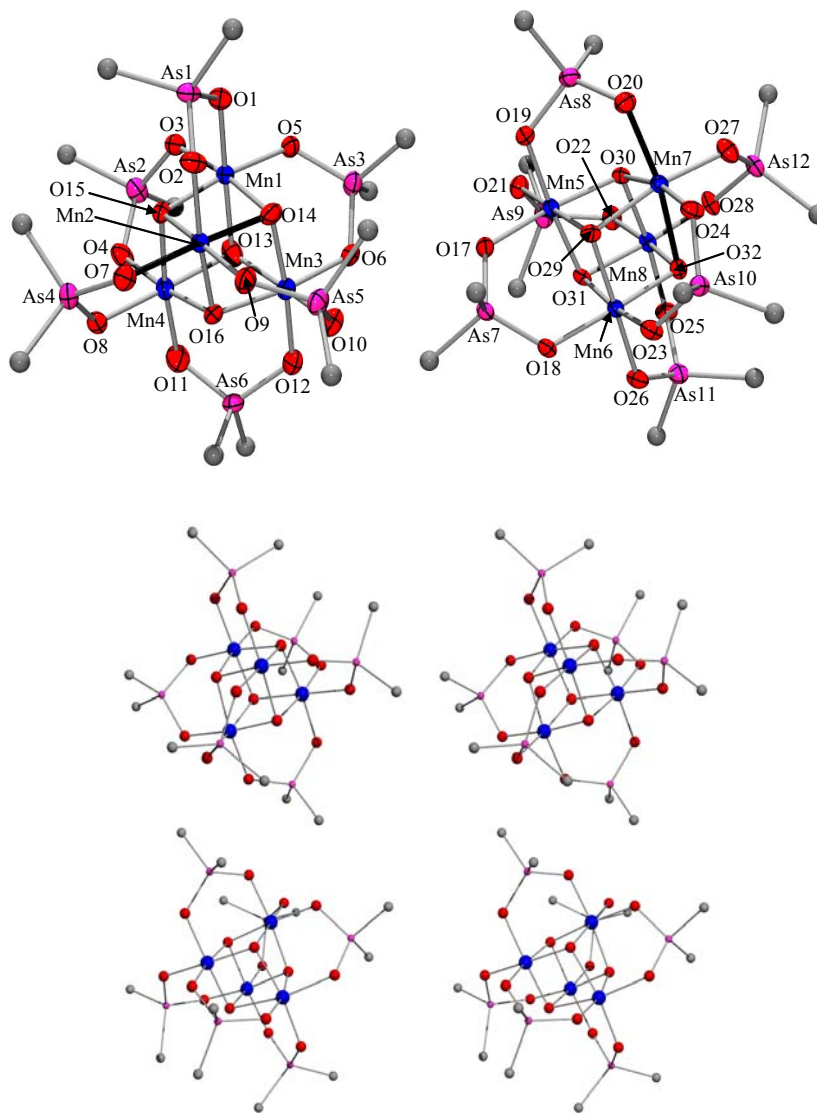


Figure 4-2. ORTEP representation in PovRay format of the cation of  $\{[\text{Mn}_4\text{O}_4(\text{O}_2\text{AsMe}_2)_6](\text{NO}_3)\}_2$  (**10**) with thermal ellipsoids at the 50% probability level except for the C atoms, together with a stereopair. Hydrogen atoms have been omitted for clarity. Mn blue; O red; As pink; C gray. The relative dispositions of the JT elongation axes are indicated as solid black bonds.

All of the Mn centers are six-coordinate, with near-octahedral geometry. Each  $\text{Mn}^{\text{III}}$  ion exhibits an axial elongation of two *trans* bonds as is typical of the Jahn-Teller distortion that is expected of a high-spin  $\text{Mn}^{\text{III}}$  ( $d^4$ ) ion. The elongation axes are oriented along the O(7)-Mn(2)-O(14) and O(20)-Mn(7)-O(32) bonds. For each  $\text{Mn}^{\text{III}}$  ion, the average axial bond length [2.004 Å for Mn(2) and 2.165 Å for Mn(7)] is  $\sim 0.1\text{-}0.2$  Å

longer than the average equatorial bond length [1.923 Å for Mn(2) and 1.936 Å for Mn(7)]. The JT elongation axes of Mn(2) and Mn(7) are oriented nearly perpendicular to each other and this point will be of particular importance to the magnetic properties of **10** (*vide infra*) because the orientation of the Mn<sup>III</sup> JT axes relative to one another is the main factor that determines the overall magnetic anisotropy of the molecules. In contrast, Mn(1), Mn(3), Mn(4), Mn(5), Mn(6) and Mn(8) exhibit shorter average Mn-O bond lengths [1.912 Å] and lack Jahn-Teller elongation axes, consistent with Mn<sup>IV</sup> ions. Table 4-4 shows a comparison of average Mn-O bond distances and angles for the two [Mn<sub>4</sub>O<sub>4</sub>(O<sub>2</sub>AsMe<sub>2</sub>)<sub>6</sub>]<sup>z-</sup> [z = 0 (**9**) and +1 (**10**)] complexes. This comparison confirms that the bond distances in the [Mn<sub>4</sub>(μ<sub>3</sub>-O)<sub>4</sub>] cores are almost superimposable.

Table 4-4. Comparison of selected bond distances (Å) and angles (°) for complexes [Mn<sub>4</sub>O<sub>4</sub>(O<sub>2</sub>AsMe<sub>2</sub>)<sub>6</sub>] (**9**) and {[Mn<sub>4</sub>O<sub>4</sub>(O<sub>2</sub>AsMe<sub>2</sub>)<sub>6</sub>](NO<sub>3</sub>)}<sub>2</sub> (**10**).

Parameter <sup>a</sup>	<b>9</b>	<b>10</b>
Mn <sup>IV</sup> – O <sub>c</sub> (ax)	1.899(3) – 1.959(3)	1.883(5) – 1.924(5)
Mn <sup>IV</sup> – O <sub>c</sub> (eq)	1.838(3) – 1.950(3)	1.865(5) – 2.004(6)
Mn <sup>III</sup> – O <sub>c</sub> (ax)	2.139(3) – 2.291(3)	2.029(6) – 2.242(5)
Mn <sup>III</sup> – O <sub>c</sub> (eq)	1.897(3) – 1.974(3)	1.907(5) – 1.985(4)
Mn <sup>IV</sup> – O <sub>eq</sub>	1.931(3) – 1.958(3)	1.864(4) – 1.971(5)
Mn <sup>IV</sup> – O <sub>ax</sub>	1.906(3) – 1.951(3)	1.885(5) – 1.917(5)
Mn <sup>III</sup> – O <sub>eq</sub>	1.909(3) – 1.938(3)	1.892(5) – 1.925(5)
Mn <sup>III</sup> – O <sub>ax</sub>	2.066(3) – 2.095(3)	1.978(5) – 2.087(5)
Mn <sup>IV</sup> ...Mn <sup>IV</sup>	2.8857(8)	2.8323(14) – 2.9281(15)
Mn <sup>III</sup> ...Mn <sup>III</sup>	3.0546(8)	—————
Mn <sup>IV</sup> ...Mn <sup>III</sup>	2.8638(8) – 3.0171(8)	2.9102(15) – 3.0079(14)
O <sub>c</sub> – Mn <sup>IV</sup> – O <sub>c</sub>	80.53(11) – 88.76(12)	80.2(2) – 88.1(2)
O <sub>c</sub> – Mn <sup>III</sup> – O <sub>c</sub>	76.77(10) – 85.46(11)	76.39(18) – 82.0(2)

<sup>a</sup> O<sub>c</sub> = cubane O<sup>2-</sup>, O<sub>ax</sub> = axial carboxylate, O<sub>eq</sub> = equatorial carboxylate.

Comparison of the O...O bite distances of the Me<sub>2</sub>AsO<sub>2</sub><sup>-</sup> ligands in complexes **9** and **10** and the Ph<sub>2</sub>PO<sub>2</sub><sup>-</sup> ligands in **5** with the corresponding distances of the MeCO<sub>2</sub><sup>-</sup> and PhSO<sub>3</sub><sup>-</sup> ligands in **1** and **2**, respectively, shows that dimethylarsinate and diphenylphosphinate groups may be preferred for formation of the cubane complex

(Table 3-5). The O···O distances for the  $\text{Me}_2\text{AsO}_2^-$ ,  $\text{Ph}_2\text{PO}_2^-$  and  $\text{PhSeO}_2^-$  ligands bridging two Mn ions are considerably longer than the corresponding distances for the  $\text{MeCO}_2^-$  and  $\text{PhSO}_3^-$  ligands and these long distances may be required to accommodate the geometry of the cubane topology.

Table 4-5. Comparison of selected bite distances (Å) for  $\text{MeCO}_2^-$ ,  $\text{PhSO}_3^-$ ,  $\text{Ph}_2\text{PO}_2^-$ ,  $\text{PhSeO}_2^-$  and  $\text{Me}_2\text{AsO}_2^-$  ligands in complexes **1**, **2**, **4**, **5**, **6**, **7**, **9** and **10**.

Acid	Compound [ $\text{Mn}_x$ ]	Bite Distance <sup>a</sup>	pK <sub>a</sub> <sup>36,70,121,129</sup>
$\text{MeCO}_2\text{H}$	<b>1</b> [ $\text{Mn}_{12}$ ]	2.235 – 2.249	4.76
$\text{PhSO}_3\text{H}$	<b>2</b> [ $\text{Mn}_{12}$ ]	2.400 – 2.422	2.55
$\text{Ph}_2\text{PO}_2\text{H}$	<b>4</b> [ $\text{Mn}_{12}$ ]	2.561 – 2.565	2.32
	<b>5</b> [ $\text{Mn}_4$ ]	2.566 – 2.617	
$\text{PhSeO}_2\text{H}$	<b>6</b> [ $\text{Mn}_7$ ]	2.654 – 2.799	4.79
	<b>7</b> [ $\text{Mn}_7$ ]	2.640 – 2.836	
$\text{MeAsO}_2\text{H}$	<b>9</b> [ $\text{Mn}_4$ ]	2.791 – 2.828	6.27
	<b>10</b> [ $\text{Mn}_4$ ]	2.749 – 2.847	

<sup>a</sup> Bite distance refers to the O···O distance between O atoms of the ligand coordinated to Mn ions in each selected cluster.

#### 4.2.2.3 X-ray crystal structure of $[\text{Mn}_{16}\text{O}_8\text{Ca}_4(\text{O}_2\text{CPh})_8(\text{O}_2\text{AsMe}_2)_{28}(\text{NO}_3)_4]$ (**11**)

A labeled ORTEP<sup>40</sup> plot in PovRay format of complex **11** is shown in Figure 4-3.

The crystallographic data and structure refinement details are collected in Table 4-6, and selected interatomic distances and angles are listed in Table A-7. The complex crystallizes in the orthorhombic space group  $I222$ , with the  $\text{Mn}_{16}$  molecule lying on a 222 symmetry site and hence, possessing  $D_2$  crystallographic symmetry with three perpendicular  $C_2$  crystallographic rotation axes bisecting the molecule (Figure 4-4). For the sake of brevity, references to specific atoms in the following discussion implicitly include their symmetry-related partners. The structure of the  $\text{Mn}_{16}$  molecule consists of four  $[\text{Mn}^{\text{III}}_4(\mu\text{-O})_2]$  “butterfly” units [atoms Mn(1), Mn(2), Mn(3), Mn(4), O(7) and O(11) and their symmetry equivalents] with the peripheral ligation to each subunit provided by six bridging  $\text{Me}_2\text{AsO}_2^-$  ligands and one bridging  $\text{PhCO}_2^-$  ligand.

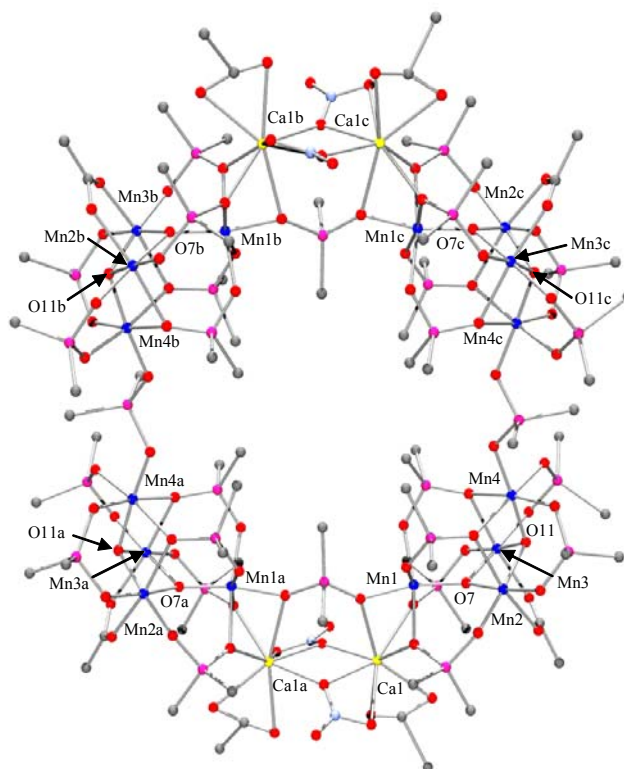


Figure 4-3. ORTEP representation in PovRay format of  $[\text{Mn}_{16}\text{O}_8\text{Ca}_4(\text{O}_2\text{CPh})_8(\text{O}_2\text{AsMe}_2)_{28}(\text{NO}_3)_4]$  (**11**). For clarity, the hydrogen atoms have been omitted and only the ipso C atoms of the phenyl groups are shown. Mn blue; O red; As pink; Ca yellow; N light blue; C gray.

The asymmetric unit of **11** is shown in Figure 4-5. The dihedral angle between the Mn(1)-Mn(2)-Mn(3) and Mn(2)-Mn(3)-Mn(4) planes is  $72.4^\circ$ . The two  $\mu_3$ -oxide atoms O(7) and O(11) lie 0.31 and 0.78 Å below their respective  $\text{Mn}_3$  planes. On one side of the  $[\text{Mn}_4\text{O}_2]$  “butterfly” subunit is another  $[\text{Mn}_4\text{O}_2]$  subunit that is bridged and connected to Mn ions and  $\text{Me}_2\text{AsO}_2^-$  groups of the former by a  $[\text{Ca}_2(\text{O}_2\text{CPh})_2(\text{O}_2\text{AsMe}_2)(\text{NO}_3)_2]$  moiety. On the other side of the  $[\text{Mn}_4\text{O}_2]$  “butterfly” subunit is another  $[\text{Mn}_4\text{O}_2]$  subunit attached to the former by a single  $\text{Me}_2\text{AsO}_2^-$  ligand [As(8), O(14)] that is coordinated to Mn(4).

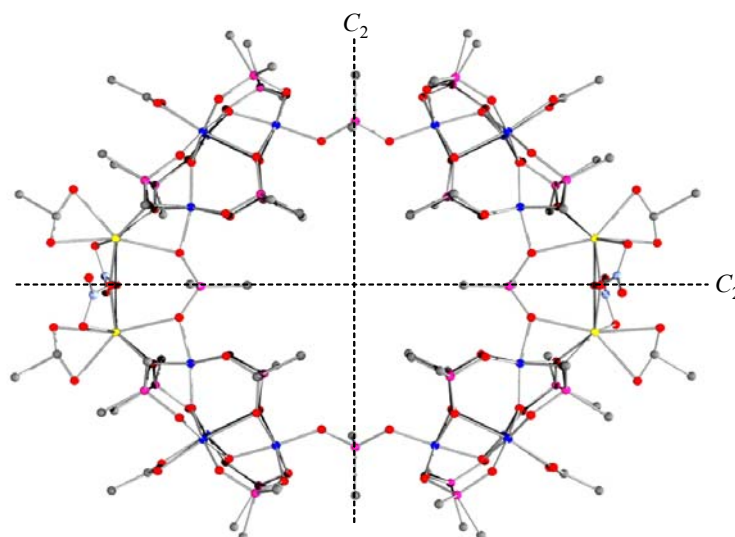
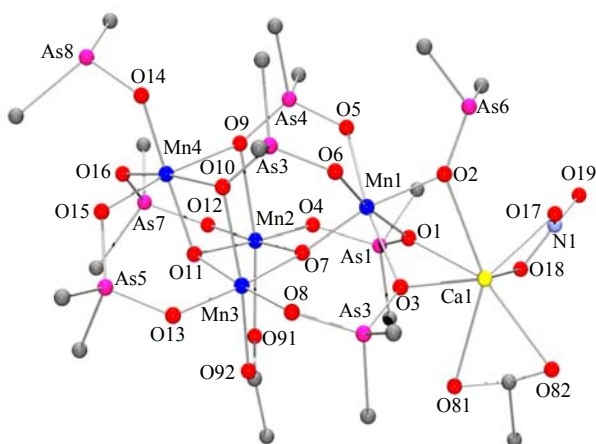


Figure 4-4. ORTEP representation in PovRay format of complex **11** showing the crystallographic  $D_2$  symmetry. Another  $C_2$  rotation axis (not shown) passes through the center of the molecule. For clarity, the hydrogen atoms have been omitted and only the ipso C atoms of the phenyl groups are shown. Mn blue; O red; As pink; Ca yellow; N light blue; C gray.

Table 4-6. Crystallographic data for  $[\text{Mn}_{16}\text{O}_8\text{Ca}_4(\text{O}_2\text{CPh})_8(\text{O}_2\text{AsMe}_2)_{28}(\text{NO}_3)_4] \cdot 32\text{MeCN}$  and  $[\text{Mn}_{16}\text{O}_8\text{Sr}_4(\text{O}_2\text{CPh})_{16}(\text{O}_2\text{AsMe}_2)_{24}] \cdot 16\text{MeCN}$ .

Parameter	<b>11</b> ·32MeCN	<b>12</b> ·16MeCN
formula <sup>a</sup>	$\text{C}_{160}\text{H}_{280}\text{N}_{28}\text{Ca}_4\text{As}_{28}\text{Mn}_{16}\text{O}_{92}$	$\text{C}_{192}\text{H}_{272}\text{N}_{16}\text{Sr}_4\text{As}_{24}\text{Mn}_{16}\text{O}_{88}$
fw, g mol <sup>-1</sup>	7365.52	7239.89
space group	$I222$	$P2_1/c$
<i>a</i> , Å	17.1626(16)	20.862(3)
<i>b</i> , Å	23.758(2)	36.594(5)
<i>c</i> , Å	31.136(3)	18.644(2)
$\alpha$ , deg	90	90
$\beta$ , deg	90	101.370(2)
$\gamma$ , deg	90	90
<i>V</i> , Å <sup>3</sup>	12696(2)	13953(3)
<i>Z</i>	8	2
<i>T</i> , °C	-100(2)	-100(2)
radiation, Å <sup>b</sup>	0.71073	0.71073
$\rho_{\text{calc}}$ , g cm <sup>-3</sup>	2.066	1.725
$\mu$ , cm <sup>-1</sup>	50.80	43.47
<i>R1</i> ( <i>wR2</i> ), % <sup>c,d</sup>	8.76 (22.86)	8.72 (22.12)

<sup>a</sup> Including solvent molecules. <sup>b</sup> Graphite monochromator. <sup>c</sup>  $R1 = \sum ||F_o| - |F_c|| / \sum |F_o|$ . <sup>d</sup>  $wR2 = [\sum [w(F_o^2 - F_c^2)^2] / \sum [wF_o^2]^2]^{1/2}$  where  $S = [\sum [w(F_o^2 - F_c^2)^2] / (n-p)]^{1/2}$ ,  $w = 1/[\sigma^2(F_o^2) + (mp)^2 + np]$ ,  $p = [\max(F_o^2, 0) + 2F_c^2]/3$ , and *m* and *n* are constants.



remaining equatorial bonds, Mn(1)-O(2) = 1.949(8) Å and Mn(1)-O(7) = 1.858(7) Å, exhibit distances typical for Mn<sup>III</sup>-O<sub>eq</sub> and Mn<sup>III</sup>-O<sup>2-</sup> bonds, respectively. Similarly for Mn(4), all four equatorial bonds, [Mn(4)-O(9) = 2.15(2) Å, Mn(4)-O(15) = 1.990(17) Å, Mn(4)-O(10) = 2.184(18) Å and Mn(4)-O(16) = 2.041(17) Å] are elongated with respect to the axial ones [Mn(4)-O(11) = 1.915(8) Å and Mn(4)-O(14) = 1.888(9) Å]. The abnormal distances around Mn(1) and Mn(4) suggest a static disorder of a JT elongation axis about two bonds, O(3)-Mn(1)-O(5) and O(1)-Mn(1)-O(6) for Mn(1) and O(9)-Mn(4)-O(15) and O(10)-Mn(4)-O(16) for Mn(4). Ca(1) is eight-coordinate with bond distances in the range of 2.344(16) – 2.66(2) Å.

Table 4-7. Bond valence sum<sup>a</sup> calculations for complexes **11**·32MeCN and **12**·16MeCN.

Atom	<b>11</b> ·32MeCN			<b>12</b> ·16MeCN		
	Mn <sup>2+</sup>	Mn <sup>3+</sup>	Mn <sup>4+</sup>	Mn <sup>2+</sup>	Mn <sup>3+</sup>	Mn <sup>4+</sup>
Mn(1)	3.093	<u>2.829</u>	2.970	3.120	<u>2.854</u>	2.996
Mn(2)	3.062	<u>2.801</u>	2.940	3.207	<u>2.934</u>	3.080
Mn(3)	3.384	<u>3.095</u>	3.250	3.243	<u>2.967</u>	3.115
Mn(4)	3.078	<u>2.815</u>	2.956	3.178	<u>2.907</u>	3.051
Mn(5)				3.007	<u>2.750</u>	2.887
Mn(6)				3.212	<u>2.938</u>	3.085
Mn(7)				3.231	<u>2.955</u>	3.103
Mn(8)				3.037	<u>2.777</u>	2.916

<sup>a</sup> The underlined value is the one closest to the actual charge for which it was calculated. The oxidation state of a particular atom can be taken as the nearest whole number to the underlined value.

Table 4-8. Bond valence sum calculations<sup>a</sup> for selected oxygen atoms in complexes **11**·32MeCN and **12**·16MeCN.

<b>11</b> ·32MeCN			<b>12</b> ·16MeCN		
Atom	$V_i$	Assignment	Atom	$V_i$	Assignment
O(7)	2.052	O <sup>2-</sup>	O(5)	2.054	O <sup>2-</sup>
O(11)	1.993	O <sup>2-</sup>	O(6)	2.052	O <sup>2-</sup>
		O <sup>2-</sup>	O(33)	2.043	O <sup>2-</sup>
		O <sup>2-</sup>	O(34)	2.029	O <sup>2-</sup>

<sup>a</sup> The oxygen atoms is O<sup>2-</sup> if  $V_i \approx 2$ , OH<sup>-</sup> if  $V_i \approx 1$ , and H<sub>2</sub>O if  $V_i \approx 0$ .

As shown in Figure 4-6, the eight benzoate ligands exhibit two types of binding modes: four bridge Mn ions in the common *syn, syn, μ* mode (I) and four are chelating Ca(1) in mode II. Additionally, there are four  $\text{NO}_3^-$  anions that are chelating Ca(1) and bridging to the nearest symmetry-related Ca(1) ion in the *syn, anti, syn, μ* bridging mode III. Of the 28 dimethylarsinate ligands, eight are bridging Mn ions in the *syn, syn, μ* bridging mode (IV), eight are bridging three Mn ions in the *syn, syn, anti, μ<sub>3</sub>* bridging mode (V), eight are bridging two Mn and one Ca ion in the *syn, syn, anti, μ<sub>3</sub>* bridging mode (VI), two are bridging Mn ions in the *anti, anti, μ* bridging mode (VII), and the final two are bridging two Mn and two Ca ions in the  $\mu_4$  bridging mode (VIII).

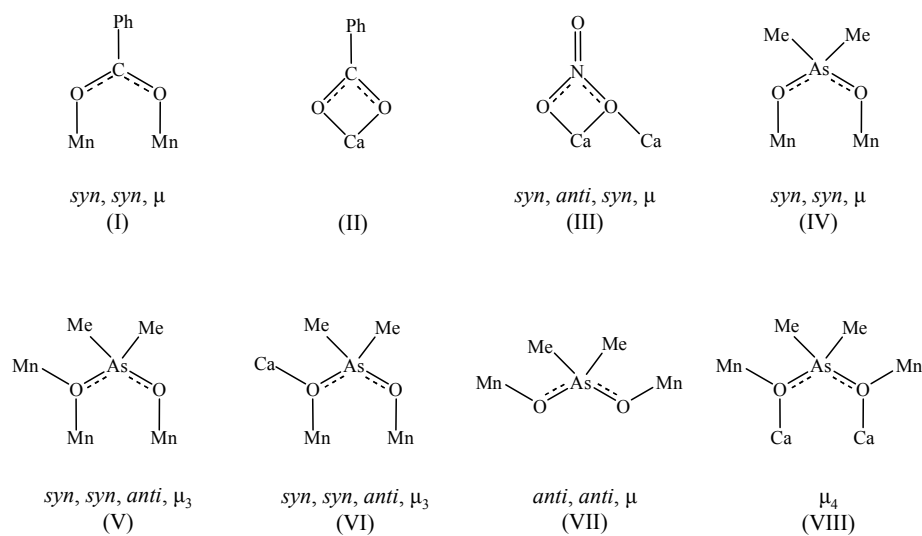


Figure 4-6. Schematic representation of the eight chelating and/or bridging modes found in complex **11**.

Complex **11** is only the second structurally characterized molecular species containing both Mn and Ca ions, the first being the recently reported  $[\text{Mn}_{13}\text{Ca}_2\text{O}_{10}(\text{OH})_2(\text{OMe})_2(\text{O}_2\text{CPh})_{18}(\text{H}_2\text{O})_4]$  complex.<sup>130</sup>

#### 4.2.2.4 X-ray crystal structure of $[\text{Mn}_{16}\text{O}_8\text{Sr}_4(\text{O}_2\text{CPh})_{16}(\text{O}_2\text{AsMe}_2)_{24}]$ (**12**)

A labeled ORTEP<sup>40</sup> plot in PovRay format of complex **12** is shown in Figure 4-7. The crystallographic data and structure refinement details are collected in Table 4-6, and selected interatomic distances and angles are listed in Table A-8. The complex crystallizes in the monoclinic space group  $P2_1/c$ , with the  $\text{Mn}_{16}$  molecule lying on a crystallographic  $C_2$  rotation axis. For the sake of brevity, references to specific atoms in the following discussion implicitly include their symmetry-related partners. The structure of **12** is very similar to that of **11** with essentially two exceptions: (i) the  $\text{Ca}^{2+}$  ions and chelating  $\text{NO}_3^-$  groups in the latter have been replaced by  $\text{Sr}^{2+}$  ions and chelating  $\text{PhCO}_2^-$  groups; and (ii) four of the  $\text{Me}_2\text{AsO}_2^-$  bridging ligands in the latter have been replaced with  $\text{PhCO}_2^-$  groups.

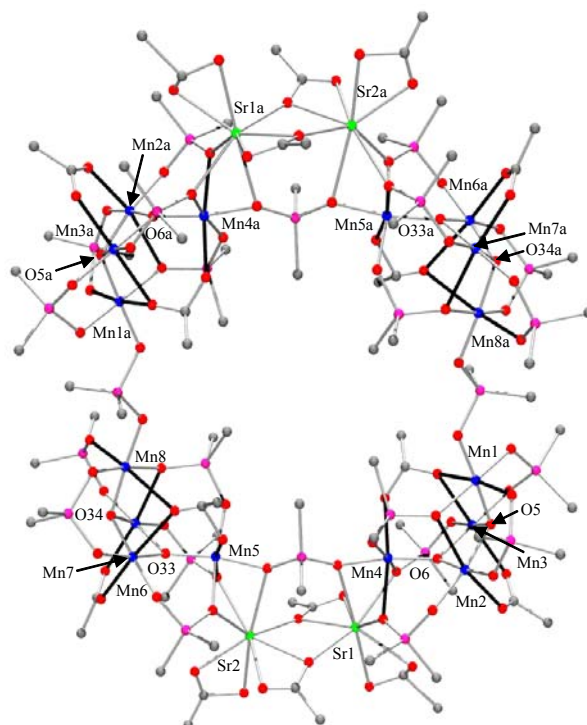


Figure 4-7. ORTEP representation in PovRay format of  $[\text{Mn}_{16}\text{O}_8\text{Sr}_4(\text{O}_2\text{CPh})_{16}(\text{O}_2\text{AsMe}_2)_{24}]$  (**12**).  $\text{Mn}^{\text{III}}$  elongation axes are shown as solid black bonds. For clarity, the hydrogen atoms have been omitted and only the ipso C atoms of the phenyl groups are shown. Mn blue; O red; As pink; Sr green; C gray.

Hence, the structure of the  $\text{Mn}_{16}$  molecule consists of four  $[\text{Mn}^{\text{III}}_4(\mu\text{-O})_2]$  “butterfly” units [atoms Mn(1), Mn(2), Mn(3), Mn(4) and Mn(5), Mn(6), Mn(7), Mn(8) and their symmetry equivalents] with the peripheral ligation to each subunit provided by five bridging  $\text{Me}_2\text{AsO}_2^-$  and two bridging  $\text{PhCO}_2^-$  ligands. The asymmetric unit of **12** is shown in Figure 4-8. The dihedral angle between the Mn(1)-Mn(2)-Mn(3) and Mn(2)-Mn(3)-Mn(4) planes is  $71.2^\circ$ . The two  $\mu_3$ -oxide atoms O(5) and O(6) lie 0.72 and 0.28 Å below their respective  $\text{Mn}_3$  planes. Similarly, the dihedral angle between the Mn(5)-Mn(6)-Mn(7) and Mn(6)-Mn(7)-Mn(8) planes in the other crystallographically independent  $[\text{Mn}_4\text{O}_2]$  subunit is  $72.3^\circ$ . The  $\mu_3$ -oxide atoms O(33) and O(34) lie 0.29 and 0.74 Å below their respective  $\text{Mn}_3$  planes.

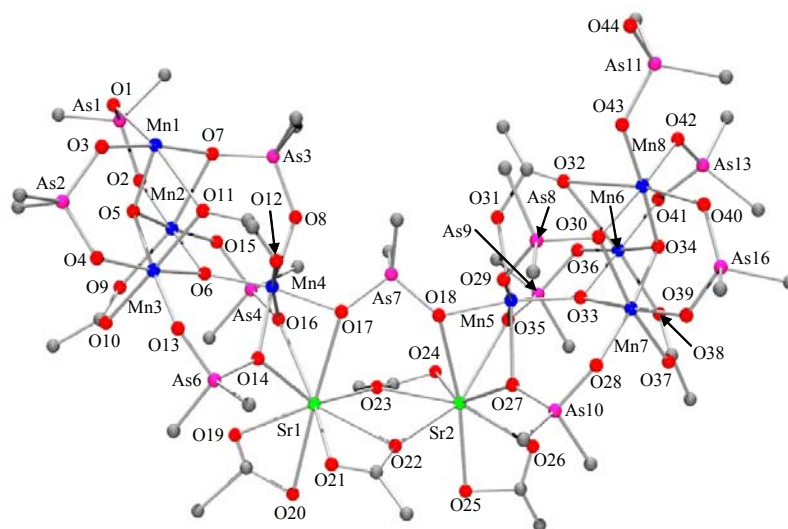


Figure 4-8. ORTEP representation in PovRay format of the asymmetric unit of  $[\text{Mn}_{16}\text{O}_8\text{Sr}_4(\text{O}_2\text{CPh})_{16}(\text{O}_2\text{AsMe}_2)_{24}]$  (**12**). For clarity, the hydrogen atoms have been omitted and only the *ipso* C atoms of the phenyl groups are shown. Mn blue; O red; As pink; Sr green; C gray.

Again, one  $\text{Me}_2\text{AsO}_2^-$  ligand coordinated to Mn(1) bridges one  $[\text{Mn}_4\text{O}_2]$  subunit to Mn(8) of a neighboring  $[\text{Mn}_4\text{O}_2]$  subunit. On the other side, a  $[\text{Sr}_2(\text{O}_2\text{CPh})_4(\text{O}_2\text{AsMe}_2)]$  moiety bridges and connects the former  $[\text{Mn}_4\text{O}_2]$  “butterfly” subunit to another through Mn ions and  $\text{Me}_2\text{AsO}_2^-$  ligands. Bond valence sum calculations, again, indicate a  $16 \text{ Mn}^{\text{III}}$

trapped-valence situation (Table 4-4). The core has the nearly same structure as **11**, the main difference involves two relatively weak bonds in **12** [Mn(1)-O(11) = 2.56(1) Å and Mn(8)-O(32) = 2.72(2) Å] that are markedly shorter in **11**. The substitution of Sr<sup>2+</sup> for Ca<sup>2+</sup> and the replacement of the NO<sub>3</sub><sup>-</sup> groups in **11** for the PhCO<sub>2</sub><sup>-</sup> groups in **12** causes an almost insignificant perturbation of the core otherwise. A side-view of **12** emphasizes the planarity of the Mn<sub>16</sub> molecule as shown in Figure 4-9.

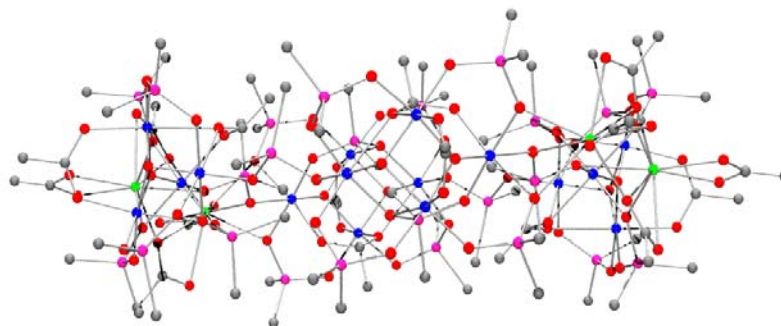


Figure 4-9. ORTEP representation in PovRay format of the side-view of complex **12**, emphasizing the planarity of the molecule. For clarity, the hydrogen atoms have been omitted and only the *ipso* C atoms of the phenyl groups are shown. Mn blue; O red; As pink; Sr green; C gray.

All of the Mn atoms are six-coordinate with near-octahedral geometry and show the expected Jahn-Teller (JT) distortion, which takes the form of an axial elongation in every case. The average JT elongated bond distance is 2.229 Å, approximately 0.30 Å longer than the average non-JT elongated bond distance of 1.925 Å (disregarding the weak Mn(1)-O(11) and Mn(8)-O(32) bond distances). The JT elongation axes of Mn(2) and Mn(3) and their symmetry partners are aligned approximately parallel to each other within each [Mn<sub>4</sub>O<sub>2</sub>] subunit while essentially perpendicular to those of Mn(1) and Mn(4). Similarly, the JT elongation axes of Mn(6) and Mn(7) are aligned parallel to each other, but perpendicular to Mn(5) and Mn(8). Hence, as with **11**, there is an overall nearly

random alignment of the magnetic anisotropy axes of the  $\text{Mn}^{\text{III}}$  ions that will strongly affect the magnetic properties to be discussed below.

As shown in Figure 4-10, the 16 benzoate ligands exhibit four types of binding modes: four bridge Mn ions in the common *syn, syn,  $\mu$*  mode (I), four are bridging three Mn ions in the *syn, anti, syn  $\mu$*  bridging mode II, four are chelating Sr(1) or Sr(2) in mode III, and the final four are chelating Sr(1) or Sr(2) and bridging Sr(2) or Sr(1), respectively, in the *syn, anti, syn  $\mu$*  bridging mode IV. Of the 24 dimethylarsinate ligands, eight are bridging Mn ions in the *syn, syn,  $\mu$*  bridging mode (V), four are bridging three Mn ions in the *syn, syn, anti,  $\mu_3$*  bridging mode (VI), eight are bridging two Mn and one Sr ion in the *syn, syn, anti,  $\mu_3$*  bridging mode (VII), two are bridging Mn ions in the *anti, anti,  $\mu$*  bridging mode (VIII), and the final two are bridging two Mn and two Sr ions in the  $\mu_4$  bridging mode (IX).

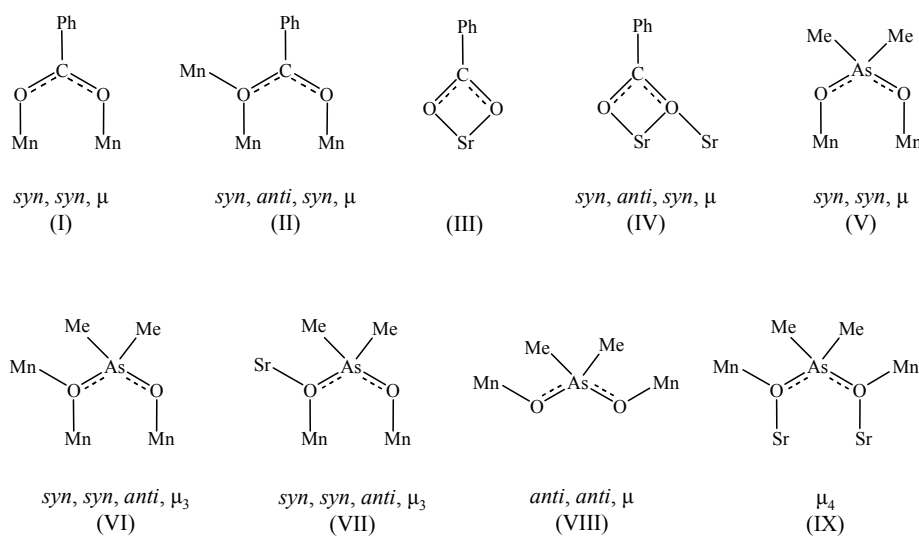


Figure 4-10. Schematic representation of the nine chelating and/or bridging modes found in complex **12**.

The  $[\text{Mn}_4\text{O}_2]$  repeating “butterfly” unit found in **11** and **12** has been found in its discrete form in complexes of the general formula  $[\text{Mn}_4\text{O}_2(\text{O}_2\text{CR})_7(\text{bpy})_2](\text{ClO}_4)^{52}$  and as

a subunit in various other clusters, including  $[\text{Na}_2\text{Mn}_9\text{O}_7(\text{O}_2\text{CPh})_{15}(\text{MeCN})_2]$ ,<sup>131</sup>  
 $[\text{Mn}_{22}\text{O}_{12}(\text{O}_3\text{PPh})_8(\text{O}_2\text{CEt})_{22}(\text{H}_2\text{O})_8]$ ,<sup>132</sup>  $[\text{Mn}_9\text{O}_6(\text{OH})(\text{CO}_3)(\text{O}_2\text{CPE}^{\prime})_{12}(\text{H}_2\text{O})_2]$ ,<sup>112</sup>  
 $[\text{Mn}_{18}\text{O}_{14}(\text{O}_2\text{CMe})_{18}(\text{hep})_4(\text{hepH})_2(\text{H}_2\text{O})_2](\text{ClO}_4)_2$  (hepH = hydroxyethylpyridine),<sup>62</sup>  
 $[\text{Mn}_{21}\text{O}_{14}(\text{OH})_2(\text{O}_2\text{CMe})_{16}(\text{hmp})_8(\text{pic})_2(\text{py})(\text{H}_2\text{O})](\text{ClO}_4)_4$  (hmpH =  
hydroxymethylpyridine and pic = picolinate)<sup>114</sup> and numerous others. However, the  
overall structure of **11** and **12** is quite different from that other previously characterized  
 $\text{Mn}_{16}$  complexes. These include  $[\text{Mn}^{\text{IV}}_6\text{Mn}^{\text{III}}_{10}\text{O}_{16}(\text{OMe})_6(\text{O}_2\text{CMe})_{16}(\text{MeOH})_3(\text{H}_2\text{O})_3]$ ,<sup>111d</sup>  
 $[\text{Mn}^{\text{IV}}_6\text{Mn}^{\text{III}}_{10}\text{O}_{16}(\text{OMe})_6(\text{O}_2\text{CR})_{16}(\text{MeOH})_6]$  (R =  $\text{CH}_2\text{Ph}$ ,  $\text{CH}_2\text{Cl}$  and  $\text{CH}_2\text{Br}$ ),<sup>111i</sup> and  
 $[\text{Mn}^{\text{III}}_8\text{Mn}^{\text{II}}_8(\text{O}_2\text{CMe})_{16}(\text{teaH})_{12}]$  (teaH<sub>3</sub> = triethanolamine).<sup>106</sup> Complex **12** is also only the  
second example of a mixed metal Mn/Sr cluster;

$[\text{Mn}_{14}\text{SrO}_{11}(\text{OMe})_3(\text{O}_2\text{CPh})_{18}(\text{MeCN})_2]$ <sup>133</sup> was the first such species.

Table 4-9. Comparison of selected bond distances (Å) and angles (°) for complexes  
**11**·32MeCN and **12**·16MeCN.

Parameter <sup>a</sup>	<b>11</b>	<b>12</b>
$\text{Mn}^w - \text{O}^a$	1.858(7) – 1.915(8)	1.866(8) – 1.900(10)
$\text{Mn}^b - \text{O}^a$	1.838(13) – 1.999(14)	1.872(10) – 1.926(8)
$\text{Mn}^b - \text{O}^b$ (ax)	2.135(16) – 2.230(12)	2.122(12) – 2.209(9)
$\text{Mn}^b - \text{O}^c$ (ax)	2.299(13) – 2.31(2)	2.305(9) – 2.475(17)
$\text{Mn}^b - \text{O}^d$ (eq)	1.897(14) – 1.962(17)	1.890(9) – 1.947(10)
$\text{Mn}^b \cdots \text{Mn}^w$	3.097(4)–3.409(4)	3.081(3) – 3.438(3)
$\text{Mn}^b \cdots \text{Mn}^b$	2.837(3)	2.822(3) – 2.826(3)
$\text{X}^{2+} \cdots \text{X}^{2+}$	3.870(6)	4.018(2)
$\text{X}^{2+} \cdots \text{Mn}^w$	3.178(3)	3.370(2) – 3.381(3)
$\text{O}^a \cdots \text{Mn}^b \cdots \text{O}^a$	80.5(6) – 85.5(6)	81.6(4) – 82.8(4)
$\text{Mn}^w \cdots \text{O}^a \cdots \text{Mn}^b$	104.6(6) – 129.6(10)	108.1(5) – 131.3(4)
$\text{Mn}^w \cdots \text{Mn}^b \cdots \text{Mn}^b$	49.23 – 65.51	48.91 – 66.68
$\text{Mn}^w \cdots \text{Mn}^b \cdots \text{Mn}^w$	92.75 – 93.49	93.21 – 94.50

<sup>a</sup>  $\text{Mn}^b$  atoms: Mn(2 and 3) in **11** and Mn(2, 3, 6 and 7) in **12**;  $\text{Mn}^w$  atoms: Mn(1 and 4) in  
**11** and Mn(1, 4, 5 and 8) in **12**;  $\text{X}^{2+}$  atoms: Ca(1) in **11** and Sr(1 and 2) in **12**;  
 $\text{O}^a$  = triply bridging  $\text{O}^{2-}$ ;  $\text{O}^b$  = axial bridging  $\text{PhCO}_2^-$ ;  $\text{O}^c$  = axial bridging  $\text{Me}_2\text{AsO}_2^-$ ;  
 $\text{O}^d$  = equatorial bridging  $\text{Me}_2\text{AsO}_2^-$ .

In Table 4-9 is shown a comparison of selected bond distances and angles of complexes **11** and **12**, emphasizing the structural similarities between the two  $\text{Mn}_{16}$  molecules. Slight differences in the values should be treated with caution and are probably reflective of the disorder associated with several  $\text{PhCO}_2^-$  and  $\text{Me}_2\text{AsO}_2^-$  ligands in both **11** and **12**.

#### 4.2.3 Magnetochemistry of Complexes **9** and **10**

Variable-temperature DC susceptibility measurements were performed on dried, microcrystalline samples of **9**· $\text{H}_2\text{O}$  and **10**· $3\text{ClCH}_2\text{CH}_2\text{Cl}$ , restrained in eicosane to prevent torquing, in a 1.0 kG field in the range of 5.0-300 K. The isotropic (Heisenberg) spin Hamiltonian describing an exchange-coupled  $\text{Mn}^{\text{III}}_2\text{Mn}^{\text{IV}}_2$  tetranuclear complex such as **9** is given by eq 4-5, using the numbering scheme of Figure 4-11, where  $S_1 = S_3 = 3/2$  and  $S_2 = S_4 = 2$ , and it is assumed that pairwise magnetic exchange interactions between pairs of  $\text{Mn}^{\text{III}}$  and  $\text{Mn}^{\text{IV}}$  ions are nearly equivalent such that  $J_{12} = J_{23} = J_{14} = J_{34} = J''$ .

$$\hat{H} = -2J(\hat{S}_2\hat{S}_4) - 2J'(\hat{S}_1\hat{S}_3) - 2J''(\hat{S}_1\hat{S}_2 + \hat{S}_1\hat{S}_4 + \hat{S}_2\hat{S}_3 + \hat{S}_3\hat{S}_4) \quad (4-5)$$

The eigenvalues of the spin Hamiltonian may be determined using the Kambe vector coupling method<sup>51</sup> with the following coupling scheme, where  $\hat{S}_A = \hat{S}_1 + \hat{S}_3$ ,  $\hat{S}_B = \hat{S}_2 + \hat{S}_4$ ,  $\hat{S}_T = \hat{S}_A + \hat{S}_B$ , and are given in eq 4-6.

$$\begin{aligned} E(S_T, S_A, S_B) = & -J[S_B(S_B + 1)] - J'[S_A(S_A + 1)] \\ & - J''[S_T(S_T + 1) - S_A(S_A + 1) - S_B(S_B + 1)] \end{aligned} \quad (4-6)$$

The overall degeneracy of the system is 400, made up of 60 individual spin states with total spin ( $S_T$ ) values in the range of 0 to 7 (Table 4-10).

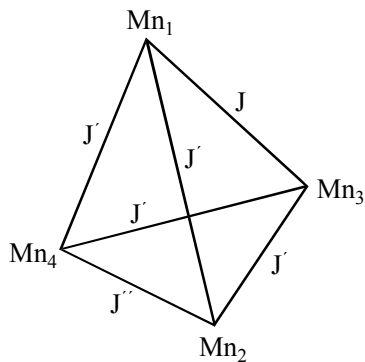


Figure 4-11. Representation of the pairwise exchange interactions  $J$ ,  $J'$  and  $J''$  between numbered Mn ions of complex **9**.

Table 4-10. Distribution of spin states for complex **9**.

$S_T$	$n^a$	$2S_T + 1$	$n(2S_T + 1)$
0	4	1	4
1	10	3	30
2	13	5	65
3	13	7	91
4	10	9	90
5	6	11	66
6	3	13	39
7	1	15	15

<sup>a</sup> number of spin states with the indicated  $S_T$  values

A theoretical  $\chi_M$  versus  $T$  expression was derived for complex **9** from the use of the Van Vleck equation,<sup>134</sup> and was modified to include a fraction ( $p$ ) of paramagnetic impurity (assumed to be mononuclear  $Mn^{II}$ ), and temperature-independent paramagnetism (TIP). The latter was kept constant at  $400 \times 10^{-6} \text{ cm}^3 \text{ K mol}^{-1}$ . The resulting equation was used to fit the experimental  $\chi_M$  vs  $T$  data for complex **9** which are plotted as  $\chi_M T$  vs  $T$  in Figure 4-12. The  $\chi_M T$  value decreases rapidly with decreasing temperature from of  $8.4 \text{ cm}^3 \text{ K mol}^{-1}$  at 300 K to  $4.6 \text{ cm}^3 \text{ K mol}^{-1}$  at 15 K, and then it sharply increases to  $5.7 \text{ cm}^3 \text{ K mol}^{-1}$  at 5.0 K. The spin-only ( $g = 2$ ) value for a molecule composed of noninteracting  $Mn^{III}_2Mn^{IV}_2$  ions is  $9.75 \text{ cm}^3 \text{ K mol}^{-1}$ . Hence, antiferromagnetic coupling dominates the overall intramolecular exchange interactions.

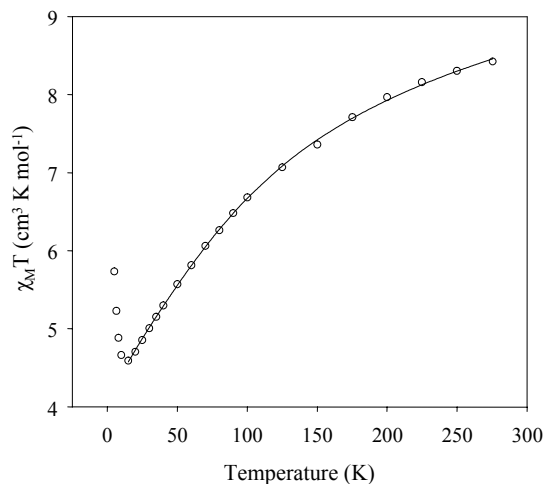


Figure 4-12. Plot of  $\chi_M T$  vs temperature for a dried, microcrystalline sample of complex **9**·H<sub>2</sub>O in eicosane.  $\chi_M$  is the DC molar magnetic susceptibility measured in a 1.0 kG field. The solid line is the fit of the data to the theoretical equation; see the text for the fit parameters.

Data below 15 K were ignored and the modified Van Vleck equation was used to fit the observed temperature dependence of the molar magnetic susceptibility as a function of the three exchange coupling parameters,  $J$ ,  $J'$  and  $J''$ , and an isotropic  $g$  value. The obtained fit (solid line in Figure 4-12) gave  $J = -0.49 \text{ cm}^{-1}$ ,  $J' = -14 \text{ cm}^{-1}$ ,  $J'' = -3.6 \text{ cm}^{-1}$ ,  $g = 1.91$  and  $p = 4.7 \times 10^{-4}$ . The obtained values indicate that the ground state of **9** is doubly degenerate, specifically  $|S_T, S_A, S_B\rangle = |0,0,0\rangle$  and  $|S_T, S_A, S_B\rangle = |1,0,1\rangle$ . There are six other spin states within  $15 \text{ cm}^{-1}$  of the ground state (Figure 4-13 and Table 4-11).

The results of the fit confirm the presence of antiferromagnetic exchange interactions (negative  $J$  values) between the Mn ions in complex **9** as was expected by comparison of **9** to various dinuclear  $[\text{Mn}_2(\mu\text{-O})_2(\mu\text{-O}_2\text{CR})]^{z+}$  ( $z = 1, 2, 3$ ) systems in which  $\text{Mn}^{\text{III}}\text{Mn}^{\text{III}}$ ,  $\text{Mn}^{\text{III}}\text{Mn}^{\text{IV}}$  and  $\text{Mn}^{\text{IV}}\text{Mn}^{\text{IV}}$  pairwise exchange interactions were found to be antiferromagnetic. The Mn-O-Mn angles are expected to play an important role in determining both the sign and magnitude of  $J$ ,  $J'$  and  $J''$  (Table 4-12). The weakly, negative (antiferromagnetic)  $J$  values are consistent with the relatively acute

$\text{Mn}^{\text{III}}\text{-O-Mn}^{\text{III}}$ ,  $\text{Mn}^{\text{III}}\text{-O-Mn}^{\text{IV}}$ , and  $\text{Mn}^{\text{IV}}\text{-O-Mn}^{\text{IV}}$  angles of  $\sim 96^\circ$ ,  $\sim 97^\circ$  and  $\sim 97^\circ$ . Also consistent with expectations is that the  $\text{Mn}^{\text{IV}}\text{Mn}^{\text{IV}}$  pairwise exchange interaction is the strongest in the molecule. Unfortunately, only qualitative comparisons between the calculated  $J$  values and those found in the literature are possible; to our knowledge there are no examples of  $[\text{Mn}_4(\mu_3\text{-O})_4(\mu\text{-O}_2\text{CR})_6]^z$  ( $z = 0$  or  $1$ ) systems for which  $J$  values have been reported. Spin frustration in the core of **9** is also expected as all of the couplings are antiferromagnetic and the spins cannot all be antiparallel to all of their neighbors.

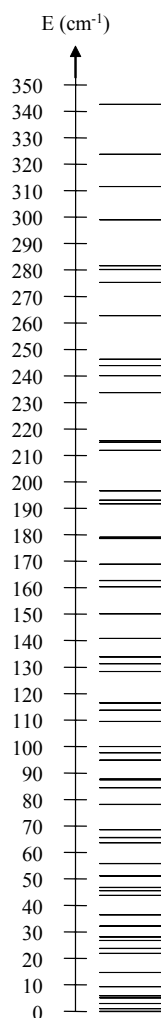


Figure 4-13. Ordering of the spin states using the calculated exchange parameters,  $J$ ,  $J'$  and  $J''$ , and the Van Vleck equation of complex **9**.

Table 4-11. Spin states of complex **9** in the  $|S_T, S_A, S_B\rangle$  format ordered as a function of their energy calculated using the exchange parameters,  $J$ ,  $J'$  and  $J''$ , and the Van Vleck equation.

$ S_T, S_A, S_B\rangle$	E (cm <sup>-1</sup> )	$ S_T, S_A, S_B\rangle$	E (cm <sup>-1</sup> )
$ 0,0,0\rangle$	0.00	$ 2,2,3\rangle$	113.82
$ 1,0,1\rangle$	0.00	$ 1,2,3\rangle$	116.46
$ 0,1,1\rangle$	0.98	$ 3,2,3\rangle$	128.34
$ 1,2,1\rangle$	2.94	$ 4,3,3\rangle$	131.28
$ 3,3,1\rangle$	5.00	$ 0,3,3\rangle$	133.92
$ 2,3,1\rangle$	5.88	$ 3,1,3\rangle$	140.90
$ 2,2,1\rangle$	9.32	$ 4,2,3\rangle$	150.12
$ 1,1,1\rangle$	14.62	$ 5,3,3\rangle$	160.32
$ 2,1,1\rangle$	21.88	$ 4,1,3\rangle$	162.68
$ 3,2,1\rangle$	23.84	$ 4,0,4\rangle$	168.96
$ 4,3,1\rangle$	26.78	$ 2,3,4\rangle$	178.58
$ 2,0,2\rangle$	28.16	$ 5,2,3\rangle$	179.16
$ 2,3,2\rangle$	32.28	$ 3,1,4\rangle$	191.72
$ 1,1,2\rangle$	36.40	$ 3,3,4\rangle$	193.10
$ 1,2,2\rangle$	43.86	$ 6,3,3\rangle$	196.62
$ 0,2,2\rangle$	45.62	$ 3,2,4\rangle$	211.94
$ 3,3,2\rangle$	46.80	$ 4,3,4\rangle$	214.88
$ 2,2,2\rangle$	51.12	$ 2,2,4\rangle$	215.46
$ 1,3,2\rangle$	55.82	$ 4,2,4\rangle$	233.72
$ 2,1,2\rangle$	63.68	$ 1,3,4\rangle$	240.18
$ 3,2,2\rangle$	65.64	$ 5,3,4\rangle$	243.92
$ 4,3,2\rangle$	68.58	$ 4,1,4\rangle$	246.28
$ 3,1,2\rangle$	78.20	$ 5,2,4\rangle$	262.76
$ 3,0,3\rangle$	84.48	$ 5,1,4\rangle$	275.32
$ 4,2,2\rangle$	87.42	$ 6,3,4\rangle$	280.22
$ 1,3,3\rangle$	87.72	$ 1,1,0\rangle$	281.60
$ 2,3,3\rangle$	94.98	$ 6,2,4\rangle$	299.06
$ 5,3,2\rangle$	97.62	$ 2,2,0\rangle$	311.62
$ 2,1,3\rangle$	99.98	$ 7,3,4\rangle$	323.78
$ 3,3,3\rangle$	109.50	$ 3,3,0\rangle$	342.62

Table 4-12. Selected Mn $\cdots$ O $\cdots$ Mn angles ( $^\circ$ ) relevant to magnetic exchange parameters  $J$ ,  $J'$  and  $J''$  for complex **9**.

Parameter <sup>a</sup>	Range
Mn <sup>III</sup> $\cdots$ O $\cdots$ Mn <sup>III</sup>	93.21(11) – 98.14(12)
Mn <sup>III</sup> $\cdots$ O $\cdots$ Mn <sup>IV</sup>	93.25(11) – 100.18(11)
Mn <sup>IV</sup> $\cdots$ O $\cdots$ Mn <sup>IV</sup>	97.11(12) – 97.69(11)

<sup>a</sup> O = triply bridging O<sup>2-</sup> ion = O(1), O(2), O(3) and O(4); Mn<sup>III</sup> ions = Mn(2) and Mn(4); Mn<sup>IV</sup> ions = Mn(1) and Mn(3)

The energies of the spin states calculated using the J parameters indicate the presence of low-lying excited states of greater S value than the ground state. This was confirmed by AC magnetic susceptibility measurements carried out on a dried, microcrystalline sample of  $\mathbf{9}\cdot\text{H}_2\text{O}$  in a 3.5 G AC field oscillating at 1000 Hz. In Figure 4-14 is shown the in-phase AC susceptibility, plotted as  $\chi_M' T$  versus  $T$ , together with the out-of-phase AC susceptibility ( $\chi_M''$ ), in the 1.8-10 K temperature range to minimize the possibility of populating excited states.

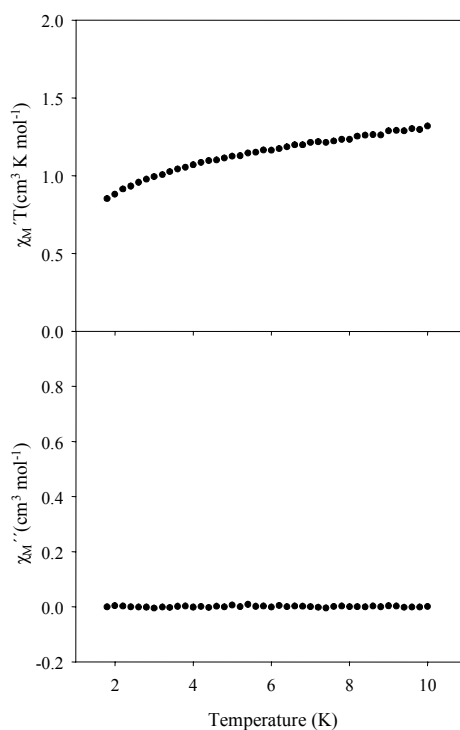


Figure 4-14. Plot of the in-phase (as  $\chi_M' T$ ) and out-of-phase ( $\chi_M''$ ) AC susceptibility signals vs temperature for a dried, microcrystalline sample of complex  $\mathbf{9}\cdot\text{H}_2\text{O}$  in eicosane in a 3.5 G AC field oscillating at 1000 Hz.

The downward sloping  $\chi_M' T$  versus  $T$  plot confirms that depopulation of excited states with greater S value than the ground state is occurring as the temperature decreases. Extrapolation of the plot to 0 K, where only the ground state will be populated, gives a  $\chi_M' T$  value of  $\sim 0.8 \text{ cm}^{-3} \text{ K mol}^{-1}$ . This value is intermediate between  $0.0 \text{ cm}^3 \text{ K}$

$\text{mol}^{-1}$  and  $1.0 \text{ cm}^3 \text{ K mol}^{-1}$ , that expected for an  $S = 0$  state and an  $S = 1$  state with  $g = 2$ , respectively. Also evident from the AC studies is the lack of an out-of-phase AC susceptibility signal ( $\chi_M''$ ). Such a signal is indicative of the onset of slow magnetic relaxation and confirms that complex **9** does not function as a single-molecule magnet in accord with the small ground state spin of the molecule.

Unfortunately, application of the Kambe vector coupling method<sup>51</sup> to determine the pairwise exchange interactions in complex **10** is not feasible. Although the crystallographic symmetry of **10**, like **9**, is  $C_i$ , it is not reasonable to assume a simplifying approximation to analyze the exchange interactions as was done for **9**. As discussed previously, there are two independent  $\text{Mn}_4$  molecules, each with significantly differing angles and interatomic distances. As an alternative, density functional theory (DFT) calculations on both **9** and **10** are currently in progress to better understand the factors that control the magnitude of the  $J$  values in these types of Mn cubane complexes.

#### **4.2.4 Magnetochemistry of Complexes 11 and 12**

##### **4.2.4.1 DC studies**

Variable-temperature DC susceptibility measurements were performed on dried, microcrystalline samples of **11**·2MeCN and **12**, restrained in eicosane to prevent torquing, in a 1.0 kG field in the range of 5.0-300 K. Evident from a comparison of the  $\chi_M T$  vs  $T$  plots is that the magnetic behavior of the two complexes is very similar (Figure 4-15). For **11**,  $\chi_M T$  smoothly decreases with decreasing temperature from  $43.9 \text{ cm}^3 \text{ K mol}^{-1}$  at 300 K to  $16.7 \text{ cm}^3 \text{ K mol}^{-1}$  at 5.0 K. Similarly for **12**,  $\chi_M T$  gradually decreases with decreasing temperature from  $42.9 \text{ cm}^3 \text{ K mol}^{-1}$  at 300 K to  $15.8 \text{ cm}^3 \text{ K mol}^{-1}$  at 5.0 K. For both  $\text{Mn}_{16}$  complexes, the value of  $\chi_M T$  at 300 K is less than that expected for a

$\text{Mn}^{\text{III}}_{16}$  complex with non-interacting metal centers ( $48 \text{ cm}^3 \text{ K mol}^{-1}$  for  $g = 2$ ), suggesting the presence of appreciable intramolecular antiferromagnetic interactions.

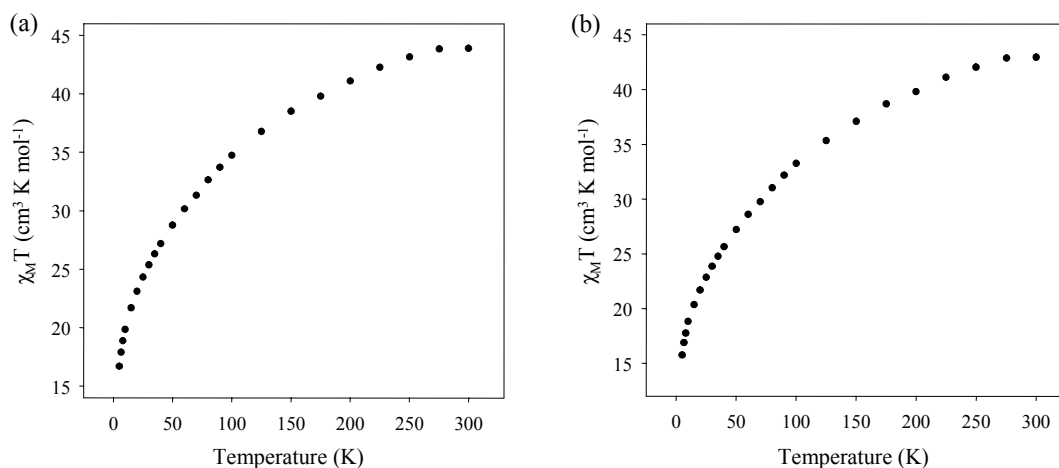


Figure 4-15. Plot of  $\chi_M T$  vs temperature for dried, microcrystalline samples of (a) complex **11**·2MeCN and (b) complex **12** in eicosane.  $\chi_M$  is the DC molar magnetic susceptibility measured in a 1.0 kG field.

Each complex contains sixteen  $\text{Mn}^{\text{III}}$  centers, with total spin ( $S$ ) values therefore ranging from 0 to 32. A matrix diagonalization approach to evaluate the various  $\text{Mn}_2$  pairwise exchange interaction constants ( $J$ ) is made challenging by the low symmetry and high nuclearity of the molecules. Such a method would involve the diagonalization of a matrix of dimensions  $153 \times 10^9$  by  $153 \times 10^9$ , and this is clearly not reasonable. An equivalent operator approach based on the Kambe vector coupling method<sup>51</sup> is also not feasible. Hence, we concentrated on determining on the ground state spin  $S$  of the complexes by the fitting of variable-temperature and -field magnetization data collected on polycrystalline samples in the 0.1-70 kG and 1.8-10.0 K field and temperature ranges. Despite many attempts to fit the data using the program MAGNET,<sup>54</sup> which assumes only the ground state of a molecule is populated, satisfactory fits were not obtained. This is likely due to the presence of low-lying excited states that are populated even at the very low temperatures employed. Unfortunately, the latter are commonly encountered in high

nuclearity clusters; weak exchange interactions between the constituent ions and/or spin frustration effects within the molecule give rise to a high density of spin states.

Reasonable fits were not obtained even using only very weak field and low temperature magnetization data (0.1-0.5 T and 1.8-4 K) where no interference from Zeeman effects in the applied DC field, i.e., excited states with larger S values crossing in energy with the ground state S, is expected.

The topology of **11** and **12** promotes spin frustration, consisting of eight edge-sharing  $[\text{Mn}_3\text{O}]$  triangular subunits found in the four  $[\text{Mn}_4\text{O}_2]$  “butterfly” units that comprise the  $\text{Mn}_{16}$  molecule. Such spin frustration effects, whereby competing antiferromagnetic exchange interactions of comparable magnitude prevent the antiparallel alignment of spins, were previously reported for the related  $[\text{Mn}^{\text{III}}_4\text{O}_2(\text{O}_2\text{CMe})_7(\text{bpy})_2](\text{ClO}_4)$  “butterfly” complex.<sup>52</sup> Very weak exchange coupling parameters (J) between the constituent  $\text{Mn}^{\text{III}}$  ions were found and it was shown further that the ground state spin of the “butterfly” molecule was very sensitive to the precise magnitude of the competing exchange interactions.<sup>52</sup> Hence, the triangular arrangement of coupled Mn ions, as found in **11** and **12**, is the classic topology for spin frustration effects, accounting for a high density of molecular spin states close in energy to the ground state spin, S. Thus, a more accurate and reliable approach of determining the ground state spin of such molecules as **11** and **12** is to measure the AC magnetic susceptibility, a method which does not involve the use of a DC field.<sup>66,106,111i,112,119</sup> Such studies have recently proven crucial in the determination of the ground state spin of other molecules reported by our group and were therefore carried out on complexes **11** and **12**.<sup>66,106,111i,112,119</sup>

#### 4.2.4.2 AC studies

In an AC magnetic susceptibility experiment, a weak field (typically in the 1 - 5 G range) oscillating at a particular AC frequency ( $\nu$ ) is applied to a sample to investigate the dynamics of its magnetization relaxation. If the magnetization vector of the molecule can reorient at the frequency of the oscillating AC field, then there is no out-of-phase ( $\chi_M''$ ) susceptibility signal, and the in-phase signal ( $\chi_M'$ ) is equal to the DC magnetic susceptibility. However, if the magnetization vector of the molecule cannot keep up with the oscillating field, then an out-of-phase signal is observed, indicating an energy barrier to magnetization relaxation that is comparable in energy to that of the thermal energy. The  $\chi_M''$  signal is dependent on the frequency of the oscillating AC field, i.e., faster the oscillation of the AC field, the higher the temperatures at which the  $\chi_M''$  signal is observed, and is accompanied by a frequency-dependent decrease in the in-phase signal (as  $\chi_M' T$ ). Such signals are a characteristic signature of the superparamagnet-like properties of a SMM, however, should not be taken as proof that a molecule behaves as a SMM; intermolecular interactions and phonon bottlenecks have been shown to also lead to such signals. Thus, AC magnetic susceptibility data were collected on dried, microcrystalline samples of **11**·2MeCN and **12** in the temperature range 1.8-10 K in a zero DC field and a 3.5 G AC field oscillating at several frequencies in the 25-997 Hz range. The data for complex **11**·2MeCN are plotted as  $\chi_M' T$  and  $\chi_M''$  in Figure 4-16 and show a frequency-dependent  $\chi_M''$  signal below 3 K; the  $\chi_M''$  signals at the given frequencies are merely the tails of peaks whose maxima clearly lie below the 1.8 K operating limit of our SQUID instrument.

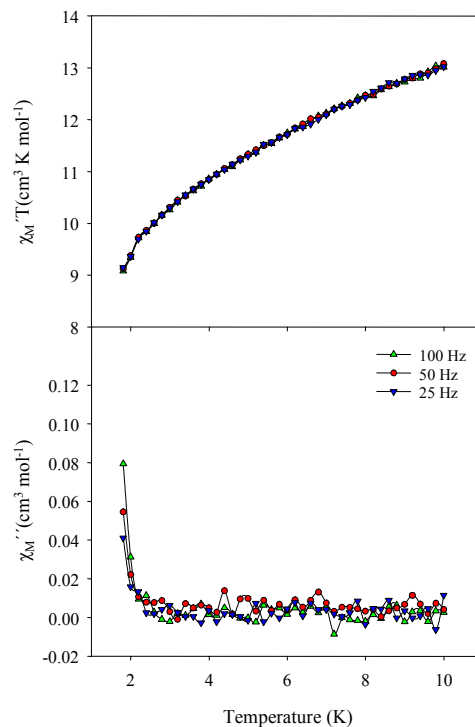


Figure 4-16. Plot of the in-phase (as  $\chi_M' T$ ) and out-of-phase ( $\chi_M''$ ) AC susceptibility signals vs temperature for a dried, microcrystalline sample of complex **11**·2MeCN in eicosane at the indicated oscillation frequencies.

The in-phase signal, plotted as  $\chi_M' T$  appears frequency-dependent at the lowest temperatures and decreases gradually with decreasing temperature, hence confirming the population of low-lying excited states of the molecule since occupation of only the ground state would give an essentially temperature-independent value. The downward sloping of the  $\chi_M' T$  vs  $T$  plot indicates depopulation of excited states with  $S$  values greater than the ground state with decreasing temperature. Extrapolation to 0 K, where only the ground state will be populated, suggests the plot is heading to a  $\chi_M' T$  value of  $\sim 10 \text{ cm}^3 \text{ K mol}^{-1}$ . This is the value expected for an  $S = 4$  state with  $g \sim 2.00$ . Similar results were obtained for complex **12**, and we conclude that the ground state spin of **11** and **12** is  $S = 4$ . The out-of-phase  $\chi_M''$  signals exhibited by **11** and **12** appear at very low temperatures, suggesting only very small effective energy barriers to magnetization

relaxation. Nevertheless, we decided to investigate the magnetic behavior at lower temperatures, where the origin of the slow magnetization behavior could be resolved.

#### 4.2.4.3 Hysteresis studies below 1.8 K

Hysteresis loops are the definitive property of a magnet and can provide unquestionable proof that a molecule behaves as a single-molecule magnet. Thus, DC magnetization field studies below 1.8 K were collected on wet crystals of complex **11**·32MeCN in order to determine whether the slow magnetization relaxation suggested by the tails of the  $\chi_M''$  signals in the AC magnetic susceptibility was due to single-molecule magnetism or to some other effect, such as phonon bottleneck. DC magnetization field scans were performed in the 0.04-7.0 K temperature range using a fixed field sweep rate of 0.070 T/s as shown in Figure 4-17a. Magnetization responses measured at different field sweep rates in the range from 0.004 to 0.56 T/s at a constant temperature of 0.04 K are given in Figure 4-17b.

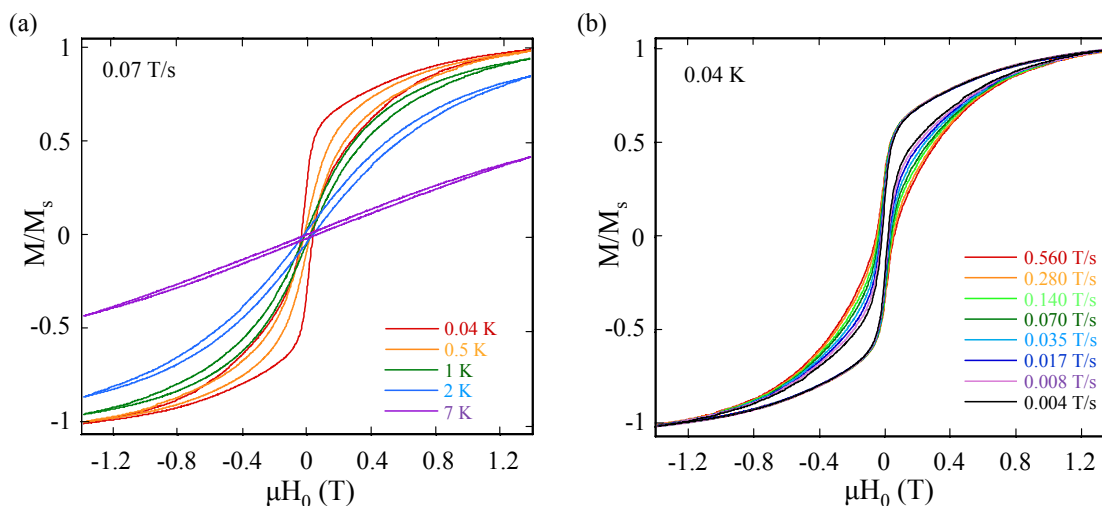


Figure 4-17. Magnetization vs DC field plots for a single crystal of complex **11**·32MeCN at (a) the indicated temperatures and a fixed field sweep rate of 0.07 T/s; and (b) the indicated sweep rates and a fixed temperature of 0.04 K. The magnetization is normalized to its maximum value,  $M_s$ .

Hysteresis loops become evident in the scans at 7 K, and their coercivities increase with decreasing temperature and with increasing field sweep rate, as expected for the superparamagnetic-like behavior of a SMM. Thus, complex **11** (and given the structural similarities, **12**) are new additions to the family of SMMs. In contrast to the hysteresis loops of several other SMMs, such as Mn<sub>12</sub> complexes, the loops for **11** do not show the steplike features indicative of quantum tunneling of magnetization (QTM) between the energy states of the molecule.<sup>27,61,104,113</sup> The absence of such steps is a common finding for higher nuclearity SMMs<sup>62,63,66,98,105,106,111g,111h,111i,114</sup> and is primarily a consequence of a distribution of local molecular environments owing to solvent and ligand disorder, both of which are prevalent in **11** and **12**. In addition, weak intermolecular interactions and low-lying excited states likely also contribute to broadening of the steps. Although the loops are smooth, there is a readily discernible step at zero field that likely corresponds to tunneling through the anisotropy barrier through the degenerate  $\pm m_s$  sublevels of the  $S = 4$  spin manifold. Tunneling through  $\pm m_s$  sublevels of excited state manifolds probably also contributes to the magnitude of the zero-field step.

Unfortunately, due to the extremely fast magnetization relaxation at zero field, DC magnetization decay measurements are not feasible; this is typically the method by which the effective energy barrier to magnetization reversal ( $U_{\text{eff}}$ ) of a SMM is determined, especially in cases where only the tail of a  $\chi_M''$  signal (and not the complete peak) is exhibited by a molecule. It is apparent, however, from the hysteresis measurements that the effective relaxation barrier for complex **11**·32MeCN is unfortunately rather small and this is likely due to efficient tunneling pathways in the ground state and/or excited state spin manifolds. The energy barrier ( $U$ ), given by  $S^2|D|$  for an integer spin system such as

**11** and **12**, would be of moderate magnitude compared to other SMMs as  $S = 4$  and a nonzero, negative  $D$  value is expected given the orientation of the anisotropy axes of the  $\text{Mn}^{\text{III}}$  ions in a non-antiparallel manner. This parameter reflects only thermal activation over the magnetization energy barrier and disregards relaxation by quantum tunneling, however, and is almost certainly greater than  $U_{\text{eff}}$ . Values of  $D$  are often obtained by monitoring the separations between the steps that occur at periodic field values in the hysteresis loops of a SMM or by single crystal high-frequency EPR (HF-EPR) measurements. Alternatively, in instances such as this when there are no steps or only small crystals unsuitable for HF-EPR measurements can be obtained,  $D$  is usually determined from fits of variable-temperature and -field magnetization measurements. We have not been able to obtain an estimate of  $D$ , however, and explanations for this have already been described. As such, we have been unable to determine values of both  $U_{\text{eff}}$  and  $U$  for either complex **11** or **12** to date, but despite the low anisotropy barriers, the frequency-dependent AC susceptibility data and the sweep rate and temperature-dependent coercivities of the hysteresis loops of **11** establish that these  $\text{Mn}_{16}$  molecules are new SMMs.

### 4.3 Conclusions

In summary, attempted ligand substitution reactions of  $[\text{Mn}_{12}\text{O}_{12}(\text{O}_2\text{CR})_{16}(\text{H}_2\text{O})_4]$  ( $\text{R} = \text{Me}$  and  $\text{Ph}$ ) with dimethylarsinic acid ( $\text{Me}_2\text{AsO}_2\text{H}$ ) have been explored and found to cause a transformation of the  $[\text{Mn}_{12}\text{O}_{12}]$  core. Two general structural types were isolated from these reactions, which vary only slightly in the conditions: (i) mixed-valence, trapped-valence tetranuclear complexes **9** and **10** which possess a manganese-oxo cubane core and the general formula  $[\text{Mn}_4(\mu_3\text{-O})_4(\text{O}_2\text{AsMe}_2)_6]^{0,+}$  and (ii) trapped-valence  $\text{Mn}^{\text{III}}_{16}$  complexes **11** and **12** which possess a novel structural topology comprised of four

[Mn<sup>III</sup><sub>4</sub>(μ-O)<sub>2</sub>] “butterfly” units. All four complexes represent the first examples of manganese clusters ligated by Me<sub>2</sub>AsO<sub>2</sub><sup>-</sup> groups.

DC and AC magnetic susceptibility studies on **9** suggest a small ground state spin and show that the complex does not behave as a single-molecule magnet. Similar studies are currently in progress for complex **10** as are more sophisticated DFT calculations on both **9** and **10**. These studies should provide considerable insight to our understanding of their magnetic properties. Similarly, magnetic studies on **11** and **12** suggest a ground state spin value of  $S = 4$  and tails of peaks in the out-of-phase AC susceptibility indicate the onset of slow magnetization relaxation. Hysteresis loops obtained from magnetization vs DC field scans establish that **11** (and by analogy **12**) are new members of the growing family of single-molecule magnets.

Hence, our efforts to extend the exploration of the reactivity of various non-carboxylate ligands with Mn<sub>12</sub> complexes continues to prove a useful strategy for the preparation of new polynuclear Mn clusters, some of which have interesting magnetic properties. Like the related non-carboxylic acid, PhSeO<sub>2</sub>H (pK<sub>a</sub> = 4.79), the use of Me<sub>2</sub>AsO<sub>2</sub>H as a reactant causes a structural rearrangement of the [Mn<sub>12</sub>O<sub>12</sub>] core. On this basis, we conclude that a combination of relatively high pK<sub>a</sub> value and large O···O bite distance compared to MeCO<sub>2</sub><sup>-</sup> are important factors to be considered for the isolation of new structural types from reactions of Mn<sub>12</sub> complexes with non-carboxylate ligands. Other studies with related non-carboxylate ligands will undoubtedly help us to better understand the causes of the structural transformations.

## 4.4 Experimental

### 4.4.1 Syntheses

All manipulations were performed under aerobic conditions using materials as received, except where otherwise noted.  $[\text{Mn}_{12}\text{O}_{12}(\text{O}_2\text{CMe})_{16}(\text{H}_2\text{O})_4]\cdot 2\text{MeCO}_2\text{H}\cdot 4\text{H}_2\text{O}$  (**1**) and  $[\text{Mn}_{12}\text{O}_{12}(\text{O}_2\text{CPh})_{16}(\text{H}_2\text{O})_4]$  (**8**) were prepared as described elsewhere.<sup>22,50</sup>

**$[\text{Mn}_4\text{O}_4(\text{O}_2\text{AsMe}_2)_6]$  (**9**)**. A solution of complex **1** (0.50 g, 0.24 mmol) in MeCN (75 cm<sup>3</sup>) was treated with Me<sub>2</sub>AsO<sub>2</sub>H (0.60 g, 4.3 mmol) in MeCN (25 cm<sup>3</sup>). The solution color changed from dark brown to deep red as it was stirred overnight. The solvent was removed *in vacuo*. Toluene (25 cm<sup>3</sup>) was added to the residue, and the solution was again evaporated to dryness. The addition and removal of toluene was repeated three more times. The residue was redissolved in CH<sub>2</sub>Cl<sub>2</sub> (50 cm<sup>3</sup>) and filtered through Celite. Diffusion of pentane into the CH<sub>2</sub>Cl<sub>2</sub> solution produced large red crystals, and these were suitable for X-ray crystallography if maintained in contact with the mother liquor to prevent the loss of interstitial solvent. After 6 days, the crystals were isolated by filtration, washed with pentane and dried *in vacuo*; yield 75%. The dried material is hygroscopic, analyzing for **9**·H<sub>2</sub>O. Anal. Calcd (found) for C<sub>12</sub>H<sub>38</sub>As<sub>6</sub>Mn<sub>4</sub>O<sub>17</sub>: C, 12.83 (12.79); H, 3.41 (3.48); N, 0.00 (0.00). Selected IR data (KBr, cm<sup>-1</sup>): 3016 (m), 2965 (m), 2926 (m), 2878 (m), 1653 (w), 1568 (s), 1473 (w), 1420 (s), 1272 (m), 1094 (s), 808 (vs), 652 (m), 622 (s), 565 (m), 500 (s), 481 (s).

**$\{[\text{Mn}_4\text{O}_4(\text{O}_2\text{AsMe}_2)_6](\text{NO}_3)\}_2$  (**10**)**. A solution of complex **1** (0.20 g, 0.10 mmol) in MeCN (30 cm<sup>3</sup>) was treated with solid Me<sub>2</sub>AsO<sub>2</sub>H (0.24 g, 1.7 mmol) and Ca(NO<sub>3</sub>)<sub>2</sub>·4H<sub>2</sub>O (0.034 g, 0.15 mmol). MeOH (1 cm<sup>3</sup>) was added and the solution was stirred for 30 min. A small amount of dark brown precipitate was removed from the deep red solution by filtration through Celite. To the filtrate was added 1,2-dichloroethane (80

cm<sup>3</sup>) and the solvent was allowed to evaporate slowly in air. Crystals formed slowly over two weeks, and these were suitable for X-ray studies if maintained in contact with the mother liquor to prevent the loss of interstitial solvent. After two weeks, the crystals were isolated by filtration, washed with large amounts of 1,2-dichloroethane, and dried under vacuum; yield ~24%. Anal. Calcd (found) for **10**·3ClCH<sub>2</sub>CH<sub>2</sub>Cl

(C<sub>30</sub>H<sub>84</sub>As<sub>12</sub>Cl<sub>6</sub>N<sub>2</sub>O<sub>38</sub>Mn<sub>8</sub>): C, 13.69 (13.67); H, 3.22 (3.36); N, 1.06 (0.96). Selected IR data (KBr, cm<sup>-1</sup>): 3422 (vs), 1559 (s), 1419 (m), 1384 (vs), 1273 (w), 828 (vs), 796 (vs), 652 (m), 616 (w), 590 (w), 490 (m).

**[Mn<sub>16</sub>Ca<sub>4</sub>O<sub>8</sub>(O<sub>2</sub>CPh)<sub>8</sub>(O<sub>2</sub>AsMe<sub>2</sub>)<sub>28</sub>](NO<sub>3</sub>)<sub>4</sub> (11)**. To a stirred slurry of complex **8** (0.25 g, 0.087 mmol) in MeCN (10 cm<sup>3</sup>) was added solid Me<sub>2</sub>AsO<sub>2</sub>H (0.22 g, 1.6 mmol) and solid Ca(NO<sub>3</sub>)<sub>2</sub>·4H<sub>2</sub>O (0.021 g, 0.087 mmol). MeOH (3 cm<sup>3</sup>) was added to the slurry with stirring for 20 min. The deep red solution containing some brown powder was filtered through Celite. Diffusion of Et<sub>2</sub>O into the solution slowly produced crystals, and these were suitable for X-ray crystallography if maintained in contact with the mother liquor to prevent the loss of interstitial solvent. After 3 days, crystals were isolated by filtration, washed with MeCN, and dried under vacuum; yield 5%. Anal. Calcd (found) for **11**·2MeCN (C<sub>116</sub>H<sub>214</sub>N<sub>6</sub>As<sub>28</sub>Ca<sub>4</sub>O<sub>92</sub>Mn<sub>16</sub>): C, 22.11 (22.04); H, 3.42 (3.65); N, 1.33 (1.18). Selected IR data (cm<sup>-1</sup>): 1597 (m), 1550 (m), 1394 (s), 1269 (w), 799 (vs), 721 (m), 649 (m), 588 (m), 484 (s).

**[Mn<sub>16</sub>O<sub>8</sub>Sr<sub>4</sub>(O<sub>2</sub>CPh)<sub>16</sub>(O<sub>2</sub>AsMe<sub>2</sub>)<sub>24</sub>] (12)**. To a stirred slurry of complex **8** (0.25 g, 0.087 mmol) in MeCN (10 cm<sup>3</sup>) was added solid Me<sub>2</sub>AsO<sub>2</sub>H (0.22 g, 1.6 mmol) and solid Sr(ClO<sub>4</sub>)<sub>2</sub>·H<sub>2</sub>O (0.025 g, 0.087 mmol). MeOH (1 cm<sup>3</sup>) was added to the slurry with stirring for 20 min. The deep red solution containing some brown powder was filtered

through Celite. Diffusion of Et<sub>2</sub>O into the solution slowly produced crystals, and these were suitable for X-ray crystallography if maintained in contact with the mother liquor to prevent the loss of interstitial solvent. After 5 days, crystals were isolated by filtration, washed with MeCN, and dried *in vacuo*; yield 7%. Anal. Calcd (found) for **12** (C<sub>160</sub>H<sub>224</sub>As<sub>24</sub>Sr<sub>4</sub>O<sub>88</sub>Mn<sub>16</sub>): C, 29.19 (29.42); H, 3.43 (3.66); N, 0.00 (0.00). Selected IR data (cm<sup>-1</sup>): 3421 (m,br), 2930 (w), 1597 (s), 1550 (s), 1394 (vs), 1268 (w), 1023 (w), 833 (vs), 800 (vs), 720 (m), 675 (m), 667 (w), 651 (m), 613 (w), 592 (w), 490 (m), 459 (w), 447 (w), 416 (w).

#### 4.4.2 X-ray Crystallography

Data were collected on a Bruker P4 (**9**) and Siemens SMART PLATFORM (**10**, **11** and **12**) platform goniometer equipped with a SMART APEX CCD area detector and a graphite monochromator utilizing MoK<sub>α</sub> radiation ( $\lambda = 0.71073 \text{ \AA}$ ). Suitable single crystals of **9**·5H<sub>2</sub>O·C<sub>5</sub>H<sub>12</sub>, **10**·½MeCN·12H<sub>2</sub>O, **11**·32MeCN and **12**·16MeCN were attached to glass fibers using silicone grease and transferred to the goniostat where they were cooled to -55 °C (**9**) and -100 °C (**10**, **11** and **12**) for characterization and data collection. Each structure was solved by direct methods (SHELXTL)<sup>64</sup> and standard Fourier techniques, and was refined on  $F^2$  using full-matrix least-squares methods. All non-hydrogen atoms were refined anisotropically. Hydrogen atoms were placed in calculated positions and refined with the use of a riding model. Cell parameters were refined using up to 8192 reflections. The intensity data for **9** was collected using the Phi-scan method with a scan step  $\Delta\text{Phi} = 0.03^\circ$ . For **10**, **11** and **12**, a full sphere of data (1850 frames) was collected using the  $\omega$ -scan method (0.3° frame width). The first 50 frames were re-measured at the end of data collection to monitor instrument and crystal stability

(maximum correction on I was < 1%). Data for **9** were corrected for Lorentz and polarization effects using the Bruker SAINT software and an absorption correction was performed using the SADABS program supplied by Bruker AXS ( $T_{\min}/T_{\max} = 0.657$ ). Absorption corrections by integration were applied based on measured indexed crystal faces for **10**, **11** and **12**.

A preliminary search of reciprocal space for  $\mathbf{9} \cdot 5\text{H}_2\text{O} \cdot \text{C}_5\text{H}_{12}$  revealed a set of reflections with no symmetry and no systematic absences. An initial choice of the centrosymmetric space group  $P\bar{1}$  was subsequently confirmed by the successful solution of the structure. The asymmetric unit contains the  $\text{Mn}_4$  molecule, five water and one pentane molecules of crystallization. The pentane molecule was significantly disordered and could not be modeled properly. Hence, the program SQUEEZE,<sup>96</sup> a part of the PLATON<sup>97</sup> package of crystallographic software, was used to calculate the solvent disorder area and remove its contribution to the overall intensity data. Correction of the X-ray data by SQUEEZE for **9** was the same as the required value, 84 electron/cell. A total of 388 parameters were refined in the final cycle of refinement using 9507 ( $R_{\text{int}} = 0.0218$ ) independent reflections with  $I > 2\sigma(I)$  to yield  $R1$  and  $wR2$  of 3.70% and 10.14%, respectively. The final difference Fourier map was reasonably clean, the largest peak being  $1.796 \text{ e } \text{\AA}^{-3}$  and the deepest hole being  $-1.122 \text{ e } \text{\AA}^{-3}$ .

Complex  $\mathbf{10} \cdot \frac{1}{2}\text{MeCN} \cdot 12\text{H}_2\text{O}$  crystallizes in the triclinic space group  $P\bar{1}$ , with the asymmetric unit consisting of two  $[\text{Mn}_4]^+$  molecules, two  $\text{NO}_3^-$  anions, half of an MeCN and twelve water molecules of crystallization. One of the  $\text{NO}_3^-$  anions [N(3), O(36), O(37), O(38)] was disordered over two sites and was constrained to be geometrically similar to the whole nitrate anion. The site occupancy factors were dependently refined to

50:50% and atoms were refined with isotropic thermal parameters. The H atoms of the water molecules of crystallization could not be located. The Me<sub>2</sub>As<sup>-</sup> group of a Me<sub>2</sub>AsO<sub>2</sub><sup>-</sup> ligand [As(6), C(11), C(12)] in one of the Mn<sub>4</sub> molecules was disordered over two positions, whose site occupancy factors were dependently refined to 76:24%. A total of 875 parameters were refined in the final cycle of refinement using 26916 reflections with  $I > 2\sigma(I)$  to yield  $R1$  and  $wR2$  of 5.15% and 12.40%, respectively. The highest peak in the electron density map is 0.82 Å from an As atom and thus was attributed to anisotropy. The final difference Fourier map was essentially featureless, the largest peak being 2.117 e Å<sup>-3</sup> and the deepest hole being -1.162 e Å<sup>-3</sup>.

For complex **11**, an initial survey of a portion of reciprocal space located a set of reflections with a orthorhombic lattice. Analysis of the full data set revealed that the space group was  $I222$ . The asymmetric unit contains one-quarter of a Mn<sub>16</sub> molecule and 8 MeCN molecules of crystallization. The latter 8 solvent molecules were disordered and could not be modeled properly, so the program SQUEEZE,<sup>96</sup> a part of the PLATON<sup>97</sup> package of crystallographic software, was used to calculate the solvent disorder area and remove its contribution to the overall intensity data. The phenyl rings in the two PhCO<sub>2</sub><sup>-</sup> ligands [C(82)-C(87) and C(92)-C(97)] were disordered and could not be resolved to satisfaction. The As atoms and their corresponding Me groups in two of the Me<sub>2</sub>AsO<sub>2</sub><sup>-</sup> ligands [As(6), C(61), C(62) and As(8), C(101), C(102)] were disordered over the crystallographic  $C_2$  rotation axes; the cluster is located on a  $222$  symmetry site. Their site occupancy factors were fixed at 50%. Additionally, the As and corresponding Me atoms of one Me<sub>2</sub>AsO<sub>2</sub><sup>-</sup> ligand not situated on a crystallographic rotation axis [As(7), C(71) and C(72)], were disordered over two main positions. Their site occupancy factors were

independently refined to 49:51. These disorders contribute significantly to the poor refinement and relatively high final  $R$  values. Over ten data sets were collected on different crystals of **11**, and all have significant disordering of the  $\text{Me}_2\text{AsO}_2^-$  ligands. In a few data sets, we were unable to locate even the carbon atoms of their Me groups. All of these data sets suggest the same structure and they refined to different levels of acceptability. The best data set is herein reported. A total of 380 parameters were refined in the final cycle of refinement using 26952 reflections with  $I > 2\sigma(I)$  to yield  $R1$  and  $wR2$  of 8.76% and 22.86%, respectively. The final difference Fourier map was reasonably clean, with the largest peak and deepest hole being  $1.496 \text{ e } \text{\AA}^{-3}$  and  $-1.451 \text{ e } \text{\AA}^{-3}$ , respectively.

Complex **12**·16MeCN crystallizes in the monoclinic space group  $P2_1/c$ , with the asymmetric unit consisting of half a  $\text{Mn}_{16}$  molecule and 8 MeCN molecules of crystallization. The latter eight molecules were disordered and could not be modeled properly. Thus, the program SQUEEZE,<sup>96</sup> a part of the PLATON<sup>97</sup> package of crystallographic software, was used to calculate the solvent disorder area and remove its contribution to the overall intensity data. The phenyl rings in two of the  $\text{PhCO}_2^-$  ligands [C(8)-C(13) and C(64)-C(69)] were disordered. Their site occupancy factors were independently refined as rigid bodies to 53:47 and 39:61, respectively. All other phenyl rings were also refined as rigid bodies, but were either not disordered or the disorder was minor and could not be resolved. The As atoms and their corresponding Me groups [As(4)/As(5), As(11)/As(12), As(13)/As(14), and As(15)/As(16)] in four of the  $\text{Me}_2\text{AsO}_2^-$  ligands were disordered about two (main) positions, and the occupancies independently refined to 62:38, 50:50, 58:42 and 47:53, respectively. A total of 967 parameters were

refined in the final cycle of refinement using 61172 reflections with  $I > 2\sigma(I)$  to yield  $R1$  and  $wR2$  of 8.72% and 22.12%, respectively. The final difference Fourier map was reasonably clean, with the largest peak and deepest hole being  $2.115 \text{ e } \text{\AA}^{-3}$  and  $-2.709 \text{ e } \text{\AA}^{-3}$ , respectively.

CHAPTER 5  
NEW POLYNUCLEAR Mn CLUSTERS FROM THE USE OF THE HYDROPHOBIC  
CARBOXYLATE LIGAND 2,2-DIMETHYLBUTYRATE

**5.1 Introduction**

One of the principal motivations for the continuing exploration of Mn carboxylate chemistry is the established potential of this area as a rich source of single-molecule magnets (SMMs),<sup>12,13,38,46,61-63,98-114</sup> a field that began in 1993 when it was shown that  $[\text{Mn}_{12}\text{O}_{12}(\text{O}_2\text{CMe})_{16}(\text{H}_2\text{O})_4]\cdot 2\text{MeCO}_2\text{H}\cdot 4\text{H}_2\text{O}$  (**1**) functions as a magnet at temperatures below its blocking temperature,  $T_B$ . A SMM possesses a significant potential energy barrier ( $U$ ) to relaxation of its magnetization vector, arising from the combination of a large ground state spin,  $S$ , and a large, negative magnetoanisotropy of the easy-axis (or Ising) type (negative axial zero-field splitting parameter,  $D$ ). The upper limit of this energy barrier is given by  $S^2|D|$  and  $(S^2 - 1/4)|D|$  for integer and half-integer  $S$  values, respectively.<sup>19,22,23,135</sup> Experimental evidence for the slow, superparamagnet-like magnetic relaxation of a SMM is provided by the observation of hysteresis, the classical macroscale property of a magnet, in magnetization versus DC field scans, and also by the observation of frequency-dependent, out-of-phase AC susceptibility signals ( $\chi_M''$ ).<sup>21,136</sup>

The calculated energy barrier,  $U$ , of complex **1** is  $50 \text{ cm}^{-1}$  (72 K), arising from  $S = 10$  and  $D = -0.50 \text{ cm}^{-1}$  (-0.72 K).<sup>19</sup> This energy barrier allows molecules of complex **1** to function as individual magnets at temperatures below 10 K. The half-life for magnetization decay is so long that it is hardly measurable if molecules of **1** are magnetized at 1.5 K by applying a magnetic field and then removing the field.<sup>19</sup> After

more than a decade of research in this area, complex **1** and carboxylate substituted derivatives still remain the molecules that function as magnets at the highest temperatures, exhibiting the most promise for use in high density memory storage devices or in quantum computing. This is in spite of the preparation of many SMMs of a different structural type, as well as research in other areas such as molecular magnetism.

There are two main routes to new SMMs. The first is the modification of a given structural type in some way that does not change the core structure. For example, such studies on Mn<sub>12</sub> complexes have included variation of the peripheral carboxylate ligation,<sup>13,38,46</sup> variation of the oxidation level by cluster reduction,<sup>13,61,100</sup> replacement of some of the Mn centers with either Fe or Cr,<sup>137,138</sup> and replacement of some of the carboxylate ligands with non-carboxylate groups.<sup>32,33,39,47,58,101</sup> The second is the use of harsher conditions, such as the reaction of a cluster with a chelating ligand, that will often cause a core structural and/or nuclearity change leading to new structural types.<sup>11,102-107</sup>

These methods have together afforded many new Mn<sub>x</sub> species when a Mn<sub>12</sub> complex was employed, such as [Mn<sub>12</sub>O<sub>12</sub>(O<sub>2</sub>CCH<sub>2</sub>Bu<sup>t</sup>)<sub>16</sub>(H<sub>2</sub>O)<sub>4</sub>],<sup>56</sup> [Mn<sub>30</sub>O<sub>24</sub>(OH)<sub>8</sub>(O<sub>2</sub>CCH<sub>2</sub>Bu<sup>t</sup>)<sub>32</sub>(H<sub>2</sub>O)<sub>2</sub>(MeNO<sub>2</sub>)<sub>4</sub>],<sup>63</sup> and [Mn<sub>84</sub>O<sub>72</sub>(O<sub>2</sub>CMe)<sub>78</sub>(OMe)<sub>24</sub>(MeOH)<sub>12</sub>(H<sub>2</sub>O)<sub>42</sub>(OH)<sub>6</sub>].<sup>66</sup>

A particularly fruitful starting material for a variety of reactions of the second type has been [Mn<sub>12</sub>O<sub>12</sub>(O<sub>2</sub>CCH<sub>2</sub>Bu<sup>t</sup>)<sub>16</sub>(H<sub>2</sub>O)<sub>4</sub>] (**13**), where Bu<sup>t</sup>CH<sub>2</sub>CO<sub>2</sub>H is 3,3-dimethylbutyric acid (*t*-butylacetic acid).<sup>63,108,139</sup> For example, the reaction of **13** with MeOH led to the isolation of the novel Mn<sub>21</sub> cluster [Mn<sub>21</sub>O<sub>24</sub>(OMe)<sub>8</sub>(O<sub>2</sub>CCH<sub>2</sub>Bu<sup>t</sup>)<sub>16</sub>(H<sub>2</sub>O)<sub>10</sub>],<sup>108</sup> while reductive destabilization with a reducing agent such as phenol led to the new Mn<sub>8</sub> cluster,

$[\text{Mn}_8\text{O}_2(\text{O}_2\text{CCH}_2\text{Bu}')_{14}(\text{HO}_2\text{CCH}_2\text{Bu}')_4]$ .<sup>139</sup> In addition, the  $\text{Mn}_{30}$  cluster mentioned above,  $[\text{Mn}_{30}\text{O}_{24}(\text{OH})_8(\text{O}_2\text{CCH}_2\text{Bu}')_{32}(\text{H}_2\text{O})_2(\text{MeNO}_2)_4]$ , was obtained by simply recrystallizing **13** from a  $\text{CH}_2\text{Cl}_2/\text{MeNO}_2$  solvent mixture.<sup>63</sup> It has been postulated that the strong basicity of the  $\text{Bu}'\text{CH}_2\text{CO}_2^-$  ligand, as reflected in the relatively high  $\text{pK}_a$  value of its conjugate acid ( $\text{pK}_a = 5.00$ ), combined with the bulky and hydrophobic nature of the  $\text{Bu}'$  group are the main reasons for the interesting products obtained with this carboxylate.

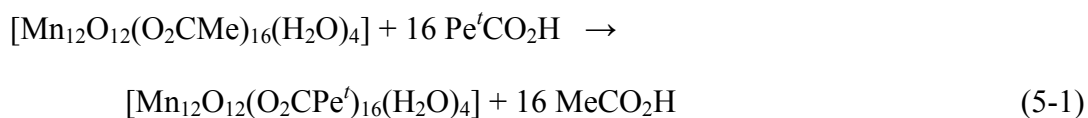
As part of our continuing interest in SMMs in general and in  $\text{Mn}_{12}$  complexes in particular, we have extended these investigations of the influence of bulky, hydrophobic groups on the nature of the obtained products. We report our findings from the use of the related carboxylic acid, 2,2-dimethylbutyric acid ( $\text{Pe}'\text{CO}_2\text{H}$ , where  $\text{Pe}'$  is the *t*-pentyl group,  $-\text{CMe}_2\text{Et}$ ) with a  $\text{pK}_a$  of 5.03, which is similar to  $\text{Bu}'\text{CH}_2\text{CO}_2\text{H}$ . We herein describe the syntheses, single crystal X-ray structures, and magnetic properties of the products obtained by the introduction of  $\text{Pe}'\text{CO}_2^-$  groups into  $\text{Mn}_{12}$  complexes.

## 5.2 Results and Discussion

### 5.2.1 Syntheses

In order to introduce the hydrophobic  $\text{Pe}'\text{CO}_2^-$  group onto the  $\text{Mn}_{12}$  core, we employed the previously developed carboxylate substitution reaction that involves the treatment of  $[\text{Mn}_{12}\text{O}_{12}(\text{O}_2\text{CMe})_{16}(\text{H}_2\text{O})_4]\cdot 2\text{MeCO}_2\text{H}\cdot 4\text{H}_2\text{O}$  (**1**) with an excess of  $\text{RCO}_2\text{H}$ .<sup>13,38</sup> Thus, a solution of complex **1** in MeCN was treated with an excess of  $\text{Pe}'\text{CO}_2\text{H}$  in  $\text{CH}_2\text{Cl}_2$ . The reaction is an equilibrium that was driven to completion by several cycles of removal of acetic acid as its toluene azeotrope (28:72%; b.p. 101 °C at one atmosphere) under reduced pressure (eq 5-1). The product was subsequently

crystallized with MeNO<sub>2</sub> and identified by infrared spectroscopy and elemental analysis as [Mn<sub>12</sub>O<sub>12</sub>(O<sub>2</sub>CPe')<sub>16</sub>(H<sub>2</sub>O)<sub>4</sub>] (**14**).



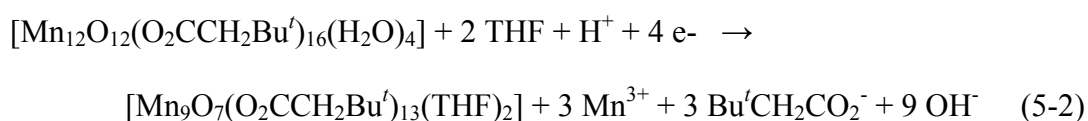
The stability of complex **14** to recrystallization from CH<sub>2</sub>Cl<sub>2</sub>/MeNO<sub>2</sub> or CH<sub>2</sub>Cl<sub>2</sub>/MeOH was investigated both in the presence and absence of the free carboxylic acid. We had previously observed<sup>56</sup> that [Mn<sub>12</sub>O<sub>12</sub>(O<sub>2</sub>CCH<sub>2</sub>Bu')<sub>16</sub>(H<sub>2</sub>O)<sub>4</sub>] (**13**) can be recrystallized without change from these solvent systems in the presence of Bu'CH<sub>2</sub>CO<sub>2</sub>H. However, in the absence of the latter, the Mn<sub>30</sub> and Mn<sub>21</sub> clusters, respectively, mentioned earlier were obtained.<sup>63,108</sup> Somewhat different results were obtained with **3**: in the presence of Pe'CO<sub>2</sub>H, recrystallization from CH<sub>2</sub>Cl<sub>2</sub>/MeOH and CH<sub>2</sub>Cl<sub>2</sub>/MeNO<sub>2</sub> gave [Mn<sub>12</sub>O<sub>12</sub>(O<sub>2</sub>CPe')<sub>16</sub>(MeOH)<sub>4</sub>] (**15**) and [Mn<sub>6</sub>O<sub>2</sub>(O<sub>2</sub>CH<sub>2</sub>)(O<sub>2</sub>CPe')<sub>11</sub>(HO<sub>2</sub>CPe')<sub>2</sub>(O<sub>2</sub>CMe)] (**16**), respectively. In the absence of Pe'CO<sub>2</sub>H, each recrystallization gave materials that, by infrared spectroscopy and elemental analysis, have not retained the Mn<sub>12</sub> core but that are not **15** or **16**. However, we have been unable to date to identify these products.

The crystallization solutions from the reaction of **14** with Pe'CO<sub>2</sub>H in a solvent mixture of CH<sub>2</sub>Cl<sub>2</sub>/MeNO<sub>2</sub> were allowed to stand for several weeks in an effort to increase the yield of complex **16**, a new structural type. Instead, several products crystallized, including complexes **14** and **16**, and a number of other materials. The reaction system is unquestionably very complicated, with several species no doubt in equilibrium in solution. The initial crystalline products were separated by filtration, the filtrate was concentrated to dryness by roto-evaporation, a small amount of Pe'CO<sub>2</sub>H was

added to the residue, and the latter was dissolved in CH<sub>2</sub>Cl<sub>2</sub>. Layering the solution with MeNO<sub>2</sub> slowly gave small crystals of [Mn<sub>9</sub>O<sub>6</sub>(OH)(CO<sub>3</sub>)(O<sub>2</sub>CPe<sup>t</sup>)<sub>12</sub>(H<sub>2</sub>O)<sub>2</sub>] (**17**) containing a bridging CO<sub>3</sub><sup>2-</sup> group. This was an unexpected result that can be rationalized by reasoning that the CO<sub>3</sub><sup>2-</sup> ligand in **17** likely arises from the oxidation of the O<sub>2</sub>CH<sub>2</sub><sup>2-</sup> ligand in **16**, which itself likely originates from the hydrolysis of CH<sub>2</sub>Cl<sub>2</sub>, a process for which there is precedent in the literature.<sup>140</sup> Alternatively, the CO<sub>3</sub><sup>2-</sup> ligand in **17** may be from the reaction of **16** with atmospheric CO<sub>2</sub> as has been previously observed with a series of hydroxo complexes [M(HB(3,5-*i*Pr<sub>2</sub>pz)<sub>3</sub>)<sub>2</sub>(OH)<sub>2</sub> (HB(3,5-*i*Pr<sub>2</sub>pz)<sub>3</sub> = hydrotris(3,5-diisopropyl-1-pyrazolyl)borate and M = Mn<sup>II</sup>, Fe<sup>II</sup>, Co<sup>II</sup>, Ni<sup>II</sup>, Cu<sup>II</sup> and Zn<sup>II</sup>).<sup>141</sup> Although mechanistic studies are not feasible for this complicated reaction system, it can be noted that neither complexes **16** nor **17** crystallize from identical reactions carried out in CHCl<sub>3</sub> instead of CH<sub>2</sub>Cl<sub>2</sub>. In addition, the infrared spectra of materials obtained from similar reactions using [Mn<sub>12</sub>O<sub>12</sub>(O<sub>2</sub>CBu<sup>t</sup>)<sub>16</sub>(H<sub>2</sub>O)<sub>4</sub>] and Bu<sup>t</sup>CO<sub>2</sub>H suggest that structural analogues of complexes **16** or **17** are not obtained. Although these results support the suggestion that the O<sub>2</sub>CH<sub>2</sub><sup>2-</sup> and CO<sub>3</sub><sup>2-</sup> ligands originate from CH<sub>2</sub>Cl<sub>2</sub> and not atmospheric CO<sub>2</sub> or carboxylate groups, the exact mechanism remains unclear.

We also investigated the reactivity of the Pe<sup>t</sup>-substituted Mn<sub>12</sub> cluster **14** under the various conditions explored earlier for the Bu<sup>t</sup>-substituted derivative, specifically with chelates and reducing agents. Reactions of complex **14** with 2,6-pyridinedimethanol (pdmH<sub>2</sub>), 2,2'-bipyridine (bpy) and phenol were carried out in CH<sub>2</sub>Cl<sub>2</sub>. Large crystals of [Mn<sub>4</sub>O<sub>2</sub>(O<sub>2</sub>CPe<sup>t</sup>)<sub>6</sub>(bpy)<sub>2</sub>] (**18**) were obtained in high yield from the reaction of **14** with bpy. IR spectra of the solids obtained from reactions with either pdmH<sub>2</sub> or phenol

suggested the product to be  $[\text{Mn}_8\text{O}_2(\text{O}_2\text{CPe}^')_{14}(\text{HO}_2\text{CPe}^')_4]$ , the  $\text{Pe}^'$  analog of  $[\text{Mn}_8\text{O}_2(\text{O}_2\text{CCH}_2\text{Bu}^')_{14}(\text{HO}_2\text{CCH}_2\text{Bu}^')_4]$ <sup>139</sup> mentioned earlier. However, not enough material was isolated from these reactions for more definitive characterization. To further understand the reaction system, recrystallization was explored of complexes **13** and **14** from solvent mixtures other than  $\text{CH}_2\text{Cl}_2/\text{MeNO}_2$ , in the absence of the corresponding acid. As mentioned earlier, the  $\text{Mn}_{30}$  complex was obtained by dissolution of complex **13** in this mixture of solvents; in fact, this transformation to  $\text{Mn}_{30}$  requires the presence of  $\text{MeNO}_2$ . Hence, several solvents were explored in place of the  $\text{CH}_2\text{Cl}_2$ , and among these was tetrahydrofuran (THF). Indeed, we obtained black needle-like crystals from a dark brown solution of **13** in THF/ $\text{MeNO}_2$ . Preliminary X-ray analysis identified the product as  $[\text{Mn}_9\text{O}_7(\text{O}_2\text{CCH}_2\text{Bu}^')_{16}(\text{THF})_2]$  (**19**), but we have been unable to obtain suitable crystals for a high quality structure refinement. The transformation of **13** into **19** is summarized in eq 5-2. The average oxidation state of the starting material is +3.33 while that of the product (**19**) is only +3. Thus, the formation of complex **19** appears to involve the reduction of **13** followed by structural rearrangement.



### 5.2.2 Electrochemistry

Previous studies have established the  $\text{Mn}_{12}$  clusters to exhibit interesting electrochemical behavior.<sup>13,61,100</sup> They normally display several oxidation and reduction processes of which at least one reduction wave is usually reversible by the common electrochemical standards (CV peak separations, DPV peak broadness,  $i_{\text{anodic}}/i_{\text{cathodic}}$  peak current ratio, and linearity of peak current vs  $\nu^{1/2}$  plots, where  $\nu$  is the scan rate). In addition, as expected the redox processes are very sensitive to the electron withdrawing

or donating ability of the carboxylate ligand, and we have reported the  $E_{1/2}$  values for a number of  $Mn_{12}$  derivatives. The range of  $E_{1/2}$  values (vs  $Fc/Fc^+$ ) for the first one-electron reduction ranges from 0.91 V for the  $R = CHCl_2$  complex to 0.00 V for the  $R = p-C_6H_4OMe$  complex. Similarly, the second reduction ranges from 0.61 V for the  $R = CHCl_2$  complex to -0.50 V for the  $R = Et$  complex. The potential of the first oxidation process varies from 1.07 V for  $R = p-C_6H_4CF_3$  to 0.70 V for  $R = p-C_6H_4OMe$  or  $p-C_6H_4Et$ . By reduction with either one or two equivalents of  $I^-$ , both the one- and two-electron reduced forms of some  $Mn_{12}$  species have been isolated and structurally characterized ( $I^-/I_2$  couple occurs at 0.21 V in  $CH_2Cl_2$  vs  $Fc/Fc^+$ ).<sup>13,61</sup> However, despite the reversible nature of the oxidation processes of several characterized  $Mn_{12}$  clusters, a one-electron oxidized  $Mn_{12}$  cluster has not yet been isolated. This is likely due in part to the high potentials associated with this process. The introduction of a strongly electron donating ligand onto the  $Mn_{12}$  complex would likely make more feasible the preparation of a one-electron oxidized  $Mn_{12}$  derivative by moving the first oxidation process to more accessible potentials, and we decided to explore this.

The cyclic voltammogram (CV) and differential pulse voltammogram (DPV) of **15** are shown in Figure 5-1. There is a quasi-reversible oxidation wave at -0.21 V and an irreversible reduction wave at -0.87 V. The CV and DPV profiles of **13** are very similar; a quasi-reversible oxidation wave occurs at -0.07 V and an irreversible reduction appears at -0.82 V. The oxidation processes of both complexes meet the standard electrochemical requirements for quasi-reversible electron transfer. A study of the scan rate ( $\nu$ ) dependence for the oxidation waves showed a linear dependence of peak current with respect to  $\nu^{1/2}$ , indicating that the process is diffusion-controlled as shown in Figure 5-2

for complex **13** and in Figure 5-3 for complex **15**. This relationship is described by the Randles-Sevcik equation (eq 5-3)

$$i_p = (2.687 \times 10^5) n^{3/2} \nu^{1/2} D^{1/2} AC \quad (5-3)$$

where  $n$  is the number of electrons appearing in the half-reaction of the redox couple,  $\nu$  is the scan rate,  $A$  is the electrode area,  $D$  is the diffusion coefficient of the analyte and  $C$  is the concentration of the analyte.

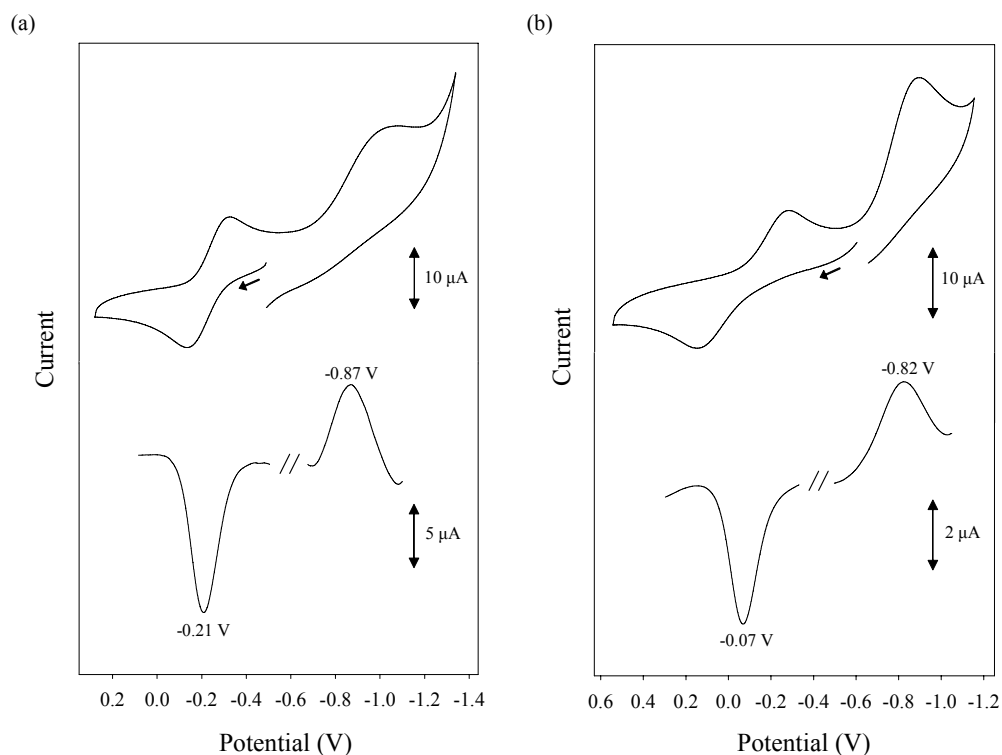


Figure 5-1. Cyclic voltammogram at  $100 \text{ mV s}^{-1}$  (top) and differential pulse voltammogram (bottom) for (a) complex **15** and (b) complex **13** in  $\text{CH}_2\text{Cl}_2$  containing  $0.1 \text{ M NBU}_4\text{PF}_6$  as supporting electrolyte. The indicated potentials are vs  $\text{Fc}/\text{Fc}^+$ .

In Table 5-1 are included values of the anodic peak current / cathodic peak current ratio ( $i_a/i_c$ ) for the -0.07 and -0.21 V oxidation waves of complexes **13** and **15**, respectively. The  $i_a/i_c$  ratio has an approximate value of  $\sim 1$  over the range of scan rates, providing support of the quasi-reversible nature of the oxidation processes.

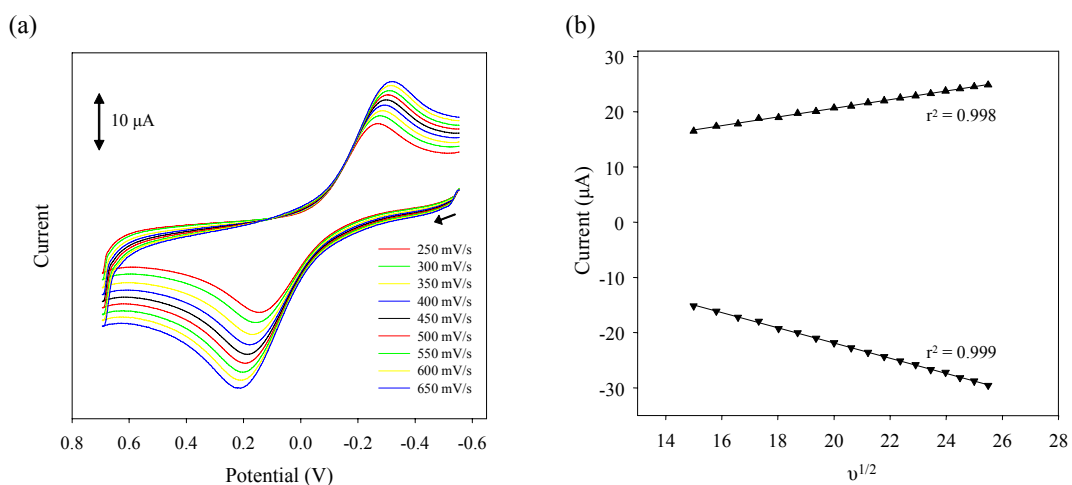


Figure 5-2. Scan rate dependence of oxidation wave at -0.07 V of complex **13** in  $\text{CH}_2\text{Cl}_2$  containing 0.1 M  $\text{NBu}_4\text{PF}_6$  as supporting electrolyte. (a) Cyclic voltammogram at the indicated scan rates. (b) Plot of cathodic (top) and anodic (bottom) peak current dependence vs  $v^{1/2}$ .

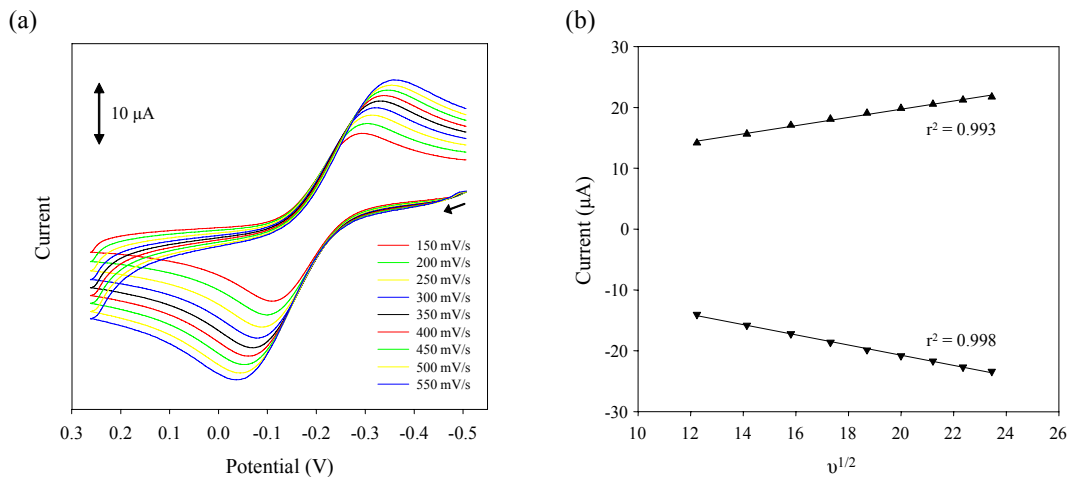


Figure 5-3. Scan rate dependence of oxidation wave at -0.21 V of complex **15** in  $\text{CH}_2\text{Cl}_2$  containing 0.1 M  $\text{NBu}_4\text{PF}_6$  as supporting electrolyte. (a) Cyclic voltammogram at the indicated scan rates. (b) Plot of cathodic (top) and anodic (bottom) peak current dependence vs  $v^{1/2}$ .

Table 5-1. Anodic peak current / cathodic peak current ratios at the indicated scan rates in  $\text{mV s}^{-1}$  for the -0.07 V and -0.21 V reduction waves of complex **13** and complex **15**, respectively.

<b>13</b>		<b>15</b>	
Scan Rate ( $\text{mV s}^{-1}$ )	$i_a/i_c$	Scan Rate ( $\text{mV s}^{-1}$ )	$i_a/i_c$
100	0.68	100	1.04
125	0.78	150	0.99
150	0.78	200	1.01
175	0.86	250	1.01
200	0.82	300	1.03
225	0.92	350	1.04
250	0.93	400	1.05
275	0.97	450	1.06
300	0.95	500	1.07
325	1.02	550	1.08
350	1.02	600	1.09
375	1.05	650	1.11
400	1.06	700	1.11
425	1.08		
450	1.09		
475	1.11		
500	1.12		
525	1.13		
550	1.15		
575	1.14		
600	1.16		
625	1.17		
650	1.19		

## 5.2.3 Description of Structures

### 5.2.3.1 X-ray crystal structure of $[\text{Mn}_{12}\text{O}_{12}(\text{O}_2\text{CPe}^t)_{16}(\text{MeOH})_4]$ (**15**)

A labeled ORTEP<sup>40</sup> plot in PovRay format of complex **15** is shown in Figure 5-4, together with a stereoview. The crystallographic data and structure refinement details are collected in Table 5-2, and selected interatomic distances and angles are listed in Table A-9. The complex crystallizes in the triclinic space group  $P\bar{1}$  with the asymmetric unit consisting of the  $\text{Mn}_{12}$  molecule and two MeCN molecules of crystallization. The structure of **15** is very similar to other previously characterized neutral  $\text{Mn}_{12}$  complexes,<sup>13,22</sup> consisting of a central  $[\text{Mn}^{\text{IV}}_4\text{O}_4]$  cubane that is surrounded by a

non-planar ring of eight Mn<sup>III</sup> atoms that are bridged and connected to the cubane by eight  $\mu_3$ -O<sup>2-</sup> ions. The eight Mn<sup>III</sup> ions separate into two groups of four Mn<sup>III</sup> ions each. In the first group, each Mn<sup>III</sup> ion is coordinated to a single Mn<sup>IV</sup> ion via two oxide bridges [Mn(5), Mn(7), Mn(9), Mn(11)], while in the second group each Mn<sup>III</sup> ion is coordinated to two Mn<sup>IV</sup> ions via two oxide bridges [Mn(6), Mn(8), Mn(10), Mn(12)].<sup>29</sup> Peripheral ligation is by sixteen bridging  $\text{Pe}'\text{CO}_2^-$  ligands and four terminal MeOH groups, which are bound in a 1:1:2 fashion to Mn(8), Mn(10) and Mn(12), respectively (Figure 5-4).

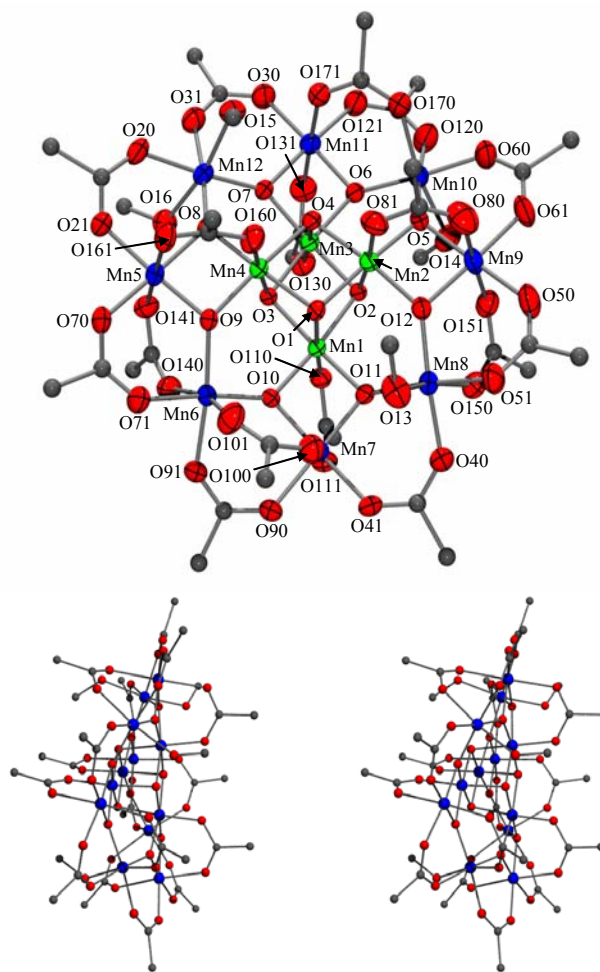


Figure 5-4. ORTEP representation in PovRay format of  $[\text{Mn}_{12}\text{O}_{12}(\text{O}_2\text{CPE}')_{16}(\text{MeOH})_4]$  (**15**) with thermal ellipsoids at the 50% probability level except for the C atoms, together with a stereopair. For clarity, the hydrogen atoms have been omitted, and only the quaternary C atoms of the ligands are shown. Mn<sup>IV</sup> green; Mn<sup>III</sup> blue; O red; C gray.

Table 5-2. Crystallographic data for  $[\text{Mn}_{12}\text{O}_{12}(\text{O}_2\text{CPe}^t)_{16}(\text{MeOH})_4]\cdot 2\text{MeCN}$ ,  $[\text{Mn}_6\text{O}_2(\text{O}_2\text{CH}_2)(\text{O}_2\text{CPe}^t)_{11}(\text{HO}_2\text{CPe}^t)_2(\text{O}_2\text{CMe})]\cdot \frac{1}{2}\text{CH}_2\text{Cl}_2$ ,  $[\text{Mn}_9\text{O}_6(\text{OH})(\text{CO}_3)(\text{O}_2\text{CPe}^t)_{12}(\text{H}_2\text{O})_2]\cdot \text{H}_2\text{O}\cdot \text{HO}_2\text{CPe}^t$  and  $[\text{Mn}_4\text{O}_2(\text{O}_2\text{CPe}^t)_6(\text{bpy})_2]\cdot 2\text{H}_2\text{O}$ .

Parameter	<b>15</b> ·2MeCN	<b>16</b> ·½CH <sub>2</sub> Cl <sub>2</sub>	<b>17</b> ·H <sub>2</sub> O·HO <sub>2</sub> CPe <sup>t</sup>	<b>18</b> ·2H <sub>2</sub> O
formula <sup>a</sup>	C <sub>104</sub> H <sub>198</sub> N <sub>2</sub> Mn <sub>12</sub> O <sub>48</sub>	C <sub>81.5</sub> H <sub>151</sub> Cl <sub>1</sub> Mn <sub>6</sub> O <sub>32</sub>	C <sub>79</sub> H <sub>151</sub> Mn <sub>9</sub> O <sub>39</sub>	C <sub>56</sub> H <sub>86</sub> N <sub>4</sub> Mn <sub>4</sub> O <sub>16</sub>
fw, g mol <sup>-1</sup>	2903.96	2008.16	2219.49	1291.07
space group	<i>P</i> $\bar{1}$	<i>P</i> 2 <sub>1</sub> / <i>c</i>	<i>C</i> mc2 <sub>1</sub>	<i>P</i> 2 <sub>1</sub> / <i>c</i>
<i>a</i> , Å	16.285(3)	15.980(2)	25.9274(14)	12.9936(10)
<i>b</i> , Å	16.556(3)	21.255(3)	19.6851(10)	18.8216(14)
<i>c</i> , Å	27.839(5)	30.570(4)	21.1978(12)	14.0822(10)
$\alpha$ , deg	83.524(3)	90	90	90
$\beta$ , deg	74.242(3)	101.675(2)	90	107.1740(10)
$\gamma$ , deg	70.340(3)	90	90	90
<i>V</i> , Å <sup>3</sup>	6801(2)	10168(2)	10819.0(10)	3290.4(4)
<i>Z</i>	2	4	4	4
<i>T</i> , °C	-100(2)	-100(2)	-55(2)	-55(2)
radiation, Å <sup>b</sup>	0.71073	0.71073	0.71073	0.71073
$\rho_{\text{calc}}$ , g cm <sup>-3</sup>	1.404	1.309	1.356	1.339
$\mu$ , cm <sup>-1</sup>	11.51	8.21	10.89	8.17
<i>R</i> 1 ( <i>wR</i> 2), % <sup>c,d</sup>	8.36 (19.93)	6.97 (17.69)	6.59 (18.05)	5.30 (15.42)

<sup>a</sup> Including solvent molecules. <sup>b</sup> Graphite monochromator. <sup>c</sup>  $R1 = \Sigma||F_o| - |F_c|| / \Sigma|F_o|$ . <sup>d</sup>  $wR2 = [\Sigma[w(F_o^2 - F_c^2)^2] / \Sigma[wF_o^2]^2]^{1/2}$  where  $S = [\Sigma[w(F_o^2 - F_c^2)^2] / (n-p)]^{1/2}$ ,  $w = 1/[\sigma^2(F_o^2) + (mp)^2 + np]$ ,  $p = [\max(F_o^2, 0) + 2F_c^2]/3$ , and  $m$  and  $n$  are constants.

The oxidation levels of the Mn ions and protonation levels of the inorganic O atoms were assigned by analysis of the Mn-O bond distances, charge considerations, and bond valence sum (BVS) calculations<sup>41</sup> (Table 5-3 and 5-4). As expected, each of the Mn<sup>III</sup> ions exhibits Jahn-Teller (JT) elongation of two *trans* bonds, as expected for a high-spin d<sup>4</sup> ion in near-octahedral geometry. The JT elongation axes of the eight Mn<sup>III</sup> ions of the outer ring are aligned approximately parallel to each other, roughly perpendicular to the [Mn<sub>12</sub>O<sub>12</sub>] disk-like core of the molecule (Figure 5-5).

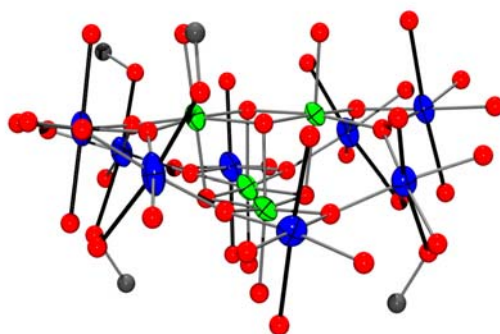


Figure 5-5. ORTEP representation of the [Mn<sub>12</sub>O<sub>44</sub>(MeOH)<sub>4</sub>] core of complex **15**, emphasizing the relative disposition of the Jahn-Teller elongation axes indicated as solid black bonds. Mn<sup>IV</sup> green; Mn<sup>III</sup> blue; O red; C gray.

Table 5-3. Bond valence sum calculations<sup>a</sup> for complex **15**·2MeCN.

Atom	Mn <sup>2+</sup>	Mn <sup>3+</sup>	Mn <sup>4+</sup>
Mn(1)	4.108	3.757	<u>3.944</u>
Mn(2)	4.126	3.774	<u>3.962</u>
Mn(3)	4.075	3.727	<u>3.913</u>
Mn(4)	4.169	3.813	<u>4.003</u>
Mn(5)	3.290	<u>3.009</u>	3.159
Mn(6)	3.274	<u>2.995</u>	3.144
Mn(7)	3.272	<u>2.993</u>	3.142
Mn(8)	3.253	<u>2.975</u>	3.123
Mn(9)	3.289	<u>3.008</u>	3.158
Mn(10)	3.284	<u>3.004</u>	3.153
Mn(11)	3.306	<u>3.024</u>	3.174
Mn(12)	3.236	<u>2.960</u>	3.107

<sup>a</sup> The underlined value is the one closest to the actual charge for which it was calculated. The oxidation state of a particular atom can be taken as the nearest whole number to the underlined value.

Table 5-4. Bond valence sum calculations<sup>a</sup> for selected oxygen atoms in complex **15**·2MeCN.

Atom	$V_i$	Assignment	Atom	$V_i$	Assignment
O(1)	2.008	O <sup>2-</sup>	O(9)	2.146	O <sup>2-</sup>
O(2)	1.968	O <sup>2-</sup>	O(10)	2.142	O <sup>2-</sup>
O(3)	1.200	O <sup>2-</sup>	O(11)	2.054	O <sup>2-</sup>
O(4)	2.018	O <sup>2-</sup>	O(12)	2.198	O <sup>2-</sup>
O(5)	2.118	O <sup>2-</sup>	O(13)	1.234	OH <sup>-</sup>
O(6)	2.189	O <sup>2-</sup>	O(14)	1.264	OH <sup>-</sup>
O(7)	2.091	O <sup>2-</sup>	O(15)	1.145	OH <sup>-</sup>
O(8)	2.162	O <sup>2-</sup>	O(16)	1.152	OH <sup>-</sup>

<sup>a</sup> The oxygen atoms is O<sup>2-</sup> if  $V_i \approx 2$ , OH<sup>-</sup> if  $V_i \approx 1$ , and H<sub>2</sub>O if  $V_i \approx 0$ .

In addition to sixteen bridging carboxylate ligands, either three or four water molecules are coordinated to the four Mn<sup>III</sup> ions in the second group described above [Mn(6), Mn(8), Mn(10), Mn(12)],<sup>20</sup> in all but two of the previously characterized Mn<sub>12</sub> complexes; the exceptions are the [Mn<sub>12</sub>O<sub>12</sub>(O<sub>2</sub>CMe)<sub>12</sub>(dpp)<sub>4</sub>] complex in which there are four five-coordinate Mn<sup>III</sup> centers and no coordinating water molecules<sup>109</sup> and the [Mn<sub>12</sub>O<sub>12</sub>(O<sub>2</sub>CMe)<sub>16</sub>(MeOH)<sub>4</sub>] complex in which there are four coordinated MeOH ligands.<sup>110</sup> Both complexes have been only recently reported. Instead of water ligands, complex **15** has four MeOH ligands coordinated to the three Mn<sup>III</sup> ions of the second group [O(13) to Mn(8), O(14) to Mn(10), O(15) and O(16) to Mn(12)]. This 1:1:2 ligand distribution pattern has also been observed for

[Mn<sub>12</sub>O<sub>12</sub>(O<sub>2</sub>CC<sub>6</sub>H<sub>4</sub>-*p*-Me)<sub>16</sub>(H<sub>2</sub>O)<sub>4</sub>]·3H<sub>2</sub>O.<sup>20,29,57</sup>

The Mn<sub>12</sub> molecules in the triclinic  $P\bar{1}$  lattice are stacked in columns along the *b* axis of the crystal; all of the molecules are oriented in the same manner with respect to the cell axes. The disordered Pe<sup>*f*</sup> groups encapsulate the [Mn<sub>12</sub>O<sub>12</sub>]<sup>16+</sup> core of **15** as shown in Figure 5-6, clearly separating individual Mn<sub>12</sub> molecules from their neighbors.

Similarly, Bu<sup>*f*</sup> groups have been found to result in the same separation between molecules

in other Mn aggregates with ligation by  $\text{Bu}'\text{CH}_2\text{CO}_2^-$ .<sup>56,63</sup> Hence, there is no evidence of intermolecular interactions in **15**. Disordered MeCN solvent molecules of crystallization are situated in the large voids separating the columns although their clear visualization is precluded by the use of the program SQUEEZE<sup>96</sup> to remove their overall electron density as discussed in the Experimental Section.

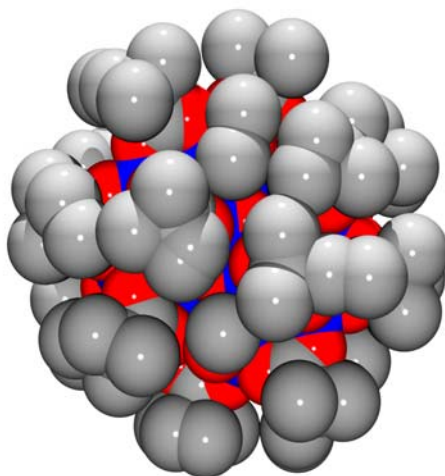


Figure 5-6. Space-filling diagram of complex **15** including all non-hydrogen atoms. Mn blue; O red; C gray.

### 5.2.3.2 X-ray crystal structure of

#### $[\text{Mn}_6\text{O}_2(\text{O}_2\text{CH}_2)(\text{O}_2\text{CPe}')_{11}(\text{HO}_2\text{CPe}')_2(\text{O}_2\text{CMe})]$ (**16**)

A labeled ORTEP<sup>40</sup> plot in PovRay format of complex **16** is shown in Figure 5-7, together with a stereoview. The crystallographic data and structure refinement details are collected in Table 5-2, and selected interatomic distances and angles are listed in Table A-10. The complex crystallizes in the monoclinic space group  $P2_1/c$  with the  $\text{Mn}_6$  molecule in a general position. The structure consists of a  $[\text{Mn}^{\text{III}}_6(\mu_3\text{-O})_2(\mu_4\text{-O}_2\text{CH}_2)]^{12+}$  core (Figure 5-7) with the peripheral ligation provided by eleven bridging  $\text{Pe}'\text{CO}_2^-$  ligands, one bridging  $\text{MeCO}_2^-$  ligand, and two terminal  $\text{Pe}'\text{CO}_2\text{H}$  ligands. Bond valence sum calculations<sup>41</sup> indicate that all of the distorted octahedral Mn centers are at the +3

oxidation level (Table 5-5). The protonation levels of the inorganic O atoms are collected in Table 5-6.

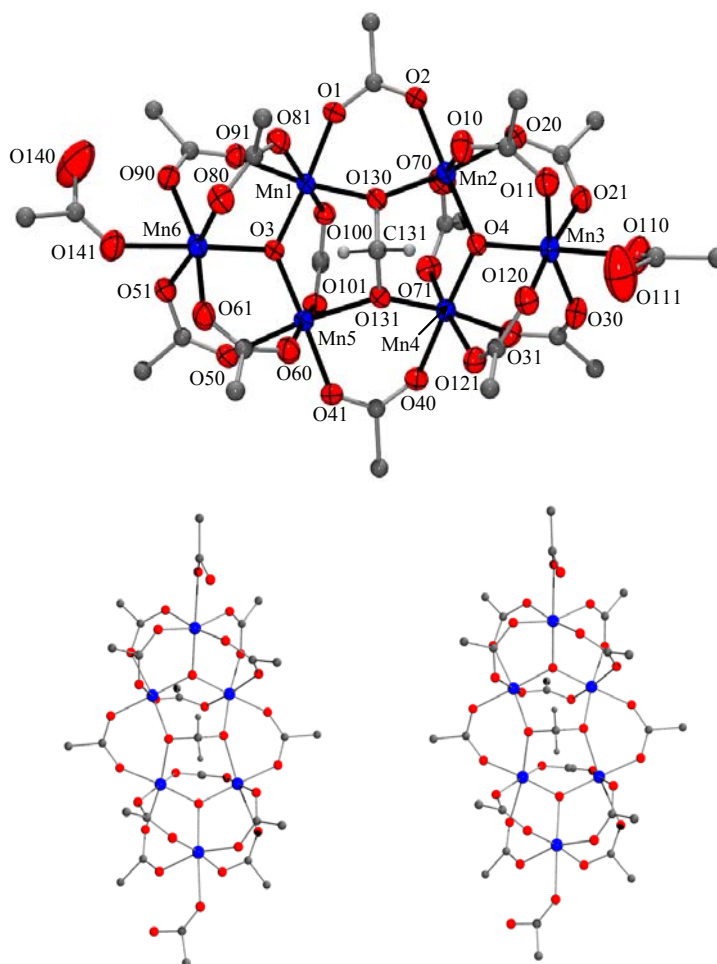


Figure 5-7. ORTEP representation in PovRay format of  $[\text{Mn}_6\text{O}_2(\text{O}_2\text{CH}_2)(\text{O}_2\text{CPe}')_{11}(\text{HO}_2\text{CPe}')_2(\text{O}_2\text{CMe})]$  (**16**) at the 50% probability level except for the C atoms, together with a stereopair. For clarity, the hydrogen atoms have been omitted, and only the quaternary C atoms of the ligands are shown.  $\text{Mn}^{\text{III}}$  blue; O red; C gray.

The six manganese ions are arranged in a twisted boat conformation, which can be described as two trinuclear  $[\text{Mn}_3(\mu_3\text{-O})]^{7+}$  units linked at one of their edges by two  $\mu\text{-Pe}'\text{CO}_2^-$  and one  $\mu_4\text{-O}_2\text{CH}_2^{2-}$  groups. The dihedral angle between the Mn(2)-Mn(3)-Mn(4) and Mn(1)-Mn(5)-Mn(6) planes is  $57.0^\circ$ . The central  $\mu_3\text{-O}^{2-}$  ion O(3) in one triangular unit is slightly ( $0.04 \text{ \AA}$ ) out of the  $\text{Mn}_3$  plane that it bridges [Mn(1), Mn(5) and

Mn(6)]. The other  $\mu_3\text{-O}^{2-}$  ion O(4) is essentially coplanar with the three Mn centers [Mn(2), Mn(3) and Mn(4)]. The remaining two  $\text{Mn}_2$  edges within each triangular unit are bridged by two  $\mu\text{-Pe}^t\text{CO}_2^-$  groups. There is an additional  $\text{Pe}^t\text{CO}_2^-$  group bridging Mn(1) and Mn(5), but the corresponding pair, Mn(2) and Mn(4), in the other triangular unit is bridged by an acetate group. Peripheral ligation at both Mn(3) and Mn(6) is completed by two monodentate  $\text{Pe}^t\text{CO}_2\text{H}$  groups. The Mn-O(3) and Mn-O(4) bond distances and Mn-O(3)-Mn and Mn-O(4)-Mn angles within each triangular unit are inequivalent, and the triangles are thus scalene. Only two other examples of a  $\mu_4\text{-O}_2\text{CH}_2^{2-}$  bridging unit as found in **16** have been previously observed in the compounds  $(\text{NBu}^n)_4[\text{CH}_2\text{Mo}_4\text{O}_{15}\text{H}]^{142}$  and  $[\text{Fe}_6\text{O}_2(\text{O}_2\text{CH}_2)(\text{O}_2\text{CCH}_2\text{Bu}^t)_{12}(\text{py})_2]^{143}$ , a compound very similar to **16**. Complexes containing somewhat similar bridging motifs include  $\text{Na}[\text{Fe}_4(\text{dhpta})_2(\mu\text{-O})(\mu\text{-OH})(\mu\text{-ala})_2]$  and  $[\text{Mn}_4(\text{dhpta})_2(\mu\text{-O})(\mu\text{-OH})(\mu\text{-O}_2\text{CMe})_2]^{4+}$  ( $\text{H}_5\text{dhpta} = 2$ -hydroxytrimethylenedinitrioloacetic acid and ala = alanine), where either four Fe or Mn ions are bridged by a hydrogen-bonded  $\text{O}^{2-}\cdots\text{HO}^-$  unit rather than a single diolate unit as in **5**.<sup>144,145</sup> The overall structure of **16** as two  $\text{M}_3$  triangular units linked at one edge has not been seen before in Mn chemistry, although it is commonly encountered in Fe chemistry.<sup>146-149</sup>

Table 5-5. Bond valence sum calculations<sup>a</sup> for complex **16**· $\frac{1}{2}\text{CH}_2\text{Cl}_2$ .

Atom	Mn <sup>2+</sup>	Mn <sup>3+</sup>	Mn <sup>4+</sup>
Mn(1)	3.214	<u>2.940</u>	3.087
Mn(2)	3.229	<u>2.954</u>	3.101
Mn(3)	3.170	<u>2.900</u>	3.044
Mn(4)	3.196	<u>2.923</u>	3.069
Mn(5)	3.240	<u>2.964</u>	3.112
Mn(6)	3.163	<u>2.893</u>	3.038

<sup>a</sup> The underlined value is the one closest to the actual charge for which it was calculated. The oxidation state of a particular atom can be taken as the nearest whole number to the underlined value.

Table 5-6. Bond valence sum calculations<sup>a</sup> for selected oxygen atoms in complex **16**·½CH<sub>2</sub>Cl<sub>2</sub>.

Atom	$V_i$	Assignment
O(3)	2.019	O <sup>2-</sup>
O(4)	2.002	O <sup>2-</sup>
O(130)	1.996	O <sup>2-</sup>
O(131)	2.014	O <sup>2-</sup>
O(110)	2.149	O <sup>2-</sup>
O(111)	1.012	OH <sup>-</sup>
O(140)	1.222	OH <sup>-</sup>
O(141)	2.176	O <sup>2-</sup>

<sup>a</sup> The oxygen atoms is O<sup>2-</sup> if  $V_i \approx 2$ , OH<sup>-</sup> if  $V_i \approx 1$ , and H<sub>2</sub>O if  $V_i \approx 0$ .

Each of the octahedral Mn<sup>III</sup> centers in **16** displays a JT axial elongation (Figure 5-8). Normally, JT elongation axes avoid Mn-oxide bonds, almost always the strongest and shortest in the molecule, but in the case of Mn(3) and Mn(6) the JT elongation axis is situated in an abnormal position containing a core O<sup>2-</sup> ion, O(4) and O(3), respectively. The JT elongation axes of Mn(2) and Mn(4) are oriented nearly parallel to each other along Mn-O(carboxylate) bonds. In addition, the JT elongation axes of Mn(1) and Mn(5) are along Mn-O(carboxylate) and Mn-O(gem-diolate) bonds, and are almost parallel to each other, but essentially perpendicular to those of Mn(2) and Mn(4). This will be of relevance to the magnetic discussion later (*vide infra*).

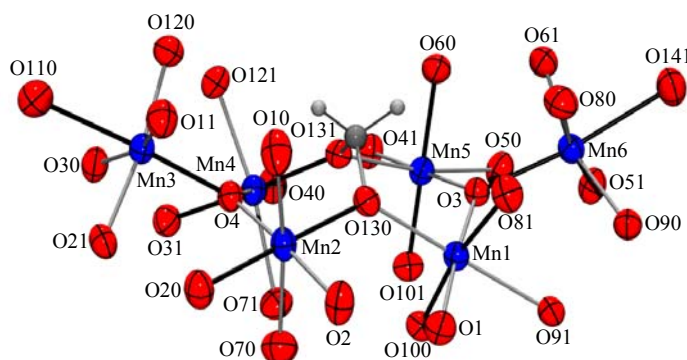


Figure 5-8. ORTEP representation of the [Mn<sub>6</sub>O<sub>30</sub>CH<sub>2</sub>] core of complex **16**, emphasizing the relative disposition of the Jahn-Teller elongation axes indicated as solid black bonds.

### 5.2.3.3 X-ray crystal structure of $[\text{Mn}_9\text{O}_6(\text{OH})(\text{CO}_3)(\text{O}_2\text{CPe}^t)_{12}(\text{H}_2\text{O})_2]$ (**17**)

A labeled ORTEP<sup>40</sup> plot in PovRay format of complex **17** is shown in Figure 5-9, together with a stereoview. The crystallographic data and structure refinement details are collected in Table 5-2, and selected interatomic distances and angles are listed in Table A-11. Complex **17** has crystallographic  $C_s$  symmetry, the mirror plane containing Mn(1), Mn(2) and Mn(3). The structure consists of a  $[\text{Mn}^{\text{III}}_9(\mu_3\text{-O})_6(\mu\text{-OH})(\mu_3\text{-CO}_3)]^{12+}$  core with peripheral ligation provided by twelve bridging  $\text{Pe}^t\text{CO}_2^-$  ligands and two terminal water molecules.

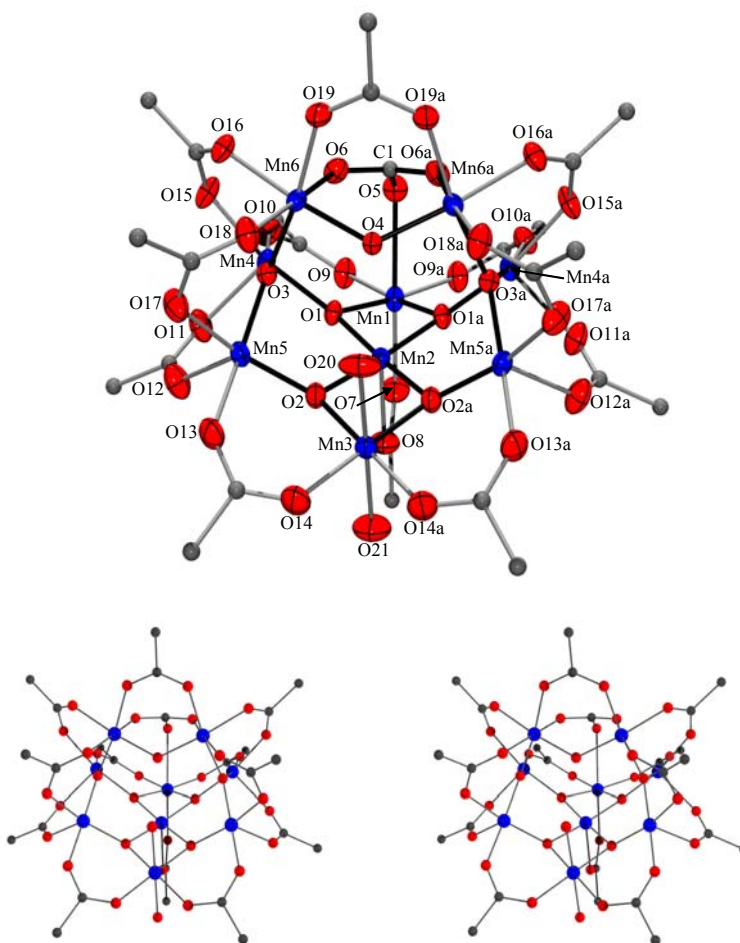


Figure 5-9. ORTEP representation in PovRay format of  $[\text{Mn}_9\text{O}_6(\text{OH})(\text{CO}_3)(\text{O}_2\text{CPe}^t)_{12}(\text{H}_2\text{O})_2]$  (**17**) at the 30% probability level except for the C atoms, together with a stereopair. For clarity, the hydrogen atoms have been omitted, and only the quaternary C atoms of the ligands are shown. Mn<sup>III</sup> blue; O red; C gray.

The base of the  $[\text{Mn}_9\text{O}_6(\text{OH})(\text{CO}_3)]$  core may be viewed as containing a  $[\text{Mn}_7\text{O}_4]$  subunit consisting of two  $[\text{Mn}_4\text{O}_2]$  “butterfly” units [atoms Mn(1), Mn(2), Mn(4), Mn(4a) and Mn(2), Mn(3), Mn(5), Mn(5a)] fused at five-coordinate Mn(2) (Figure 5-10a). These two fused “butterfly” units form a basket-like subunit of the molecule. The resultant  $[\text{Mn}_3\text{O}_4]$  base of the basket [Mn(1), Mn(2), Mn(3), O(1), O(2)] is not planar but bent with  $\text{Mn}(1)\text{-Mn}(2)\text{-Mn}(3) = 169.1^\circ$ . The remaining two Mn atoms, Mn(6) and Mn(6a), represent the “handle” of the basket and are connected to the fused-butterfly unit by a  $\eta^1, \eta^1, \eta^1, \mu_3\text{-CO}_3^{2-}$  group through atoms O(5), O(6) and O(6a) and two  $\mu_3\text{-O}^{2-}$  ions [O(3) and O(3a)]. One OH ion [O(4)] and one carboxylate ligand bridge Mn(6) and Mn(6a) across the mirror plane of the molecule.

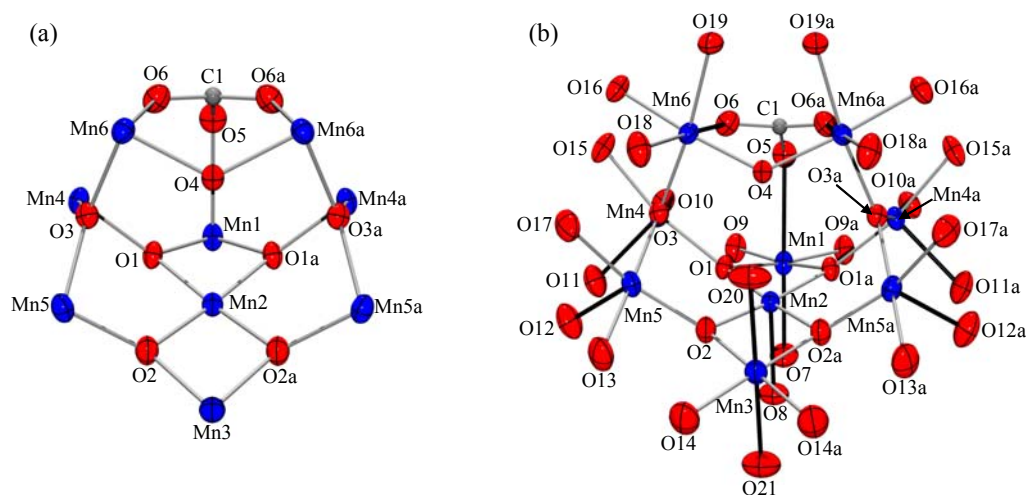


Figure 5-10. ORTEP representations in PovRay format of (a) the  $[\text{Mn}_9\text{O}_6(\text{OH})(\text{CO}_3)]^{12+}$  core of complex **17** and (b) the relative dispositions of the elongation axes, indicated as solid black bonds.  $\text{Mn}^{\text{III}}$  blue; O red; C gray.

Bond valence sum (BVS) calculations<sup>41</sup> indicate that all the Mn ions are in the +3 oxidation state (Table 5-7) and the protonation levels of the inorganic O atoms are collected in Table 5-8. Atom Mn(2) is five-coordinate with exactly square pyramidal (sp) geometry ( $\tau = 0$ , where  $\tau$  is 0 and 1 for ideal square pyramidal and trigonal bipyramidal

geometries, respectively<sup>71</sup>) as a result of the crystallographically imposed mirror plane symmetry. Atoms Mn(4) and Mn(5) are also five-coordinate with *sp* and distorted *sp* geometries ( $\tau = 0.01$  and  $0.22$ , respectively). The remaining Mn<sup>III</sup> centers all possess distorted octahedral geometries. Each octahedral Mn<sup>III</sup> displays a clear JT axial elongation, with axial Mn-O bonds approximately  $0.20 \text{ \AA}$  longer than equatorial ones. For Mn(2), the axial Mn(2)-O(8) length [ $2.192(6) \text{ \AA}$ ] is longer than basal lengths [ $1.900(3) - 1.906(4) \text{ \AA}$ ], as expected for *sp* geometry. Similarly for square pyramidal Mn(4) and Mn(5) [Mn(4)-O(11) =  $2.081(5)$  and Mn(5)-O(12) =  $2.041(5) \text{ \AA}$ ]. In effect, there is parallel alignment of the JT distortion axes of the three Mn<sup>III</sup> ions of the [Mn<sub>3</sub>O<sub>4</sub>] base [Mn(1), Mn(2), Mn(3)], whereas there is an overall random alignment of the distortion axes of the remaining Mn centers (Figure 5-10b). This will be of relevance to the magnetic discussion later (*vide infra*).

The Mn<sub>9</sub> core of **17** is very similar to that in [Mn<sub>9</sub>O<sub>7</sub>(O<sub>2</sub>CPh)<sub>13</sub>(py)<sub>2</sub>],<sup>150</sup> [Na<sub>2</sub>Mn<sub>9</sub>O<sub>7</sub>(O<sub>2</sub>CPh)<sub>15</sub>(MeCN)<sub>2</sub>]<sup>131</sup> and [K<sub>2</sub>Mn<sub>9</sub>O<sub>7</sub>(O<sub>2</sub>CBu<sup>t</sup>)<sub>15</sub>(HO<sub>2</sub>CBu<sup>t</sup>)<sub>2</sub>].<sup>151</sup> The core also appears as a subunit in the larger cluster [Mn<sub>22</sub>O<sub>12</sub>(O<sub>3</sub>PPh)<sub>8</sub>(O<sub>2</sub>CEt)<sub>22</sub>(H<sub>2</sub>O)<sub>8</sub>].<sup>132</sup> The primary difference between complex **17** and these other Mn<sub>9</sub> clusters is the triply bridging CO<sub>3</sub><sup>2-</sup> ligand that fuses the “handle” to the [Mn<sub>7</sub>O<sub>4</sub>] “basket” subunit. Triply bridging carbonate ions are somewhat rare in discrete transition metal clusters, especially in Mn chemistry. Known clusters with such  $\eta^1, \eta^1, \eta^1, \mu_3\text{-CO}_3^{2-}$  ligands include a handful of molecules containing Cu,<sup>152</sup> Z,<sup>152d,152e,153</sup> V,<sup>154</sup> and Mo.<sup>155</sup> To our knowledge, complex **17** is the first example of a triply bridging CO<sub>3</sub><sup>2-</sup> ion in molecular Mn chemistry. There is, however, a doubly bridging,  $\eta^1, \eta^1, \mu\text{-CO}_3^{2-}$  ligand in Mn<sup>II</sup> chemistry, although it was not crystallographically confirmed.<sup>141</sup> A heterometallic Mn<sub>16</sub> cluster in which a carbonate

group bridges equatorial Ba<sup>2+</sup> ions has also been reported.<sup>156</sup> The carbonate ligand in **17** is not planar; the carbon atom C(1) is slightly (0.18 Å) out of the plane formed by the three oxygen atoms [O(5), O(6), and O(6a)]. All previous  $\eta^1, \eta^1, \eta^1, \mu_3\text{-CO}_3^{2-}$  groups are planar, and we assign the slightly pyramidal structure in **17** to the strain the CO<sub>3</sub><sup>2-</sup> group experiences in the bridging mode it adopts. The bond distances C(1)-O(5) (1.274(8) Å) and C(1)-O(6) and C(1)-O(6a) (1.303(5) Å) are in agreement with a CO<sub>3</sub><sup>2-</sup> ion. The C-O bond lengths in formaldehyde, free carbonate anion, and methanol are 1.22, 1.33 and 1.43 Å, respectively.

Table 5-7. Bond valence sum calculations<sup>a</sup> for complex **17**·H<sub>2</sub>O·HO<sub>2</sub>CPe<sup>t</sup>.

Atom	Mn <sup>2+</sup>	Mn <sup>3+</sup>	Mn <sup>4+</sup>
Mn(1)	3.277	<u>2.997</u>	3.147
Mn(2)	3.070	<u>2.808</u>	2.948
Mn(3)	3.039	<u>3.027</u>	3.177
Mn(4)	3.178	<u>2.906</u>	3.051
Mn(5)	3.186	<u>2.914</u>	3.059
Mn(6)	3.311	<u>3.028</u>	3.179

<sup>a</sup> The underlined value is the one closest to the actual charge for which it was calculated. The oxidation state of a particular atom can be taken as the nearest whole number to the underlined value.

Table 5-8. Bond valence sum calculations<sup>a</sup> for selected oxygen atoms in complex **17**·H<sub>2</sub>O·HO<sub>2</sub>CPe<sup>t</sup>.

Atom	$V_i$	Assignment
O(1)	2.137	O <sup>2-</sup>
O(2)	2.116	O <sup>2-</sup>
O(3)	2.164	O <sup>2-</sup>
O(4)	1.568	OH <sup>-</sup>
O(20)	0.270	H <sub>2</sub> O
O(21)	0.259	H <sub>2</sub> O

<sup>a</sup> The oxygen atoms is O<sup>2-</sup> if  $V_i \approx 2$ , OH<sup>-</sup> if  $V_i \approx 1$ , and H<sub>2</sub>O if  $V_i \approx 0$ .

#### 5.2.3.4 X-ray crystal structure of [Mn<sub>4</sub>O<sub>2</sub>(O<sub>2</sub>CPe<sup>t</sup>)<sub>6</sub>(bpy)<sub>2</sub>] (**18**)

A labeled ORTEP<sup>40</sup> plot in PovRay format of complex **18** is shown in Figure 5-11. The crystallographic data and structure refinement details are collected in Table 5-2, and

selected interatomic distances and angles are listed in Table A-12. Complex **18**·2H<sub>2</sub>O crystallizes in the monoclinic space group  $P2_1/c$ . The asymmetric unit contains half the molecule and two H<sub>2</sub>O solvent molecules. The structure consists of a  $[\text{Mn}^{\text{III}}_2\text{Mn}^{\text{II}}_2(\mu_3\text{-O})_2]^{6+}$  core with peripheral ligation provided by six bridging  $\text{Pe}'\text{CO}_2^-$  ligands and two terminal bipyridine molecules. BVS calculations<sup>41</sup> indicate that Mn(1) and Mn(1a) are in the +3 oxidation state while Mn(2) and Mn(2a) are in the +2 oxidation level (Table 5-9) and also that triply bridging O(1) and O(1a) are  $\text{O}^{2-}$  (Table 5-10). Each  $\text{Mn}^{\text{II}}$  center is in a distorted octahedral environment while the two  $\text{Mn}^{\text{III}}$  centers are five-coordinate with distorted square pyramidal geometry ( $\tau = 0.16$ ).<sup>71</sup>

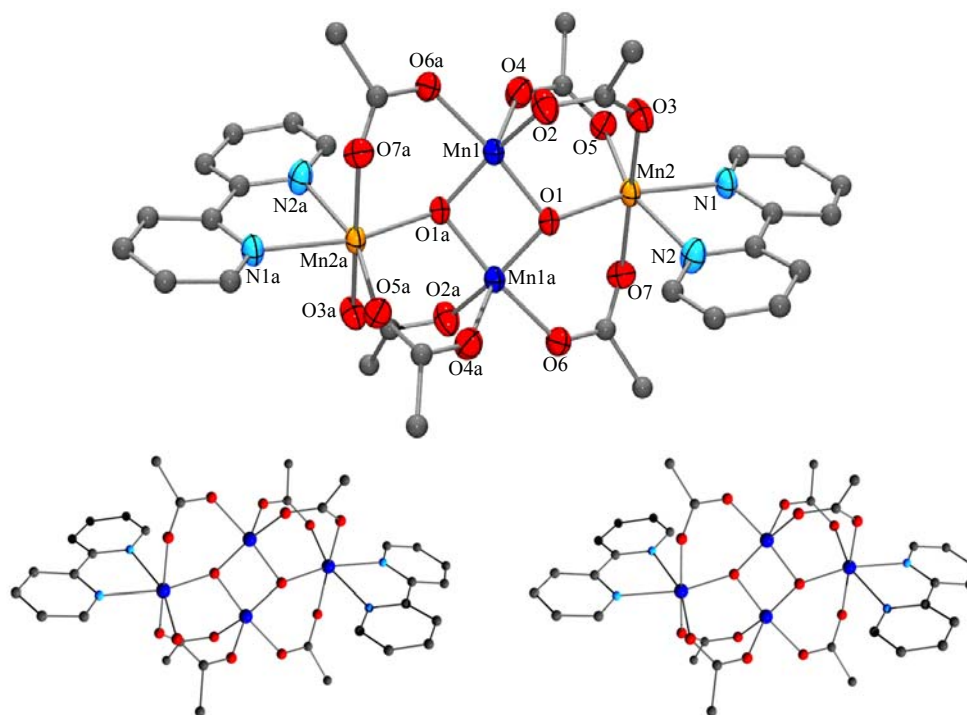


Figure 5-11. ORTEP representation in PovRay format of  $[\text{Mn}_4\text{O}_2(\text{O}_2\text{CPe}')_6(\text{bpy})_2]$  (**18**) at the 50% probability level except for C atoms, together with a stereopair. For clarity, the hydrogen atoms have been omitted, and only the quaternary C atoms of the ligands are shown.  $\text{Mn}^{\text{III}}$  blue;  $\text{Mn}^{\text{II}}$  orange; O red; C gray; N cyan.

The complex possesses an exactly planar array of four Mn atoms bridged by two  $\mu_3$ -oxide atoms, O(1) and O(1a), one above and one below the Mn<sub>4</sub> plane. The distance of the  $\mu_3$ -oxygen atoms above or below the Mn<sub>4</sub> plane is 0.60 Å. The [Mn<sup>III</sup><sub>2</sub>Mn<sup>II</sup><sub>2</sub>( $\mu_3$ -O)<sub>2</sub>]<sup>6+</sup> core can be considered as two edge-sharing [Mn<sub>3</sub>O] units. Each edge of the Mn<sub>4</sub> rhombus is bridged by either one or two  $\mu$ -Pe<sup>t</sup>CO<sub>2</sub><sup>-</sup> groups. The edges bridged by only one *t*-pentylate ligand have a slightly longer Mn···Mn separation [3.465 Å] than those bridged by two *t*-pentylate groups [3.274 Å]. The central Mn(1)···Mn(1a) separation is significantly shorter [2.775 Å], consistent with the two oxide bridges. Two terminal bpy groups complete the peripheral ligation, one at each end of the molecule. The local *z* axes of the two five-coordinate Mn<sup>III</sup> centers, Mn(1)-O(4) = 2.089(2) and Mn(1a)-O(4a) = 2.089(2), are oriented parallel to each other. The overall symmetry of the complex is *C<sub>i</sub>*. The overall structure of complex **18** is nearly identical to that observed in [Mn<sub>4</sub>O<sub>2</sub>(O<sub>2</sub>CMe)<sub>6</sub>(bpy)<sub>2</sub>].<sup>52</sup>

Table 5-9. Bond valence sum calculations<sup>a</sup> for complex **18**·2H<sub>2</sub>O.

Atom	Mn <sup>2+</sup>	Mn <sup>3+</sup>	Mn <sup>4+</sup>
Mn(1)	3.163	<u>2.893</u>	3.037
Mn(2)	<u>2.060</u>	1.919	1.959

<sup>a</sup> The underlined value is the one closest to the actual charge for which it was calculated. The oxidation state of a particular atom can be taken as the nearest whole number to the underlined value.

Table 5-10. Bond valence sum calculations<sup>a</sup> for selected oxygen atoms in complex **18**·2H<sub>2</sub>O.

Atom	<i>V<sub>i</sub></i>	Assignment
O(1)	2.039	O <sup>2-</sup>

<sup>a</sup> The oxygen atoms is O<sup>2-</sup> if *V<sub>i</sub>* ≈ 2, OH<sup>-</sup> if *V<sub>i</sub>* ≈ 1, and H<sub>2</sub>O if *V<sub>i</sub>* ≈ 0.

## 5.2.4 Magnetochemistry of Complexes 15 - 19

### 5.2.4.1 DC studies of 15

Variable-temperature DC susceptibility measurements were performed in the 5.0-300 K range on a powdered microcrystalline sample of **15**·2CH<sub>2</sub>Cl<sub>2</sub>, restrained in eicosane to prevent torquing, in a 5 kG field (Figure 5-12). The value of  $\chi_M T$  in the 150-300 K range, 20-22 cm<sup>3</sup> K mol<sup>-1</sup>, rapidly increases to a maximum of 53 cm<sup>3</sup> K mol<sup>-1</sup> at 15 K before decreasing rapidly at lower temperatures. The maximum value indicates a large ground state spin (S) value and the decrease of  $\chi_M T$  at low temperatures is primarily due to Zeeman and zero-field splitting (ZFS) effects.

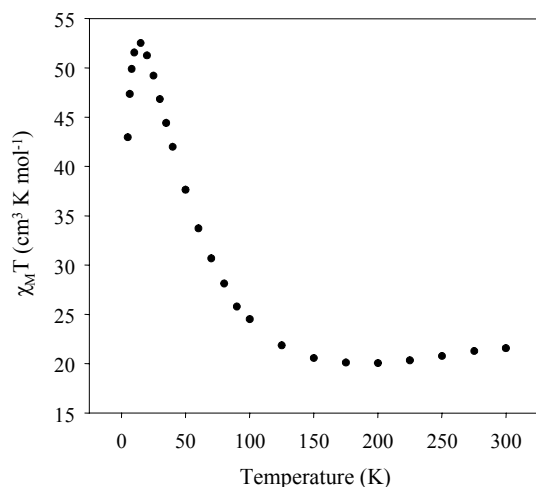


Figure 5-12. Plot of  $\chi_M T$  vs temperature for a dried, microcrystalline sample of complex **15**·2CH<sub>2</sub>Cl<sub>2</sub> in eicosane.  $\chi_M$  is the DC molar magnetic susceptibility measured in a 5.0 kG field.

A theoretical treatment of the susceptibility data using the Kambe vector coupling approach<sup>51</sup> was not feasible owing to the topological complexity and low symmetry of the Mn<sub>12</sub> cluster. Instead, our efforts were focused on the determination of the ground state spin by variable-temperature and -field magnetization (M) measurements in the 1.8-4.00 K temperature and 0.5-7 T field ranges. The data are plotted as reduced magnetization ( $M/N\mu_B$ ) versus  $H/T$  in Figure 5-13a, where N is Avogadro's number,  $\mu_B$  is

the Bohr magneton, and  $H$  is the applied magnetic field. For complexes populating only the ground state and experiencing no ZFS, the magnetization follows the Brillouin function and the isofield lines all superimpose and saturate at a value of  $gS$ . The data in Figure 5-13a show that the isofield lines do not superimpose for complex **15**, indicating that the ground state is zero-field split. The data were fit using the method described elsewhere<sup>49,52</sup> that involves diagonalization of the spin Hamiltonian matrix, assuming only the ground state is occupied at these temperatures, and including axial ZFS Zeeman interactions and a full powder average of the magnetization.<sup>54</sup> Fitting of the data gave  $S = 10$ ,  $g = 2.03$ , and  $D = -0.38 \text{ cm}^{-1}$ . These values are typical of neutral  $\text{Mn}_{12}$  complexes; complex **15** has the same spin as its parent complex **1**. Thus, replacement of the water ligands with methanol groups does not significantly perturb the properties of the  $\text{Mn}_{12}$  complex.<sup>112</sup>

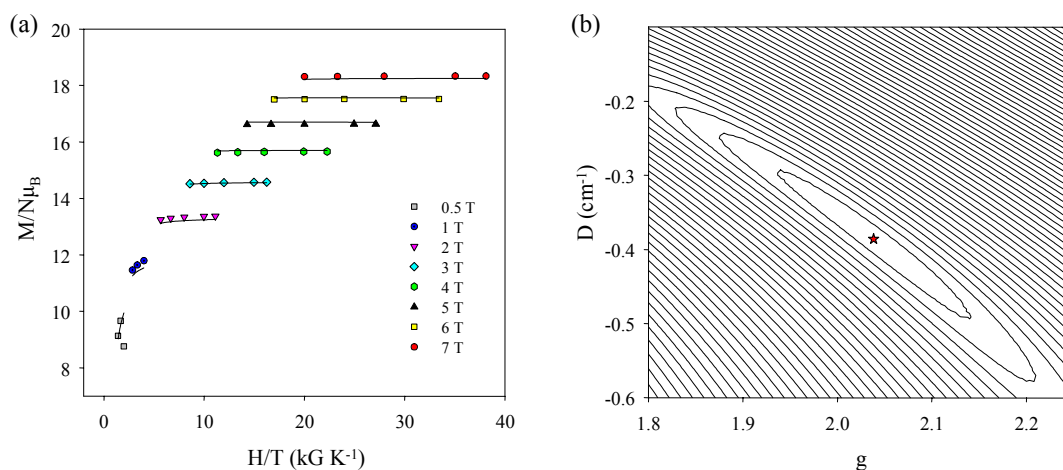


Figure 5-13. Determination of ground state spin. (a) Plot of reduced magnetization  $M/N\mu_B$  vs  $H/T$  for a dried, microcrystalline sample of complex **15**· $2\text{CH}_2\text{Cl}_2$  in eicosane; the DC field value of each of the isofield plots is indicated. (b) Two-dimensional contour plot of the error surface for the  $D$  vs  $g$  fit for complex **15**· $2\text{CH}_2\text{Cl}_2$ . The asterisk indicates the soft minimum.

In order to confirm that the obtained parameters were the true global rather than a local minimum, and to assess the uncertainty in the obtained  $g$  and  $D$  values, a root-mean

square  $D$  vs  $g$  error surface for the fit was generated using the program GRID.<sup>55</sup> The error surface is shown in Figure 5-13b as a contour plot for the  $D = -0.10$  to  $-0.60$   $\text{cm}^{-1}$  and  $g = 1.8$  to  $2.25$  ranges. One soft fitting minimum is observed; the contour describes the region of minimum error from  $D \approx -0.30$  to  $-0.49$   $\text{cm}^{-1}$  and  $g \approx 1.94$  to  $2.14$ , giving fitting parameters of  $D = -0.39 \pm 0.10$   $\text{cm}^{-1}$  and  $g = 2.0 \pm 0.1$ .

#### 5.2.4.2 AC studies of **15**

To confirm, as expected, that this new  $\text{Mn}_{12}$  complex is a SMM, and to assess further the influence of its terminal MeOH groups instead of the usual  $\text{H}_2\text{O}$  ones, AC magnetic susceptibility studies were carried out on a dried, microcrystalline sample of **15**·2 $\text{CH}_2\text{Cl}_2$  in the 1.8-10 K range in a 3.5 G AC field with oscillation frequencies ( $\nu$ ) up to 1488 Hz. All other previously characterized  $\text{Mn}_{12}$  complexes exhibit at least one frequency-dependent out-of-phase ( $\chi_M''$ ) signal that is accompanied by a frequency-dependent decrease in the in-phase ( $\chi_M'$ ) signal, indicating slow magnetization relaxation. Although such signals are not sufficient proof of the SMM property, they are a strong indicator that a complex behaves as a SMM. Indeed, frequency-dependent out-of-phase ( $\chi_M''$ ) AC susceptibility signals are clearly exhibited by complex **15**·2 $\text{CH}_2\text{Cl}_2$  (Figure 5-14). In fact, there are two such signals, corresponding to two distinct relaxation processes, a higher-temperature (HT) peak at  $\sim 6$  K and a lower-temperature (LT) peak at  $\sim 2.5$  K. The signals are accompanied by two frequency-dependent decreases in the in-phase  $\chi_M' T$  plot, first at  $T \sim 7.5$  K and then at  $T \sim 3$  K, respectively, indicating that the magnetization of **15** cannot relax fast enough to stay in-phase with the oscillating field and that complex **15** is most likely a SMM. The value of  $\chi_M' T$  in the temperature-independent region of Figure 5-14 is especially useful for estimating the ground state spin without interference from even a small DC field. The  $\chi_M' T$  value above 7 K of  $\sim 54$   $\text{cm}^3$  K

$\text{mol}^{-1}$  for **15** corresponds to an  $S = 10$  system with  $g = 1.98$ , consistent with the DC magnetization results above.

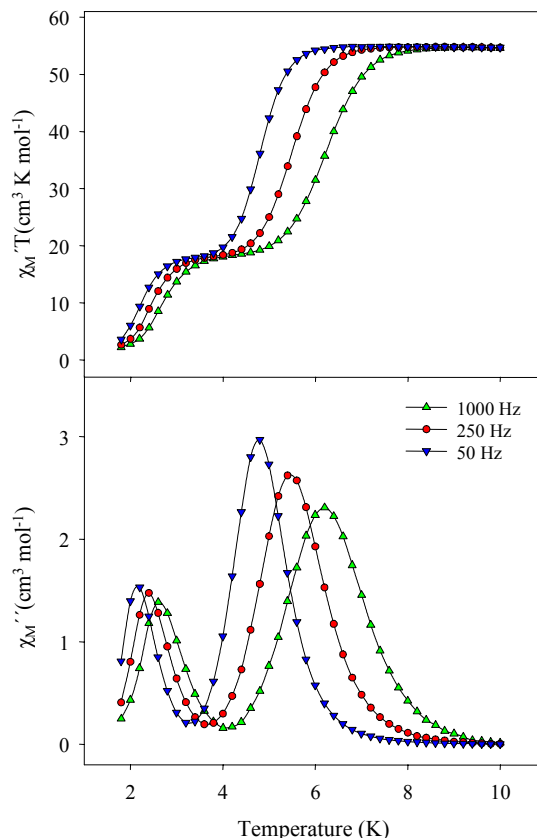


Figure 5-14. Plot of the in-phase (as  $\chi_M' T$ ) and out-of-phase ( $\chi_M''$ ) AC susceptibility signals vs temperature for a dried, microcrystalline sample of complex **15**·2CH<sub>2</sub>Cl<sub>2</sub> in eicosane at the indicated oscillation frequencies.

The presence of two peaks in the out-of-phase AC susceptibility plot of **15** is typical of Mn<sub>12</sub> complexes, and has been shown previously to be due to Jahn-Teller (JT) isomerism, in which complexes differ in the relative orientation of one or more Mn<sup>III</sup> JT elongation axes.<sup>56-59</sup> The LT (faster-relaxing) isomer is the one with the abnormal orientation of the JT axis towards the bridging oxide ions, whereas the HT (slower-relaxing) form is that with all JT axes avoiding bridging oxide ions. Normally, the HT form is the predominant form in wet crystals, with the LT form often becoming more

pronounced in dried solids as interstitial solvent of crystallization is lost. Indeed, the HT:LT ratio in dried solid of **15** is 3:1 (Figure 5-14), whereas it is 19:1 in wet crystals. The significantly smaller amount of the LT form in the latter also rationalizes why it is not observed in the X-ray crystal structure of the complex, since the small fraction of the LT form and the likely static disorder of the abnormally-oriented axis over multiple sites will dilute its effect on the structural parameters.

At the  $\chi_M''$  peak maximum, the magnetization relaxation rate ( $1/\tau$ , where  $\tau$  is the relaxation time) is equal to the angular frequency ( $2\pi\nu$ ) of the AC field, and thus  $\chi_M''$  versus  $\nu$  studies provide rate vs  $T$  kinetic data,<sup>157</sup> and these were fit to the Arrhenius equation (eq 5-4). This is the characteristic behavior of a thermally-activated Orbach process, where  $U_{\text{eff}}$  is the effective energy barrier,  $k$  is the Boltzmann constant, and  $1/\tau_0$  is the pre-exponential term.

$$1/\tau = 1/\tau_0 \exp(-U_{\text{eff}}/kT) \quad (5-4)$$

The frequency dependencies of the  $\chi_M''$  peaks for **15** were determined at different oscillation frequencies in the 5-1500 Hz range. A plot of  $\ln(1/\tau)$  vs  $1/T$  using this  $\chi_M''$  vs  $T$  data is shown in Figure 5-15, with the least-squares fit to eq 5-4 shown as solid lines for both the HT (●) and LT (▲) signals. The effective energy barrier to magnetization relaxation ( $U_{\text{eff}}$ ) for the HT signal (slower-relaxing species) is  $43 \text{ cm}^{-1}$  (62 K) while that of the LT signal (faster-relaxing species) is much smaller,  $24 \text{ cm}^{-1}$  (35 K). These are very similar to the values previously found for such HT and LT signals within the  $[\text{Mn}_{12}\text{O}_{12}(\text{O}_2\text{CR})_{16}(\text{H}_2\text{O})_4]$  family.<sup>56</sup> The values of the pre-exponential factor,  $1/\tau_0$ ,  $1.29 \times 10^8 \text{ s}^{-1}$  for the HT peak and  $2.98 \times 10^{10} \text{ s}^{-1}$  for the LT peak, are also within the range normally found for the  $[\text{Mn}_{12}\text{O}_{12}(\text{O}_2\text{CR})_{16}(\text{H}_2\text{O})_4]$  family.

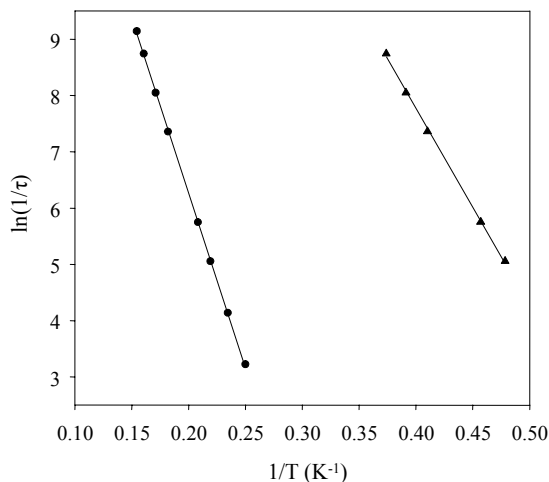


Figure 5-15. Plot of the natural logarithm of relaxation rate,  $\ln(1/\tau)$ , vs  $1/T$  for a dried, microcrystalline sample of complex **15**· $2\text{CH}_2\text{Cl}_2$  in eicosane using AC  $\chi_M''$  data; (●) corresponds to the HT peak (slower-relaxing species) and (▲) corresponds to the LT peak (faster-relaxing species). The solid lines are fits to the Arrhenius equation; see the text for the fit parameters.

Finally, we should add that we have not complemented the above results on **15** with single crystal hysteresis studies using a micro-SQUID apparatus to investigate the effect, if any, of the bulky carboxylate groups on the hysteresis loops. While we are very interested in this general point, such studies are instead currently in progress in great detail with the  $\text{Bu}^i\text{CH}_2\text{CO}_2^-$  derivatives, and these results will be reported separately.

#### 5.2.4.3 DC and AC susceptibility studies of complexes **16** - **19**

Variable-temperature DC susceptibility measurements were performed on dried, microcrystalline samples of **16**· $\frac{1}{2}\text{CH}_2\text{Cl}_2$ · $4\text{H}_2\text{O}$ , **17**· $\text{HO}_2\text{CPe}^t$ , **18**· $2\text{H}_2\text{O}$  and **19**· $\frac{1}{2}\text{MeNO}_2$ , restrained in eicosane to prevent torquing, in a 1 kG field in the range of 5.0-300 K. For **16**,  $\chi_M T$  smoothly decreases from  $15.8 \text{ cm}^3 \text{ K mol}^{-1}$  at 300 K to  $3.9 \text{ cm}^3 \text{ K mol}^{-1}$  at 5.0 K (Figure 5-16). The value at 300 K is less than the  $18 \text{ cm}^3 \text{ K mol}^{-1}$  spin-only value ( $g = 2.0$ ) expected for a  $\text{Mn}^{\text{III}}_6$  complex with non-interacting metal centers, indicating the presence of appreciable antiferromagnetic interactions between the manganese centers. For **17**, the  $\chi_M T$  value of  $4.0 \text{ cm}^3 \text{ K mol}^{-1}$  at 300 K decreases gradually with decreasing

temperature to  $0.35 \text{ cm}^3 \text{ K mol}^{-1}$  at 5.0 K (Figure 5-17a), while the  $\chi_M T$  value for **19** of  $19.3 \text{ cm}^3 \text{ K mol}^{-1}$  at 300 K decreases gradually to  $2.4 \text{ cm}^3 \text{ K mol}^{-1}$  at 5.0 K (Figure 5-18a). The spin-only ( $g = 2$ ) value for a molecule composed of non-interacting  $\text{Mn}^{\text{III}}$  ions is  $27 \text{ cm}^3 \text{ K mol}^{-1}$ . The  $\chi_M T$  value of  $7.4 \text{ cm}^3 \text{ K mol}^{-1}$  at 300 K for complex **18** gradually decreases with decreasing temperature to  $3.5 \text{ cm}^3 \text{ K mol}^{-1}$  at 5.0 K (Figure 5-19a). The value of  $\chi_M T$  at 300 K is less than the spin-only value for a unit composed of non-interacting  $\text{Mn}^{\text{II}}_2\text{Mn}^{\text{III}}_2$  ions ( $14.75 \text{ cm}^3 \text{ K mol}^{-1}$ ). Hence, the molecules all appear to have appreciable intramolecular antiferromagnetic interactions and relatively low or zero ground state spin values.

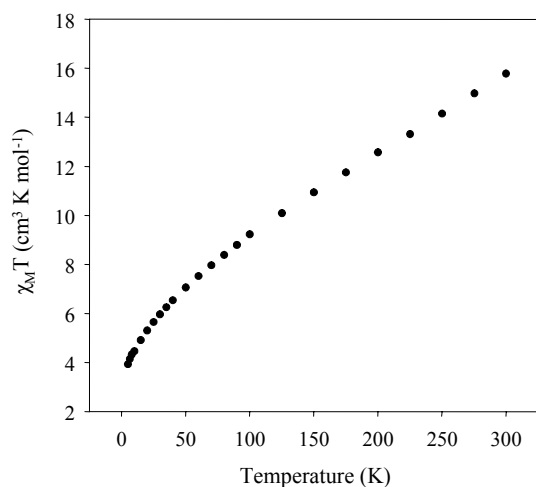


Figure 5-16. Plot of  $\chi_M T$  vs temperature for a dried, microcrystalline sample of complex **16**· $\frac{1}{2}\text{CH}_2\text{Cl}_2$ · $4\text{H}_2\text{O}$ .  $\chi_M$  is the DC molar magnetic susceptibility measured in a 1 kG field.

Complex **16** contains six  $\text{Mn}^{\text{III}}$  centers with total spin values ranging from 0 to 12 while complexes **17** and **19** each contain nine  $\text{Mn}^{\text{III}}$  centers with total spin values ranging from 0 to 18. Again, it is not possible to easily evaluate the various exchange parameters between the Mn centers as a result of the complexity and low symmetry of the clusters. In addition, magnetization data collected in the 0.1-70 kG and 1.8-10.0 K field and temperature ranges could not be satisfactorily fit to a model that assumes only the ground

state is populated. This behavior is typical of (i) complexes with low ground state  $S$  values, which cross with excited states with larger  $S$  values as a result of Zeeman effects in the applied DC field, and/or (ii) low-lying excited states from weak exchange interactions and/or spin frustration effects<sup>85,86</sup> within the complicated topologies present in most of these complexes. The exception to the latter is tetranuclear complex **7**, but even this has  $Mn^{II}/Mn^{III}$  interactions, which are typically very weak, and spin frustration within the triangular  $Mn_3$  subunits. In any event, further analysis of the exchange interactions within **18** was not pursued since the DC magnetic susceptibility behavior of such “butterfly” clusters has been already thoroughly studied.<sup>52</sup>

Overall, the low temperature DC magnetic susceptibility studies and the profiles of the susceptibility vs  $T$  plots suggest small ground state spin values of  $S \leq 2$  for complexes **16**·½CH<sub>2</sub>Cl<sub>2</sub>·4H<sub>2</sub>O, **17**·HO<sub>2</sub>CPe', **18**·2H<sub>2</sub>O and **19**·½MeNO<sub>2</sub>. Further assessment of the values was carried out using AC susceptibility studies in a 3.5 G AC field oscillating at frequencies up to 997 Hz. While the appearance of an out-of-phase AC susceptibility signal ( $\chi_M''$ ) is indicative of the onset of slow magnetic relaxation, the in-phase signal ( $\chi_M'$ ) can indicate, as mentioned earlier, the ground state  $S$  value and whether low-lying excited states are populated even at very low temperatures. Specifically, a temperature-independent  $\chi_M' T$  vs  $T$  plot indicates that only the ground state spin state is populated, while a sloping  $\chi_M' T$  vs  $T$  plot indicates population of low-lying excited states. As expected on the basis of the DC studies, the  $\chi_M' T$  vs  $T$  plots of each of the complexes are strongly sloping with decreasing values of  $\chi_M' T$  with decreasing temperature, indicating population of excited states with greater  $S$  values than the ground state. Comparison of the AC susceptibility data ( $\chi_M' T$ ) with the DC data ( $\chi_M T$ ) over the same  $T$  range shows

that the two are essentially superimposable for each of the clusters, as shown in Figure 5-17b for representative complex **17**·HO<sub>2</sub>CPe<sup>f</sup>.

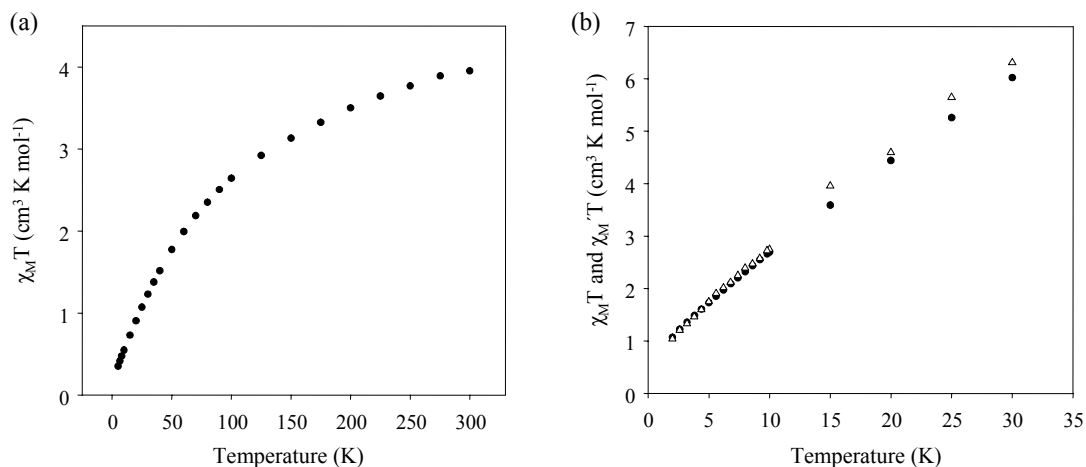


Figure 5-17. Determination of ground state spin. (a) Plot of  $\chi_M T$  vs temperature for a dried, microcrystalline sample of complex **17**·HO<sub>2</sub>CPe<sup>f</sup>.  $\chi_M$  is the DC molar magnetic susceptibility measured in a 1 kG field. (b) Plot of  $\chi_M' T$  vs temperature for complex **17**·HO<sub>2</sub>CPe<sup>f</sup> in the 2.0-30.0 K range from AC magnetic susceptibility measurements ( $\Delta$ ), and including the DC  $\chi_M T$  data ( $\bullet$ ) for this temperature range. The AC data were measured with a 3.5 G AC field oscillating at 997 Hz.

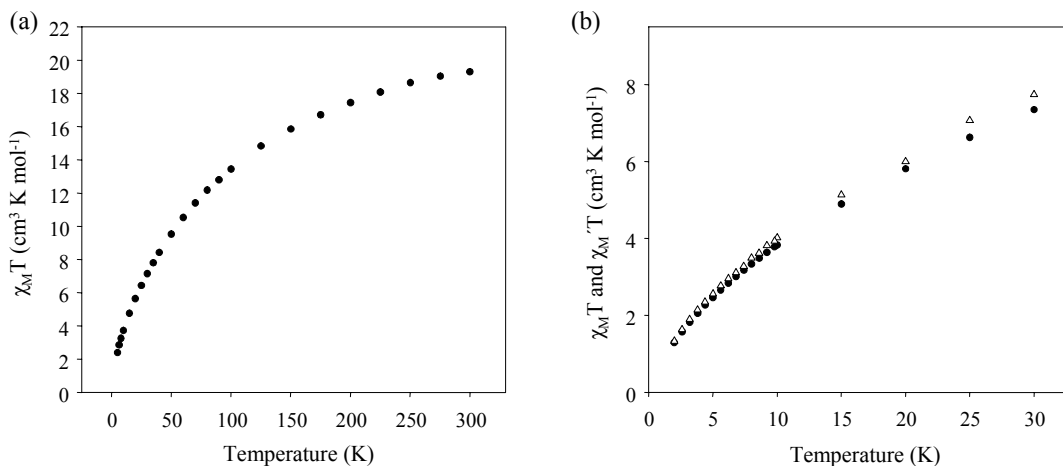


Figure 5-18. Determination of ground state spin. (a) Plot of  $\chi_M T$  vs temperature for a dried, microcrystalline sample of complex **19**· $\frac{1}{2}$ MeNO<sub>2</sub>.  $\chi_M$  is the DC molar magnetic susceptibility measured in a 1 kG field. (b) Plot of  $\chi_M' T$  vs temperature for complex **19**· $\frac{1}{2}$ MeNO<sub>2</sub> in the 2.0-30.0 K range from AC magnetic susceptibility measurements ( $\Delta$ ), and including the DC  $\chi_M T$  data ( $\bullet$ ) for this temperature range. The AC data were measured with a 3.5 G AC field oscillating at 997 Hz.

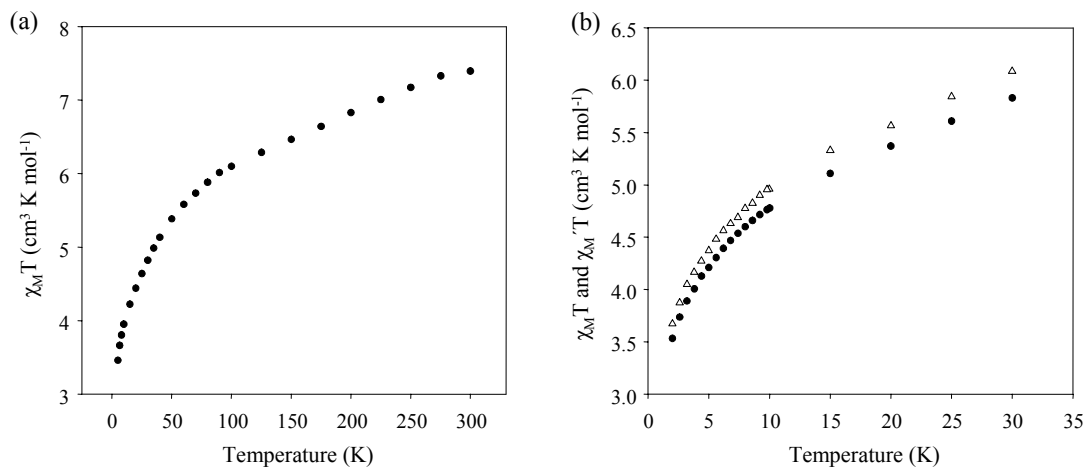


Figure 5-19. Determination of ground state spin. (a) Plot of  $\chi_M T$  vs temperature for a dried, microcrystalline sample of complex  $\mathbf{18} \cdot 2\text{H}_2\text{O}$ .  $\chi_M$  is the DC molar magnetic susceptibility measured in a 1 kG field. (b) Plot of  $\chi_M' T$  vs temperature for complex  $\mathbf{18} \cdot 2\text{H}_2\text{O}$  in the 2.0-30.0 K range from AC magnetic susceptibility measurements ( $\Delta$ ), and including the DC  $\chi_M T$  data ( $\bullet$ ) for this temperature range. The AC data were measured with a 3.5 G AC field oscillating at 997 Hz.

Linear extrapolation suggests that the plot for  $\mathbf{17}$  is heading for  $\chi_M T \leq 0.6 \text{ cm}^3 \text{K mol}^{-1}$  at 0 K, a value consistent with at most an  $S = 1$  ground state spin, and more likely  $S = 0$ . Similarly, the AC data for  $\mathbf{16}$ ,  $\mathbf{18}$  (Figure 5-19b) and  $\mathbf{19}$  (Figure 5-18b) suggest  $S \leq 2$  (and probably 1 or 0), but with very low-lying excited states that are populated even at 1.8 K and which make a more precise assignment of a ground state value very difficult.

### 5.3 Conclusions

The use of the basic, hydrophobic carboxylic acid, *t*-pentylic acid, as a reactant in  $\text{Mn}_{12}$  chemistry has led to the isolation of several new Mn clusters, two of which are new structural types in Mn chemistry. The reaction of  $[\text{Mn}_{12}\text{O}_{12}(\text{O}_2\text{CPe}^t)_{16}(\text{H}_2\text{O})_4]$  ( $\mathbf{14}$ ) with MeOH in the presence of *t*-pentylic acid has led to the isolation of  $[\text{Mn}_{12}\text{O}_{12}(\text{O}_2\text{CPe}^t)_{16}(\text{MeOH})_4]$  ( $\mathbf{15}$ ), a new member of a sub-class of  $\text{Mn}_{12}$  clusters in which the water ligands that coordinate to either three or four  $\text{Mn}^{\text{III}}$  ions in the outer ring of the cluster have been replaced by another ligand, MeOH. Magnetic studies on  $\mathbf{15}$

suggest that the complex retains an  $S = 10$  ground state spin as expected for a neutral  $Mn_{12}$  cluster. Additionally, peaks in the out-of-phase AC susceptibility indicate the onset of slow magnetization relaxation and suggest that **15** functions as a SMM.

In contrast, recrystallization of **14** from  $CH_2Cl_2/MeNO_2$  in the presence of *t*-pentylic acid causes a structural change and affords two new structural types in Mn chemistry,  $[Mn_6O_2(O_2CH_2)(O_2CPe^t)_{11}(HO_2CPe^t)_2(O_2CMe)]$  (**16**) and  $[Mn_9O_6(OH)(CO_3)(O_2CPe^t)_{12}(H_2O)_2]$  (**17**). Complex **16** contains only the third example of a  $\mu_4$ -methanediolate unit, while complex **17** possesses a non-planar triply bridging  $CO_3^{2-}$  anion and is the first example of a discrete complex with Mn ions bridged by a carbonate group. These investigations emphasize the differences in the reactivity of the nearly identical  $Mn_{12}$  complexes, **13** and **14**; recrystallization of **13** under similar conditions results in the retention of the  $[Mn_{12}O_{12}]^{16+}$  core. In addition, the reaction of **14** with the chelating ligand, 2,2'-bipyridine, has afforded  $[Mn_4O_2(O_2CPe^t)_6(bpy)_2]$  (**18**). Structural rearrangement of the  $[Mn_{12}O_{12}]^{16+}$  core is also observed when **13** undergoes reactions with other chelating ligands. Further investigations to probe the reactivity of **13** with various solvents, including THF, have led to the isolation of a new enneanuclear cluster,  $[Mn_9O_7(O_2CCH_2Bu^t)_{13}(THF)_2]$  (**19**). Magnetic studies on complexes **16-19** suggest ground state spin values of  $S \leq 2$  and show that the complexes do not function as single-molecule magnets.

Electrochemical studies on both complexes **13** and **15** reveal that in contrast to most other characterized  $Mn_{12}$  clusters, these molecules exhibit irreversible reduction processes, supporting the proposal that reductive destabilization of the  $[Mn_{12}O_{12}]$  core followed by structural rearrangement occurs to yield new clusters of differing nuclearity

and topology. While the strongly electron donating nature of the ligands coordinated to the metal centers in **13** and **15** accounts for the unwillingness of the cluster to accept another electron reversibly, it also accounts for the quasi-reversible oxidation wave, a process that occurs at a potential nearly one volt lower than previously found for other Mn<sub>12</sub> clusters.

## 5.4 Experimental

### 5.4.1 Syntheses

All manipulations were performed under aerobic conditions using materials as received, except where otherwise noted. [Mn<sub>12</sub>O<sub>12</sub>(O<sub>2</sub>CMe)<sub>16</sub>(H<sub>2</sub>O)<sub>4</sub>]·2MeCO<sub>2</sub>H·4H<sub>2</sub>O (**1**)<sup>50</sup> and [Mn<sub>12</sub>O<sub>12</sub>(O<sub>2</sub>CCH<sub>2</sub>Bu<sup>t</sup>)<sub>16</sub>(H<sub>2</sub>O)<sub>4</sub>] (**13**)<sup>13</sup> were prepared as described elsewhere.

[Mn<sub>12</sub>O<sub>12</sub>(O<sub>2</sub>CPe<sup>t</sup>)<sub>16</sub>(H<sub>2</sub>O)<sub>4</sub>] (**14**). A solution of complex **1** (2.0 g, 0.97 mmol) in MeCN (75 cm<sup>3</sup>) was treated with a solution of HO<sub>2</sub>CPe<sup>t</sup> (3.89 cm<sup>3</sup>, 31.0 mmol) in CH<sub>2</sub>Cl<sub>2</sub> (25 cm<sup>3</sup>). The solution was stirred overnight, and the solvent was then removed *in vacuo*. The residue was dissolved in toluene (20 cm<sup>3</sup>), and the solution was again evaporated to dryness. The addition and removal of toluene was repeated two more times. The residue was then dissolved in CH<sub>2</sub>Cl<sub>2</sub> (75 cm<sup>3</sup>) and treated again with HO<sub>2</sub>CPe<sup>t</sup> (3.89 cm<sup>3</sup>, 31.0 mmol) in CH<sub>2</sub>Cl<sub>2</sub> (25 cm<sup>3</sup>). After 3 h, three more cycles of addition and removal of toluene were performed. The residue was re-dissolved in CH<sub>2</sub>Cl<sub>2</sub> (50 cm<sup>3</sup>), the solution was filtered, and MeNO<sub>2</sub> (50 cm<sup>3</sup>) was added. The solution was then maintained undisturbed at 4 °C for 4 days. The resulting black crystals were collected by filtration, washed with MeNO<sub>2</sub>, and dried *in vacuo*; the yield was ~83%. Anal. Calcd (found) for **14**·CH<sub>2</sub>Cl<sub>2</sub> (C<sub>97</sub>H<sub>186</sub>Cl<sub>2</sub>O<sub>48</sub>Mn<sub>12</sub>): C, 40.87 (40.78); H, 6.58 (6.53); N, 0.00 (0.00). Selected IR data (cm<sup>-1</sup>): 1584 (s), 1557 (s), 1524 (s), 1499 (m), 1477 (vs), 1459 (m), 1419 (vs), 1374 (s), 1356 (m), 1326 (m), 1284 (m), 1229 (w), 1209 (m), 1061 (w), 1006

(w), 931 (w), 883 (w), 801 (w), 786 (w), 726 (m), 680 (m), 613 (s), 545 (m), 508 (w), 473 (w), 440 (w).

**[Mn<sub>12</sub>O<sub>12</sub>(O<sub>2</sub>CPe<sup>f</sup>)<sub>16</sub>(MeOH)<sub>4</sub>] (15)**. A solution of complex **14** (0.40 g, 0.14 mmol) in CH<sub>2</sub>Cl<sub>2</sub> (20 cm<sup>3</sup>) was treated with HO<sub>2</sub>CPe<sup>f</sup> (2.0 cm<sup>3</sup>, 16.0 mmol) and MeOH (10 cm<sup>3</sup>). The solution was maintained undisturbed at 4 °C for 6 days. The resulting black crystals were collected by filtration, washed with MeOH, and dried *in vacuo*; the yield was ~82%. A sample for crystallography was maintained in contact with the mother liquor to prevent the loss of interstitial solvent. Anal. Calcd (found) for **15**·2CH<sub>2</sub>Cl<sub>2</sub> (C<sub>102</sub>H<sub>196</sub>Cl<sub>4</sub>O<sub>48</sub>Mn<sub>12</sub>): C, 40.95 (40.79); H, 6.60 (6.68); N, 0.00 (0.00). Selected IR data (cm<sup>-1</sup>): 1587 (s), 1559 (s), 1524 (s), 1479 (vs), 1459 (m), 1419 (vs), 1374 (s), 1359 (m), 1324 (m), 1289 (m), 1206 (m), 1179 (m), 1069 (w), 1008 (w), 933 (w), 873 (w), 803 (w), 783 (w), 721 (m), 670 (m), 638 (m), 615 (s), 543 (m), 510 (w), 478 (w), 445 (w).

**[Mn<sub>6</sub>O<sub>2</sub>(O<sub>2</sub>CH<sub>2</sub>)(O<sub>2</sub>CPe<sup>f</sup>)<sub>11</sub>(HO<sub>2</sub>CPe<sup>f</sup>)<sub>2</sub>(O<sub>2</sub>CMe)] (16)**. A solution of complex **14** (0.40 g, 0.14 mmol) in CH<sub>2</sub>Cl<sub>2</sub> (20 cm<sup>3</sup>) was treated with HO<sub>2</sub>CPe<sup>f</sup> (2.0 cm<sup>3</sup>, 16.0 mmol). The solution was layered with MeNO<sub>2</sub> (80 cm<sup>3</sup>), and black crystals slowly grew. After one week, the crystals were collected by filtration, washed with MeNO<sub>2</sub>, and dried *in vacuo*; the yield was ~10%. A sample for crystallography was maintained in contact with the mother liquor to prevent the loss of interstitial solvent. Dried solid appeared to be hygroscopic. Anal. Calcd (found) for **16**·½CH<sub>2</sub>Cl<sub>2</sub>·4H<sub>2</sub>O (C<sub>81.5</sub>H<sub>159</sub>Cl<sub>1</sub>O<sub>36</sub>Mn<sub>6</sub>): C, 47.06 (47.09); H, 7.70 (7.73); N, 0.00 (0.11). Selected IR data (cm<sup>-1</sup>): 1710 (m), 1627 (vs), 1539 (vs), 1477 (vs), 1459 (s), 1437 (m), 1417 (s), 1359 (m), 1326 (w), 1286 (s), 1204 (s), 1066 (m), 1051 (m), 1008 (m), 971 (m), 928 (w), 886 (w), 803 (m), 781 (m), 763 (w), 678 (m), 635 (s), 603 (m), 545 (m), 475 (m), 445 (m).

**[Mn<sub>9</sub>O<sub>6</sub>(OH)(CO<sub>3</sub>)(O<sub>2</sub>CPe<sup>f</sup>)<sub>12</sub>(H<sub>2</sub>O)<sub>2</sub>] (17)**. To a solution of complex **14** (0.40 g, 0.14 mmol) in CH<sub>2</sub>Cl<sub>2</sub> (20 cm<sup>3</sup>) was added HO<sub>2</sub>CPe<sup>f</sup> (2.0 cm<sup>3</sup>, 16.0 mmol). The solution was layered with MeNO<sub>2</sub> (80 cm<sup>3</sup>), and black crystals of **16** slowly grew. After two weeks, these were removed by filtration through Celite, and the filtrate was evaporated to dryness *in vacuo*. The residue was re-dissolved in CH<sub>2</sub>Cl<sub>2</sub> (10 cm<sup>3</sup>), HO<sub>2</sub>CPe<sup>f</sup> (1.3 cm<sup>3</sup>, 10.0 mmol) was added, and the solution layered with MeNO<sub>2</sub> (40 cm<sup>3</sup>). Black crystals slowly grew over 4 weeks, and these were suitable for X-ray studies if maintained in contact with the mother liquor to prevent the loss of interstitial solvent. After 4 weeks, the crystals were isolated by filtration, washed with small volumes of MeNO<sub>2</sub>, and dried *in vacuo*; the yield was ~5%. Anal. Calcd (found) for **17**·HO<sub>2</sub>CPe<sup>f</sup> (C<sub>79</sub>H<sub>149</sub>O<sub>38</sub>Mn<sub>9</sub>): C, 43.10 (43.16); H, 6.82 (6.77); N, 0.00 (0.02). Selected IR data (cm<sup>-1</sup>): 1697 (w), 1557 (vs), 1537 (vs), 1474 (vs), 1459 (w), 1419 (vs), 1379 (m), 1364 (m), 1326 (w), 1289 (m), 1204 (m), 1066 (w), 1051 (w), 1006 (w), 808 (w), 783 (w), 690 (w), 665 (w), 653 (w), 613 (m), 413 (w).

**[Mn<sub>4</sub>O<sub>2</sub>(O<sub>2</sub>CPe<sup>f</sup>)<sub>6</sub>(bpy)<sub>2</sub>] (18)**. To a solution of complex **14** (0.25 g, 0.090 mmol) in CH<sub>2</sub>Cl<sub>2</sub> (10 cm<sup>3</sup>) was added 2,2'-bipyridine (0.23 g, 1.4 mmol), and the resulting solution was stirred for 3 h and filtered through Celite. The filtrate was layered with MeNO<sub>2</sub> (25 cm<sup>3</sup>). Black crystals slowly grew, and these were suitable for X-ray crystallography if maintained in contact with the mother liquor to prevent the loss of interstitial solvent. After 3 days, the crystals were isolated by filtration, washed with MeNO<sub>2</sub>, and dried *in vacuo*; the yield was 35%. Anal. Calcd (found) for **18**·2H<sub>2</sub>O (C<sub>56</sub>H<sub>86</sub>N<sub>4</sub>O<sub>16</sub>Mn<sub>4</sub>): C, 52.10 (52.17); H, 6.71 (6.65); N, 4.34 (4.34). Selected IR data (cm<sup>-1</sup>): 1584 (vs), 1547 (s), 1476 (s), 1442 (m), 1420 (vs), 1370 (m), 1357 (m), 1290 (m),

1205 (w), 1161 (w), 1054 (w), 1016 (w), 804(w), 786 (w), 764 (s), 738 (m), 696(m), 653 (m), 630 (s), 415 (m).

**[Mn<sub>9</sub>O<sub>7</sub>(O<sub>2</sub>CCH<sub>2</sub>Bu<sup>t</sup>)<sub>13</sub>(THF)<sub>2</sub>] (19)**. To a solution of complex **13** (0.20 g, 0.072 mmol) in THF (30 cm<sup>3</sup>) was added MeNO<sub>2</sub> (50 cm<sup>3</sup>). The solution was filtered, and the filtrate was allowed to stand undisturbed at 4 °C. Black crystals formed slowly over two weeks, and these were suitable for X-ray studies if maintained in contact with the mother liquor to prevent the loss of interstitial solvent. After 2 weeks, the crystals were isolated by filtration, washed with MeNO<sub>2</sub>, and dried *in vacuo*; the yield was ~30%. Anal. Calcd (found) for **19**·½MeNO<sub>2</sub> (C<sub>86.5</sub>H<sub>160.5</sub>N<sub>0.5</sub>O<sub>36</sub>Mn<sub>9</sub>): C, 45.61 (45.36); H, 7.10 (7.16); N, 0.31 (0.30). Selected IR data (cm<sup>-1</sup>): 1564 (vs), 1479 (m), 1434 (s), 1409 (vs), 1362 (m), 1306 (w), 1274 (w), 1234 (m), 1196 (w), 1149 (w), 1046 (w), 973 (w), 903 (w), 803 (w), 733 (m), 693 (s), 665 (s), 633 (s), 605 (m), 568 (w), 515 (w), 463 (w).

#### 5.4.2 X-ray Crystallography

Diffraction intensities were collected at 173 K (**15**·2MeCN, **16**·½CH<sub>2</sub>Cl<sub>2</sub>) and 218 K (**17**·H<sub>2</sub>O·HO<sub>2</sub>CPe<sup>t</sup>, **18**·2H<sub>2</sub>O), respectively, with a Bruker SMART 1000 and a Bruker P3 diffractometer equipped with a CCD area detector and a graphite monochromator utilizing MoK<sub>α</sub> radiation (λ = 0.71073 Å). Space groups were determined on the basis of systematic absences (**16**, **18**), intensity statistics (**15**), or both (**17**). Absorption corrections were applied based on measured indexed crystal faces (**15**, **16**) and by SADABS (**17**, **18**). Structures were solved by direct methods and standard Fourier techniques, and they were refined on F<sup>2</sup> using full-matrix least-squares procedures.

The MeCN molecules in **15** and the HO<sub>2</sub>CPe<sup>t</sup> group in **17** are disordered, and they were treated by the SQUEEZE<sup>96</sup> program, a part of the PLATON<sup>97</sup> package of crystallographic software; the correction of the X-ray data was 361 electron/cell and the

required value is 256 electron/cell (**17**). A common feature in each of the structures is a disorder of Me and Et groups in some bridging *t*-pentylate groups. The Me and Et groups are disordered in six groups in **15**, seven groups in **16**, and two groups in **17** and **18**. Additionally, the Me group of the MeOH ligand coordinated to Mn(12) in **15** was disordered over two positions [C(14) and C(15)], and the occupancies refined to 61:39%. The models for these disorders included refinements over two sites with correlated site occupation factors. Non-hydrogen atoms were refined anisotropically, except those of disordered groups, which were refined with isotropic thermal parameters. In **17**, all carbon atoms in the  $\text{Pe}'$  groups were refined with isotropic thermal parameters. Hydrogen atoms were placed in calculated positions and refined with a riding group model. The H atoms in some highly disordered groups, solvent water molecules and the  $\text{OH}^-$  group in **17** were not included. Restrictions for the C-C distances in ligands were used in the refinement of **17**. The non-centrosymmetric crystal of **17** was treated as a racemic twin; the Flack parameter is 0.52(2). Maximum and minimum peaks on the residual densities in **15-18** are in the range between  $1.093 \text{ e } \text{\AA}^{-3}$  and  $-0.643 \text{ e } \text{\AA}^{-3}$ .

CHAPTER 6  
SINGLE-MOLECULE MAGNETS: STRUCTURAL CHARACTERIZATION,  
MAGNETIC PROPERTIES AND  $^{19}\text{F}$  NMR SPECTROSCOPY OF A  $\text{Mn}_{12}$  FAMILY  
SPANNING THREE OXIDATION LEVELS

**6.1 Introduction**

Slow magnetization relaxation in molecules at low temperatures was first recognized in 1993 when hysteresis loops, the fundamental property of a magnet, were exhibited by single molecules of  $[\text{Mn}_{12}\text{O}_{12}(\text{O}_2\text{CMe})_{16}(\text{H}_2\text{O})_4]\cdot 2\text{MeCO}_2\text{H}\cdot 4\text{H}_2\text{O}$  (**1**).<sup>23</sup> This finding led to the birth of a new research area, whose objective includes the discovery of a single-molecule magnet (SMM) that exhibits magnetization hysteresis at technologically relevant temperatures.<sup>12,19,22,31,66,98,99,119,101-108</sup> Such a breakthrough would ultimately enable the use of molecules such as  $[\text{Mn}_{12}\text{O}_{12}(\text{O}_2\text{CR})_{16}(\text{H}_2\text{O})_4]$  complexes in a number of applications, one of the most important of these being high density information storage at the molecular level. The basis for such “molecular memory” is the storage of one bit of digital information on a single molecule.<sup>158,159</sup>

In addition to the obvious applications of these complexes in nanotechnology, there are other important fundamental properties that can be better understood through the study of SMMs. Close examination of the hysteresis loops of **1** reveals a predicted quantum phenomenon that had never before been observed – quantum tunneling of magnetization (QTM).<sup>20,27,28,61</sup> This realization has prompted an explosion of research involving single-molecule magnetism in the physics area.<sup>135,136,160</sup> Molecules of **1** are of sub-nanoscale dimensions, ~1.5 nm in diameter. Hence, they represent the point at which classical and quantum worlds meet, being macroscopic entities which display quantum

effects.<sup>27,136,159,161</sup> The presence of QTM is evidenced by step-like features that occur at regular intervals in magnetization vs DC field sweeps.<sup>27,61,65,113,162</sup> One consequence of QTM, a process by which a molecule exists as a quantum superposition of states, is that SMMs can potentially function as qubits in quantum computers.<sup>163</sup>

In recent years there has been a rapid increase in the number of molecules which behave as SMMs. Complexes of varying nuclearity, topology and peripheral ligation have been prepared through the use of various transition metals. These include V,<sup>115</sup> Co,<sup>116</sup> Ni,<sup>117</sup> Fe,<sup>95,118</sup> and particularly Mn.<sup>13,32,33,38,39,46,47,56-59,61-63,66,94,98-114</sup> However, although several new SMMs have been isolated and characterized, the temperature at which the reversal of magnetization is frozen (i.e., the blocking temperature,  $T_B$ ) is still only ~3 K, that which is exhibited by complex **1**.

The properties of a molecule that give rise to an energy barrier for magnetization reversal and hence allow it to behave as a SMM include a large ground state spin,  $S$ , and a large, negative magnetic anisotropy as gauged by the zero-field splitting parameter,  $D$ .<sup>12,19,21-23</sup> Researchers are striving to gain a thorough understanding of the structural influences of a molecule on both  $S$  and  $D$  in order to design new SMMs with increased blocking temperatures. Hence, the study of the effects of chemical and/or physical variations of a molecule is extremely useful.  $Mn_{12}$  complexes have been modified in a number of ways,<sup>13,32,33,38,39,46,47,58,61,100,101,137,138</sup> the magnetic properties measured to gauge the effect of the changes on the behavior. One of the most exciting changes made to this system was the preparation and isolation of the one-electron reduced  $Mn_{12}$  species,  $(PPh_4)[Mn_{12}O_{12}(O_2CEt)(H_2O)_4]$ .<sup>13</sup> This was shortly followed by the isolation of the two-electron reduced species,  $(PPh_4)_2[Mn_{12}O_{12}(O_2CCHCl_2)_{16}(H_2O)_4]$ .<sup>61</sup> Both complexes

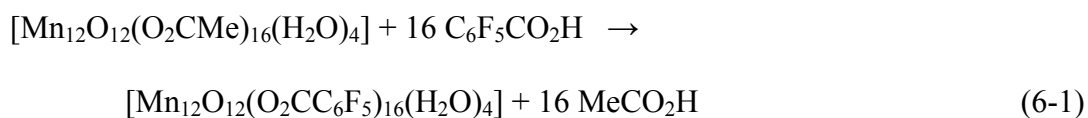
behave as SMMs, albeit at slightly lower temperatures than the neutral Mn<sub>12</sub> species. A complete study, including hysteresis measurements on single crystals, of such a family of Mn<sub>12</sub> complexes is lacking in the literature however.

We herein describe the results of this work, the syntheses, single crystal X-ray structures and magnetic properties of a family of Mn<sub>12</sub> clusters with identical peripheral ligation spanning three oxidation levels: [Mn<sub>12</sub>O<sub>12</sub>(O<sub>2</sub>CC<sub>6</sub>F<sub>5</sub>)<sub>16</sub>(H<sub>2</sub>O)<sub>4</sub>] (**20**), (NMe<sub>4</sub>)[Mn<sub>12</sub>O<sub>12</sub>(O<sub>2</sub>CC<sub>6</sub>F<sub>5</sub>)<sub>16</sub>(H<sub>2</sub>O)<sub>4</sub>] (**21**) and (NMe<sub>4</sub>)<sub>2</sub>[Mn<sub>12</sub>O<sub>12</sub>(O<sub>2</sub>CC<sub>6</sub>F<sub>5</sub>)<sub>16</sub>(H<sub>2</sub>O)<sub>4</sub>] (**22**). Low temperature magnetization measurements and AC susceptibility measurements on all three complexes show a progressive decrease in the magnetic anisotropy parameter, *D*, and hence, the effective energy barrier for magnetization reversal, *U*<sub>eff</sub>, as the Mn<sub>12</sub> complex is successively reduced. Parameters obtained from inelastic neutron scattering (INS) measurements on deuterated analogues of the complexes are in agreement with the trend.<sup>164</sup>

## 6.2 Results and Discussion

### 6.2.1 Syntheses and Electrochemistry

Employing the previously developed ligand substitution procedure, which involves the treatment of **1** with an excess of a carboxylic acid, pentafluorobenzoate ligands were introduced onto the Mn<sub>12</sub> complex.<sup>13,38</sup> The transformation of **1** into **20** is summarized in eq 6-1.



The ligand substitution reaction is an equilibrium that favors the product side when the p*K*<sub>a</sub> of the added acid is lower than that of acetic acid; the p*K*<sub>a</sub> of C<sub>6</sub>F<sub>5</sub>CO<sub>2</sub>H is 1.48<sup>37</sup> while that of MeCO<sub>2</sub>H is 4.76. A consequence of this considerable difference is that the

fully-substituted derivative can be obtained in high yield when only a slight excess of  $C_6F_5CO_2H$  is used to treat complex **1**. In addition, acetic acid removal from the reaction system under low pressure as its toluene azeotrope (28/72%; b.p. 101 °C at atmospheric pressure) guarantees complete substitution.<sup>13,38</sup>

The redox chemistry of a number of  $Mn_{12}$  derivatives has been thoroughly explored.<sup>13,61,100,113</sup> Cyclic voltammograms typically exhibit at least one quasi-reversible reduction wave and frequently a second quasi-reversible one as well. The reduction potentials are highly dependent on the electron donating or withdrawing nature of the carboxylate ligand ( $RCO_2^-$ ). The first reduction potential occurs over a wide range, from 0.00 V for  $R = C_6H_4-p-OMe$  to 0.91 V for  $R = CHCl_2$  (vs the  $Fc/Fc^+$  couple).<sup>13,61</sup> In previous reports, it was shown that with the use of stoichiometric amounts of  $I^-$  as a reducing agent ( $I^-/I_2$  couple occurs at 0.21 V in  $CH_2Cl_2$  vs  $Fc/Fc^+$ ), both the one- and two-electron reduced  $Mn_{12}$  species could be generated in bulk in  $CH_2Cl_2$ . The isolation and structural characterization of both  $(PPh_4)[Mn_{12}O_{12}(O_2CET)_{16}(H_2O)_4]$  and  $(PPh_4)_2[Mn_{12}O_{12}(O_2CCHCl_2)_{16}(H_2O)_4]$  as well as others have been described.<sup>13,61,100</sup>

The cyclic voltammogram (CV) and differential pulse voltammogram (DPV) for complex **20** are shown in Figure 6-1. Two reduction processes are displayed at 0.64 V and 0.30 V, each of which appears quasi-reversible. This reversibility was assessed on the basis of the usual electrochemical criteria, including CV peak separations, anodic/cathodic peak current ratio, DPV peak broadness, and proportionality of the peak current to the square root of the scan rate ( $v$ ). In the latter, a study of the scan rate dependence for the 0.64 V and 0.30 V reduction processes showed a linear dependence of the peak current with  $v^{1/2}$ , indicating that the reductions are diffusion-controlled

processes (Figure 6-2). As expected, the  $E_{1/2}$  values are rather positive, in accord with the strongly electron withdrawing substituents in  $C_6F_5CO_2^-$ , and both the first and second reductions are consequently within the capability of the reducing agent,  $I^-$ .

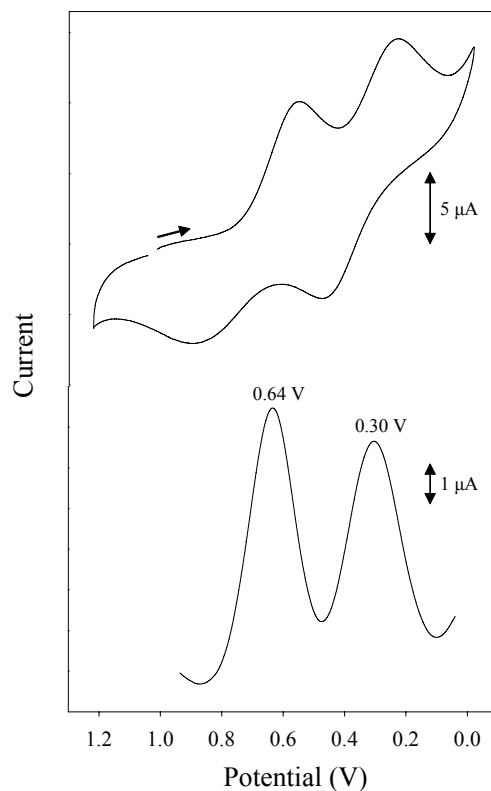


Figure 6-1. Cyclic voltammogram at  $100 \text{ mV s}^{-1}$  (top) and differential pulse voltammogram (bottom) of complex **20** in  $CH_2Cl_2$  containing  $0.1 \text{ M}$   $NBu_4PF_6$  as supporting electrolyte. The indicated potentials are vs  $Fc/Fc^+$ .

In Table 6-1 are included values of the anodic peak current / cathodic peak current ratios for the 0.64 and 0.30 V reduction waves of complex **20**. The  $i_a/i_c$  ratio of the 0.64 V reduction wave has an approximate value of nearly one over the range of scan rates, providing support of the quasi-reversible nature of the one-electron reduction process. The  $i_a/i_c$  ratio of the second reduction wave at 0.30 V is nearly constant at a value of  $\sim 0.30$  over the range of scan rates.

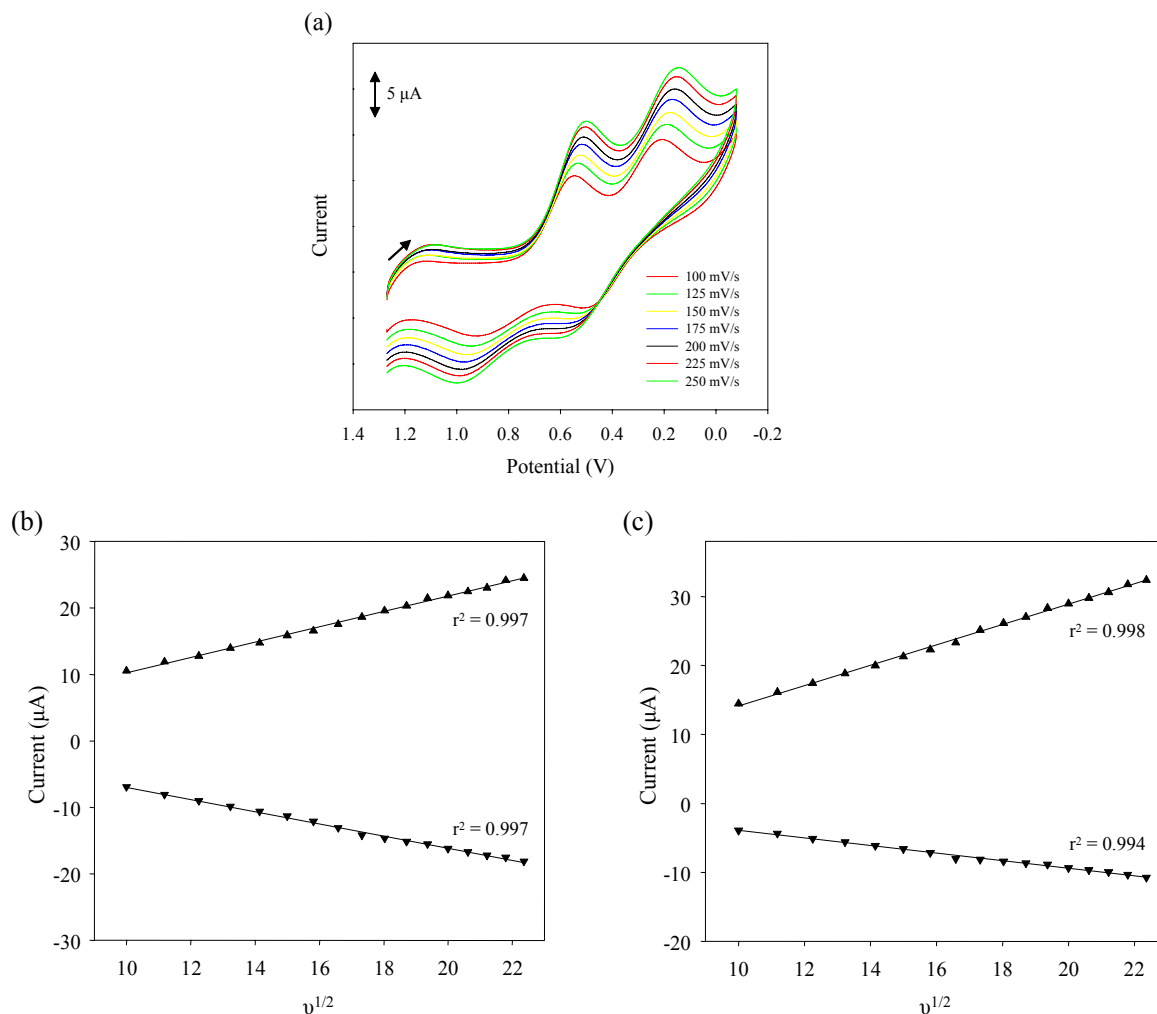


Figure 6-2. Scan rate dependence of reduction waves at 0.64 V and 0.30 V of complex **20** in  $\text{CH}_2\text{Cl}_2$  containing 0.1 M  $\text{NBu}_4^+\text{PF}_6^-$  as supporting electrolyte. (a) Cyclic voltammogram at the indicated scan rates with corresponding plot of cathodic (top) and anodic (bottom) peak current dependence vs  $v^{1/2}$  for (b) 0.64 V reduction wave and (c) 0.30 V reduction wave.

Thus,  $[\text{Mn}_{12}\text{O}_{12}(\text{O}_2\text{CC}_6\text{F}_5)_{16}(\text{H}_2\text{O})_4]$  (**20**) was treated with one and two equivalents of  $\text{NMe}_4\text{I}$  in  $\text{MeCN}$ ; the formation of  $\text{I}_2$  was confirmed by its extraction into a hexanes phase. Removal of  $\text{MeCN}$  *in vacuo* and recrystallization of the residue from  $\text{CH}_2\text{Cl}_2$  with heptane or heptane/toluene (1:1) gave black crystals of the desired one- and two-electron reduced complexes, **21** and **22** in good yield ( $\geq 70\%$ ) and analytical purity. The transformation of **20** into both **21** and **22** is summarized in eq 6-2, where  $n = 1$  or 2.

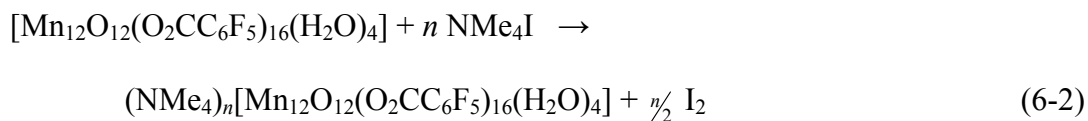


Table 6-1. Anodic peak current / cathodic peak current ratios at the indicated scan rate in  $\text{mV s}^{-1}$  for the 0.64 V and 0.30 V reduction waves of complex **20**.

0.64 V Reduction Wave		0.30 V Reduction Wave	
Scan Rate ( $\text{mV s}^{-1}$ )	$i_a/i_c$	Scan Rate ( $\text{mV s}^{-1}$ )	$i_a/i_c$
100	-0.66	100	-0.27
125	-0.68	125	-0.27
150	-0.71	150	-0.29
175	-0.71	175	-0.30
200	-0.72	200	-0.31
225	-0.71	225	-0.31
250	-0.74	250	-0.32
275	-0.75	275	-0.34
300	-0.76	300	-0.32
325	-0.75	325	-0.32
350	-0.75	350	-0.32
375	-0.72	375	-0.31
400	-0.74	400	-0.32
425	-0.74	425	-0.32
450	-0.74	450	-0.32
475	-0.72	475	-0.33
500	-0.74	500	-0.33

## 6.2.2 Description of Structures

### 6.2.2.1 X-ray crystal structure of $[\text{Mn}_{12}\text{O}_{12}(\text{O}_2\text{CC}_6\text{F}_5)_{16}(\text{H}_2\text{O})_4]$ (**20**)

Labeled ORTEP<sup>40</sup> plots in PovRay format of complexes **20**, **21**, and **22** are presented in Figures 6-3, 6-4 and 6-6, together with stereoviews. The crystallographic data and structure refinement details are collected in Table 6-2, and selected interatomic distances and angles are listed in Tables A-13, A-14 and A-15, respectively.

Complex **20**·3CH<sub>2</sub>Cl<sub>2</sub> crystallizes in the triclinic space group  $P\bar{1}$  (Figure 6-3). The structure consists of a central  $[\text{Mn}^{\text{IV}}_4\text{O}_4]$  cubane core that is surrounded by a non-planar ring of eight Mn<sup>III</sup> ions that are bridged and connected to the cubane by eight  $\mu_3\text{-O}^{2-}$  ions. The eight Mn<sup>III</sup> ions separate into two groups of four Mn<sup>III</sup> ions each. In the first group,

each Mn<sup>III</sup> ion is coordinated to a single Mn<sup>IV</sup> ion via two oxide bridges [Mn(1), Mn(4), Mn(5), Mn(8)], while in the second group each Mn<sup>III</sup> ion is coordinated to two Mn<sup>IV</sup> ions via two oxide bridges [Mn(9), Mn(10), Mn(11), Mn(12)].<sup>29</sup> Peripheral ligation is provided by sixteen bridging C<sub>6</sub>F<sub>5</sub>CO<sub>2</sub><sup>-</sup> ligands and four terminal H<sub>2</sub>O molecules [O(33), O(36), O(41), O(44)], which are bound in a 2:2 fashion to two *trans* Mn<sup>III</sup> ions, Mn(9) and Mn(12), respectively (Figure 6-3). This disposition of two pairs of H<sub>2</sub>O ligands has also been observed for [Mn<sub>12</sub>O<sub>12</sub>(O<sub>2</sub>CPh)<sub>16</sub>(H<sub>2</sub>O)<sub>4</sub>], [Mn<sub>12</sub>O<sub>12</sub>(O<sub>2</sub>CC<sub>6</sub>H<sub>4</sub>-*p*-Cl)<sub>16</sub>(H<sub>2</sub>O)<sub>4</sub>], [Mn<sub>12</sub>O<sub>12</sub>(O<sub>2</sub>CMe)<sub>8</sub>(O<sub>3</sub>SPh)<sub>8</sub>(H<sub>2</sub>O)<sub>4</sub>] and others.<sup>20,29,39</sup>

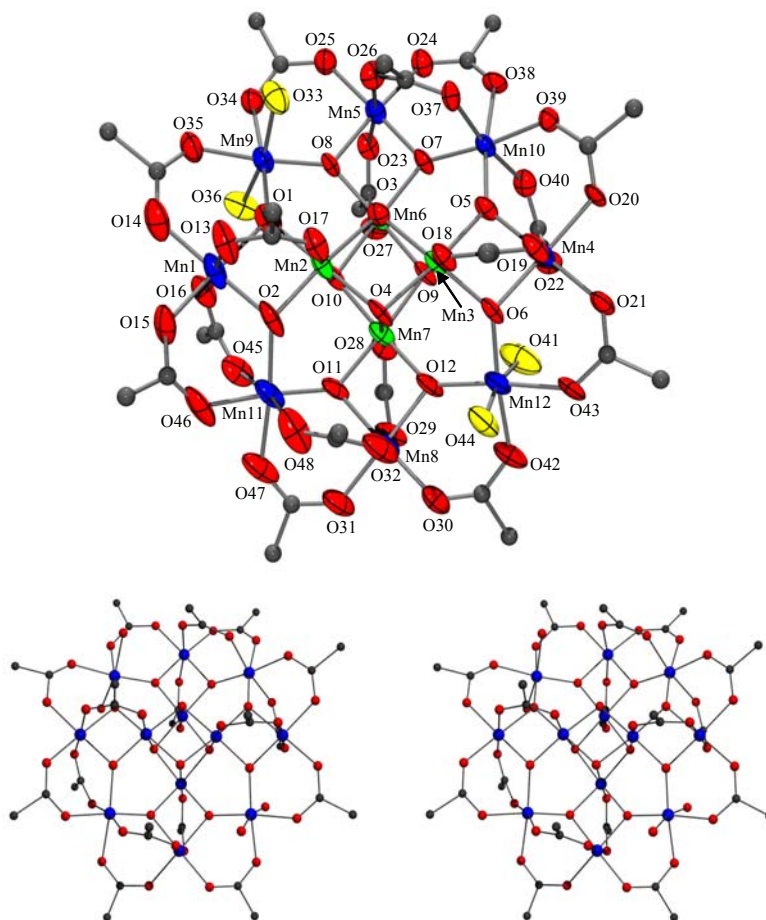


Figure 6-3. ORTEP representation in PovRay format of [Mn<sub>12</sub>O<sub>12</sub>(O<sub>2</sub>CC<sub>6</sub>F<sub>5</sub>)<sub>16</sub>(H<sub>2</sub>O)<sub>4</sub>] (**20**) with thermal ellipsoids at the 50% probability level except for the C atoms, together with a stereopair. For clarity, only the *ipso* C atoms of the pentafluorobenzoate groups are shown. Mn<sup>IV</sup> green; Mn<sup>III</sup> blue; O red; H<sub>2</sub>O yellow; C gray.

All of the Mn centers are six-coordinate, with near-octahedral geometry. Assignment of the oxidation states of the metal centers was done qualitatively by charge consideration and also by comparison of the bond distances around the Mn centers. These assignments were confirmed quantitatively by bond valence sum (BVS) calculations,<sup>41</sup> indicating that Mn(2), Mn(3), Mn(6) and Mn(7) are Mn<sup>IV</sup> while the remaining Mn centers are Mn<sup>III</sup> (Table 6-3). The protonation levels of the inorganic O atoms were confirmed by a similar BVS calculation and are collected in Table 6-4. The structure of **20** is very similar to other previously characterized neutral Mn<sub>12</sub> complexes. The eight Mn<sup>III</sup> centers exhibit a Jahn-Teller (JT) distortion, as expected for a high-spin d<sup>4</sup> ion in near-octahedral geometry. As is almost always the case for Mn<sup>III</sup> ions, the JT distortion takes the form of an axial elongation of two *trans* bonds, typically lengthening bond distances by 0.1-0.2 Å. The JT elongation axes avoid the Mn-O<sup>2-</sup> bonds, the shortest and strongest in the molecule, and thus the JT axes are all axially disposed, roughly perpendicular to the [Mn<sub>12</sub>O<sub>12</sub>] disk-like core. As a result, there is a near parallel alignment of the eight Mn<sup>III</sup> JT elongation axes. This is also the origin of the significant magnetic anisotropy in the *z* direction that greatly influences the observed magnetic properties (*vide infra*).

Table 6-2. Crystallographic data for  $[\text{Mn}_{12}\text{O}_{12}(\text{O}_2\text{CC}_6\text{F}_5)_{16}(\text{H}_2\text{O})_4] \cdot 3\text{CH}_2\text{Cl}_2$ ,  $(\text{NMe}_4)[\text{Mn}_{12}\text{O}_{12}(\text{O}_2\text{CC}_6\text{F}_5)_{16}(\text{H}_2\text{O})_4] \cdot 4.5\text{CH}_2\text{Cl}_2 \cdot \frac{1}{2}\text{H}_2\text{O}$ , and  $(\text{NMe}_4)_2[\text{Mn}_{12}\text{O}_{12}(\text{O}_2\text{CC}_6\text{F}_5)_{16}(\text{H}_2\text{O})_4] \cdot 6\text{C}_7\text{H}_8$ .

Parameter	$[\text{Mn}_{12}]$ ( <b>20</b> )	$[\text{Mn}_{12}]^{1-}$ ( <b>21</b> )	$[\text{Mn}_{12}]^{2-}$ ( <b>22</b> )
formula <sup>a</sup>	$\text{C}_{115}\text{H}_{14}\text{Cl}_6\text{Mn}_{12}\text{F}_{80}\text{O}_{48}$	$\text{C}_{120.5}\text{H}_{30}\text{Cl}_9\text{Mn}_{12}\text{N}_1\text{F}_{80}\text{O}_{48.5}$	$\text{C}_{162}\text{H}_{80}\text{Mn}_{12}\text{N}_2\text{F}_{80}\text{O}_{48}$
fw, g mol <sup>-1</sup>	4555.19	4765.74	5001.53
space group	$P\bar{1}$	$P2/c$	$C2/c$
<i>a</i> , Å	18.519(4)	33.6633(2)	21.7892(15)
<i>b</i> , Å	18.895(4)	17.3311(9)	27.0937(19)
<i>c</i> , Å	26.169(5)	27.2564(2)	31.623(2)
$\alpha$ , deg	70.073(2)	90	90
$\beta$ , deg	72.616(2)	94.2090(2)	91.640(2)
$\gamma$ , deg	73.364(3)	90	90
<i>V</i> , Å <sup>3</sup>	8040(3)	15859.1(2)	18661(2)
<i>Z</i>	2	4	4
<i>T</i> , °C	-80(2)	-80(2)	-100(2)
radiation, Å <sup>b</sup>	0.71073	0.71073	0.71073
$\rho_{\text{calc}}$ , g cm <sup>-3</sup>	1.882	1.996	1.780
$\mu$ , cm <sup>-1</sup>	11.77	12.48	9.40
<i>R1</i> ( <i>wR2</i> ), % <sup>c,d</sup>	8.80 (21.79)	5.34 (13.25)	5.81 (14.31)

<sup>a</sup> Including solvent molecules. <sup>b</sup> Graphite monochromator. <sup>c</sup>  $R1 = \sum||F_o| - |F_c|| / \sum|F_o|$ . <sup>d</sup>  $wR2 = [\sum[w(F_o^2 - F_c^2)^2] / \sum[wF_o^2]]^{1/2}$  where  $S = [\sum[w(F_o^2 - F_c^2)^2] / (n-p)]^{1/2}$ ,  $w = 1/[\sigma^2(F_o^2) + (m^*p)^2 + n^*p]$ ,  $p = [\max(F_o^2, 0) + 2^*F_c^2]/3$ , and *m* and *n* are constants.

Table 6-3. Bond valence sum calculations<sup>a</sup> for complexes **20**·3CH<sub>2</sub>Cl<sub>2</sub>, **21**·4.5CH<sub>2</sub>Cl<sub>2</sub>·½H<sub>2</sub>O, and **22**·6C<sub>7</sub>H<sub>8</sub>.

Atom	<b>20</b> ·3CH <sub>2</sub> Cl <sub>2</sub>			<b>21</b> ·4.5CH <sub>2</sub> Cl <sub>2</sub> ·½H <sub>2</sub> O			<b>22</b> ·6C <sub>7</sub> H <sub>8</sub>		
	Mn <sup>2+</sup>	Mn <sup>3+</sup>	Mn <sup>4+</sup>	Mn <sup>2+</sup>	Mn <sup>3+</sup>	Mn <sup>4+</sup>	Mn <sup>2+</sup>	Mn <sup>3+</sup>	Mn <sup>4+</sup>
Mn(1)	3.265	<u>2.987</u>	3.136	4.193	3.835	<u>4.026</u>	4.187	3.830	<u>4.021</u>
Mn(2)	4.189	3.832	<u>4.023</u>	4.126	3.774	<u>3.962</u>	4.184	3.827	<u>4.018</u>
Mn(3)	4.126	3.774	<u>3.962</u>	4.128	3.776	<u>3.964</u>	3.299	<u>3.018</u>	3.168
Mn(4)	3.304	<u>3.022</u>	3.173	4.121	3.770	<u>3.957</u>	3.284	<u>3.004</u>	3.153
Mn(5)	3.343	<u>3.058</u>	3.210	3.297	<u>3.007</u>	3.157	3.262	<u>2.984</u>	3.133
Mn(6)	4.172	3.816	<u>4.006</u>	3.268	<u>2.989</u>	3.138	<u>2.101</u>	1.922	2.017
Mn(7)	4.239	3.878	<u>4.071</u>	3.264	<u>2.985</u>	3.134			
Mn(8)	3.248	<u>2.971</u>	3.119	<u>2.121</u>	1.940	2.036			
Mn(9)	3.289	<u>3.008</u>	3.158	3.296	<u>3.015</u>	3.166			
Mn(10)	3.278	<u>2.998</u>	3.148	3.297	<u>3.016</u>	3.166			
Mn(11)	3.333	<u>3.039</u>	3.201	3.252	<u>2.974</u>	3.122			
Mn(12)	3.259	<u>2.981</u>	3.130	3.265	<u>2.987</u>	3.135			

<sup>a</sup> The underlined value is the one closest to the actual charge for which it was calculated. The oxidation state of a particular atom can be taken as the nearest whole number to the underlined value.

Table 6-4. Bond valence sum calculations<sup>a</sup> for selected oxygen atoms in complexes **20**·3CH<sub>2</sub>Cl<sub>2</sub>, **21**·4.5CH<sub>2</sub>Cl<sub>2</sub>·½H<sub>2</sub>O, and **22**·6C<sub>7</sub>H<sub>8</sub>.

Atom	<b>20</b> ·3CH <sub>2</sub> Cl <sub>2</sub>			<b>21</b> ·4.5CH <sub>2</sub> Cl <sub>2</sub> ·½H <sub>2</sub> O			<b>22</b> ·6C <sub>7</sub> H <sub>8</sub>		
	$V_i$	Assignment		Atom	$V_i$	Assignment	Atom	$V_i$	Assignment
O(1)	2.135	O <sup>2-</sup>		O(1)	O <sup>2-</sup>	2.027	O(1)	1.994	O <sup>2-</sup>
O(2)	2.042	O <sup>2-</sup>		O(2)	O <sup>2-</sup>	1.980	O(2)	2.007	O <sup>2-</sup>
O(3)	1.995	O <sup>2-</sup>		O(3)	O <sup>2-</sup>	1.987	O(3)	2.141	O <sup>2-</sup>
O(4)	2.053	O <sup>2-</sup>		O(4)	O <sup>2-</sup>	2.030	O(4)	2.001	O <sup>2-</sup>
O(5)	2.156	O <sup>2-</sup>		O(5)	O <sup>2-</sup>	2.192	O(6)	2.139	O <sup>2-</sup>
O(6)	2.128	O <sup>2-</sup>		O(6)	O <sup>2-</sup>	2.081	O(7)	2.102	O <sup>2-</sup>
O(7)	2.109	O <sup>2-</sup>		O(7)	O <sup>2-</sup>	2.142	O(20)	0.308	H <sub>2</sub> O
O(8)	2.168	O <sup>2-</sup>		O(8)	O <sup>2-</sup>	1.979	O(23)	0.264	H <sub>2</sub> O
O(9)	2.057	O <sup>2-</sup>		O(9)	O <sup>2-</sup>	2.123			
O(10)	2.042	O <sup>2-</sup>		O(10)	O <sup>2-</sup>	2.142			
O(11)	2.141	O <sup>2-</sup>		O(11)	O <sup>2-</sup>	2.138			
O(12)	2.199	O <sup>2-</sup>		O(12)	O <sup>2-</sup>	2.081			
O(33)	0.293	H <sub>2</sub> O		O(17)	H <sub>2</sub> O	0.323			
O(36)	0.327	H <sub>2</sub> O		O(46)	H <sub>2</sub> O	0.341			
O(41)	0.293	H <sub>2</sub> O		O(47)	H <sub>2</sub> O	0.296			
O(44)	0.301	H <sub>2</sub> O		O(48)	H <sub>2</sub> O	0.286			

<sup>a</sup> The oxygen atoms is O<sup>2-</sup> if  $V_i \approx 2$ , OH<sup>-</sup> if  $V_i \approx 1$ , and H<sub>2</sub>O if  $V_i \approx 0$ .

The JT elongation axis of Mn(11) is not clearly defined, however. The axial bonds, Mn(11)-O(45) = 2.015(8) Å and Mn(11)-O(48) = 2.010(9), are slightly shorter than is typical for an axially-elongated JT bond of a Mn<sup>III</sup> ion. In addition, the equatorial bonds, Mn(11)-O(47) = 2.053(10) and Mn(11)-O(2) = 1.978(8), are slightly longer than is typical for a Mn<sup>III</sup>-O<sub>eq</sub> and Mn<sup>III</sup>-O<sup>2-</sup> bond, respectively, in a Mn<sub>12</sub> complex (Table 6-5). These abnormal distances around Mn(11) suggest a static disorder between a normal, axially disposed JT elongation axis and one abnormally-oriented in the plane of the molecule. We have previously called such molecules (differing only in the orientation of one or more JT axes) Jahn-Teller isomers.<sup>56-59</sup> Examples include [Mn<sub>12</sub>O<sub>12</sub>(O<sub>2</sub>CCH<sub>2</sub>Bu<sup>t</sup>)<sub>16</sub>(H<sub>2</sub>O)<sub>4</sub>],<sup>56</sup> [Mn<sub>12</sub>O<sub>12</sub>(O<sub>2</sub>CC<sub>6</sub>H<sub>4</sub>-*p*-Me)<sub>16</sub>(H<sub>2</sub>O)<sub>4</sub>]<sup>57</sup> and [Mn<sub>12</sub>O<sub>12</sub>(O<sub>2</sub>CCF<sub>3</sub>)<sub>16</sub>(H<sub>2</sub>O)<sub>4</sub>].<sup>59</sup>

Table 6-5. Interatomic distances (Å) of Mn(11) in complex **20**.

Bond	Distance	Type <sup>a</sup>
Mn(11)-O(11)	1.884(7)	O <sub>r</sub>
Mn(11)-O(2)	1.978(8)	O <sub>r</sub>
Mn(11)-O(46)	1.978(10)	O <sub>eq</sub>
Mn(11)-O(47)	2.053(10)	O <sub>eq</sub>
Mn(11)-O(48)	2.010(9)	O <sub>ax</sub>
Mn(11)-O(45)	2.015(8)	O <sub>ax</sub>

<sup>a</sup> O<sub>r</sub> = ring O<sup>2-</sup>, O<sub>ax</sub> = axial carboxylate, O<sub>eq</sub> = equatorial carboxylate

#### 6.2.2.2 X-ray crystal structure of (NMe<sub>4</sub>)[Mn<sub>12</sub>O<sub>12</sub>(O<sub>2</sub>CC<sub>6</sub>F<sub>5</sub>)<sub>16</sub>(H<sub>2</sub>O)<sub>4</sub>] (**21**)

Complex **21**·4.5CH<sub>2</sub>Cl<sub>2</sub>·½H<sub>2</sub>O crystallizes in the monoclinic space group *P2/c*. The anion consists again of a central [Mn<sup>IV</sup><sub>4</sub>O<sub>4</sub>] cubane surrounded by a non-planar ring of eight Mn atoms bridged by eight μ<sub>3</sub>-O<sup>2-</sup> ions, sixteen bridging C<sub>6</sub>F<sub>5</sub>CO<sub>2</sub><sup>-</sup> ligands and four terminal H<sub>2</sub>O molecules (Figure 6-4). Examination of the Mn-O bond lengths unequivocally establishes that the added electron has converted a formerly Mn<sup>III</sup> atom to a Mn<sup>II</sup> ion [Mn(8)]. JT axial elongations are observed at the other seven ring Mn atoms,

as expected for a high-spin  $d^4$  ion in near-octahedral geometry. All of the JT elongation axes are approximately perpendicular to the plane of the molecule. The Mn oxidation levels were determined by a BVS<sup>41</sup> calculation (Table 6-3 and 6-4). Therefore, the  $[\text{Mn}_{12}]^-$  anion is a trapped-valence  $\text{Mn}^{\text{II}}$ ,  $\text{Mn}_7^{\text{III}}$ ,  $\text{Mn}_4^{\text{IV}}$  cluster.

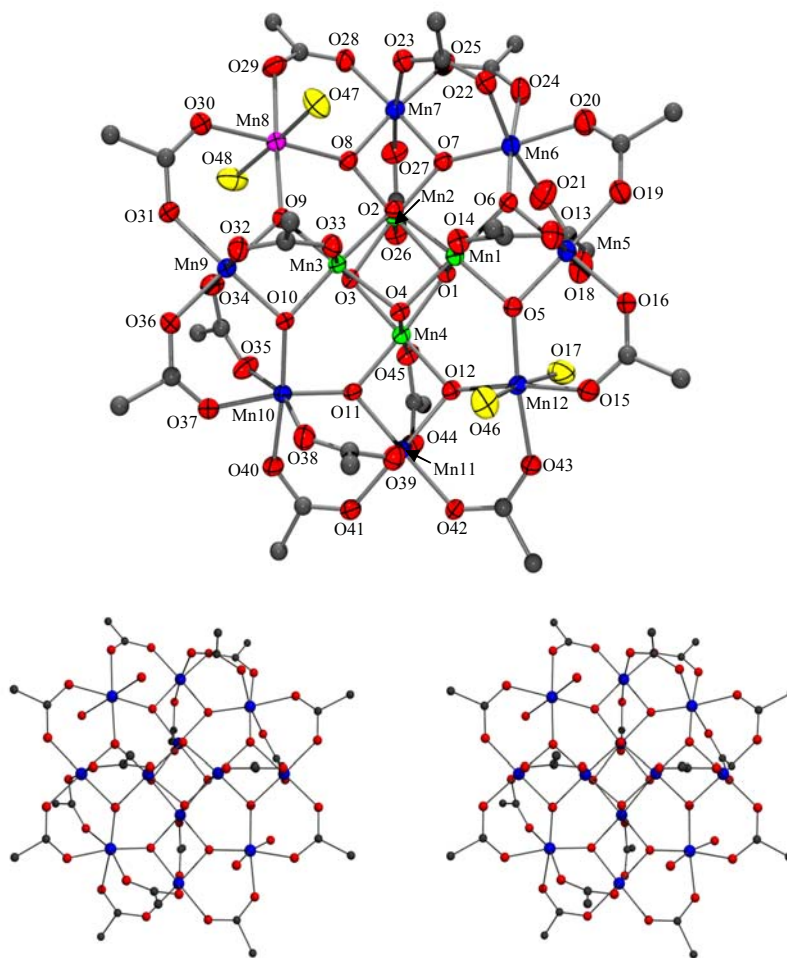


Figure 6-4. ORTEP representation in PovRay format of the anion of  $(\text{NMe}_4)[\text{Mn}_{12}\text{O}_{12}(\text{O}_2\text{CC}_6\text{F}_5)_{16}(\text{H}_2\text{O})_4]$  (**21**) with thermal ellipsoids at the 50% probability level except for the C atoms, together with a stereopair. For clarity, only the *ipso* C atoms of the pentafluorobenzoate groups are shown.  $\text{Mn}^{\text{IV}}$  green;  $\text{Mn}^{\text{III}}$  blue;  $\text{Mn}^{\text{II}}$  purple; O red;  $\text{H}_2\text{O}$  yellow; C gray.

A static disorder between one carboxylate group and an adjacent water molecule is observed in the crystal structure of **21**. Hence, the structure is a mixture of two isomers, the 2:2 form (77%) and the 1:1:2 form (23%), the notation describing the distribution of

the four H<sub>2</sub>O molecules among the Mn ions. Figure 6-4 shows the form with 77% occupancy, where the carboxylate is bridging Mn(6) and Mn(5) [O(21)-C(64)-O(18)] and the water molecule [O(17)] is coordinated to Mn(12). The minor form has the carboxylate bridging Mn(12) and Mn(5) [O(17)-C(57)-O(18)] and the water molecule [O(21)] coordinated to Mn(6).

The [Mn<sub>12</sub>]<sup>-</sup> molecules are stacked in columns with all of the molecules oriented in the same way with respect to the cell axes. There is a  $\pi$ -stacking interaction of the pentafluorophenyl rings bridging Mn(5) and Mn(6) between [Mn<sub>12</sub>]<sup>-</sup> anions in adjacent columns along the  $\bar{1}01$  direction of the cell as shown in Figure 6-5 as dashed lines. The dihedral angle between the rings is 1° and the ring separation is ~3.5 Å.

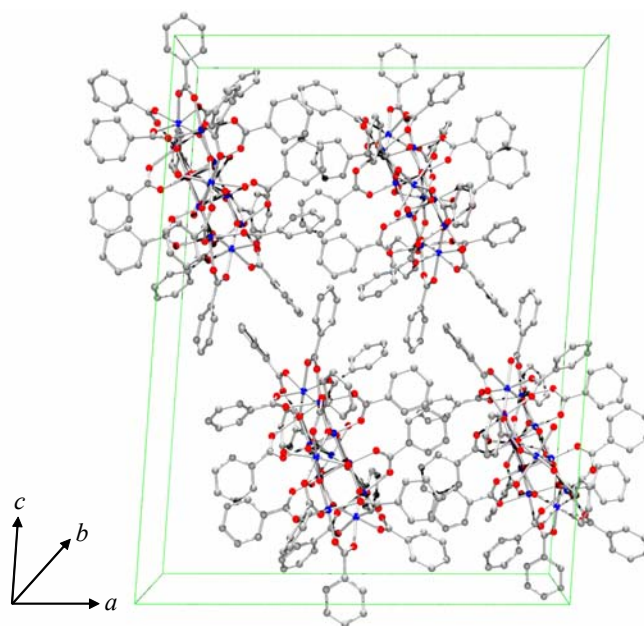


Figure 6-5. Packing diagram for **21**, emphasizing intermolecular  $\pi$ -stacking of carboxylate aromatic rings (dashed lines).

### 6.2.2.3 X-ray crystal structure of (NMe<sub>4</sub>)<sub>2</sub>[Mn<sub>12</sub>O<sub>12</sub>(O<sub>2</sub>CC<sub>6</sub>F<sub>5</sub>)<sub>16</sub>(H<sub>2</sub>O)<sub>4</sub>] (**22**)

Complex **22**·6C<sub>7</sub>H<sub>8</sub> crystallizes in the monoclinic space group *C2/c* (Figure 6-6).

The [Mn<sub>12</sub>]<sup>2-</sup> cluster is located on a crystallographic *C*<sub>2</sub> rotation axis perpendicular to the

plane of the molecule and passing through the central cubane unit. The anion again consists of a central  $[\text{Mn}^{\text{IV}}_4\text{O}_4]$  cubane surrounded by a non-planar ring of eight Mn atoms bridged by eight  $\mu_3\text{-O}^{2-}$  ions, sixteen bridging  $\text{C}_6\text{F}_5\text{CO}_2^-$  ligands and four terminal  $\text{H}_2\text{O}$  molecules, which are bound in a 2:2 fashion to two *trans* Mn atoms, Mn(6) and Mn(6a), respectively.

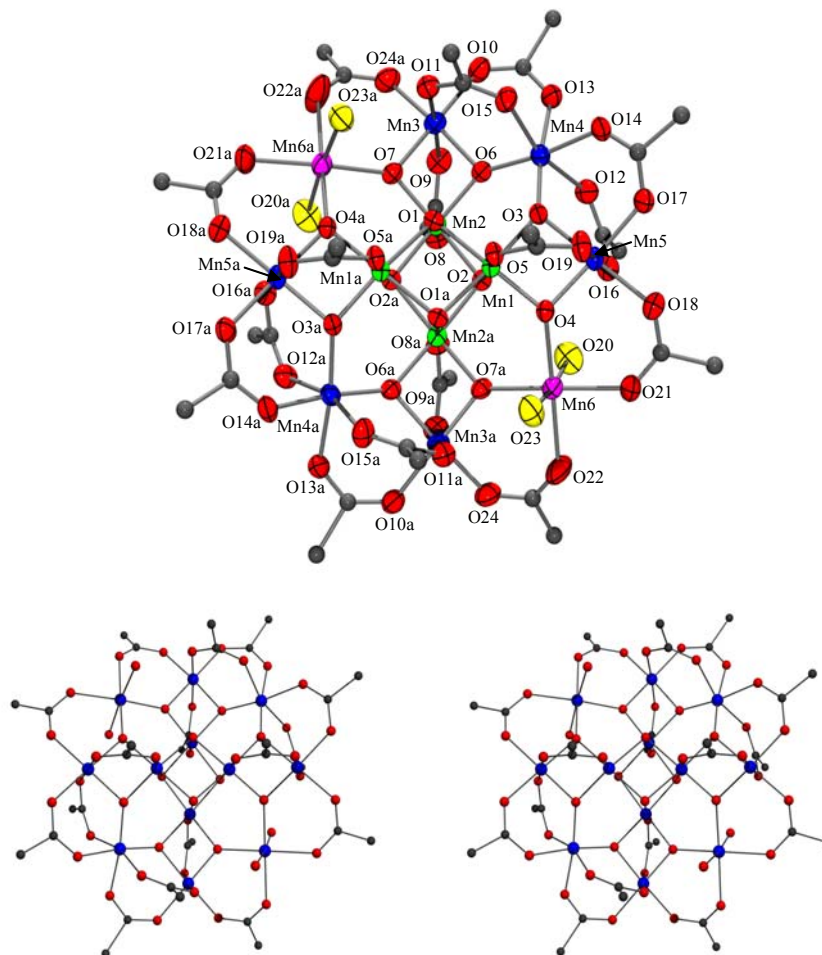


Figure 6-6. ORTEP representation in PovRay format of the anion of  $(\text{NMe}_4)_2[\text{Mn}_{12}\text{O}_{12}(\text{O}_2\text{CC}_6\text{F}_5)_{16}(\text{H}_2\text{O})_4]$  (**22**) with thermal ellipsoids at the 50% probability level except for the C atoms, together with a stereopair. For clarity, only the *ipso* C atoms of the pentafluorobenzoate groups are shown.  $\text{Mn}^{\text{IV}}$  green;  $\text{Mn}^{\text{III}}$  blue;  $\text{Mn}^{\text{II}}$  purple; O red;  $\text{H}_2\text{O}$  yellow; C gray.

Analysis of the Mn-O bond lengths again establishes that the central cubane Mn atoms are  $\text{Mn}^{\text{IV}}$  ions, and that the added electrons have gone one each on two formerly

Mn<sup>III</sup> atoms converting them to Mn<sup>II</sup> ions [Mn(6) and Mn(6a)], to which the water molecules are coordinated. The distances around Mn(6) and Mn(6a) are typical of Mn<sup>II</sup> ions in near-octahedral geometry. The other six outer ring Mn atoms display bond distances and JT axial elongations typical of Mn<sup>III</sup>. All JT elongation axes are perpendicular to the plane of the molecule. The Mn oxidation levels were confirmed by a BVS<sup>41</sup> calculation (Table 6-3 and 6-4). Thus, the [Mn<sub>12</sub>]<sup>2-</sup> anion is a trapped-valence Mn<sub>2</sub><sup>II</sup>, Mn<sub>6</sub><sup>III</sup>, Mn<sub>4</sub><sup>IV</sup> species.

Table 6-6 shows a comparison of average Mn-O bond distances for the three [Mn<sub>12</sub>O<sub>12</sub>(O<sub>2</sub>CC<sub>6</sub>F<sub>5</sub>)<sub>16</sub>(H<sub>2</sub>O)<sub>4</sub>]<sup>z-</sup> [*z* = 0 (**20**), 1- (**21**) and 2- (**22**)] complexes. This comparison confirms that the bond distances in the [Mn<sub>12</sub>O<sub>12</sub>] cores are almost superimposable except for those positions that involve Mn<sup>II</sup> ions being compared with Mn<sup>III</sup> ions.

### 6.2.3 <sup>19</sup>F Nuclear Magnetic Resonance Spectroscopy

In order to assess the structures and stability of the complexes in solution, a <sup>19</sup>F NMR spectroscopic investigation of complexes **20**, **21** and **22** in CD<sub>2</sub>Cl<sub>2</sub> was carried out. Chemical shifts and *T*<sub>1</sub> times for **20-22** are listed in Table 6-7. <sup>1</sup>H NMR spectroscopy has proven in the past to be a convenient tool for the study of Mn<sub>12</sub> complexes, and the use of <sup>19</sup>F NMR spectroscopy in the present work is a useful complement, providing a rare example of this type of NMR spectroscopy on a paramagnetic system. The <sup>19</sup>F NMR spectrum of complex **20** in CD<sub>2</sub>Cl<sub>2</sub> in Figure 6-7 (bottom) shows eight resonances with a 4:2:2:1:2:1:2:4 integration ratio. As with other Mn<sub>12</sub> derivatives, there are only three distinct types of bridging carboxylates in the NMR spectrum: (i) four axial ligands bridging Mn<sup>III</sup>...Mn<sup>IV</sup> pairs, (ii) four axial ligands bridging Mn<sup>III</sup>...Mn<sup>III</sup> pairs, and (iii) eight equatorial ligands bridging Mn<sup>III</sup>...Mn<sup>III</sup> pairs.

Table 6-6. Selected interatomic distances (Å) and angles (°) for [Mn<sub>12</sub>O<sub>12</sub>(O<sub>2</sub>CC<sub>6</sub>F<sub>5</sub>)<sub>16</sub>(H<sub>2</sub>O)<sub>4</sub>] (**20**), (NMe<sub>4</sub>)[Mn<sub>12</sub>O<sub>12</sub>(O<sub>2</sub>CC<sub>6</sub>F<sub>5</sub>)<sub>16</sub>(H<sub>2</sub>O)<sub>4</sub>] (**21**), and (NMe<sub>4</sub>)<sub>2</sub>[Mn<sub>12</sub>O<sub>12</sub>(O<sub>2</sub>CC<sub>6</sub>F<sub>5</sub>)<sub>16</sub>(H<sub>2</sub>O)<sub>4</sub>] (**22**).

Parameter <sup>a</sup>	<b>20</b>	<b>21</b>	<b>22</b>
Mn <sup>IV</sup> – O <sub>c</sub> (ax)	1.898(6) – 1.906(6)	1.874(3) – 1.915(3)	1.889(3) – 1.893(3)
Mn <sup>IV</sup> – O <sub>c</sub> (eq)	1.895(7) – 1.927(6)	1.905(3) – 1.967(3)	1.921(4) – 1.945(4)
Mn <sup>IV</sup> – O <sub>r</sub>	1.850(7) – 1.894(6)	1.818(3) – 1.903(3)	1.830(4) – 1.877(4)
Mn <sup>IV</sup> – O <sub>ax</sub>	1.914(7) – 1.931(6)	1.924(3) – 1.951(3)	1.940(4) – 1.947(3)
Mn <sup>IIIb</sup> – O <sub>r</sub>	1.874(7) – 1.915(7)	1.842(3) – 1.919(3)	1.841(4) – 1.904(4)
Mn <sup>IIIc</sup> – O <sub>r</sub>	1.865(6) – 1.903(6)	1.860(3) – 1.915(3)	1.878(4) – 1.882(4)
Mn <sup>IIIb</sup> – O <sub>eq</sub>	1.909(8) – 1.960(6)	1.919(3) – 1.981(3)	1.944(5) – 1.980(4)
Mn <sup>IIIc</sup> – O <sub>eq</sub>	1.956(6) – 1.978(7)	1.947(3) – 2.031(4)	1.967(4) – 1.979(4)
Mn <sup>IIIb</sup> – O <sub>ax</sub>	2.161(7) – 2.244(10)	2.164(3) – 2.236(4)	2.171(4) – 2.268(4)
Mn <sup>IIIc</sup> – O <sub>ax</sub>	2.148(7) – 2.162(8)	2.069(4) – 2.163(3)	2.151(4) – 2.180(4)
Mn <sup>IIIc</sup> – O <sub>w</sub>	2.168(7) – 2.212(7)	2.207(4) – 2.221(4)	—————
Mn <sup>II d</sup> – O <sub>r</sub>	—————	2.080(3) – 2.153(3)	2.075(4) – 2.117(4)
Mn <sup>II d</sup> – O <sub>eq</sub>	—————	2.135(3) – 2.164(3)	2.126(5) – 2.139(5)
Mn <sup>II d</sup> – O <sub>ax</sub>	—————	—————	—————
Mn <sup>II d</sup> – O <sub>w</sub>	—————	2.179(4) – 2.200(4)	2.219(4) – 2.281(4)
O <sub>r</sub> – Mn <sup>IV</sup> – O <sub>r</sub>	83.9(3) – 84.8(3)	83.36(13) – 84.46(13)	84.07(16) – 84.26(16)
O <sub>r</sub> – Mn <sup>IIIb</sup> – O <sub>r</sub>	82.3(3) – 83.4(3)	82.53(13) – 83.91(13)	82.49(15) – 83.09(16)
O <sub>r</sub> – Mn <sup>IIIc</sup> – O <sub>r</sub>	91.7(3) – 95.1(3)	93.64(13) – 95.31(13)	93.88(15)
O <sub>r</sub> – Mn <sup>II d</sup> – O <sub>r</sub>	—————	88.63(12)	93.37(14)

<sup>a</sup> O<sub>c</sub> = cubane O<sup>2-</sup>, O<sub>r</sub> = ring O<sup>2-</sup>, O<sub>ax</sub> = axial carboxylate, O<sub>eq</sub> = equatorial carboxylate, O<sub>w</sub> = water; <sup>b</sup> Mn<sup>IIIb</sup> atoms: Mn(1, 4, 5 and 8) in **20**, Mn(5, 7, 9 and 11) in **21**, and Mn(3 and 5) in **22**; <sup>c</sup> Mn<sup>IIIc</sup> atoms: Mn(9, 10, 11 and 12) in **20**, Mn(6, 10 and 12) in **21**, and Mn(4) in **22**; <sup>d</sup> Mn<sup>II</sup> atoms: Mn(8) in **21**, and Mn(6) in **22**. Distances around Mn(11) in complex **20** are not considered because of disorder in the structure.

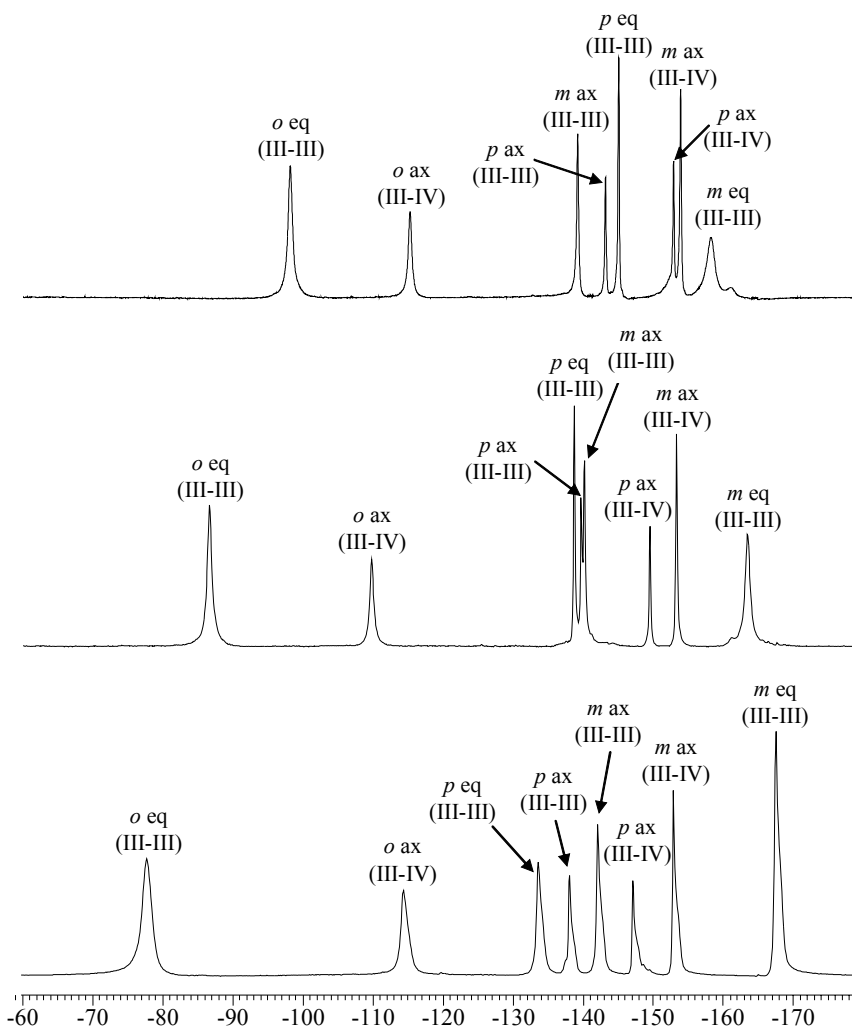


Figure 6-7.  $^{19}\text{F}$  NMR (282 MHz) spectra at  $\sim 23^\circ\text{C}$  in  $\text{CD}_2\text{Cl}_2$  of **20** (bottom), **21** (middle) and **22** (top).

Solution studies of  $\text{Mn}_{12}$  molecules at room temperature have shown that there is a fluxional process that is fast on the NMR timescale that rapidly exchanges the water ligands with one type of axial carboxylate ligand,<sup>32,165</sup> the one that has both its O atoms located on the JT elongation axes of the  $\text{Mn}^{\text{III}}\cdots\text{Mn}^{\text{III}}$  pairs. This introduces dihedral mirror planes, which make all of the equatorial carboxylate groups equivalent. In effect, the solution state symmetry of a  $\text{Mn}_{12}$  molecule is  $D_{2d}$ , giving three resonances in a 1:1:2 relative integration ratio (axial:axial:equatorial). Hence, **20** should exhibit three resonances each for the *o*-, *m*- and *p*- positions of the three types of ligands, giving a total

of nine signals. Only eight are observed however; the *o*- resonance of the axial ligands bridging Mn<sup>III</sup>...Mn<sup>III</sup> pairs cannot be clearly located, and we have concluded that it is probably too paramagnetically broadened to be observed. The resonances in the <sup>19</sup>F NMR spectra of **20-22** are shown in Figure 6-7. The spectra are all very similar, exhibiting eight signals each with only minor shifts of the resonances.

Table 6-7. Solution <sup>19</sup>F NMR spectral data for [Mn<sub>12</sub>O<sub>12</sub>(O<sub>2</sub>CC<sub>6</sub>F<sub>5</sub>)<sub>16</sub>(H<sub>2</sub>O)<sub>4</sub>]<sup>0, -, 2-</sup> complexes.

<b>20</b>			<b>21</b>			<b>22</b>		
Peak <sup>a</sup>	Assignment <sup>b</sup>	T <sub>1</sub> <sup>c</sup>	Peak <sup>a</sup>	Assignment <sup>b</sup>	T <sub>1</sub> <sup>c</sup>	Peak <sup>a</sup>	Assignment <sup>b</sup>	T <sub>1</sub> <sup>c</sup>
-77.8	<i>o</i> eq (III-III)	2.8	-86.6	<i>o</i> eq (III-III)	2.4	-98.2	<i>o</i> eq (III-III)	2.2
-114.4	<i>o</i> ax (III-IV)	3.4	-109.8	<i>o</i> ax (III-IV)	3.4	-115.3	<i>o</i> ax (III-IV)	3.3
-133.7	<i>p</i> eq (III-III)	35.5	-138.8	<i>p</i> eq (III-III)	30.2	-139.3	<i>m</i> ax (III-III)	7.5
-138.2	<i>p</i> ax (III-III)	22.5	-139.7	<i>p</i> ax (III-III)	19.3	-143.3	<i>p</i> ax (III-III)	16.6
-142.2	<i>m</i> ax (III-III)	11.2	-140.3	<i>m</i> ax (III-III)	9.3	-145.1	<i>p</i> eq (III-III)	24.8
-147.1	<i>p</i> ax (III-IV)	24.8	-149.6	<i>p</i> ax (III-IV)	22.3	-153.0	<i>p</i> ax (III-IV)	19.3
-152.9	<i>m</i> ax (III-IV)	15.0	-153.4	<i>m</i> ax (III-IV)	12.8	-154.0	<i>m</i> ax (III-IV)	11.5
-167.6	<i>m</i> eq (III-III)	19.0	-163.5	<i>m</i> eq (III-III)	15.1	-158.4	<i>m</i> eq (III-III)	13.1

<sup>a</sup> ppm, at ~ 23 °C. <sup>b</sup> ax = axial, eq = equatorial; III-III and III-IV refer to ligands bridging Mn<sup>III</sup>Mn<sup>III</sup> and Mn<sup>III</sup>Mn<sup>IV</sup> pairs, respectively; *o* = ortho, *m* = meta and *p* = para. <sup>c</sup> ms.

Spin-lattice relaxation time (*T*<sub>1</sub>) measurements were performed to aid in the assignment of the peaks. Unpaired electrons on metal centers relax at very fast rates, providing efficient pathways for nuclear relaxation; in general, the longitudinal relaxation time is directly related to the distance of a nucleus from a paramagnetic center.<sup>166,167</sup> Resonances were also assigned on the basis of relative integration ratios, peak broadness (*r*<sup>-6</sup> dependence, where *r* is the distance to the paramagnetic centers), and comparisons with Mn<sub>12</sub> derivatives possessing other carboxylate groups.<sup>13,61</sup> For each of the three complexes, the *T*<sub>1</sub> times can be separated into three distinct groups, two resonances with very short *T*<sub>1</sub> times, three with intermediate *T*<sub>1</sub> times and three with long *T*<sub>1</sub> times. The resonances with the shortest times were assigned to the *o*-F nuclei; these are the resonances that are broadened and shifted the most. The resonances with the longest *T*<sub>1</sub>

times were assigned to the *p*-F nuclei while those with the intermediate  $T_1$  times were assigned to the *m*-F nuclei.

The paramagnetic shifts are expected to have both contact (through-bond) and dipolar (through-space) contributions.<sup>166-168</sup> Unpaired spin density on the paramagnetic metal centers is primarily in  $d_\pi$  orbitals, and  $\pi$ -symmetry overlap with the carboxylate  $\pi$  system will result in direct delocalization of positive spin density from the metal onto the  $-\text{CO}_2$   $\pi$  system. Direct  $\pi$  delocalization of the positive spin density onto the *o*- and *p*-positions of the aromatic pentafluorophenyl rings then occurs. This results in direct  $\pi$  delocalization of the positive spin density from the aromatic ring to the *o*- and *p*-F nuclei, giving downfield paramagnetic shifts of these NMR resonances. Spin polarization effects give a negative spin density at the *m*-positions of the pentafluorophenyl rings, giving an upfield paramagnetic shift of these resonances. Indeed, the observed alternating downfield-upfield-downfield shifts of the *ortho-meta-para* resonances in **20-22** are characteristic of a dominant  $\pi$ -spin delocalization mechanism for the contact shifts.<sup>167,169</sup> Isotropic shifts from dipolar contributions likely also affect the paramagnetic shifts of the fluorine nuclei in these magnetically anisotropic molecules, and probably are the reason for the difference in the magnitude of the shifts of the *o*- and *p*- resonances of a particular carboxylate group, which are usually much more similar on the basis of only a  $\pi$  delocalization mechanism.<sup>167,168</sup>

If the added electron(s) in **21** and **22** is (are) trapped on the NMR timescale, then unique resonances for carboxylates coordinated to the  $\text{Mn}^{\text{II}}$  site(s) should be observed. This is not seen. Instead, **21** and **22** display the same  $D_{2d}$  solution symmetry as **20**,

indicating that the added electrons are detrapping at a fast rate versus the  $^{19}\text{F}$  NMR timescale among the outer ring of Mn ions.

#### 6.2.4 Inelastic Neutron Scattering Spectroscopy

To obtain a larger ground state spin  $S$  and/or a more negative anisotropy  $D$ , it is crucial to better understand the effects of chemical and physical variations on these magnetic parameters. Consequently, we have undertaken an inelastic neutron scattering (INS) study of these three  $\text{Mn}_{12}$  derivatives. In such systems, INS is a powerful tool to obtain detailed magnetic information including magnetic anisotropy parameters (axial, rhombic, and up to the fourth order) as it does not rely on an applied magnetic field. Previous experiments on complex **1**<sup>170</sup> and other molecular magnets<sup>171</sup> have shown that the anisotropy parameters can be derived with great accuracy.

In Figure 6-8 are shown the low temperature neutron energy loss side spectra of  $[\text{Mn}_{12}\text{O}_{12}(\text{O}_2\text{CC}_6\text{F}_5)_{16}(\text{D}_2\text{O})_4]$  (**23**),  $(\text{NMe}_4)[\text{Mn}_{12}\text{O}_{12}(\text{O}_2\text{CC}_6\text{F}_5)_{16}(\text{D}_2\text{O})_4]$  (**24**) and  $(\text{NMe}_4)_2[\text{Mn}_{12}\text{O}_{12}(\text{O}_2\text{CC}_6\text{F}_5)_{16}(\text{D}_2\text{O})_4]$  (**25**) taken at 1.8 K (**23** and **25**) and 2.0 K (**24**), respectively. Two peaks were observed in the spectra of complexes **23** and **24**. The peaks labeled  $I_a$  and  $I_b$  are centered at about 10 and 9.3  $\text{cm}^{-1}$ , respectively, in the spectrum of **23** while  $I_c$  and  $I_d$  are observed at about 7.4 and 6.9  $\text{cm}^{-1}$ , respectively, in the spectrum of **24**. The spectrum of **25** shows no resolved peaks in the observed energy region, but weak intensity between about 3 and 6  $\text{cm}^{-1}$ . The asterisk marks the energy transfer position of an impurity of complex **24** in **25**. In Figure 6-9 are shown the spectra of complexes **23** and **24** at 20 K and 9.9 K, respectively. For **23**, new transitions, labeled  $\text{II}_a - \text{VI}_a$  and  $\text{II}_b - \text{VI}_b$ , appear at energies between about 3 and 9  $\text{cm}^{-1}$  as the temperature is increased. Three new peaks appear in **24** upon raising the temperature to 9.9 K, labeled  $\text{II}_c - \text{IV}_c$  and

$\text{II}_d - \text{IV}_d$ . The solid lines (blue) in each spectrum in Figures 6-8 and 6-9 correspond to the sum of the gaussians underlined (dashed green lines) in the analysis.

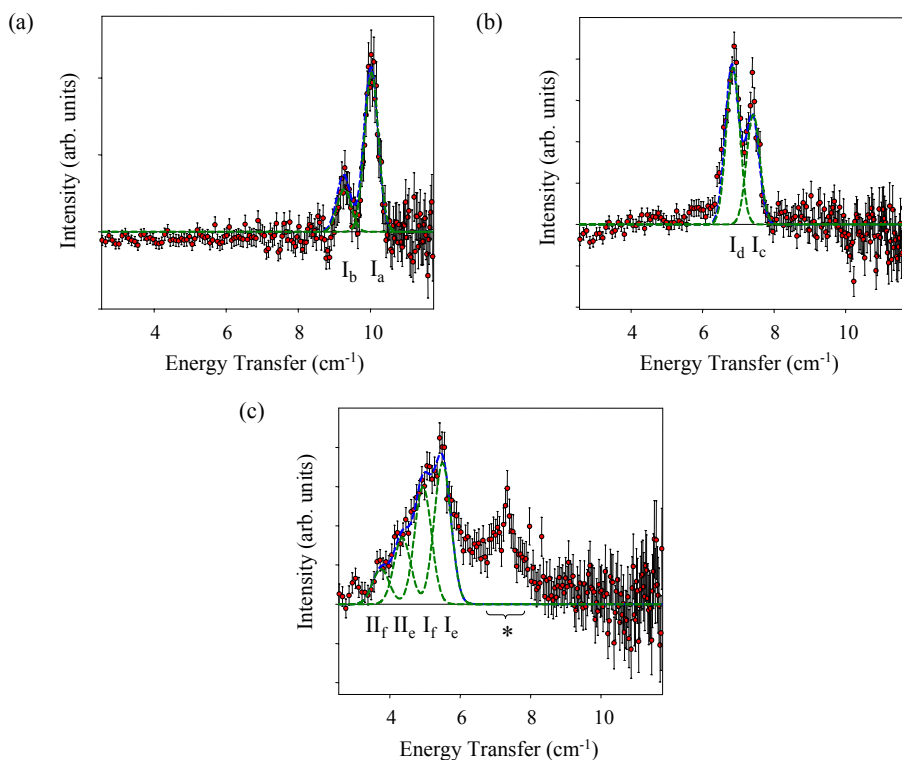


Figure 6-8. Neutron energy loss side INS spectrum of (a) complex **23** at 1.8 K, (b) complex **24** at 2.0 K and (c) complex **25** at 1.8 K obtained at an incident neutron wavelength  $\lambda = 6.0 \text{ \AA}$ . The solid lines (blue) correspond to the sum of the gaussians underlined (dashed green lines) in the analysis; see the text for the fit parameters.

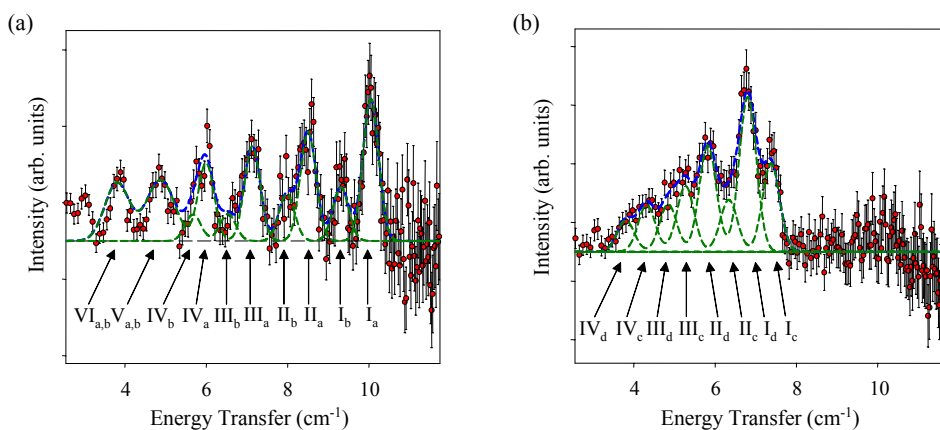


Figure 6-9. Neutron energy loss side INS spectrum of (a) complex **23** at 20 K and (b) complex **24** at 9.9 K obtained at an incident neutron wavelength  $\lambda = 6.0 \text{ \AA}$ . The solid lines (blue) correspond to the sum of the gaussians underlined (dashed green lines) in the analysis; see the text for the fit parameters.

The average energy of transitions  $I_a$  and  $I_b$  of complex **23** in Figure 6-8a is centered at about  $9.8 \text{ cm}^{-1}$ . Assuming that this corresponds to the first allowed transition between the  $m_s = \pm 10$  and  $m_s = \pm 9$  sublevels in the  $S = 10$  ground state, its energy is given by  $19D$ , which means that  $D \sim -0.51 \text{ cm}^{-1}$ . Taking this value, the observation of two transitions at 1.8 K for complex **23** in Figure 6-8a is puzzling. According to Boltzmann statistics, just the  $m_s = \pm 10$  state is populated at 1.8 K (99.9%). Thus, due to the INS selection rule within a given  $S$  state,  $\Delta m_s = \pm 1$ , only one transition should be observed, as is the case for complex **1**.<sup>170a</sup> The observation of two peaks in the low temperature spectra of **23** is attributed to two isomers present in the sample, either due to Jahn-Teller isomerism known in  $\text{Mn}_{12}$  compounds<sup>56-59</sup> or to structural isomers.<sup>172,173</sup> Thus, the peaks  $I_a$  and  $I_b$  correspond to transitions from  $m_s = \pm 10$  to  $m_s = \pm 9$  energy levels in isomer **a** and isomer **b**, respectively. The ratio of **a** to **b** is about 3:1 with the assumption that the INS intensities are proportional, within a good accuracy, to the amount of each isomer in the sample. The same explanation is valid for complex **24**, where the observation of two peaks is also seen. Here, the two peaks labeled  $I_c$  and  $I_d$  correspond to the isomers **c** and **d** (ratio **c/d** = 0.7). A closer examination of the data in Figure 6-9c also reveals the existence of two isomers in **25**, but in this case higher energy states are already populated at 1.8 K. Thus, hot peaks superimpose with the cold ones and lead to the broad band observed between 3 and  $7 \text{ cm}^{-1}$ . The two isomers identified are named **e** and **f**. The ratio **e/f** could not be determined from the present data.

On the basis of this information, data are fitted with gaussians of equal width for each sample, shown as dashed lines (green) in Figures 6-8 and 6-9. The width (fwhm) of the gaussians for the elevated temperature data are fixed to the width of the

corresponding transition I at low temperature (about 60  $\mu\text{eV}$ ). Exceptions are transitions  $V_a/V_b$  and  $VI_a/VI_b$ , respectively. For those it is not possible to locate their four individual positions, because they are superimposed. Thus,  $V_a/V_b$  and  $VI_a/VI_b$  are treated as one transition for their position with fwhm of about 100  $\mu\text{eV}$ . The results of this procedure are presented in Table 6-8 for the neutral species **23**, and the resulting energy splitting patterns for the two isomers **a** and **b** in **23** are shown in Figure 6-10.

Table 6-8. Experimental (neutron energy loss side) and calculated energies and relative intensities of the INS transitions of isomers **a** and **b** in  $[\text{Mn}_{12}\text{O}_{12}(\text{O}_2\text{CC}_6\text{F}_5)_{16}(\text{D}_2\text{O})_4]$  (**23**) at  $\lambda = 6.0 \text{ \AA}$ .<sup>a</sup>

Isomer	Transition	Energy ( $\text{cm}^{-1}$ )		Normalized Intensity (arb. units)			
		exp	calc	2.0 K		20.0 K	
				exp	calc	exp	calc
<b>a</b>	I <sub>a</sub>	10.03(2)	10.01	1.00(3)	1.00	0.37(2)	0.44
	II <sub>a</sub>	8.48(2)	8.51			0.29(2)	0.41
	III <sub>a</sub>	7.11(2)	7.16			0.24(2)	0.31
	IV <sub>a</sub>	5.98(3)	5.94			0.19(2)	0.24
	V <sub>a</sub>	4.86(2)	4.83				0.18
	VI <sub>a</sub>	3.79(2)	3.82				0.14
<b>b</b>	I <sub>b</sub>	9.30(5)	9.28	1.00(8)	1.00	0.35(2)	0.42
	II <sub>b</sub>	7.90(1)	7.94			0.29(2)	0.41
	III <sub>b</sub>	6.69(2)	6.72			0.24(2)	0.33
	IV <sub>b</sub>	5.65(1)	5.61			0.18(2)	0.25
	V <sub>b</sub>	4.86(2)	4.59				0.20
	VI <sub>b</sub>	3.79(2)	3.65				0.16

<sup>a</sup> The intensities were scaled to a value of 1.0 for transitions I<sub>a</sub> and I<sub>b</sub> at 2.0 K. For the calculation the following sets of parameters were used: for isomer **a**,  $D = -0.463 \text{ cm}^{-1}$  and  $B_4^0 = -2.09 \times 10^{-5} \text{ cm}^{-1}$  with  $\chi^2 = 7.7 \times 10^{-4}$ ; for isomer **b**:  $D = -0.437 \text{ cm}^{-1}$  and  $B_4^0 = -1.69 \times 10^{-5} \text{ cm}^{-1}$  with  $\chi^2 = 5.4 \times 10^{-4}$ .

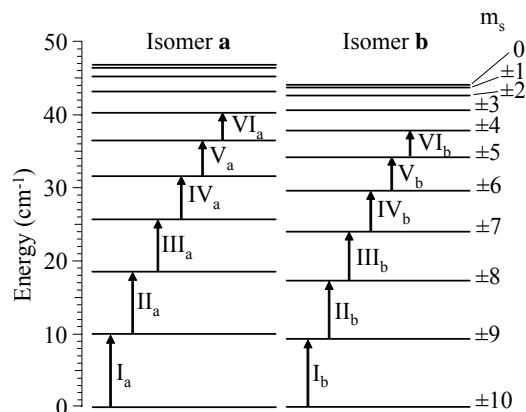


Figure 6-10. Energy level diagram for complex **23** calculated using the parameters given in Table 6-8.

In the following analysis, the bands V and VI are not included, due to their overlap problem mentioned above. The experimental energy patterns in Figure 6-10 are reproduced by applying the following axial Hamiltonian for the magneto-crystalline anisotropy (eq 6-3), where  $B_4^0$  is the axial fourth order term to the zero-field splitting, and  $\hat{O}_4^0 = 35\hat{S}_z^4 - [30S(S+1) - 25]\hat{S}_z^2 - 6S(S+1) + 3\hat{S}^2(S+1)^2$ .

$$\hat{H} = D \left[ \hat{S}_z^2 - \frac{1}{3} S(S+1) \right] + B_4^0 \hat{O}_4^0 \quad (6-3)$$

Small deviations from tetragonal symmetry have been neglected in our analysis as they only marginally influence the low energy levels. Calculations using only the D parameter cannot reproduce the experimental data. Thus, the  $B_4^0$  term is significant. This allows us to reproduce the deviations of our experimental peak positions from a pure Landé pattern, observed for complexes **23** and **24**. For **25**, the data do not contain enough information to extract the  $B_4^0$  parameter and thus this is neglected in the analysis of **25**. Fitting the data with the Hamiltonian (eq 6-3) allowed the determination of the zero-field splitting parameters for the six isomers. The results are collected in Table 6-9.

Table 6-9. Zero-field splitting parameters  $D$  and  $B_4^0$  (in  $\text{cm}^{-1}$ ) for complexes **23**, **24** and **25**.

Parameter	Isomer					
	<b>a</b> [ $\text{Mn}_{12}$ ]	<b>b</b> [ $\text{Mn}_{12}$ ]	<b>c</b> [ $\text{Mn}_{12}$ ] <sup>1-</sup>	<b>d</b> [ $\text{Mn}_{12}$ ] <sup>1-</sup>	<b>e</b> [ $\text{Mn}_{12}$ ] <sup>2-</sup>	<b>f</b> [ $\text{Mn}_{12}$ ] <sup>2-</sup>
$D$	-0.463	-0.437	-0.368	-0.332	-0.274	-0.241
$B_4^0$ ( $10^{-5}$ )	-2.09	-1.69	-1.59	-1.80		
$\chi^2$ ( $10^{-3}$ )	0.8	0.5	0.4	3.8	4	7

Using INS, not only is information on peak positions obtained, but also on their relative intensities. Since the intensity of a given transition is a function of the underlying wave functions of the initial and final states, it is very sensitive to the applied model parameters. Comparing experimental intensities and calculated ones is therefore an excellent way to validate the chosen model. The differential magnetic neutron cross section for a transition  $\Psi_i \rightarrow \Psi_j$  is given by eq 6-4.<sup>174</sup>

$$\begin{aligned}
 \frac{d^2\sigma}{d\Omega dE} = & \frac{N}{4} \left\{ \frac{\gamma e^2}{m_e c^2} \right\} \frac{|k'|}{|k|} \exp^{-2W(\mathbf{Q})} F^2(\mathbf{Q}) \\
 & \times \sum_{\alpha,\beta} \left\{ \delta_{\alpha,\beta} - \frac{Q_\alpha Q_\beta}{Q^2} \right\} \\
 & \times \sum_{i,j} \exp^{i\vec{Q}(\vec{R}_i - \vec{R}_j)} \langle \Psi_i | \hat{S}_j^\alpha | \Psi_j \rangle \\
 & \times \langle \Psi_j | \hat{S}_j^\beta | \Psi_i \rangle \delta(\hbar\omega + E_j - E_i)
 \end{aligned} \tag{6-4}$$

In this equation  $k$  and  $k'$  are the wavenumbers of the incoming and scattered neutrons,  $\mathbf{Q}$  is the scattering vector,  $\exp(-2W)$  is the Debye – Waller factor,  $\hbar\omega$  is the neutron energy, and  $\Psi_i$  and  $\Psi_j$  are the cluster wave functions with energies  $E_i$  and  $E_j$ , respectively.  $g_i$  is the  $g$  factor and  $F(\mathbf{Q})$  is the magnetic form factor,  $\vec{R}_i$  is the space vector of the  $i$ th Mn ion in the cluster and  $\alpha$  and  $\beta$  stand for the spatial coordinates  $x$ ,  $y$  and  $z$ .  $e$  and  $m_e$  are the charge and mass of the electron, respectively,  $c$  is the speed of light, and  $\gamma = -1.91$  is the gyromagnetic constant of the neutron. For a powder sample, eq 6-4 must be averaged in

$Q$ -space. For the relative intensities we are then left with eq 6-5, where  $S_{\perp}$  is the spin component perpendicular to the scattering vector  $\mathbf{Q}$ , and  $p_i$  is the Boltzmann factor of level  $i$ .<sup>175</sup> The results of these calculations are given in Table 6-9 for both isomers of complex **23**. The overall agreement with the experimental data is very good.

$$\frac{d^2\sigma}{d\Omega dE} \approx \sum_{i,f} p_i \left| \langle \Psi_i | S_{\perp} | \Psi_j \rangle \right|^2 \quad (6-5)$$

The  $S = 10$  ground state of the neutral compound is empirically understood by considering the ferrimagnetic arrangement first suggested for **1**. As one  $\text{Mn}^{\text{III}}$  ion is reduced to a  $\text{Mn}^{\text{II}}$ , one would intuitively expect a ground state spin  $S = 21/2$  instead of  $19/2$ . With one more electron reduction step, we recover  $S = 10$  again, but we would naively expect  $S = 11$ . This pattern clearly shows that the canonical picture of the  $\text{Mn}_{12}$  ground state should be handled with care, as the wrong ground state can easily be predicted. This is due to several factors; the ground state is extremely dependent on the competition between the various exchange couplings in the cluster and any change, for example converting one  $\text{Mn}^{\text{III}}$  to a  $\text{Mn}^{\text{II}}$  ion, can considerably modify the low energy levels. We know that in **1**, low energy spin states lie close in energy to the ground state, the first one as low as  $40 \text{ cm}^{-1}$ ,<sup>170b,170c</sup> and a minor change in the exchange couplings can easily alter the energy level ordering. The anisotropy parameter  $D$  decreases as these  $\text{Mn}_{12}$  complexes get successively reduced. The  $D$  values given in Table 6-9 are approximate values because the fitting model assumes axial symmetry, and these complexes are all crystallographically occupying non-axial sites.<sup>113</sup> The upper limit for the energy barrier  $U$  can be evaluated for the three compounds as the following:  $U = S^2|D| = 45 \text{ cm}^{-1}$  for  $z = 0$ ,  $U = (S^2 - 1/4)|D| = 31 \text{ cm}^{-1}$  for  $z = 1-$  and  $U = S^2|D| = 26 \text{ cm}^{-1}$  for  $z = 2-$ .

Using INS spectroscopy, we have clearly shown the effect of electron reduction in  $\text{Mn}_{12}$  derivatives. The ground state spin varies from  $S = 10$  for the neutral and two-electron reduced compounds to  $S = 19/2$  for the one-electron reduced species. Only the knowledge of all the exchange couplings will permit a definitive rationalization of the ground state evolution as a function of electron reduction. The anisotropy is clearly reduced upon addition of electrons to the neutral species, as expected for the loss of a JT elongation axis as a  $\text{Mn}^{\text{III}}$  ion is converted to a  $\text{Mn}^{\text{II}}$  ion.

## 6.2.5 Magnetochemistry of Complexes **20** - **22**

### 6.2.5.1 DC studies

Variable-temperature DC susceptibility measurements were performed on powdered, microcrystalline samples of **20**, **21** and  $\mathbf{22} \cdot 2.5\text{C}_7\text{H}_8$ , restrained in eicosane to prevent torquing, in a 5.0 kG field in the range of 5.0-300 K. The  $\chi_{\text{M}}T$  versus  $T$  dependences of complexes **20** and  $\mathbf{22} \cdot 2.5\text{C}_7\text{H}_8$  are similar to those of previously studied  $[\text{Mn}_{12}\text{O}_{12}(\text{O}_2\text{CR})_{16}(\text{H}_2\text{O})_4]$  complexes with  $S = 10$  ground states, exhibiting a nearly temperature-independent value of 17-19  $\text{cm}^3 \text{K mol}^{-1}$  (**20**) and 18-20  $\text{cm}^3 \text{K mol}^{-1}$  ( $\mathbf{22} \cdot 2.5\text{C}_7\text{H}_8$ ) in the 150-300 K range which then increases rapidly to a maximum of 47-49  $\text{cm}^3 \text{K mol}^{-1}$  (**20**) and 49-53  $\text{cm}^3 \text{K mol}^{-1}$  ( $\mathbf{22} \cdot 2.5\text{C}_7\text{H}_8$ ) at  $\sim 15$  K before decreasing rapidly at lower temperatures (Figure 6-11).<sup>13,22</sup> The data for the  $[\text{Mn}_{12}]$  complex **21** show a similar temperature dependence. The  $\chi_{\text{M}}T$  value of **21** slowly increases from 19.65  $\text{cm}^3 \text{K mol}^{-1}$  at 300 K to a maximum of 51.35  $\text{cm}^3 \text{K mol}^{-1}$  at 15.0 K and then decreases rapidly at lower temperatures. The maximum value indicates a high ground state spin ( $S$ ) value for each of the complexes, with the low temperature decrease primarily due to a combination of Zeeman and zero-field splitting effects. The spin-only ( $g = 2$ ) values for units composed of non-interacting  $\text{Mn}^{\text{IV}}_4\text{Mn}^{\text{III}}_8$  (**20**),  $\text{Mn}^{\text{IV}}_4\text{Mn}^{\text{III}}_7\text{Mn}^{\text{II}}$  (**21**) and

$\text{Mn}^{\text{IV}}_4\text{Mn}^{\text{III}}_6\text{Mn}^{\text{II}}_2$  (**22**) ions are  $31.5 \text{ cm}^3 \text{ K mol}^{-1}$ ,  $32.9 \text{ cm}^3 \text{ K mol}^{-1}$  and  $34.3 \text{ cm}^3 \text{ K mol}^{-1}$ , respectively. The  $\chi_{\text{M}}T$  value at 300 K of each of the complexes is less than that expected for non-interacting metal ions, indicating the presence of appreciable intramolecular exchange interactions.

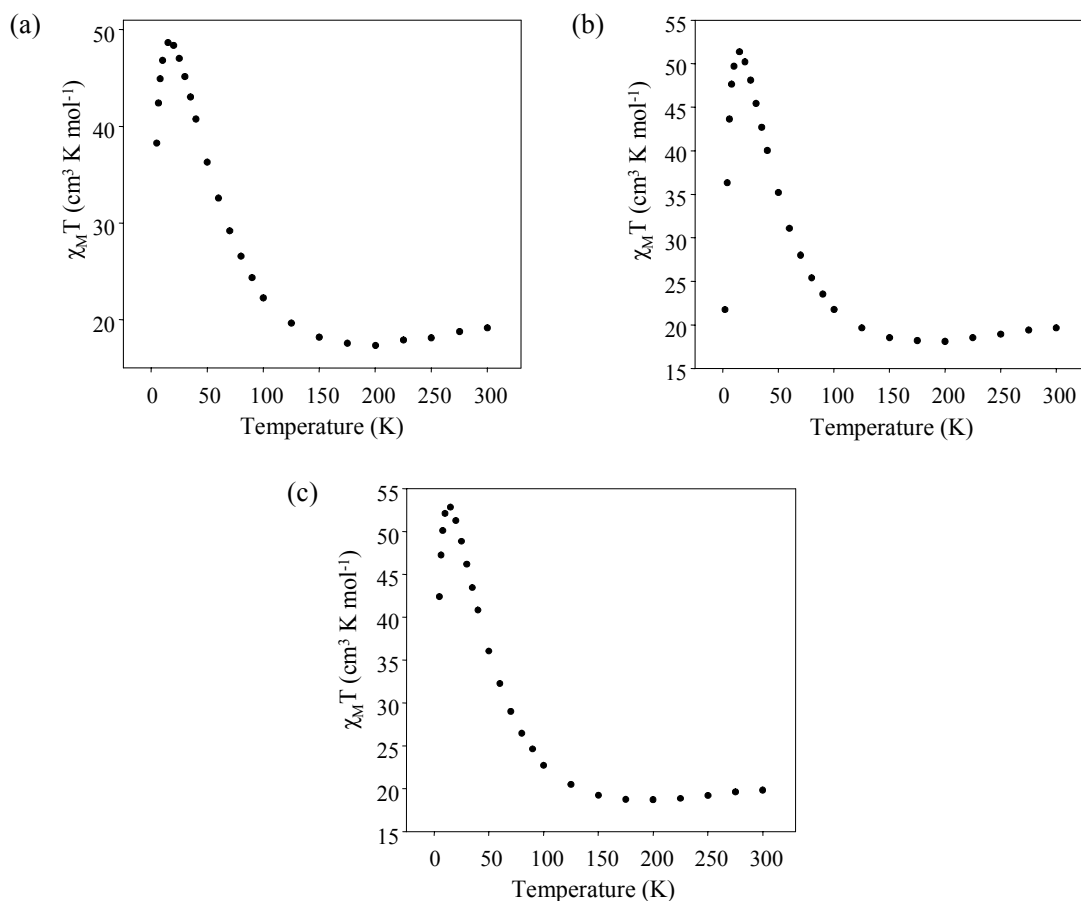


Figure 6-11. Plot of  $\chi_{\text{M}}T$  versus  $T$  for dried, microcrystalline samples of (a)  $[\text{Mn}_{12}]$  complex **20**, (b)  $[\text{Mn}_{12}]^-$  complex **21** and (c)  $[\text{Mn}_{12}]^{2-}$  complex **22**· $2.5\text{C}_7\text{H}_8$  in eicosane.  $\chi_{\text{M}}$  is the molar DC magnetic susceptibility measured at 5.0 kG.

As with other  $\text{Mn}_{12}$  clusters, a theoretical treatment of the DC magnetic susceptibility data<sup>51</sup> as a means of determining the magnitude of the exchange parameters between the Mn ions is not simple. Instead, we concentrated only on determining the ground state spin of the molecules using magnetization measurements in the 1-70 kG and 1.80-10.0 K ranges. The data, plotted as reduced magnetization ( $M/N\mu_{\text{B}}$ ) vs  $H/T$ , are

shown for the three complexes in Figure 6-12, where  $N$  is Avogadro's number and  $\mu_B$  is the Bohr magneton. For a system occupying only the ground state and experiencing no zero-field splitting (ZFS), the various isofield lines would be superimposed and  $M/N\mu_B$  would saturate at a value of  $gS$ . The non-superimposition of the isofield lines clearly indicates the presence of ZFS. The data were fit using MAGNET,<sup>54</sup> which assumes only the ground state is populated at these temperatures and is based on the method described elsewhere involving diagonalization of the spin Hamiltonian matrix, including axial ZFS ( $D\hat{S}_z^2$ ) and Zeeman interactions, and incorporating a full powder average.<sup>53</sup> The best fits are shown as solid lines in Figure 6-12 for complexes **20-22**, and the fitting parameters are listed in Table 6-10. Attempts to fit the data with  $S = 17/2$  (**21**) or  $S = 9$  (**22**) gave unreasonable  $g$  values of 2.26 and 2.28, respectively; a  $g$  value significantly greater than 2 is not expected for a  $\text{Mn}^{\text{IV}}_4\text{Mn}^{\text{III}}_7\text{Mn}^{\text{II}}$  or  $\text{Mn}^{\text{IV}}_4\text{Mn}^{\text{III}}_6\text{Mn}^{\text{II}}_2$  cluster, and these possibilities were therefore discounted. Reasonable (but not as good) fits for **21** and **22** can also be obtained with other  $S$  values, however: the data for **21** can be fit with  $S = 21/2$ ,  $g = 2.01$  and  $D = -0.32 \text{ cm}^{-1}$ , and that for **22** with  $S = 11$ ,  $g = 1.87$  and  $D = -0.24 \text{ cm}^{-1}$ . Nevertheless, note that the  $S = 10$  (**20**),  $S = 19/2$  (**21**) and  $S = 10$  (**22**) ground state values obtained from the best fits of the magnetization data are in agreement with these same values obtained from INS measurements on dried, microcrystalline deuterated analogues of **20-22**.<sup>164</sup>

Table 6-10.  $M/N\mu_B$  vs  $H/T$  fitting parameters for  $[\text{Mn}_{12}]^z$  ( $z = 0, 1-, 2-$ ) complexes.

Parameter	$[\text{Mn}_{12}]$ ( <b>20</b> )	$[\text{Mn}_{12}]^-$ ( <b>21</b> )	$[\text{Mn}_{12}]^{2-}$ ( <b>22</b> )
$S$	10	19/2	10
$g$	1.87	2.04	2.05
$D, \text{cm}^{-1}$	-0.40	-0.34	-0.29
$D, \text{K}$	-0.58	-0.49	-0.42
$D/g, \text{cm}^{-1}$	0.21	0.17	0.14
$U, \text{K}$	58	44	42

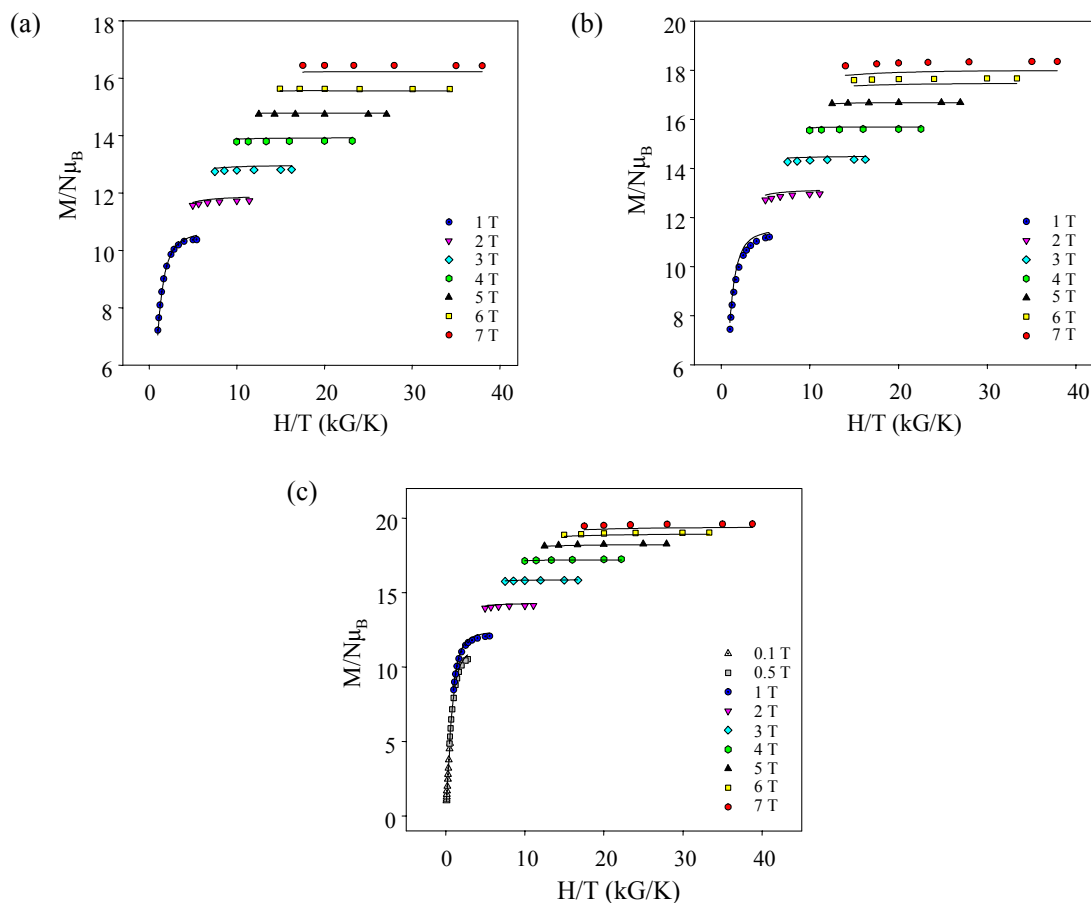


Figure 6-12. Plot of  $M/N\mu_B$  versus  $H/T$  for dried, microcrystalline samples of (a)  $[\text{Mn}_{12}]$  complex **20**, (b)  $[\text{Mn}_{12}]^-$  complex **21** and (c)  $[\text{Mn}_{12}]^{2-}$  complex **22**· $2.5\text{C}_7\text{H}_8$  in eicosane at the indicated applied fields. The solid lines are the fit of the data; see the table for the fit parameters.

In order to confirm that the obtained parameters were the true global rather than local error minima, and to assess the uncertainty in the obtained  $g$  and  $D$  values, root-mean square  $D$  vs  $g$  error surfaces for the fits were generated using the program GRID.<sup>55</sup> The error surfaces for **20-22** are shown in Figure 6-13 as contour plots for the  $D = -0.10$  to  $-0.70 \text{ cm}^{-1}$  and  $g = 1.7$  to  $2.1$  ranges (**20**),  $D = -0.10$  to  $-0.55 \text{ cm}^{-1}$  and  $g = 1.8$  to  $2.25$  ranges (**21**),  $D = -0.05$  to  $-0.50 \text{ cm}^{-1}$  and  $g = 1.9$  to  $2.2$  ranges (**22**). For each, one very soft fitting minimum is observed indicating significant uncertainty in the fit values; the lowest indicated contour describes the region of minimum error for **20** from  $D \approx -0.33$  to

$-0.48 \text{ cm}^{-1}$  and  $g \approx 1.81$  to  $1.93$ , giving fitting parameters of  $D = -0.40 \pm 0.08 \text{ cm}^{-1}$  and  $g = 1.87 \pm 0.06$ , for **21** from  $D \approx -0.30$  to  $-0.39 \text{ cm}^{-1}$  and  $g \approx 1.99$  to  $2.09$ , giving fitting parameters of  $D = -0.34 \pm 0.04 \text{ cm}^{-1}$  and  $g = 2.04 \pm 0.05$ , and for **22** from  $D \approx -0.26$  to  $-0.32 \text{ cm}^{-1}$  and  $g \approx 2.01$  to  $2.09$ , giving fitting parameters of  $D = -0.29 \pm 0.03 \text{ cm}^{-1}$  and  $g = 2.05 \pm 0.04$ .

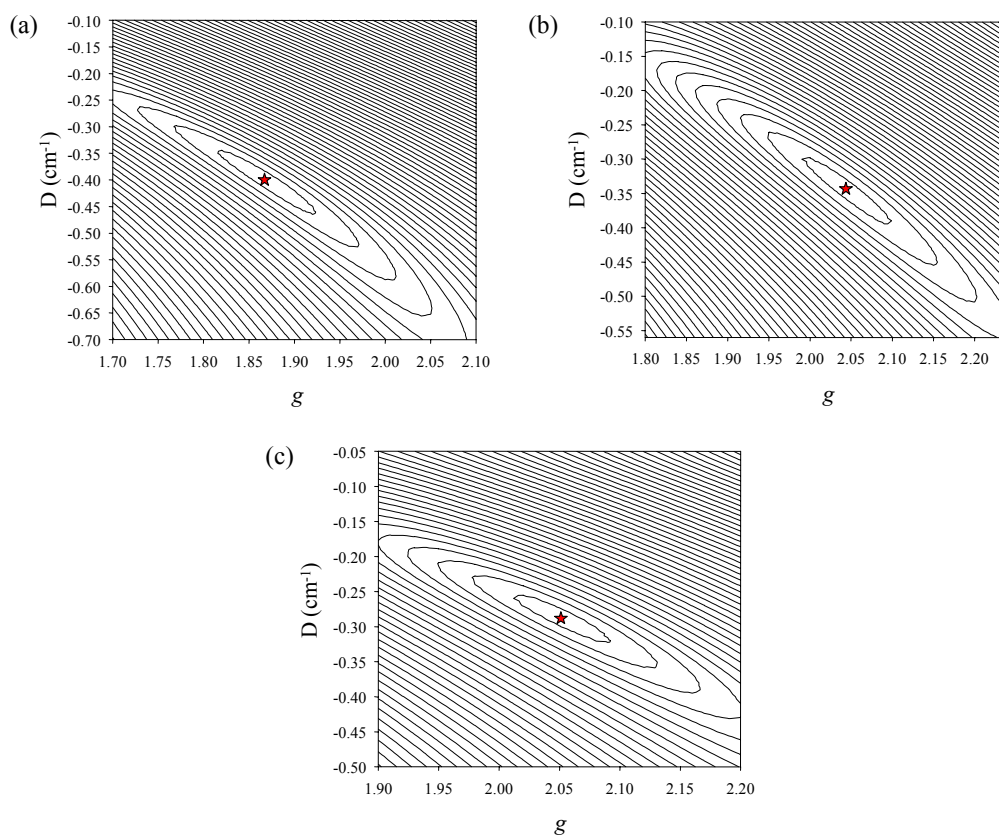


Figure 6-13. Two-dimensional contour plot of the error surface for the  $D$  vs  $g$  fit for (a)  $[\text{Mn}_{12}]$  complex **20**, (b)  $[\text{Mn}_{12}]^-$  complex **21** and (c)  $[\text{Mn}_{12}]^{2-}$  complex **22**· $2.5\text{C}_7\text{H}_8$ . The asterisk indicates the soft minimum.

The soft (shallow) fitting minima and the resulting large uncertainties are undoubtedly the primary reason that the  $g$  values are slightly  $> 2$  in some cases; this is not expected for Mn. We did not feel it appropriate to fix  $g$  at  $2.0$ , preferring to quote in Table 6-10 the values given by the fit. The similarly significant uncertainties in the  $D$  values quoted in Table 6-10 mean that they are most useful for relative comparisons, and

their absolute values should be treated with some caution. Also note that the  $D/g$  values obtained from the magnetization fits will be useful for comparisons with the more reliable  $D/g$  values obtained from hysteresis studies (*vide infra*). More reliable values of  $D$  have also been obtained from the INS measurements:<sup>164</sup> this sensitive technique detected two species present in each sample with  $D$  values of  $-0.463$  and  $-0.437$   $\text{cm}^{-1}$  for **20**,  $-0.368$  and  $-0.332$   $\text{cm}^{-1}$  for **21**, and  $-0.274$  and  $-0.241$   $\text{cm}^{-1}$  for **22**, in satisfying agreement with the single values obtained from the magnetization fits given in Table 6-10.

A comparison of the fitting parameters shows that the ground state spin of each of the complexes changes only slightly as the  $\text{Mn}_{12}$  molecule is progressively reduced. The spin value does not change at all on two-electron reduction, suggesting that the complexes act as “spin buffers”, accepting electrons with little or no change to the  $S$  value.<sup>61</sup> This behavior is in contrast to that observed with the axial magnetic anisotropy parameter,  $D$ ; as the  $\text{Mn}_{12}$  molecule is progressively reduced, the magnetic anisotropy decreases, as reflected in the decreasing absolute value of  $D$ . This trend is expected; the molecular anisotropy of a cluster is primarily a consequence of the single-ion anisotropies of the constituent metal ions and the relative orientations of the anisotropy axes of these ions with respect to each other. The primary source of the magnetic anisotropy in a  $\text{Mn}_{12}$  molecule is from Jahn-Teller distorted  $\text{Mn}^{\text{III}}$  ions;  $\text{Mn}^{\text{II}}$  and  $\text{Mn}^{\text{IV}}$  are fairly isotropic ions. The addition of electrons to the neutral  $\text{Mn}_{12}$  molecule on reduction converts a formerly  $\text{Mn}^{\text{III}}$  ion to a  $\text{Mn}^{\text{II}}$  ion. This results in a decrease in the number of  $\text{Mn}^{\text{III}}$  ions and a concomitant decrease in the molecular anisotropy.

The combination of a large ground state spin and a negative magnetic anisotropy that has been decreased but is still reasonably large implies that in addition to complex **20**, the reduced complexes, **21** and **22**, might still function as SMMs as has been previously found for other one- and two-electron reduced species.<sup>13,61,100</sup> In order for these molecules to behave as SMMs, they must possess a sufficiently large energy barrier to magnetization reversal such that they display slow magnetization relaxation rates. The upper limit (U) of this energy barrier is given by  $U = S^2|D|$  and  $U = (S^2 - 1/4)|D|$  for integer and non-integer spins, respectively.<sup>12,19,22,23</sup> These values of U for **20-22** are included in Table 6-10. Both AC susceptibility studies and DC magnetization studies below 1.8 K using a micro-SQUID<sup>92</sup> apparatus were therefore performed.

#### 6.2.5.2 AC studies

On the basis of similar measurements on other  $[\text{Mn}_{12}]$ ,  $[\text{Mn}_{12}]^-$  and  $[\text{Mn}_{12}]^{2-}$  systems,<sup>13,61,100</sup> we expected that **20-22** would exhibit at least one frequency-dependent out-of-phase AC susceptibility signal ( $\chi_M''$ ), an indicator of slow magnetization relaxation. Such signals have been observed for all  $\text{Mn}_{12}$  SMMs and are considered a signature of the SMM property although only hysteresis loops obtained from magnetization vs DC field scans provide definitive evidence of the SMM property. Key kinetic parameters can be obtained from  $\chi_M''$  vs  $T$  data, including  $U_{\text{eff}}$ , the true or effective barrier to relaxation.  $U_{\text{eff}}$  is smaller than U, since quantum tunneling of the magnetization (QTM) represents a short-cut through the barrier via higher lying  $m_s$  levels of the ground state S spin manifold. In addition, the in-phase AC susceptibility ( $\chi_M'$ ) is invaluable for the determination of the ground-state spin of a molecule.<sup>66,106,111i,112,119</sup> In Figure 6-14 are shown the  $\chi_M' T$  vs  $T$  plots for **20-22** at different AC oscillation frequencies. The  $\chi_M' T$  values are temperature-independent down to the temperatures at which decreases due to

slow magnetization relaxation are reached. The temperature-independent  $\chi_M'T$  values show that only the ground states of the molecules are populated at these temperatures, and can be used to calculate the ground state S values without complications from a DC field. The  $\chi_M'T$  values of  $\sim 48$ ,  $\sim 47$ , and  $\sim 54 \text{ cm}^3 \text{ K mol}^{-1}$  for **20**, **21**, and **22**, respectively, correspond to  $S = 10 / g = 1.87$ ,  $S = 19/2 / g = 1.95$ , and  $S = 10 / g = 1.98$ , respectively, consistent with the fits of the DC magnetization data above.

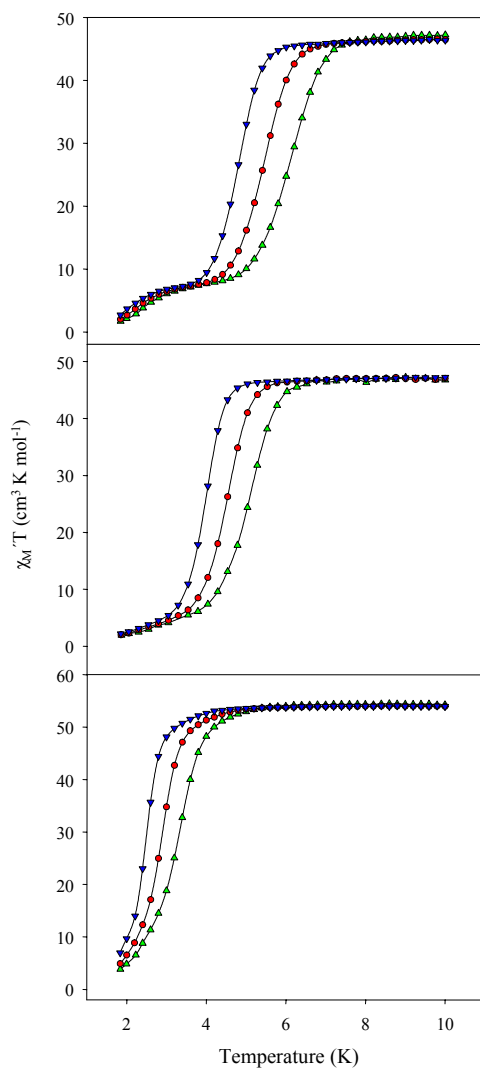


Figure 6-14.  $\chi_M'T$  vs  $T$  plots for vacuum-dried  $[\text{Mn}_{12}]$  complex **20** (top),  $[\text{Mn}_{12}]^-$  complex **21** (middle), and  $[\text{Mn}_{12}]^{2-}$  complex **22** (bottom) at 1000 ( $\blacktriangle$ ), 250 ( $\bullet$ ) and 50 Hz ( $\blacktriangledown$ ).

The sharp decreases in the  $\chi_M' T$  signal at the lowest temperatures are accompanied by the appearance of frequency-dependent out-of-phase ( $\chi_M''$ ) signals, the characteristic signature of a superparamagnet-like species such as a SMM. These were studied in detail, for both dried samples and those maintained in contact with their mother liquor to avoid solvent loss. Previous studies have shown that environmental factors strongly influence the magnetic behavior of a SMM. Disordered solvent molecules of crystallization, the loss of such solvent molecules, and other environmental factors such as the site-symmetry of a molecule (the crystal space group) have accounted for: (i) a broadening or smearing out of QTM steps in hysteresis loops such that the loops appear smooth, without the periodic steps expected for a SMM;<sup>62,63,66,114,111i</sup> (ii) the appearance of a second peak in the out-of-phase AC susceptibility that is indicative of a second relaxation process<sup>56</sup> and (iii) differences in the effective energy barrier ( $U_{\text{eff}}$ ) for magnetization reversal between seemingly identical molecules.<sup>61</sup> Hence, it is important to probe the relaxation behavior of SMMs by measurements on both vacuum-dried samples and on wet samples maintained in mother liquor to prevent solvent loss. For this reason, AC susceptibilities were measured in a 3.5 G AC field oscillating at frequencies up to 1500 Hz for dried samples **20**, **21** and **22**·2.5C<sub>7</sub>H<sub>8</sub> and wet crystals of **20**·3CH<sub>2</sub>Cl<sub>2</sub>, **21**·4.5CH<sub>2</sub>Cl<sub>2</sub>·½H<sub>2</sub>O and **22**·6C<sub>7</sub>H<sub>8</sub>, facilitating an assessment of the effect of solvent loss on the magnetic properties.

A comparison of the  $\chi_M''$  vs  $T$  plots for dry and wet samples of **20** at three AC oscillation frequencies is shown in the top panels of Figures 6-15 and 6-16, respectively. In each plot are shown two peaks corresponding to two distinct relaxation processes. In the dry sample, the higher-temperature (HT) peak at ~ 6 K predominates with a relative

integration ratio of approximately eleven times that of the lower-temperature (LT) peak at  $\sim 2.5$  K, whereas in the wet sample, the HT signal predominates over the LT form by more than thirty-fold.

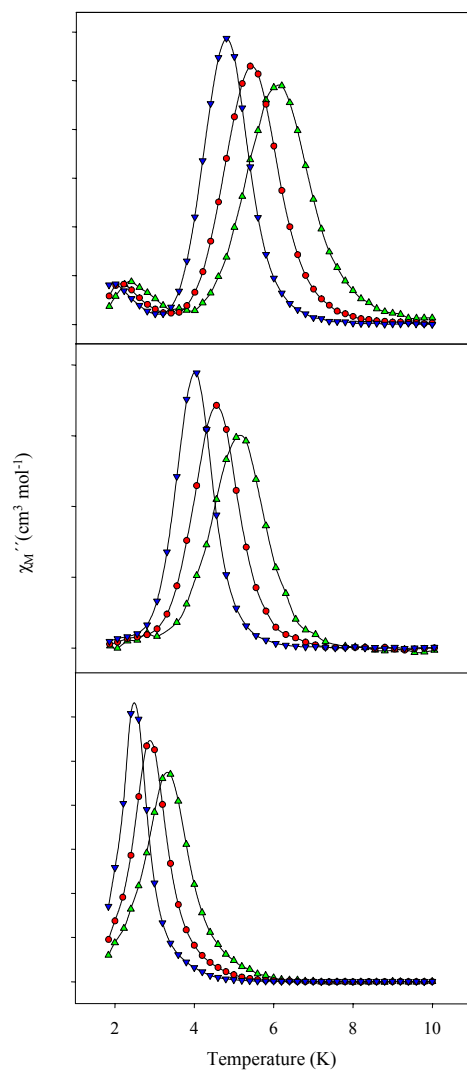


Figure 6-15.  $\chi_M''$  vs  $T$  plots for vacuum-dried  $[\text{Mn}_{12}]$  complex **20** (top),  $[\text{Mn}_{12}]^-$  complex **21** (middle), and  $[\text{Mn}_{12}]^{2-}$  complex **22** (bottom) at 1000 ( $\blacktriangle$ ), 250 ( $\bullet$ ) and 50 Hz ( $\blacktriangledown$ ).

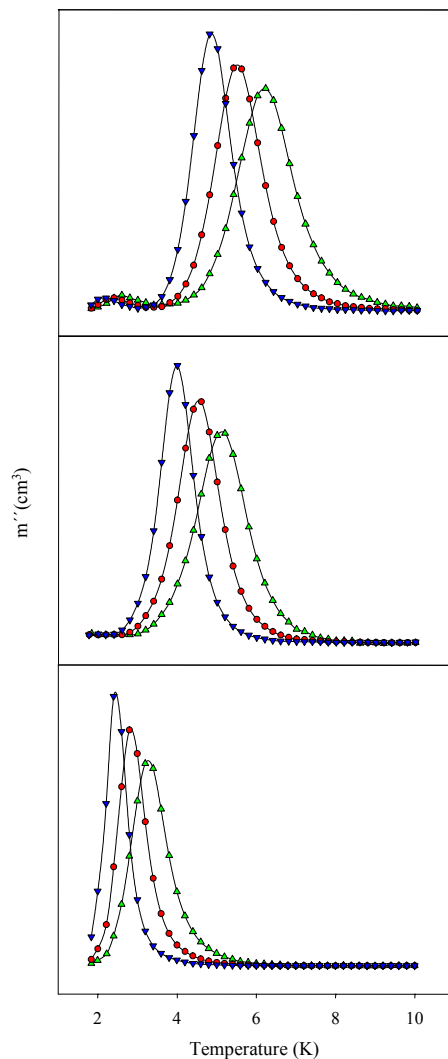


Figure 6-16.  $m''$  vs  $T$  plots for wet crystals of  $[\text{Mn}_{12}]$  complex **20** (top),  $[\text{Mn}_{12}]^-$  complex **21** (middle), and  $[\text{Mn}_{12}]^{2-}$  complex **22** (bottom) at 1000 ( $\blacktriangle$ ), 250 ( $\bullet$ ) and 50 Hz ( $\blacktriangledown$ ).

Because the integration ratio of HT:LT is much larger for the wet crystals than for the dry sample, it seems reasonable that the LT peak arises as a result of the loss of highly volatile  $\text{CH}_2\text{Cl}_2$  solvent molecules of crystallization. This solvent loss is deliberate and complete in the vacuum-dried sample, giving two molecular environments that each give a  $\chi_M''$  signal. The presence of two  $\chi_M''$  signals is commonly encountered for  $\text{Mn}_{12}$  complexes and has been previously attributed to Jahn-Teller isomerism,<sup>56-59</sup> a phenomenon by which molecules differ in the relative orientation of one or more  $\text{Mn}^{\text{III}}$  JT

elongation axis. The LT  $\chi_M''$  signal corresponds to the isomer with at least one abnormally-oriented JT elongation axis towards a bridging oxide ion while the HT  $\chi_M''$  signal corresponds to the isomer with eight normally-oriented JT elongation axes. Consistent with most previous findings, the LT form in **20** is the minor species not just in the dried, microcrystalline sample, but especially in wet crystals. The X-ray crystal structure of **20** reveals that the JT elongation axis of Mn(11) is not clearly defined as already discussed, suggesting that a static disorder of the abnormally-oriented JT axis of this ion might exist and that the JT elongation axis of Mn(11) might be reorienting as interstitial solvent molecules of crystallization are lost. Note that instead of molar susceptibility, the figure ordinates for a sample maintained in mother liquor are simply the total magnetization (plotted as  $m'T$  and  $m''$ ) as the mass of a wet sample cannot be accurately determined. A comparison of the  $U_{\text{eff}}$  and pre-exponential factor  $1/\tau_0$  values in Table 6-11 for the HT peak of the wet and dry samples shows that the relaxation process is probably the same in each sample.

Table 6-11. Arrhenius parameters ( $U_{\text{eff}}$  and  $\tau_0$ ) for wet<sup>a</sup> and dried<sup>b</sup> complexes **20-22**.

		$\tau_0$ , s	$U_{\text{eff}}$ , K
Wet <sup>a,c</sup>	<b>20</b> <sup>e</sup>	$2.9 \times 10^{-9}$	64
	<b>21</b> <sup>f</sup>	$4.9 \times 10^{-9}$	53
	<b>22</b> <sup>g</sup>	$3.3 \times 10^{-8}$	28
Dried <sup>b,c</sup>	<b>20</b> <sup>h</sup>	$3.3 \times 10^{-9}$	66
	<b>21</b> <sup>h</sup>	$4.0 \times 10^{-9}$	54
	<b>22</b> <sup>i</sup>	$2.7 \times 10^{-8}$	29
Wet <sup>a,d</sup>	<b>20</b> <sup>e</sup>	$8.1 \times 10^{-9}$	59
	<b>21</b> <sup>f,j</sup>	$3.0 \times 10^{-10}$	49
	<b>21</b> <sup>f,k</sup>	$1.3 \times 10^{-10}$	21
	<b>22</b> <sup>g</sup>	$9.1 \times 10^{-8}$	25

<sup>a</sup> crystals maintained in contact with mother liquor. <sup>b</sup> vacuum-dried crystals. <sup>c</sup> AC data only. <sup>d</sup> combined AC and DC data. <sup>e</sup> **20**·3CH<sub>2</sub>Cl<sub>2</sub> <sup>f</sup> **21**·4.5CH<sub>2</sub>Cl<sub>2</sub>·½H<sub>2</sub>O <sup>g</sup> **22**·6C<sub>7</sub>H<sub>8</sub> <sup>h</sup> unsolvated. <sup>i</sup> **22**·2.5C<sub>7</sub>H<sub>8</sub> <sup>j</sup> slower-relaxing species. <sup>k</sup> faster-relaxing species.

The  $\chi_M''$  vs  $T$  plot for dry and wet samples of both **21** and **22**·2.5C<sub>7</sub>H<sub>8</sub> at three frequencies are shown in the middle and bottom panels of Figures 6-15 and 6-16, respectively. Only one peak is observed for each molecule at temperatures above 1.8 K, suggesting effectively only one molecular environment, a small range of axial and rhombic anisotropy parameters D and E, and consequently a small range of  $U_{\text{eff}}$  values. For **21**, the crystal structure reveals a static disorder between a carboxylate group and an adjacent water molecule, as described earlier, giving a mixture of isomers (77:23%) differing in the distribution of the four H<sub>2</sub>O ligands. However, only one  $\chi_M''$  peak is seen, suggesting either (i) the two isomers have very similar D and  $U_{\text{eff}}$  values and thus relax at essentially the same rate, or (ii) the differences in D and  $U_{\text{eff}}$  are so large that the faster-relaxing form gives signals at < 1.8 K, the operating limit of our SQUID instrument. Studies to lower temperatures are needed to address this point further (*vide infra*).

In accord with the decreasing Mn<sup>III</sup> content, the  $\chi_M''$  signals shift to lower temperatures on progressive reduction: 6-8 K [Mn<sub>12</sub>], 4-6 K range for [Mn<sub>12</sub>]<sup>-</sup>, and 2-4 K range for [Mn<sub>12</sub>]<sup>2-</sup>. This shift reflects the decreasing energy barrier to magnetization relaxation,  $U_{\text{eff}}$ . As expected, the change in  $U_{\text{eff}}$  with decreasing Mn<sup>III</sup> content is not linear.  $U_{\text{eff}}$  depends on a number of factors, including S, the axial (D) and rhombic (E) ZFS parameters, fourth order spin Hamiltonian parameters, and others. Qualitative comparisons, however, are reasonable, and display a monotonic decrease of  $U_{\text{eff}}$  with Mn<sup>III</sup> content.

### 6.2.5.3 Relaxation studies using AC and DC data

The temperature at the peak of the  $\chi_M''$  signal is the point at which the rate of reorientation (relaxation) of the magnetization vector equals the operating frequency of the oscillating field. This is thus a source of kinetic data, and  $U_{\text{eff}}$  can be determined by

fitting the resulting relaxation rate ( $1/\tau$ ) vs  $T$  data to the Arrhenius equation (eq 6-6), where  $\tau$  is the relaxation time.

$$\tau = \tau_0 \exp(U_{\text{eff}}/kT) \quad (6-6)$$

This is the characteristic behavior of a thermally-activated Orbach process, where  $k$  is the Boltzmann constant and  $1/\tau_0$  is the pre-exponential term. The frequency dependence of the  $\chi_M''$  peak for **20-22** was determined at eight oscillation frequencies in the 5-1500 Hz range. Plots of  $\tau$  vs  $1/T$  for wet crystals of **20-22** are shown in Figure 6-17, with the least-squares fit to eq 6-6 shown as a solid line. The  $U_{\text{eff}}$  and  $\tau_0$  values for both dried, microcrystalline samples and wet crystals are compiled in Table 6-11 and are similar to values previously obtained for  $[\text{Mn}_{12}]$ ,  $[\text{Mn}_{12}]^-$  and  $[\text{Mn}_{12}]^{2-}$  systems. Within experimental uncertainty, the  $U_{\text{eff}}$  and  $\tau_0$  values for wet and dried samples are almost identical.

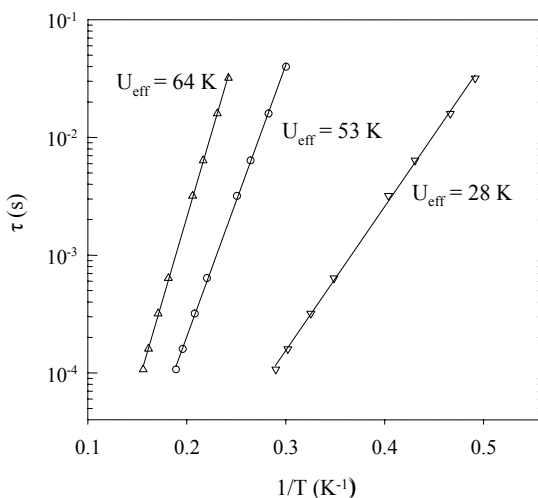


Figure 6-17. Plots of relaxation time ( $\tau$ ) vs  $1/T$  for wet crystals of complexes **20** ( $\Delta$ ), **21** ( $\circ$ ) and **22** ( $\nabla$ ) using AC  $\chi_M''$  data. The solid lines are the fits to the Arrhenius equation. See Table 6-11 for the fit parameters.

To supplement the AC data, additional relaxation vs time measurements were obtained at temperatures below 1.8 K by DC magnetization decay vs time measurements. These data were obtained on single crystals using a micro-SQUID apparatus. First, a

large DC field of 1.4 T was applied to the sample at  $\sim 5$  K to saturate its magnetization in one direction, and the temperature was lowered to a chosen value between 0.04 and 3.5 K. When the temperature was stable, the field was swept from 1.4 to 0 T at a rate of 0.14 T/s, and then the magnetization in zero field was measured as a function of time. This gave a set of relaxation time ( $\tau$ ) vs  $T$  data, which were combined with the AC data and used to construct an Arrhenius plot. The data are plotted as  $\tau$  vs  $1/T$  in Figures 6-18, 6-19, 6-20 and 6-21 together with the fits (dotted lines) to eq 6-6 for complex **20**, the slower-relaxing species of complex **21**, the faster-relaxing species of complex **21** and for complex **22**, respectively; the fit parameters are given in Table 6-11. Good fits of the combined AC and DC data were obtained for **20** and **22**; the  $U_{\text{eff}}$  for the HT JT isomer of **20** is 59 K, a typical value for  $\text{Mn}_{12}$ , while  $U_{\text{eff}}$  for **22** is 25 K. These can be compared with 64 and 28 K, respectively, for wet crystals over the smaller  $T$  range of Figure 6-17.

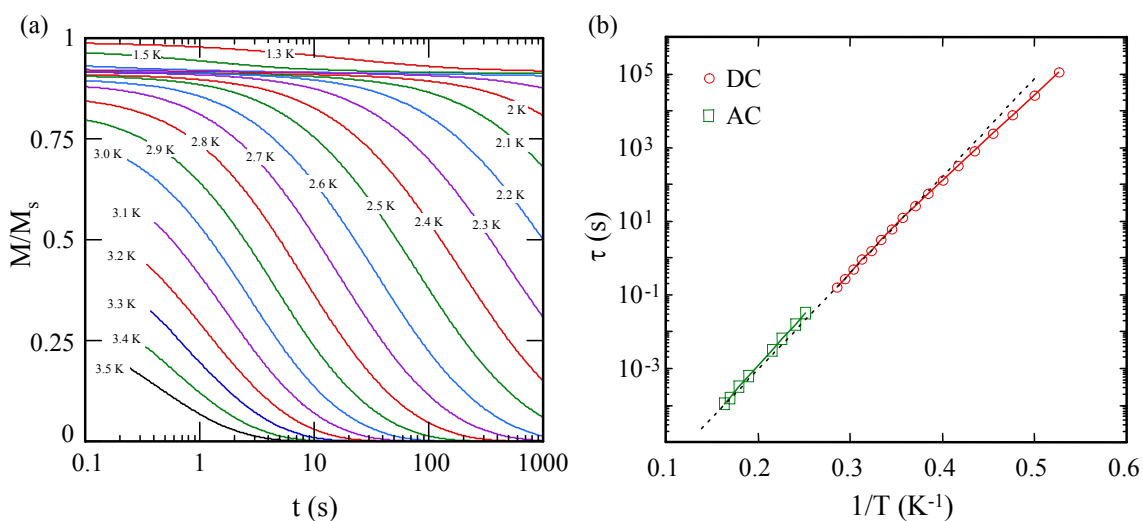


Figure 6-18. Relaxation time vs temperature studies for a single crystal of  $\mathbf{20} \cdot 3\text{CH}_2\text{Cl}_2$ . (a) Plot of magnetization vs time decay in zero field. The magnetization is normalized to its saturation value,  $M_s$ . (b) Plot of relaxation time ( $\tau$ ) vs  $1/T$  for using AC  $\chi_M''$  and DC decay data. The dotted lines are fits to the Arrhenius equation. See Table 6-11 for the fit parameters.

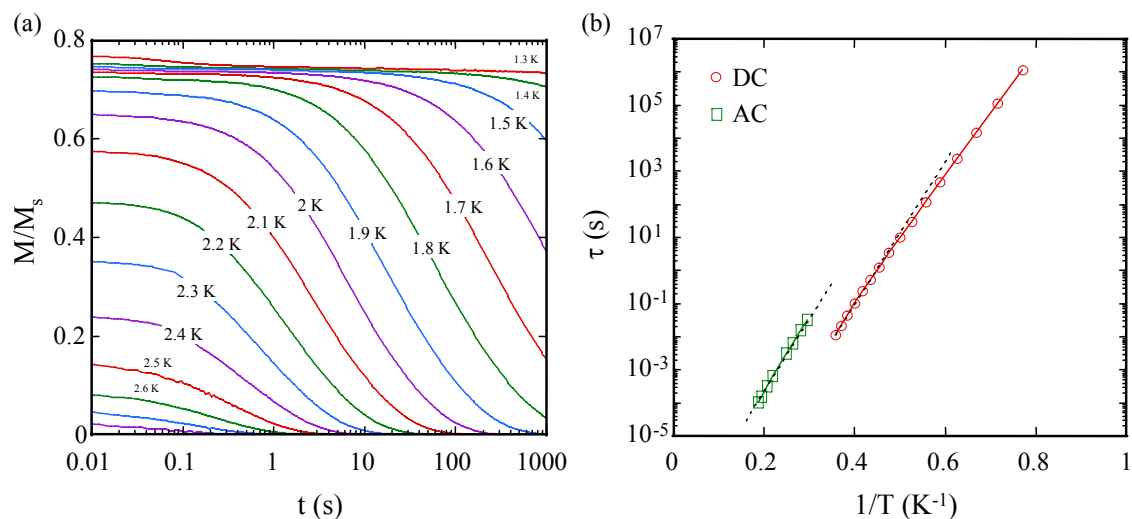


Figure 6-19. Relaxation time vs temperature studies for the slower-relaxing species of complex  $21 \cdot 4.5\text{CH}_2\text{Cl}_2 \cdot \frac{1}{2}\text{H}_2\text{O}$ . (a) Plot of magnetization vs time decay in zero field. The magnetization is normalized to its saturation value,  $M_s$ . (b) Plot of relaxation time ( $\tau$ ) vs  $1/T$  for using AC  $\chi_M''$  and DC decay data. The dotted lines are fits to the Arrhenius equation. See Table 6-11 for the fit parameters.

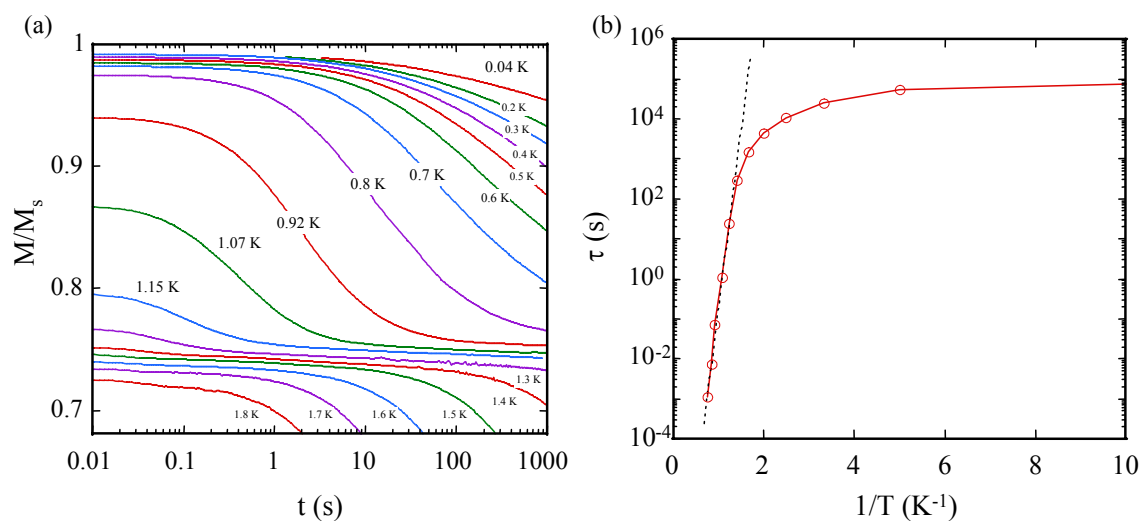


Figure 6-20. Relaxation time vs temperature studies for the faster-relaxing species of complex  $21 \cdot 4.5\text{CH}_2\text{Cl}_2 \cdot \frac{1}{2}\text{H}_2\text{O}$ . (a) Plot of magnetization vs time decay in zero field. The magnetization is normalized to its saturation value,  $M_s$ . (b) Plot of relaxation time ( $\tau$ ) vs  $1/T$  for using AC  $\chi_M''$  and DC decay data. The dotted lines are fits to the Arrhenius equation. See Table 6-11 for the fit parameters.

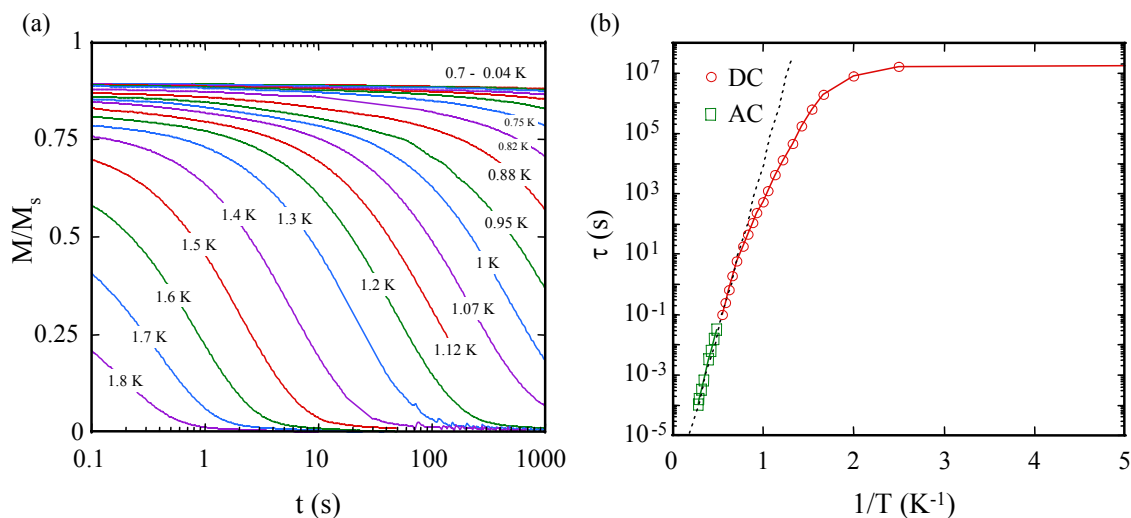


Figure 6-21. Relaxation time vs temperature studies for a single crystal of complex **22**·6C<sub>7</sub>H<sub>8</sub>. (a) Plot of magnetization vs time decay in zero field. The magnetization is normalized to its saturation value,  $M_s$ . (b) Plot of relaxation time ( $\tau$ ) vs  $1/T$  for using AC  $\chi_M''$  and DC decay data. The dotted lines are fits to the Arrhenius equation. See Table 6-11 for the fit parameters.

There is an interesting discrepancy between the AC and DC data for **21** in Figure 6-19, which give  $U_{\text{eff}} = 53$  K,  $\tau_0 = 4.9 \times 10^{-9}$  s and  $U_{\text{eff}} = 49$  K,  $\tau_0 = 3.0 \times 10^{-10}$  s, respectively. Thus, the slopes of the plots (i.e., the  $U_{\text{eff}}$  values) are almost the same within experimental uncertainty, but the significant difference in  $\tau_0$  values (almost an order of magnitude) causes a noticeable offset. Both the AC and DC measurements were repeated several times on different crystals with the same result. We are not sure of the exact origin of this difference, but it may be due to differences caused by the differing mounting conditions; the AC data were obtained on crystals, maintained in mother liquor, that were quickly transferred to the SQUID and cooled to low temperatures to avoid solvent loss, whereas the DC data were on single crystals in Apiezon grease. Crystals of **21**·4.5CH<sub>2</sub>Cl<sub>2</sub>·½H<sub>2</sub>O are very sensitive to solvent loss and readily fracture even under grease, making handling very difficult. Note that hysteresis loops described below also

show greater complexity for **21**·4.5CH<sub>2</sub>Cl<sub>2</sub>·½H<sub>2</sub>O compared with those for **20**·3CH<sub>2</sub>Cl<sub>2</sub> and **22**·6C<sub>7</sub>H<sub>8</sub>.

#### 6.2.5.4 Variable-frequency AC susceptibility studies

To further understand the nature of the magnetization relaxation processes in these clusters, more detailed AC experiments were carried out on wet crystals of **20**·3CH<sub>2</sub>Cl<sub>2</sub>, **21**·4.5CH<sub>2</sub>Cl<sub>2</sub>·½H<sub>2</sub>O, and **22**·6C<sub>7</sub>H<sub>8</sub>. At a fixed temperature of 4.0 K (**20**), 3.4 K (**21**) and 2.2 K (**22**), the in-phase ( $m'$ ) and out-of-phase ( $m''$ ) components of the AC magnetic susceptibility were measured as the frequency ( $\nu$ ) of oscillating AC field was varied in the range of 0.1-1500 Hz. For a single relaxation process, the  $m'$  and  $m''$  behavior as a function of angular frequency ( $\omega$ ) is given by eqs 6-7 and 6-8, respectively, while for a distribution of single relaxation processes, the  $m'$  and  $m''$  behavior is expressed by eqs 6-9 and 6-10, respectively,

$$\chi'(\omega) = \chi_s + \frac{(\chi_T - \chi_s)}{1 + \omega^2 \tau^2} \quad (6-7)$$

$$\chi''(\omega) = \frac{(\chi_T - \chi_s)\omega\tau}{1 + \omega^2 \tau^2} \quad (6-8)$$

$$\chi'(\omega) = \chi_s + \frac{(\chi_T - \chi_s)[1 + (\omega\tau)^{1-\alpha} \sin(\alpha\pi/2)]}{1 + 2(\omega\tau)^{1-\alpha} \sin(\alpha\pi/2) + (\omega\tau)^{2(1-\alpha)}} \quad (6-9)$$

$$\chi''(\omega) = \chi_s + \frac{(\chi_T - \chi_s)(\omega\tau)^{1-\alpha} \cos(\alpha\pi/2)}{1 + 2(\omega\tau)^{1-\alpha} \sin(\alpha\pi/2) + (\omega\tau)^{2(1-\alpha)}} \quad (6-10)$$

where  $\chi_s$  is the adiabatic susceptibility,  $\chi_T$  is the isothermal susceptibility,  $\omega = 2\pi\nu$  is the angular frequency, and  $\tau$  is the magnetization relaxation time. An additional parameter,  $\alpha$ , which takes a value between 0 and 1 and gauges the width of the distribution, is included in the expressions for a distribution of single relaxation processes. Plots of  $m'$  vs  $m''$  (Cole-Cole or Argand plots) are shown for complexes **20-22** in the top, middle, and

bottom panels of Figure 6-22, respectively.<sup>176</sup> A least-squares fitting of the data to a single relaxation process is shown as a dashed line while the fitting to a distribution of single relaxation processes is shown as a solid line; clearly, significantly improved fits are obtained for the latter. On this basis, it is concluded that in wet crystals of complexes **20-22** the magnetization relaxes via only a single process and that there is a distribution in this single relaxation process (i.e., a distribution of relaxation barriers).

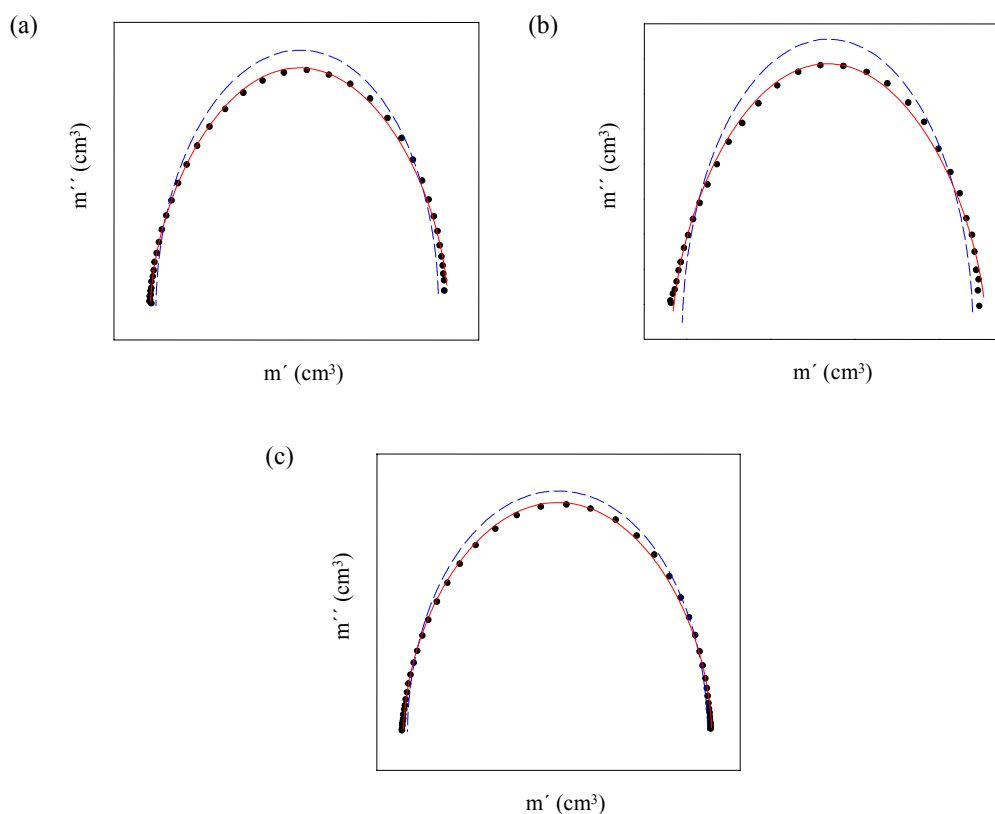


Figure 6-22. Argand plot of  $m'$  vs  $m''$  for wet crystals of (a) complex **20**· $3\text{CH}_2\text{Cl}_2$  at 4.0 K, (b) complex **21**· $4.5\text{CH}_2\text{Cl}_2 \cdot \frac{1}{2}\text{H}_2\text{O}$  at 3.4 K and (c) complex **22**· $6\text{C}_7\text{H}_8$  at 2.2 K. The dashed lines (blue) are a least-squares fitting of the data to a single relaxation process as described by eqs 6-7 and 6-8. The solid lines (red) are a least-squares fitting of the data to a distribution of single relaxation processes as described by eqs 6-9 and 6-10; see Table 6-12 for the fit parameters.

In Figures 6-23, 6-24 and 6-25 are shown plots of  $m'$  vs frequency and  $m''$  vs frequency for wet crystals of complexes **20-22**. As expected, least-squares fitting of the data to a distribution of single relaxation processes (solid red line) is better than that to

only a single relaxation process (dashed blue line). The relaxation times ( $\tau$ ) obtained from the two fitting schemes are very similar for each complex, and the main difference in the fitting parameters occurs in the values of the adiabatic and isothermal susceptibility.

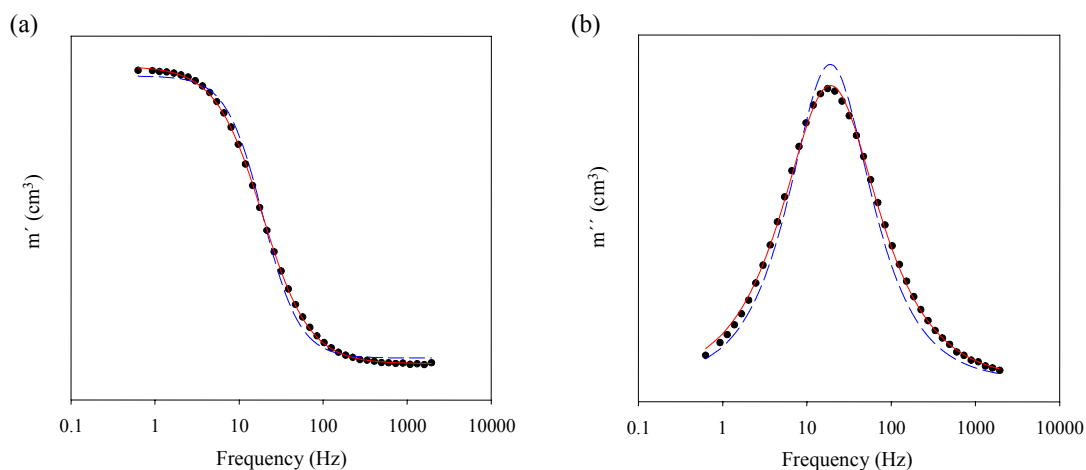


Figure 6-23. Plot of (a) the in-phase ( $m'$ ) and (b) the out-of-phase ( $m''$ ) AC magnetic susceptibility vs frequency at 4.0 K for complex  $20 \cdot 3\text{CH}_2\text{Cl}_2$ . The dotted lines (blue) are a least-squares fitting of the data to a single relaxation process. The solid lines (red) are a least-squares fitting of the data to a distribution of single relaxation processes; see Table 6-12 for the fit parameters.

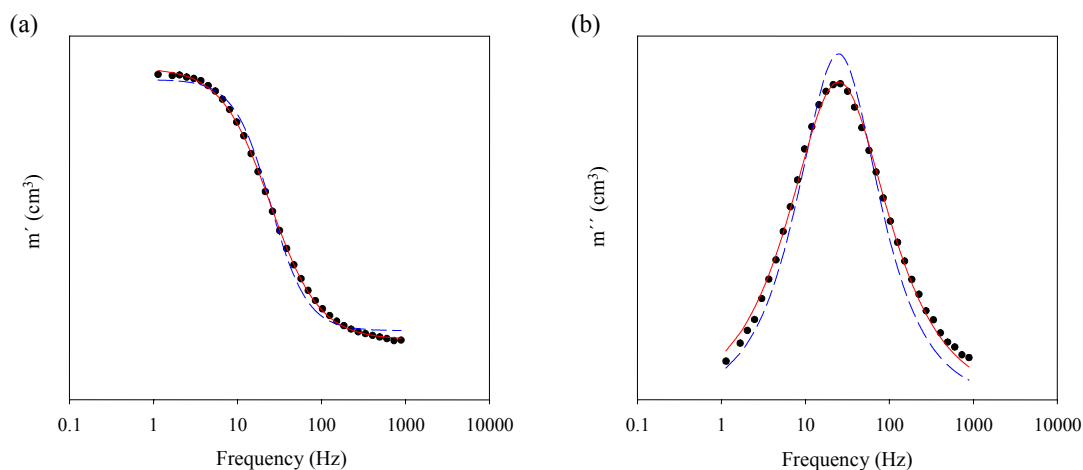


Figure 6-24. Plot of (a) the in-phase ( $m'$ ) and (b) the out-of-phase ( $m''$ ) AC magnetic susceptibility vs frequency at 3.4 K for complex  $21 \cdot 4.5\text{CH}_2\text{Cl}_2 \cdot \frac{1}{2}\text{H}_2\text{O}$ . The dotted lines (blue) are a least-squares fitting of the data to a single relaxation process. The solid lines (red) are a least-squares fitting of the data to a distribution of single relaxation processes; see Table 6-12 for the fit parameters.

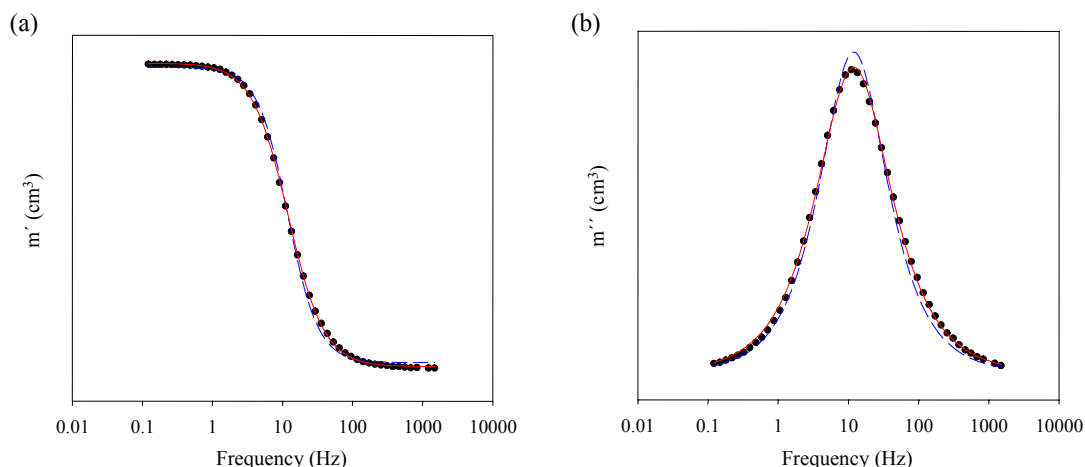


Figure 6-25. Plot of (a) the in-phase ( $m'$ ) and (b) the out-of-phase ( $m''$ ) AC magnetic susceptibility vs frequency at 2.2 K for complex **22**· $6C_7H_8$ . The dotted lines (blue) are a least-squares fitting of the data to a single relaxation process. The solid lines (red) are a least-squares fitting of the data to a distribution of single relaxation processes; see Table 6-12 for the fit parameters.

Table 6-12. Least-squares fitting parameters of the in-phase ( $m'$ ) and out-of-phase ( $m''$ ) AC magnetic susceptibility vs frequency data at 4.0 K for complex **20**· $3CH_2Cl_2$ , 3.4 K for complex **21**· $4.5CH_2Cl_2 \cdot \frac{1}{2}H_2O$  and 2.2 K for complex **22**· $6C_7H_8$  to a single relaxation process or to a distribution of a single relaxation processes.

Compound	Single relaxation process			Distribution of single relaxation processes		
		$m'$	$m''$		$m'$	$m''$
<b>20</b> · $3CH_2Cl_2$	$\chi_S$ ( $cm^3$ )	$2.19 \times 10^{-5}$	0.50	$\chi_S$ ( $cm^3$ )	$1.89 \times 10^{-5}$	-7.00
	$\chi_T$ ( $cm^3$ )	$1.69 \times 10^{-4}$	0.50	$\chi_T$ ( $cm^3$ )	$1.74 \times 10^{-4}$	-7.00
	$\tau$ (s)	0.0515	0.0526	$\tau$ (s)	0.0525	0.0525
				$\alpha$	0.216	0.137
<b>21</b> · $4.5CH_2Cl_2 \cdot \frac{1}{2}H_2O$	$\chi_S$ ( $cm^3$ )	$9.48 \times 10^{-6}$	6.50	$\chi_S$ ( $cm^3$ )	$8.26 \times 10^{-6}$	-7.00
	$\chi_T$ ( $cm^3$ )	$4.40 \times 10^{-5}$	6.50	$\chi_T$ ( $cm^3$ )	$4.57 \times 10^{-5}$	-7.00
	$\tau$ (s)	0.0401	0.0403	$\tau$ (s)	0.0407	0.0401
				$\alpha$	0.249	0.170
<b>22</b> · $6C_7H_8$	$\chi_S$ ( $cm^3$ )	$2.64 \times 10^{-5}$	0.500	$\chi_S$ ( $cm^3$ )	$2.14 \times 10^{-5}$	-7.00
	$\chi_T$ ( $cm^3$ )	$3.82 \times 10^{-4}$	0.500	$\chi_T$ ( $cm^3$ )	$3.86 \times 10^{-4}$	-7.00
	$\tau$ (s)	0.0133	0.0133	$\tau$ (s)	0.0133	0.0133
				$\alpha$	0.155	0.0963

The width of the distribution is gauged by the fitting parameter  $\alpha$ ; average values of  $\alpha$  obtained from fitting of plots of  $m'$  vs frequency and  $m''$  vs frequency to a distribution of single relaxation processes are 0.177 (**20**), 0.210 (**21**), and 0.126 (**22**). A complete listing of the fitting parameters is included in Table 6-12. These results are consistent

with similar studies done on other  $Mn_{12}$  complexes,<sup>100</sup> the main conclusion is that the samples have a distribution of energy relaxation barriers, i.e., a distribution of  $D$  values due to a distribution in local molecular environments. It should be noted that at the temperature was which the measurement was carried out for complex **21**, only the HT (slower-relaxing) isomer was studied. Similar measurements at much lower temperatures are needed to study the LT (faster-relaxing) isomer of **21**.

#### 6.2.5.5 Hysteresis studies below 1.8 K

The AC measurements suggest that complexes **20-22** function as SMMs, and this was confirmed by hysteresis loops obtained from magnetization vs DC field scans. These were performed on single crystals of **20**·3CH<sub>2</sub>Cl<sub>2</sub>, **21**·4.5CH<sub>2</sub>Cl<sub>2</sub>·½H<sub>2</sub>O, and **22**·6C<sub>7</sub>H<sub>8</sub> using a micro-SQUID apparatus.<sup>92</sup> In Figure 6-26 are shown the temperature and scan-rate dependence studies. The coercivities clearly increase with decreasing temperature and increasing scan rate, as expected for the superparamagnet-like behavior of SMMs. The loops also clearly show the steps at periodic values of applied field due to QTM, which causes a surge in the relaxation as  $m_s$  levels on opposite sides of the  $S = 10$  double well potential energy barrier come into resonance at those field positions. The field separation,  $\Delta H$ , between the steps is proportional to  $D$  and is given by eq 6-11.

$$\Delta H = \frac{|D|}{g\mu_B} \quad (6-11)$$

Measurement of the step positions in Figure 6-26 gave an average  $\Delta H$  of 0.475 T, and a resulting  $|D|/g$  value of 0.22 cm<sup>-1</sup>, consistent with both the values obtained from fits of the magnetization data for dried **20** (0.21 cm<sup>-1</sup>) and from the INS studies (0.22 cm<sup>-1</sup>).<sup>164</sup>

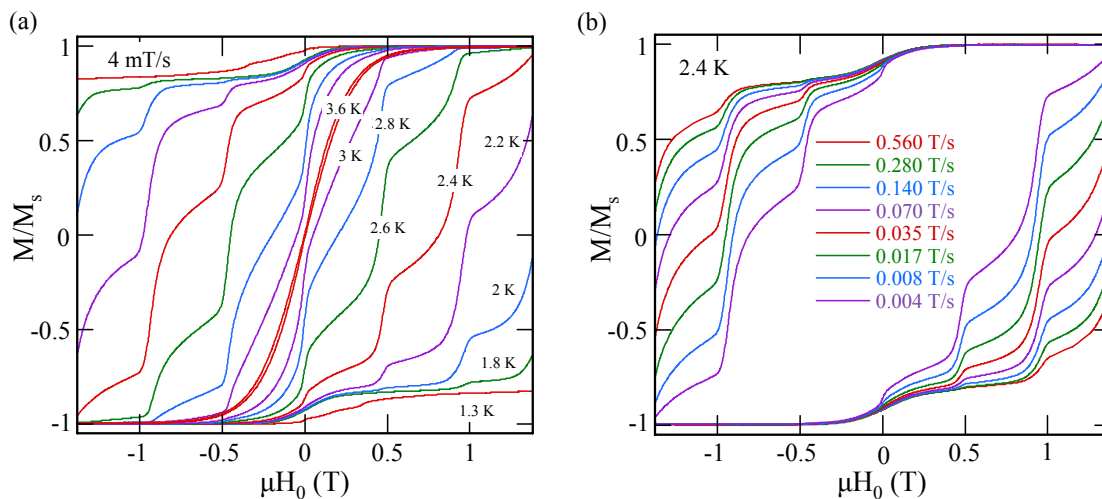


Figure 6-26. Magnetization hysteresis loops for a single crystal of  $20 \cdot 3\text{CH}_2\text{Cl}_2$ : (a) temperature dependence at a fixed scan rate of 4 mT/s; (b) scan-rate dependence at a fixed temperature of 2.4 K.  $M$  is normalized to its saturation value,  $M_s$ .

The corresponding hysteresis loops on **21** are shown in Figures 6-27 and 6-28.

They clearly reveal two different species within the crystal. Approximately 28% of the molecules have smaller  $U_{\text{eff}}$  and  $D$  values than the remaining 72%. Analysis of the step positions of the faster-relaxing species (28%) gave an average  $\Delta H \approx 0.18$  T and  $|D|/g \approx 0.042$   $\text{cm}^{-1}$ , whereas the slower-relaxing species (72%) gave  $\Delta H \approx 0.33$  T and  $|D|/g \approx 0.15$   $\text{cm}^{-1}$ . The logical conclusion is that the two isomers of **21** detected in the crystal structure in  $\sim 77:23\%$  ratio correspond to the two species detected in the hysteresis loops of Figures 6-27 and 6-28 in a  $\sim 72:28\%$  ratio. The much smaller  $D$  value of the minor component and the resulting small  $U_{\text{eff}}$  would be consistent with the AC  $\chi_M''$  signal occurring at  $< 1.8$  K and thus not observed in Figures 6-15 and 6-16. Of course, we cannot rule out that the same  $\sim 3:1$  ratio of two species in the crystal structure and the hysteresis loops may just be a coincidence, and the faster-relaxing species may in reality be due to a JT isomer with an abnormally-oriented JT axis statically disordered about multiple  $\text{Mn}^{\text{III}}$  ions and thus not showing up in the structural parameters of the X-ray

structure. Finally, examination of the loop coercivities for each sub-species shows that both exhibit the temperature and scan-rate dependence of a SMM.

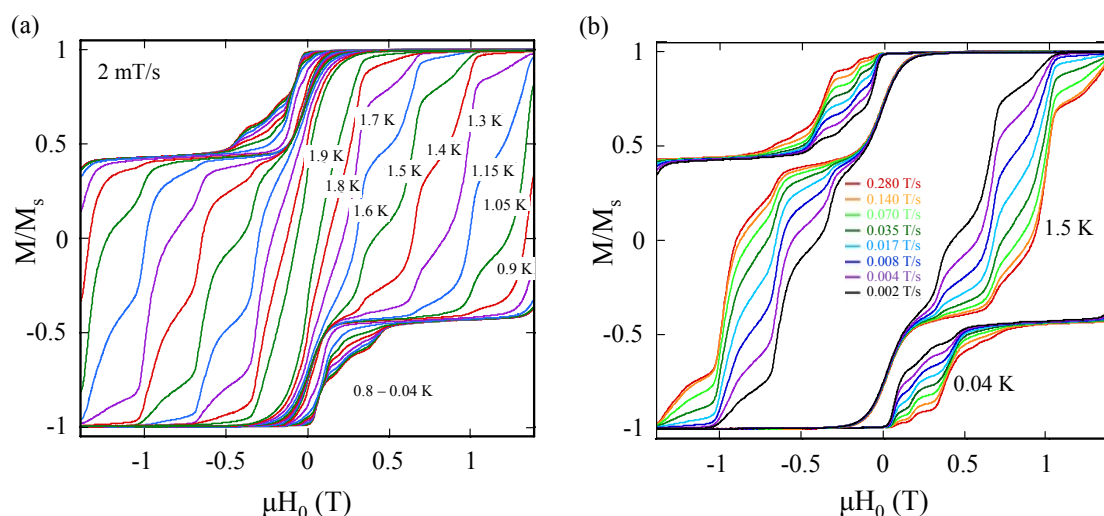


Figure 6-27. Magnetization hysteresis loops for a single crystal of  $21 \cdot 4.5\text{CH}_2\text{Cl}_2 \cdot \frac{1}{2}\text{H}_2\text{O}$ : (a) temperature dependence at a fixed scan rate of 2 mT/s; (b) scan-rate dependence at a fixed temperature of 0.04 K. Loops for both the faster- and slower-relaxing species are shown.  $M$  is normalized to its saturation value,  $M_s$ .

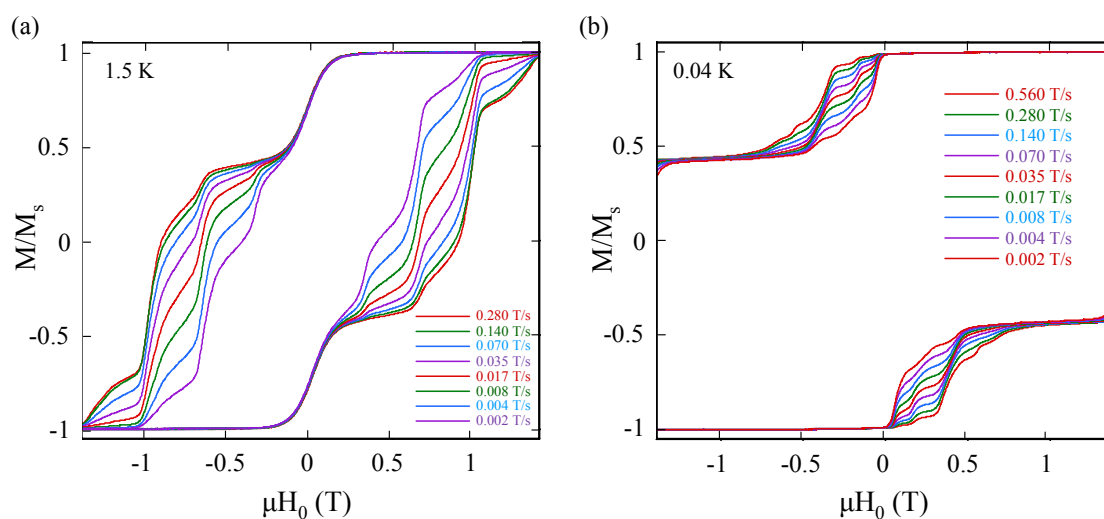


Figure 6-28. Magnetization hysteresis loops for a single crystal of  $21 \cdot 4.5\text{CH}_2\text{Cl}_2 \cdot \frac{1}{2}\text{H}_2\text{O}$ : (a) scan-rate dependence at a fixed temperature of 1.5 K of the slower-relaxing species; (b) scan-rate dependence at a fixed temperature of 0.04 K of the faster-relaxing species.  $M$  is normalized to its saturation value,  $M_s$ .

The corresponding hysteresis loops on **22** are shown in Figure 6-29, and they are overall similar to those for **20**. There is only one species present, and the step pattern is well defined. Again, the coercivities increase with decreasing temperature and increasing scan rate, as expected for a SMM, and as seen previously for another  $[\text{Mn}_{12}]^{2-}$  salt.<sup>61</sup> Analysis of the step positions gave  $|D|/g \approx 0.15 \text{ cm}^{-1}$ , a value consistent with that obtained from both INS<sup>164</sup> and magnetization vs field studies on a dried sample of this complex.

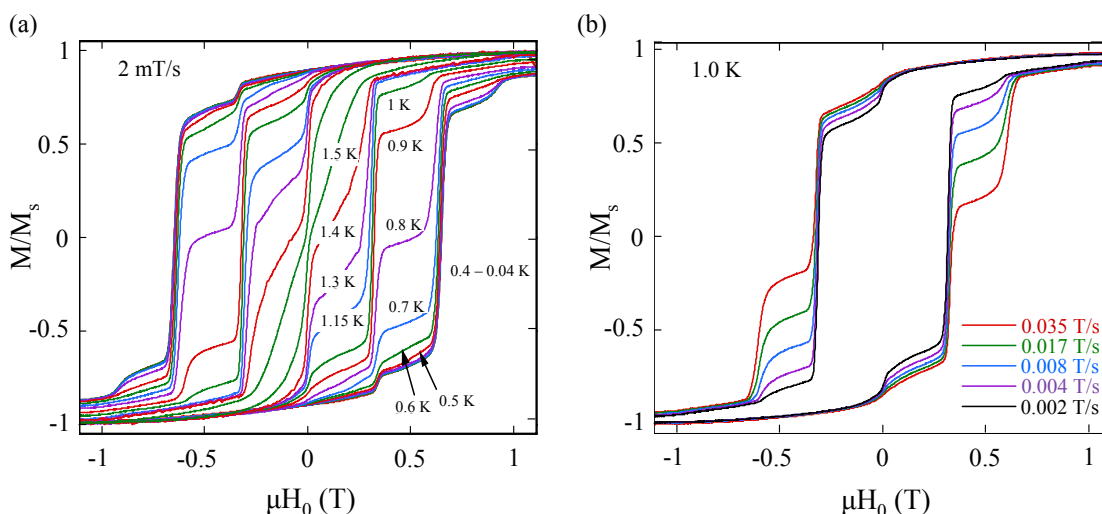


Figure 6-29. Magnetization hysteresis loops for a single crystal of **22**·6C<sub>7</sub>H<sub>8</sub>: (a) temperature dependence at a fixed scan rate of 4 mT/s; (b) scan-rate dependence at a fixed temperature of 2.4 K. *M* is normalized to its saturation value, *M<sub>s</sub>*

### 6.3 Conclusions

The goal of this investigation was to study the effect of reduction on the magnetic properties of a family of Mn<sub>12</sub> SMMs with identical peripheral ligation. The syntheses, crystal structures and magnetic properties have been obtained on such a family with pentafluorobenzoate ligands spanning three oxidation levels. <sup>19</sup>F NMR spectra have been obtained on all three complexes, establishing retention of the structures on dissolution, with fast de-trapping (on the <sup>19</sup>F NMR timescale) of the added electrons leading to effective *D*<sub>2d</sub> solution symmetry in every case. AC and DC susceptibility studies on dried,

microcrystalline samples of **20-22** establish that  $S = 10, 19/2,$  and  $10$  for **20-22**, respectively, and show a decrease in the  $|D|$  value with decreasing  $\text{Mn}^{\text{III}}$  content, i.e., the magnetic anisotropy decreases with reduction, and the magnetization relaxation rate thus increases. Magnetization vs DC field scans exhibit hysteresis, establishing all the compounds to be SMMs. The hysteresis loops also exhibit the steps characteristic of QTM.

AC susceptibility measurements carried out on wet crystals maintained in mother liquor to prevent the loss of interstitial solvent and on dried, microcrystalline samples gave only small differences in  $U_{\text{eff}}$  and  $\tau_0$  between wet and dry samples. However, measurements on wet crystals do avoid certain complications associated with solvent loss, such as an increase in the amount of the faster-relaxing form of **20**. This again emphasizes the importance of comparing data from different techniques using samples maintained in the same way. For example, the data from micro-SQUID hysteresis studies on wet single crystals are best compared to magnetization studies on similarly wet crystals.

## 6.4 Experimental

### 6.4.1 Syntheses

All manipulations were performed under aerobic conditions using materials as received, except where otherwise noted.  $[\text{Mn}_{12}\text{O}_{12}(\text{O}_2\text{CMe})_{16}(\text{H}_2\text{O})_4] \cdot 2\text{MeCO}_2\text{H} \cdot 4\text{H}_2\text{O}$  (**1**) was prepared as described elsewhere.<sup>50</sup>

$[\text{Mn}_{12}\text{O}_{12}(\text{O}_2\text{CC}_6\text{F}_5)_{16}(\text{H}_2\text{O})_4]$  (**20**). A slurry of complex **1** (2.0 g, 0.97 mmol) in  $\text{CH}_2\text{Cl}_2$  (50  $\text{cm}^3$ ) was treated with  $\text{HO}_2\text{CC}_6\text{F}_5$  (3.7 g, 0.017 mol). The solution was stirred overnight and the solvent was removed *in vacuo*. Toluene (20  $\text{cm}^3$ ) was added to the residue, and the solution was again evaporated to dryness. The addition and removal of

toluene was repeated two more times. The remaining solid was redissolved in  $\text{CH}_2\text{Cl}_2$  ( $50\text{ cm}^3$ ) and treated again with  $\text{HO}_2\text{CC}_6\text{F}_5$  (0.41 g, 1.9 mmol). After 12 h, three more cycles of addition and removal of toluene were performed. The residue was redissolved in  $\text{CH}_2\text{Cl}_2$  ( $50\text{ cm}^3$ ) and filtered. An equal volume of heptane was added and the solution was allowed to stand undisturbed at room temperature for 4 days. The resulting black crystals were collected by filtration, washed with heptane, and dried *in vacuo*; yield 91%. Anal. Calcd (found) for  $\mathbf{20} \cdot \text{HO}_2\text{CC}_6\text{F}_5$  ( $\text{C}_{119}\text{H}_9\text{F}_{85}\text{Mn}_{12}\text{O}_{50}$ ): C, 31.86% (31.90%); H, 0.21% (0.38%). A crystallography sample was grown slowly from  $\text{CH}_2\text{Cl}_2$ /heptane and maintained in mother liquor to avoid solvent loss. Selected IR data (KBr,  $\text{cm}^{-1}$ ): 1699 (w), 1604 (vs), 1552 (s), 1507 (s), 1471 (m), 1417 (vs), 1351 (s), 1302 (m), 1231 (s), 1152 (vs), 1091 (m), 1015 (m), 857 (s), 797 (w), 778 (vs), 692 (m), 667 (m), 632 (s, br), 549 (m), 520 (m), 500 (m), 441 (w), 418 (w).

For the preparation of the INS sample, the  $\text{H}_2\text{O}$  molecules were exchanged with  $\text{D}_2\text{O}$  by treatment of  $\mathbf{20}$  (6.0 g, 1.4 mmol) in MeCN ( $100\text{ cm}^3$ ) with  $\text{D}_2\text{O}$  ( $0.50\text{ cm}^3$ , 0.028 mol) under a nitrogen atmosphere. The solution was stirred overnight and the solvent was removed *in vacuo*. The residue was redissolved in  $\text{CH}_2\text{Cl}_2$  ( $150\text{ cm}^3$ ) and filtered. Crystallization of the residue was performed as described above. Anal. Calcd (found) for  $[\text{Mn}_{12}\text{O}_{12}(\text{O}_2\text{CC}_6\text{F}_5)_{16}(\text{D}_2\text{O})_4]$   $\mathbf{23}$  ( $\text{C}_{112}\text{D}_8\text{F}_{80}\text{Mn}_{12}\text{O}_{48}$ ): C, 31.22% (31.30%); H, 0.00% (0.00%).

$(\text{NMe}_4)[\text{Mn}_{12}\text{O}_{12}(\text{O}_2\text{CC}_6\text{F}_5)_{16}(\text{H}_2\text{O})_4]$  ( $\mathbf{21}$ ). Solid NMe<sub>4</sub>I (0.047 g, 0.23 mmol) was added to a stirred dark brown solution of complex  $\mathbf{20}$  (1.0 g, 0.23 mmol) in MeCN ( $70\text{ cm}^3$ ). The solution was stirred overnight with no noticeable color change. Hexanes ( $25\text{ cm}^3$ ) were added to the reaction solution to facilitate the extraction of  $\text{I}_2$ , the hexanes

layer removed, and the MeCN layer evaporated to dryness. The residue was redissolved in MeCN (50 cm<sup>3</sup>), hexanes (25 cm<sup>3</sup>) were again added to extract further I<sub>2</sub>, separated, and the MeCN solution evaporated to dryness. This process was repeated six more times to complete the removal of I<sub>2</sub>. The residue was dissolved in CH<sub>2</sub>Cl<sub>2</sub> (50 cm<sup>3</sup>) and filtered. An equal volume of heptane was added and the solution was allowed to stand undisturbed for 4 days. The resulting black microcrystalline product was recrystallized twice more, filtered, washed with heptane and dried *in vacuo*; yield 74%. Anal. Calcd (found) for **21** (C<sub>116</sub>H<sub>20</sub>F<sub>80</sub>N<sub>1</sub>Mn<sub>12</sub>O<sub>48</sub>): C, 31.85% (32.00%); H, 0.46% (0.47%); N, 0.32% (0.33%). X-ray quality crystals were grown slowly from CH<sub>2</sub>Cl<sub>2</sub>/heptane and maintained in mother liquor to avoid solvent loss. Selected IR data (KBr, cm<sup>-1</sup>): 1649 (s), 1604 (s), 1557 (m), 1522 (s), 1492 (vs), 1417 (vs), 1387 (vs), 1294 (m), 1116 (m), 996 (s), 948 (m), 936 (m), 823 (w), 758 (s), 746 (s), 708 (m), 653 (m), 608 (m), 583 (m), 560 (m), 525 (m), 505 (w), 455 (w), 420 (w).

For the preparation of the INS sample, the H<sub>2</sub>O molecules coordinated to the complex were exchanged with D<sub>2</sub>O by treatment of **21** (6.0 g, 1.3 mmol) in MeCN (100 cm<sup>3</sup>) with D<sub>2</sub>O (0.48 cm<sup>3</sup>, 0.027 mol) under a nitrogen atmosphere. The solution was stirred overnight and the solvent was removed *in vacuo*. The residue was redissolved in CH<sub>2</sub>Cl<sub>2</sub> (150 cm<sup>3</sup>) and filtered. Crystallization of the residue was performed as described above. Anal Calcd. (found) for (NMe<sub>4</sub>)[Mn<sub>12</sub>O<sub>12</sub>(O<sub>2</sub>CC<sub>6</sub>F<sub>5</sub>)<sub>16</sub>(D<sub>2</sub>O)<sub>4</sub>] **24** (C<sub>116</sub>H<sub>12</sub>D<sub>8</sub>F<sub>80</sub>N<sub>1</sub>Mn<sub>12</sub>O<sub>48</sub>): C, 31.79% (31.79%); H, 0.28% (0.21%); N, 0.32% (0.30%).

(NMe<sub>4</sub>)<sub>2</sub>[Mn<sub>12</sub>O<sub>12</sub>(O<sub>2</sub>CC<sub>6</sub>F<sub>5</sub>)<sub>16</sub>(H<sub>2</sub>O)<sub>4</sub>] (**22**). Solid NMe<sub>4</sub>I (0.094 g, 0.47 mmol) was added to a stirred dark brown solution of complex **20** (1.0 g, 0.23 mmol) in MeCN (70 cm<sup>3</sup>). The solution was stirred overnight with no noticeable color change. Hexanes

(25 cm<sup>3</sup>) were added to the reaction solution to facilitate the extraction of I<sub>2</sub> as for **21**, and the separated MeCN solution was evaporated to dryness. The residue was redissolved in MeCN (50 cm<sup>3</sup>), hexanes (25 cm<sup>3</sup>) were again added, and the solution was evaporated to dryness. This process was repeated six more times to complete the removal of I<sub>2</sub>. The residue was dissolved in CH<sub>2</sub>Cl<sub>2</sub> (50 cm<sup>3</sup>) and filtered. Crystals were obtained by addition of a mixture of heptane and toluene to the CH<sub>2</sub>Cl<sub>2</sub> solution. The resulting black microcrystalline product was recrystallized twice, filtered, washed with heptane and dried *in vacuo*; yield 70%. Anal Calcd. (found) for **22** (C<sub>120</sub>H<sub>32</sub>F<sub>80</sub>N<sub>2</sub>Mn<sub>12</sub>O<sub>48</sub>): C, 32.40% (32.39%); H, 0.73% (0.68%); N, 0.63% (0.63%). X-ray quality crystals were grown slowly from CH<sub>2</sub>Cl<sub>2</sub>/heptane-toluene (1:1), and maintained in mother liquor to avoid solvent loss. Selected IR data (KBr, cm<sup>-1</sup>): 1616 (vs), 1523 (vs), 1489 (vs), 1381 (vs), 1356 (s), 1291 (m), 1105 (m), 993 (s), 950 (m), 930 (m), 832 (w), 764 (s), 752 (s), 738 (s), 583 (s, br), 508 (m).

For the preparation of the INS sample, the H<sub>2</sub>O molecules coordinated to the complex were exchanged with D<sub>2</sub>O by treatment of **22** (6.0 g, 1.3 mmol) in MeCN (100 cm<sup>3</sup>) with D<sub>2</sub>O (0.46 cm<sup>3</sup>, 0.026 mol) under a nitrogen atmosphere. The solution was stirred overnight and the solvent was removed *in vacuo*. The residue was redissolved in CH<sub>2</sub>Cl<sub>2</sub> (150 cm<sup>3</sup>) and filtered. Crystallization of the residue was performed as described above. Anal Calcd. (found) for (NMe<sub>4</sub>)<sub>2</sub>[Mn<sub>12</sub>O<sub>12</sub>(O<sub>2</sub>CC<sub>6</sub>F<sub>5</sub>)<sub>16</sub>(D<sub>2</sub>O)<sub>4</sub>] **25** (C<sub>120</sub>H<sub>24</sub>D<sub>8</sub>F<sub>80</sub>N<sub>2</sub>Mn<sub>12</sub>O<sub>48</sub>): C, 32.34% (32.47%); H, 0.54% (0.41%); N, 0.63% (0.70%).

#### 6.4.2 X-ray Crystallography

Data were collected using a Siemens SMART PLATFORM equipped with a CCD area detector and a graphite monochromator utilizing MoK $\alpha$  radiation ( $\lambda = 0.71073 \text{ \AA}$ ). Suitable single crystals of **20**·3CH<sub>2</sub>Cl<sub>2</sub>, **21**·4.5CH<sub>2</sub>Cl<sub>2</sub>·½H<sub>2</sub>O and **22**·6C<sub>7</sub>H<sub>8</sub> were attached

to glass fibers using silicone grease and transferred to the goniostat where they were cooled to  $-80^{\circ}\text{C}$  (**20** and **21**) and  $-80^{\circ}\text{C}$  (**22**) for characterization and data collection. Each structure was solved by direct methods (SHELXTL)<sup>64</sup> and standard Fourier techniques, and was refined using full-matrix least-squares methods. All non-hydrogen atoms were refined anisotropically. Cell parameters were refined using up to 8192 reflections. For each complex, a full sphere of data (1850 frames) was collected using the  $\omega$ -scan method ( $0.3^{\circ}$  frame width). The first 50 frames were re-measured at the end of data collection to monitor instrument and crystal stability (maximum correction on I was  $< 1\%$ ). Absorption corrections by integration were applied based on measured indexed crystal faces.

A preliminary search of reciprocal space for **20** $\cdot 3\text{CH}_2\text{Cl}_2$  revealed a set of reflections with no symmetry and no systematic absences. An initial choice of the centrosymmetric space group  $P\bar{1}$  was subsequently confirmed by the successful solution of the structure. The asymmetric unit contains the  $\text{Mn}_{12}$  molecule and three disordered  $\text{CH}_2\text{Cl}_2$  molecules of crystallization. The solvent molecules were significantly disordered and could not be modeled properly. Hence, the program SQUEEZE,<sup>96</sup> a part of the PLATON<sup>97</sup> package of crystallographic software, was used to calculate the solvent disorder area and remove its contribution to the overall intensity data. The pentafluorophenyl rings in two of the  $\text{C}_6\text{F}_5\text{CO}_2^-$  ligands [C(9)-C(14) and C(16)-C(21)] were disordered over two positions, whose site occupancy factors were dependently refined to 70:30% and 54:46%, respectively. Hydrogen atoms of the water ligands were not located and therefore not included in the final cycle of refinement. A total of 2266 parameters were refined in the final cycle of refinement using 10424 reflections with  $I >$

$2\sigma(I)$  to yield  $R1$  and  $wR2$  of 8.80% and 21.79%, respectively. The final difference Fourier map was essentially featureless, the largest peak being  $1.211 \text{ e } \text{\AA}^{-3}$  and the deepest hole being  $-0.702 \text{ e } \text{\AA}^{-3}$ .

For complex **21**· $4.5\text{CH}_2\text{Cl}_2 \cdot \frac{1}{2}\text{H}_2\text{O}$ , an initial survey of a portion of reciprocal space located a set of reflections with a monoclinic lattice. Analysis of the full data set revealed that the space group was  $P2/c$ . The asymmetric unit contains the  $\text{Mn}_{12}$  molecule, two one-half  $\text{NMe}_4^+$  cations, 4.5  $\text{CH}_2\text{Cl}_2$  molecules, and half of a water molecule of crystallization. Hydrogen atoms of the cations and solvent molecules were calculated in ideal positions and were refined with the use of a riding model. The hydrogen atoms of the four coordinated water molecules were located from a difference Fourier map and refined freely. A disorder was observed involving a water molecule [O(17)] and a pentafluorobenzoate ligand [O(21)-C(64)-C(18)]. Each was refined in two positions with their site occupancies being 77:23%. Atoms of the minor disorder position were refined with isotropic thermal parameters. A total of 2479 parameters were refined in the final cycle of refinement using 18144 reflections with  $I > 2\sigma(I)$  to yield  $R1$  and  $wR2$  of 5.34% and 13.25%, respectively. The final difference Fourier map was essentially featureless, with the largest peak and deepest hole being  $1.704$  and  $-1.540 \text{ e } \text{\AA}^{-3}$ , respectively.

A preliminary search of reciprocal space for **22**· $6\text{C}_7\text{H}_8$  revealed a set of reflections with a monoclinic lattice. An initial choice of the space group  $C2/c$  was subsequently confirmed by the successful solution of the structure. The asymmetric unit contains half of the  $\text{Mn}_{12}$  molecule, two toluene molecules in general positions, two one-half toluene molecules, each of which is disordered over a center of inversion, and one  $\text{NMe}_4^+$  cation. Hydrogen atoms were calculated in ideal positions and were refined with the use of a

riding model. The pentafluorophenyl rings in two of the  $\text{C}_6\text{F}_5\text{CO}_2^-$  ligands [C(16)-C(21) and C(51)-C(56)] were disordered over two sites, whose site occupancy factors were dependently refined to 58:42% and 50:50%, respectively. A total of 1415 parameters were refined in the final cycle of refinement using 7055 reflections with  $I > 2\sigma(I)$  to yield  $R1$  and  $wR2$  of 5.81% and 14.31%, respectively. The final difference Fourier maps were reasonably clean, the maximum and minimum residual electron density being  $0.933 \text{ e } \text{\AA}^{-3}$  and  $-0.620 \text{ e } \text{\AA}^{-3}$ , respectively.

CHAPTER 7  
EFFECT OF SYMMETRY ON MAGNETIC BEHAVIOR: A STUDY OF THE HIGH-  
SYMMETRY  $Mn_{12}$  SINGLE-MOLECULE MAGNET  $[Mn_{12}O_{12}(O_2CCH_2Br)_{16}(H_2O)_4]$

**7.1 Introduction**

Mesoscopic physics, an area of research that focuses on the boundary between classical and quantum behavior, has become a very attractive and intensely studied field, particularly since the discovery of quantum effects in single-molecule magnets (SMMs) in 1996.<sup>19,27,92,135,136,160,177,178</sup> The crossover between the classical and quantum regimes of behavior can be explored experimentally by observing signatures of quantum mechanical behavior, including quantum tunneling of magnetization (QTM), quantum phase interference and quantum coherence, in macroscopic systems.<sup>160,162,163</sup> Materials that exhibit such mesoscopic quantum phenomena have potential applications in numerous areas, including quantum computing and magnetic information storage,<sup>135,158,159</sup> and as such, are actively investigated both for fundamental scientific and for technological interests.<sup>20,28,179,180</sup>

Single-molecule magnets, or molecules that function as single-domain magnetic particles are ideal systems for the investigation of quantum effects on macroscopic magnetization, offering numerous advantages over higher dimensionality, more complex magnetic systems. These advantages are largely a consequence of their well-defined structure; a single crystal of a SMM is an ordered ensemble of non-interacting molecules with a defined orientation with respect to the cell axes (Figure 7-1). The magnetic

response is amplified by the number of molecules in the crystal and macroscopic measurements give direct access to single-molecule properties.

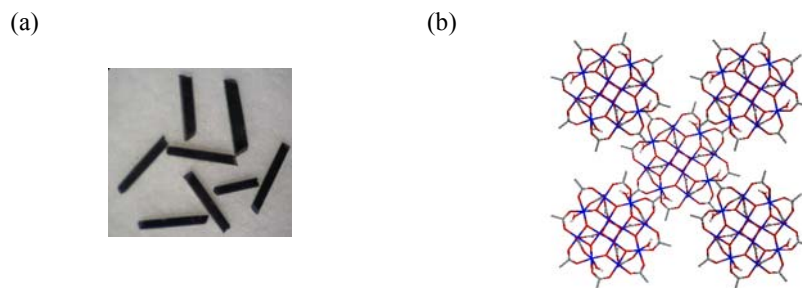


Figure 7-1. Representations of the structure of **1**. (a) Photograph of seven crystals and (b) packing diagram showing the orientation of molecules of **1** relative to each other with respect to the *z* axis (long axis) of an individual crystal.

In 1996 it was reported that the dodecanuclear mixed-valence, trapped-valence manganese-oxo cluster [Mn<sub>12</sub>O<sub>12</sub>(O<sub>2</sub>CMe)<sub>16</sub>(H<sub>2</sub>O)<sub>4</sub>]·2MeCO<sub>2</sub>H·4H<sub>2</sub>O (**1**), exhibits quantum tunneling of magnetization (QTM) as evidenced by a previously unseen field dependence of the relaxation rate of the magnetization (Figure 7-2).<sup>27</sup> With this observation of quantum tunneling of magnetization as step-like features in the hysteresis loops of **1**, the interface between classical and quantum behavior was finally bridged. Not only unique to this molecule, the quantum phenomenon was also observed in the octanuclear Fe<sup>III</sup> oxo-hydroxo cluster [Fe<sub>8</sub>O<sub>2</sub>(OH)<sub>12</sub>(tacn)<sub>6</sub>]<sup>8+</sup> (tacn = 1, 4, 7-triazacyclononane)<sup>31</sup> and has since been seen in numerous other SMMs. Subsequently, much research was devoted to an in-depth understanding of the magnetic behavior of single-molecule magnets, specifically complex **1**. This cluster was the first known member of the Mn<sub>12</sub> SMM family and until recently was the most ideal candidate for study by numerous techniques, owing to its crystallographic tetragonal symmetry.

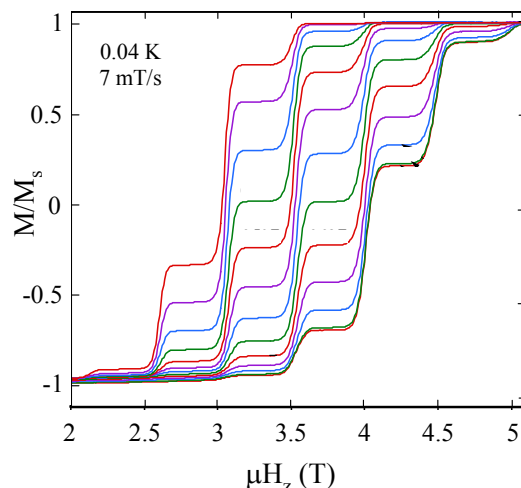


Figure 7-2. Magnetization ( $M$ ) vs field of a single crystal of complex **1** at the indicated field sweep rate at 0.04 K. Transverse fields are applied along the  $z$  axis of the crystal and  $M$  is normalized to its saturation value,  $M_s$ .

The symmetry of a SMM strongly influences its magnetic behavior, dictating selection rules as described by certain terms in the spin Hamiltonian of the molecule, an example of which is given in eq 7-1.

$$\hat{H} = D\hat{S}_z^2 + E(\hat{S}_x^2 + \hat{S}_y^2) + \mu_B \vec{H} \cdot \vec{g} \cdot \hat{S} + B_4^0 \hat{O}_4^0 + B_4^4 \hat{O}_4^4 + \hat{H}' \quad (7-1)$$

The first term represents the second order uniaxial magnetic anisotropy of the molecule ( $D$  is the axial anisotropy constant and  $\hat{S}_z$  is the spin projection operator along the easy-axis of the molecule), the second term represents the second order transverse anisotropy ( $E$  is the rhombic anisotropy constant and  $\hat{S}_x$  and  $\hat{S}_y$  are the  $x$  and  $y$  projections of the total spin operator  $\hat{S}$ ), the third term represents the Zeeman interaction with an applied magnetic field  $H$ , the third and fourth terms represent the fourth order uniaxial and transverse anisotropy ( $B_4^0$  and  $B_4^4$  are the fourth order uniaxial and transverse anisotropy constants), respectively, and  $\hat{H}'$  represents environmental couplings such as hyperfine, dipolar and exchange interactions.<sup>26</sup> Quantum tunneling of magnetization is predicted when there are transverse terms in the spin Hamiltonian that do not commute with  $\hat{S}_z$ .

Such terms are provided by: (i) allowed transverse anisotropy terms for systems in which  $x \neq y \neq z$  directions; (ii) transverse components of the magnetic fields due to dipolar interactions and/or hyperfine nuclear fields; and (iii) the Zeeman interaction associated with the transverse component of the external magnetic field. Mixing of degenerate  $m_s$  sublevels on opposite sides of the double well potential describing the  $S = 10$  ground state spin of the  $Mn_{12}$  molecule occurs in the presence of transverse interactions, causing a small tunnel splitting,  $\Delta$ , and allowing relaxation of the magnetization by quantum tunneling through the two  $m_s$  sublevels separated in energy by the tunnel splitting. A few of the techniques that have been used to study the magnetic behavior of the model  $Mn_{12}$  system,  $[Mn_{12}O_{12}(O_2CMe)_{16}(H_2O)_4] \cdot 2MeCO_2H \cdot 4H_2O$ , include inelastic neutron scattering (INS), high-frequency electron paramagnetic resonance (HFEP), low-temperature hysteresis/magnetization measurements, and  $^{55}Mn$  nuclear magnetic resonance. Although these techniques have provided substantial information about the magnetic properties of the cluster, many questions still remain concerning certain abnormal features exhibited by **1** at low temperatures. These include the absence of tunneling selection rules and multiple, broad EPR absorption peaks.

Until recently, it was assumed on the basis of X-ray diffraction studies that molecules of **1** possess strict axial symmetry, i.e., the second order transverse anisotropy constant,  $E$ , is zero. The remaining terms in the spin Hamiltonian allow quantum tunneling of magnetization only from even-numbered  $m_s$  to odd-numbered  $m_s$  sublevels. However, hysteresis loops collected on single crystals of **1** reveal that in addition to even-to-odd resonances, there are also steps that correspond to tunneling from odd-to-even  $m_s$  sublevels. These resonances are forbidden by a spin Hamiltonian that assumes strict axial

symmetry, and hence there is not an obvious explanation to account for these resonances. Several reasons have been proposed to account for this strange magnetic behavior of **1** however. These include crystal dislocations that give rise to local rotations of the anisotropy axes (Figure 7-3). These local rotations give rise to a broad distribution of tunneling rates and account for odd tunneling resonances. Unfortunately, the predicted distributions are considerably broader than those observed experimentally.<sup>181</sup> Very recently, on the basis of X-ray studies, Cornia and others have proposed a more realistic model involving a discrete disorder associated with the acetic acid molecule of crystallization of **1**. This disorder also gives rise to a locally varying rhombicity and hence a distribution of tunneling rates. However, the predicted distribution in this case more closely resembles that which is experimentally observed.<sup>173</sup>

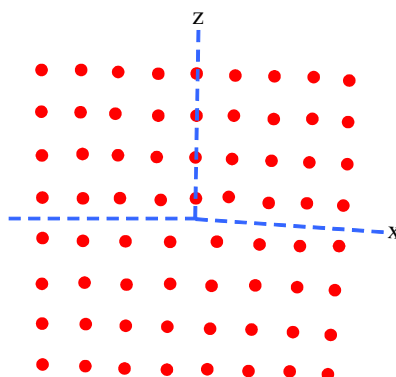


Figure 7-3. Edge dislocation along the  $y$  axis with the extra plane  $y, z$  inserted at  $z > 0$ .

Until recently, there was only one  $Mn_{12}$  complex that met the requirements for strict axial symmetry.<sup>50</sup> Unfortunately, the majority of mono-substituted neutral  $Mn_{12}$  clusters crystallize in space groups in which the crystallographic symmetry is two-fold or less. In fact, the only two mono-substituted published  $Mn_{12}$  clusters with 3-fold or greater symmetry are  $[Mn_{12}O_{12}(O_2CMe)_{16}(H_2O)_4] \cdot 2MeCO_2H \cdot 4H_2O$  (**1**) and  $[Mn_{12}O_{12}(O_2CCH_2Br)_{16}(H_2O)_4]$  (**26**).<sup>50,182</sup> Each of these complexes crystallizes in a

tetragonal space group,  $I\bar{4}$  for **1** and  $I4_1/a$  for **26**, with the molecules possessing  $S_4$  crystallographic symmetry. The difference of space group is of no consequence for the magnetic properties of these complexes; instead, the primary difference between the two clusters involves the nature of the solvent molecules of crystallization. In the case of **1**, the cluster crystallizes with four  $H_2O$  and two  $MeCO_2H$  molecules. The acetic acid molecules are disordered over sites with two-fold symmetry so the site occupancy is 50:50% (Figure 7-4).

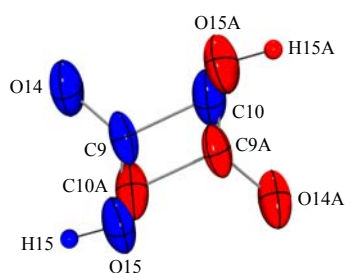


Figure 7-4. ORTEP representation in PovRay format of the two-fold disorder of the  $MeCO_2H$  solvent molecules of crystallization in complex **1**. A crystallographic  $C_2$  rotation axis (not shown) passes through the center of the two  $MeCO_2H$  molecules.

Disordered acetic acid molecules have been proposed to give rise to a locally varying rhombic anisotropy that breaks the axial symmetry of complex **1** and accounts for some of the abnormal behavior of the molecule.<sup>172</sup> This disordered acetic acid molecule is strongly hydrogen-bonded to an acetate ligand on the cluster that bridges two  $Mn^{III}$  ions (Figure 7-5) [ $O(15)\cdots O(6) = 2.866(6)$  Å and  $O(15)-H(15)\cdots O(6) = 174.6(3)^\circ$ ]. Complex **26** also possesses crystallographic axial symmetry, but instead of having acetic acid molecules of crystallization, the molecule crystallizes with four relatively inert dichloromethane molecules (Figure 7-6b).

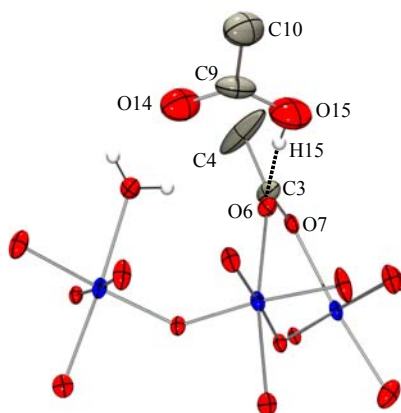


Figure 7-5. ORTEP representation in PovRay format of the hydrogen-bonding interaction between an MeCO<sub>2</sub>H molecule of crystallization [O(14), O(15), C(9), C(10), H(15)] and an MeCO<sub>2</sub><sup>-</sup> ligand [O(6), O(7), C(3), C(4)] bridging Mn<sup>III</sup>Mn<sup>III</sup> pairs in complex **1**.

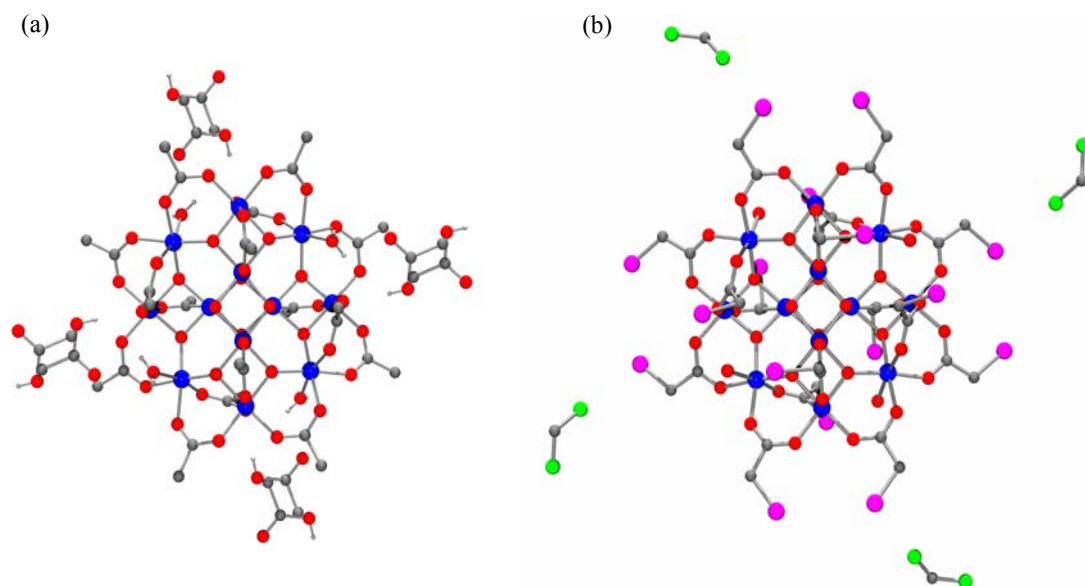


Figure 7-6. ORTEP representation in PovRay format of (a) [Mn<sub>12</sub>O<sub>12</sub>(O<sub>2</sub>CMe)<sub>16</sub>(H<sub>2</sub>O)<sub>4</sub>] with MeCO<sub>2</sub>H solvent molecules of crystallization and (b) [Mn<sub>12</sub>O<sub>12</sub>(O<sub>2</sub>CCH<sub>2</sub>Br)<sub>16</sub>(H<sub>2</sub>O)<sub>4</sub>] with CH<sub>2</sub>Cl<sub>2</sub> solvent molecules of crystallization. Mn blue; O red; C gray; Br pink; Cl green; H light gray.

The abnormal features in the hysteresis loops and EPR spectra of **1** constitute a key reason for an in-depth study of complex **26**, to see if the same features are observed in the absence of hydrogen-bonding of a carboxylate ligand of the cluster with the solvent. The acetate ligand that is involved in this strong hydrogen-bonding interaction is the one

shown in Figure 7-5, consisting of atoms O(6), O(7), C(3), and C(4). Atom O(6) and the neighboring methyl C(4) atom exhibit unusually large displacement parameters at room temperature compared with the remaining acetate ligands, possibly reflecting unresolved disorder (Table 7-1). To investigate this issue in more detail, Cornia and others collected a new set of X-ray diffraction data at 83 K.<sup>173</sup> Preliminary structure refinement showed abnormal elongation of the displacements ellipsoids of atoms O(6) and C(4) and to a lesser extent, O(7) and C(3). This MeCO<sub>2</sub><sup>-</sup> ligand was consequently modeled over two positions, A and B, shown in green and purple colors, respectively; site occupancy factors refined to 0.46 and 0.54, respectively. When the acetate ligand occupies the A position, the hydrogen-bonding interaction with the MeCO<sub>2</sub>H solvent molecule exists (Figure 7-7).

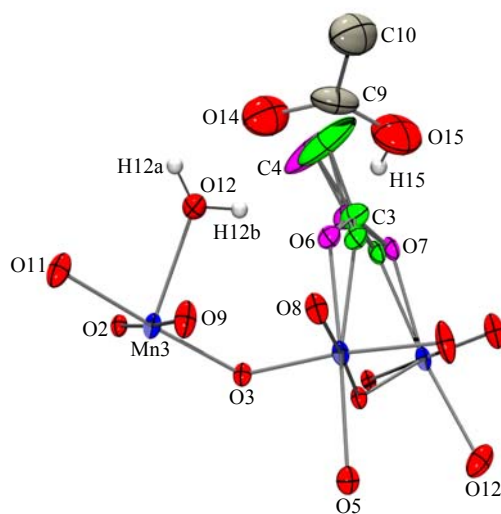


Figure 7-7. ORTEP representation in PovRay format with thermal ellipsoids at the 50% probability level of the coordination sphere of Mn(2) and Mn(3) of complex **1**, showing the model of the MeCO<sub>2</sub><sup>-</sup> ligand over two positions. A = green and B = purple.

Table 7-1. Debye-Waller thermal parameters for (i) atoms of MeCO<sub>2</sub><sup>-</sup> ligand involved in hydrogen-bonding interaction with MeCO<sub>2</sub>H solvent molecules of crystallization and (ii) atoms of MeCO<sub>2</sub><sup>-</sup> ligands not involved in this interaction.

$B_{\text{eq}}, \text{\AA}^2$	C	O
Disordered MeCO <sub>2</sub> <sup>-</sup>	15.06 [C(4)]	4.35 [O(6)]
Normal MeCO <sub>2</sub> <sup>-</sup>	4.07 – 4.38	2.19 – 3.25

The new study shows that the disorder of the acetic acid molecule is transmitted to the  $Mn_{12}$  units via a strong hydrogen-bonding interaction. Since the number of hydrogen-bonded acetic acid molecules which surround each  $Mn_{12}$  unit can, in principle, range from zero to four, up to six isomeric forms of the cluster can be envisioned and these are shown in Figure 7-8.<sup>173</sup> Two of them, the ones in which there are zero ( $n = 0$ ) or four ( $n = 4$ ) hydrogen-bond interactions possess  $S_4$  symmetry, while the remaining isomers have either  $C_2$  ( $n = 2$ , *trans*) or  $C_1$  ( $n = 1$  and  $n = 2$ , *cis*) symmetry. Non-axial isomers must then be present in the lattice, which provides a possible explanation for the intriguing tunneling behavior of complex **1**.

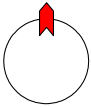
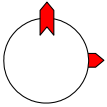
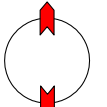
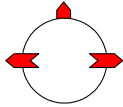
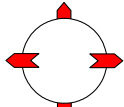
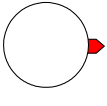
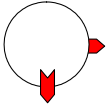
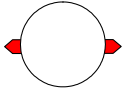
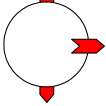
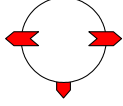
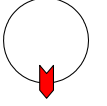
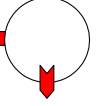
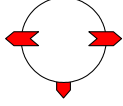
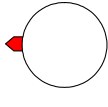
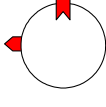
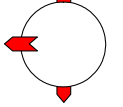
$n = 0$	$n = 1$	$n = 2$ 'cis'	$n = 2$ 'trans'	$n = 3$	$n = 4$
					
					
					
					
6.25 %	25 %	25 %	12.5 %	25 %	6.25 %

Figure 7-8. Depiction of the six isomers of complex **1** that differ in the number of hydrogen-bonded  $MeCO_2H$  molecules of crystallization as discussed in the text. The red arrow is representative of such a hydrogen-bond interaction.

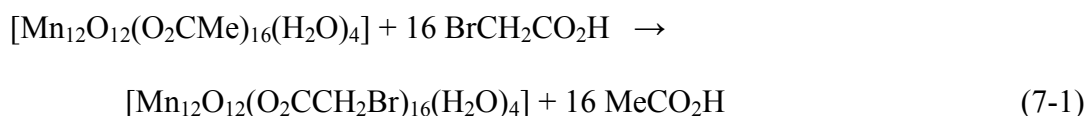
It is therefore of importance to study the magnetic behavior of a high symmetry  $Mn_{12}$  cluster that consists of only one species with strict axial symmetry, i.e.,  $[Mn_{12}O_{12}(O_2CCH_2Br)_{16}(H_2O)_4] \cdot 4CH_2Cl_2$  (**26**· $4CH_2Cl_2$ ). We herein describe the results of

this work, the synthesis, single crystal X-ray structure, single crystal  $^{55}\text{Mn}$  NMR spectrum, high-frequency electron paramagnetic resonance (HFEP) spectra and magnetic properties of the high symmetry  $\text{Mn}_{12}$  complex.

## 7.2 Results and Discussion

### 7.2.1 Synthesis

In a manner similar to the preparation of most  $\text{Mn}_{12}$  derivatives, we employed the previously developed carboxylate substitution procedure that involves the treatment of  $[\text{Mn}_{12}\text{O}_{12}(\text{O}_2\text{CMe})_{16}(\text{H}_2\text{O})_4] \cdot 2\text{MeCO}_2\text{H} \cdot 4\text{H}_2\text{O}$  (**1**) with an excess of  $\text{RCO}_2\text{H}$  to introduce the  $\text{BrCH}_2\text{CO}_2^-$  ligands onto the  $\text{Mn}_{12}$  core.<sup>13,38</sup> Thus, a solution of complex **1** in a solvent mixture of MeCN and  $\text{CH}_2\text{Cl}_2$  was treated with an excess of  $\text{BrCH}_2\text{CO}_2\text{H}$ . The transformation of **1** into **26** is summarized in eq 7-1.



The ligand substitution reaction is an equilibrium that favors the product side when the  $\text{pK}_a$  of the reactant acid is lower than that of acetic acid; the  $\text{pK}_a$  of  $\text{BrCH}_2\text{CO}_2\text{H}$  is 2.90 while that of  $\text{MeCO}_2\text{H}$  is 4.76.<sup>34</sup> Acetic acid was removed from the reaction system by multiple cycles of addition and removal of under reduced pressure as its toluene azeotrope (28:72%; b.p. 101 °C at one atmosphere). This procedure successfully led to the isolation and crystallization of  $[\text{Mn}_{12}\text{O}_{12}(\text{O}_2\text{CCH}_2\text{Br})_{16}(\text{H}_2\text{O})_4]$  (**26**) in nearly quantitative yield (~ 96%). Crystallization from  $\text{CH}_2\text{Cl}_2$ /hexanes gave dark brown crystals of  $\text{26} \cdot 4\text{CH}_2\text{Cl}_2$  suitable for X-ray crystallography.

### 7.2.2 Electrochemistry

Electrochemical studies on  $\text{Mn}_{12}$  complexes have revealed that they have a rich redox chemistry involving several oxidation and reduction processes, the  $E_{1/2}$  potentials

of which are very sensitive to the electron withdrawing or donating ability of the carboxylate ( $\text{RCO}_2^-$ ). By ligand substitution of complex **1** ( $\text{R} = \text{Me}$ ) with an appropriate electron withdrawing  $\text{RCO}_2^-$  group, the  $E_{1/2}$  reduction potentials have been shifted to relatively positive values. The shift of potentials can be correlated to the relative  $\text{pK}_a$  values of the carboxylic acids. As the  $\text{pK}_a$  of the acid decreases, the electron withdrawing ability of the  $\text{RCO}_2^-$  group increases; an electron withdrawing substituent causes the carboxylate to become less basic, reducing the electron density on the metal center and thereby making the aggregate easier to reduce and concomitantly harder to oxidize. On this basis,  $E_{1/2}$  potentials have been shifted to chemically accessible values, leading to the isolation of the one- and two-electron reduced  $\text{Mn}_{12}$  species.<sup>13,61,100</sup>

The cyclic voltammogram (CV) and differential pulse voltammogram (DPV) of **26** are typical of the  $\text{Mn}_{12}$  family of complexes, and are shown in Figure 7-9. There are two quasi-reversible reduction waves at 0.57 and 0.21 V. Standard electrochemical requirements for quasi-reversible electron transfer, including CV peak separations, anodic/cathodic peak current ratio, DPV peak broadness, are fulfilled by each redox process. A study of the scan rate ( $\nu$ ) dependence of each reduction showed a linear dependence of peak current with respect to  $\nu^{1/2}$ , indicating that the processes are diffusion-controlled. This relationship is described by the Randles-Sevcik equation (eq 7-2)

$$i_p = (2.687 \times 10^5) n^{3/2} \nu^{1/2} D^{1/2} AC \quad (7-2)$$

where  $n$  is the number of electrons appearing in the half-reaction of the redox couple,  $\nu$  is the scan rate,  $A$  is the electrode area,  $D$  is the diffusion coefficient of the analyte and  $C$  is the concentration of the analyte. As expected, the  $E_{1/2}$  values of the first and second

reduction process are shifted to more positive values than those of **1** (0.18 and -0.06 V, respectively) and are very similar to those of the monochloroacetate-substituted  $\text{Mn}_{12}$  derivative ( $\text{R} = \text{ClCH}_2\text{CO}_2^-$ ), 0.60 and 0.30 V, respectively. This was expected on the basis of the similarity of the  $\text{pK}_a$  values of  $\text{ClCH}_2\text{CO}_2\text{H}$  (2.85) and  $\text{BrCH}_2\text{CO}_2\text{H}$  (2.90).

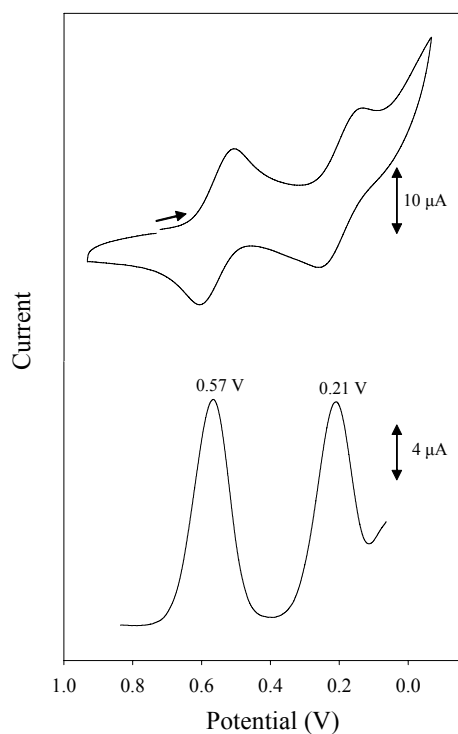


Figure 7-9. Cyclic voltammogram at  $100 \text{ mV s}^{-1}$  (top) and differential pulse voltammogram (bottom) for complex **26** in  $\text{CH}_2\text{Cl}_2$  containing 0.1 M  $\text{NBu}_4\text{PF}_6$  as supporting electrolyte. The indicated potentials are vs  $\text{Fc}/\text{Fc}^+$ .

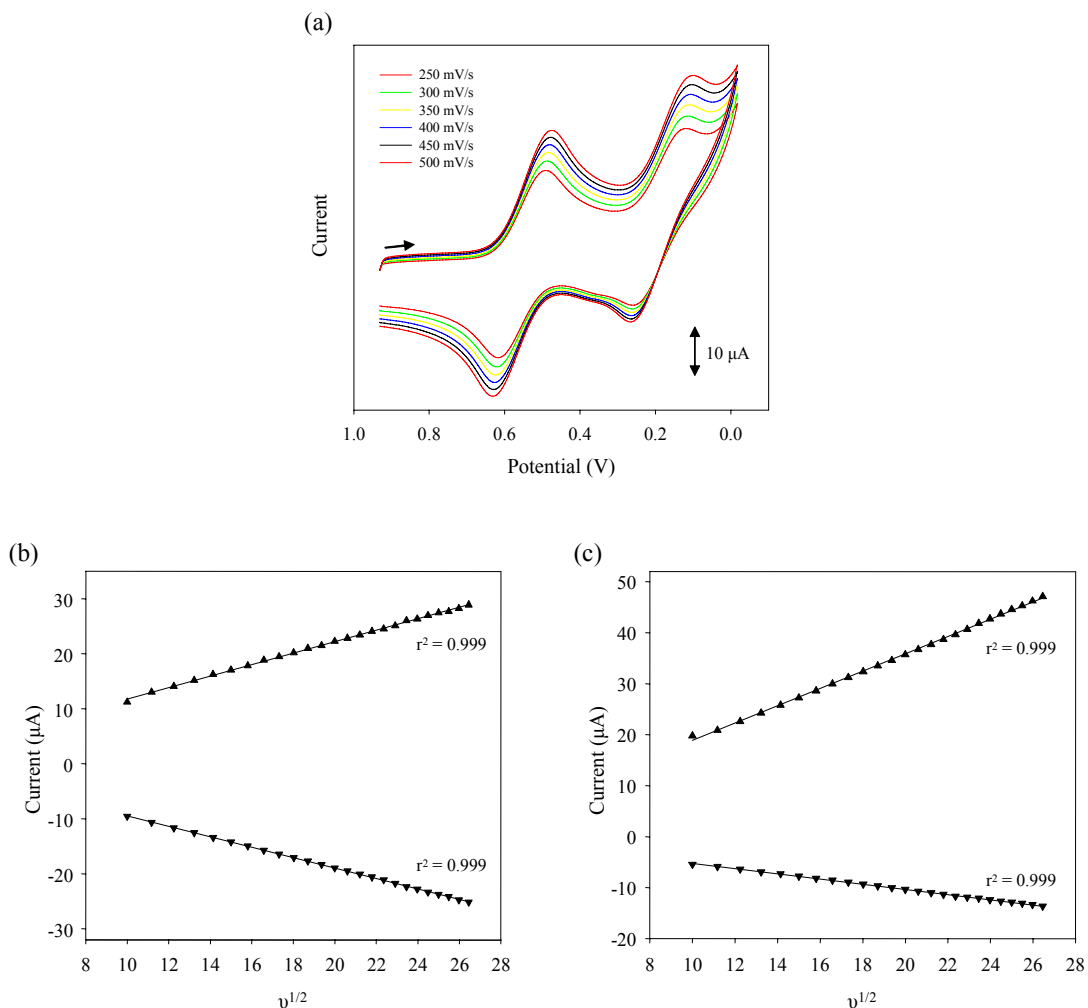


Figure 7-10. Scan rate dependence of the reduction waves at 0.57 V and 0.21 V of complex **26** in  $\text{CH}_2\text{Cl}_2$  containing 0.1 M  $\text{NBu}^n_4\text{PF}_6$  as supporting electrolyte. (a) Cyclic voltammogram at the indicated scan rates with corresponding plot of cathodic (top) and anodic (bottom) peak current dependence vs  $v^{1/2}$  for (b) 0.57 V reduction wave and (c) 0.21 V reduction wave.

### 7.2.3 X-Ray Crystal Structure of $[\text{Mn}_{12}\text{O}_{12}(\text{O}_2\text{CCH}_2\text{Br})_{16}(\text{H}_2\text{O})_4]$ (**26**)

A labeled ORTEP<sup>40</sup> plot in PovRay format of complex **26** is shown in Figure 7-11, together with a stereoview. The crystallographic data and structure refinement details are collected in Table 7-2, and selected interatomic distances and angles are listed in Table A-16. Complex **26**·4 $\text{CH}_2\text{Cl}_2$  crystallizes in the tetragonal space group  $I4_1/a$  (Figure 7-11). The  $\text{Mn}_{12}$  molecule is located on a crystallographic  $S_4$  improper rotation axis

perpendicular to the plane of the molecule and passing through the central cubane unit. For the sake of brevity, references to specific atoms in the following discussion implicitly include their symmetry-related partners. The complex has the same structure as previously characterized  $[\text{Mn}_{12}\text{O}_{12}(\text{O}_2\text{CR})_{16}(\text{H}_2\text{O})_4]$  complexes, possessing a central  $[\text{Mn}^{\text{IV}}_4\text{O}_4]^{8+}$  cubane moiety held within a non-planar ring of eight  $\text{Mn}^{\text{III}}$  ions by eight  $\mu_3\text{-O}^{2-}$  ions. The eight  $\text{Mn}^{\text{III}}$  ions separate into two groups of four  $\text{Mn}^{\text{III}}$  ions each. In the first group, each  $\text{Mn}^{\text{III}}$  ion is coordinated to a single  $\text{Mn}^{\text{IV}}$  ion via two oxide bridges [Mn(2)], while in the second group each  $\text{Mn}^{\text{III}}$  ion is coordinated to two  $\text{Mn}^{\text{IV}}$  ions via two oxide bridges [Mn(1)].<sup>29</sup> Peripheral ligation is provided by sixteen bridging  $\text{BrCH}_2\text{CO}_2^-$  and four water molecules [O(1)].

Table 7-2. Crystallographic data for  $[\text{Mn}_{12}\text{O}_{12}(\text{O}_2\text{CCH}_2\text{Br})_{16}(\text{H}_2\text{O})_4] \cdot 4\text{CH}_2\text{Cl}_2$ .

Parameter	<b>26</b> ·4CH <sub>2</sub> Cl <sub>2</sub>
formula <sup>a</sup>	C <sub>36</sub> H <sub>48</sub> Cl <sub>8</sub> Mn <sub>12</sub> Br <sub>16</sub> O <sub>48</sub>
fw, g mol <sup>-1</sup>	3470.09
space group	<i>I</i> 4 <sub>1</sub> / <i>a</i>
<i>a</i> , Å	26.9948(16)
<i>b</i> , Å	26.9948(16)
<i>c</i> , Å	12.7245(11)
$\alpha$ , deg	90
$\beta$ , deg	90
$\gamma$ , deg	90
<i>V</i> , Å <sup>3</sup>	9272.6(11)
<i>Z</i>	4
<i>T</i> , °C	-100(2)
radiation, Å <sup>b</sup>	0.71073
$\rho_{\text{calc}}$ , g cm <sup>-3</sup>	2.480
$\mu$ , cm <sup>-1</sup>	87.86
<i>R</i> 1 ( <i>wR</i> 2), % <sup>c,d</sup>	5.68 (15.43)

<sup>a</sup> Including solvent molecules. <sup>b</sup> Graphite monochromator. <sup>c</sup>  $R1 = \Sigma||F_o| - |F_c|| / \Sigma|F_o|$ . <sup>d</sup>  $wR2 = [\Sigma[w(F_o^2 - F_c^2)^2] / \Sigma[wF_o^2]^2]^{1/2}$  where  $S = [\Sigma[w(F_o^2 - F_c^2)^2] / (n-p)]^{1/2}$ ,  $w = 1/[\sigma^2(F_o^2) + (m^*p)^2 + n^*p]$ ,  $p = [\max(F_o^2, 0) + 2^*F_c^2]/3$ , and *m* and *n* are constants.

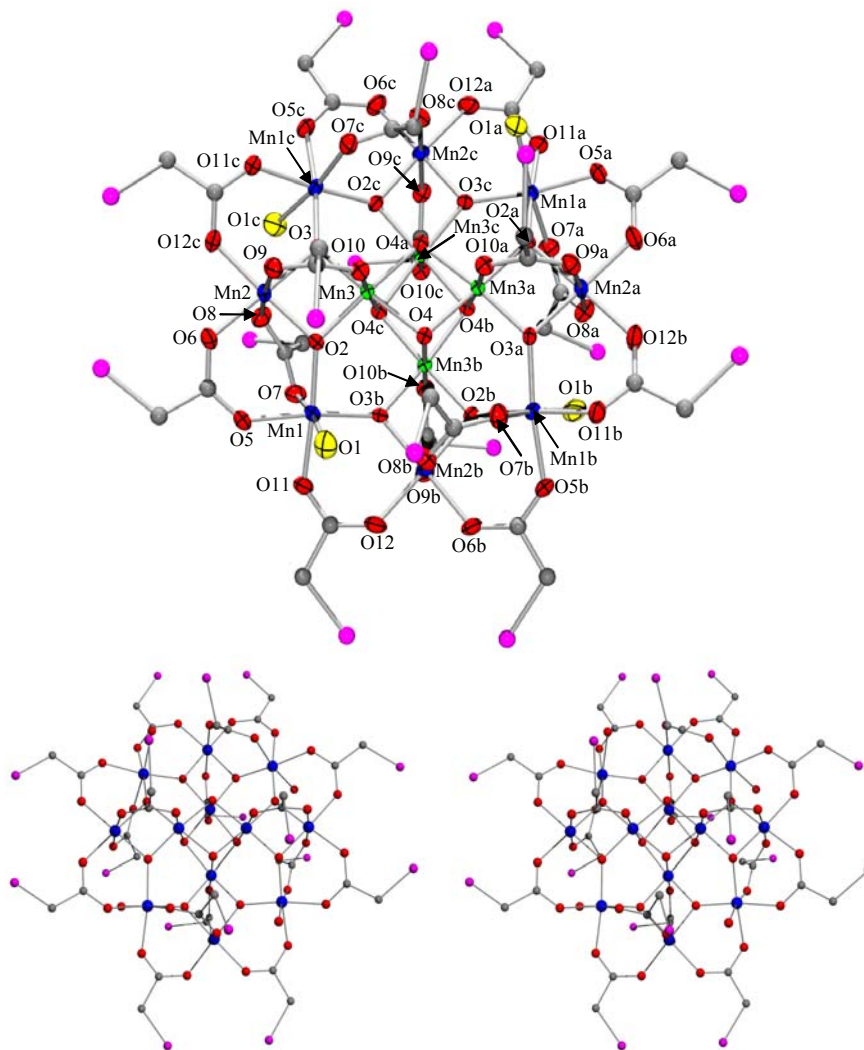


Figure 7-11. ORTEP representation in PovRay format of  $[\text{Mn}_{12}\text{O}_{12}(\text{O}_2\text{CCH}_2\text{Br})_{16}(\text{H}_2\text{O})_4]$  (**26**) with thermal ellipsoids at the 50% probability level except for the C and Br atoms, together with a stereopair. For clarity, the hydrogen atoms have been omitted.  $\text{Mn}^{\text{IV}}$  green;  $\text{Mn}^{\text{III}}$  blue; O red;  $\text{H}_2\text{O}$  yellow; Br pink; C gray.

In all  $[\text{Mn}_{12}\text{O}_{12}(\text{O}_2\text{CR})_{16}(\text{H}_2\text{O})_4]$  complexes studied to date, the four water ligands coordinate only to the four  $\text{Mn}^{\text{III}}$  ions in the second group described above [ $\text{Mn}(1)$ ], either one water on each Mn, two each on two Mn, or similar.<sup>20</sup> Seven different isomeric forms of monosubstituted, neutral  $\text{Mn}_{12}$  clusters which differ in the arrangement of the four water ligands have been identified: (1,1,1,1), (2,2), (1,1,1), (1,1,2), (1,2,1), (2), and (0) (Figure 7-12). In complex **26**, the four water ligands are coordinated to  $\text{Mn}(1)$  in a 1:1:1:1

pattern (Figure 7-12a). This disposition of one H<sub>2</sub>O ligand on each Mn<sup>III</sup> that is bridged to two Mn<sup>IV</sup> ions by two oxide bridges has also been observed for [Mn<sub>12</sub>O<sub>12</sub>(O<sub>2</sub>CMe)<sub>16</sub>(H<sub>2</sub>O)<sub>4</sub>]<sup>50</sup> and [Mn<sub>12</sub>O<sub>12</sub>(O<sub>2</sub>CC<sub>12</sub>H<sub>9</sub>)<sub>16</sub>(H<sub>2</sub>O)<sub>4</sub>] (C<sub>12</sub>H<sub>9</sub> = biphenyl).

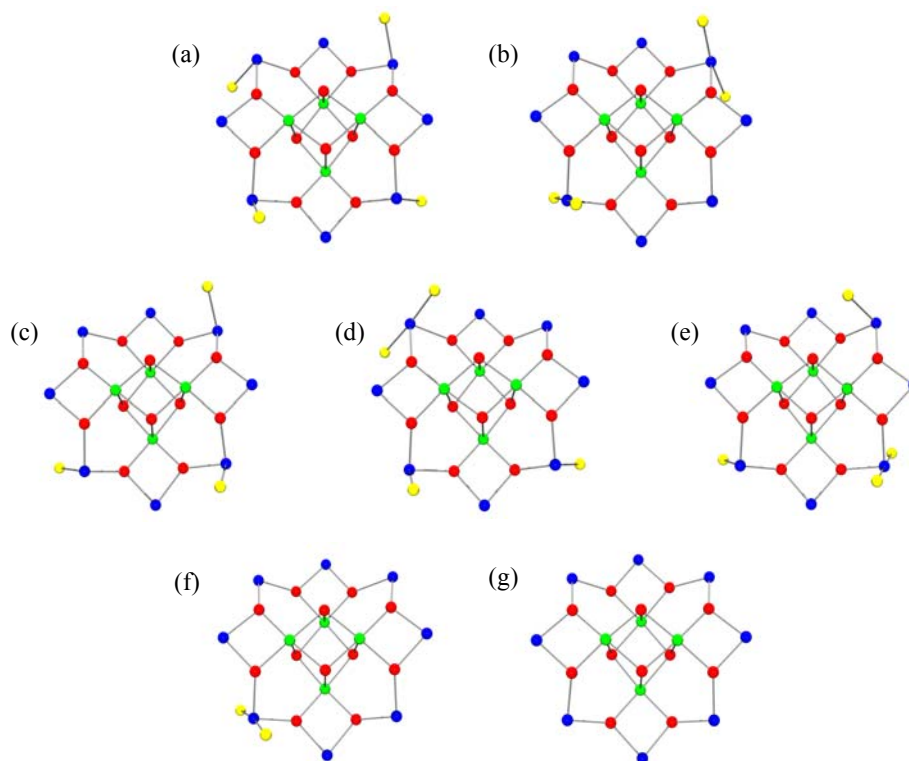


Figure 7-12. Seven different geometric isomers of Mn<sub>12</sub> SMMs found in structurally characterized molecules: (a) (1,1,1,1); (b) (2,2); (c) (1,1,1); (d) (1,1,2); (e) (1,2,1); (f) (2); (g) (0) isomer.

All of the Mn centers are six-coordinate with near-octahedral geometry. The Mn oxidation levels were qualitatively determined by charge consideration and also by evaluation of the bond distances around the Mn centers. These assignments were confirmed quantitatively by bond valence sum (BVS)<sup>41</sup> calculations, indicating that Mn(1) and Mn(2) are Mn<sup>III</sup> and the remaining Mn center, Mn(3), is Mn<sup>IV</sup> (Table 7-3). The protonation levels of the inorganic O atoms were also confirmed by a BVS calculation and the results are collected in Table 7-4. The eight Mn<sup>III</sup> centers exhibit a Jahn-Teller (JT) distortion, as expected for a high-spin d<sup>4</sup> ion in near-octahedral

geometry. As is almost always the case for Mn<sup>III</sup> ions, the JT distortion takes the form of an axial elongation of two *trans* bonds. The elongation typically lengthens bond distances by 0.1-0.2 Å. The JT elongation axes avoid the Mn-O<sup>2-</sup> bonds, the shortest and strongest in the molecule, and thus are all axially disposed, roughly perpendicular to the [Mn<sub>12</sub>O<sub>12</sub>] disk-like core. As a result, there is a near parallel alignment of the eight Mn<sup>III</sup> JT elongation axes. This is the predominant factor that determines the overall magnetic anisotropy of the molecule and hence, greatly influences the observed magnetic properties (*vide infra*).

Table 7-3. Bond valence sum calculations<sup>a</sup> for complex **26**·4CH<sub>2</sub>Cl<sub>2</sub>.

Atom	Mn <sup>2+</sup>	Mn <sup>3+</sup>	Mn <sup>4+</sup>
Mn(1)	3.2665	<u>2.9878</u>	3.1368
Mn(2)	3.3000	<u>3.0185</u>	3.1689
Mn(3)	4.1305	3.7781	<u>3.9664</u>

<sup>a</sup> The underlined value is the one closest to the actual charge for which it was calculated. The oxidation state of a particular atom can be taken as the nearest whole number to the underlined value.

Table 7-4. Bond valence sum calculations<sup>a</sup> for selected oxygen atoms in complex **26**·4CH<sub>2</sub>Cl<sub>2</sub>.

Atom	$V_i$	Assignment
O(3)	2.019	O <sup>2-</sup>
O(4)	2.002	O <sup>2-</sup>
O(130)	1.996	O <sup>2-</sup>

<sup>a</sup> The oxygen atoms is O<sup>2-</sup> if  $V_i \approx 2$ , OH<sup>-</sup> if  $V_i \approx 1$ , and H<sub>2</sub>O if  $V_i \approx 0$ .

The local JT axes of the two Mn<sup>III</sup> ions, Mn(1) and Mn(2), are canted away from the crystallographic symmetry (*z*) axis by  $\theta = 34.0^\circ$  and  $7.9^\circ$ , respectively; the local Mn<sup>III</sup> symmetry axes are defined by the O···O elongation axis of the Mn<sup>III</sup> coordination sphere (Figure 7-13). The direction of the local JT axis is the direction of the principal hyperfine field of the Mn<sup>III</sup> ion, and the difference in  $\theta$  of the two Mn<sup>III</sup> ions will be of relevance to the <sup>55</sup>Mn spectroscopic measurements (*vide infra*).

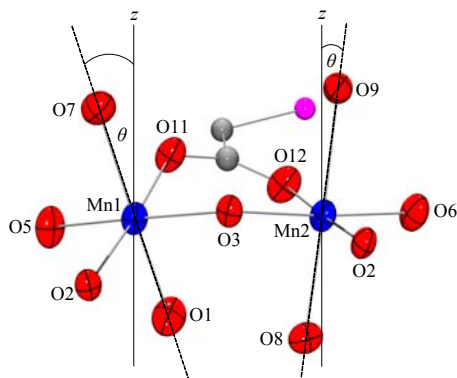


Figure 7-13. ORTEP representation in PovRay format of the anisotropy axes (dashed lines) of Mn(1) and Mn(2) in complex **26**, where  $\theta$  is the angle of the local Mn<sup>III</sup> anisotropy axis with respect to the crystallographic  $z$  axis. Mn<sup>III</sup> blue; O red; Br pink; C gray.

There is evidence of weak intermolecular interactions between separate Mn<sub>12</sub> molecules. The Br(8)⋯Br(8) distance shown as a dashed line between neighboring molecules in Figure 7-14 is 3.487 Å, significantly longer than the sum of the covalent radii of Br (2.28 Å), but much shorter than the sum of their van der Waals radii (3.70 Å).<sup>183</sup> This interaction is complicated by the disorder over seven sites of the BrCH<sub>2</sub>CO<sub>2</sub><sup>-</sup> ligand involved in this interaction. The Br⋯Br distance given is between Br(8) and Br(8) on adjacent Mn<sub>12</sub> molecules; the site occupancy factor of Br(8) is only 19% however as will be discussed in the Experimental Section. The CH<sub>2</sub>Cl<sub>2</sub> solvent molecules of crystallization are included in the packing diagram in Figure 7-14 and it is clear that there are four CH<sub>2</sub>Cl<sub>2</sub> solvent molecules per Mn<sub>12</sub> unit. There is no evidence of hydrogen-bonding and/or other types of interactions between the solvent molecules and the Mn<sub>12</sub> molecule as have been found in **1** by Cornia and others.<sup>173</sup> In Table 7-5 is shown a comparison of selected interatomic distances and angles for complexes **1** and **26**; the closeness of the parameters emphasizes the structural similarities of the two complexes.

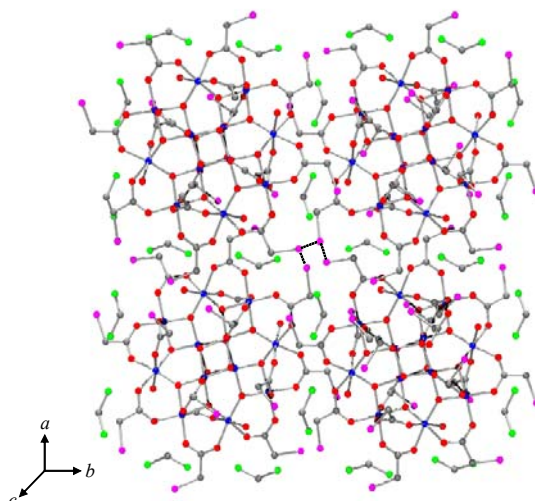


Figure 7-14. ORTEP representation in PovRay format of the packing of complex **26**. For clarity, the hydrogen atoms have been omitted. Representative pairs of interacting Br $\cdots$ Br atoms between neighboring molecules are indicated by the dashed lines. Mn blue; O red; Br pink; C gray; Cl green.

Table 7-5. Comparison of selected interatomic distances (Å) and angles (°) for [Mn<sub>12</sub>O<sub>12</sub>(O<sub>2</sub>CMe)<sub>16</sub>(H<sub>2</sub>O)<sub>4</sub>] $\cdot$ 2MeCO<sub>2</sub>H $\cdot$ 4H<sub>2</sub>O (**1**) and [Mn<sub>12</sub>O<sub>12</sub>(O<sub>2</sub>CCH<sub>2</sub>Br)<sub>16</sub>(H<sub>2</sub>O)<sub>4</sub>] (**26**).

Parameter <sup>a</sup>	<b>1</b>	<b>26</b>
Mn <sup>IV</sup> – O <sub>c</sub> (ax)	1.8954(13)	1.902(4)
Mn <sup>IV</sup> – O <sub>c</sub> (eq)	1.9116(11), 1.9196(10)	1.922(4), 1.934(4)
Mn <sup>IV</sup> – O <sub>r</sub>	1.8592(11), 1.8795(11)	1.865(4), 1.878(4)
Mn <sup>IV</sup> – O <sub>ax</sub>	1.9131(13)	1.923(4)
Mn <sup>IIIb</sup> – O <sub>r</sub>	1.8770(11), 1.8983(11)	1.871(4), 1.902(4)
Mn <sup>IIIc</sup> – O <sub>r</sub>	1.8860(11), 1.8964(11)	1.898(4), 1.898(4)
Mn <sup>IIIb</sup> – O <sub>eq</sub>	1.9371(13), 1.9393(12)	1.932(5), 1.948(5)
Mn <sup>IIIc</sup> – O <sub>eq</sub>	1.9655(12), 1.9884(13)	1.959(4), 1.970(5)
Mn <sup>IIIb</sup> – O <sub>ax</sub>	2.111(5) <sup>*</sup> , 2.228(3), 2.2318(13)	2.187(5), 2.220(5)
Mn <sup>IIIc</sup> – O <sub>ax</sub>	2.117(11), 2.151(17) <sup>*</sup>	2.114(5)
Mn <sup>IIIc</sup> – O <sub>w</sub>	2.1735(15)	2.193(5)
O <sub>r</sub> – Mn <sup>IV</sup> – O <sub>r</sub>	84.96(5)	83.75(17)
O <sub>r</sub> – Mn <sup>IIIb</sup> – O <sub>r</sub>	83.95(5)	82.91(17)
O <sub>r</sub> – Mn <sup>IIIc</sup> – O <sub>r</sub>	93.29(5)	92.35(17)
Mn <sup>IV</sup> $\cdots$ Mn <sup>IV</sup>	2.8166(4), 2.8166(4), 2.9271(4)	2.8180(14), 2.8180(14), 2.9851(16)
Mn <sup>IIIb</sup> $\cdots$ Mn <sup>IIIc</sup>	3.321, 3.414	3.332, 3.388
Mn <sup>IIIb</sup> $\cdots$ Mn <sup>IV</sup> $\cdots$ Mn <sup>IV</sup>	120.688(13), 122.594(13)	119.24(5), 121.28(5)
	178.380(14)	177.25(4)
Mn <sup>IIIb</sup> $\cdots$ Mn <sup>IV</sup>	2.7643(3)	2.7938(12)
Mn <sup>IIIc</sup> $\cdots$ Mn <sup>IV</sup>	3.445, 3.448	3.460, 3.461

<sup>a</sup> O<sub>c</sub> = cubane O<sup>2-</sup>, O<sub>r</sub> = ring O<sup>2-</sup>, O<sub>ax</sub> = axial carboxylate, O<sub>eq</sub> = equatorial carboxylate, O<sub>w</sub> = water; <sup>b</sup> Mn<sup>IIIb</sup> atoms: Mn(2) in **1** and Mn(2) in **26**; <sup>c</sup> Mn<sup>IIIc</sup> atoms: Mn(3) in **1** and Mn(1) in **26**. <sup>\*</sup> Involves the acetate ligand disorder bridging Mn(2) and Mn(3).

### 7.2.4 $^1\text{H}$ Nuclear Magnetic Resonance Spectroscopy

In order to assess the solution state structure and stability of the complex, an NMR spectroscopic investigation of complex **26** in  $\text{CD}_2\text{Cl}_2$  was carried out. Chemical shifts and  $T_1$  times are listed in Table 7-6.  $^1\text{H}$  NMR spectroscopy has been used extensively in the past to investigate the behavior in solution of  $[\text{Mn}_{12}\text{O}_{12}(\text{O}_2\text{CR})_{16}(\text{H}_2\text{O})_4]^{z-}$  ( $z = 0, 1-,$  and  $2-$ ) complexes.<sup>13,46,57,165</sup>  $\text{Mn}^{\text{III}}$  has a relatively fast electron relaxation time. As such, electron relaxation cannot facilitate nuclear relaxation efficiently, making the  $\text{Mn}^{\text{III}}$  ion generally suitable for NMR spectroscopic study. The  $^1\text{H}$  NMR spectrum of complex **26** in  $\text{CD}_2\text{Cl}_2$  in Figure 7-15 shows three resonances with a 1:2:1 integration ratio.

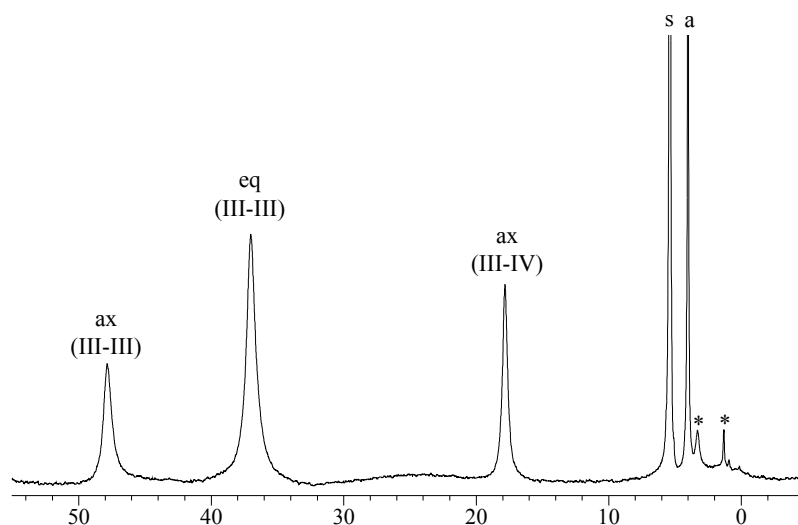


Figure 7-15.  $^1\text{H}$  NMR (300 MHz) spectrum at  $\sim 23$  °C in  $\text{CD}_2\text{Cl}_2$  of **26**; ax = axial, eq = equatorial, s = solvent protio-impurity; a =  $\text{HO}_2\text{CCH}_2\text{Br}$  impurity, \* = solvent impurities.

As with other  $\text{Mn}_{12}$  derivatives, there are only three distinct types of bridging carboxylates in the NMR spectrum: (i) four axial ligands bridging  $\text{Mn}^{\text{III}}\cdots\text{Mn}^{\text{IV}}$  pairs, (ii) four axial ligands bridging  $\text{Mn}^{\text{III}}\cdots\text{Mn}^{\text{III}}$  pairs, and (iii) eight equatorial ligands bridging  $\text{Mn}^{\text{III}}\cdots\text{Mn}^{\text{III}}$  pairs. Solution studies of  $\text{Mn}_{12}$  molecules at room temperature have shown that there is a fluxional process that is fast on the NMR timescale that rapidly exchanges

the water ligands with one type of axial carboxylate ligand;<sup>32</sup> the one that has both its O atoms located on the JT elongation axes of the  $\text{Mn}^{\text{III}}\cdots\text{Mn}^{\text{III}}$  pairs (Figure 7-16). This introduces dihedral mirror planes which make all of the equatorial carboxylate groups equivalent. In effect, the solution state symmetry of a  $\text{Mn}_{12}$  molecule is  $D_{2d}$ , giving three resonances in a 1:1:2 relative integration ratio (axial:axial:equatorial) as shown in Figure 7-17.

Table 7-6. Solution  $^1\text{H}$  NMR spectral data for complexes **1** and **26**.

Compound	Peak <sup>a</sup>	Assignment <sup>b</sup>	$T_1$ <sup>c</sup>
R = $\text{CH}_2\text{Br}$ ( <b>26</b> )	47.8	ax (III-III)	2.9
	37.0	eq (III-III)	3.1
	17.8	ax (III-IV)	5.1
R = Me ( <b>1</b> )	48.7	ax (III-III)	3.6
	41.7	eq (III-III)	3.4
	14.0	ax (III-IV)	5.6

<sup>a</sup> ppm, at  $\sim 23$  °C. <sup>b</sup> ax = axial, eq = equatorial; III-III and III-IV refer to the ligand bridging a  $\text{Mn}^{\text{III}}\text{Mn}^{\text{III}}$  and  $\text{Mn}^{\text{III}}\text{Mn}^{\text{IV}}$  pair, respectively. <sup>c</sup> ms.

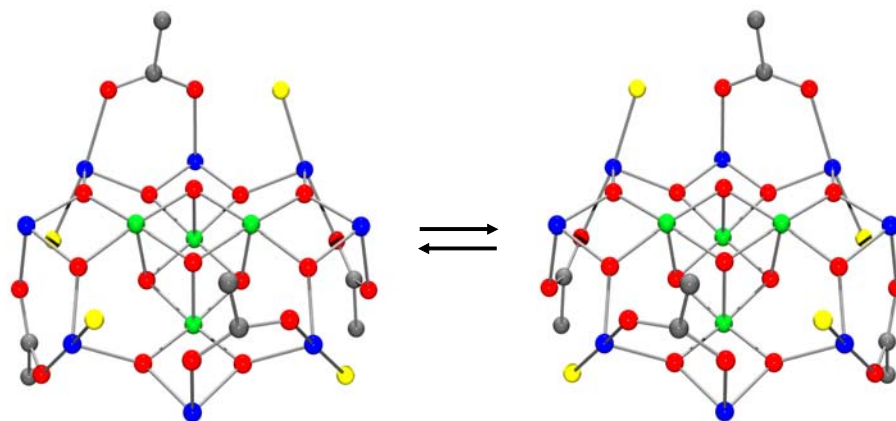


Figure 7-16. ORTEP representation of the fluxional process that takes place between the water ligand and the axial carboxylate bridging a  $\text{Mn}^{\text{III}}\text{Mn}^{\text{III}}$  pair in a typical  $[\text{Mn}_{12}\text{O}_{12}(\text{O}_2\text{CR})_{16}(\text{H}_2\text{O})_4]$  molecule.  $\text{Mn}^{\text{IV}}$  green;  $\text{Mn}^{\text{III}}$  blue; O red; C gray;  $\text{H}_2\text{O}$  yellow.

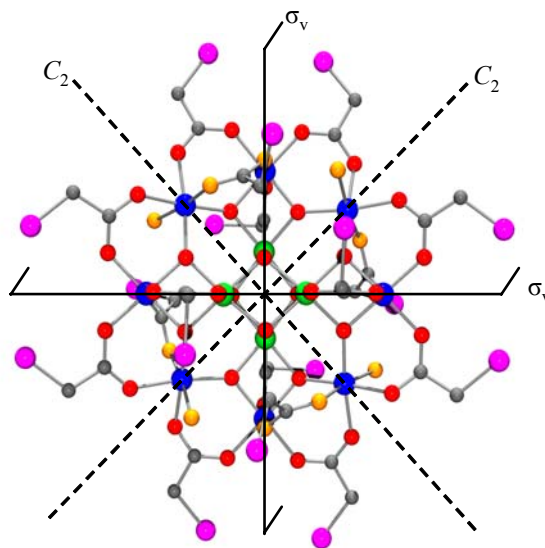


Figure 7-17. ORTEP representation in PovRay format of  $[\text{Mn}_{12}\text{O}_{12}(\text{O}_2\text{CCH}_2\text{Br})_{16}(\text{H}_2\text{O})_4]$  (**26**) showing the  $D_{2d}$  symmetry typical of a  $[\text{Mn}_{12}\text{O}_{12}(\text{O}_2\text{CR})_{16}(\text{H}_2\text{O})_4]$  molecule in solution. Another  $C_2$  rotation axis (not shown) passes through the central cubane unit of the molecule.  $\text{Mn}^{\text{IV}}$  green;  $\text{Mn}^{\text{III}}$  blue; Br pink; C gray; O red (except those O atoms in orange that are involved in the fluxional process).

Longitudinal (spin-lattice) relaxation times ( $T_1$ ) were determined using the inversion-recovery pulse method ( $180^\circ - \tau - 90^\circ$ ) to aid in the assignment of the peaks. Electrons on metal centers relax at very fast rates, providing efficient pathways for nuclear relaxation. In general, the longitudinal relaxation time is directly related to the distance of a nucleus from a paramagnetic center.<sup>166,167</sup> The sequence consists of a  $180^\circ$  pulse that inverts the magnetization as far as possible out of its equilibrium direction, followed by a variable delay ( $\tau$ ) and finally a  $90^\circ$  pulse to monitor the magnetization. In Figure 7-18 are shown several spectra of **26** obtained at selected values of  $\tau$ , showing the evolution of the magnetization relaxation as a function of time. Resonances were also assigned on the basis of relative integration ratios, peak broadness ( $r^{-6}$  dependence, where  $r$  is the distance to the paramagnetic centers), and comparisons with  $\text{Mn}_{12}$  derivatives

possessing other carboxylate groups. The  $^1\text{H}$  NMR spectrum of complex **1** in  $\text{CD}_3\text{CN}$  is shown in Figure 7-19 for comparison; similarly,  $T_1$  times for **1** are included in Table 7-6.

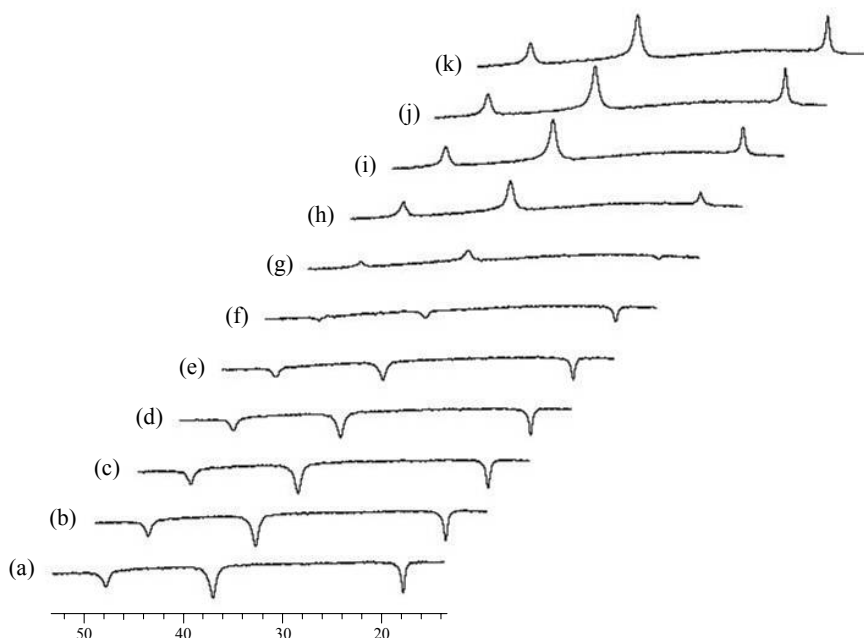


Figure 7-18. Array of inversion recovery data of **26** in  $\text{CD}_2\text{Cl}_2$  at  $23\text{ }^\circ\text{C}$ . The number of transients measured at each  $\tau$  value is 32. The delay times  $\tau$  were (a)  $4.16 \times 10^{-5}$  s, (b)  $8.32 \times 10^{-5}$  s, (c)  $1.16 \times 10^{-4}$  s, (d)  $3.33 \times 10^{-4}$  s, (e)  $6.66 \times 10^{-5}$  s, (f)  $1.33 \times 10^{-3}$  s, (g)  $2.66 \times 10^{-3}$  s, (h)  $5.32 \times 10^{-3}$  s, (i)  $1.06 \times 10^{-2}$  s, (j)  $2.13 \times 10^{-2}$  s, and (k)  $4.26 \times 10^{-2}$  s after the  $180^\circ$  pulse.

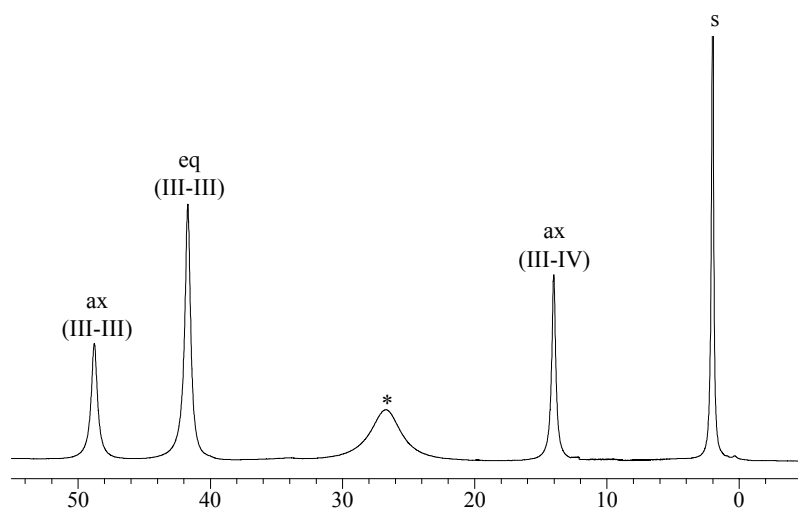


Figure 7-19.  $^1\text{H}$  NMR (300 MHz) spectrum at  $\sim 23\text{ }^\circ\text{C}$  in  $\text{CD}_3\text{CN}$  of **1**; ax = axial, eq = equatorial, s = the solvent protio-impurity; \* =  $\text{H}_2\text{O}$ .

The isotropic shifts of the nuclei are expected to have both contact (through-bond) and pseudocontact, or dipolar (through-space), contributions<sup>166-168</sup> (eq 7-3).

$$\left(\frac{\Delta\nu}{\nu_0}\right)_{\text{iso}} = \left(\frac{\Delta\nu}{\nu_0}\right)_{\text{dipolar}} + \left(\frac{\Delta\nu}{\nu_0}\right)_{\text{contact}} \quad (7-3)$$

The dipolar shift arises from dipolar interactions, or direct through-space interactions between the nuclear and electronic magnetic moments and the contact shift involves the interaction of electronic and nuclear magnetic moments via the metal-ligand bonding framework. The contact component of the isotropic shift is dominated by two mechanisms: (i) direct delocalization whereby unpaired spin density is delocalized onto a ligand orbital of appropriate symmetry via direct overlap of the magnetic orbitals with the ligand orbitals and (ii) spin polarization whereby unpaired spin density polarizes the spin density in an orthogonal, filled orbital. Direct  $\pi$  delocalization of unpaired spin density in the  $d_{\pi}$  orbitals on the paramagnetic metal center to the  $-\text{CO}_2$   $\pi$  system occurs by  $\pi$ -symmetry overlap. Similarly, direct  $\pi$  delocalization of the positive spin density onto the  $-\text{CH}_2\text{Br}$  nuclei occurs, giving downfield paramagnetic shifts of these NMR resonances. In addition, pseudocontact (dipolar) contributions also likely affect the hydrogen paramagnetic shifts; derivatives such as **26** exhibit too wide of a range of shifts for nuclei located in the three different sites of the cluster on the basis of only a  $\pi$  delocalization mechanism.

### 7.2.5 Single Crystal <sup>55</sup>Mn Nuclear Magnetic Resonance Spectroscopy

In addition to our examination of the solution state structure and stability of both **26** (and for comparison **1**), a solid state NMR spectroscopic investigation of complexes **1** and **26** was carried out. This technique can be used to directly probe the magnetic structure and individual Mn ions in these interesting molecules, and for this reason, we

have carried out  $^{55}\text{Mn}$  NMR measurements on single crystals of complexes **1** and **26** and on an aligned dried, microcrystalline sample of **26**.<sup>184</sup> Such a study allows the assessment of the influence of the hydrogen-bonding of the  $\text{MeCO}_2\text{H}$  solvent molecules of crystallization in **1** on the symmetry of the  $\text{Mn}_{12}$  core by comparison of the resulting NMR spectrum with that of **26**, which has no significant such hydrogen-bonding perturbation of its  $\text{Mn}_{12}$  core. In addition, comparisons can be made between the NMR spectra obtained on an aligned powder and single crystal of **26**. As will be shown, there are significant differences between the single crystal and aligned powder spectra. Specifically, the single crystals afford significantly higher spectral resolution than the aligned powder, and moreover, that significant differences in the chemical structure of **26** are induced upon vacuum-drying and powdering of the sample. Furthermore, angular dependence studies are now possible because of the use of high quality, large single crystals. Such studies were conducted with rotations in the *ab* and *ac* planes in 1 T and 2 T fields, respectively.

A comparison of  $^{55}\text{Mn}$  NMR signals obtained from (a)  $[\text{Mn}_{12}\text{O}_{12}(\text{O}_2\text{CCH}_2\text{Br})_{16}(\text{H}_2\text{O})_4]$  (**26**) powder, (b) a single crystal of  $[\text{Mn}_{12}\text{O}_{12}(\text{O}_2\text{CCH}_2\text{Br})_{16}(\text{H}_2\text{O})_4]\cdot 4\text{CH}_2\text{Cl}_2$  (**26** $\cdot 4\text{CH}_2\text{Cl}_2$ ), and (c) a single crystal of  $[\text{Mn}_{12}\text{O}_{12}(\text{O}_2\text{CMe})_{16}(\text{H}_2\text{O})_4]\cdot 2\text{MeCO}_2\text{H}\cdot 4\text{H}_2\text{O}$  (**1**), all in zero external field is presented in Figure 7-20. The observed peaks are assigned to the three types of Mn ions expected assuming  $S_4$  symmetry (Figure 7-21), following Goto and co-workers<sup>185</sup> and Furukawa et al.,<sup>186</sup> who reported oriented powder NMR spectra for **1**.

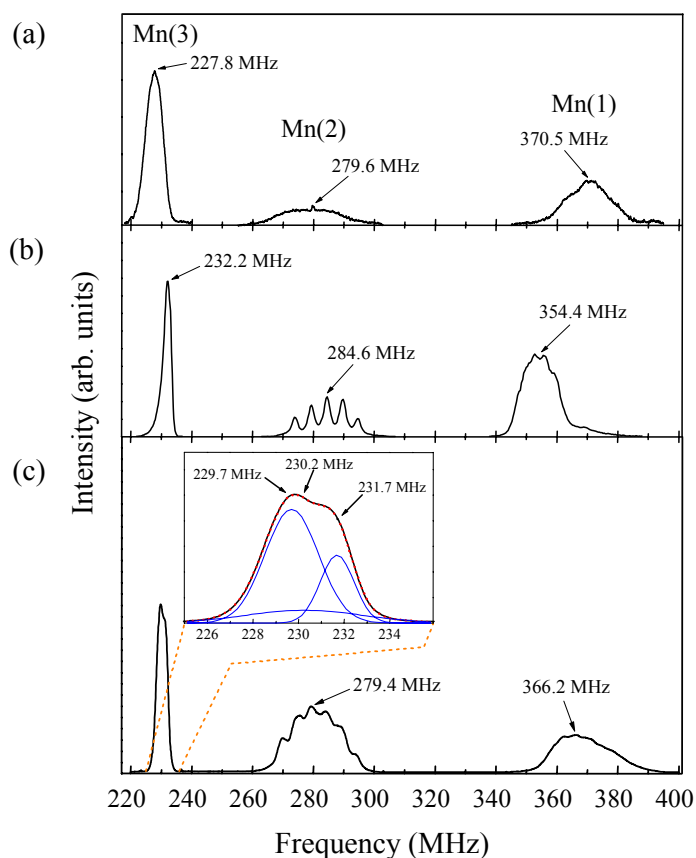


Figure 7-20. Comparison of zero-field  $^{55}\text{Mn}$  NMR spectra of (a) an aligned dried, microcrystalline sample of  $[\text{Mn}_{12}\text{O}_{12}(\text{O}_2\text{CCH}_2\text{Br})_{16}(\text{H}_2\text{O})_4]$  (**26**), (b) a single crystal of  $[\text{Mn}_{12}\text{O}_{12}(\text{O}_2\text{CCH}_2\text{Br})_{16}(\text{H}_2\text{O})_4]\cdot 4\text{CH}_2\text{Cl}_2$  (**26}\cdot 4\text{CH}\_2\text{Cl}\_2) and (c) a single crystal of  $[\text{Mn}_{12}\text{O}_{12}(\text{O}_2\text{CMe})_{16}(\text{H}_2\text{O})_4]\cdot 2\text{MeCO}_2\text{H}\cdot 4\text{H}_2\text{O}$  (**1**).**

Assignments were made on the basis of individual resonance profiles, including central frequency and quadrupole splitting, and also by comparison of spectra with those already reported for powdered samples of complex **1**.<sup>185</sup> The position and width of the three peaks in the NMR spectrum can be explained by a combination of large internal hyperfine field and a small quadrupolar interaction. The internal field determines the resonance frequency of the lines and describes the interaction of the nuclear magnetic dipole moment with the local magnetic moment of the electron spin on the manganese centers. The quadrupole effect yields the observed line width and is related to the local



this axis and the molecular  $z$  axis is  $34.0^\circ$  for Mn(1) and  $7.9^\circ$  for Mn(2). As this angle increases, the quadrupolar splitting is expected to decrease. Hence, we expect that the experimentally observed quadrupolar splitting of the peak corresponding to Mn(1) will be smaller than that of the peak corresponding to Mn(2), and this is one point that is helpful in the assignment of the peaks in the spectrum. Also of use is the relationship between  $\theta$  and the magnitude of the internal field; as  $\theta$  increases, the magnitude of the internal field also increases. Hence, the peak for Mn(1) should occur in the spectrum at a higher resonance frequency than does the peak of Mn(2). A knowledge of the angle of the local principal axis of the electric field gradient with respect to the molecular  $z$  axis allows us to definitively assign these two peaks in the NMR spectrum to the corresponding Mn<sup>III</sup> ions, consistent with previous assignments.<sup>185,186</sup> Specifically, the peak centered at 230 MHz [labeled Mn(3) in Figure 7-21] is assigned to the four Mn<sup>IV</sup> ions in the central [Mn<sub>4</sub>O<sub>4</sub>] cubane core of the Mn<sub>12</sub> molecules. The second signal at 284 MHz [labeled Mn(2)], with well-resolved quadrupolar splitting in the crystals, is assigned to four of the eight Mn<sup>III</sup> ions in the outer ring, and the broad signal around 355 MHz [labeled Mn(1)] is assigned to the remaining four Mn<sup>III</sup> ions. Hyperfine fields can be calculated using  $\gamma_n^{55} = 10.5$  MHz/T, giving the field values collected in Table 7-7 for an aligned powder and single crystal of **26**. Two significant conclusions are evident from Figure 7-20:

(i) Comparison of the oriented powder (Figure 7-20a) and single crystal (Figure 7-20b) spectra of **26** demonstrates the impressive increase in the spectral resolution gained using a crystal. A significant broadening of all of the peaks in Figure 7-20a as compared to those in Figure 7-20b and, in particular, the complete loss of quadrupolar splitting on the Mn(2) peak and up to 16 MHz shifts in the peak positions [e.g., for

Mn(1)] provide clear evidence that aligned powders could lead to erroneous structural and magnetic information.

Table 7-7. Comparison of parameters obtained from  $^{55}\text{Mn}$  NMR spectra of an aligned powder and single crystal of **26**.

<b>26</b>	Peak <sup>a</sup>	Frequency (MHz)	FWHM (MHz)	Hyperfine Field (T)
Aligned Powder	1	227.8	6.52	21.69
	2	279.6	24.74	26.60
	3	370.5	16.67	35.25
Single Crystal	1	232.2	2.89	22.11
	2	284.6	2.91	27.10
	3	354.4	13.82	33.76

<sup>a</sup> Using the numbering scheme described in the text

Indeed, the single crystal data enable measurement of the quadrupole coupling parameter  $e^2qQ$  through the quadrupole splitting,  $\Delta\nu_Q$ , using the equation for the energy, where  $I$  and  $m$  are the nuclear spin and its projection quantum numbers, and  $\theta$  is the angle between the internal magnetic field (molecular  $z$  axis) and the local symmetry axis of the electric field gradient tensor.<sup>185,187</sup>

$$E_m = -\gamma_n \hbar H_0 m + \frac{e^2 q Q}{4I(2I-1)} \left( \frac{3\cos^2\theta - 1}{2} \right) [3m^2 - I(I+1)] \quad (7-4)$$

From the crystallographic data for **26**, it is known that the local Jahn-Teller axes, and hence the principal hyperfine field directions of Mn(2) and Mn(1) ions, are canted away from the  $c$  axis at angles of  $7.9^\circ$  and  $34.0^\circ$ , respectively. With  $I = 5/2$ ,  $\Delta\nu_Q = 5.15 \pm 0.05$  MHz for the Mn(2) peak and  $\Delta\nu_Q = 3.3 \pm 0.10$  MHz for the Mn(1) peak, resulting in  $e^2qQ$  values of  $35.33 \pm 0.35$  and  $41.43 \pm 1.26$  MHz, respectively. No such information can be obtained from the oriented powder data. Vacuum-drying and crushing the crystals obviously changes the environment of the Mn ions, most likely due to the pressure and temperature change placed on the crystals during this process. Further studies of these

effects are underway to determine the exact cause of the transformation. More significant to this work is the knowledge that an aligned powder does not represent a statistical average of the crystal, as is seen by the large shift of the peaks in the aligned powdered spectra, suggesting that studies on aligned powders should be treated with caution.

(ii) Comparison of the single crystal spectrum of **1** (Figure 7-20c) with those reported earlier using oriented powders shows qualitative differences. In particular, the splitting reported on the Mn(3) peak, at ~230 MHz, was earlier assigned to a partially resolved quadrupolar interaction. In contrast, our data demonstrate three gaussian lines (Figure 7-20), instead of five lines expected from this interpretation. Rather, these peaks could originate from structural isomers of **1** (with very little or no quadrupolar splitting), as was inferred from X-ray analysis<sup>172</sup> and supported by recent high-field EPR<sup>26,188</sup> and magnetization data.<sup>189</sup> Additional measurements are needed to identify the origin of the powdering effects. From the line positions (obtained from fitting with three gaussians) shown in the inset of Figure 7-20c and  $\gamma_n^{55}$ , we deduce that the three variants of **1** have internal fields of 21.89, 21.93 and 22.07 T for the [Mn<sub>4</sub>O<sub>4</sub>] core. These should be contrasted with the average value of 21.8 T reported by Goto and co-workers<sup>185</sup> and 22.11 T for **26**.

The higher resolution afforded by the single crystal of complex **26** allows the investigation of the anisotropic behavior of the hyperfine field of the Mn(3) site. Measurements were made with a Zeeman field of 1 T in the *ac* plane and 2 T in the *ab* plane, which allows resolution for observing the critical structures in the spectra. For example, in Figure 7-22, we observe an evolution of the zero-field single peak, splitting first into two peaks at low angles and then into four distinct peaks when the field is at

large angles with respect to the  $a$  or  $b$  axis. This result can only be attributed to four magnetically distinct (but crystallographically equivalent)  $\text{Mn}^{\text{IV}}$  ions in the  $[\text{Mn}_4\text{O}_4]$  core. Our preliminary analysis suggests that the hyperfine fields at each of the atoms in the core are canted away from the  $c$  axis with a small but finite perpendicular component. Consequently, this implies that the interaction among the local electronic moments in the core leads to a spin structure that is not purely ferromagnetically aligned, as suggested earlier by EPR data.<sup>190</sup> Because **26** is even more symmetric than **1**, our results imply that earlier conclusions based on the hyperfine fields being parallel to the easy-axis need to be reexamined.

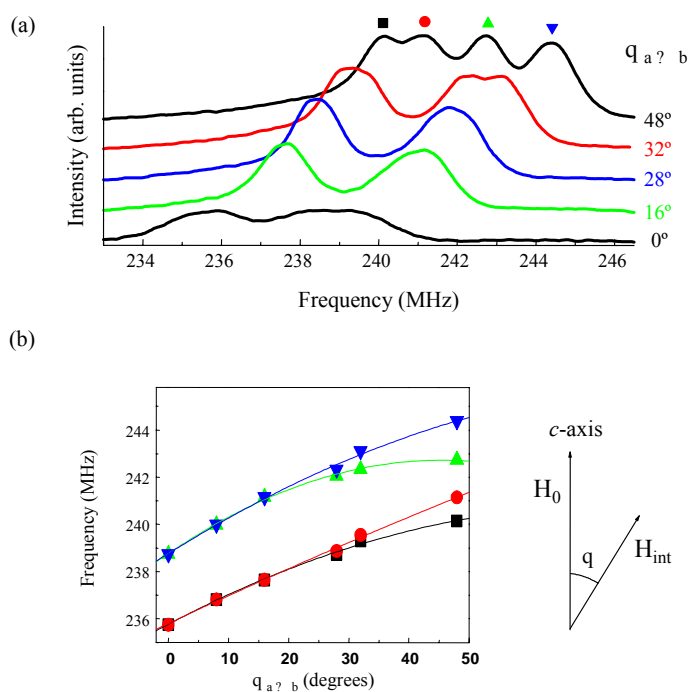


Figure 7-22. Angular dependence of  $^{55}\text{Mn}$  NMR in the  $ab$  plane of a single crystal of complex **26**· $4\text{CH}_2\text{Cl}_2$ .

Angular dependence of the  $\text{Mn}(3)$  peak of **26** was also conducted from the easy to hard axis, as shown in Figure 7-23. Rotation in the  $ac$  plane was prepared by cooling the crystal in zero field, so signals from both  $m_s = \pm 10$  states are discernable, separated by

twice the Zeeman frequency at the applied field of 1 T. The angular variation in the  $ac$  plane is described by the eq 7-5, where  $\nu_{CF}$  represents the central frequency and  $\theta$  is the angle between the applied field  $H_0$  and the  $c$  axis of the crystal.

$$\text{Peak frequency} = \nu_{CF} \pm (^{55}\gamma / 2\pi)(H_0)(\cos\theta) \quad (7-5)$$

As the crystal is rotated, the effective field,  $H_{\text{eff}}$ , felt by the nuclei is the sum of the projection of  $H_0$  onto the hyperfine field,  $H_N$  ( $H_{\text{eff}} = H_N \pm H_0 \cos\theta$ ). Thus, a maximum in the splitting is seen when  $H_0$  is parallel to the  $c$ -axis ( $\theta = 90^\circ$ ). One interesting result is the splitting observed when the crystallographic  $c$ -axis is perpendicular to the external field,  $H_0$ . When the crystal is in this configuration and an external field is applied, we observe two peaks as opposed to the expected one peak. We tentatively assign this to two different orientations of the hyperfine fields at the  $\text{Mn}^{\text{IV}}$  sites.

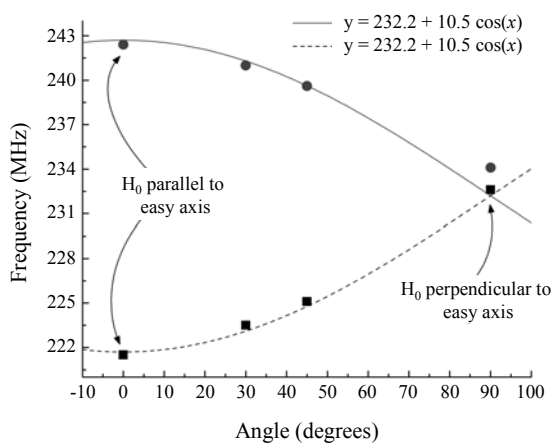


Figure 7-23. Angular dependence of  $^{55}\text{Mn}$  NMR in the  $ac$  plane of a single crystal of complex  $26 \cdot 4\text{CH}_2\text{Cl}_2$ .

The  $^{55}\text{Mn}$  spectrum gives information on the coupling of the nuclear magnetic moments of the Mn nuclei with the local magnetic moments of the electrons, and for this reason, the spectrum is only visible at very low temperatures. At temperatures above the blocking temperature  $T_B$  of a SMM, that is the temperature at which the molecule

functions as a magnet, the magnetization vectors of the electrons are rapidly changing orientations. Hence, the manganese nuclei relax at very fast rates because of the fast electronic relaxation and the peaks are broadened to such an extent that the spectrum appears to be featureless. Once the temperature at which measurements are taken is below  $T_B$ , the local magnetic moments couple to only one orientation of the local magnetic moments of the electrons of the Mn center, giving a sharp signal. Hence, low temperatures are essential for this technique (Figure 7-24).

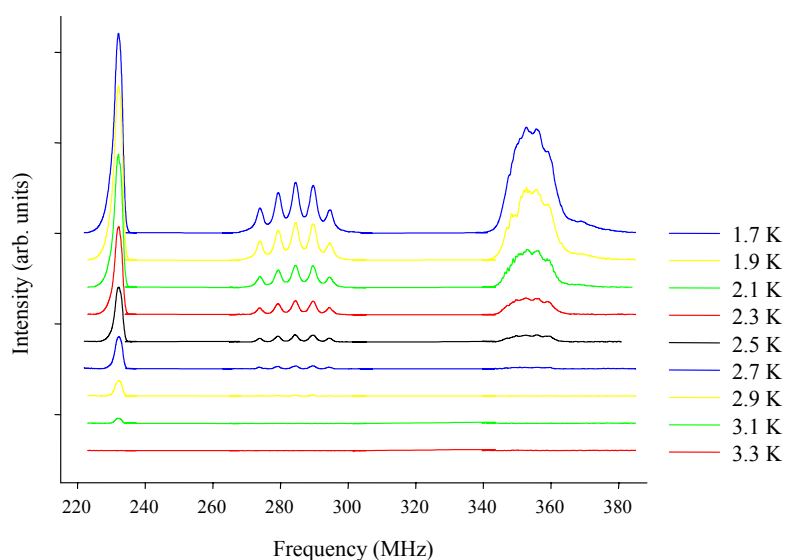


Figure 7-24. Temperature dependence of the  $^{55}\text{Mn}$  NMR spectrum of a single crystal of complex  $26 \cdot 4\text{CH}_2\text{Cl}_2$  at the indicated temperatures.

In conclusion, the ability to probe individual Mn sites within the  $\text{Mn}_{12}$  core represents a powerful new tool to study factors such as symmetry lowering in SMMs due to extrinsic perturbation. Single crystal  $^{55}\text{Mn}$  NMR spectroscopy affords a significant resolution enhancement over oriented powder spectroscopy, allowing information to be obtained that would otherwise not be achievable, including more accurate measurements of hyperfine fields and quadrupole coupling constants. It also shows that vacuum-drying and powdering of these SMM crystals introduced a significant structural perturbation.

Angular dependence studies show that there are further studies to be done to better understand the magnetic structure of this molecule. The higher symmetry of **26**, a result of the absence of hydrogen-bonding of lattice solvent molecules with the Mn<sub>12</sub> molecule, produces a less convoluted spectrum than **1**, suggesting that **26** is a model system to study for understanding magnetic tunneling in the Mn<sub>12</sub> family.

## 7.2.6 Magnetochemistry of Complex **26**

### 7.2.6.1 DC studies

Variable-temperature DC magnetic susceptibility ( $\chi_M$ ) data were collected on a microcrystalline powdered sample of **26**, restrained in eicosane to prevent torquing, in a 5.0 kG magnetic field in the 5.0-300 K range (Figure 7-25). The  $\chi_M T$  versus  $T$  dependence is similar to those of previously studied [Mn<sub>12</sub>O<sub>12</sub>(O<sub>2</sub>CR)<sub>16</sub>(H<sub>2</sub>O)<sub>4</sub>] complexes with  $S = 10$  ground states, exhibiting a nearly temperature-independent value of 19-20 cm<sup>3</sup> K mol<sup>-1</sup> in the 150-300 K range which then increases rapidly to a maximum of 51 cm<sup>3</sup> K mol<sup>-1</sup> at 15 K before decreasing rapidly at lower temperatures.<sup>13,22</sup>

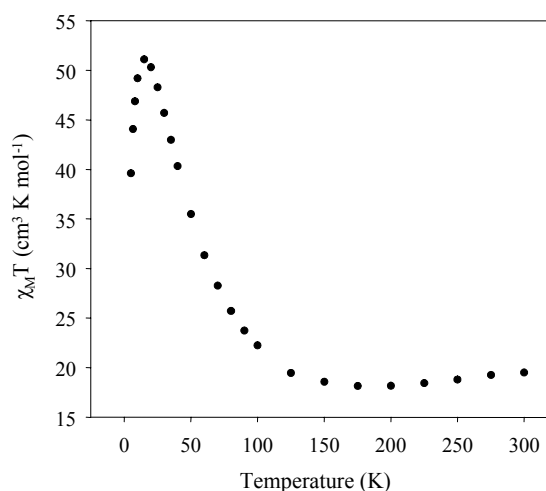


Figure 7-25. Plot of  $\chi_M T$  vs temperature for a dried, microcrystalline sample of complex **26** in eicosane.  $\chi_M$  is the DC molar magnetic susceptibility measured in a 5.0 kG field.

The maximum suggests a large ground state spin (S) value for the complex, with the sharp decrease at low temperatures primarily due to a combination of Zeeman and zero-field splitting effects. The spin-only ( $g = 2$ ) value for a unit composed of noninteracting  $\text{Mn}^{\text{IV}}_4\text{Mn}^{\text{III}}_8$  ions is  $31.3 \text{ cm}^3 \text{ K mol}^{-1}$ . The  $\chi_{\text{M}}T$  value at 300 K of **26** is less than that expected for noninteracting metal ions, indicating the presence of appreciable intramolecular exchange interactions.

A matrix diagonalization of the spin Hamiltonian of the complex to evaluate the various  $\text{Mn}_2$  exchange parameters would allow the determination of all of the possible spin states and their energies and hence, is a method by which the ground state spin of **26** could be determined. Such a matrix diagonalization approach is not so simple however as it involves a matrix of  $1.0 \times 10^8$  by  $1.0 \times 10^8$  dimensions. Additionally, as with other  $\text{Mn}_{12}$  complexes, it is not feasible to apply the Kambe equivalent operator method<sup>51</sup> to evaluate the exchange parameters (J) between the Mn ions because of the size and complexity of the molecule. Thus, variable-temperature, variable-field DC magnetization (M) data were collected in the 1.8-4.0 K range at applied DC fields (H) ranging from 1-70 kG. The data in Figure 7-26a are shown as reduced magnetization ( $M/N\mu_{\text{B}}$ ) plotted versus  $H/T$ , where M is the magnetization, N is Avogadro's number,  $\mu_{\text{B}}$  is the Bohr magneton, and H is the magnetic field. For complexes populating only the ground state and experiencing no zero-field splitting (ZFS), the magnetization follows the Brillouin function and the isofield lines all superimpose and saturate at a value of  $gS$ . The nonsuperimposition of the isofield lines clearly indicates the presence of ZFS. The  $M/N\mu_{\text{B}}$  versus  $H/T$  data were fit using the program MAGNET<sup>54</sup> that assumes only that the ground state is populated at these temperatures and magnetic fields.<sup>53</sup> A spin

Hamiltonian including a isotropic Zeeman interactions and axial zero-field splitting ZFS ( $D\hat{S}_z^2$ ) was used to least-squares-fit the data. The matrix was diagonalized on each cycle, and a powder average was calculated. The best fit is shown as solid lines in Figure 7-26a, and the fitting parameters were  $S = 10$ ,  $g = 1.87$ , and  $D = -0.38 \text{ cm}^{-1} = -0.54 \text{ K}$ . The values are typical members of the  $\text{Mn}_{12}$  family.

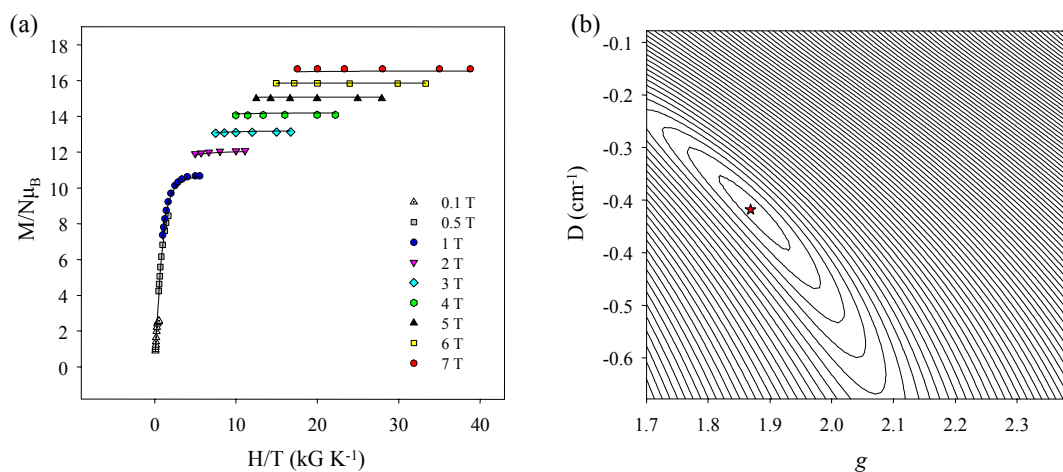


Figure 7-26. Determination of the ground state spin. (a) Plot of  $M/N\mu_B$  versus  $H/T$  for a dried, microcrystalline sample of complex **26** in eicosane at the indicated applied fields. The solid lines are the fit of the data; see the text for the fit parameters. (b) Two-dimensional contour plot of the error surface for the  $D$  vs  $g$  fit for complex **26**. The asterisk indicates the minimum.

Other  $S$  values were also explored in the fitting; attempts to fit the magnetization data either with an  $S = 9$  or a  $S = 11$  ground state spin gave fitting parameters of  $g = 2.08$  and  $D = -0.47 \text{ cm}^{-1}$  and  $g = 1.71$  and  $D = -0.32 \text{ cm}^{-1}$ , respectively. Each fit was of similar quality to that obtained for  $S = 10$ , but the  $g$  value is too high in the case of  $S = 9$ ; a  $g$  value significantly greater than that of a free electron (2.0023) is unreasonable. Similarly, the  $g$  and  $D$  values obtained for the  $S = 11$  fit are slightly lower than that expected for a neutral  $\text{Mn}_{12}$  species. In order to confirm that the obtained parameters were the true global rather than local minimum, and to assess the uncertainty in the obtained  $g$  and  $D$

values, a root-mean square  $D$  vs  $g$  error surface for the fit was generated using the program GRID.<sup>55</sup> The error surface is shown in Figure 7-26b as a contour plot for the  $D = -0.07$  to  $-0.70$   $\text{cm}^{-1}$  and  $g = 1.7$  to  $2.3$  ranges. One soft fitting minimum is observed; the contour describes the region of minimum error from  $D \approx -0.32$  to  $-0.44$   $\text{cm}^{-1}$  and  $g \approx 1.81$  to  $1.93$ , giving fitting parameters of  $D = -0.38 \pm 0.06$   $\text{cm}^{-1}$  and  $g = 1.87 \pm 0.06$ .

### 7.2.6.2 AC studies

In order to probe the dynamics of the relaxation of the magnetization of the complex, AC susceptibility studies were collected on a dried, microcrystalline sample of **26** and on wet crystals of **26**·4CH<sub>2</sub>Cl<sub>2</sub> in the 1.8-10 K range in a 3.5 G AC field with eight oscillation frequencies ( $\nu$ ) from 5 to 1488 Hz. In Figure 7-27 are shown the resulting in-phase (as  $\chi_M' T$ ) and out-of-phase ( $\chi_M''$ ) AC susceptibility signals for a vacuum-dried sample of **26**. In an AC susceptibility experiment, a weak field (typically 1-5 G) oscillating at a particular frequency ( $\nu$ ) is applied to a sample. The magnetization vector of the molecule oscillates with the AC field, and there is no out-of-phase AC susceptibility signal ( $\chi_M''$ ) until the temperature is lowered to a value at which the barrier to magnetization relaxation is comparable to the thermal energy. A frequency-dependent  $\chi_M''$  signal is observed and there is a concomitant frequency-dependent decrease in the in-phase ( $\chi_M'$ ) signal. The value of  $\chi_M' T$  in the temperature-independent region provides especially useful support for conclusions drawn concerning the ground state spin of a cluster from DC magnetization measurements described above. A value of  $\chi_M' T$  that is independent of temperature indicates the ground state is well-isolated, and hence, DC magnetization measurements within the temperature-independent range, can be fitted to give the true ground state spin of the molecule. The  $\chi_M' T$  value of  $\sim 50$   $\text{cm}^3$  K mol<sup>-1</sup> for

**26** corresponds to an  $S = 10$  system with  $g = 1.91$ , consistent with the DC magnetization results above.

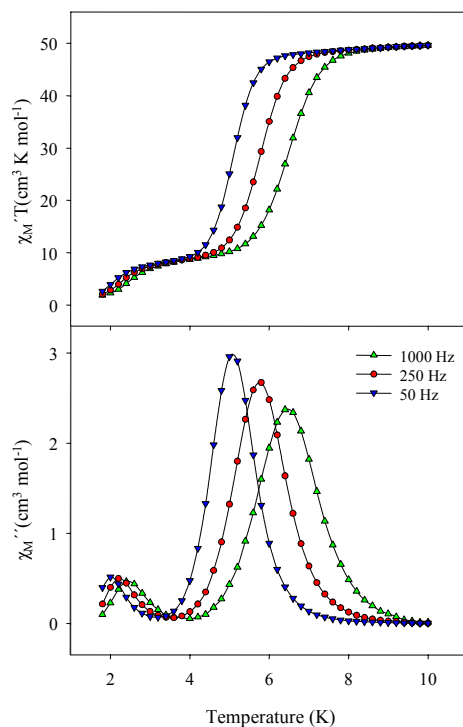


Figure 7-27. Plot of the in-phase (as  $\chi_M' T$ ) and out-of-phase ( $\chi_M''$ ) AC susceptibility signals vs temperature for a dried, microcrystalline sample of complex **26** at the indicated oscillation frequencies.

A comparison of the  $\chi_M''$  vs  $T$  plot for dry and wet samples of **26** for a field oscillating at 1000 Hz can be made using the top and bottom portions of Figure 7-28, respectively. The dried, microcrystalline sample of **26** exhibits two signals in the out-of-phase AC susceptibility, a higher-temperature (HT) peak at  $\sim 6$  K and a lower-temperature (LT) peak at  $\sim 2.5$  K. The signals are accompanied by two frequency-dependent decreases in the in-phase  $\chi_M' T$  plot, first at  $T \sim 7$  K and then at  $T \sim 3$  K, respectively, and correspond to two distinct relaxation processes. Consistent with measurements on other  $Mn_{12}$  complexes, the HT peak of **26** predominates over the LT form by a factor of more than ten. The LT species arises as a result of the loss of highly

volatile  $\text{CH}_2\text{Cl}_2$  solvent molecules of crystallization and corresponds to a fraction of molecules in which the magnetization relaxation occurs by a different mechanism.

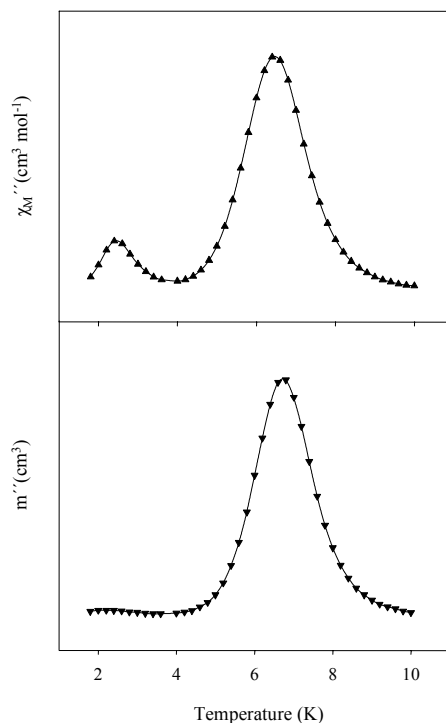


Figure 7-28. Plot of the out-of-phase AC susceptibility signals vs temperature for dried, microcrystalline complex **26** (top) and for wet crystals of complex **26**·4 $\text{CH}_2\text{Cl}_2$  (bottom) at 1000 Hz.

The presence of two such peaks in the  $\chi_M''$  vs  $T$  plots of  $\text{Mn}_{12}$  molecules is very common and has been previously attributed to Jahn-Teller isomerism, a situation whereby molecules differ in the relative orientation of at least one  $\text{Mn}^{\text{III}}$  JT elongation axis.<sup>56-59</sup> The LT (faster-relaxing) isomer is the one with the abnormal orientation of the JT axis towards the bridging oxide ions, whereas the HT (slower-relaxing) species is that with all JT axes avoiding bridging oxide ions. The  $\chi_M''$  vs  $T$  plot obtained from crystals of **26** maintained in mother liquor shows only the HT  $\chi_M''$  signal at  $\sim 7$  K, the signal expected at  $T \sim 3$  K corresponding to the LT isomer is virtually absent. Note that instead of molar susceptibility, the figure ordinates for a sample maintained in mother liquor are

simply the total magnetization (plotted as  $m''$ ) as the mass of the sample cannot be accurately determined. This finding emphasizes the importance that measurements be made on wet crystals whenever possible in order to minimize the range of molecular environments.

These AC susceptibility measurements at a given oscillation frequency as a function of temperature were supplemented with further AC susceptibility measurements on wet crystals of  $26 \cdot 4\text{CH}_2\text{Cl}_2$  at a constant temperature and a variable frequency of oscillation of the 3.5 G AC field. Such measurements have become a routine method of studying the nature of the magnetization relaxation process in SMMs<sup>100,103,113</sup> as well as spin glasses.<sup>176,191</sup> At a fixed temperature of 4.6 K, the in-phase (as  $m'$ ) and out-of-phase ( $m''$ ) components of the AC magnetic susceptibility were measured as the frequency of the AC field was varied from 0.1 to 1488 Hz. As with similar measurements on other  $\text{Mn}_{12}$  complexes,<sup>100,113</sup> the data were best fit to a distribution of single relaxation processes rather than to a single relaxation process. The  $m'$  and  $m''$  behavior as a function of angular frequency ( $\omega$ ) for a single relaxation process is given by eqs 7-6 and 7-7, respectively, while for a distribution of single relaxation processes, the  $m'$  and  $m''$  behavior is expressed by eqs 7-8 and 7-9, respectively,

$$\chi'(\omega) = \chi_s + \frac{(\chi_T - \chi_s)}{1 + \omega^2 \tau^2} \quad (7-6)$$

$$\chi''(\omega) = \frac{(\chi_T - \chi_s)\omega\tau}{1 + \omega^2 \tau^2} \quad (7-7)$$

$$\chi'(\omega) = \chi_s + \frac{(\chi_T - \chi_s)[1 + (\omega\tau)^{1-\alpha} \sin(\alpha\pi/2)]}{1 + 2(\omega\tau)^{1-\alpha} \sin(\alpha\pi/2) + (\omega\tau)^{2(1-\alpha)}} \quad (7-8)$$

$$\chi''(\omega) = \chi_s + \frac{(\chi_T - \chi_s)(\omega\tau)^{1-\alpha} \cos(\alpha\pi/2)}{1 + 2(\omega\tau)^{1-\alpha} \sin(\alpha\pi/2) + (\omega\tau)^{2(1-\alpha)}} \quad (7-9)$$

where  $\chi_s$  is the adiabatic susceptibility,  $\chi_T$  is the isothermal susceptibility,  $\omega = 2\pi\nu$  is the angular frequency, and  $\tau$  is the magnetization relaxation time. The primary importance of this measurement involves an additional parameter  $\alpha$ , a value between 0 and 1 that is included in the expressions for a distribution of single relaxation processes as a gauge of the width of the distribution. In Figure 7-29 are shown plots of  $m'$  vs frequency and  $m''$  vs frequency for wet crystals of  $26.4\text{CH}_2\text{Cl}_2$ . A least-squares fitting of the data to a single relaxation process is shown as a dashed line while the fitting to a distribution of single relaxation processes is shown as a solid line.

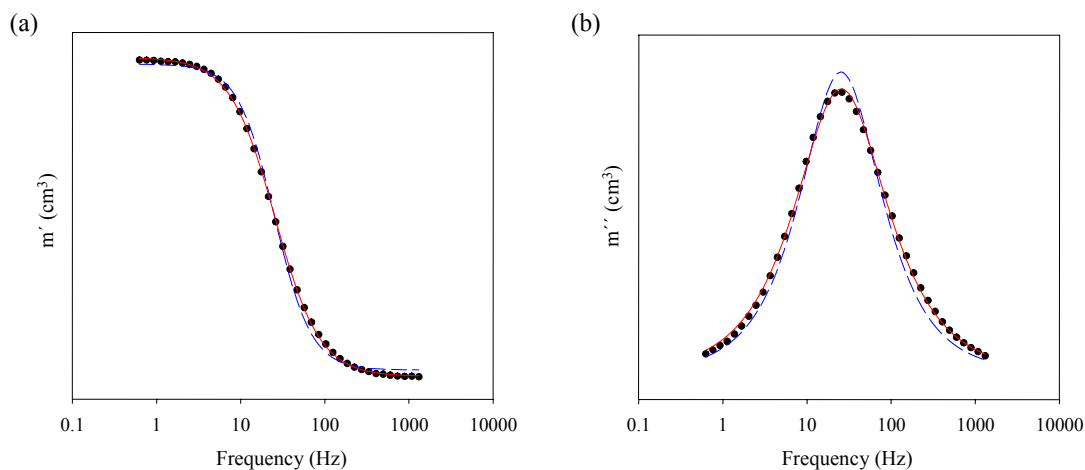


Figure 7-29. Plots of (a)  $m'$  vs frequency and (b)  $m''$  vs frequency at 4.6 K for wet crystals of  $26.4\text{CH}_2\text{Cl}_2$ . The dashed lines are a least-squares fitting of the data to a single relaxation process as described by eqs 7-6 and 7-7; the solid lines are a least-squares fitting of the data to a distribution of single relaxation processes as described by eqs 7-8 and 7-9; see the test for the fitting parameters.

Clearly, significantly improved fits are obtained for the latter, and hence, it is concluded that the magnetization relaxes via a distribution of single relaxation processes. The relaxation times ( $\tau$ ) obtained from the two fitting schemes are very similar,  $\tau = 0.0393$  s (single relaxation process) and  $\tau = 0.0392$  s (distribution of single relaxation processes) and the main difference in the fitting parameters occurs in the values of the

adiabatic and isothermal susceptibility. A Cole-Cole (or Argand) plot of  $m'$  vs  $m''$  can be used to determine the number of distinct magnetization relaxation processes. Such a plot of  $m'$  vs  $m''$  for wet crystals of  $26\cdot4\text{CH}_2\text{Cl}_2$  is shown in Figure 7-30, and the symmetric shape of the plot is indicative of only one relaxation process.<sup>176</sup>

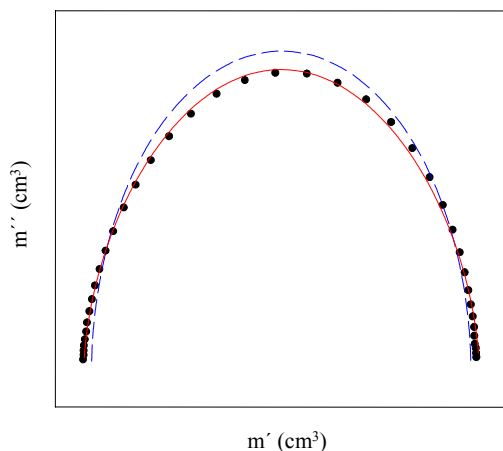


Figure 7-30. Argand plot of  $m'$  vs  $m''$  of wet crystals of  $26\cdot4\text{CH}_2\text{Cl}_2$  at 4.6 K. The dashed line is a least-squares fitting of the data to a single relaxation process as described by eqs 7-6 and 7-7. The solid line is a least-squares fitting of the data to a distribution of single relaxation processes as described by eqs 7-8 and 7-9.

Hence, the magnetization in wet crystals of  $26\cdot4\text{CH}_2\text{Cl}_2$  relaxes via a single process and there is a distribution in this single relaxation process, the width of which is gauged by the fitting parameter  $\alpha$ . The average value of  $\alpha$  obtained from the fitting of plots of  $m'$  and  $m''$  vs frequency to a distribution of single relaxation processes is 0.149. These results are very similar to those obtained on other  $\text{Mn}_{12}$  SMMs<sup>100,113</sup> and are consistent with a narrow range of energy relaxation barriers due to a distribution of environments of the molecules.

### 7.2.6.3 Relaxation studies using AC and DC data

AC susceptibility studies at several oscillation frequencies can be used as a means of determining the effective energy barrier,  $U_{\text{eff}}$ , to magnetization relaxation of a

molecule, since at the  $\chi_M''$  peak maximum the magnetization relaxation rate ( $1/\tau$ , where  $\tau$  is the relaxation time) is equal to the angular frequency ( $2\pi\nu$ ) of the AC field. Hence, out-of-phase AC measurements at different oscillating field frequencies are a valuable source of rate vs  $T$  kinetic data<sup>157</sup> that can be fitted to the Arrhenius equation (eq 7-10), where  $U_{\text{eff}}$  is the effective energy barrier to relaxation,  $k$  is the Boltzmann constant,  $\tau$  is the relaxation time and  $1/\tau_0$  is the pre-exponential factor.

$$\tau = \tau_0 \exp(U_{\text{eff}}/kT) \quad (7-10)$$

To supplement these AC data and to provide for a more accurate analysis over a wider range of temperatures, DC magnetization decay data were collected and combined with the AC  $\chi_M''$  vs  $T$  data. These data were obtained on a single crystal of  $26.4\text{CH}_2\text{Cl}_2$  using a micro-SQUID apparatus. First, a large DC field of 1.4 T was applied to the sample at about 5 K to saturate its magnetization in one direction, and the temperature was lowered to a chosen value between 1.3 and 4.4 K. When the temperature was stable, the field was swept from 1.4 to 0 T at a rate of 0.14 T/s, and then the magnetization in zero field was measured as a function of time (Figure 7-31a). An Arrhenius plot was constructed using the combined data sets and is shown in Figure 7-31b as  $\tau$  vs  $1/T$ . The fit of the thermally-activated region above  $\sim 3.3$  K gave  $\tau_0 = 2.9 \times 10^{-9}$  s and  $U_{\text{eff}} = 75$  K, consistent with values obtained from similar measurements on other neutral  $\text{Mn}_{12}$  species.

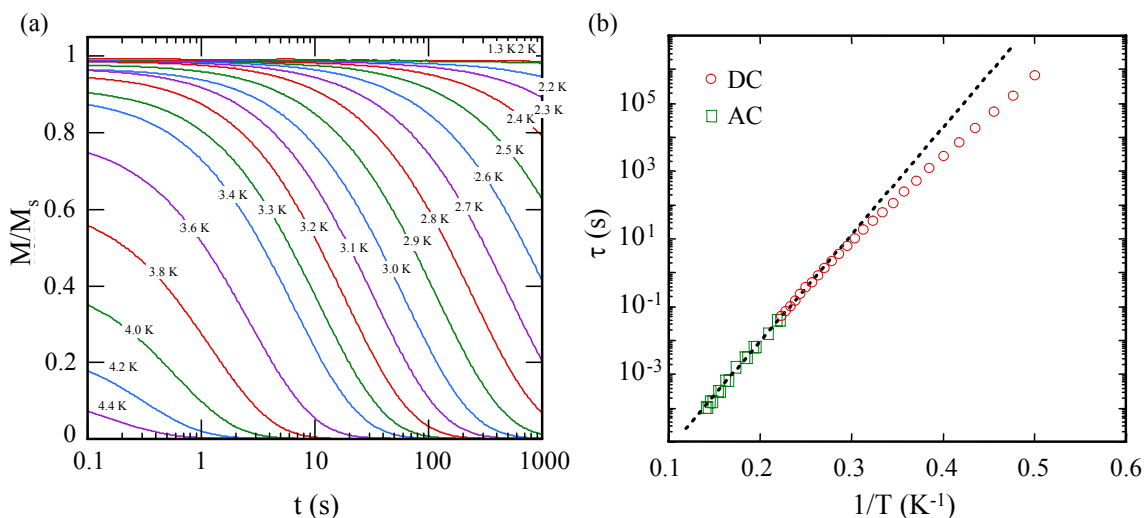


Figure 7-31. Relaxation time vs temperature studies on a single crystal of **26**·4CH<sub>2</sub>Cl<sub>2</sub>. (a) Magnetization vs time decay plots in zero field.  $M$  is normalized to its saturation value,  $M_s$ ; (b) Plot of relaxation time ( $\tau$ ) vs  $1/T$  for complex **26** using AC  $\chi_M''$  and DC decay data. The solid line is a fit to the Arrhenius equation. See the text for the fitting parameters.

#### 7.2.6.4 Hysteresis studies below 1.8 K

Like all of the reported Mn<sub>12</sub> derivatives, complex **26** is also expected to function as a SMM. Out-of-phase AC susceptibility signals exhibited by **26** are not sufficient proof of the SMM property however, and for this reason, hysteresis loops from magnetization vs DC field scans on an aligned single crystal of **26**·4CH<sub>2</sub>Cl<sub>2</sub> using a micro-SQUID apparatus were obtained. The resulting hysteresis loops are given in Figure 7-32, showing the temperature dependence at a constant field sweep rate of 2 mT/s and the field sweep rate dependence at a constant temperature of 3 K. The loops are very typical of neutral Mn<sub>12</sub> complexes, exhibiting well-defined steps that correspond to quantum tunneling of magnetization (QTM). These sharp increases in the magnetization relaxation rate occur at regular intervals of the applied field, and the field separation,  $\Delta H$ , between the steps is proportional to  $D$  as given in eq 7-11.

$$\Delta H = \frac{|D|}{g\mu_B} \quad (7-11)$$

Measurement of the step positions in Figure 7-32 gave an average  $\Delta H$  of 0.45 T and a  $|D|/g$  value of  $0.21 \text{ cm}^{-1}$  (assuming  $g = 2.0$ ). This is consistent with value of  $D$  obtained from magnetization vs field measurements on a dried sample of complex **26**. The coercivities of the hysteresis loops increase with decreasing temperature at a constant field sweep rate and increase with increasing sweep rate at a constant temperature; this is as expected for the superparamagnetic properties of a SMM.

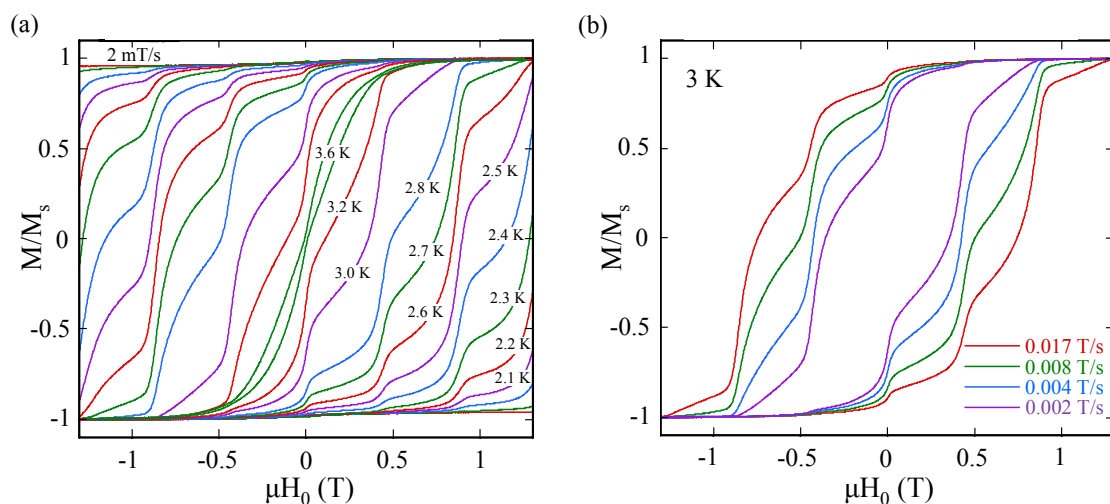


Figure 7-32. (a) Magnetization ( $M$ ) vs magnetic field hysteresis loops for complex **26**·4CH<sub>2</sub>Cl<sub>2</sub> at the indicated temperatures and sweep rate. (b) Magnetization ( $M$ ) vs magnetic field hysteresis loops for complex **26**·4CH<sub>2</sub>Cl<sub>2</sub> at the indicated sweeping rates at 3.0 K.  $M$  is normalized to its saturation value,  $M_s$ .

### 7.2.7 Single Crystal High-Frequency Electron Paramagnetic Resonance

In order to obtain detailed information on the spin Hamiltonian and to verify the  $S = 10$  ground state spin of complex **26**·4CH<sub>2</sub>Cl<sub>2</sub>, a high-frequency electron paramagnetic resonance (HFEP) spectroscopy study was performed on a single crystal. This technique is ideally suited for complexes that have appreciable zero-field splitting<sup>192</sup> and since the microwave energies employed are relatively large (110-550 GHz), it is possible

to observe direct transitions between the zero-field split sublevels of the high ground state spin. HF-EPR has been used in this capacity to characterize the ground state of several high-spin complexes.<sup>111b,111a,177,193,194</sup> Detailed analysis of the EPR spectra at various frequencies and angles gives direct access to the energy differences between spin levels and because changes in the relative intensities of EPR peaks reflect changes in the Boltzmann population of states, the sign and precise values of the zero-field splitting parameters can be determined. This then enables a precise determination of the spin Hamiltonian parameters. In an ideal case, the spin of the ground state can be determined by simply counting the number of peaks in the EPR spectrum, and the zero-field splitting parameter can be evaluated from the spacing between successive peaks.

The giant spin Hamiltonian describing the  $S = 10$  ground state spin of **26** is given by eq 7-12:

$$\hat{H} = D\hat{S}_z^2 + \mu_B \vec{H} \cdot \vec{g} \cdot \hat{S} + B_4^0 \hat{O}_4^0 + B_4^4 \hat{O}_4^4 \quad (7-12)$$

where the first term is the second order uniaxial anisotropy with a negative  $D$  value, the second term is the Zeeman interaction, and  $\hat{O}_4^0$  and  $\hat{O}_4^4$  represent the fourth order uniaxial and transverse anisotropies. In contrast to **1**, a detailed structural analysis of **26** shows the absence of any symmetry-lowering solvent disorder. On this basis, only anisotropy terms that obey the crystallographic symmetry are allowed in the spin Hamiltonian, i.e., the  $E$  parameter should equal zero.

Our initial studies on **26** at lower frequencies confirmed that the ground state spin of the molecule is  $S = 10$ , with a low-lying  $S = 9$  excited state.<sup>195</sup> Though we did obtain a reasonable estimate of the zero-field splitting (ZFS) parameters from lower frequency data ( $D = -0.456 \text{ cm}^{-1}$  and  $B_4^0 = 2.0 \times 10^{-5} \text{ cm}^{-1}$ ) (*vide infra*), this precise determination

should be carried out at higher frequencies (up to frequencies above the zero-field splitting energy of the ground state transition), and, in particular, the angle-dependent studies must be performed in order to obtain the transverse anisotropy terms (with fields applied close to the hard plane). To accurately determine the uniaxial ZFS parameters, the magnetic field is applied along the easy-axis. In this situation, the transverse anisotropy terms operate at very high orders of perturbation theory, and, essentially, vanish. Thus, the energy of each spin state is solely determined by the uniaxial anisotropy terms and the Zeeman energy  $m_s g \mu_B H$ . The energy difference diagram between adjacent levels can then be constructed accordingly as function of magnetic field. Experimentally, such a diagram is obtained by identifying the fields at which the EPR absorptions occur from EPR spectra taken at various frequencies. As shown in Figure 7-33 the solid squares mark the EPR absorptions observed in EPR spectra taken at different frequencies. The Hamiltonian parameters,  $D$ ,  $B_4^0$ , and the easy-axis  $g$  value,  $g_z$ , are obtained by minimizing the square difference between the data and simulation, which is shown in Figure 7-34a for a field applied along the easy-axis of the molecule. A similar simulation for a field applied perpendicular to the easy-axis (i.e., in the hard plane) is shown in Figure 7-34b. Though there are three parameters to be determined, the huge volume of data involved in the least squares analysis yields a precise determination of all three parameters. The solid lines plotted in Figure 7-33 present the optimal fit with  $D = -0.468 \text{ cm}^{-1}$ ,  $B_4^0 = -2.5 \times 10^{-5} \text{ cm}^{-1}$ , and  $g_z = 1.97$ .

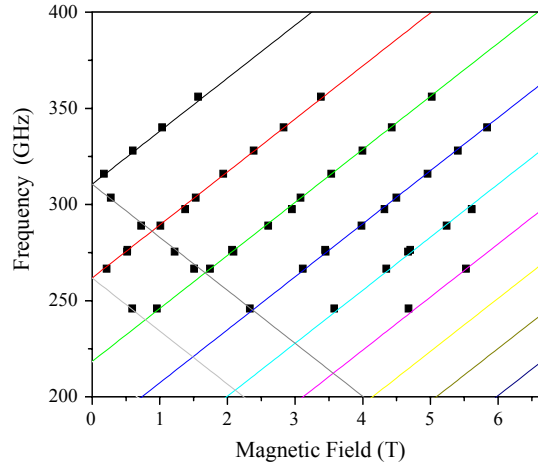


Figure 7-33. Plot of HFEPR peak positions deduced from easy-axis measurements at different frequencies in the range from 240 GHz to 360 GHz at 15 K. Solid lines represent a single fit to the data using the Hamiltonian described in the text.

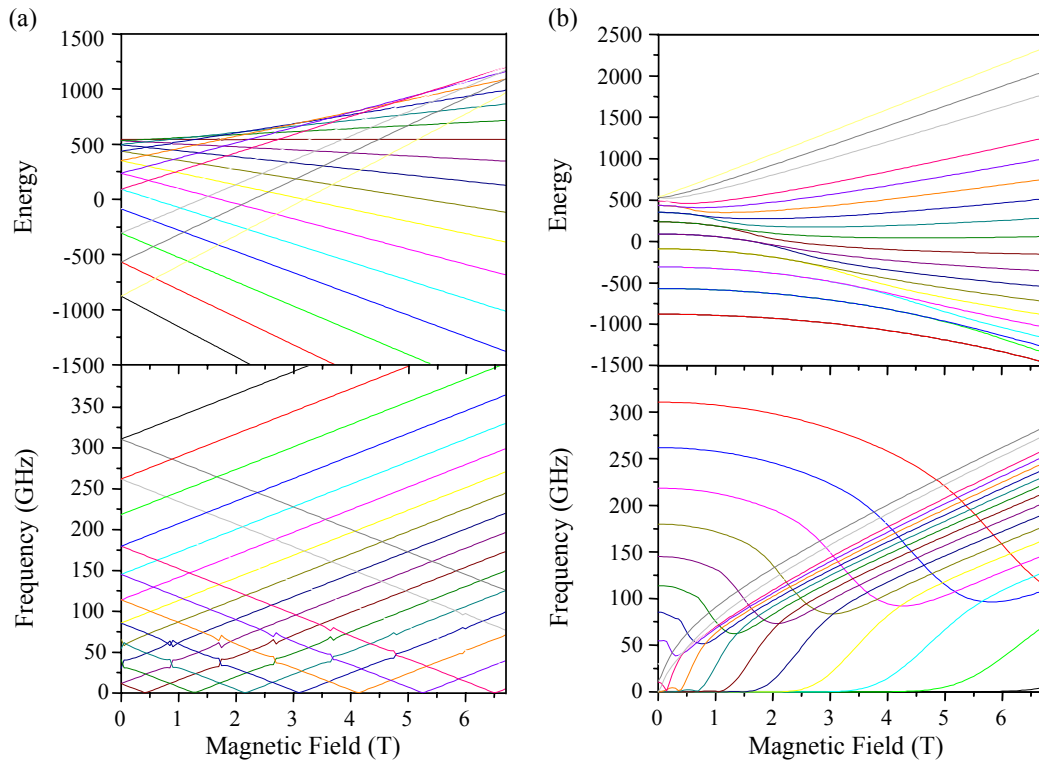


Figure 7-34. Plot of the energy and frequency of the  $m_s$  sublevels of the  $S = 10$  ground state of **26** versus applied magnetic field where (a) the applied magnetic field is parallel to the easy-axis and (b) the applied magnetic field is perpendicular to the easy-axis. The solid lines are a simulation produced using the optimal fit parameters given in the text.

When the DC magnetic field is in the hard plane, the good quantum number is no longer solely determined by the zero-field spin Hamiltonian, but also by the field direction. In this situation, the transverse anisotropy, which essentially vanishes in the axial case, becomes a zero order perturbation to the Hamiltonian, and the energies of spin levels are determined by both uniaxial and transverse ZFS parameters. Therefore, to determine the transverse anisotropy, EPR spectra were taken at 51.3 GHz, and the field was rotated within the hard plane.<sup>8,196</sup> A contour plot of the EPR absorption intensity taken over a 125° angle range, is shown in Figure 7-35. There is a clear four-fold shift of the EPR absorption peaks, and the fine structure previously observed in **1** is not seen in **26**, hence confirming the absence of discrete solvent disorder in this Mn<sub>12</sub> molecule. The four-fold shift is caused by the presence of the transverse anisotropy  $B_4^4$  term. The precise determination of  $B_4^4$  is obtained by simulating the four-fold shift with  $B_4^4 = 3 \times 10^{-5} \text{ cm}^{-1}$  and  $g_{x,y} = 1.945$  using the previously determined axial parameters.

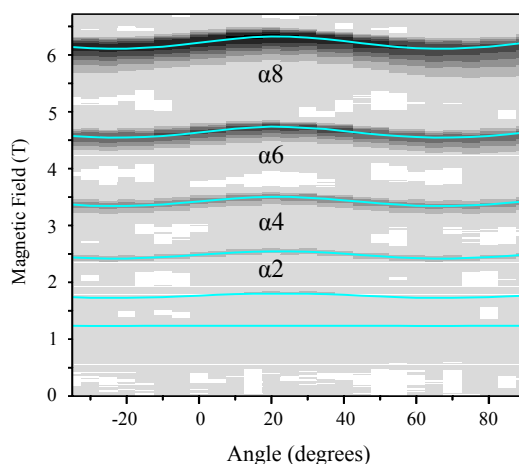


Figure 7-35. Contour plot of the angle-dependent EPR spectra with the field rotating in the hard plane. Darker shades correspond to stronger EPR absorption. Superimposed on the data is a single fit to all of the peak positions (blue lines).

It should be noted that the spectra we obtained in Figure 7-35 are not as sharp as our earlier study.<sup>195</sup> This is attributed to the poor quality of the crystal in this study relative to the crystal previously measured; this can be seen visually by the poor surface quality of the crystal in this study. The crystal was thermo-cycled *in situ* to 300 K and recooled to 15 K and the resulting EPR spectrum shows even broader resonant peaks. The comparisons of previously obtained spectra and the present data before and after thermo-cycling are shown in Figure 7-36 and the comparison indicates that the broadening of the EPR absorptions is likely caused by random solvent loss and poor handling of the crystals in the present study.

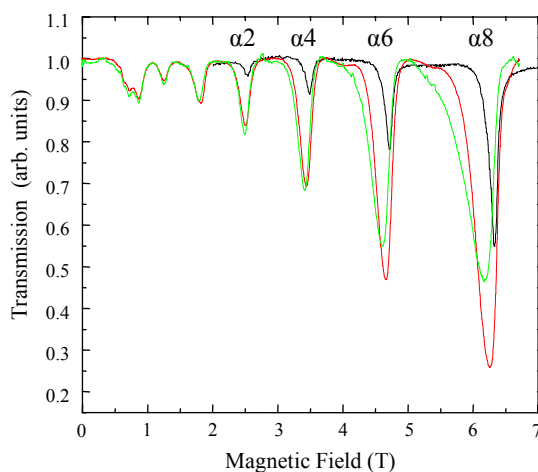


Figure 7-36. Spectra of complex **26**·4CH<sub>2</sub>Cl<sub>2</sub> taken under different conditions. The spectrum shown in black is from our earlier studies and represents the best crystal that was cooled under optimal conditions. The remaining spectra shown in red and green were obtained from the present studies, measured after the crystal was cooled only once and then after thermo-cycling, respectively.

In addition to our studies with the field applied along the easy-axis of the molecule to determine the spin Hamiltonian parameters and to characterize the ground state spin of the molecule, we also undertook a detailed investigation of the EPR spectrum with the applied field in the hard plane of the molecule. Such an investigation allows a study of the spin-energy levels of the ground state as well as excited spin states of complex **26**. In

order to align the hard plane ( $x, y$ ) of the sample with respect to the applied DC magnetic field, angle dependent measurements of the EPR spectra were performed and these are shown in Figure 7-37.

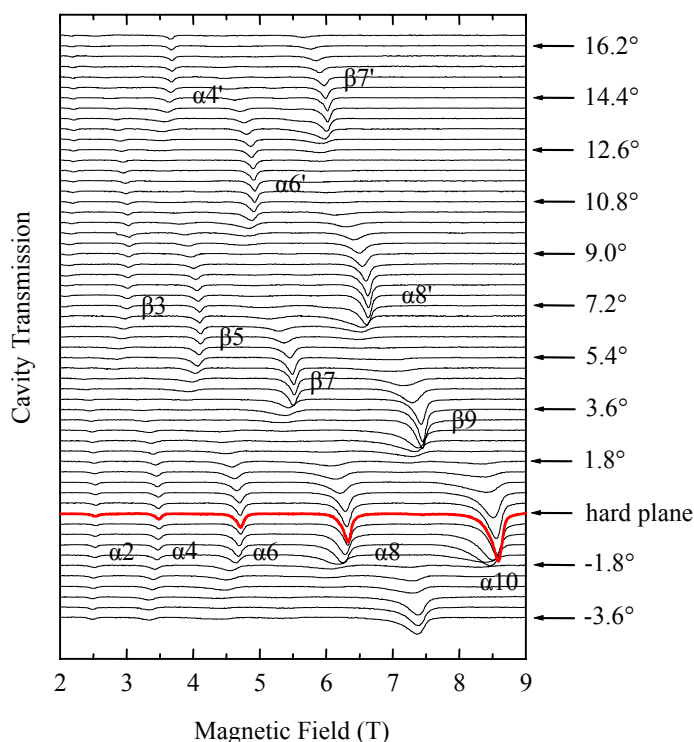


Figure 7-37. Angle dependence of the EPR spectrum of  $26 \cdot 4\text{CH}_2\text{Cl}_2$  in the range of  $\pm 3.6^\circ$  on either side of the hard plane, with an angular step of  $0.36^\circ$ .

In general, the hard plane spectra of complex  $26 \cdot 4\text{CH}_2\text{Cl}_2$  look very similar to those of complex **1**.<sup>196,197</sup> In the high-field limit ( $g\mu_B H_0 > |D|S$ ), a total of 20 EPR transitions with the  $2S + 1$  ( $S = 10$ ) multiplet are expected, as shown in Figure 7-34b by solid curves. The  $\alpha$  resonances correspond to transitions within the Zeeman-split  $\pm m_s$  zero-field sublevels and comprise half of this total. The quantization axis is defined by the uniaxial crystal field tensor in the zero-field limit and is along the  $z$  direction. In the high-field limit however, the quantization axis points along the applied field vector; the 10  $\alpha$  resonances then correspond to transitions from  $m_s = \text{even-to-odd}$  transitions, e.g.  $m_s = -10$

to -9. Because the  $\alpha$  resonances originate from pairs of levels ( $\pm m_s$ ) which are (approximately) degenerate in zero field, one expects the resonance frequencies, when plotted against field, to tend to zero as the field tends to zero, as shown in Figure 7-38. The simulation has been performed by exact diagonalization of eq 7-12, and this procedure is described in detail elsewhere.<sup>196,197</sup> In order to fit the experimental data (open circles), crystal field parameters obtained from our earlier studies of **26**·4CH<sub>2</sub>Cl<sub>2</sub> with the field along the easy-axis,  $D = -0.456 \text{ cm}^{-1}$ ,  $B_4^0 = -2.0 \times 10^{-5} \text{ cm}^{-1}$ , were used.<sup>198</sup> These Hamiltonian parameters are very close to the accepted crystal field parameters for **1** ( $D = -0.454 \text{ cm}^{-1}$ ,  $B_4^0 = -2.0 \times 10^{-5} \text{ cm}^{-1}$ ),<sup>170a,188,197</sup> thus emphasizing the close similarity of physical properties of these two Mn<sub>12</sub> derivatives.

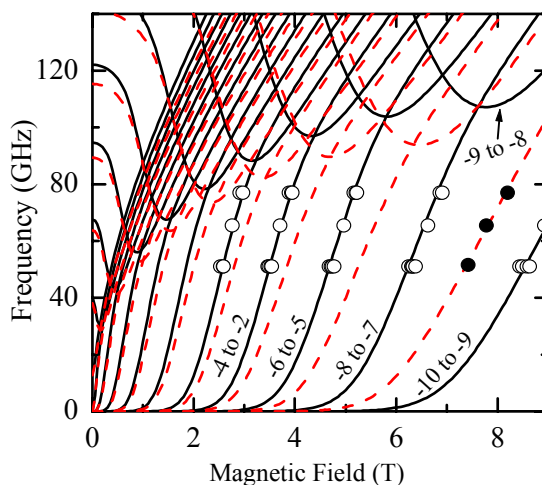


Figure 7-38. Fits to eq 7-12 for the frequency dependence of the hard plane spectra for the  $S = 10$  state (solid black curves, open circles) and for the  $S = 9$  state (dotted red curves, solid circles); the crystal field parameters for this simulation are given in the text. Open and closed circles are experimental data at frequencies of 51.5, 65.4 and 76.9 GHz.

In earlier investigations of **1** it was pointed out that EPR spectra obtained for a field applied perpendicular to the easy-axis of the molecule revealed a number of anomalous transitions which were labeled  $\beta$ ,<sup>196,197</sup> as opposed to the  $\alpha$  resonances which nicely fit the

accepted  $S = 10$  Hamiltonian (eq 7-12). Initially, these  $\beta$  transitions were tentatively ascribed to the  $m_s = \text{odd-to-even}$  transitions (e.g.,  $m_s = -9$  to  $-8$ ).<sup>196</sup> However, they should not be observable below a cutoff frequency, which is about 95 GHz at high fields for the given CF parameters, as depicted in Figure 7-38. In full agreement with these calculations we do not observe these  $\beta$  resonances until we slightly misalign the hard plane of the sample with respect to the applied magnetic field (Figure 7-37). Indeed, at  $\pm 3.6^\circ$  away from the hard plane, the  $\beta$  resonances become highly pronounced. Meanwhile, the  $\alpha_{10}$ ,  $\alpha_8$  and  $\alpha_6$  resonances disappear over this same angle range and there is even an approximately  $0.75^\circ$  range over which neither  $\alpha_{10}$  or  $\beta_9$  are observed and, although  $\alpha_4$  and  $\alpha_2$  peaks remain visible at  $\theta = \pm 3.6^\circ$ , it is clear that their intensities diminish substantially. This symmetry effect between the out-of-plane angle dependence of the  $\beta$  and  $\alpha$  resonances was recently reported for **1**, and is discussed in more detail elsewhere.<sup>26</sup> For comparison, Figure 7-39b shows simulations of the EPR spectra for the same angle range, generated using the program SIM.<sup>199</sup> These simulations agree well with our observations, i.e., the  $\alpha$  peaks disappear, and the  $\beta_9$  appears, as the field is tilted away from the hard plane. The simulations predict accurately the angles at which the  $\alpha$  peaks disappear and  $\beta_9$  peaks appear. This contrasts the behavior seen in molecules of **1**, where a significant overlap of the  $\alpha$  and  $\beta$  peaks has been attributed to a distribution of tilts of the easy axes of the molecules (up to  $\pm 1.7^\circ$ ), induced by a discrete disorder associated with the two acetic acid molecules of crystallization.<sup>26</sup> A small distribution of tilts can be inferred from the present data, as seen from the overlap of the  $\alpha_{10}$  and  $\beta_9$  resonances (Figure 7-40), and from the absence of some of the features in the simulations

which disperse strongly with angle. However, the width of the distribution must be on the order of, or less than, the angle resolution employed in these measurements, i.e.,  $\sim \pm 0.2^\circ$ .

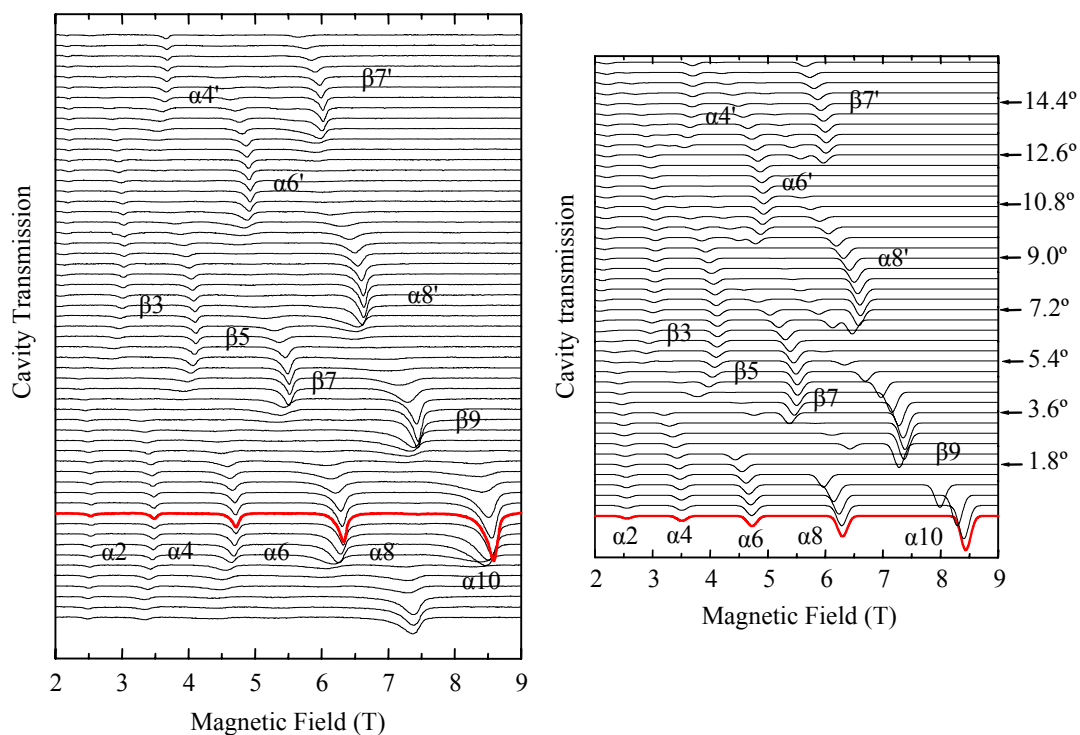


Figure 7-39. Comparison of EPR spectrum of  $26 \cdot 4\text{CH}_2\text{Cl}_2$  with simulated spectrum. (a) Angle dependence of the EPR spectrum in the range of  $\pm 3.6^\circ$  on either side of the hard plane, with an angular step of  $0.36^\circ$ . (b)  $\text{SIM}^{199}$  simulations of the EPR spectrum for the field tilted up to  $\pm 3.6^\circ$  away from the hard plane.

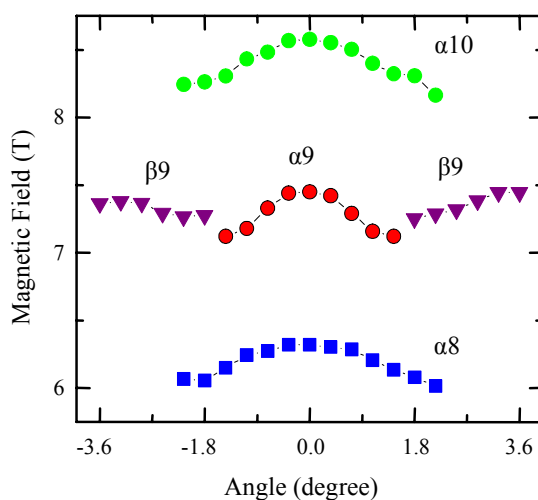


Figure 7-40. Angle dependence of several of the most important resonances.

It is also apparent from the data in Figure 7-37 that, for the most part, the resonances are extremely symmetric and much sharper than those of **1**.<sup>26</sup> In particular, none of the fine structures seen in the hard axis spectra of **1** are seen for the present complex; e.g., the pronounced high-field shoulders on the  $\alpha$  resonances. Consequently, we conclude that the discrete solvent disorder<sup>26,172,173,188,189</sup> that is now well established in **1** is absent in **26**. This observation is consistent with the full complement of four solvent molecules per formula unit, and suggests that complex **26** probably represents a more suitable candidate for measurements of quantum effects in high-symmetry  $S = 10$  SMMs.

In Figure 7-41a is shown the temperature dependence of the EPR spectra of **25** at 51.5 GHz for a field applied perpendicular to the easy-axis to within an accuracy of  $\pm 0.1^\circ$ , as inferred from the angle dependent data in Figure 7-37. As the temperature is increased from 10 K up to 40 K, an extra resonance is found at 7.42 T. Since this peak is located between the  $\alpha_{10}$  and  $\alpha_8$  resonances, it is labeled as  $\alpha_9$ . Similar peaks at 65.4 and 76.9 GHz were also observed, which are located, respectively, at 7.77 and 8.22 T between the  $\alpha_8$  and  $\alpha_{10}$  peaks (Figure 7-41b).

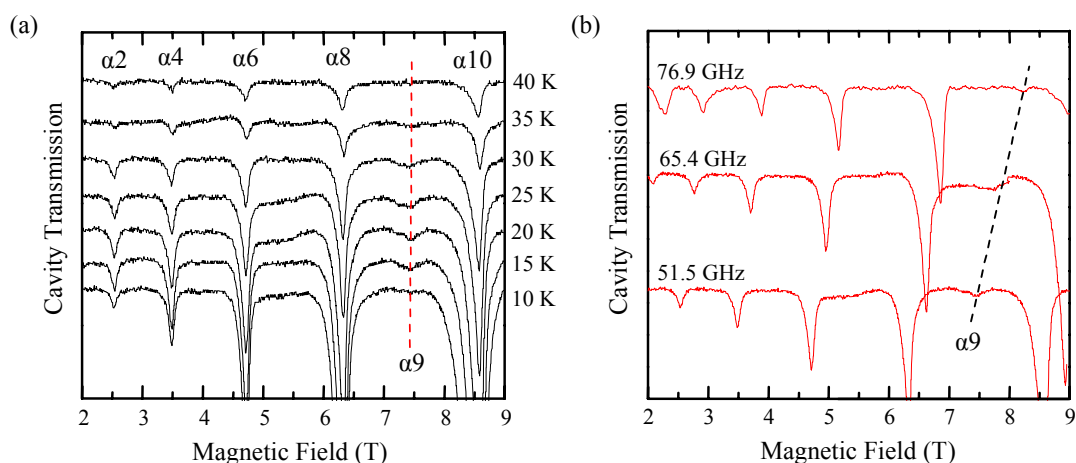


Figure 7-41. EPR spectra for a single crystal of complex **26**·4CH<sub>2</sub>Cl<sub>2</sub> measured at (a) different temperatures at 51.5 GHz and (b) different frequencies, specifically 51.5, 65.4 and 76.9 GHz.

The positions of  $\alpha_9$  peaks as a function of frequency are plotted as solid circles in Figure 7-40. It is tempting to attribute these  $\alpha$  resonances to the onset of the  $\beta_9$  transitions, which could occur if a small minority of molecules have their easy-axes tilted with respect to the majority of molecules, whose easy-axes are exactly perpendicular to the applied magnetic field, as has recently been found for **1**.<sup>26</sup> However, a careful angle-dependent study of the EPR spectra shows that the positions of  $\alpha_9$  and  $\beta_9$  exhibit completely different angle dependencies. The temperature dependencies of the intensities of the  $\alpha_9$  and  $\beta_9$  peaks reveal even more discrepancies. The areas under the  $\alpha_9$  and  $\beta_9$  peaks were calculated by integration and plotted as a function of temperature (Figure 7-42a). This procedure does not employ any fitting functions and is sensitive only to the noise background of the data; the corresponding uncertainty is depicted by error bars in Figure 7-42a. Again, the nature of the  $\alpha_9$  resonance is different from the  $\beta_9$  resonance and, thus, cannot be explained within the framework of the  $S = 10$  picture.

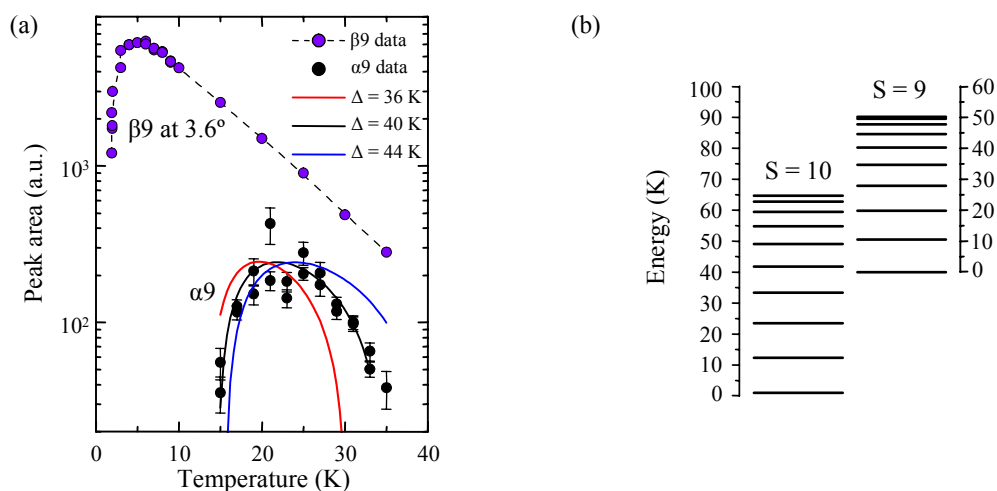


Figure 7-42. Determination of relative energy of  $S = 9$  excited state. (a) Temperature dependence of the area of the  $\alpha_9$  and  $\beta_9$  resonances. The curves through the solid circles represent the calculated  $\alpha_9$  resonance areas assuming  $\Delta = 36$  K,  $\Delta = 40$  K and  $\Delta = 44$  K. (b) Schematic for the energy levels of both the  $S = 10$  and  $S = 9$  states in zero magnetic field. The  $S = 9$  state is located at an energy  $\Delta = 40 \pm 2$  K above the bottom of the  $S = 10$  state.

Further examination of Figures 7-41 and 7-42 reveals that the  $\alpha_9$  resonance diminishes in intensity as the temperature decreases to 15 K, becoming invisible at 10 K. This fact proves beyond any doubt that the  $\alpha_9$  resonance originates from an excited state of the  $\text{Mn}_{12}$  molecule. We therefore conclude that, at low frequencies, the  $\alpha_9$  resonance corresponds to a transition within an excited state of complex **26**. For comparison, Figure 7-38 includes dashed red curves corresponding to fits to the  $\alpha_9$  data; this fit assumes  $S = 9$  and, due to the limited number of data points, allows only for the variation of  $D$ . For an odd total spin state, the low field limiting behavior of odd-to-even  $m_s$  and even-to-odd  $m_s$  transitions is the reverse of that for an even total spin state. Consequently, one does expect the frequency of the  $m_s = -9$  to  $-8$  transition to go to zero in the low field limit within the  $S = 9$  manifold. The fit to the data for  $S = 9$  yields the Hamiltonian parameter  $D = -0.430 \text{ cm}^{-1}$  ( $-0.62 \text{ K}$ ), which is 5% smaller than for  $S = 10$ . The low frequency  $\alpha_9$  resonance data lie perfectly on the  $S = 9$  curves. Therefore, the anisotropy barrier for the  $S = 9$  state is  $|D|S^2 \approx 50 \text{ K}$ , which is 23% smaller than that for  $S = 10$  (65 K). Having established that the low-frequency  $\alpha_9$  transition corresponds to an  $S = 9$  state, we can estimate its approximate location relative to  $S = 10$ . Using the CF parameters for both  $S = 10$  and  $S = 9$  states, the energy levels  $E_{10}(m_s)$  and  $E_9(m_s)$  for the two states, and both partition functions for a given temperature  $T$ , where  $\Delta$  is the energy difference between the bottoms of the  $S = 10$  and  $S = 9$  manifolds were calculated using eq 7-13.

$$Z_{10}(m_s) = \sum_{m_s=-10}^{10} e^{-E_{10}(m_s)/T} \text{ and } Z_9(m_s) = \sum_{m_s=-9}^9 e^{(-E_9(m_s)+\Delta)/T} \quad (7-13)$$

The area under the  $\alpha_9$  peak, at a given temperature, is proportional to the difference in populations of the corresponding levels (eq 7-14).

$$A_{\alpha 9}(\Delta, T) \propto \frac{N_{-9} - N_{-8}}{Z} = \frac{e^{\{E_9(-8) - E_9(-9)\} / T}}{Z_{10}(T) + Z_9(\Delta, T)} \quad (7-14)$$

Thus, by varying the only parameter  $\Delta$ , we have found that the  $S = 9$  manifold is located at  $\Delta = 40 \pm 2$  K above the bottom of the  $S = 10$  state (Figure 7-42b). This implies that the  $S = 9$  state lies very close to the  $m_s = \pm 6$  excited state within the  $S = 10$  multiplet. We have also performed similar calculations of the temperature dependence of the  $\alpha 9$  peak area for the values of  $\Delta = 36$  K and  $\Delta = 44$  K, and both dependencies were inconsistent with our experimental data, as depicted in Figure 7-42a. The obtained location of the  $S = 9$  excited state at  $\Delta = 40 \pm 2$  K is in perfect agreement with recent calculations.<sup>200</sup>

In summary, detailed analysis of the EPR spectra obtained on a single crystal of **26**·4CH<sub>2</sub>Cl<sub>2</sub> show very similar ZFS parameters to the acetate-substituted derivative. However, our spectroscopic analysis does not show any evidence of second order transverse anisotropy, which confirms that the discrete solvent disorder is not present in the molecules. It is worth noting that the crystals are very susceptible to solvent loss, even more so than crystals of complex **1**, and hence, must be treated very carefully prior to measurements. Similar frequency and temperature dependent EPR studies with the applied field in the hard plane of the molecule reveal the existence of an  $S = 9$  state located only  $40 \pm 2$  K above the  $S = 10$ ,  $m_s = \pm 10$  ground state. This result is in perfect agreement with theoretical predictions.<sup>200,201</sup> The effects of the coexistence of an excited  $S = 9$  state and the ground  $S = 10$  state in the Mn<sub>12</sub> molecule are not known, and we hope these investigations will stimulate further studies. Our experiments also indicate that **26** is an intrinsically cleaner system than **1**, which we believe to be connected with the fact that the former possesses a full complement of four solvent molecules per formula unit. Thus,

further investigations of the title compound may provide further insights into the quantum magnetization dynamics of giant spin ( $S = 10$ ) SMMs.

### 7.3 Conclusions

The goal of this investigation included (i) a detailed study of the structure, magnetic properties, and high-frequency electron paramagnetic resonance spectrum of  $[\text{Mn}_{12}\text{O}_{12}(\text{O}_2\text{CCH}_2\text{Br})_{16}(\text{H}_2\text{O})_4]$  and (ii) the confirmation of the origin of the abnormal features present in the hysteresis loops and EPR spectra of molecules of  $[\text{Mn}_{12}\text{O}_{12}(\text{O}_2\text{CMe})_{16}(\text{H}_2\text{O})_4] \cdot 2\text{MeCO}_2\text{H} \cdot 4\text{H}_2\text{O}$  by comparison of the former to those obtained on the high-symmetry  $\text{Mn}_{12}$  molecule in the present work. To assess the presence or absence of interactions between the  $\text{Mn}_{12}$  molecule and interstitial solvent molecules, our X-ray crystal structure of **26** included the refinement of the four  $\text{CH}_2\text{Cl}_2$  solvent molecules of crystallization, and a detailed structural analysis subsequently revealed almost no symmetry-lowering contacts between  $\text{Mn}_{12}$  molecules. This is in contrast to molecules of **1**, where hydrogen-bonding interactions between the  $\text{Mn}_{12}$  molecule and acetic acid molecules of crystallization break the tetragonal symmetry of the molecule, giving rise to up to six isomers in the crystalline lattice.

Similar to other typical neutral  $\text{Mn}_{12}$  species, DC studies establish that the ground state spin of **26** is  $S = 10$  and that the molecule possesses a significant uniaxial magnetic anisotropy. Magnetization vs DC field scans exhibit hysteresis, establishing that **26** is a single-molecule magnet. AC susceptibility studies carried out on wet crystals maintained in mother liquor to prevent the loss of interstitial solvent and on a dried, microcrystalline sample showed that solvent loss increases the fraction of faster-relaxing molecules in a sample of **26**. This result is consistent with differences observed between the  $^{55}\text{Mn}$  NMR spectra obtained on a single crystal of **26** maintained in mother liquor and on a dried,

microcrystalline sample of **26** and emphasizes the importance of the environment and local symmetry of a molecule on the resulting magnetic properties of a SMM. More in-depth HFEPN measurements on a single crystal of **26** reveal that in contrast to **1**, there is no second order transverse magnetic anisotropy. Further analysis shows that the spectra obtained on a single crystal of **26** are generally much sharper, with more symmetric resonance profiles, than those of **1**. The higher symmetry of **26**, a result of the absence of hydrogen-bonding of lattice solvent molecules with the Mn<sub>12</sub> molecule, suggests that **26** is a model system to better our understanding of the quantum magnetization dynamics in the Mn<sub>12</sub> family.

## 7.4 Experimental

### 7.4.1 Synthesis

All manipulations were performed under aerobic conditions using materials as received, except where otherwise noted. [Mn<sub>12</sub>O<sub>12</sub>(O<sub>2</sub>CMe)<sub>16</sub>(H<sub>2</sub>O)<sub>4</sub>] $\cdot$ 2MeCO<sub>2</sub>H $\cdot$ 4H<sub>2</sub>O (**1**) was prepared as described elsewhere.<sup>50</sup>

[Mn<sub>12</sub>O<sub>12</sub>(O<sub>2</sub>CCH<sub>2</sub>Br)<sub>16</sub>(H<sub>2</sub>O)<sub>4</sub>] (**26**). To a solution of complex **1** (2.0 g, 0.97 mmol) in a mixture of MeCN (50 cm<sup>3</sup>) and CH<sub>2</sub>Cl<sub>2</sub> (50 cm<sup>3</sup>) was added BrCH<sub>2</sub>CO<sub>2</sub>H (4.3 g, 31 mmol). The mixture was stirred for 1 hr, and the solvent was removed *in vacuo*. Toluene (20 cm<sup>3</sup>) was added to the residue, and the solution was again evaporated to dryness. The addition and removal of toluene was repeated two more times. The remaining solid was redissolved in CH<sub>2</sub>Cl<sub>2</sub> (75 cm<sup>3</sup>) and treated again with BrCH<sub>2</sub>CO<sub>2</sub>H (4.3 g, 31 mmol). After 1 h, three more cycles of addition and removal of toluene were performed. The residue was redissolved in CH<sub>2</sub>Cl<sub>2</sub> (100 cm<sup>3</sup>) and filtered. Hexanes (25 cm<sup>3</sup>) were added and the solution was allowed to stand undisturbed at room temperature for 4 days. The resulting black crystals were collected by filtration, washed

with hexanes, and dried *in vacuo*; yield 96%. A sample for crystallography was maintained in contact with the mother liquor to prevent the loss of interstitial solvent. Anal. Calcd (found) for **26** (C<sub>32</sub>H<sub>40</sub>Mn<sub>12</sub>O<sub>48</sub>Br<sub>16</sub>): C, 12.28 (12.61); H, 1.29 (1.30); N, 0.00 (0.00). Selected IR data (cm<sup>-1</sup>): 1720 (w), 1597 (vs), 1574 (vs), 1557 (s), 1534 (s), 1419 (vs), 1402 (vs), 1359 (s), 1209 (m), 1116 (w), 958 (w), 896 (w), 733 (m), 680 (s), 645 (s), 603 (s), 553 (s), 525 (m).

#### 7.4.2 X-ray Crystallography

Data were collected using a Siemens SMART PLATFORM equipped with a CCD area detector and a graphite monochromator utilizing MoK<sub>α</sub> radiation ( $\lambda = 0.71073 \text{ \AA}$ ). A suitable single crystal of **26**·4CH<sub>2</sub>Cl<sub>2</sub> was attached to a glass fiber using silicone grease and transferred to the goniostat where it was cooled to -100 °C for characterization and data collection. The structure was solved by direct methods (SHELXTL)<sup>64</sup> and standard Fourier techniques and was refined using full-matrix least-squares methods. All non-hydrogen atoms were refined anisotropically. Hydrogen atoms were placed in calculated positions and refined with the use of a riding model. Cell parameters were refined using up to 8192 reflections. A full sphere of data (1850 frames) was collected using the  $\omega$ -scan method (0.3° frame width). The first 50 frames were re-measured at the end of data collection to monitor instrument and crystal stability (maximum correction on I was < 1%). Absorption corrections by integration were applied based on measured indexed crystal faces.

An initial survey of reciprocal space revealed a set of reflections with a tetragonal lattice. Analysis of the full data set revealed that the space group was *I4<sub>1</sub>/a*. The asymmetric unit contains one-quarter of the Mn<sub>12</sub> molecule and one disordered CH<sub>2</sub>Cl<sub>2</sub> molecule. The bromine atoms [Br(2) and Br(3)] in two of the BrCH<sub>2</sub>CO<sub>2</sub><sup>-</sup> ligands were

slightly disordered. Their site occupancy factors were each dependently refined to 94:6%. A more complex disorder was observed for Br(4). Seven possible positions for the atom were located, and the occupancies of the seven atoms refined to a sum of 1.0. The disorder of Br(4) was coupled as a result of proximity with the disordered CH<sub>2</sub>Cl<sub>2</sub> molecule of crystallization. The CH<sub>2</sub>Cl<sub>2</sub> molecule was disordered over three positions and was refined using a model having only one C atom and two Cl atoms, each disordered over three positions. Three possible positions for each Cl atom were located, and the occupancies of the three atoms refined to a sum of 1.34 and 0.75 for Cl(1) and Cl(2), respectively. The corresponding C atom disorder could not be resolved. A total of 321 parameters were refined in the final cycle of refinement using 3860 reflections with  $I > 2\sigma(I)$  to yield  $R1$  and  $wR2$  of 5.68% and 15.43%, respectively. The final difference Fourier map was essentially featureless, the largest peak being  $1.905 \text{ e } \text{\AA}^{-3}$  and the deepest hole being  $-1.185 \text{ e } \text{\AA}^{-3}$ .

## CHAPTER 8 GENERAL CONCLUSIONS

In summary, the strategies and methods employed in the present work have resulted in: (i) the expansion of existing families of single-molecule magnets with new members which differ appreciably by one or more factors, e.g. peripheral ligation or oxidation level; (ii) the preparation of several novel  $Mn_x$  clusters, some of which behave as either new SMMs or new SCMs; (iii) the realization of the importance of single crystal measurements on crystals maintained in mother liquor to prevent the loss of interstitial solvent in lieu of previously employed measurements on dried, polycrystalline studies of SMMs. Such studies are valuable for the determination of the various factors, structural, synthetic and otherwise, that influence the magnetic properties of a  $Mn_x$  cluster, and ultimately might prove useful for the rational design of an improved single-molecule magnet that behaves as a magnet at technologically relevant temperatures.

Our investigation of the reactivity of  $Mn_{12}$  complexes with various non-carboxylate ligands has led us to conclude the importance of the following properties of the non-carboxylate ligand: solubility, steric considerations, acid dissociation constant and geometry (i.e., O...O bite distance). A combination of these factors and others strongly influences the identity of the products obtained from reactions carried out under seemingly identical conditions with different non-carboxylic acids. Our initial interest in the expansion of our understanding in this area was spurred by the isolation of the diphenylphosphinate-substituted  $Mn_{12}$  derivative. Although the  $[Mn_{12}O_{12}]$  core of the molecule was retained upon substitution of the organic groups, structural distortions were

evident upon close examination of the bond distances and angles of the new derivative. Such ligand-induced distortions were subsequently shown to not significantly perturb the magnetic properties of the  $\text{Mn}_{12}$  molecule, but the strategy of fine-tuning the magnitude of the exchange interactions between the Mn centers by distorting the geometry still appeared to be a promising means by which the magnetic anisotropy or ground state spin of the  $\text{Mn}_{12}$  molecule might be improved. An additional aim of the use of non-carboxylate organic ligands includes the site-specific replacement of carboxylate ligands on the  $\text{Mn}_{12}$  molecule. Such replacement of certain ligands, e.g. all axial or all equatorial, is essential to make regioselective reactions possible in a complex with so many carboxylate ligands and make more feasible important objectives such as the binding of groups that might enhance the shape anisotropy or magnetic properties of the  $\text{Mn}_{12}$  complexes, and/or facilitate the binding of the latter to surfaces or to each other to give dimers of  $\text{Mn}_{12}$  species. Unfortunately, the diphenylphosphinate groups distributed themselves equally between four axial and four equatorial sites about the  $\text{Mn}_{12}$  molecule, and this is likely a consequence of the steric bulk of the ligand. This conclusion is further supported by our inability to isolate a fully-substituted diphenylphosphinate  $\text{Mn}_{12}$  derivative. To this end, we studied the reactivity of  $\text{Mn}_{12}$  complexes with a similar organic acid, benzenesulfonic acid, both to obtain a mixed-ligand derivative with two types of ligands in specific positions on the  $\text{Mn}_{12}$  molecule and to study the effects of substitution on the  $\text{Mn}_{12}$  structure and on the resulting magnetic properties. We obtained a new  $\text{Mn}_{12}$  derivative in which benzenesulfonate groups occupy only axial positions about the  $\text{Mn}_{12}$  core with acetate ligands in the equatorial sites. The distribution of ligands was rationalized on the basis of the relative basicities of acetate and

benzenesulfonate, with the more basic, stronger donor acetate ligands favoring occupation of the equatorial sites where shorter, stronger Mn-O bonds can be formed, to the benefit of the overall energy stabilization of the molecule, and the less basic benzenesulfonate ligands thus occupying axial positions with one or both of their O atoms on the more labile, JT elongation axes. Hence, as with diphenylphosphinic acid, the use of benzenesulfonic acid has allowed access to a novel mixed-ligand Mn<sub>12</sub> derivative that retains the SMM properties of its parent Mn<sub>12</sub> complex and might ultimately prove practical for regioselective reactions. Examination of the bond distances and angles of the new benzenesulfonate-substituted Mn<sub>12</sub> derivative shows that there is virtually no distortion of the [Mn<sub>12</sub>O<sub>12</sub>] core. This is in contrast to the diphenylphosphinate-substituted derivative, and considering the similar acid dissociation constants, 2.32 for Ph<sub>2</sub>PO<sub>2</sub>H and 2.55 for PhSO<sub>3</sub>H, can be rationalized by considering the dissimilar average O···O bite distances of the ligands in the two derivatives, 2.56 Å for Ph<sub>2</sub>PO<sub>2</sub><sup>-</sup> and 2.42 Å for PhSO<sub>3</sub><sup>-</sup> (Table 8-1). The latter is much closer to that which is found in the acetate-substituted derivative of 2.24 Å, and as a result, we conclude that a combination of steric bulk of the phenyl groups of the Ph<sub>2</sub>PO<sub>2</sub><sup>-</sup> ligand and the large O···O bite distance prevent the formation of a fully-substituted Mn<sub>12</sub> derivative. This conclusion is supported by the isolation of a manganese-oxo cubane cluster, and not a fully-substituted Mn<sub>12</sub> derivative, from the reaction of the benzenesulfonate-substituted Mn<sub>12</sub> derivative with diphenylphosphinic acid. We attribute our inability to isolate a fully-substituted benzenesulfonate Mn<sub>12</sub> derivative to the relatively insoluble nature of the ligand.

Table 8-1. Comparison of selected bite distances (Å) for  $\text{MeCO}_2^-$ ,  $\text{PhSO}_3^-$ ,  $\text{Ph}_2\text{PO}_2^-$ ,  $\text{PhSeO}_2^-$  and  $\text{Me}_2\text{AsO}_2^-$  ligands in complexes **1**, **2**·4 $\text{CH}_2\text{Cl}_2$ , **4**, **5**, **6**·6 $\text{MeCN}$ , **7**·2 $\text{CH}_2\text{Cl}_2$ , **9**·5 $\text{H}_2\text{O}$ · $\text{C}_5\text{H}_{12}$  and **10**·½ $\text{MeCN}$ ·12 $\text{H}_2\text{O}$ .

Ligand	Compound, $[\text{Mn}_x]$	Bite Distance <sup>a</sup>	$\text{pK}_a$ <sup>171</sup>
$\text{MeCO}_2\text{H}$	<b>1</b> , $[\text{Mn}_{12}]$	2.235 – 2.249	4.76
$\text{PhSO}_3\text{H}$	<b>2</b> , $[\text{Mn}_{12}]$	2.400 – 2.422	2.55
$\text{Ph}_2\text{PO}_2\text{H}$	<b>4</b> , $[\text{Mn}_{12}]$	2.561 – 2.565	2.32
	<b>5</b> , $[\text{Mn}_4]$	2.566 – 2.617	
$\text{PhSeO}_2\text{H}$	<b>6</b> , $[\text{Mn}_7]$	2.654 – 2.799	4.79
	<b>7</b> , $[\text{Mn}_7]$	2.640 – 2.836	
$\text{MeAsO}_2\text{H}$	<b>9</b> , $[\text{Mn}_4]$	2.791 – 2.828	6.27
	<b>10</b> , $[\text{Mn}_4]$	2.749 – 2.847	

<sup>a</sup> Bite distance refers to the  $\text{O}\cdots\text{O}$  distance between O atoms of the carboxylate coordinated to Mn ions in each selected cluster.

Our results with diphenylphosphinic acid and benzenesulfonic acid are in contrast to those results obtained from similar attempted ligand substitution reactions with benzeneseleninic acid and dimethylarsinic acid, where the  $[\text{Mn}_{12}\text{O}_{12}]$  core was completely transformed into products with considerably different topological arrangements. The use of benzeneseleninic acid ( $\text{PhSeO}_2\text{H}$ ) has afforded two new heptanuclear Mn clusters, which possess a novel structural type in Mn chemistry and represent the first examples of transition metal clusters ligated by benzeneseleninate groups. The  $\text{pK}_a$  of benzeneseleninic acid (4.79) is very similar to that of acetic acid (4.76), but there is a significant difference in the  $\text{O}\cdots\text{O}$  bite distances; such distances are in the range of 2.64 – 2.84 Å for the two  $\text{Mn}_7$  clusters obtained. Hence, the rupture of the  $[\text{Mn}_{12}\text{O}_{12}]$  core followed by structural rearrangement confirms our suspicions that there is a limit to the number of organic ligands with a significantly increased  $\text{O}\cdots\text{O}$  bite distance that can be ligated to a  $\text{Mn}_{12}$  derivative without causing structural transformation. Magnetic studies on the two  $\text{Mn}_7$  clusters reveal that these species are not new additions to the growing family of single-molecule magnets. Instead, the slow relaxation is caused

by single-chain magnetism behavior, with the relaxation barrier arising from a combination of the molecular anisotropy and the exchange interaction between the individual  $\text{Mn}_7$  molecules. These two clusters are the first single-chain magnets (SCMs) which are composed of polynuclear metal clusters and are also the first SCMs to show quantum tunneling of magnetization.

As an extension of this work, we studied the reactivity of  $\text{Mn}_{12}$  derivatives with an even more basic ligand with an even greater O...O bite distance, dimethylarsinic acid. Again as expected, attempted ligand substitution reactions caused a transformation of the  $[\text{Mn}_{12}\text{O}_{12}]$  core, giving two tetranuclear complexes possessing a manganese-oxo cubane core and two  $\text{Mn}_{16}$  complexes possessing a novel structural topology comprised of four  $[\text{Mn}^{\text{III}}_4(\mu\text{-O})_2]$  “butterfly” units. All four complexes represent the first examples of manganese clusters ligated by dimethylarsinate groups and magnetic studies establish that the two  $\text{Mn}_{16}$  complexes behave as single-molecule magnets. A comparison of dimethylarsinic acid to the similar reactant diphenylphosphinic acid reveals two main dissimilarities: (i) a large difference in  $\text{pK}_a$  (6.27 for  $\text{Me}_2\text{AsO}_2\text{H}$  and 2.32 for  $\text{Ph}_2\text{PO}_2\text{H}$ ) and (ii) a considerable difference in steric bulk of the substituents, i.e., Me vs Ph. For each acid, the bite distance is relatively large compared with that of acetate and on this basis, we might expect that at least a partially-substituted  $\text{Mn}_{12}$  complex would be obtained with dimethylarsinate ligands. However, even with the replacement of the bulky phenyl groups with sterically unhindered methyl groups, we did not isolate even a partially-substituted  $\text{Mn}_{12}$  derivative as was found with diphenylphosphinic acid. The most obvious explanation for this result is the high basicity of the dimethylarsinate ligand as reflected in the relatively high  $\text{pK}_a$  value. Other factors including relative solubilities

and crystallization kinetics almost certainly play important roles in determining the exact species that preferentially crystallizes from the reactions however. In conclusion, these studies have proven that an effective strategy for the preparation of new polynuclear Mn aggregates involves the use of a chelating ligand with (i) a  $pK_a$  significantly higher than that of acetic acid; (ii) a O...O (or otherwise) bite distance that is appreciably greater than that found in typical  $Mn_{12}$  derivatives; and (iii) a combination of the above-mentioned properties.

The other approach used in the present work to obtain new polynuclear  $Mn_x$  clusters that might possess a significant enough magnetic anisotropy and high ground state spin to behave as single-molecule magnets involves the use of a bulky, hydrophobic carboxylate ligand to destabilize the  $Mn_{12}$  molecule and induce a structural rearrangement. This idea was stimulated by the preparation of novel high nuclearity single-molecule magnets from reactions of a *t*-butylacetate-substituted  $Mn_{12}$  derivative. It has been postulated that the strong basicity of the  $Bu^tCH_2CO_2^-$  ligand, as reflected in the relatively high  $pK_a$  value of its conjugate acid ( $pK_a = 5.00$ ), combined with the bulky and hydrophobic nature of the  $Bu^t$  group are the main reasons for the interesting products obtained with this carboxylate and as a result, we have extended these investigations of the influence of bulky, hydrophobic groups on the nature of the obtained products through the use of the related carboxylic acid, 2,2-dimethylbutyric acid with a  $pK_a$  of 5.03, which is similar to  $Bu^tCH_2CO_2H$ . Reactions of the 2,2-dimethylbutyrate-substituted  $Mn_{12}$  derivative similar to those which led to the isolation of new polynuclear  $Mn_x$  clusters in the case of the *t*-butylacetate-substituted  $Mn_{12}$  complex afforded several new Mn clusters, two of which are new structural types in Mn chemistry and one of which is

only the second member of a new sub-class of  $Mn_{12}$  derivatives in which the water ligands that coordinate to either three or four  $Mn^{III}$  ions in the outer ring of the cluster have been replaced by another ligand, MeOH. Magnetic studies reveal that the new  $Mn_{12}$  complex likely still functions as a single-molecule magnet, with an effective energy barrier to magnetization reversal that is comparable to that of the parent  $Mn_{12}$  complex. Unfortunately, magnetic studies on the other new clusters, reveal insufficiently small ground state spin values to allow large enough energy barriers to magnetization relaxation. As such, these new complexes do not function as single-molecule magnets. However, despite this outcome, the introduction of the hydrophobic, bulky ligand onto the  $Mn_{12}$  complex did allow access to new Mn aggregates as predicted, confirming our suspicions that a  $Mn_{12}$  complex substituted with a strongly electron donating ligand is easily destabilized and can undergo structural rearrangement.

As important as development of new synthetic methodologies for the preparation of new single-molecule magnets with novel topologies is a more thorough understanding of the structural factors that influence the ground state spin and magnetic anisotropy of a known molecule. Chemical variation of a known SMM is useful towards this end and such modifications on  $Mn_{12}$  complexes include variation of the peripheral carboxylate ligation, variation of the oxidation level by cluster reduction, replacement of some of the Mn centers with either Fe or Cr, and replacement of some of the carboxylate ligands with non-carboxylate groups. With each perturbation, the magnetic properties of the resulting clusters were measured to gauge the effects and from these studies we have realized the importance of symmetry, solvent or ligand disorder, intermolecular interactions, the loss of interstitial solvent molecules as well as numerous others. To extend further our

knowledge in this area, we have investigated the effect of reduction on the magnetic properties of a family of  $\text{Mn}_{12}$  single-molecule magnets with identical peripheral ligation spanning three oxidation levels. Low temperature magnetization measurements and AC magnetic susceptibility measurements on all three complexes show that (i) the ground state spin of each of the complexes changes only slightly and (ii) the axial magnetic anisotropy decreases as the  $\text{Mn}_{12}$  molecule is progressively reduced. This trend is consistent with our expectations as the successive reduction decreases the number of  $\text{Mn}^{\text{III}}$  ions, the primary source of the magnetic anisotropy in a  $\text{Mn}_{12}$  molecule. To investigate the effect of solvent loss on the magnetic properties, AC susceptibility measurements were carried out on crystals maintained in mother liquor to prevent the loss of interstitial solvent and on dried, microcrystalline samples and only small differences in the obtained kinetic parameters were found between wet and dry samples. These studies did reveal, however, that measurements on wet crystals are without certain complications associated with solvent loss and minimize local environmental differences between neighboring molecules in a crystal, giving a narrower range of anisotropy parameters and also effective energy barrier to magnetization reversal. This finding emphasizes the importance that parameters obtained from measurements made on wet crystals, such as single crystal micro-SQUID hysteresis measurements, should not be quantitatively compared with those values obtained from measurements on dried, microcrystalline samples, but rather should be compared only with those obtained from similar measurements on wet crystals.

Similarly, our work on the the tetragonal symmetry bromoacetate-substituted  $\text{Mn}_{12}$  complex has shown that that measurements on single crystals produces data of far

superior quality than that obtained from similar measurements on dried, microcrystalline samples of single-molecule magnets. Evidence for this conclusion is supported by a comparison of the  $^{55}\text{Mn}$  NMR spectra obtained on a single crystal and on a powdered sample of the bromoacetate-substituted  $\text{Mn}_{12}$  complex, where the single crystal spectrum showed several features which were absent in the powder spectrum, including well-resolved quadrupolar splitting of two peaks. The single crystal  $^{55}\text{Mn}$  NMR study of this complex represents the first of its kind; there are only two other  $^{55}\text{Mn}$  NMR spectroscopic studies of  $\text{Mn}_{12}$  SMMs and these were carried out on dried, polycrystalline samples. HFEPR measurements on the cluster reveal that in contrast to the “model” high symmetry acetate-substituted  $\text{Mn}_{12}$  derivative, there is no measureable rhombic anisotropy term. This is consistent with our structural analysis, which revealed almost no symmetry-lowering contacts between  $\text{Mn}_{12}$  molecules, i.e., no interaction of the interstitial solvent molecules with the  $\text{Mn}_{12}$  molecules as seen with the “model” system. Hence, we conclude that this  $\text{Mn}_{12}$  complex is a cleaner, truly axial  $\text{Mn}_{12}$  single-molecule magnet and is a model system to study for understanding magnetic tunneling in the  $\text{Mn}_{12}$  family.

Consistent with previous research, this work has confirmed that  $\text{Mn}_{12}$  complexes represent excellent starting materials, affording a diversity of novel  $\text{Mn}_x$  topologies. In conclusion, the strategies employed in the present work have proven effective methods by which a better understanding of the factors that affect both the spin and magnetic anisotropy of a molecule has been attained. Such studies will prove useful for the rational design of a synthetic method for an improved single-molecule magnet.

APPENDIX A  
BOND DISTANCES AND ANGLES

Table A-1. Selected interatomic distances (Å) and angles (°) for  
[Mn<sub>12</sub>O<sub>12</sub>(O<sub>2</sub>CMe)<sub>8</sub>(O<sub>3</sub>SPh)<sub>8</sub>(H<sub>2</sub>O)<sub>4</sub>]·4CH<sub>2</sub>Cl<sub>2</sub> (2·4CH<sub>2</sub>Cl<sub>2</sub>).

Mn(1)-O(46)	1.883(2)	Mn(6)-O(26)	2.220(2)
Mn(1)-O(47)	1.909(2)	Mn(6)-O(27)	2.222(2)
Mn(1)-O(1)	1.925(2)	Mn(7)-O(52)	1.895(2)
Mn(1)-O(42)	1.942(2)	Mn(7)-O(53)	1.903(2)
Mn(1)-O(38)	2.163(2)	Mn(7)-O(29)	1.920(2)
Mn(1)-O(43)	2.238(2)	Mn(7)-O(28)	1.931(2)
Mn(1)-Mn(9)	2.7905(6)	Mn(7)-O(33)	2.171(2)
Mn(2)-O(56)	1.903(2)	Mn(7)-O(30)	2.254(2)
Mn(2)-O(47)	1.907(2)	Mn(7)-Mn(12)	2.7934(6)
Mn(2)-O(3)	1.948(2)	Mn(8)-O(46)	1.895(2)
Mn(2)-O(2)	1.954(2)	Mn(8)-O(52)	1.906(2)
Mn(2)-O(5)	2.216(2)	Mn(8)-O(36)	1.935(2)
Mn(2)-O(4)	2.221(2)	Mn(8)-O(40)	1.951(2)
Mn(3)-O(57)	1.899(2)	Mn(8)-O(34)	2.174(2)
Mn(3)-O(56)	1.901(2)	Mn(8)-O(37)	2.184(2)
Mn(3)-O(7)	1.932(2)	Mn(9)-O(46)	1.854(2)
Mn(3)-O(6)	1.933(2)	Mn(9)-O(47)	1.8643(19)
Mn(3)-O(8)	2.198(3)	Mn(9)-O(54)	1.865(2)
Mn(3)-O(11)	2.261(2)	Mn(9)-O(44)	1.923(2)
Mn(3)-Mn(10)	2.8015(6)	Mn(9)-O(48)	1.9258(19)
Mn(4)-O(51)	1.880(2)	Mn(9)-O(49)	1.9260(19)
Mn(4)-O(57)	1.910(2)	Mn(9)-Mn(12)	2.8069(6)
Mn(4)-O(14)	1.929(2)	Mn(9)-Mn(10)	2.8117(6)
Mn(4)-O(15)	1.962(2)	Mn(9)-Mn(11)	2.9353(6)
Mn(4)-O(9)	2.176(2)	Mn(10)-O(49)	1.866(2)
Mn(4)-O(16)	2.190(2)	Mn(10)-O(56)	1.871(2)
Mn(5)-O(51)	1.883(2)	Mn(10)-O(57)	1.872(2)
Mn(5)-O(50)	1.905(2)	Mn(10)-O(55)	1.9174(19)
Mn(5)-O(20)	1.926(2)	Mn(10)-O(12)	1.924(2)
Mn(5)-O(19)	1.940(2)	Mn(10)-O(54)	1.9393(19)
Mn(5)-O(17)	2.185(3)	Mn(10)-Mn(11)	2.8054(6)
Mn(5)-O(21)	2.255(3)	Mn(10)-Mn(12)	2.9478(6)
Mn(5)-Mn(11)	2.8016(6)	Mn(11)-O(51)	1.859(2)
Mn(6)-O(50)	1.889(2)	Mn(11)-O(50)	1.870(2)
Mn(6)-O(53)	1.910(2)	Mn(11)-O(55)	1.876(2)
Mn(6)-O(25)	1.946(2)	Mn(11)-O(22)	1.907(2)
Mn(6)-O(24)	1.952(2)	Mn(11)-O(49)	1.9227(19)

Table A-1. Continued.

Mn(11)-O(48)	1.925(2)	Mn(12)-O(52)	1.874(2)
Mn(11)-Mn(12)	2.8117(6)	Mn(12)-O(54)	1.9157(19)
Mn(12)-O(48)	1.863(2)	Mn(12)-O(55)	1.935(2)
Mn(12)-O(53)	1.874(2)	Mn(12)-O(31)	1.945(2)
O(46)-Mn(1)-O(47)	82.12(8)	O(56)-Mn(3)-O(6)	95.09(9)
O(46)-Mn(1)-O(1)	177.95(9)	O(7)-Mn(3)-O(6)	86.43(10)
O(47)-Mn(1)-O(1)	95.88(9)	O(57)-Mn(3)-O(8)	96.67(9)
O(46)-Mn(1)-O(42)	95.24(9)	O(56)-Mn(3)-O(8)	96.19(10)
O(47)-Mn(1)-O(42)	174.95(10)	O(7)-Mn(3)-O(8)	87.28(11)
O(1)-Mn(1)-O(42)	86.72(9)	O(6)-Mn(3)-O(8)	87.17(10)
O(46)-Mn(1)-O(38)	92.17(9)	O(57)-Mn(3)-O(11)	88.57(9)
O(47)-Mn(1)-O(38)	90.80(9)	O(56)-Mn(3)-O(11)	89.08(9)
O(1)-Mn(1)-O(38)	88.32(10)	O(7)-Mn(3)-O(11)	87.57(10)
O(42)-Mn(1)-O(38)	93.61(10)	O(6)-Mn(3)-O(11)	87.81(10)
O(46)-Mn(1)-O(43)	88.72(9)	O(8)-Mn(3)-O(11)	173.02(10)
O(47)-Mn(1)-O(43)	87.72(9)	O(57)-Mn(3)-Mn(10)	41.66(6)
O(1)-Mn(1)-O(43)	90.75(10)	O(56)-Mn(3)-Mn(10)	41.63(6)
O(42)-Mn(1)-O(43)	87.92(9)	O(7)-Mn(3)-Mn(10)	135.93(7)
O(38)-Mn(1)-O(43)	178.16(9)	O(6)-Mn(3)-Mn(10)	134.80(7)
O(46)-Mn(1)-Mn(9)	41.30(6)	O(8)-Mn(3)-Mn(10)	106.26(8)
O(47)-Mn(1)-Mn(9)	41.69(6)	O(11)-Mn(3)-Mn(10)	80.72(6)
O(1)-Mn(1)-Mn(9)	136.66(7)	O(51)-Mn(4)-O(57)	94.94(9)
O(42)-Mn(1)-Mn(9)	134.85(7)	O(51)-Mn(4)-O(14)	172.60(10)
O(38)-Mn(1)-Mn(9)	98.57(7)	O(57)-Mn(4)-O(14)	92.45(10)
O(43)-Mn(1)-Mn(9)	81.04(6)	O(51)-Mn(4)-O(15)	90.63(10)
O(56)-Mn(2)-O(47)	95.52(9)	O(57)-Mn(4)-O(15)	174.09(9)
O(56)-Mn(2)-O(3)	91.05(9)	O(14)-Mn(4)-O(15)	81.98(10)
O(47)-Mn(2)-O(3)	171.95(10)	O(51)-Mn(4)-O(9)	87.32(9)
O(56)-Mn(2)-O(2)	171.70(10)	O(57)-Mn(4)-O(9)	93.84(9)
O(47)-Mn(2)-O(2)	91.19(9)	O(14)-Mn(4)-O(9)	92.04(10)
O(3)-Mn(2)-O(2)	82.69(10)	O(15)-Mn(4)-O(9)	84.42(10)
O(56)-Mn(2)-O(5)	98.37(9)	O(51)-Mn(4)-O(16)	92.36(9)
O(47)-Mn(2)-O(5)	84.36(9)	O(57)-Mn(4)-O(16)	92.83(9)
O(3)-Mn(2)-O(5)	90.10(10)	O(14)-Mn(4)-O(16)	87.42(10)
O(2)-Mn(2)-O(5)	87.12(10)	O(15)-Mn(4)-O(16)	88.92(10)
O(56)-Mn(2)-O(4)	87.14(9)	O(9)-Mn(4)-O(16)	173.33(10)
O(47)-Mn(2)-O(4)	96.15(9)	O(51)-Mn(5)-O(50)	81.70(9)
O(3)-Mn(2)-O(4)	88.80(10)	O(51)-Mn(5)-O(20)	176.10(10)
O(2)-Mn(2)-O(4)	87.29(10)	O(50)-Mn(5)-O(20)	95.35(9)
O(5)-Mn(2)-O(4)	174.40(9)	O(51)-Mn(5)-O(19)	96.10(9)
O(57)-Mn(3)-O(56)	82.11(9)	O(50)-Mn(5)-O(19)	174.94(10)
O(57)-Mn(3)-O(7)	96.15(9)	O(20)-Mn(5)-O(19)	86.64(10)
O(56)-Mn(3)-O(7)	176.27(10)	O(51)-Mn(5)-O(17)	93.77(9)
O(57)-Mn(3)-O(6)	175.46(10)	O(50)-Mn(5)-O(17)	92.48(9)

Table A-1. Continued.

O(20)-Mn(5)-O(17)	88.89(10)	O(29)-Mn(7)-Mn(12)	136.12(7)
O(19)-Mn(5)-O(17)	92.22(10)	O(28)-Mn(7)-Mn(12)	135.86(7)
O(51)-Mn(5)-O(21)	86.30(9)	O(33)-Mn(7)-Mn(12)	103.31(6)
O(50)-Mn(5)-O(21)	90.37(9)	O(30)-Mn(7)-Mn(12)	80.82(6)
O(20)-Mn(5)-O(21)	91.18(10)	O(46)-Mn(8)-O(52)	94.83(8)
O(19)-Mn(5)-O(21)	84.93(10)	O(46)-Mn(8)-O(36)	172.45(9)
O(17)-Mn(5)-O(21)	177.13(9)	O(52)-Mn(8)-O(36)	92.72(9)
O(51)-Mn(5)-Mn(11)	41.20(6)	O(46)-Mn(8)-O(40)	90.54(9)
O(50)-Mn(5)-Mn(11)	41.61(6)	O(52)-Mn(8)-O(40)	174.29(9)
O(20)-Mn(5)-Mn(11)	135.37(7)	O(36)-Mn(8)-O(40)	81.91(9)
O(19)-Mn(5)-Mn(11)	135.21(7)	O(46)-Mn(8)-O(34)	88.53(9)
O(17)-Mn(5)-Mn(11)	101.58(7)	O(52)-Mn(8)-O(34)	94.23(9)
O(21)-Mn(5)-Mn(11)	80.35(6)	O(36)-Mn(8)-O(34)	90.76(10)
O(50)-Mn(6)-O(53)	95.42(8)	O(40)-Mn(8)-O(34)	83.94(9)
O(50)-Mn(6)-O(25)	171.13(10)	O(46)-Mn(8)-O(37)	93.61(9)
O(53)-Mn(6)-O(25)	91.72(9)	O(52)-Mn(8)-O(37)	93.20(9)
O(50)-Mn(6)-O(24)	90.77(9)	O(36)-Mn(8)-O(37)	86.12(10)
O(53)-Mn(6)-O(24)	171.61(10)	O(40)-Mn(8)-O(37)	88.40(10)
O(25)-Mn(6)-O(24)	82.68(10)	O(34)-Mn(8)-O(37)	172.07(9)
O(50)-Mn(6)-O(26)	96.48(9)	O(46)-Mn(9)-O(47)	84.13(9)
O(53)-Mn(6)-O(26)	86.16(9)	O(46)-Mn(9)-O(54)	92.89(9)
O(25)-Mn(6)-O(26)	89.24(10)	O(47)-Mn(9)-O(54)	90.04(9)
O(24)-Mn(6)-O(26)	87.53(10)	O(46)-Mn(9)-O(44)	94.16(9)
O(50)-Mn(6)-O(27)	85.54(9)	O(47)-Mn(9)-O(44)	94.29(9)
O(53)-Mn(6)-O(27)	101.45(9)	O(54)-Mn(9)-O(44)	172.07(9)
O(25)-Mn(6)-O(27)	87.89(11)	O(46)-Mn(9)-O(48)	95.57(8)
O(24)-Mn(6)-O(27)	84.64(10)	O(47)-Mn(9)-O(48)	173.32(9)
O(26)-Mn(6)-O(27)	171.94(9)	O(54)-Mn(9)-O(48)	83.31(8)
O(52)-Mn(7)-O(53)	82.74(8)	O(44)-Mn(9)-O(48)	92.39(9)
O(52)-Mn(7)-O(29)	95.83(9)	O(46)-Mn(9)-O(49)	175.18(9)
O(53)-Mn(7)-O(29)	176.84(10)	O(47)-Mn(9)-O(49)	99.39(8)
O(52)-Mn(7)-O(28)	176.12(10)	O(54)-Mn(9)-O(49)	83.85(8)
O(53)-Mn(7)-O(28)	95.73(9)	O(44)-Mn(9)-O(49)	88.88(9)
O(29)-Mn(7)-O(28)	85.52(10)	O(48)-Mn(9)-O(49)	80.54(8)
O(52)-Mn(7)-O(33)	96.02(9)	O(46)-Mn(9)-Mn(1)	42.08(6)
O(53)-Mn(7)-O(33)	93.08(9)	O(47)-Mn(9)-Mn(1)	42.94(6)
O(29)-Mn(7)-O(33)	89.87(10)	O(54)-Mn(9)-Mn(1)	98.82(6)
O(28)-Mn(7)-O(33)	87.60(9)	O(44)-Mn(9)-Mn(1)	88.86(6)
O(52)-Mn(7)-O(30)	90.68(8)	O(48)-Mn(9)-Mn(1)	137.55(6)
O(53)-Mn(7)-O(30)	86.39(9)	O(49)-Mn(9)-Mn(1)	141.90(6)
O(29)-Mn(7)-O(30)	90.81(9)	O(46)-Mn(9)-Mn(12)	89.26(6)
O(28)-Mn(7)-O(30)	85.66(9)	O(47)-Mn(9)-Mn(12)	131.98(7)
O(33)-Mn(7)-O(30)	173.16(8)	O(54)-Mn(9)-Mn(12)	42.76(6)
O(52)-Mn(7)-Mn(12)	41.88(6)	O(44)-Mn(9)-Mn(12)	133.67(7)
O(53)-Mn(7)-Mn(12)	41.89(6)	O(48)-Mn(9)-Mn(12)	41.35(6)

Table A-1. Continued.

O(49)-Mn(9)-Mn(12)	85.94(6)	O(54)-Mn(10)-Mn(11)	85.43(6)
Mn(1)-Mn(9)-Mn(12)	121.51(2)	Mn(3)-Mn(10)-Mn(11)	123.71(2)
O(46)-Mn(9)-Mn(10)	135.94(7)	O(49)-Mn(10)-Mn(9)	42.97(6)
O(47)-Mn(9)-Mn(10)	89.82(6)	O(56)-Mn(10)-Mn(9)	89.48(6)
O(54)-Mn(9)-Mn(10)	43.38(6)	O(57)-Mn(10)-Mn(9)	134.61(7)
O(44)-Mn(9)-Mn(10)	129.85(7)	O(55)-Mn(10)-Mn(9)	85.85(6)
O(48)-Mn(9)-Mn(10)	85.75(6)	O(12)-Mn(10)-Mn(9)	130.36(7)
O(49)-Mn(9)-Mn(10)	41.34(6)	O(54)-Mn(10)-Mn(9)	41.35(6)
Mn(1)-Mn(9)-Mn(10)	124.39(2)	Mn(3)-Mn(10)-Mn(9)	123.94(2)
Mn(12)-Mn(9)-Mn(10)	63.290(16)	Mn(11)-Mn(10)-Mn(9)	63.010(16)
O(46)-Mn(9)-Mn(11)	135.90(6)	O(49)-Mn(10)-Mn(12)	82.95(6)
O(47)-Mn(9)-Mn(11)	139.48(6)	O(56)-Mn(10)-Mn(12)	138.00(6)
O(54)-Mn(9)-Mn(11)	83.02(6)	O(57)-Mn(10)-Mn(12)	137.87(6)
O(44)-Mn(9)-Mn(11)	89.38(6)	O(55)-Mn(10)-Mn(12)	40.29(6)
O(48)-Mn(9)-Mn(11)	40.33(6)	O(12)-Mn(10)-Mn(12)	88.89(6)
O(49)-Mn(9)-Mn(11)	40.26(6)	O(54)-Mn(10)-Mn(12)	39.83(6)
Mn(1)-Mn(9)-Mn(11)	177.17(2)	Mn(3)-Mn(10)-Mn(12)	177.21(2)
Mn(12)-Mn(9)-Mn(11)	58.585(15)	Mn(11)-Mn(10)-Mn(12)	58.450(15)
Mn(10)-Mn(9)-Mn(11)	58.392(15)	Mn(9)-Mn(10)-Mn(12)	58.276(15)
O(49)-Mn(10)-O(56)	90.70(9)	O(51)-Mn(11)-O(50)	83.27(9)
O(49)-Mn(10)-O(57)	92.16(9)	O(51)-Mn(11)-O(55)	92.73(9)
O(56)-Mn(10)-O(57)	83.62(9)	O(50)-Mn(11)-O(55)	91.12(9)
O(49)-Mn(10)-O(55)	83.92(8)	O(51)-Mn(11)-O(22)	96.08(10)
O(56)-Mn(10)-O(55)	174.51(9)	O(50)-Mn(11)-O(22)	93.39(9)
O(57)-Mn(10)-O(55)	97.62(8)	O(55)-Mn(11)-O(22)	170.51(9)
O(49)-Mn(10)-O(12)	171.70(9)	O(51)-Mn(11)-O(49)	95.85(9)
O(56)-Mn(10)-O(12)	94.36(9)	O(50)-Mn(11)-O(49)	174.52(9)
O(57)-Mn(10)-O(12)	94.94(9)	O(55)-Mn(11)-O(49)	83.52(8)
O(55)-Mn(10)-O(12)	90.87(9)	O(22)-Mn(11)-O(49)	92.08(9)
O(49)-Mn(10)-O(54)	83.46(8)	O(51)-Mn(11)-O(48)	175.22(9)
O(56)-Mn(10)-O(54)	98.27(8)	O(50)-Mn(11)-O(48)	99.92(8)
O(57)-Mn(10)-O(54)	175.23(9)	O(55)-Mn(11)-O(48)	83.68(8)
O(55)-Mn(10)-O(54)	80.09(8)	O(22)-Mn(11)-O(48)	87.32(9)
O(12)-Mn(10)-O(54)	89.29(9)	O(49)-Mn(11)-O(48)	80.64(8)
O(49)-Mn(10)-Mn(3)	99.84(6)	O(51)-Mn(11)-Mn(5)	41.84(6)
O(56)-Mn(10)-Mn(3)	42.45(6)	O(50)-Mn(11)-Mn(5)	42.58(6)
O(57)-Mn(10)-Mn(3)	42.38(6)	O(55)-Mn(11)-Mn(5)	100.24(6)
O(55)-Mn(10)-Mn(3)	139.64(6)	O(22)-Mn(11)-Mn(5)	88.70(6)
O(12)-Mn(10)-Mn(3)	88.32(7)	O(49)-Mn(11)-Mn(5)	137.36(6)
O(54)-Mn(10)-Mn(3)	140.22(6)	O(48)-Mn(11)-Mn(5)	141.92(6)
O(49)-Mn(10)-Mn(11)	43.01(6)	O(51)-Mn(11)-Mn(10)	89.28(7)
O(56)-Mn(10)-Mn(11)	133.11(7)	O(50)-Mn(11)-Mn(10)	133.06(7)
O(57)-Mn(10)-Mn(11)	90.09(7)	O(55)-Mn(11)-Mn(10)	42.88(6)
O(55)-Mn(10)-Mn(11)	41.73(6)	O(22)-Mn(11)-Mn(10)	133.52(7)
O(12)-Mn(10)-Mn(11)	132.51(7)	O(49)-Mn(11)-Mn(10)	41.46(6)

Table A-1. Continued.

O(48)-Mn(11)-Mn(10)	85.94(6)	O(54)-Mn(12)-O(31)	90.02(9)
Mn(5)-Mn(11)-Mn(10)	122.52(2)	O(55)-Mn(12)-O(31)	91.81(9)
O(51)-Mn(11)-Mn(12)	135.64(7)	O(48)-Mn(12)-Mn(7)	98.46(6)
O(50)-Mn(11)-Mn(12)	91.00(6)	O(53)-Mn(12)-Mn(7)	42.69(6)
O(55)-Mn(11)-Mn(12)	43.27(6)	O(52)-Mn(12)-Mn(7)	42.47(6)
O(22)-Mn(11)-Mn(12)	128.21(7)	O(54)-Mn(12)-Mn(7)	140.70(6)
O(49)-Mn(11)-Mn(12)	85.86(6)	O(55)-Mn(12)-Mn(7)	139.05(6)
O(48)-Mn(11)-Mn(12)	41.25(6)	O(31)-Mn(12)-Mn(7)	88.63(6)
Mn(5)-Mn(11)-Mn(12)	125.58(2)	O(48)-Mn(12)-Mn(9)	43.07(6)
Mn(10)-Mn(11)-Mn(12)	63.308(16)	O(53)-Mn(12)-Mn(9)	132.98(7)
O(51)-Mn(11)-Mn(9)	136.18(6)	O(52)-Mn(12)-Mn(9)	90.13(6)
O(50)-Mn(11)-Mn(9)	140.17(6)	O(54)-Mn(12)-Mn(9)	41.38(6)
O(55)-Mn(11)-Mn(9)	83.04(6)	O(55)-Mn(12)-Mn(9)	85.66(6)
O(22)-Mn(11)-Mn(9)	88.16(6)	O(31)-Mn(12)-Mn(9)	131.09(6)
O(49)-Mn(11)-Mn(9)	40.34(6)	Mn(7)-Mn(12)-Mn(9)	123.35(2)
O(48)-Mn(11)-Mn(9)	40.35(6)	O(48)-Mn(12)-Mn(11)	42.93(6)
Mn(5)-Mn(11)-Mn(9)	175.99(2)	O(53)-Mn(12)-Mn(11)	88.20(6)
Mn(10)-Mn(11)-Mn(9)	58.599(15)	O(52)-Mn(12)-Mn(11)	133.51(7)
Mn(12)-Mn(11)-Mn(9)	58.424(15)	O(54)-Mn(12)-Mn(11)	85.68(6)
O(48)-Mn(12)-O(53)	90.32(9)	O(55)-Mn(12)-Mn(11)	41.65(6)
O(48)-Mn(12)-O(52)	91.22(9)	O(31)-Mn(12)-Mn(11)	133.32(7)
O(53)-Mn(12)-O(52)	84.10(9)	Mn(7)-Mn(12)-Mn(11)	122.18(2)
O(48)-Mn(12)-O(54)	83.63(8)	Mn(9)-Mn(12)-Mn(11)	62.991(16)
O(53)-Mn(12)-O(54)	173.46(9)	O(48)-Mn(12)-Mn(10)	82.94(6)
O(52)-Mn(12)-O(54)	98.46(8)	O(53)-Mn(12)-Mn(10)	136.41(6)
O(48)-Mn(12)-O(55)	83.74(8)	O(52)-Mn(12)-Mn(10)	138.80(6)
O(53)-Mn(12)-O(55)	96.68(8)	O(54)-Mn(12)-Mn(10)	40.42(6)
O(52)-Mn(12)-O(55)	174.91(9)	O(55)-Mn(12)-Mn(10)	39.86(6)
O(54)-Mn(12)-O(55)	80.24(8)	O(31)-Mn(12)-Mn(10)	90.00(6)
O(48)-Mn(12)-O(31)	172.78(9)	Mn(7)-Mn(12)-Mn(10)	178.21(2)
O(53)-Mn(12)-O(31)	95.86(9)	Mn(9)-Mn(12)-Mn(10)	58.434(15)
O(52)-Mn(12)-O(31)	93.11(9)	Mn(11)-Mn(12)-Mn(10)	58.242(15)

Table A-2. Selected interatomic distances (Å) and angles (°) for [Mn<sub>4</sub>O<sub>4</sub>(O<sub>2</sub>PPh<sub>2</sub>)<sub>6</sub>] (**5**).

Mn(1)-O(1)	2.008(6)	Mn(5)-O(13)	1.841(6)
Mn(1)-O(1a)	1.860(6)	Mn(5)-O(13a)	1.999(6)
Mn(1)-O(2)	1.919(5)	Mn(5)-O(14)	1.909(5)
Mn(1)-O(3)	1.910(7)	Mn(5)-O(15)	1.930(5)
Mn(1)-O(4a)	1.998(8)	Mn(5)-O(16)	1.964(7)
Mn(1)-O(5)	1.960(6)	Mn(5)-O(17)	1.928(6)
Mn(1)-Mn(1a)	2.908(3)	Mn(5)-Mn(5a)	2.874(2)
Mn(1)-Mn(2)	2.947(3)	Mn(5)-Mn(6)	2.9694(18)
Mn(2)-O(1)	1.951(7)	Mn(6)-O(13)	2.007(7)
Mn(2)-O(6)	1.967(7)	Mn(6)-O(18)	1.972(5)
Mn(3)-O(7)	1.891(5)	Mn(7)-O(19)	1.904(7)
Mn(3)-O(7a)	2.051(7)	Mn(7)-O(19b)	2.045(9)
Mn(3)-O(8)	1.978(6)	Mn(7)-O(20)	1.973(5)
Mn(3)-O(9)	1.921(6)	Mn(7)-O(21)	2.020(7)
Mn(3)-O(10b)	1.977(8)	Mn(7)-O(22b)	1.915(7)
Mn(3)-O(11)	1.997(7)	Mn(7)-O(23)	2.007(8)
Mn(3)-Mn(3a)	2.986(3)	Mn(7)-Mn(7a)	2.970(3)
Mn(3)-Mn(4)	2.888(2)	Mn(7)-Mn(8)	2.884(3)
Mn(4)-O(7)	1.873(6)	Mn(8)-O(19)	1.909(7)
Mn(4)-O(12)	1.928(6)	Mn(8)-O(24)	1.943(7)
O(1a)-Mn(1)-O(1)	81.0(4)	O(3)-Mn(1)-Mn(1a)	130.8(2)
O(1a)-Mn(1)-O(2)	83.2(3)	O(3)-Mn(1)-Mn(1b)	86.4(2)
O(1a)-Mn(1)-O(3)	171.8(3)	O(3)-Mn(1)-Mn(2)	134.0(2)
O(1a)-Mn(1)-O(4a)	87.5(3)	O(4a)-Mn(1)-Mn(1a)	83.4(2)
O(1a)-Mn(1)-O(5)	90.6(3)	O(4a)-Mn(1)-Mn(1b)	132.2(2)
O(2)-Mn(1)-O(1)	79.4(3)	O(4a)-Mn(1)-Mn(2)	127.9(2)
O(2)-Mn(1)-O(3)	90.2(3)	O(5)-Mn(1)-Mn(1a)	133.77(19)
O(2)-Mn(1)-O(4a)	91.5(3)	O(5)-Mn(1)-Mn(1b)	128.4(2)
O(2)-Mn(1)-O(5)	167.7(3)	O(5)-Mn(1)-Mn(2)	84.17(18)
O(3)-Mn(1)-O(1)	93.0(3)	Mn(1a)-Mn(1)-Mn(1b)	60.0
O(3)-Mn(1)-O(4a)	97.7(3)	Mn(1a)-Mn(1)-Mn(2)	60.44(3)
O(3)-Mn(1)-O(5)	94.9(3)	O(1)-Mn(2)-O(1a)	80.2(3)
O(4a)-Mn(1)-O(1)	166.0(3)	O(1)-Mn(2)-O(6)	89.9(3)
O(4a)-Mn(1)-O(5)	98.8(3)	O(1)-Mn(2)-O(6a)	167.7(3)
O(5)-Mn(1)-O(1)	89.1(3)	O(1a)-Mn(2)-O(6)	91.0(3)
O(1)-Mn(1)-Mn(1a)	82.87(18)	O(6a)-Mn(2)-O(6)	97.6(3)
O(1)-Mn(1)-Mn(1b)	39.36(18)	O(1)-Mn(2)-Mn(1)	42.64(19)
O(1)-Mn(1)-Mn(2)	41.15(18)	O(1)-Mn(2)-Mn(1a)	82.7(2)
O(1a)-Mn(1)-Mn(1a)	43.2(2)	O(1a)-Mn(2)-Mn(1)	38.23(18)
O(1a)-Mn(1)-Mn(1b)	85.4(2)	O(6)-Mn(2)-Mn(1)	85.06(19)
O(1a)-Mn(1)-Mn(2)	40.5(2)	O(6)-Mn(2)-Mn(1a)	133.6(2)
O(2)-Mn(1)-Mn(1a)	40.74(16)	O(6a)-Mn(2)-Mn(1)	128.1(2)
O(2)-Mn(1)-Mn(1b)	40.74(16)	Mn(1)-Mn(2)-Mn(1a)	59.12(7)
O(2)-Mn(1)-Mn(2)	84.2(3)	Mn(1b)-O(1)-Mn(1)	97.4(3)

Table A-2. Continued.

Mn(1b)-O(1)-Mn(2)	101.3(3)	O(7)-Mn(4)-Mn(3b)	87.7(2)
Mn(2)-O(1)-Mn(1)	96.2(3)	O(12)-Mn(4)-Mn(3)	85.49(19)
Mn(1a)-O(2)-Mn(1)	98.5(3)	O(12)-Mn(4)-Mn(3a)	136.2(2)
O(7)-Mn(3)-O(7a)	79.5(4)	O(12)-Mn(4)-Mn(3b)	129.2(2)
O(7)-Mn(3)-O(8)	83.0(3)	Mn(3a)-Mn(4)-Mn(3)	62.26(6)
O(7)-Mn(3)-O(9)	169.2(3)	Mn(4)-O(7)-Mn(3)	100.2(3)
O(7)-Mn(3)-O(10b)	89.0(3)	Mn(4)-O(7)-Mn(3a)	94.7(3)
O(7)-Mn(3)-O(11)	91.9(3)	Mn(3)-O(7)-Mn(3a)	98.4(3)
O(8)-Mn(3)-O(7a)	79.0(3)	Mn(3a)-O(8)-Mn(3)	98.0(4)
O(8)-Mn(3)-O(9)	89.4(3)	O(13)-Mn(5)-O(13a)	83.1(4)
O(8)-Mn(3)-O(10b)	92.0(3)	O(13)-Mn(5)-O(14)	84.4(2)
O(8)-Mn(3)-O(11)	167.0(3)	O(13)-Mn(5)-O(15)	172.2(3)
O(9)-Mn(3)-O(7a)	91.5(3)	O(13)-Mn(5)-O(16)	91.4(3)
O(9)-Mn(3)-O(10b)	99.0(4)	O(13)-Mn(5)-O(17)	90.1(2)
O(9)-Mn(3)-O(11)	93.8(3)	O(14)-Mn(5)-O(13a)	80.2(2)
O(10b)-Mn(3)-O(7a)	166.2(3)	O(14)-Mn(5)-O(15)	89.0(3)
O(10b)-Mn(3)-O(11)	99.9(3)	O(14)-Mn(5)-O(16)	90.2(3)
O(11)-Mn(3)-O(7a)	88.3(2)	O(14)-Mn(5)-O(17)	170.7(3)
O(7)-Mn(3)-Mn(3a)	84.5(2)	O(15)-Mn(5)-O(13a)	91.7(3)
O(7)-Mn(3)-Mn(3b)	42.8(2)	O(15)-Mn(5)-O(16)	92.7(3)
O(7)-Mn(3)-Mn(4)	39.66(18)	O(15)-Mn(5)-O(17)	95.9(3)
O(7a)-Mn(3)-Mn(3a)	38.79(15)	O(16)-Mn(5)-O(13a)	169.3(3)
O(7a)-Mn(3)-Mn(3b)	81.96(16)	O(16)-Mn(5)-O(17)	97.4(3)
O(7a)-Mn(3)-Mn(4)	40.27(17)	O(17)-Mn(5)-O(13a)	91.8(2)
O(8)-Mn(3)-Mn(3a)	40.98(19)	O(13)-Mn(5)-Mn(5a)	86.52(18)
O(8)-Mn(3)-Mn(3b)	40.98(19)	O(13)-Mn(5)-Mn(5b)	43.69(18)
O(8)-Mn(3)-Mn(4)	82.7(3)	O(13)-Mn(5)-Mn(6)	41.6(2)
O(9)-Mn(3)-Mn(3a)	84.7(2)	O(13a)-Mn(5)-Mn(5a)	39.50(16)
O(9)-Mn(3)-Mn(3b)	130.4(2)	O(13a)-Mn(5)-Mn(5b)	83.75(16)
O(9)-Mn(3)-Mn(4)	131.7(3)	O(13a)-Mn(5)-Mn(6)	42.26(19)
O(10b)-Mn(3)-Mn(3a)	132.9(3)	O(14)-Mn(5)-Mn(5a)	41.16(15)
O(10b)-Mn(3)-Mn(3b)	84.4(2)	O(14)-Mn(5)-Mn(5b)	41.16(15)
O(10b)-Mn(3)-Mn(4)	128.7(2)	O(14)-Mn(5)-Mn(6)	85.6(2)
O(11)-Mn(3)-Mn(3a)	126.8(2)	O(15)-Mn(5)-Mn(5a)	85.8(2)
O(11)-Mn(3)-Mn(3b)	134.7(2)	O(15)-Mn(5)-Mn(5b)	130.1(2)
O(11)-Mn(3)-Mn(4)	85.78(19)	O(15)-Mn(5)-Mn(6)	133.90(19)
Mn(3a)-Mn(3)-Mn(3b)	60.0	O(16)-Mn(5)-Mn(5a)	131.3(2)
Mn(3)-Mn(3b)-Mn(4)	58.87(3)	O(16)-Mn(5)-Mn(5b)	85.97(19)
O(7)-Mn(4)-O(7a)	84.7(3)	O(16)-Mn(5)-Mn(6)	133.0(2)
O(7)-Mn(4)-O(12)	91.2(3)	O(17)-Mn(5)-Mn(5a)	131.20(19)
O(7a)-Mn(4)-O(12)	89.2(3)	O(17)-Mn(5)-Mn(5b)	133.80(17)
O(7b)-Mn(4)-O(12)	172.9(3)	O(17)-Mn(5)-Mn(6)	85.27(17)
O(12a)-Mn(4)-O(12)	94.5(3)	Mn(5a)-Mn(5)-Mn(5b)	60.0
O(7)-Mn(4)-Mn(3)	40.12(17)	Mn(5a)-Mn(5)-Mn(6)	61.06(3)
O(7)-Mn(4)-Mn(3a)	45.1(2)	O(13)-Mn(6)-O(13a)	78.9(2)

Table A-2. Continued.

O(13)-Mn(6)-O(18)	90.5(2)	O(19b)-Mn(7)-Mn(7a)	83.3(2)
O(13)-Mn(6)-O(18a)	164.4(2)	O(19b)-Mn(7)-Mn(7b)	39.5(2)
O(18)-Mn(6)-O(13a)	87.9(2)	O(19b)-Mn(7)-Mn(8)	41.3(2)
O(18)-Mn(6)-O(18a)	100.6(2)	O(20)-Mn(7)-Mn(7a)	41.18(17)
O(18)-Mn(6)-Mn(5a)	125.38(19)	O(20)-Mn(7)-Mn(7b)	41.18(17)
O(18)-Mn(6)-Mn(5)	83.55(17)	O(20)-Mn(7)-Mn(8)	83.2(3)
O(18a)-Mn(6)-Mn(5)	132.52(19)	O(21)-Mn(7)-Mn(7a)	82.8(2)
O(13)-Mn(6)-Mn(5)	37.50(16)	O(21)-Mn(7)-Mn(7b)	130.1(2)
O(13)-Mn(6)-Mn(5a)	81.12(16)	O(21)-Mn(7)-Mn(8)	129.2(2)
O(13a)-Mn(6)-Mn(5)	42.07(16)	O(22b)-Mn(7)-Mn(7a)	132.2(2)
Mn(5a)-Mn(6)-Mn(5)	57.88(5)	O(22b)-Mn(7)-Mn(7b)	85.7(2)
Mn(5)-O(13)-Mn(5b)	96.8(3)	O(22b)-Mn(7)-Mn(8)	131.5(3)
Mn(5)-O(13)-Mn(6)	100.9(3)	O(23)-Mn(7)-Mn(7a)	133.1(2)
Mn(5b)-O(13)-Mn(6)	95.7(2)	O(23)-Mn(7)-Mn(7b)	127.7(2)
Mn(5)-O(14)-Mn(5b)	97.7(3)	O(23)-Mn(7)-Mn(8)	85.1(2)
O(19)-Mn(7)-O(19b)	81.9(4)	Mn(7a)-Mn(7)-Mn(7b)	60.0
O(19)-Mn(7)-O(20)	83.7(3)	Mn(7b)-Mn(7)-Mn(8)	59.01(4)
O(19)-Mn(7)-O(21)	88.4(3)	O(19)-Mn(8)-O(19b)	85.5(4)
O(19)-Mn(7)-O(22b)	171.1(4)	O(19)-Mn(8)-O(24)	92.6(3)
O(19)-Mn(7)-O(23)	90.1(3)	O(19)-Mn(8)-O(24b)	173.6(4)
O(20)-Mn(7)-O(19b)	80.1(3)	O(24)-Mn(8)-O(19b)	88.2(3)
O(20)-Mn(7)-O(21)	88.9(3)	O(24)-Mn(8)-O(24b)	93.5(3)
O(20)-Mn(7)-O(22b)	91.0(3)	O(19)-Mn(8)-Mn(7)	40.8(2)
O(20)-Mn(7)-O(23)	167.5(3)	O(19)-Mn(8)-Mn(7b)	88.0(3)
O(21)-Mn(7)-O(19b)	166.1(3)	O(19b)-Mn(8)-Mn(7)	45.0(3)
O(21)-Mn(7)-O(22b)	98.7(3)	O(24)-Mn(8)-Mn(7b)	128.8(2)
O(21)-Mn(7)-O(23)	101.7(3)	O(24)-Mn(8)-Mn(7a)	137.6(2)
O(22b)-Mn(7)-O(19b)	90.2(3)	O(24)-Mn(8)-Mn(7)	86.52(19)
O(22b)-Mn(7)-O(23)	93.7(3)	Mn(7a)-Mn(8)-Mn(7)	61.98(8)
O(23)-Mn(7)-O(19b)	88.3(3)	Mn(7)-O(19)-Mn(8)	98.3(3)
O(19)-Mn(7)-Mn(7a)	43.0(3)	Mn(7)-O(19)-Mn(7a)	97.5(3)
O(19)-Mn(7)-Mn(7b)	85.6(3)	Mn(8)-O(19)-Mn(7a)	93.6(4)
O(19)-Mn(7)-Mn(8)	40.9(2)	Mn(7)-O(20)-Mn(7a)	97.6(3)

---

Table A-3. Selected interatomic distances (Å) and angles (°) for  
 $[\text{Mn}_7\text{O}_8(\text{O}_2\text{CMe})(\text{O}_2\text{SePh})_8(\text{H}_2\text{O})] \cdot 6\text{MeCN}$  (**6**·6MeCN).

Mn(1)-O(1)	1.788(6)	Mn(4)-O(26)	2.180(7)
Mn(1)-O(2)	1.839(7)	Mn(4)-O(7)	2.278(6)
Mn(1)-O(3)	1.914(6)	Mn(4)-Mn(5)	2.829(2)
Mn(1)-O(11)	1.944(6)	Mn(4)-Mn(6)	3.018(2)
Mn(1)-O(9)	1.961(6)	Mn(4)-Mn(7)	3.036(2)
Mn(1)-O(13)	1.998(6)	Mn(5)-O(5)	1.880(6)
Mn(1)-Mn(2)	2.722(2)	Mn(5)-O(6)	1.907(6)
Mn(2)-O(1)	1.813(6)	Mn(5)-O(18)	1.909(7)
Mn(2)-O(2)	1.844(7)	Mn(5)-O(21)	1.950(6)
Mn(2)-O(5)	1.905(6)	Mn(5)-O(27)	2.172(8)
Mn(2)-O(12)	1.948(6)	Mn(5)-O(16)	2.530(7)
Mn(2)-O(10)	1.992(7)	Mn(5)-Mn(7)	3.126(2)
Mn(2)-O(15)	2.002(6)	Mn(6)-O(8)	1.831(6)
Mn(3)-O(3)	1.893(6)	Mn(6)-O(7)	1.848(6)
Mn(3)-O(4)	1.898(6)	Mn(6)-O(4)	1.899(7)
Mn(3)-O(17)	1.918(6)	Mn(6)-O(23)	1.909(7)
Mn(3)-O(19)	1.923(6)	Mn(6)-O(20)	1.963(6)
Mn(3)-O(25)	2.289(8)	Mn(6)-O(14)	1.994(6)
Mn(3)-O(14)	2.478(7)	Mn(6)-Mn(7)	2.758(2)
Mn(3)-Mn(4)	2.856(2)	Mn(7)-O(8)	1.819(6)
Mn(3)-Mn(6)	3.111(2)	Mn(7)-O(7)	1.852(5)
Mn(4)-O(5)	1.895(6)	Mn(7)-O(6)	1.886(6)
Mn(4)-O(3)	1.907(6)	Mn(7)-O(24)	1.935(7)
Mn(4)-O(4)	1.944(6)	Mn(7)-O(16)	1.960(6)
Mn(4)-O(6)	1.949(6)	Mn(7)-O(22)	1.964(6)
O(1)-Mn(1)-O(2)	83.7(3)	O(11)-Mn(1)-Mn(2)	91.2(2)
O(1)-Mn(1)-O(3)	93.3(3)	O(9)-Mn(1)-Mn(2)	139.3(2)
O(2)-Mn(1)-O(3)	90.0(3)	O(13)-Mn(1)-Mn(2)	130.64(18)
O(1)-Mn(1)-O(11)	92.8(3)	O(1)-Mn(2)-O(2)	82.8(3)
O(2)-Mn(1)-O(11)	90.0(3)	O(1)-Mn(2)-O(5)	92.3(3)
O(3)-Mn(1)-O(11)	173.9(3)	O(2)-Mn(2)-O(5)	91.3(3)
O(1)-Mn(1)-O(9)	176.4(3)	O(1)-Mn(2)-O(12)	92.7(3)
O(2)-Mn(1)-O(9)	97.0(3)	O(2)-Mn(2)-O(12)	89.8(3)
O(3)-Mn(1)-O(9)	90.3(3)	O(5)-Mn(2)-O(12)	174.9(3)
O(11)-Mn(1)-O(9)	83.6(3)	O(1)-Mn(2)-O(10)	179.0(3)
O(1)-Mn(1)-O(13)	89.4(3)	O(2)-Mn(2)-O(10)	97.0(3)
O(2)-Mn(1)-O(13)	173.0(3)	O(5)-Mn(2)-O(10)	88.7(3)
O(3)-Mn(1)-O(13)	91.5(3)	O(12)-Mn(2)-O(10)	86.3(3)
O(11)-Mn(1)-O(13)	89.3(3)	O(1)-Mn(2)-O(15)	90.9(3)
O(9)-Mn(1)-O(13)	89.8(3)	O(2)-Mn(2)-O(15)	173.7(3)
O(1)-Mn(1)-Mn(2)	41.24(19)	O(5)-Mn(2)-O(15)	89.8(3)
O(2)-Mn(1)-Mn(2)	42.4(2)	O(12)-Mn(2)-O(15)	89.7(3)
O(3)-Mn(1)-Mn(2)	92.92(19)	O(10)-Mn(2)-O(15)	89.2(3)

Table A-3. Continued.

O(1)-Mn(2)-Mn(1)	40.57(19)	O(3)-Mn(4)-O(7)	99.8(2)
O(2)-Mn(2)-Mn(1)	42.3(2)	O(4)-Mn(4)-O(7)	75.4(2)
O(5)-Mn(2)-Mn(1)	93.05(19)	O(6)-Mn(4)-O(7)	74.4(2)
O(12)-Mn(2)-Mn(1)	91.0(2)	O(26)-Mn(4)-O(7)	160.8(2)
O(10)-Mn(2)-Mn(1)	139.3(2)	O(5)-Mn(4)-Mn(5)	41.25(18)
O(15)-Mn(2)-Mn(1)	131.42(19)	O(3)-Mn(4)-Mn(5)	141.3(2)
O(3)-Mn(3)-O(4)	83.5(3)	O(4)-Mn(4)-Mn(5)	136.79(19)
O(3)-Mn(3)-O(17)	93.9(3)	O(6)-Mn(4)-Mn(5)	42.22(18)
O(4)-Mn(3)-O(17)	177.1(3)	O(26)-Mn(4)-Mn(5)	83.0(2)
O(3)-Mn(3)-O(19)	173.5(3)	O(7)-Mn(4)-Mn(5)	92.84(14)
O(4)-Mn(3)-O(19)	90.7(3)	O(5)-Mn(4)-Mn(3)	141.48(19)
O(17)-Mn(3)-O(19)	91.9(3)	O(3)-Mn(4)-Mn(3)	41.09(19)
O(3)-Mn(3)-O(25)	89.0(3)	O(4)-Mn(4)-Mn(3)	41.34(18)
O(4)-Mn(3)-O(25)	89.4(3)	O(6)-Mn(4)-Mn(3)	136.16(19)
O(17)-Mn(3)-O(25)	89.3(3)	O(26)-Mn(4)-Mn(3)	91.5(2)
O(19)-Mn(3)-O(25)	94.0(3)	O(7)-Mn(4)-Mn(3)	91.69(14)
O(3)-Mn(3)-O(14)	90.0(2)	Mn(5)-Mn(4)-Mn(3)	174.10(8)
O(4)-Mn(3)-O(14)	74.4(2)	O(5)-Mn(4)-Mn(6)	135.9(2)
O(17)-Mn(3)-O(14)	106.9(3)	O(3)-Mn(4)-Mn(6)	92.4(2)
O(19)-Mn(3)-O(14)	85.4(3)	O(4)-Mn(4)-Mn(6)	37.72(19)
O(25)-Mn(3)-O(14)	163.8(2)	O(6)-Mn(4)-Mn(6)	82.01(18)
O(3)-Mn(3)-Mn(4)	41.46(18)	O(26)-Mn(4)-Mn(6)	130.1(2)
O(4)-Mn(3)-Mn(4)	42.59(18)	O(7)-Mn(4)-Mn(6)	37.67(14)
O(17)-Mn(3)-Mn(4)	134.7(2)	Mn(5)-Mn(4)-Mn(6)	118.37(7)
O(19)-Mn(3)-Mn(4)	133.17(19)	Mn(3)-Mn(4)-Mn(6)	63.88(5)
O(25)-Mn(3)-Mn(4)	83.75(19)	O(5)-Mn(4)-Mn(7)	90.58(19)
O(14)-Mn(3)-Mn(4)	84.85(14)	O(3)-Mn(4)-Mn(7)	137.2(2)
O(3)-Mn(3)-Mn(6)	89.9(2)	O(4)-Mn(4)-Mn(7)	83.72(19)
O(4)-Mn(3)-Mn(6)	35.0(2)	O(6)-Mn(4)-Mn(7)	36.95(18)
O(17)-Mn(3)-Mn(6)	146.6(2)	O(26)-Mn(4)-Mn(7)	126.3(2)
O(19)-Mn(3)-Mn(6)	83.7(2)	O(7)-Mn(4)-Mn(7)	37.49(13)
O(25)-Mn(3)-Mn(6)	123.98(18)	Mn(5)-Mn(4)-Mn(7)	64.31(5)
O(14)-Mn(3)-Mn(6)	39.82(14)	Mn(3)-Mn(4)-Mn(7)	118.05(7)
Mn(4)-Mn(3)-Mn(6)	60.59(5)	Mn(6)-Mn(4)-Mn(7)	54.20(5)
O(5)-Mn(4)-O(3)	100.4(3)	O(5)-Mn(5)-O(6)	83.8(3)
O(5)-Mn(4)-O(4)	173.6(3)	O(5)-Mn(5)-O(18)	96.2(3)
O(3)-Mn(4)-O(4)	81.9(3)	O(6)-Mn(5)-O(18)	176.2(4)
O(5)-Mn(4)-O(6)	82.3(3)	O(5)-Mn(5)-O(21)	172.1(3)
O(3)-Mn(4)-O(6)	174.0(3)	O(6)-Mn(5)-O(21)	90.2(3)
O(4)-Mn(4)-O(6)	94.9(3)	O(18)-Mn(5)-O(21)	89.3(3)
O(5)-Mn(4)-O(26)	90.9(3)	O(5)-Mn(5)-O(27)	90.1(3)
O(3)-Mn(4)-O(26)	95.0(3)	O(6)-Mn(5)-O(27)	89.4(3)
O(4)-Mn(4)-O(26)	94.9(3)	O(18)-Mn(5)-O(27)	94.5(4)
O(6)-Mn(4)-O(26)	90.3(3)	O(21)-Mn(5)-O(27)	95.1(3)
O(5)-Mn(4)-O(7)	98.3(2)	O(5)-Mn(5)-O(16)	87.5(3)

Table A-3. Continued.

O(6)-Mn(5)-O(16)	72.7(2)	O(8)-Mn(6)-Mn(3)	130.8(2)
O(18)-Mn(5)-O(16)	103.4(4)	O(7)-Mn(6)-Mn(3)	93.19(18)
O(21)-Mn(5)-O(16)	85.7(3)	O(4)-Mn(6)-Mn(3)	34.96(18)
O(27)-Mn(5)-O(16)	162.1(3)	O(23)-Mn(6)-Mn(3)	141.73(19)
O(5)-Mn(5)-Mn(4)	41.67(19)	O(20)-Mn(6)-Mn(3)	84.6(2)
O(6)-Mn(5)-Mn(4)	43.38(18)	O(14)-Mn(6)-Mn(3)	52.73(19)
O(18)-Mn(5)-Mn(4)	137.3(2)	Mn(7)-Mn(6)-Mn(3)	118.75(7)
O(21)-Mn(5)-Mn(4)	133.3(2)	Mn(4)-Mn(6)-Mn(3)	55.53(5)
O(27)-Mn(5)-Mn(4)	81.6(2)	O(8)-Mn(7)-O(7)	82.8(2)
O(16)-Mn(5)-Mn(4)	84.83(14)	O(8)-Mn(7)-O(6)	93.5(3)
O(5)-Mn(5)-Mn(7)	88.1(2)	O(7)-Mn(7)-O(6)	86.8(3)
O(6)-Mn(5)-Mn(7)	34.28(19)	O(8)-Mn(7)-O(24)	88.4(3)
O(18)-Mn(5)-Mn(7)	141.9(3)	O(7)-Mn(7)-O(24)	91.7(3)
O(21)-Mn(5)-Mn(7)	84.0(2)	O(6)-Mn(7)-O(24)	177.4(3)
O(27)-Mn(5)-Mn(7)	123.5(2)	O(8)-Mn(7)-O(16)	174.4(3)
O(16)-Mn(5)-Mn(7)	38.77(14)	O(7)-Mn(7)-O(16)	91.9(3)
Mn(4)-Mn(5)-Mn(7)	61.06(5)	O(6)-Mn(7)-O(16)	88.2(3)
O(8)-Mn(6)-O(7)	82.6(2)	O(24)-Mn(7)-O(16)	89.7(3)
O(8)-Mn(6)-O(4)	95.8(3)	O(8)-Mn(7)-O(22)	96.4(3)
O(7)-Mn(6)-O(4)	87.6(3)	O(7)-Mn(7)-O(22)	175.5(3)
O(8)-Mn(6)-O(23)	87.5(3)	O(6)-Mn(7)-O(22)	88.8(3)
O(7)-Mn(6)-O(23)	92.1(3)	O(24)-Mn(7)-O(22)	92.8(3)
O(4)-Mn(6)-O(23)	176.6(3)	O(16)-Mn(7)-O(22)	89.0(3)
O(8)-Mn(6)-O(20)	95.8(3)	O(8)-Mn(7)-Mn(6)	41.09(18)
O(7)-Mn(6)-O(20)	175.5(3)	O(7)-Mn(7)-Mn(6)	41.75(17)
O(4)-Mn(6)-O(20)	88.3(3)	O(6)-Mn(7)-Mn(6)	90.60(18)
O(23)-Mn(6)-O(20)	92.1(3)	O(24)-Mn(7)-Mn(6)	89.66(18)
O(8)-Mn(6)-O(14)	172.1(3)	O(16)-Mn(7)-Mn(6)	133.64(19)
O(7)-Mn(6)-O(14)	90.2(2)	O(22)-Mn(7)-Mn(6)	137.3(2)
O(4)-Mn(6)-O(14)	87.2(3)	O(8)-Mn(7)-Mn(4)	87.8(2)
O(23)-Mn(6)-O(14)	89.4(3)	O(7)-Mn(7)-Mn(4)	48.44(19)
O(20)-Mn(6)-O(14)	91.6(2)	O(6)-Mn(7)-Mn(4)	38.39(18)
O(8)-Mn(6)-Mn(7)	40.76(18)	O(24)-Mn(7)-Mn(4)	140.07(19)
O(7)-Mn(6)-Mn(7)	41.88(16)	O(16)-Mn(7)-Mn(4)	90.27(19)
O(4)-Mn(6)-Mn(7)	92.70(19)	O(22)-Mn(7)-Mn(4)	127.2(2)
O(23)-Mn(6)-Mn(7)	89.30(19)	Mn(6)-Mn(7)-Mn(4)	62.57(5)
O(20)-Mn(6)-Mn(7)	136.47(19)	O(8)-Mn(7)-Mn(5)	128.2(2)
O(14)-Mn(6)-Mn(7)	131.97(17)	O(7)-Mn(7)-Mn(5)	93.09(19)
O(8)-Mn(6)-Mn(4)	88.1(2)	O(6)-Mn(7)-Mn(5)	34.70(18)
O(7)-Mn(6)-Mn(4)	48.88(19)	O(24)-Mn(7)-Mn(5)	143.46(19)
O(4)-Mn(6)-Mn(4)	38.78(18)	O(16)-Mn(7)-Mn(5)	53.93(19)
O(23)-Mn(6)-Mn(4)	140.9(2)	O(22)-Mn(7)-Mn(5)	83.9(2)
O(20)-Mn(6)-Mn(4)	126.9(2)	Mn(6)-Mn(7)-Mn(5)	117.07(7)
O(14)-Mn(6)-Mn(4)	89.73(19)	Mn(4)-Mn(7)-Mn(5)	54.63(5)
Mn(7)-Mn(6)-Mn(4)	63.24(5)	Mn(1)-O(1)-Mn(2)	98.2(3)

Table A-3. Continued.

Mn(1)-O(2)-Mn(2)	95.3(3)	Mn(7)-O(6)-Mn(5)	111.0(3)
Mn(3)-O(3)-Mn(4)	97.5(3)	Mn(7)-O(6)-Mn(4)	104.7(3)
Mn(3)-O(3)-Mn(1)	130.7(3)	Mn(5)-O(6)-Mn(4)	94.4(3)
Mn(4)-O(3)-Mn(1)	121.3(3)	Mn(6)-O(7)-Mn(7)	96.4(3)
Mn(3)-O(4)-Mn(6)	110.0(3)	Mn(6)-O(7)-Mn(4)	93.5(2)
Mn(3)-O(4)-Mn(4)	96.1(3)	Mn(7)-O(7)-Mn(4)	94.1(2)
Mn(6)-O(4)-Mn(4)	103.5(3)	Mn(7)-O(8)-Mn(6)	98.2(3)
Mn(5)-O(5)-Mn(4)	97.1(3)	Mn(6)-O(14)-Mn(3)	87.4(2)
Mn(5)-O(5)-Mn(2)	133.7(3)	Mn(7)-O(16)-Mn(5)	87.3(2)
Mn(4)-O(5)-Mn(2)	122.3(3)		

---

Table A-4. Selected interatomic distances (Å) and angles (°) for  
 $[\text{Mn}_7\text{O}_8(\text{O}_2\text{SePh})_9(\text{H}_2\text{O})] \cdot 2\text{CH}_2\text{Cl}_2$  ( $7 \cdot 2\text{CH}_2\text{Cl}_2$ ).

Mn(1)-O(14)	1.800(6)	Mn(2)-Mn(3)	3.113(2)
Mn(1)-O(15)	1.845(7)	Mn(3)-O(11)	1.822(5)
Mn(1)-O(12)	1.886(7)	Mn(3)-O(16)	1.843(5)
Mn(1)-O(3)	1.932(7)	Mn(3)-O(13)	1.894(8)
Mn(1)-O(4)	1.983(8)	Mn(3)-O(10)	1.923(7)
Mn(1)-O(6)	2.010(8)	Mn(3)-O(9)	1.952(8)
Mn(1)-Mn(1a)	2.760(3)	Mn(3)-O(7)	2.005(7)
Mn(2)-O(13)	1.873(8)	Mn(3)-Mn(3a)	2.741(3)
Mn(2)-O(12)	1.902(7)	Mn(3)-Mn(4)	3.033(3)
Mn(2)-O(5)	1.903(10)	Mn(4)-O(12)	1.913(7)
Mn(2)-O(8)	1.935(8)	Mn(4)-O(13)	1.963(7)
Mn(2)-O(2)	2.001(17)	Mn(4)-O(1)	2.160(12)
Mn(2)-Mn(4)	2.8427(19)	Mn(4)-O(16)	2.276(9)
O(12)-Mn(1)-O(3)	173.8(3)	O(2)-Mn(2)-Mn(4)	88.2(5)
O(14)-Mn(1)-O(4)	177.2(4)	O(13)-Mn(2)-Mn(3)	34.5(2)
O(15)-Mn(1)-O(4)	98.8(4)	O(12)-Mn(2)-Mn(3)	89.5(2)
O(12)-Mn(1)-O(4)	89.9(4)	O(5)-Mn(2)-Mn(3)	147.9(4)
O(3)-Mn(1)-O(4)	84.1(4)	O(8)-Mn(2)-Mn(3)	82.3(3)
O(14)-Mn(1)-O(6)	90.2(3)	O(2)-Mn(2)-Mn(3)	125.5(7)
O(15)-Mn(1)-O(6)	171.7(3)	Mn(4)-Mn(2)-Mn(3)	61.03(6)
O(12)-Mn(1)-O(6)	91.5(3)	O(11)-Mn(3)-O(16)	83.1(3)
O(3)-Mn(1)-O(6)	89.9(3)	O(11)-Mn(3)-O(13)	94.6(4)
O(4)-Mn(1)-O(6)	89.3(4)	O(16)-Mn(3)-O(13)	87.3(3)
O(14)-Mn(1)-Mn(1a)	40.0(2)	O(11)-Mn(3)-O(10)	89.4(4)
O(15)-Mn(1)-Mn(1a)	41.6(2)	O(16)-Mn(3)-O(10)	92.1(3)
O(12)-Mn(1)-Mn(1a)	92.6(2)	O(13)-Mn(3)-O(10)	175.9(3)
O(3)-Mn(1)-Mn(1a)	91.2(3)	O(11)-Mn(3)-O(9)	96.3(3)
O(4)-Mn(1)-Mn(1a)	140.3(3)	O(16)-Mn(3)-O(9)	176.3(4)
O(6)-Mn(1)-Mn(1a)	130.2(2)	O(13)-Mn(3)-O(9)	89.1(3)
O(13)-Mn(2)-O(12)	84.5(3)	O(10)-Mn(3)-O(9)	91.6(3)
O(13)-Mn(2)-O(5)	176.4(4)	O(11)-Mn(3)-O(7)	173.7(3)
O(12)-Mn(2)-O(5)	92.7(4)	O(16)-Mn(3)-O(7)	90.9(3)
O(13)-Mn(2)-O(8)	88.9(4)	O(13)-Mn(3)-O(7)	86.9(3)
O(12)-Mn(2)-O(8)	171.7(4)	O(10)-Mn(3)-O(7)	89.0(3)
O(5)-Mn(2)-O(8)	94.1(5)	O(9)-Mn(3)-O(7)	89.8(3)
O(13)-Mn(2)-O(2)	92.0(7)	O(11)-Mn(3)-Mn(3a)	41.21(19)
O(12)-Mn(2)-O(2)	95.5(5)	O(16)-Mn(3)-Mn(3a)	41.94(19)
O(5)-Mn(2)-O(2)	86.1(8)	O(13)-Mn(3)-Mn(3a)	92.6(2)
O(8)-Mn(2)-O(2)	89.8(6)	O(10)-Mn(3)-Mn(3a)	89.66(19)
O(13)-Mn(2)-Mn(4)	43.4(2)	O(9)-Mn(3)-Mn(3a)	137.5(3)
O(12)-Mn(2)-Mn(4)	42.0(2)	O(7)-Mn(3)-Mn(3a)	132.72(19)
O(5)-Mn(2)-Mn(4)	133.4(3)	O(11)-Mn(3)-Mn(4)	87.6(3)
O(8)-Mn(2)-Mn(4)	132.1(4)	O(16)-Mn(3)-Mn(4)	48.4(3)

Table A-4. Continued.

O(13)-Mn(3)-Mn(4)	39.0(2)	O(13a)-Mn(4)-Mn(2)	136.7(2)
O(10)-Mn(3)-Mn(4)	140.5(2)	O(1)-Mn(4)-Mn(2)	87.55(6)
O(9)-Mn(3)-Mn(4)	127.9(3)	O(16)-Mn(4)-Mn(2)	91.86(6)
O(7)-Mn(3)-Mn(4)	89.8(2)	Mn(2)-Mn(4)-Mn(2a)	174.45(12)
Mn(3a)-Mn(3)-Mn(4)	63.13(3)	O(12)-Mn(4)-Mn(3a)	136.1(2)
O(11)-Mn(3)-Mn(2)	128.6(3)	O(13)-Mn(4)-Mn(3a)	82.9(2)
O(16)-Mn(3)-Mn(2)	93.0(2)	Mn(2)-Mn(4)-Mn(3a)	117.56(8)
O(13)-Mn(3)-Mn(2)	34.1(2)	O(12)-Mn(4)-Mn(3)	91.7(2)
O(10)-Mn(3)-Mn(2)	142.0(2)	O(13)-Mn(4)-Mn(3)	37.3(2)
O(9)-Mn(3)-Mn(2)	84.5(3)	O(1)-Mn(4)-Mn(3)	127.5(3)
O(7)-Mn(3)-Mn(2)	53.3(2)	O(16)-Mn(4)-Mn(3)	37.29(14)
Mn(3a)-Mn(3)-Mn(2)	118.15(5)	Mn(2)-Mn(4)-Mn(3)	63.88(5)
Mn(4)-Mn(3)-Mn(2)	55.08(5)	Mn(3a)-Mn(4)-Mn(3)	53.73(7)
O(12)-Mn(4)-O(12a)	99.9(4)	Mn(3a)-O(11)-Mn(3)	97.6(4)
O(12)-Mn(4)-O(13)	81.8(3)	Mn(1)-O(12)-Mn(2)	132.2(4)
O(12)-Mn(4)-O(13a)	173.5(3)	Mn(1)-O(12)-Mn(4)	122.5(3)
O(13)-Mn(4)-O(13a)	95.8(4)	Mn(2)-O(12)-Mn(4)	96.4(3)
O(12)-Mn(4)-O(1)	94.0(3)	Mn(2)-O(13)-Mn(3)	111.5(4)
O(13)-Mn(4)-O(1)	92.2(3)	Mn(2)-O(13)-Mn(4)	95.6(3)
O(12)-Mn(4)-O(16)	98.9(3)	Mn(3)-O(13)-Mn(4)	103.7(3)
O(13)-Mn(4)-O(16)	74.6(3)	Mn(1)-O(14)-Mn(1a)	100.1(4)
O(1)-Mn(4)-O(16)	160.0(4)	Mn(1a)-O(15)-Mn(1)	96.8(5)
O(12)-Mn(4)-Mn(2)	41.7(2)	Mn(3)-O(16)-Mn(3a)	96.1(4)
O(12a)-Mn(4)-Mn(2)	141.4(2)	Mn(3)-O(16)-Mn(4)	94.3(3)
O(13)-Mn(4)-Mn(2)	41.0(2)		

---

Table A-5. Selected interatomic distances (Å) and angles (°) for  
 $[\text{Mn}_4\text{O}_4(\text{O}_2\text{AsMe}_2)_6] \cdot 5\text{H}_2\text{O} \cdot \text{C}_5\text{H}_{12}$  (**9**·5H<sub>2</sub>O·C<sub>5</sub>H<sub>12</sub>).

Mn(1)-O(2)	1.855(3)	Mn(2)-Mn(3)	2.8638(8)
Mn(1)-O(3)	1.873(3)	Mn(2)-Mn(4)	3.0546(8)
Mn(1)-O(1)	1.899(3)	Mn(3)-O(4)	1.838(3)
Mn(1)-O(9)	1.906(3)	Mn(3)-O(8)	1.933(3)
Mn(1)-O(5)	1.931(3)	Mn(3)-O(1)	1.950(3)
Mn(1)-O(7)	1.940(2)	Mn(3)-O(12)	1.951(3)
Mn(1)-Mn(4)	2.8646(8)	Mn(3)-O(15)	1.958(3)
Mn(1)-Mn(3)	2.8857(8)	Mn(3)-O(3)	1.959(3)
Mn(1)-Mn(2)	2.9375(8)	Mn(3)-Mn(4)	3.0171(8)
Mn(2)-O(4)	1.897(3)	Mn(4)-O(2)	1.899(3)
Mn(2)-O(13)	1.909(3)	Mn(4)-O(16)	1.929(3)
Mn(2)-O(6)	1.921(3)	Mn(4)-O(14)	1.938(3)
Mn(2)-O(1)	1.933(3)	Mn(4)-O(3)	1.974(3)
Mn(2)-O(11)	2.066(3)	Mn(4)-O(10)	2.095(3)
Mn(2)-O(2)	2.139(3)	Mn(4)-O(4)	2.291(3)
O(2)-Mn(1)-O(3)	83.47(11)	O(2)-Mn(1)-Mn(2)	46.55(9)
O(2)-Mn(1)-O(1)	86.57(12)	O(3)-Mn(1)-Mn(2)	85.87(8)
O(3)-Mn(1)-O(1)	84.09(11)	O(1)-Mn(1)-Mn(2)	40.38(8)
O(2)-Mn(1)-O(9)	92.87(12)	O(9)-Mn(1)-Mn(2)	139.28(8)
O(3)-Mn(1)-O(9)	93.71(12)	O(5)-Mn(1)-Mn(2)	88.28(9)
O(1)-Mn(1)-O(9)	177.78(12)	O(7)-Mn(1)-Mn(2)	131.07(8)
O(2)-Mn(1)-O(5)	93.62(12)	Mn(4)-Mn(1)-Mn(2)	63.519(19)
O(3)-Mn(1)-O(5)	173.95(12)	Mn(3)-Mn(1)-Mn(2)	58.909(19)
O(1)-Mn(1)-O(5)	90.45(12)	O(4)-Mn(2)-O(13)	93.12(12)
O(9)-Mn(1)-O(5)	91.73(12)	O(4)-Mn(2)-O(6)	173.07(12)
O(2)-Mn(1)-O(7)	175.09(11)	O(13)-Mn(2)-O(6)	91.67(13)
O(3)-Mn(1)-O(7)	92.17(11)	O(4)-Mn(2)-O(1)	81.66(11)
O(1)-Mn(1)-O(7)	90.75(11)	O(13)-Mn(2)-O(1)	171.85(12)
O(9)-Mn(1)-O(7)	89.65(11)	O(6)-Mn(2)-O(1)	93.02(12)
O(5)-Mn(1)-O(7)	90.50(12)	O(4)-Mn(2)-O(11)	92.54(13)
O(2)-Mn(1)-Mn(4)	40.82(8)	O(13)-Mn(2)-O(11)	96.52(13)
O(3)-Mn(1)-Mn(4)	43.25(8)	O(6)-Mn(2)-O(11)	91.89(13)
O(1)-Mn(1)-Mn(4)	89.35(8)	O(1)-Mn(2)-O(11)	89.99(12)
O(9)-Mn(1)-Mn(4)	88.83(8)	O(4)-Mn(2)-O(2)	85.46(11)
O(5)-Mn(1)-Mn(4)	134.37(9)	O(13)-Mn(2)-O(2)	95.19(11)
O(7)-Mn(1)-Mn(4)	135.13(8)	O(6)-Mn(2)-O(2)	89.12(12)
O(2)-Mn(1)-Mn(3)	87.22(8)	O(1)-Mn(2)-O(2)	78.23(10)
O(3)-Mn(1)-Mn(3)	42.27(8)	O(11)-Mn(2)-O(2)	168.21(11)
O(1)-Mn(1)-Mn(3)	42.12(8)	O(4)-Mn(2)-Mn(3)	39.18(8)
O(9)-Mn(1)-Mn(3)	135.73(9)	O(13)-Mn(2)-Mn(3)	132.30(10)
O(5)-Mn(1)-Mn(3)	132.48(9)	O(6)-Mn(2)-Mn(3)	135.74(9)
O(7)-Mn(1)-Mn(3)	88.04(7)	O(1)-Mn(2)-Mn(3)	42.72(8)
Mn(4)-Mn(1)-Mn(3)	63.291(19)	O(11)-Mn(2)-Mn(3)	88.28(9)

Table A-5. Continued.

O(2)-Mn(2)-Mn(3)	82.83(7)	O(8)-Mn(3)-Mn(4)	129.98(8)
O(4)-Mn(2)-Mn(1)	85.51(8)	O(1)-Mn(3)-Mn(4)	84.06(8)
O(13)-Mn(2)-Mn(1)	134.19(9)	O(12)-Mn(3)-Mn(4)	141.53(9)
O(6)-Mn(2)-Mn(1)	87.56(9)	O(15)-Mn(3)-Mn(4)	86.39(8)
O(1)-Mn(2)-Mn(1)	39.53(8)	O(3)-Mn(3)-Mn(4)	40.10(7)
O(11)-Mn(2)-Mn(1)	129.29(9)	Mn(2)-Mn(3)-Mn(4)	62.522(19)
O(2)-Mn(2)-Mn(1)	39.01(7)	Mn(1)-Mn(3)-Mn(4)	58.014(18)
Mn(3)-Mn(2)-Mn(1)	59.643(19)	O(2)-Mn(4)-O(16)	170.58(11)
O(4)-Mn(2)-Mn(4)	48.48(9)	O(2)-Mn(4)-O(14)	92.63(11)
O(13)-Mn(2)-Mn(4)	88.56(9)	O(16)-Mn(4)-O(14)	94.21(12)
O(6)-Mn(2)-Mn(4)	126.73(10)	O(2)-Mn(4)-O(3)	79.67(11)
O(1)-Mn(2)-Mn(4)	83.30(8)	O(16)-Mn(4)-O(3)	92.20(11)
O(11)-Mn(2)-Mn(4)	140.98(9)	O(14)-Mn(4)-O(3)	165.14(11)
O(2)-Mn(2)-Mn(4)	37.98(7)	O(2)-Mn(4)-O(10)	91.52(12)
Mn(3)-Mn(2)-Mn(4)	61.197(19)	O(16)-Mn(4)-O(10)	93.97(12)
Mn(1)-Mn(2)-Mn(4)	57.079(18)	O(14)-Mn(4)-O(10)	97.66(11)
O(4)-Mn(3)-O(8)	176.71(12)	O(3)-Mn(4)-O(10)	95.25(11)
O(4)-Mn(3)-O(1)	82.69(11)	O(2)-Mn(4)-O(4)	81.26(11)
O(8)-Mn(3)-O(1)	94.07(11)	O(16)-Mn(4)-O(4)	92.31(11)
O(4)-Mn(3)-O(12)	92.26(12)	O(14)-Mn(4)-O(4)	89.68(11)
O(8)-Mn(3)-O(12)	88.46(12)	O(3)-Mn(4)-O(4)	76.66(10)
O(1)-Mn(3)-O(12)	92.90(12)	O(10)-Mn(4)-O(4)	169.95(10)
O(4)-Mn(3)-O(15)	92.44(12)	O(2)-Mn(4)-Mn(1)	39.69(8)
O(8)-Mn(3)-O(15)	90.68(12)	O(16)-Mn(4)-Mn(1)	132.67(8)
O(1)-Mn(3)-O(15)	170.28(11)	O(14)-Mn(4)-Mn(1)	132.15(9)
O(12)-Mn(3)-O(15)	95.70(13)	O(3)-Mn(4)-Mn(1)	40.55(7)
O(4)-Mn(3)-O(3)	88.76(12)	O(10)-Mn(4)-Mn(1)	89.18(8)
O(8)-Mn(3)-O(3)	90.15(11)	O(4)-Mn(4)-Mn(1)	80.80(7)
O(1)-Mn(3)-O(3)	80.53(11)	O(2)-Mn(4)-Mn(3)	82.68(8)
O(12)-Mn(3)-O(3)	173.18(12)	O(16)-Mn(4)-Mn(3)	88.04(8)
O(15)-Mn(3)-O(3)	90.99(11)	O(14)-Mn(4)-Mn(3)	127.12(9)
O(4)-Mn(3)-Mn(2)	40.69(8)	O(3)-Mn(4)-Mn(3)	39.72(8)
O(8)-Mn(3)-Mn(2)	136.13(8)	O(10)-Mn(4)-Mn(3)	134.95(8)
O(1)-Mn(3)-Mn(2)	42.25(8)	O(4)-Mn(4)-Mn(3)	37.46(7)
O(12)-Mn(3)-Mn(2)	89.91(9)	Mn(1)-Mn(4)-Mn(3)	58.695(19)
O(15)-Mn(3)-Mn(2)	133.06(8)	O(2)-Mn(4)-Mn(2)	43.88(9)
O(3)-Mn(3)-Mn(2)	86.46(7)	O(16)-Mn(4)-Mn(2)	130.50(8)
O(4)-Mn(3)-Mn(1)	88.11(9)	O(14)-Mn(4)-Mn(2)	84.63(8)
O(8)-Mn(3)-Mn(1)	89.06(8)	O(3)-Mn(4)-Mn(2)	81.02(8)
O(1)-Mn(3)-Mn(1)	40.77(8)	O(10)-Mn(4)-Mn(2)	135.33(8)
O(12)-Mn(3)-Mn(1)	133.23(9)	O(4)-Mn(4)-Mn(2)	38.31(7)
O(15)-Mn(3)-Mn(1)	131.03(9)	Mn(1)-Mn(4)-Mn(2)	59.403(19)
O(3)-Mn(3)-Mn(1)	40.04(8)	Mn(3)-Mn(4)-Mn(2)	56.281(18)
Mn(2)-Mn(3)-Mn(1)	61.45(2)	Mn(1)-O(1)-Mn(2)	100.09(12)
O(4)-Mn(3)-Mn(4)	49.29(9)	Mn(1)-O(1)-Mn(3)	97.11(12)

Table A-5. Continued.

Mn(2)-O(1)-Mn(3)	95.04(12)	Mn(1)-O(3)-Mn(4)	96.20(11)
Mn(1)-O(2)-Mn(4)	99.49(12)	Mn(3)-O(3)-Mn(4)	100.18(11)
Mn(1)-O(2)-Mn(2)	94.44(12)	Mn(3)-O(4)-Mn(2)	100.12(13)
Mn(4)-O(2)-Mn(2)	98.14(12)	Mn(3)-O(4)-Mn(4)	93.25(11)
Mn(1)-O(3)-Mn(3)	97.69(11)	Mn(2)-O(4)-Mn(4)	93.21(11)

---

Table A-6. Selected interatomic distances (Å) and angles (°) for  
 $\{[\text{Mn}_4\text{O}_4(\text{O}_2\text{AsMe}_2)_6](\text{NO}_3)\}_2 \cdot \frac{1}{2}\text{MeCN} \cdot 12\text{H}_2\text{O}$  (**10**· $\frac{1}{2}\text{MeCN} \cdot 12\text{H}_2\text{O}$ ).

Mn(1)-O(5)	1.897(5)	Mn(5)-O(19)	1.885(5)
Mn(1)-O(3)	1.922(5)	Mn(5)-O(17)	1.897(4)
Mn(1)-O(15)	1.923(4)	Mn(5)-O(29)	1.903(4)
Mn(1)-O(1)	1.929(5)	Mn(5)-O(21)	1.907(5)
Mn(1)-O(13)	1.930(5)	Mn(5)-O(30)	1.908(4)
Mn(1)-O(14)	1.956(5)	Mn(5)-O(31)	1.917(5)
Mn(1)-Mn(4)	2.8791(14)	Mn(5)-Mn(6)	2.8691(15)
Mn(1)-Mn(2)	2.9236(15)	Mn(5)-Mn(8)	2.8756(14)
Mn(1)-Mn(3)	2.9281(15)	Mn(5)-Mn(7)	2.9178(13)
Mn(2)-O(9)	1.901(5)	Mn(6)-O(32)	1.872(4)
Mn(2)-O(15)	1.907(5)	Mn(6)-O(23)	1.892(5)
Mn(2)-O(2)	1.925(5)	Mn(6)-O(18)	1.905(4)
Mn(2)-O(16)	1.960(5)	Mn(6)-O(26)	1.911(5)
Mn(2)-O(7)	1.978(5)	Mn(6)-O(29)	1.920(5)
Mn(2)-O(14)	2.029(6)	Mn(6)-O(31)	1.925(5)
Mn(2)-Mn(4)	2.9102(15)	Mn(6)-Mn(8)	2.8323(14)
Mn(2)-Mn(3)	2.9400(16)	Mn(6)-Mn(7)	3.0000(13)
Mn(3)-O(14)	1.884(5)	Mn(7)-O(24)	1.892(5)
Mn(3)-O(12)	1.905(6)	Mn(7)-O(27)	1.912(5)
Mn(3)-O(6)	1.906(5)	Mn(7)-O(30)	1.954(5)
Mn(3)-O(16)	1.924(5)	Mn(7)-O(29)	1.985(4)
Mn(3)-O(10)	1.971(5)	Mn(7)-O(20)	2.087(5)
Mn(3)-O(13)	2.004(6)	Mn(7)-O(32)	2.242(5)
Mn(3)-Mn(4)	2.9016(15)	Mn(7)-Mn(8)	3.0079(14)
Mn(4)-O(13)	1.883(5)	Mn(8)-O(28)	1.864(4)
Mn(4)-O(4)	1.887(5)	Mn(8)-O(32)	1.865(5)
Mn(4)-O(11)	1.889(6)	Mn(8)-O(31)	1.914(4)
Mn(4)-O(16)	1.906(5)	Mn(8)-O(22)	1.916(5)
Mn(4)-O(8)	1.911(5)	Mn(8)-O(25)	1.917(5)
Mn(4)-O(15)	1.967(5)	Mn(8)-O(30)	1.923(5)
O(5)-Mn(1)-O(3)	92.7(2)	O(1)-Mn(1)-O(14)	91.6(2)
O(5)-Mn(1)-O(15)	173.5(2)	O(13)-Mn(1)-O(14)	82.0(2)
O(3)-Mn(1)-O(15)	90.8(2)	O(5)-Mn(1)-Mn(4)	131.80(17)
O(5)-Mn(1)-O(1)	91.1(2)	O(3)-Mn(1)-Mn(4)	88.62(15)
O(3)-Mn(1)-O(1)	92.0(2)	O(15)-Mn(1)-Mn(4)	42.85(14)
O(15)-Mn(1)-O(1)	94.2(2)	O(1)-Mn(1)-Mn(4)	137.04(15)
O(5)-Mn(1)-O(13)	91.6(2)	O(13)-Mn(1)-Mn(4)	40.36(14)
O(3)-Mn(1)-O(13)	94.2(2)	O(14)-Mn(1)-Mn(4)	84.83(15)
O(15)-Mn(1)-O(13)	82.8(2)	O(5)-Mn(1)-Mn(2)	136.65(16)
O(1)-Mn(1)-O(13)	173.2(2)	O(3)-Mn(1)-Mn(2)	130.60(16)
O(5)-Mn(1)-O(14)	92.9(2)	O(15)-Mn(1)-Mn(2)	40.03(14)
O(3)-Mn(1)-O(14)	173.2(2)	O(1)-Mn(1)-Mn(2)	88.36(15)
O(15)-Mn(1)-O(14)	83.2(2)	O(13)-Mn(1)-Mn(2)	85.39(16)

Table A-6. Continued.

O(14)-Mn(1)-Mn(2)	43.78(16)	Mn(1)-Mn(2)-Mn(3)	59.92(4)
Mn(4)-Mn(1)-Mn(2)	60.20(4)	O(14)-Mn(3)-O(12)	173.8(2)
O(5)-Mn(1)-Mn(3)	88.92(16)	O(14)-Mn(3)-O(6)	91.9(2)
O(3)-Mn(1)-Mn(3)	137.06(16)	O(12)-Mn(3)-O(6)	91.5(2)
O(15)-Mn(1)-Mn(3)	84.80(14)	O(14)-Mn(3)-O(16)	83.8(2)
O(1)-Mn(1)-Mn(3)	130.93(16)	O(12)-Mn(3)-O(16)	92.1(2)
O(13)-Mn(1)-Mn(3)	42.88(17)	O(6)-Mn(3)-O(16)	171.7(2)
O(14)-Mn(1)-Mn(3)	39.42(15)	O(14)-Mn(3)-O(10)	92.5(2)
Mn(4)-Mn(1)-Mn(3)	59.95(4)	O(12)-Mn(3)-O(10)	92.4(2)
Mn(2)-Mn(1)-Mn(3)	60.32(4)	O(6)-Mn(3)-O(10)	94.9(2)
O(9)-Mn(2)-O(15)	173.2(2)	O(16)-Mn(3)-O(10)	92.5(2)
O(9)-Mn(2)-O(2)	92.8(2)	O(14)-Mn(3)-O(13)	81.8(2)
O(15)-Mn(2)-O(2)	93.0(2)	O(12)-Mn(3)-O(13)	92.9(2)
O(9)-Mn(2)-O(16)	91.8(2)	O(6)-Mn(3)-O(13)	92.2(2)
O(15)-Mn(2)-O(16)	82.0(2)	O(16)-Mn(3)-O(13)	80.2(2)
O(2)-Mn(2)-O(16)	170.6(2)	O(10)-Mn(3)-O(13)	171.1(2)
O(9)-Mn(2)-O(7)	91.2(2)	O(14)-Mn(3)-Mn(4)	85.43(15)
O(15)-Mn(2)-O(7)	91.77(19)	O(12)-Mn(3)-Mn(4)	88.41(16)
O(2)-Mn(2)-O(7)	94.8(2)	O(6)-Mn(3)-Mn(4)	132.19(18)
O(16)-Mn(2)-O(7)	93.3(2)	O(16)-Mn(3)-Mn(4)	40.52(14)
O(9)-Mn(2)-O(14)	94.7(2)	O(10)-Mn(3)-Mn(4)	132.93(16)
O(15)-Mn(2)-O(14)	81.7(2)	O(13)-Mn(3)-Mn(4)	40.16(14)
O(2)-Mn(2)-O(14)	92.3(2)	O(14)-Mn(3)-Mn(1)	41.23(16)
O(16)-Mn(2)-O(14)	79.2(2)	O(12)-Mn(3)-Mn(1)	133.76(19)
O(7)-Mn(2)-O(14)	170.6(2)	O(6)-Mn(3)-Mn(1)	88.62(16)
O(9)-Mn(2)-Mn(4)	132.01(17)	O(16)-Mn(3)-Mn(1)	83.46(15)
O(15)-Mn(2)-Mn(4)	42.09(14)	O(10)-Mn(3)-Mn(1)	133.72(16)
O(2)-Mn(2)-Mn(4)	135.13(15)	O(13)-Mn(3)-Mn(1)	40.93(15)
O(16)-Mn(2)-Mn(4)	40.48(14)	Mn(4)-Mn(3)-Mn(1)	59.19(4)
O(7)-Mn(2)-Mn(4)	87.85(14)	O(14)-Mn(3)-Mn(2)	43.18(17)
O(14)-Mn(2)-Mn(4)	82.77(15)	O(12)-Mn(3)-Mn(2)	133.23(16)
O(9)-Mn(2)-Mn(1)	136.45(15)	O(6)-Mn(3)-Mn(2)	135.10(17)
O(15)-Mn(2)-Mn(1)	40.44(13)	O(16)-Mn(3)-Mn(2)	41.26(14)
O(2)-Mn(2)-Mn(1)	88.03(15)	O(10)-Mn(3)-Mn(2)	87.49(16)
O(16)-Mn(2)-Mn(1)	83.02(15)	O(13)-Mn(3)-Mn(2)	83.69(15)
O(7)-Mn(2)-Mn(1)	132.18(15)	Mn(4)-Mn(3)-Mn(2)	59.76(4)
O(14)-Mn(2)-Mn(1)	41.84(15)	Mn(1)-Mn(3)-Mn(2)	59.76(4)
Mn(4)-Mn(2)-Mn(1)	59.14(4)	O(13)-Mn(4)-O(4)	91.9(2)
O(9)-Mn(2)-Mn(3)	88.83(16)	O(13)-Mn(4)-O(11)	91.5(2)
O(15)-Mn(2)-Mn(3)	84.73(14)	O(4)-Mn(4)-O(11)	90.5(3)
O(2)-Mn(2)-Mn(3)	131.56(16)	O(13)-Mn(4)-O(16)	83.8(2)
O(16)-Mn(2)-Mn(3)	40.36(14)	O(4)-Mn(4)-O(16)	173.9(2)
O(7)-Mn(2)-Mn(3)	133.56(16)	O(11)-Mn(4)-O(16)	94.0(2)
O(14)-Mn(2)-Mn(3)	39.47(14)	O(13)-Mn(4)-O(8)	174.8(2)
Mn(4)-Mn(2)-Mn(3)	59.47(4)	O(4)-Mn(4)-O(8)	91.7(2)

Table A-6. Continued.

O(11)-Mn(4)-O(8)	92.2(2)	O(29)-Mn(5)-Mn(6)	41.59(14)
O(16)-Mn(4)-O(8)	92.3(2)	O(21)-Mn(5)-Mn(6)	133.19(16)
O(13)-Mn(4)-O(15)	82.8(2)	O(30)-Mn(5)-Mn(6)	83.98(14)
O(4)-Mn(4)-O(15)	93.4(2)	O(31)-Mn(5)-Mn(6)	41.80(13)
O(11)-Mn(4)-O(15)	173.2(2)	O(19)-Mn(5)-Mn(8)	134.42(14)
O(16)-Mn(4)-O(15)	81.8(2)	O(17)-Mn(5)-Mn(8)	134.38(16)
O(8)-Mn(4)-O(15)	93.3(2)	O(29)-Mn(5)-Mn(8)	84.85(14)
O(13)-Mn(4)-Mn(1)	41.57(16)	O(21)-Mn(5)-Mn(8)	88.86(15)
O(4)-Mn(4)-Mn(1)	88.74(15)	O(30)-Mn(5)-Mn(8)	41.55(14)
O(11)-Mn(4)-Mn(1)	133.00(18)	O(31)-Mn(5)-Mn(8)	41.31(12)
O(16)-Mn(4)-Mn(1)	85.15(14)	Mn(6)-Mn(5)-Mn(8)	59.08(4)
O(8)-Mn(4)-Mn(1)	134.84(15)	O(19)-Mn(5)-Mn(7)	87.70(14)
O(15)-Mn(4)-Mn(1)	41.67(13)	O(17)-Mn(5)-Mn(7)	133.88(15)
O(13)-Mn(4)-Mn(3)	43.33(18)	O(29)-Mn(5)-Mn(7)	42.43(13)
O(4)-Mn(4)-Mn(3)	135.15(16)	O(21)-Mn(5)-Mn(7)	134.50(15)
O(11)-Mn(4)-Mn(3)	88.55(17)	O(30)-Mn(5)-Mn(7)	41.53(14)
O(16)-Mn(4)-Mn(3)	41.00(14)	O(31)-Mn(5)-Mn(7)	88.61(13)
O(8)-Mn(4)-Mn(3)	133.17(15)	Mn(6)-Mn(5)-Mn(7)	62.44(3)
O(15)-Mn(4)-Mn(3)	84.78(13)	Mn(8)-Mn(5)-Mn(7)	62.55(3)
Mn(1)-Mn(4)-Mn(3)	60.86(4)	O(32)-Mn(6)-O(23)	93.5(2)
O(13)-Mn(4)-Mn(2)	86.59(16)	O(32)-Mn(6)-O(18)	173.1(2)
O(4)-Mn(4)-Mn(2)	133.71(17)	O(23)-Mn(6)-O(18)	93.3(2)
O(11)-Mn(4)-Mn(2)	135.77(19)	O(32)-Mn(6)-O(26)	90.8(2)
O(16)-Mn(4)-Mn(2)	41.86(15)	O(23)-Mn(6)-O(26)	94.4(2)
O(8)-Mn(4)-Mn(2)	88.25(14)	O(18)-Mn(6)-O(26)	87.6(2)
O(15)-Mn(4)-Mn(2)	40.52(14)	O(32)-Mn(6)-O(29)	88.1(2)
Mn(1)-Mn(4)-Mn(2)	60.66(4)	O(23)-Mn(6)-O(29)	91.0(2)
Mn(3)-Mn(4)-Mn(2)	60.78(4)	O(18)-Mn(6)-O(29)	92.9(2)
O(19)-Mn(5)-O(17)	91.2(2)	O(26)-Mn(6)-O(29)	174.6(2)
O(19)-Mn(5)-O(29)	95.8(2)	O(32)-Mn(6)-O(31)	82.85(19)
O(17)-Mn(5)-O(29)	92.02(19)	O(23)-Mn(6)-O(31)	172.5(2)
O(19)-Mn(5)-O(21)	89.4(2)	O(18)-Mn(6)-O(31)	90.55(19)
O(17)-Mn(5)-O(21)	91.6(2)	O(26)-Mn(6)-O(31)	92.2(2)
O(29)-Mn(5)-O(21)	173.6(2)	O(29)-Mn(6)-O(31)	82.42(19)
O(19)-Mn(5)-O(30)	93.16(19)	O(32)-Mn(6)-Mn(8)	40.63(14)
O(17)-Mn(5)-O(30)	173.4(2)	O(23)-Mn(6)-Mn(8)	134.02(14)
O(29)-Mn(5)-O(30)	82.62(19)	O(18)-Mn(6)-Mn(8)	132.66(15)
O(21)-Mn(5)-O(30)	93.4(2)	O(26)-Mn(6)-Mn(8)	89.96(14)
O(19)-Mn(5)-O(31)	175.59(19)	O(29)-Mn(6)-Mn(8)	85.78(13)
O(17)-Mn(5)-O(31)	93.1(2)	O(31)-Mn(6)-Mn(8)	42.30(13)
O(29)-Mn(5)-O(31)	83.08(19)	O(32)-Mn(6)-Mn(5)	87.93(15)
O(21)-Mn(5)-O(31)	91.5(2)	O(23)-Mn(6)-Mn(5)	132.06(16)
O(30)-Mn(5)-O(31)	82.47(18)	O(18)-Mn(6)-Mn(5)	88.37(15)
O(19)-Mn(5)-Mn(6)	137.35(16)	O(26)-Mn(6)-Mn(5)	133.57(16)
O(17)-Mn(5)-Mn(6)	89.45(15)	O(29)-Mn(6)-Mn(5)	41.14(13)

Table A-6. Continued.

O(31)-Mn(6)-Mn(5)	41.59(14)	Mn(6)-Mn(7)-Mn(8)	56.26(3)
Mn(8)-Mn(6)-Mn(5)	60.57(4)	O(28)-Mn(8)-O(32)	93.8(2)
O(32)-Mn(6)-Mn(7)	48.26(15)	O(28)-Mn(8)-O(31)	173.8(2)
O(23)-Mn(6)-Mn(7)	86.61(14)	O(32)-Mn(8)-O(31)	83.34(19)
O(18)-Mn(6)-Mn(7)	133.41(15)	O(28)-Mn(8)-O(22)	90.8(2)
O(26)-Mn(6)-Mn(7)	138.95(14)	O(32)-Mn(8)-O(22)	175.3(2)
O(29)-Mn(6)-Mn(7)	40.59(13)	O(31)-Mn(8)-O(22)	91.99(19)
O(31)-Mn(6)-Mn(7)	86.08(13)	O(28)-Mn(8)-O(25)	94.8(2)
Mn(8)-Mn(6)-Mn(7)	62.01(3)	O(32)-Mn(8)-O(25)	91.8(2)
Mn(5)-Mn(6)-Mn(7)	59.57(3)	O(31)-Mn(8)-O(25)	90.80(19)
O(24)-Mn(7)-O(27)	94.4(2)	O(22)-Mn(8)-O(25)	88.6(2)
O(24)-Mn(7)-O(30)	167.65(19)	O(28)-Mn(8)-O(30)	92.2(2)
O(27)-Mn(7)-O(30)	93.33(19)	O(32)-Mn(8)-O(30)	86.9(2)
O(24)-Mn(7)-O(29)	90.95(19)	O(31)-Mn(8)-O(30)	82.16(18)
O(27)-Mn(7)-O(29)	165.8(2)	O(22)-Mn(8)-O(30)	92.1(2)
O(30)-Mn(7)-O(29)	79.37(18)	O(25)-Mn(8)-O(30)	172.94(19)
O(24)-Mn(7)-O(20)	97.2(2)	O(28)-Mn(8)-Mn(6)	134.61(15)
O(27)-Mn(7)-O(20)	96.1(2)	O(32)-Mn(8)-Mn(6)	40.81(13)
O(30)-Mn(7)-O(20)	91.47(19)	O(31)-Mn(8)-Mn(6)	42.61(13)
O(29)-Mn(7)-O(20)	96.21(19)	O(22)-Mn(8)-Mn(6)	134.54(14)
O(24)-Mn(7)-O(32)	94.06(19)	O(25)-Mn(8)-Mn(6)	89.71(14)
O(27)-Mn(7)-O(32)	89.55(19)	O(30)-Mn(8)-Mn(6)	84.75(13)
O(30)-Mn(7)-O(32)	76.39(18)	O(28)-Mn(8)-Mn(5)	133.22(17)
O(29)-Mn(7)-O(32)	76.94(17)	O(32)-Mn(8)-Mn(5)	87.86(15)
O(20)-Mn(7)-O(32)	166.91(18)	O(31)-Mn(8)-Mn(5)	41.40(14)
O(24)-Mn(7)-Mn(5)	131.11(15)	O(22)-Mn(8)-Mn(5)	88.38(15)
O(27)-Mn(7)-Mn(5)	133.66(15)	O(25)-Mn(8)-Mn(5)	131.91(15)
O(30)-Mn(7)-Mn(5)	40.33(13)	O(30)-Mn(8)-Mn(5)	41.15(13)
O(29)-Mn(7)-Mn(5)	40.31(13)	Mn(6)-Mn(8)-Mn(5)	60.34(3)
O(20)-Mn(7)-Mn(5)	87.22(13)	O(28)-Mn(8)-Mn(7)	87.98(15)
O(32)-Mn(7)-Mn(5)	80.35(12)	O(32)-Mn(8)-Mn(7)	48.06(15)
O(24)-Mn(7)-Mn(6)	87.94(14)	O(31)-Mn(8)-Mn(7)	86.05(13)
O(27)-Mn(7)-Mn(6)	127.97(16)	O(22)-Mn(8)-Mn(7)	131.45(16)
O(30)-Mn(7)-Mn(6)	79.70(13)	O(25)-Mn(8)-Mn(7)	139.86(15)
O(29)-Mn(7)-Mn(6)	39.01(13)	O(30)-Mn(8)-Mn(7)	39.50(13)
O(20)-Mn(7)-Mn(6)	135.16(14)	Mn(6)-Mn(8)-Mn(7)	61.73(3)
O(32)-Mn(7)-Mn(6)	38.54(11)	Mn(5)-Mn(8)-Mn(7)	59.41(3)
Mn(5)-Mn(7)-Mn(6)	57.98(3)	Mn(4)-O(13)-Mn(1)	98.1(2)
O(24)-Mn(7)-Mn(8)	132.29(16)	Mn(4)-O(13)-Mn(3)	96.5(2)
O(27)-Mn(7)-Mn(8)	86.71(14)	Mn(1)-O(13)-Mn(3)	96.2(2)
O(30)-Mn(7)-Mn(8)	38.74(14)	Mn(3)-O(14)-Mn(1)	99.4(2)
O(29)-Mn(7)-Mn(8)	79.98(13)	Mn(3)-O(14)-Mn(2)	97.3(2)
O(20)-Mn(7)-Mn(8)	130.14(14)	Mn(1)-O(14)-Mn(2)	94.4(2)
O(32)-Mn(7)-Mn(8)	38.23(12)	Mn(2)-O(15)-Mn(1)	99.5(2)
Mn(5)-Mn(7)-Mn(8)	58.04(3)	Mn(2)-O(15)-Mn(4)	97.4(2)

Table A-6. Continued.

Mn(1)-O(15)-Mn(4)	95.5(2)	Mn(5)-O(30)-Mn(7)	98.1(2)
Mn(4)-O(16)-Mn(3)	98.5(2)	Mn(8)-O(30)-Mn(7)	101.8(2)
Mn(4)-O(16)-Mn(2)	97.7(2)	Mn(8)-O(31)-Mn(5)	97.29(19)
Mn(3)-O(16)-Mn(2)	98.4(2)	Mn(8)-O(31)-Mn(6)	95.10(19)
Mn(5)-O(29)-Mn(6)	97.3(2)	Mn(5)-O(31)-Mn(6)	96.6(2)
Mn(5)-O(29)-Mn(7)	97.26(19)	Mn(8)-O(32)-Mn(6)	98.6(2)
Mn(6)-O(29)-Mn(7)	100.4(2)	Mn(8)-O(32)-Mn(7)	93.7(2)
Mn(5)-O(30)-Mn(8)	97.31(19)	Mn(6)-O(32)-Mn(7)	93.20(19)

---

Table A-7. Selected interatomic distances (Å) and angles (°) for  
 $[\text{Mn}_{16}\text{O}_8\text{Ca}_4(\text{O}_2\text{CPh})_8(\text{O}_2\text{AsMe}_2)_{28}(\text{NO}_3)_4] \cdot 32\text{MeCN}$  (**11**·32MeCN).

Mn(1)-O(7)	1.858(7)	Mn(3)-O(13)	1.962(17)
Mn(1)-O(2)	1.949(8)	Mn(3)-O(92)	2.135(16)
Mn(1)-O(1)	2.016(16)	Mn(3)-O(10)	2.299(13)
Mn(1)-O(5)	2.06(2)	Mn(3)-Mn(4)	3.131(5)
Mn(1)-O(3)	2.117(14)	Mn(4)-O(14)	1.888(9)
Mn(1)-O(6)	2.14(2)	Mn(4)-O(11)	1.915(8)
Mn(1)-Mn(2)	3.403(4)	Mn(4)-O(15)	1.990(17)
Mn(1)-Mn(3)	3.409(4)	Mn(4)-O(16)	2.041(17)
Mn(2)-O(4)	1.897(14)	Mn(4)-O(9)	2.15(2)
Mn(2)-O(12)	1.902(13)	Mn(4)-O(10)	2.184(18)
Mn(2)-O(7)	1.938(15)	Ca(1)-O(1)	2.344(16)
Mn(2)-O(11)	1.999(14)	Ca(1)-O(17)	2.37(2)
Mn(2)-O(91)	2.230(12)	Ca(1)-O(3)	2.373(17)
Mn(2)-O(9)	2.31(2)	Ca(1)-O(17a)	2.39(2)
Mn(2)-Mn(3)	2.837(3)	Ca(1)-O(82)	2.54(2)
Mn(2)-Mn(4)	3.097(4)	Ca(1)-O(2)	2.542(10)
Mn(3)-O(11)	1.838(13)	Ca(1)-O(81)	2.603(12)
Mn(3)-O(8)	1.900(18)	Ca(1)-O(18)	2.66(2)
Mn(3)-O(7)	1.909(16)	Ca(1)-Ca(1a)	3.870(6)
O(7)-Mn(1)-O(2)	167.7(4)	O(4)-Mn(2)-O(9)	97.4(7)
O(7)-Mn(1)-O(1)	92.4(6)	O(12)-Mn(2)-O(9)	87.1(7)
O(2)-Mn(1)-O(1)	77.2(6)	O(7)-Mn(2)-O(9)	88.6(6)
O(7)-Mn(1)-O(5)	99.7(7)	O(11)-Mn(2)-O(9)	79.8(6)
O(2)-Mn(1)-O(5)	87.6(7)	O(91)-Mn(2)-O(9)	168.7(7)
O(1)-Mn(1)-O(5)	93.0(8)	O(4)-Mn(2)-Mn(3)	137.8(5)
O(7)-Mn(1)-O(3)	88.1(6)	O(12)-Mn(2)-Mn(3)	135.2(4)
O(2)-Mn(1)-O(3)	84.4(6)	O(7)-Mn(2)-Mn(3)	42.1(5)
O(1)-Mn(1)-O(3)	85.0(4)	O(11)-Mn(2)-Mn(3)	40.2(3)
O(5)-Mn(1)-O(3)	172.0(7)	O(91)-Mn(2)-Mn(3)	81.3(4)
O(7)-Mn(1)-O(6)	96.6(7)	O(9)-Mn(2)-Mn(3)	91.6(6)
O(2)-Mn(1)-O(6)	93.2(6)	O(4)-Mn(2)-Mn(4)	141.0(4)
O(1)-Mn(1)-O(6)	169.4(5)	O(12)-Mn(2)-Mn(4)	86.1(4)
O(5)-Mn(1)-O(6)	91.0(6)	O(7)-Mn(2)-Mn(4)	88.8(4)
O(3)-Mn(1)-O(6)	89.6(8)	O(11)-Mn(2)-Mn(4)	36.8(3)
O(4)-Mn(2)-O(12)	86.6(6)	O(91)-Mn(2)-Mn(4)	124.8(4)
O(4)-Mn(2)-O(7)	96.8(6)	O(9)-Mn(2)-Mn(4)	43.9(6)
O(12)-Mn(2)-O(7)	174.8(5)	Mn(3)-Mn(2)-Mn(4)	63.51(14)
O(4)-Mn(2)-O(11)	176.2(5)	O(11)-Mn(3)-O(8)	174.2(6)
O(12)-Mn(2)-O(11)	95.9(5)	O(11)-Mn(3)-O(7)	85.5(6)
O(7)-Mn(2)-O(11)	80.5(6)	O(8)-Mn(3)-O(7)	95.2(6)
O(4)-Mn(2)-O(91)	93.7(6)	O(11)-Mn(3)-O(13)	90.6(7)
O(12)-Mn(2)-O(91)	91.8(5)	O(8)-Mn(3)-O(13)	88.4(8)
O(7)-Mn(2)-O(91)	91.9(4)	O(7)-Mn(3)-O(13)	175.5(7)

Table A-7. Continued.

O(11)-Mn(2)-O(91)	89.1(4)	O(14)-Mn(4)-Mn(3)	139.4(7)
O(11)-Mn(3)-O(92)	93.0(5)	O(11)-Mn(4)-Mn(3)	32.7(4)
O(8)-Mn(3)-O(92)	92.7(7)	O(15)-Mn(4)-Mn(3)	85.6(5)
O(7)-Mn(3)-O(92)	91.4(5)	O(16)-Mn(4)-Mn(3)	124.1(5)
O(13)-Mn(3)-O(92)	91.1(7)	O(9)-Mn(4)-Mn(3)	87.2(6)
O(11)-Mn(3)-O(10)	78.4(5)	O(10)-Mn(4)-Mn(3)	47.2(3)
O(8)-Mn(3)-O(10)	95.8(7)	Mn(2)-Mn(4)-Mn(3)	54.20(6)
O(7)-Mn(3)-O(10)	89.7(5)	Mn(1)-O(7)-Mn(3)	129.6(10)
O(13)-Mn(3)-O(10)	87.2(7)	Mn(1)-O(7)-Mn(2)	127.3(10)
O(92)-Mn(3)-O(10)	171.3(6)	Mn(3)-O(7)-Mn(2)	95.0(3)
O(11)-Mn(3)-Mn(2)	44.6(4)	Mn(4)-O(9)-Mn(2)	87.8(8)
O(8)-Mn(3)-Mn(2)	137.4(5)	Mn(4)-O(10)-Mn(3)	88.5(5)
O(7)-Mn(3)-Mn(2)	42.9(4)	Mn(3)-O(11)-Mn(4)	113.1(6)
O(13)-Mn(3)-Mn(2)	133.9(6)	Mn(3)-O(11)-Mn(2)	95.3(3)
O(92)-Mn(3)-Mn(2)	82.8(5)	Mn(4)-O(11)-Mn(2)	104.6(6)
O(10)-Mn(3)-Mn(2)	92.2(5)	O(1)-Ca(1)-O(17)	96.9(6)
O(11)-Mn(3)-Mn(4)	34.2(3)	O(1)-Ca(1)-O(3)	72.6(3)
O(8)-Mn(3)-Mn(4)	139.9(5)	O(17)-Ca(1)-O(3)	146.4(5)
O(7)-Mn(3)-Mn(4)	88.3(4)	O(1)-Ca(1)-O(17a)	143.6(5)
O(13)-Mn(3)-Mn(4)	87.2(5)	O(17)-Ca(1)-O(17a)	70.8(5)
O(92)-Mn(3)-Mn(4)	127.1(4)	O(3)-Ca(1)-O(17a)	98.4(6)
O(10)-Mn(3)-Mn(4)	44.2(5)	O(1)-Ca(1)-O(82)	138.6(6)
Mn(2)-Mn(3)-Mn(4)	62.29(14)	O(17)-Ca(1)-O(82)	91.3(5)
O(14)-Mn(4)-O(11)	171.9(9)	O(3)-Ca(1)-O(82)	118.0(6)
O(14)-Mn(4)-O(15)	88.8(7)	O(17a)-Ca(1)-O(82)	77.1(4)
O(11)-Mn(4)-O(15)	88.4(6)	O(1)-Ca(1)-O(2)	60.7(5)
O(14)-Mn(4)-O(16)	96.3(8)	O(17)-Ca(1)-O(2)	79.5(4)
O(11)-Mn(4)-O(16)	91.5(6)	O(3)-Ca(1)-O(2)	67.5(5)
O(15)-Mn(4)-O(16)	94.6(5)	O(17a)-Ca(1)-O(2)	83.2(4)
O(14)-Mn(4)-O(9)	96.1(8)	O(82)-Ca(1)-O(2)	160.1(4)
O(11)-Mn(4)-O(9)	86.0(7)	O(1)-Ca(1)-O(81)	90.7(5)
O(15)-Mn(4)-O(9)	172.7(8)	O(17)-Ca(1)-O(81)	130.6(5)
O(16)-Mn(4)-O(9)	90.2(9)	O(3)-Ca(1)-O(81)	82.3(5)
O(14)-Mn(4)-O(10)	92.4(7)	O(17a)-Ca(1)-O(81)	123.7(5)
O(11)-Mn(4)-O(10)	79.9(5)	O(82)-Ca(1)-O(81)	55.0(3)
O(15)-Mn(4)-O(10)	87.3(7)	O(2)-Ca(1)-O(81)	142.8(3)
O(16)-Mn(4)-O(10)	171.1(5)	O(1)-Ca(1)-O(18)	75.5(6)
O(9)-Mn(4)-O(10)	87.2(4)	O(17)-Ca(1)-O(18)	50.7(6)
O(14)-Mn(4)-Mn(2)	144.3(6)	O(3)-Ca(1)-O(18)	145.4(6)
O(11)-Mn(4)-Mn(2)	38.7(4)	O(17a)-Ca(1)-O(18)	115.3(6)
O(15)-Mn(4)-Mn(2)	126.7(5)	O(82)-Ca(1)-O(18)	78.9(7)
O(16)-Mn(4)-Mn(2)	84.2(4)	O(2)-Ca(1)-O(18)	107.5(7)
O(9)-Mn(4)-Mn(2)	48.3(6)	O(81)-Ca(1)-O(18)	85.0(6)
O(10)-Mn(4)-Mn(2)	87.8(4)	Ca(1)-O(17)-Ca(1a)	108.9(5)

Table A-8. Selected interatomic distances (Å) and angles (°) for  
 [Mn<sub>16</sub>O<sub>8</sub>Sr<sub>4</sub>(O<sub>2</sub>CPh)<sub>16</sub>(O<sub>2</sub>AsMe<sub>2</sub>)<sub>24</sub>]·16MeCN (**12**·16MeCN).

Mn(1)-O(44)	1.874(9)	Mn(6)-O(36)	1.896(9)
Mn(1)-O(5)	1.890(9)	Mn(6)-O(33)	1.908(8)
Mn(1)-O(3)	1.957(10)	Mn(6)-O(41)	1.931(9)
Mn(1)-O(7)	2.013(9)	Mn(6)-O(38)	2.166(12)
Mn(1)-O(1)	2.070(10)	Mn(6)-O(32)	2.475(17)
Mn(1)-O(11)	2.56(1)	Mn(6)-Mn(7)	2.826(3)
Mn(1)-Mn(2)	3.107(3)	Mn(6)-Mn(8)	3.151(3)
Mn(1)-Mn(3)	3.157(3)	Mn(7)-O(34)	1.905(9)
Mn(2)-O(2)	1.890(9)	Mn(7)-O(33)	1.906(9)
Mn(2)-O(6)	1.907(9)	Mn(7)-O(28)	1.919(11)
Mn(2)-O(15)	1.917(9)	Mn(7)-O(39)	1.947(10)
Mn(2)-O(5)	1.926(8)	Mn(7)-O(37)	2.122(12)
Mn(2)-O(9)	2.184(10)	Mn(7)-O(30)	2.341(10)
Mn(2)-O(7)	2.399(9)	Mn(7)-Mn(8)	3.081(3)
Mn(2)-Mn(3)	2.822(3)	Mn(8)-O(43)	1.891(9)
Mn(2)-Mn(4)	3.438(3)	Mn(8)-O(34)	1.900(10)
Mn(3)-O(5)	1.872(10)	Mn(8)-O(42)	1.952(11)
Mn(3)-O(6)	1.916(8)	Mn(8)-O(30)	1.985(10)
Mn(3)-O(13)	1.922(9)	Mn(8)-O(40)	2.103(11)
Mn(3)-O(4)	1.929(8)	Mn(8)-O(32)	2.72(2)
Mn(3)-O(10)	2.209(9)	Sr(1)-O(23)	2.468(10)
Mn(3)-O(11)	2.305(9)	Sr(1)-O(14)	2.523(9)
Mn(3)-Mn(4)	3.377(3)	Sr(1)-O(19)	2.58(3)
Mn(4)-O(6)	1.866(8)	Sr(1)-O(16)	2.585(9)
Mn(4)-O(14)	1.947(9)	Sr(1)-O(22)	2.596(10)
Mn(4)-O(8)	1.952(10)	Sr(1)-O(20)	2.66(2)
Mn(4)-O(17)	1.973(9)	Sr(1)-O(21)	2.676(10)
Mn(4)-O(16)	2.180(9)	Sr(1)-O(17)	2.718(9)
Mn(4)-O(12)	2.203(10)	Sr(1)-Sr(2)	4.018(2)
Mn(5)-O(33)	1.878(8)	Sr(2)-O(22)	2.514(10)
Mn(5)-O(29)	1.970(10)	Sr(2)-O(26)	2.525(15)
Mn(5)-O(35)	1.977(9)	Sr(2)-O(27)	2.543(9)
Mn(5)-O(18)	1.986(9)	Sr(2)-O(25)	2.552(15)
Mn(5)-O(27)	2.200(9)	Sr(2)-O(35)	2.568(10)
Mn(5)-O(31)	2.246(12)	Sr(2)-O(23)	2.603(10)
Mn(5)-Mn(6)	3.388(12)	Sr(2)-O(18)	2.743(10)
Mn(5)-Mn(7)	3.432(12)	Sr(2)-O(24)	2.750(12)
Mn(6)-O(34)	1.893(10)		
O(44)-Mn(1)-O(5)	174.6(5)	O(3)-Mn(1)-Mn(3)	82.7(3)
O(44)-Mn(1)-O(3)	90.0(4)	O(7)-Mn(1)-Mn(3)	89.2(3)
O(5)-Mn(1)-O(3)	89.7(4)	O(1)-Mn(1)-Mn(3)	124.2(3)
O(44)-Mn(1)-O(7)	93.9(4)	Mn(2)-Mn(1)-Mn(3)	53.54(6)
O(5)-Mn(1)-O(7)	85.7(4)	O(2)-Mn(2)-O(6)	174.8(4)

Table A-8. Continued.

O(3)-Mn(1)-O(7)	171.0(4)	O(5)-Mn(3)-O(10)	91.4(4)
O(44)-Mn(1)-O(1)	93.7(4)	O(6)-Mn(3)-O(10)	90.3(3)
O(5)-Mn(1)-O(1)	91.7(4)	O(13)-Mn(3)-O(10)	93.6(4)
O(3)-Mn(1)-O(1)	95.7(4)	O(4)-Mn(3)-O(10)	90.5(4)
O(7)-Mn(1)-O(1)	92.1(4)	O(5)-Mn(3)-O(11)	85.9(4)
O(44)-Mn(1)-Mn(2)	144.4(3)	O(6)-Mn(3)-O(11)	89.2(3)
O(5)-Mn(1)-Mn(2)	35.9(3)	O(13)-Mn(3)-O(11)	89.1(4)
O(3)-Mn(1)-Mn(2)	125.5(3)	O(4)-Mn(3)-O(11)	89.6(4)
O(7)-Mn(1)-Mn(2)	50.5(3)	O(10)-Mn(3)-O(11)	177.3(4)
O(1)-Mn(1)-Mn(2)	86.4(2)	O(5)-Mn(3)-Mn(2)	42.8(3)
O(44)-Mn(1)-Mn(3)	141.9(4)	O(6)-Mn(3)-Mn(2)	42.3(3)
O(5)-Mn(1)-Mn(3)	32.8(3)	O(13)-Mn(3)-Mn(2)	138.5(3)
O(2)-Mn(2)-O(15)	89.9(4)	O(4)-Mn(3)-Mn(2)	130.4(3)
O(6)-Mn(2)-O(15)	93.9(4)	O(10)-Mn(3)-Mn(2)	80.3(2)
O(2)-Mn(2)-O(5)	94.2(4)	O(11)-Mn(3)-Mn(2)	97.6(3)
O(6)-Mn(2)-O(5)	81.6(4)	O(5)-Mn(3)-Mn(1)	33.1(2)
O(15)-Mn(2)-O(5)	171.6(4)	O(6)-Mn(3)-Mn(1)	88.2(3)
O(2)-Mn(2)-O(9)	89.5(4)	O(13)-Mn(3)-Mn(1)	141.9(3)
O(6)-Mn(2)-O(9)	93.8(4)	O(4)-Mn(3)-Mn(1)	85.0(3)
O(15)-Mn(2)-O(9)	94.9(4)	O(10)-Mn(3)-Mn(1)	124.2(3)
O(5)-Mn(2)-O(9)	92.4(4)	O(11)-Mn(3)-Mn(1)	53.2(3)
O(2)-Mn(2)-O(7)	85.5(4)	Mn(2)-Mn(3)-Mn(1)	62.32(7)
O(6)-Mn(2)-O(7)	90.4(3)	O(6)-Mn(4)-O(14)	90.8(4)
O(15)-Mn(2)-O(7)	98.2(4)	O(6)-Mn(4)-O(8)	97.0(4)
O(5)-Mn(2)-O(7)	74.9(3)	O(8)-Mn(4)-O(16)	94.7(4)
O(9)-Mn(2)-O(7)	165.9(4)	O(17)-Mn(4)-O(16)	80.9(3)
O(2)-Mn(2)-Mn(3)	134.1(3)	O(6)-Mn(4)-O(12)	96.6(3)
O(6)-Mn(2)-Mn(3)	42.6(2)	O(14)-Mn(4)-O(12)	88.9(4)
O(15)-Mn(2)-Mn(3)	135.8(3)	O(8)-Mn(4)-O(12)	88.6(4)
O(5)-Mn(2)-Mn(3)	41.3(3)	O(17)-Mn(4)-O(12)	90.1(4)
O(9)-Mn(2)-Mn(3)	83.5(3)	O(16)-Mn(4)-O(12)	170.4(4)
O(7)-Mn(2)-Mn(3)	90.6(2)	O(14)-Mn(4)-O(8)	172.1(4)
O(2)-Mn(2)-Mn(1)	84.9(3)	O(6)-Mn(4)-O(17)	170.5(4)
O(6)-Mn(2)-Mn(1)	89.9(3)	O(14)-Mn(4)-O(17)	82.6(4)
O(15)-Mn(2)-Mn(1)	138.5(3)	O(8)-Mn(4)-O(17)	89.9(4)
O(5)-Mn(2)-Mn(1)	35.1(3)	O(6)-Mn(4)-O(16)	91.9(3)
O(9)-Mn(2)-Mn(1)	126.1(3)	O(14)-Mn(4)-O(16)	86.6(4)
O(7)-Mn(2)-Mn(1)	40.4(2)	O(33)-Mn(5)-O(29)	97.6(4)
Mn(3)-Mn(2)-Mn(1)	64.14(7)	O(33)-Mn(5)-O(35)	90.3(4)
O(5)-Mn(3)-O(6)	82.8(4)	O(29)-Mn(5)-O(35)	172.1(4)
O(5)-Mn(3)-O(13)	174.9(4)	O(33)-Mn(5)-O(18)	169.8(4)
O(6)-Mn(3)-O(13)	97.2(4)	O(29)-Mn(5)-O(18)	89.4(4)
O(5)-Mn(3)-O(4)	89.5(4)	O(35)-Mn(5)-O(18)	82.9(4)
O(6)-Mn(3)-O(4)	172.3(4)	O(33)-Mn(5)-O(27)	91.7(4)
O(13)-Mn(3)-O(4)	90.4(4)	O(29)-Mn(5)-O(27)	92.0(4)

Table A-8. Continued.

O(35)-Mn(5)-O(27)	88.7(4)	O(34)-Mn(7)-O(30)	75.5(4)
O(18)-Mn(5)-O(27)	80.6(4)	O(33)-Mn(7)-O(30)	90.1(3)
O(33)-Mn(5)-O(31)	96.5(4)	O(28)-Mn(7)-O(30)	96.0(4)
O(29)-Mn(5)-O(31)	90.6(5)	O(39)-Mn(7)-O(30)	87.9(4)
O(35)-Mn(5)-O(31)	87.5(4)	O(37)-Mn(7)-O(30)	169.9(4)
O(18)-Mn(5)-O(31)	90.8(4)	O(34)-Mn(7)-Mn(6)	41.8(3)
O(27)-Mn(5)-O(31)	171.0(4)	O(33)-Mn(7)-Mn(6)	42.2(2)
O(34)-Mn(6)-O(36)	176.4(5)	O(28)-Mn(7)-Mn(6)	138.2(3)
O(34)-Mn(6)-O(33)	82.1(4)	O(39)-Mn(7)-Mn(6)	134.2(3)
O(36)-Mn(6)-O(33)	97.8(4)	O(37)-Mn(7)-Mn(6)	83.3(3)
O(34)-Mn(6)-O(41)	91.6(4)	O(30)-Mn(7)-Mn(6)	90.7(3)
O(36)-Mn(6)-O(41)	88.2(4)	O(34)-Mn(7)-Mn(8)	35.9(3)
O(33)-Mn(6)-O(41)	172.9(4)	O(33)-Mn(7)-Mn(8)	89.3(3)
O(34)-Mn(6)-O(38)	93.0(4)	O(28)-Mn(7)-Mn(8)	135.9(4)
O(36)-Mn(6)-O(38)	90.6(4)	O(39)-Mn(7)-Mn(8)	86.9(4)
O(33)-Mn(6)-O(38)	90.4(4)	O(37)-Mn(7)-Mn(8)	129.8(3)
O(41)-Mn(6)-O(38)	93.2(4)	O(34)-Mn(8)-O(30)	84.9(4)
O(34)-Mn(6)-O(32)	89.6(5)	O(42)-Mn(8)-O(30)	171.4(4)
O(36)-Mn(6)-O(32)	86.8(5)	O(43)-Mn(8)-O(40)	93.0(4)
O(33)-Mn(6)-O(32)	85.2(4)	O(34)-Mn(8)-O(40)	90.2(4)
O(41)-Mn(6)-O(32)	91.5(4)	O(42)-Mn(8)-O(40)	99.2(5)
O(38)-Mn(6)-O(32)	174.6(5)	O(30)-Mn(8)-O(40)	88.7(4)
O(34)-Mn(6)-Mn(7)	42.1(3)	O(43)-Mn(8)-Mn(7)	142.9(3)
O(36)-Mn(6)-Mn(7)	138.7(3)	O(34)-Mn(8)-Mn(7)	36.0(3)
O(33)-Mn(6)-Mn(7)	42.2(3)	O(42)-Mn(8)-Mn(7)	127.6(3)
O(41)-Mn(6)-Mn(7)	132.5(3)	O(30)-Mn(8)-Mn(7)	49.4(3)
O(38)-Mn(6)-Mn(7)	81.8(3)	O(40)-Mn(8)-Mn(7)	84.0(3)
O(32)-Mn(6)-Mn(7)	97.0(3)	O(43)-Mn(8)-Mn(6)	143.1(3)
O(34)-Mn(6)-Mn(8)	33.9(3)	O(34)-Mn(8)-Mn(6)	33.8(3)
O(36)-Mn(6)-Mn(8)	142.5(3)	O(42)-Mn(8)-Mn(6)	83.9(3)
O(33)-Mn(6)-Mn(8)	87.2(3)	O(30)-Mn(8)-Mn(6)	88.9(3)
O(41)-Mn(6)-Mn(8)	85.8(3)	O(40)-Mn(8)-Mn(6)	123.8(3)
O(38)-Mn(6)-Mn(8)	126.6(3)	Mn(7)-Mn(8)-Mn(6)	53.91(7)
O(32)-Mn(6)-Mn(8)	56.4(4)	Mn(3)-O(5)-Mn(1)	114.1(4)
Mn(7)-Mn(6)-Mn(8)	61.78(8)	Mn(3)-O(5)-Mn(2)	96.0(4)
O(34)-Mn(7)-O(33)	81.8(4)	Mn(1)-O(5)-Mn(2)	109.0(4)
O(34)-Mn(7)-O(28)	171.3(5)	Mn(4)-O(6)-Mn(2)	131.3(4)
O(33)-Mn(7)-O(28)	96.4(4)	Mn(4)-O(6)-Mn(3)	126.4(4)
O(34)-Mn(7)-O(39)	94.2(4)	Mn(2)-O(6)-Mn(3)	95.1(4)
O(33)-Mn(7)-O(39)	175.9(4)	Mn(1)-O(7)-Mn(2)	89.1(3)
O(28)-Mn(7)-O(39)	87.4(4)	Mn(8)-O(30)-Mn(7)	90.4(4)
O(34)-Mn(7)-O(37)	94.7(4)	Mn(5)-O(33)-Mn(7)	130.2(4)
O(33)-Mn(7)-O(37)	90.8(4)	Mn(5)-O(33)-Mn(6)	127.0(5)
O(28)-Mn(7)-O(37)	93.9(5)	Mn(7)-O(33)-Mn(6)	95.6(4)
O(39)-Mn(7)-O(37)	90.5(5)	Mn(6)-O(34)-Mn(8)	112.3(5)

Table A-8. Continued.

Mn(6)-O(34)-Mn(7)	96.2(4)	O(22)-Sr(2)-O(26)	125.5(5)
Mn(8)-O(34)-Mn(7)	108.1(5)	O(22)-Sr(2)-O(27)	89.9(3)
O(23)-Sr(1)-O(14)	142.7(3)	O(26)-Sr(2)-O(27)	86.6(5)
O(23)-Sr(1)-O(19)	111.4(7)	O(22)-Sr(2)-O(25)	83.8(7)
O(14)-Sr(1)-O(19)	85.2(7)	O(26)-Sr(2)-O(25)	51.5(9)
O(23)-Sr(1)-O(16)	83.0(3)	O(27)-Sr(2)-O(25)	117.7(6)
O(14)-Sr(1)-O(16)	67.4(3)	O(22)-Sr(2)-O(35)	142.9(3)
O(19)-Sr(1)-O(16)	78.2(8)	O(26)-Sr(2)-O(35)	85.1(5)
O(23)-Sr(1)-O(22)	73.7(3)	O(27)-Sr(2)-O(35)	69.8(3)
O(14)-Sr(1)-O(22)	117.2(3)	O(25)-Sr(2)-O(35)	132.9(7)
O(19)-Sr(1)-O(22)	137.2(8)	O(22)-Sr(2)-O(23)	72.9(3)
O(16)-Sr(1)-O(22)	142.8(3)	O(26)-Sr(2)-O(23)	128.2(5)
O(23)-Sr(1)-O(20)	91.6(8)	O(27)-Sr(2)-O(23)	145.0(3)
O(14)-Sr(1)-O(20)	122.8(9)	O(25)-Sr(2)-O(23)	91.0(7)
O(19)-Sr(1)-O(20)	50.0(11)	O(35)-Sr(2)-O(23)	106.2(3)
O(16)-Sr(1)-O(20)	121.6(8)	O(22)-Sr(2)-O(18)	84.1(3)
O(22)-Sr(1)-O(20)	88.2(10)	O(26)-Sr(2)-O(18)	137.8(4)
O(23)-Sr(1)-O(21)	122.2(3)	O(27)-Sr(2)-O(18)	61.6(3)
O(14)-Sr(1)-O(21)	79.9(3)	O(25)-Sr(2)-O(18)	167.8(7)
O(19)-Sr(1)-O(21)	108.1(8)	O(35)-Sr(2)-O(18)	59.1(3)
O(16)-Sr(1)-O(21)	146.2(3)	O(23)-Sr(2)-O(18)	86.0(3)
O(22)-Sr(1)-O(21)	48.7(3)	O(22)-Sr(2)-O(24)	119.2(3)
O(20)-Sr(1)-O(21)	82.8(6)	O(26)-Sr(2)-O(24)	89.1(5)
O(23)-Sr(1)-O(17)	87.3(3)	O(27)-Sr(2)-O(24)	146.3(3)
O(14)-Sr(1)-O(17)	59.0(3)	O(25)-Sr(2)-O(24)	84.4(6)
O(19)-Sr(1)-O(17)	133.0(8)	O(35)-Sr(2)-O(24)	76.5(3)
O(22)-Sr(1)-O(17)	88.7(3)	O(23)-Sr(2)-O(24)	48.0(3)
O(22)-Sr(1)-O(17)	88.7(3)	O(18)-Sr(2)-O(24)	102.1(4)
O(20)-Sr(1)-O(17)	177.0(10)	Sr(2)-O(22)-Sr(1)	103.6(4)
O(21)-Sr(1)-O(17)	95.3(3)	Sr(1)-O(23)-Sr(2)	104.8(4)

Table A-9. Selected interatomic distances (Å) and angles (°) for  
 $[\text{Mn}_{12}\text{O}_{12}(\text{O}_2\text{CPe}')_{16}(\text{MeOH})_4]\cdot 2\text{MeCN}$  (**15**·2MeCN).

Mn(1)-O(10)	1.870(4)	Mn(6)-O(140)	2.150(6)
Mn(1)-O(11)	1.879(4)	Mn(6)-O(101)	2.168(6)
Mn(1)-O(1)	1.913(4)	Mn(7)-O(10)	1.898(4)
Mn(1)-O(110)	1.913(5)	Mn(7)-O(11)	1.916(4)
Mn(1)-O(2)	1.921(4)	Mn(7)-O(41)	1.942(5)
Mn(1)-O(3)	1.940(4)	Mn(7)-O(90)	1.956(5)
Mn(1)-Mn(7)	2.7873(14)	Mn(7)-O(100)	2.153(6)
Mn(1)-Mn(4)	2.8263(14)	Mn(7)-O(111)	2.162(5)
Mn(1)-Mn(2)	2.8399(14)	Mn(8)-O(12)	1.870(4)
Mn(1)-Mn(3)	2.9656(14)	Mn(8)-O(11)	1.904(4)
Mn(2)-O(12)	1.860(4)	Mn(8)-O(40)	1.930(5)
Mn(2)-O(5)	1.883(4)	Mn(8)-O(51)	1.988(5)
Mn(2)-O(4)	1.908(4)	Mn(8)-O(150)	2.156(6)
Mn(2)-O(2)	1.912(4)	Mn(8)-O(13)	2.239(6)
Mn(2)-O(81)	1.930(5)	Mn(9)-O(5)	1.897(5)
Mn(2)-O(1)	1.934(4)	Mn(9)-O(12)	1.898(4)
Mn(2)-Mn(9)	2.7914(15)	Mn(9)-O(61)	1.930(5)
Mn(2)-Mn(3)	2.8348(16)	Mn(9)-O(50)	1.960(6)
Mn(2)-Mn(4)	2.9421(14)	Mn(9)-O(151)	2.160(6)
Mn(3)-O(6)	1.869(4)	Mn(9)-O(80)	2.191(7)
Mn(3)-O(7)	1.894(4)	Mn(10)-O(6)	1.877(5)
Mn(3)-O(4)	1.898(5)	Mn(10)-O(5)	1.886(5)
Mn(3)-O(3)	1.914(4)	Mn(10)-O(60)	1.949(6)
Mn(3)-O(2)	1.939(4)	Mn(10)-O(120)	1.970(6)
Mn(3)-O(130)	1.940(5)	Mn(10)-O(170)	2.138(6)
Mn(3)-Mn(11)	2.7920(15)	Mn(10)-O(14)	2.241(6)
Mn(3)-Mn(4)	2.8265(15)	Mn(11)-O(6)	1.885(4)
Mn(4)-O(8)	1.869(4)	Mn(11)-O(7)	1.915(5)
Mn(4)-O(9)	1.873(4)	Mn(11)-O(30)	1.941(5)
Mn(4)-O(3)	1.901(5)	Mn(11)-O(121)	1.951(5)
Mn(4)-O(1)	1.903(4)	Mn(11)-O(171)	2.156(6)
Mn(4)-O(160)	1.918(5)	Mn(11)-O(131)	2.162(6)
Mn(4)-O(4)	1.939(4)	Mn(12)-O(7)	1.872(5)
Mn(4)-Mn(5)	2.7699(15)	Mn(12)-O(8)	1.873(5)
Mn(5)-O(9)	1.886(4)	Mn(12)-O(31)	1.969(5)
Mn(5)-O(8)	1.903(4)	Mn(12)-O(20)	1.978(5)
Mn(5)-O(70)	1.931(5)	Mn(12)-O(15)	2.208(6)
Mn(5)-O(21)	1.951(5)	Mn(12)-O(16)	2.211(5)
Mn(5)-O(141)	2.165(6)	O(13)-C(12)	1.404(11)
Mn(5)-O(161)	2.214(6)	O(14)-C(13)	1.393(13)
Mn(6)-O(10)	1.886(4)	O(15)-C(15)	1.41(3)
Mn(6)-O(9)	1.893(4)	O(15)-C(14)	1.447(18)
Mn(6)-O(91)	1.964(5)	O(16)-C(16)	1.443(10)
Mn(6)-O(71)	1.972(5)		

Table A-9. Continued.

O(10)-Mn(1)-O(11)	84.97(19)	O(12)-Mn(2)-O(5)	84.44(19)
O(10)-Mn(1)-O(1)	92.67(19)	O(12)-Mn(2)-O(4)	173.72(19)
O(11)-Mn(1)-O(1)	88.85(19)	O(5)-Mn(2)-O(4)	100.78(19)
O(10)-Mn(1)-O(110)	92.8(2)	O(12)-Mn(2)-O(2)	92.87(18)
O(11)-Mn(1)-O(110)	92.61(19)	O(5)-Mn(2)-O(2)	89.07(19)
O(1)-Mn(1)-O(110)	174.5(2)	O(4)-Mn(2)-O(2)	83.79(18)
O(10)-Mn(1)-O(2)	173.97(18)	O(12)-Mn(2)-O(81)	93.4(2)
O(11)-Mn(1)-O(2)	99.82(18)	O(5)-Mn(2)-O(81)	91.4(2)
O(1)-Mn(1)-O(2)	83.82(18)	O(4)-Mn(2)-O(81)	90.0(2)
O(110)-Mn(1)-O(2)	90.67(19)	O(2)-Mn(2)-O(81)	173.8(2)
O(10)-Mn(1)-O(3)	95.38(18)	O(12)-Mn(2)-O(1)	94.32(18)
O(11)-Mn(1)-O(3)	172.1(2)	O(5)-Mn(2)-O(1)	172.4(2)
O(1)-Mn(1)-O(3)	83.22(18)	O(4)-Mn(2)-O(1)	80.04(18)
O(110)-Mn(1)-O(3)	95.28(19)	O(2)-Mn(2)-O(1)	83.52(18)
O(2)-Mn(1)-O(3)	79.37(17)	O(81)-Mn(2)-O(1)	96.1(2)
O(10)-Mn(1)-Mn(7)	42.67(13)	O(12)-Mn(2)-Mn(9)	42.54(14)
O(11)-Mn(1)-Mn(7)	43.27(13)	O(5)-Mn(2)-Mn(9)	42.58(14)
O(1)-Mn(1)-Mn(7)	98.17(14)	O(4)-Mn(2)-Mn(9)	143.09(14)
O(110)-Mn(1)-Mn(7)	86.53(14)	O(2)-Mn(2)-Mn(9)	97.28(13)
O(2)-Mn(1)-Mn(7)	142.64(13)	O(81)-Mn(2)-Mn(9)	87.25(17)
O(3)-Mn(1)-Mn(7)	137.99(13)	O(1)-Mn(2)-Mn(9)	136.85(13)
O(10)-Mn(1)-Mn(4)	88.42(13)	O(12)-Mn(2)-Mn(3)	135.65(14)
O(11)-Mn(1)-Mn(4)	130.11(14)	O(5)-Mn(2)-Mn(3)	89.99(15)
O(1)-Mn(1)-Mn(4)	42.09(13)	O(4)-Mn(2)-Mn(3)	41.72(14)
O(110)-Mn(1)-Mn(4)	137.14(14)	O(2)-Mn(2)-Mn(3)	42.96(12)
O(2)-Mn(1)-Mn(4)	85.69(12)	O(81)-Mn(2)-Mn(3)	130.80(17)
O(3)-Mn(1)-Mn(4)	42.09(13)	O(1)-Mn(2)-Mn(3)	85.67(14)
Mn(7)-Mn(1)-Mn(4)	120.44(5)	Mn(9)-Mn(2)-Mn(3)	123.54(5)
O(10)-Mn(1)-Mn(2)	135.11(15)	O(12)-Mn(2)-Mn(1)	87.88(14)
O(11)-Mn(1)-Mn(2)	88.93(14)	O(5)-Mn(2)-Mn(1)	130.30(15)
O(1)-Mn(1)-Mn(2)	42.69(13)	O(4)-Mn(2)-Mn(1)	86.08(13)
O(110)-Mn(1)-Mn(2)	131.96(14)	O(2)-Mn(2)-Mn(1)	42.33(12)
O(2)-Mn(1)-Mn(2)	42.07(13)	O(81)-Mn(2)-Mn(1)	138.12(16)
O(3)-Mn(1)-Mn(2)	85.23(13)	O(1)-Mn(2)-Mn(1)	42.13(13)
Mn(7)-Mn(1)-Mn(2)	123.64(5)	Mn(9)-Mn(2)-Mn(1)	119.20(5)
Mn(4)-Mn(1)-Mn(2)	62.56(3)	Mn(3)-Mn(2)-Mn(1)	63.01(4)
O(10)-Mn(1)-Mn(3)	134.72(13)	O(12)-Mn(2)-Mn(4)	133.86(14)
O(11)-Mn(1)-Mn(3)	139.45(14)	O(5)-Mn(2)-Mn(4)	140.93(15)
O(1)-Mn(1)-Mn(3)	82.37(14)	O(4)-Mn(2)-Mn(4)	40.50(13)
O(110)-Mn(1)-Mn(3)	93.08(14)	O(2)-Mn(2)-Mn(4)	82.60(12)
O(2)-Mn(1)-Mn(3)	40.02(12)	O(81)-Mn(2)-Mn(4)	93.15(17)
O(3)-Mn(1)-Mn(3)	39.36(12)	O(1)-Mn(2)-Mn(4)	39.56(12)
Mn(7)-Mn(1)-Mn(3)	177.28(5)	Mn(9)-Mn(2)-Mn(4)	176.41(5)
Mn(4)-Mn(1)-Mn(3)	58.36(4)	Mn(3)-Mn(2)-Mn(4)	58.55(4)
Mn(2)-Mn(1)-Mn(3)	58.41(4)	Mn(1)-Mn(2)-Mn(4)	58.49(3)

Table A-9. Continued.

O(6)-Mn(3)-O(7)	84.80(19)	Mn(2)-Mn(3)-Mn(1)	58.58(3)
O(6)-Mn(3)-O(4)	90.8(2)	O(8)-Mn(4)-O(9)	85.47(19)
O(7)-Mn(3)-O(4)	87.3(2)	O(8)-Mn(4)-O(3)	89.6(2)
O(6)-Mn(3)-O(3)	172.4(2)	O(9)-Mn(4)-O(3)	91.14(19)
O(7)-Mn(3)-O(3)	100.65(19)	O(8)-Mn(4)-O(1)	173.2(2)
O(4)-Mn(3)-O(3)	84.20(19)	O(9)-Mn(4)-O(1)	98.03(19)
O(6)-Mn(3)-O(2)	94.16(18)	O(3)-Mn(4)-O(1)	84.54(18)
O(7)-Mn(3)-O(2)	170.5(2)	O(8)-Mn(4)-O(160)	93.2(2)
O(4)-Mn(3)-O(2)	83.33(18)	O(9)-Mn(4)-O(160)	90.8(2)
O(3)-Mn(3)-O(2)	79.59(17)	O(3)-Mn(4)-O(160)	176.7(2)
O(6)-Mn(3)-O(130)	92.3(2)	O(1)-Mn(4)-O(160)	92.6(2)
O(7)-Mn(3)-O(130)	90.3(2)	O(8)-Mn(4)-O(4)	95.95(19)
O(4)-Mn(3)-O(130)	175.9(2)	O(9)-Mn(4)-O(4)	174.38(19)
O(3)-Mn(3)-O(130)	93.0(2)	O(3)-Mn(4)-O(4)	83.44(18)
O(2)-Mn(3)-O(130)	99.1(2)	O(1)-Mn(4)-O(4)	80.02(18)
O(6)-Mn(3)-Mn(11)	42.16(13)	O(160)-Mn(4)-O(4)	94.6(2)
O(7)-Mn(3)-Mn(11)	43.16(14)	O(8)-Mn(4)-Mn(5)	43.22(14)
O(4)-Mn(3)-Mn(11)	94.00(13)	O(9)-Mn(4)-Mn(5)	42.73(13)
O(4)-Mn(3)-Mn(11)	94.00(13)	O(3)-Mn(4)-Mn(5)	95.54(13)
O(3)-Mn(3)-Mn(11)	143.76(13)	O(1)-Mn(4)-Mn(5)	140.74(14)
O(2)-Mn(3)-Mn(11)	136.30(13)	O(160)-Mn(4)-Mn(5)	87.68(16)
O(130)-Mn(3)-Mn(11)	86.50(16)	O(4)-Mn(4)-Mn(5)	139.13(13)
O(6)-Mn(3)-Mn(4)	133.78(16)	O(8)-Mn(4)-Mn(1)	132.34(15)
O(7)-Mn(3)-Mn(4)	88.58(15)	O(9)-Mn(4)-Mn(1)	89.13(13)
O(4)-Mn(3)-Mn(4)	43.12(13)	O(3)-Mn(4)-Mn(1)	43.16(13)
O(3)-Mn(3)-Mn(4)	42.01(13)	O(1)-Mn(4)-Mn(1)	42.35(13)
O(2)-Mn(3)-Mn(4)	85.37(13)	O(160)-Mn(4)-Mn(1)	134.22(17)
O(130)-Mn(3)-Mn(4)	133.51(16)	O(4)-Mn(4)-Mn(1)	85.90(12)
Mn(11)-Mn(3)-Mn(4)	121.34(5)	Mn(5)-Mn(4)-Mn(1)	120.59(5)
O(6)-Mn(3)-Mn(2)	86.61(15)	O(8)-Mn(4)-Mn(3)	86.89(14)
O(7)-Mn(3)-Mn(2)	128.33(16)	O(9)-Mn(4)-Mn(3)	132.89(15)
O(4)-Mn(3)-Mn(2)	41.99(13)	O(3)-Mn(4)-Mn(3)	42.36(13)
O(3)-Mn(3)-Mn(2)	85.85(14)	O(1)-Mn(4)-Mn(3)	86.46(14)
O(2)-Mn(3)-Mn(2)	42.23(13)	O(160)-Mn(4)-Mn(3)	136.06(18)
O(130)-Mn(3)-Mn(2)	140.95(16)	O(4)-Mn(4)-Mn(3)	41.99(13)
Mn(11)-Mn(3)-Mn(2)	116.43(5)	Mn(5)-Mn(4)-Mn(3)	119.39(5)
Mn(4)-Mn(3)-Mn(2)	62.62(4)	Mn(1)-Mn(4)-Mn(3)	63.29(4)
O(6)-Mn(3)-Mn(1)	133.68(14)	O(8)-Mn(4)-Mn(2)	135.53(14)
O(7)-Mn(3)-Mn(1)	140.07(14)	O(9)-Mn(4)-Mn(2)	138.21(14)
O(4)-Mn(3)-Mn(1)	82.69(13)	O(3)-Mn(4)-Mn(2)	83.04(13)
O(3)-Mn(3)-Mn(1)	40.02(12)	O(1)-Mn(4)-Mn(2)	40.31(13)
O(2)-Mn(3)-Mn(1)	39.59(12)	O(160)-Mn(4)-Mn(2)	93.75(16)
O(130)-Mn(3)-Mn(1)	97.08(16)	O(4)-Mn(4)-Mn(2)	39.72(13)
Mn(11)-Mn(3)-Mn(1)	174.88(5)	Mn(5)-Mn(4)-Mn(2)	178.22(6)
Mn(4)-Mn(3)-Mn(1)	58.35(3)	Mn(1)-Mn(4)-Mn(2)	58.95(3)

Table A-9. Continued.

Mn(3)-Mn(4)-Mn(2)	58.83(4)	O(41)-Mn(7)-O(100)	87.0(2)
O(9)-Mn(5)-O(8)	84.16(18)	O(90)-Mn(7)-O(100)	88.4(2)
O(9)-Mn(5)-O(70)	95.7(2)	O(10)-Mn(7)-O(111)	87.53(19)
O(8)-Mn(5)-O(70)	174.9(2)	O(11)-Mn(7)-O(111)	85.74(19)
O(9)-Mn(5)-O(21)	175.8(2)	O(41)-Mn(7)-O(111)	90.1(2)
O(8)-Mn(5)-O(21)	94.0(2)	O(90)-Mn(7)-O(111)	87.0(2)
O(70)-Mn(5)-O(21)	85.9(2)	O(100)-Mn(7)-O(111)	174.6(2)
O(9)-Mn(5)-O(141)	95.3(2)	O(10)-Mn(7)-Mn(1)	41.89(13)
O(8)-Mn(5)-O(141)	93.8(2)	O(11)-Mn(7)-Mn(1)	42.22(13)
O(70)-Mn(5)-O(141)	91.2(2)	O(41)-Mn(7)-Mn(1)	136.06(16)
O(21)-Mn(5)-O(141)	88.6(2)	O(90)-Mn(7)-Mn(1)	134.35(15)
O(9)-Mn(5)-O(161)	85.0(2)	O(100)-Mn(7)-Mn(1)	106.61(15)
O(8)-Mn(5)-O(161)	84.6(2)	O(111)-Mn(7)-Mn(1)	78.59(13)
O(70)-Mn(5)-O(161)	90.3(2)	O(12)-Mn(8)-O(11)	93.68(19)
O(21)-Mn(5)-O(161)	91.2(2)	O(12)-Mn(8)-O(40)	173.8(2)
O(141)-Mn(5)-O(161)	178.4(2)	O(11)-Mn(8)-O(40)	92.2(2)
O(9)-Mn(5)-Mn(4)	42.37(13)	O(12)-Mn(8)-O(51)	91.1(2)
O(8)-Mn(5)-Mn(4)	42.26(13)	O(11)-Mn(8)-O(51)	171.8(2)
O(70)-Mn(5)-Mn(4)	136.71(17)	O(40)-Mn(8)-O(51)	82.8(2)
O(21)-Mn(5)-Mn(4)	135.19(16)	O(12)-Mn(8)-O(150)	95.4(2)
O(141)-Mn(5)-Mn(4)	101.07(15)	O(11)-Mn(8)-O(150)	99.6(2)
O(161)-Mn(5)-Mn(4)	78.03(14)	O(40)-Mn(8)-O(150)	85.4(2)
O(10)-Mn(6)-O(9)	93.67(18)	O(51)-Mn(8)-O(150)	86.6(2)
O(10)-Mn(6)-O(91)	91.5(2)	O(12)-Mn(8)-O(13)	92.1(2)
O(9)-Mn(6)-O(91)	172.5(2)	O(11)-Mn(8)-O(13)	92.8(2)
O(10)-Mn(6)-O(71)	174.3(2)	O(40)-Mn(8)-O(13)	85.8(2)
O(9)-Mn(6)-O(71)	91.5(2)	O(51)-Mn(8)-O(13)	80.4(2)
O(91)-Mn(6)-O(71)	83.6(2)	O(150)-Mn(8)-O(13)	165.1(2)
O(10)-Mn(6)-O(140)	95.0(2)	O(5)-Mn(9)-O(12)	83.05(19)
O(9)-Mn(6)-O(140)	92.2(2)	O(5)-Mn(9)-O(61)	95.3(2)
O(91)-Mn(6)-O(140)	82.0(2)	O(12)-Mn(9)-O(61)	177.4(2)
O(71)-Mn(6)-O(140)	87.2(2)	O(5)-Mn(9)-O(50)	172.6(3)
O(10)-Mn(6)-O(101)	95.7(2)	O(12)-Mn(9)-O(50)	95.8(2)
O(9)-Mn(6)-O(101)	97.6(2)	O(61)-Mn(9)-O(50)	85.6(2)
O(91)-Mn(6)-O(101)	87.3(2)	O(5)-Mn(9)-O(151)	98.8(2)
O(71)-Mn(6)-O(101)	81.3(2)	O(12)-Mn(9)-O(151)	93.3(2)
O(140)-Mn(6)-O(101)	165.1(2)	O(61)-Mn(9)-O(151)	88.9(3)
O(10)-Mn(7)-O(11)	83.18(18)	O(50)-Mn(9)-O(151)	88.5(2)
O(10)-Mn(7)-O(41)	177.2(2)	O(5)-Mn(9)-O(80)	84.9(2)
O(11)-Mn(7)-O(41)	95.2(2)	O(12)-Mn(9)-O(80)	86.9(2)
O(10)-Mn(7)-O(90)	95.02(19)	O(61)-Mn(9)-O(80)	91.0(3)
O(11)-Mn(7)-O(90)	172.6(2)	O(50)-Mn(9)-O(80)	87.7(3)
O(41)-Mn(7)-O(90)	86.3(2)	O(151)-Mn(9)-O(80)	176.3(2)
O(10)-Mn(7)-O(100)	95.5(2)	O(5)-Mn(9)-Mn(2)	42.20(14)
O(11)-Mn(7)-O(100)	99.0(2)	O(12)-Mn(9)-Mn(2)	41.51(13)

Table A-9. Continued.

O(61)-Mn(9)-Mn(2)	136.52(19)	O(7)-Mn(12)-O(15)	93.5(2)
O(50)-Mn(9)-Mn(2)	135.19(18)	O(8)-Mn(12)-O(15)	94.6(2)
O(151)-Mn(9)-Mn(2)	103.83(14)	O(31)-Mn(12)-O(15)	86.5(2)
O(80)-Mn(9)-Mn(2)	78.75(18)	O(20)-Mn(12)-O(15)	84.9(2)
O(6)-Mn(10)-O(5)	93.86(19)	O(7)-Mn(12)-O(16)	94.2(2)
O(6)-Mn(10)-O(60)	174.7(3)	O(8)-Mn(12)-O(16)	93.0(2)
O(5)-Mn(10)-O(60)	91.4(2)	O(31)-Mn(12)-O(16)	85.2(2)
O(6)-Mn(10)-O(120)	90.8(2)	O(20)-Mn(12)-O(16)	86.9(2)
O(5)-Mn(10)-O(120)	172.3(2)	O(15)-Mn(12)-O(16)	168.9(2)
O(60)-Mn(10)-O(120)	83.9(3)	Mn(4)-O(1)-Mn(1)	95.6(2)
O(6)-Mn(10)-O(170)	94.1(2)	Mn(4)-O(1)-Mn(2)	100.1(2)
O(5)-Mn(10)-O(170)	97.8(2)	Mn(1)-O(1)-Mn(2)	95.18(19)
O(60)-Mn(10)-O(170)	85.0(3)	Mn(2)-O(2)-Mn(1)	95.61(19)
O(120)-Mn(10)-O(170)	88.0(3)	Mn(2)-O(2)-Mn(3)	94.81(18)
O(6)-Mn(10)-O(14)	92.9(2)	Mn(1)-O(2)-Mn(3)	100.39(18)
O(5)-Mn(10)-O(14)	92.2(2)	Mn(4)-O(3)-Mn(3)	95.63(19)
O(60)-Mn(10)-O(14)	87.1(3)	Mn(4)-O(3)-Mn(1)	94.8(2)
O(120)-Mn(10)-O(14)	81.5(3)	Mn(3)-O(3)-Mn(1)	100.62(19)
O(170)-Mn(10)-O(14)	167.4(2)	Mn(3)-O(4)-Mn(2)	96.29(18)
O(6)-Mn(11)-O(7)	83.78(18)	Mn(3)-O(4)-Mn(4)	94.89(19)
O(6)-Mn(11)-O(30)	177.9(2)	Mn(2)-O(4)-Mn(4)	99.8(2)
O(7)-Mn(11)-O(30)	94.7(2)	Mn(2)-O(5)-Mn(10)	131.8(3)
O(6)-Mn(11)-O(121)	95.6(2)	Mn(2)-O(5)-Mn(9)	95.2(2)
O(7)-Mn(11)-O(121)	173.0(3)	Mn(10)-O(5)-Mn(9)	127.8(2)
O(6)-Mn(11)-O(171)	94.0(2)	Mn(3)-O(6)-Mn(10)	135.5(3)
O(7)-Mn(11)-O(171)	97.3(2)	Mn(3)-O(6)-Mn(11)	96.1(2)
O(30)-Mn(11)-O(171)	87.5(2)	Mn(10)-O(6)-Mn(11)	123.1(2)
O(121)-Mn(11)-O(171)	89.7(3)	Mn(12)-O(7)-Mn(3)	132.8(3)
O(6)-Mn(11)-O(131)	86.2(2)	Mn(12)-O(7)-Mn(11)	127.7(2)
O(7)-Mn(11)-O(131)	84.6(2)	Mn(3)-O(7)-Mn(11)	94.3(2)
O(30)-Mn(11)-O(131)	92.3(3)	Mn(4)-O(8)-Mn(12)	134.4(2)
O(121)-Mn(11)-O(131)	88.4(3)	Mn(4)-O(8)-Mn(5)	94.5(2)
O(171)-Mn(11)-O(131)	178.1(2)	Mn(12)-O(8)-Mn(5)	128.8(2)
O(6)-Mn(11)-Mn(3)	41.74(13)	Mn(4)-O(9)-Mn(5)	94.9(2)
O(7)-Mn(11)-Mn(3)	42.56(13)	Mn(4)-O(9)-Mn(6)	133.4(2)
O(30)-Mn(11)-Mn(3)	136.56(17)	Mn(5)-O(9)-Mn(6)	123.8(2)
O(121)-Mn(11)-Mn(3)	135.53(17)	Mn(1)-O(10)-Mn(6)	134.5(2)
O(171)-Mn(11)-Mn(3)	102.77(15)	Mn(1)-O(10)-Mn(7)	95.44(19)
O(131)-Mn(11)-Mn(3)	78.70(16)	Mn(6)-O(10)-Mn(7)	123.1(2)
O(7)-Mn(12)-O(8)	93.25(19)	Mn(1)-O(11)-Mn(8)	132.8(2)
O(7)-Mn(12)-O(31)	91.8(2)	Mn(1)-O(11)-Mn(7)	94.51(19)
O(8)-Mn(12)-O(31)	174.8(2)	Mn(8)-O(11)-Mn(7)	127.3(2)
O(7)-Mn(12)-O(20)	175.3(2)	Mn(2)-O(12)-Mn(8)	135.2(2)
O(8)-Mn(12)-O(20)	91.3(2)	Mn(2)-O(12)-Mn(9)	95.9(2)
O(31)-Mn(12)-O(20)	83.7(2)	Mn(8)-O(12)-Mn(9)	123.6(2)

Table A-9. Continued.

C(12)-O(13)-Mn(8)	122.1(5)	C(14)-O(15)-Mn(12)	120.7(8)
C(13)-O(14)-Mn(10)	120.2(5)	C(16)-O(16)-Mn(12)	123.8(6)
C(15)-O(15)-Mn(12)	120.8(13)		

---

Table A-10. Selected interatomic distances (Å) and angles (°) for  
 $[\text{Mn}_6\text{O}_2(\text{O}_2\text{CH}_2)(\text{O}_2\text{CPe}^f)_{11}(\text{HO}_2\text{CPe}^f)_2(\text{O}_2\text{CMe})] \cdot \frac{1}{2}\text{CH}_2\text{Cl}_2$  (**16**·½CH<sub>2</sub>Cl<sub>2</sub>).

Mn(1)-O(3)	1.838(3)	Mn(4)-O(40)	1.963(4)
Mn(1)-O(1)	1.934(3)	Mn(4)-O(31)	1.966(4)
Mn(1)-O(100)	1.997(3)	Mn(4)-O(121)	2.216(4)
Mn(1)-O(81)	2.055(4)	Mn(4)-O(71)	2.231(4)
Mn(1)-O(130)	2.088(3)	Mn(5)-O(3)	1.850(3)
Mn(1)-O(91)	2.152(4)	Mn(5)-O(41)	1.931(4)
Mn(2)-O(4)	1.856(3)	Mn(5)-O(101)	1.956(4)
Mn(2)-O(130)	1.913(3)	Mn(5)-O(60)	2.017(4)
Mn(2)-O(2)	1.948(4)	Mn(5)-O(131)	2.128(3)
Mn(2)-O(20)	1.996(4)	Mn(5)-O(50)	2.176(4)
Mn(2)-O(10)	2.173(4)	Mn(6)-O(51)	1.903(4)
Mn(2)-O(70)	2.211(4)	Mn(6)-O(80)	1.923(4)
Mn(3)-O(21)	1.935(4)	Mn(6)-O(61)	1.955(4)
Mn(3)-O(30)	1.947(4)	Mn(6)-O(90)	1.981(4)
Mn(3)-O(120)	1.947(4)	Mn(6)-O(3)	2.065(3)
Mn(3)-O(11)	1.982(4)	Mn(6)-O(141)	2.323(4)
Mn(3)-O(4)	2.015(3)	O(130)-C(131)	1.410(6)
Mn(3)-O(110)	2.277(5)	O(131)-C(131)	1.398(6)
Mn(4)-O(4)	1.866(3)	C(131)-H(13d)	0.9900
Mn(4)-O(131)	1.903(3)	C(131)-H(13e)	0.9900
O(3)-Mn(1)-O(1)	175.89(15)	O(2)-Mn(2)-O(10)	89.01(17)
O(3)-Mn(1)-O(100)	93.33(14)	O(20)-Mn(2)-O(10)	86.55(16)
O(1)-Mn(1)-O(100)	88.39(15)	O(4)-Mn(2)-O(70)	92.69(15)
O(3)-Mn(1)-O(81)	91.54(15)	O(130)-Mn(2)-O(70)	102.01(15)
O(1)-Mn(1)-O(81)	86.21(15)	O(2)-Mn(2)-O(70)	84.12(17)
O(100)-Mn(1)-O(81)	170.20(15)	O(20)-Mn(2)-O(70)	81.93(16)
O(3)-Mn(1)-O(130)	94.06(14)	O(10)-Mn(2)-O(70)	167.04(16)
O(1)-Mn(1)-O(130)	89.24(14)	O(21)-Mn(3)-O(30)	87.83(17)
O(100)-Mn(1)-O(130)	101.42(14)	O(21)-Mn(3)-O(120)	172.06(16)
O(81)-Mn(1)-O(130)	86.70(14)	O(30)-Mn(3)-O(120)	91.99(17)
O(3)-Mn(1)-O(91)	91.66(14)	O(21)-Mn(3)-O(11)	89.50(16)
O(1)-Mn(1)-O(91)	84.77(14)	O(30)-Mn(3)-O(11)	161.36(16)
O(100)-Mn(1)-O(91)	85.01(14)	O(120)-Mn(3)-O(11)	88.14(16)
O(81)-Mn(1)-O(91)	86.35(14)	O(21)-Mn(3)-O(4)	92.06(15)
O(130)-Mn(1)-O(91)	171.11(14)	O(30)-Mn(3)-O(4)	96.78(15)
O(4)-Mn(2)-O(130)	92.94(14)	O(120)-Mn(3)-O(4)	95.84(15)
O(4)-Mn(2)-O(2)	176.41(17)	O(11)-Mn(3)-O(4)	101.75(15)
O(130)-Mn(2)-O(2)	89.34(15)	O(21)-Mn(3)-O(110)	85.53(16)
O(4)-Mn(2)-O(20)	92.86(15)	O(30)-Mn(3)-O(110)	80.71(17)
O(130)-Mn(2)-O(20)	172.82(15)	O(120)-Mn(3)-O(110)	86.61(16)
O(2)-Mn(2)-O(20)	85.07(15)	O(11)-Mn(3)-O(110)	80.69(17)
O(4)-Mn(2)-O(10)	93.80(16)	O(4)-Mn(3)-O(110)	176.58(15)
O(130)-Mn(2)-O(10)	88.84(15)	O(4)-Mn(4)-O(131)	92.74(14)

Table A-10. Continued.

O(4)-Mn(4)-O(40)	177.90(15)	O(80)-Mn(6)-O(61)	88.67(17)
O(131)-Mn(4)-O(40)	89.37(15)	O(51)-Mn(6)-O(90)	87.87(16)
O(4)-Mn(4)-O(31)	93.38(15)	O(80)-Mn(6)-O(90)	90.36(17)
O(131)-Mn(4)-O(31)	172.99(16)	O(61)-Mn(6)-O(90)	162.29(16)
O(40)-Mn(4)-O(31)	84.52(16)	O(51)-Mn(6)-O(3)	96.08(15)
O(4)-Mn(4)-O(121)	90.71(14)	O(80)-Mn(6)-O(3)	91.95(15)
O(131)-Mn(4)-O(121)	89.13(14)	O(61)-Mn(6)-O(3)	95.61(14)
O(40)-Mn(4)-O(121)	89.29(15)	O(90)-Mn(6)-O(3)	102.09(14)
O(31)-Mn(4)-O(121)	87.38(15)	O(51)-Mn(6)-O(141)	87.89(17)
O(4)-Mn(4)-O(71)	90.98(14)	O(80)-Mn(6)-O(141)	84.13(17)
O(131)-Mn(4)-O(71)	99.62(14)	O(61)-Mn(6)-O(141)	78.89(15)
O(40)-Mn(4)-O(71)	88.71(15)	O(90)-Mn(6)-O(141)	83.42(15)
O(31)-Mn(4)-O(71)	83.70(15)	O(3)-Mn(6)-O(141)	173.29(15)
O(121)-Mn(4)-O(71)	171.00(14)	Mn(1)-O(3)-Mn(5)	123.77(17)
O(3)-Mn(5)-O(41)	177.89(15)	Mn(1)-O(3)-Mn(6)	117.95(16)
O(3)-Mn(5)-O(101)	93.50(15)	Mn(5)-O(3)-Mn(6)	118.14(16)
O(41)-Mn(5)-O(101)	85.88(16)	Mn(2)-O(4)-Mn(4)	124.19(17)
O(3)-Mn(5)-O(60)	93.31(15)	Mn(2)-O(4)-Mn(3)	117.25(16)
O(41)-Mn(5)-O(60)	87.12(16)	Mn(4)-O(4)-Mn(3)	118.56(17)
O(101)-Mn(5)-O(60)	171.21(16)	C(131)-O(130)-Mn(2)	113.9(3)
O(3)-Mn(5)-O(131)	93.12(13)	C(131)-O(130)-Mn(1)	115.0(3)
O(41)-Mn(5)-O(131)	88.97(14)	Mn(2)-O(130)-Mn(1)	126.61(17)
O(101)-Mn(5)-O(131)	99.79(14)	C(131)-O(131)-Mn(4)	117.3(3)
O(60)-Mn(5)-O(131)	85.38(14)	C(131)-O(131)-Mn(5)	111.9(3)
O(3)-Mn(5)-O(50)	92.11(14)	Mn(4)-O(131)-Mn(5)	126.40(17)
O(41)-Mn(5)-O(50)	85.80(15)	O(131)-C(131)-O(130)	109.4(4)
O(101)-Mn(5)-O(50)	88.39(15)	O(131)-C(131)-H(13d)	109.8
O(60)-Mn(5)-O(50)	85.80(15)	O(130)-C(131)-H(13d)	109.8
O(131)-Mn(5)-O(50)	169.99(14)	O(131)-C(131)-H(13e)	109.8
O(51)-Mn(6)-O(80)	171.97(17)	O(130)-C(131)-H(13e)	109.8
O(51)-Mn(6)-O(61)	90.63(17)	H(13d)-C(131)-H(13e)	108.2

Table A-11. Selected interatomic distances (Å) and angles (°) for  
 $[\text{Mn}_9\text{O}_6(\text{OH})(\text{CO}_3)(\text{O}_2\text{CPe}^t)_{12}(\text{H}_2\text{O})_2] \cdot \text{H}_2\text{O} \cdot \text{HO}_2\text{CPe}^t$  (**17**· $\text{H}_2\text{O} \cdot \text{HO}_2\text{CPe}^t$ ).

Mn(1)-O(1)	1.885(3)	Mn(4)-O(15)	1.943(4)
Mn(1)-O(9)	1.933(4)	Mn(4)-O(11)	2.081(5)
Mn(1)-O(7)	2.111(7)	Mn(4)-Mn(6)	3.1767(10)
Mn(1)-O(5)	2.425(7)	Mn(5)-O(3)	1.865(3)
Mn(1)-Mn(2)	2.8126(14)	Mn(5)-O(2)	1.882(4)
Mn(2)-O(1)	1.900(3)	Mn(5)-O(13)	1.923(4)
Mn(2)-O(2)	1.906(4)	Mn(5)-O(17)	1.975(4)
Mn(2)-O(8)	2.192(6)	Mn(5)-O(12)	2.041(5)
Mn(2)-Mn(3)	2.8313(15)	Mn(6)-O(4)	1.849(2)
Mn(3)-O(2)	1.868(4)	Mn(6)-O(3)	1.885(3)
Mn(3)-O(14)	1.936(5)	Mn(6)-O(19)	1.928(4)
Mn(3)-O(20)	2.245(6)	Mn(6)-O(16)	1.969(4)
Mn(3)-O(21)	2.261(10)	Mn(6)-O(18)	2.155(4)
Mn(4)-O(1)	1.861(3)	Mn(6)-O(6)	2.321(4)
Mn(4)-O(3)	1.882(3)	O(5)-C(1)	1.274(8)
Mn(4)-O(10)	1.934(4)	O(6)-C(1)	1.303(5)
O(1)-Mn(1)-O(1a)	81.4(2)	O(2)-Mn(3)-O(14a)	177.7(3)
O(1)-Mn(1)-O(9)	95.16(15)	O(2)-Mn(3)-O(14)	96.0(2)
O(1)-Mn(1)-O(9a)	172.72(18)	O(14)-Mn(3)-O(14a)	84.6(3)
O(9)-Mn(1)-O(9a)	87.5(2)	O(2)-Mn(3)-O(20)	90.74(17)
O(1)-Mn(1)-O(7)	94.74(19)	O(14)-Mn(3)-O(20)	91.4(2)
O(9)-Mn(1)-O(7)	91.9(2)	O(2)-Mn(3)-O(21)	91.0(3)
O(1)-Mn(1)-O(5)	90.38(15)	O(14)-Mn(3)-O(21)	86.9(3)
O(9)-Mn(1)-O(5)	83.20(18)	O(20)-Mn(3)-O(21)	177.7(3)
O(7)-Mn(1)-O(5)	173.2(2)	O(2)-Mn(3)-Mn(2)	41.89(11)
O(1)-Mn(1)-Mn(2)	42.22(10)	O(14)-Mn(3)-Mn(2)	137.07(17)
O(9)-Mn(1)-Mn(2)	136.14(12)	O(20)-Mn(3)-Mn(2)	96.19(15)
O(7)-Mn(1)-Mn(2)	83.9(2)	O(21)-Mn(3)-Mn(2)	86.1(3)
O(5)-Mn(1)-Mn(2)	102.85(14)	O(1)-Mn(4)-O(3)	90.49(14)
O(1)-Mn(2)-O(1a)	80.6(2)	O(1)-Mn(4)-O(10)	93.93(16)
O(1)-Mn(2)-O(2a)	175.19(18)	O(3)-Mn(4)-O(10)	169.19(19)
O(1)-Mn(2)-O(2)	98.88(15)	O(1)-Mn(4)-O(15)	168.4(2)
O(2)-Mn(2)-O(2a)	81.2(2)	O(3)-Mn(4)-O(15)	89.98(15)
O(1)-Mn(2)-O(8)	92.72(18)	O(10)-Mn(4)-O(15)	83.72(17)
O(2)-Mn(2)-O(8)	92.08(19)	O(1)-Mn(4)-O(11)	99.1(2)
O(1)-Mn(2)-Mn(1)	41.80(10)	O(3)-Mn(4)-O(11)	99.88(16)
O(2)-Mn(2)-Mn(1)	139.04(11)	O(10)-Mn(4)-O(11)	89.16(19)
O(8)-Mn(2)-Mn(1)	81.40(18)	O(15)-Mn(4)-O(11)	92.2(2)
O(1)-Mn(2)-Mn(3)	139.68(10)	O(1)-Mn(4)-Mn(6)	98.50(10)
O(2)-Mn(2)-Mn(3)	40.87(11)	O(3)-Mn(4)-Mn(6)	32.52(11)
O(8)-Mn(2)-Mn(3)	87.72(18)	O(10)-Mn(4)-Mn(6)	136.78(15)
Mn(1)-Mn(2)-Mn(3)	169.12(5)	O(15)-Mn(4)-Mn(6)	75.99(12)
O(2)-Mn(3)-O(2a)	83.3(2)	O(11)-Mn(4)-Mn(6)	128.80(13)

Table A-11. Continued.

O(3)-Mn(5)-O(2)	90.94(16)	O(16)-Mn(6)-O(6)	83.19(16)
O(3)-Mn(5)-O(13)	172.4(2)	O(18)-Mn(6)-O(6)	173.50(17)
O(2)-Mn(5)-O(13)	92.3(2)	O(4)-Mn(6)-Mn(4)	102.71(16)
O(3)-Mn(5)-O(17)	90.89(18)	O(3)-Mn(6)-Mn(4)	32.46(10)
O(2)-Mn(5)-O(17)	159.4(2)	O(19)-Mn(6)-Mn(4)	143.06(14)
O(13)-Mn(5)-O(17)	83.7(2)	O(16)-Mn(6)-Mn(4)	76.41(11)
O(3)-Mn(5)-O(12)	99.57(18)	O(18)-Mn(6)-Mn(4)	121.44(12)
O(2)-Mn(5)-O(12)	105.5(2)	O(6)-Mn(6)-Mn(4)	52.55(12)
O(13)-Mn(5)-O(12)	86.1(2)	Mn(4)-O(1)-Mn(1)	126.33(19)
O(17)-Mn(5)-O(12)	94.5(2)	Mn(4)-O(1)-Mn(2)	129.48(16)
O(4)-Mn(6)-O(3)	93.14(18)	Mn(1)-O(1)-Mn(2)	95.98(15)
O(4)-Mn(6)-O(19)	94.4(2)	Mn(3)-O(2)-Mn(5)	121.8(2)
O(3)-Mn(6)-O(19)	172.31(18)	Mn(3)-O(2)-Mn(2)	97.24(16)
O(4)-Mn(6)-O(16)	173.7(2)	Mn(5)-O(2)-Mn(2)	128.2(2)
O(3)-Mn(6)-O(16)	89.27(17)	Mn(5)-O(3)-Mn(4)	123.00(19)
O(19)-Mn(6)-O(16)	83.08(19)	Mn(5)-O(3)-Mn(6)	121.98(17)
O(4)-Mn(6)-O(18)	92.7(2)	Mn(4)-O(3)-Mn(6)	115.02(17)
O(3)-Mn(6)-O(18)	91.57(16)	Mn(6)-O(4)-Mn(6a)	126.4(3)
O(19)-Mn(6)-O(18)	89.68(19)	C(1)-O(5)-Mn(1)	118.6(5)
O(16)-Mn(6)-O(18)	93.04(17)	C(1)-O(6)-Mn(6)	133.5(3)
O(4)-Mn(6)-O(6)	91.35(18)	O(5)-C(1)-O(6)	118.0(3)
O(3)-Mn(6)-O(6)	83.12(15)	O(6)-C(1)-O(6a)	118.3(5)
O(19)-Mn(6)-O(6)	95.10(18)		

---

Table A-12. Selected interatomic distances (Å) and angles (°) for  
 $[\text{Mn}_4\text{O}_2(\text{O}_2\text{CPE}^{\text{t}})_6(\text{bpy})_2]\cdot 2\text{H}_2\text{O}$  (**18**·2H<sub>2</sub>O).

Mn(1)-O(1a)	1.8537(18)	Mn(2)-O(1)	2.0906(18)
Mn(1)-O(1)	1.8560(18)	Mn(2)-O(5)	2.1201(19)
Mn(1)-O(2)	1.957(2)	Mn(2)-O(3)	2.184(2)
Mn(1)-O(6a)	1.965(2)	Mn(2)-O(7)	2.212(2)
Mn(1)-O(4)	2.089(2)	Mn(2)-N(1)	2.259(2)
Mn(1)-Mn(1a)	2.7755(8)	Mn(2)-N(2)	2.281(2)
O(1a)-Mn(1)-O(1)	83.13(8)	O(5)-Mn(2)-O(3)	91.87(8)
O(1a)-Mn(1)-O(2)	159.64(9)	O(1)-Mn(2)-O(7)	89.56(7)
O(1)-Mn(1)-O(2)	92.51(9)	O(5)-Mn(2)-O(7)	94.47(8)
O(1a)-Mn(1)-O(6a)	94.04(9)	O(3)-Mn(2)-O(7)	173.39(8)
O(1)-Mn(1)-O(6a)	169.43(9)	O(1)-Mn(2)-N(1)	165.17(8)
O(2)-Mn(1)-O(6a)	86.62(10)	O(5)-Mn(2)-N(1)	88.97(8)
O(1a)-Mn(1)-O(4)	103.54(9)	O(3)-Mn(2)-N(1)	94.81(8)
O(1)-Mn(1)-O(4)	102.84(8)	O(7)-Mn(2)-N(1)	87.18(8)
O(2)-Mn(1)-O(4)	96.82(10)	O(1)-Mn(2)-N(2)	93.62(8)
O(6a)-Mn(1)-O(4)	87.72(10)	O(5)-Mn(2)-N(2)	160.42(9)
O(1a)-Mn(1)-Mn(1a)	41.60(5)	O(3)-Mn(2)-N(2)	86.07(9)
O(1)-Mn(1)-Mn(1a)	41.54(5)	O(7)-Mn(2)-N(2)	88.57(9)
O(2)-Mn(1)-Mn(1a)	130.95(8)	N(1)-Mn(2)-N(2)	71.84(9)
O(6a)-Mn(1)-Mn(1a)	134.78(7)	Mn(1a)-O(1)-Mn(1)	96.87(8)
O(4)-Mn(1)-Mn(1a)	107.76(7)	Mn(1a)-O(1)-Mn(2)	122.80(10)
O(1)-Mn(2)-O(5)	105.72(8)	Mn(1)-O(1)-Mn(2)	111.95(9)
O(1)-Mn(2)-O(3)	86.93(7)		

Table A-13. Selected interatomic distances (Å) and angles (°) for  
 $[\text{Mn}_{12}\text{O}_{12}(\text{O}_2\text{CC}_6\text{F}_5)_{16}(\text{H}_2\text{O})_4]\cdot 3\text{CH}_2\text{Cl}_2$  (**20**·3CH<sub>2</sub>Cl<sub>2</sub>).

Mn(1)-O(2)	1.874(8)	Mn(6)-O(3)	1.904(6)
Mn(1)-O(1)	1.915(7)	Mn(6)-O(10)	1.917(6)
Mn(1)-O(15)	1.933(9)	Mn(6)-O(27)	1.920(7)
Mn(1)-O(14)	1.958(10)	Mn(6)-Mn(7)	2.941(2)
Mn(1)-O(13)	2.184(8)	Mn(7)-O(12)	1.850(7)
Mn(1)-O(16)	2.207(8)	Mn(7)-O(11)	1.868(6)
Mn(1)-Mn(2)	2.779(2)	Mn(7)-O(4)	1.898(6)
Mn(2)-O(1)	1.864(7)	Mn(7)-O(10)	1.909(7)
Mn(2)-O(2)	1.864(6)	Mn(7)-O(28)	1.920(7)
Mn(2)-O(10)	1.905(6)	Mn(7)-O(9)	1.922(6)
Mn(2)-O(17)	1.914(7)	Mn(7)-Mn(8)	2.796(2)
Mn(2)-O(4)	1.920(7)	Mn(8)-O(11)	1.903(7)
Mn(2)-O(3)	1.926(6)	Mn(8)-O(31)	1.909(8)
Mn(2)-Mn(6)	2.814(2)	Mn(8)-O(12)	1.910(6)
Mn(2)-Mn(7)	2.840(2)	Mn(8)-O(30)	1.927(10)
Mn(2)-Mn(3)	2.962(2)	Mn(8)-O(29)	2.227(8)
Mn(3)-O(6)	1.874(7)	Mn(8)-O(32)	2.244(10)
Mn(3)-O(5)	1.880(6)	Mn(9)-O(8)	1.865(6)
Mn(3)-O(9)	1.906(6)	Mn(9)-O(1)	1.880(7)
Mn(3)-O(4)	1.907(6)	Mn(9)-O(35)	1.957(8)
Mn(3)-O(3)	1.927(6)	Mn(9)-O(34)	1.978(7)
Mn(3)-O(18)	1.931(6)	Mn(9)-O(36)	2.168(7)
Mn(3)-Mn(4)	2.795(2)	Mn(9)-O(33)	2.212(7)
Mn(3)-Mn(7)	2.813(2)	Mn(10)-O(5)	1.891(6)
Mn(3)-Mn(6)	2.834(2)	Mn(10)-O(7)	1.903(6)
Mn(4)-O(5)	1.876(7)	Mn(10)-O(39)	1.956(6)
Mn(4)-O(6)	1.913(6)	Mn(10)-O(38)	1.964(6)
Mn(4)-O(21)	1.926(8)	Mn(10)-O(37)	2.148(7)
Mn(4)-O(20)	1.960(6)	Mn(10)-O(40)	2.162(8)
Mn(4)-O(22)	2.161(7)	Mn(11)-O(11)	1.884(7)
Mn(4)-O(19)	2.195(7)	Mn(11)-O(46)	1.978(10)
Mn(5)-O(7)	1.874(7)	Mn(11)-O(2)	1.978(8)
Mn(5)-O(8)	1.909(6)	Mn(11)-O(48)	2.010(9)
Mn(5)-O(25)	1.934(7)	Mn(11)-O(45)	2.015(8)
Mn(5)-O(24)	1.947(7)	Mn(11)-O(47)	2.053(10)
Mn(5)-O(26)	2.161(7)	Mn(12)-O(12)	1.869(7)
Mn(5)-O(23)	2.172(7)	Mn(12)-O(6)	1.875(7)
Mn(5)-Mn(6)	2.785(2)	Mn(12)-O(42)	1.963(9)
Mn(6)-O(8)	1.869(7)	Mn(12)-O(43)	1.974(8)
Mn(6)-O(7)	1.894(6)	Mn(12)-O(44)	2.201(8)
Mn(6)-O(9)	1.895(7)	Mn(12)-O(41)	2.211(8)
O(2)-Mn(1)-O(1)	82.7(3)	O(1)-Mn(1)-O(15)	171.5(3)
O(2)-Mn(1)-O(15)	93.6(3)	O(2)-Mn(1)-O(14)	177.7(3)

Table A-13. Continued.

O(1)-Mn(1)-O(14)	96.8(4)	O(1)-Mn(2)-Mn(7)	129.4(2)
O(15)-Mn(1)-O(14)	86.7(4)	O(2)-Mn(2)-Mn(7)	89.2(3)
O(2)-Mn(1)-O(13)	89.9(3)	O(10)-Mn(2)-Mn(7)	41.9(2)
O(1)-Mn(1)-O(13)	84.3(3)	O(17)-Mn(2)-Mn(7)	137.5(2)
O(15)-Mn(1)-O(13)	88.0(4)	O(4)-Mn(2)-Mn(7)	41.64(19)
O(14)-Mn(1)-O(13)	87.8(4)	O(3)-Mn(2)-Mn(7)	85.4(2)
O(2)-Mn(1)-O(16)	93.8(3)	Mn(1)-Mn(2)-Mn(7)	120.96(7)
O(1)-Mn(1)-O(16)	93.4(3)	Mn(6)-Mn(2)-Mn(7)	62.68(6)
O(15)-Mn(1)-O(16)	94.5(4)	O(1)-Mn(2)-Mn(3)	139.1(2)
O(14)-Mn(1)-O(16)	88.5(3)	O(2)-Mn(2)-Mn(3)	135.5(3)
O(13)-Mn(1)-O(16)	175.4(3)	O(10)-Mn(2)-Mn(3)	82.15(19)
O(2)-Mn(1)-Mn(2)	41.8(2)	O(17)-Mn(2)-Mn(3)	92.6(2)
O(1)-Mn(1)-Mn(2)	42.0(2)	O(4)-Mn(2)-Mn(3)	39.13(17)
O(15)-Mn(1)-Mn(2)	132.5(3)	O(3)-Mn(2)-Mn(3)	39.78(19)
O(14)-Mn(1)-Mn(2)	137.1(3)	Mn(1)-Mn(2)-Mn(3)	177.50(8)
O(13)-Mn(1)-Mn(2)	78.6(2)	Mn(6)-Mn(2)-Mn(3)	58.70(5)
O(16)-Mn(1)-Mn(2)	102.4(2)	Mn(7)-Mn(2)-Mn(3)	57.97(5)
O(1)-Mn(2)-O(2)	84.3(3)	O(6)-Mn(3)-O(5)	84.1(3)
O(1)-Mn(2)-O(10)	88.2(3)	O(6)-Mn(3)-O(9)	88.3(3)
O(2)-Mn(2)-O(10)	92.6(3)	O(5)-Mn(3)-O(9)	92.3(3)
O(1)-Mn(2)-O(17)	93.1(3)	O(6)-Mn(3)-O(4)	101.0(3)
O(2)-Mn(2)-O(17)	94.2(3)	O(5)-Mn(3)-O(4)	173.5(3)
O(10)-Mn(2)-O(17)	173.2(3)	O(9)-Mn(3)-O(4)	83.8(3)
O(1)-Mn(2)-O(4)	170.9(3)	O(6)-Mn(3)-O(3)	171.1(3)
O(2)-Mn(2)-O(4)	96.4(3)	O(5)-Mn(3)-O(3)	95.1(3)
O(10)-Mn(2)-O(4)	82.7(3)	O(9)-Mn(3)-O(3)	82.8(3)
O(17)-Mn(2)-O(4)	96.0(3)	O(4)-Mn(3)-O(3)	79.2(3)
O(1)-Mn(2)-O(3)	99.9(3)	O(6)-Mn(3)-O(18)	91.3(3)
O(2)-Mn(2)-O(3)	174.5(3)	O(5)-Mn(3)-O(18)	93.2(3)
O(10)-Mn(2)-O(3)	84.0(3)	O(9)-Mn(3)-O(18)	174.3(3)
O(17)-Mn(2)-O(3)	89.1(3)	O(4)-Mn(3)-O(18)	90.7(3)
O(4)-Mn(2)-O(3)	78.9(3)	O(3)-Mn(3)-O(18)	97.6(3)
O(1)-Mn(2)-Mn(1)	43.4(2)	O(6)-Mn(3)-Mn(4)	42.99(18)
O(2)-Mn(2)-Mn(1)	42.1(2)	O(5)-Mn(3)-Mn(4)	41.9(2)
O(10)-Mn(2)-Mn(1)	98.38(19)	O(9)-Mn(3)-Mn(4)	96.6(2)
O(17)-Mn(2)-Mn(1)	87.1(2)	O(4)-Mn(3)-Mn(4)	143.7(2)
O(4)-Mn(2)-Mn(1)	138.44(19)	O(3)-Mn(3)-Mn(4)	136.98(19)
O(3)-Mn(2)-Mn(1)	142.7(2)	O(18)-Mn(3)-Mn(4)	87.0(2)
O(1)-Mn(2)-Mn(6)	87.8(2)	O(6)-Mn(3)-Mn(7)	88.17(19)
O(2)-Mn(2)-Mn(6)	135.0(2)	O(5)-Mn(3)-Mn(7)	134.85(19)
O(10)-Mn(2)-Mn(6)	42.76(18)	O(9)-Mn(3)-Mn(7)	42.91(18)
O(17)-Mn(2)-Mn(6)	130.6(2)	O(4)-Mn(3)-Mn(7)	42.19(19)
O(4)-Mn(2)-Mn(6)	85.26(19)	O(3)-Mn(3)-Mn(7)	86.07(19)
O(3)-Mn(2)-Mn(6)	42.42(18)	O(18)-Mn(3)-Mn(7)	131.45(19)
Mn(1)-Mn(2)-Mn(6)	123.22(7)	Mn(4)-Mn(3)-Mn(7)	122.07(7)

Table A-13. Continued.

O(6)-Mn(3)-Mn(6)	129.1(2)	O(8)-Mn(5)-O(26)	89.4(3)
O(5)-Mn(3)-Mn(6)	88.69(19)	O(25)-Mn(5)-O(26)	85.5(3)
O(9)-Mn(3)-Mn(6)	41.6(2)	O(24)-Mn(5)-O(26)	97.8(3)
O(4)-Mn(3)-Mn(6)	84.9(2)	O(7)-Mn(5)-O(23)	90.1(3)
O(3)-Mn(3)-Mn(6)	41.98(18)	O(8)-Mn(5)-O(23)	84.9(3)
O(18)-Mn(3)-Mn(6)	139.4(2)	O(25)-Mn(5)-O(23)	89.6(3)
Mn(4)-Mn(3)-Mn(6)	118.95(7)	O(24)-Mn(5)-O(23)	88.1(3)
Mn(7)-Mn(3)-Mn(6)	62.76(5)	O(26)-Mn(5)-O(23)	172.2(3)
O(6)-Mn(3)-Mn(2)	139.90(19)	O(7)-Mn(5)-Mn(6)	42.60(18)
O(5)-Mn(3)-Mn(2)	134.8(2)	O(8)-Mn(5)-Mn(6)	41.94(19)
O(9)-Mn(3)-Mn(2)	82.1(2)	O(25)-Mn(5)-Mn(6)	135.7(2)
O(4)-Mn(3)-Mn(2)	39.5(2)	O(24)-Mn(5)-Mn(6)	134.3(2)
O(3)-Mn(3)-Mn(2)	39.75(18)	O(26)-Mn(5)-Mn(6)	100.44(19)
O(18)-Mn(3)-Mn(2)	94.6(2)	O(23)-Mn(5)-Mn(6)	78.8(2)
Mn(4)-Mn(3)-Mn(2)	176.52(7)	O(8)-Mn(6)-O(7)	83.9(3)
Mn(7)-Mn(3)-Mn(2)	58.84(5)	O(8)-Mn(6)-O(9)	172.0(3)
Mn(6)-Mn(3)-Mn(2)	58.04(5)	O(7)-Mn(6)-O(9)	97.9(3)
O(5)-Mn(4)-O(6)	83.2(3)	O(8)-Mn(6)-O(3)	88.4(3)
O(5)-Mn(4)-O(21)	178.3(3)	O(7)-Mn(6)-O(3)	91.6(3)
O(6)-Mn(4)-O(21)	95.8(3)	O(9)-Mn(6)-O(3)	83.7(3)
O(5)-Mn(4)-O(20)	95.8(3)	O(8)-Mn(6)-O(10)	98.1(3)
O(6)-Mn(4)-O(20)	174.5(3)	O(7)-Mn(6)-O(10)	175.4(3)
O(21)-Mn(4)-O(20)	85.1(3)	O(9)-Mn(6)-O(10)	79.6(3)
O(5)-Mn(4)-O(22)	92.7(3)	O(3)-Mn(6)-O(10)	84.3(3)
O(6)-Mn(4)-O(22)	91.8(3)	O(8)-Mn(6)-O(27)	92.5(3)
O(21)-Mn(4)-O(22)	88.7(3)	O(7)-Mn(6)-O(27)	93.8(3)
O(20)-Mn(4)-O(22)	93.6(3)	O(9)-Mn(6)-O(27)	95.1(3)
O(5)-Mn(4)-O(19)	86.6(3)	O(3)-Mn(6)-O(27)	174.5(3)
O(6)-Mn(4)-O(19)	86.0(3)	O(10)-Mn(6)-O(27)	90.2(3)
O(21)-Mn(4)-O(19)	92.0(3)	O(8)-Mn(6)-Mn(5)	43.05(18)
O(20)-Mn(4)-O(19)	88.6(3)	O(7)-Mn(6)-Mn(5)	42.1(2)
O(22)-Mn(4)-O(19)	177.7(3)	O(9)-Mn(6)-Mn(5)	139.79(19)
O(5)-Mn(4)-Mn(3)	41.98(18)	O(3)-Mn(6)-Mn(5)	97.93(19)
O(6)-Mn(4)-Mn(3)	41.9(2)	O(10)-Mn(6)-Mn(5)	140.6(2)
O(21)-Mn(4)-Mn(3)	136.7(2)	O(27)-Mn(6)-Mn(5)	86.4(2)
O(20)-Mn(4)-Mn(3)	136.0(2)	O(8)-Mn(6)-Mn(2)	86.71(19)
O(22)-Mn(4)-Mn(3)	98.98(19)	O(7)-Mn(6)-Mn(2)	133.9(2)
O(19)-Mn(4)-Mn(3)	79.08(19)	O(9)-Mn(6)-Mn(2)	86.5(2)
O(7)-Mn(5)-O(8)	83.4(3)	O(3)-Mn(6)-Mn(2)	43.02(19)
O(7)-Mn(5)-O(25)	178.3(3)	O(10)-Mn(6)-Mn(2)	42.43(18)
O(8)-Mn(5)-O(25)	95.0(3)	O(27)-Mn(6)-Mn(2)	131.6(2)
O(7)-Mn(5)-O(24)	94.6(3)	Mn(5)-Mn(6)-Mn(2)	121.73(7)
O(8)-Mn(5)-O(24)	172.7(3)	O(8)-Mn(6)-Mn(3)	130.5(2)
O(25)-Mn(5)-O(24)	87.0(3)	O(7)-Mn(6)-Mn(3)	90.03(19)
O(7)-Mn(5)-O(26)	94.6(3)	O(9)-Mn(6)-Mn(3)	41.93(19)

Table A-13. Continued.

O(3)-Mn(6)-Mn(3)	42.61(19)	O(10)-Mn(7)-Mn(2)	41.83(18)
O(10)-Mn(6)-Mn(3)	85.54(19)	O(28)-Mn(7)-Mn(2)	135.6(2)
O(27)-Mn(6)-Mn(3)	136.9(2)	O(9)-Mn(7)-Mn(2)	85.2(2)
Mn(5)-Mn(6)-Mn(3)	122.19(7)	Mn(8)-Mn(7)-Mn(2)	120.81(8)
Mn(2)-Mn(6)-Mn(3)	63.26(5)	Mn(3)-Mn(7)-Mn(2)	63.19(6)
O(8)-Mn(6)-Mn(7)	137.39(19)	O(12)-Mn(7)-Mn(6)	137.4(2)
O(7)-Mn(6)-Mn(7)	137.7(2)	O(11)-Mn(7)-Mn(6)	136.9(2)
O(9)-Mn(6)-Mn(7)	39.94(18)	O(4)-Mn(7)-Mn(6)	82.1(2)
O(3)-Mn(6)-Mn(7)	82.89(19)	O(10)-Mn(7)-Mn(6)	39.87(18)
O(10)-Mn(6)-Mn(7)	39.7(2)	O(28)-Mn(7)-Mn(6)	93.5(2)
O(27)-Mn(6)-Mn(7)	92.8(2)	O(9)-Mn(7)-Mn(6)	39.3(2)
Mn(5)-Mn(6)-Mn(7)	179.13(8)	Mn(8)-Mn(7)-Mn(6)	179.00(9)
Mn(2)-Mn(6)-Mn(7)	59.09(6)	Mn(3)-Mn(7)-Mn(6)	58.96(5)
Mn(3)-Mn(6)-Mn(7)	58.28(5)	Mn(2)-Mn(7)-Mn(6)	58.23(5)
O(12)-Mn(7)-O(11)	84.8(3)	O(11)-Mn(8)-O(31)	96.6(3)
O(12)-Mn(7)-O(4)	89.3(3)	O(11)-Mn(8)-O(12)	82.3(3)
O(11)-Mn(7)-O(4)	92.8(3)	O(31)-Mn(8)-O(12)	174.2(3)
O(12)-Mn(7)-O(10)	172.3(3)	O(11)-Mn(8)-O(30)	176.0(4)
O(11)-Mn(7)-O(10)	97.1(3)	O(31)-Mn(8)-O(30)	84.8(4)
O(4)-Mn(7)-O(10)	83.2(3)	O(12)-Mn(8)-O(30)	96.0(3)
O(12)-Mn(7)-O(28)	93.2(3)	O(11)-Mn(8)-O(29)	85.8(3)
O(11)-Mn(7)-O(28)	91.2(3)	O(31)-Mn(8)-O(29)	90.7(3)
O(4)-Mn(7)-O(28)	175.5(3)	O(12)-Mn(8)-O(29)	83.5(3)
O(10)-Mn(7)-O(28)	94.2(3)	O(30)-Mn(8)-O(29)	90.5(4)
O(12)-Mn(7)-O(9)	98.5(3)	O(11)-Mn(8)-O(32)	92.1(3)
O(11)-Mn(7)-O(9)	175.0(3)	O(31)-Mn(8)-O(32)	94.1(3)
O(4)-Mn(7)-O(9)	83.6(3)	O(12)-Mn(8)-O(32)	91.6(3)
O(10)-Mn(7)-O(9)	79.1(3)	O(30)-Mn(8)-O(32)	91.5(5)
O(28)-Mn(7)-O(9)	92.3(3)	O(29)-Mn(8)-O(32)	174.9(3)
O(12)-Mn(7)-Mn(8)	42.8(2)	O(11)-Mn(8)-Mn(7)	41.67(19)
O(11)-Mn(7)-Mn(8)	42.6(2)	O(31)-Mn(8)-Mn(7)	136.6(3)
O(4)-Mn(7)-Mn(8)	97.0(2)	O(12)-Mn(8)-Mn(7)	41.2(2)
O(10)-Mn(7)-Mn(8)	139.71(19)	O(30)-Mn(8)-Mn(7)	136.1(3)
O(28)-Mn(7)-Mn(8)	87.4(2)	O(29)-Mn(8)-Mn(7)	77.6(2)
O(9)-Mn(7)-Mn(8)	141.1(2)	O(32)-Mn(8)-Mn(7)	97.8(2)
O(12)-Mn(7)-Mn(3)	87.1(2)	O(8)-Mn(9)-O(1)	91.7(3)
O(11)-Mn(7)-Mn(3)	134.6(2)	O(8)-Mn(9)-O(35)	174.1(3)
O(4)-Mn(7)-Mn(3)	42.44(18)	O(1)-Mn(9)-O(35)	93.7(3)
O(10)-Mn(7)-Mn(3)	86.26(18)	O(8)-Mn(9)-O(34)	92.6(3)
O(28)-Mn(7)-Mn(3)	133.9(2)	O(1)-Mn(9)-O(34)	175.2(3)
O(9)-Mn(7)-Mn(3)	42.46(19)	O(35)-Mn(9)-O(34)	82.1(3)
Mn(8)-Mn(7)-Mn(3)	120.56(7)	O(8)-Mn(9)-O(36)	92.7(3)
O(12)-Mn(7)-Mn(2)	131.0(2)	O(1)-Mn(9)-O(36)	95.2(3)
O(11)-Mn(7)-Mn(2)	89.8(2)	O(35)-Mn(9)-O(36)	89.3(3)
O(4)-Mn(7)-Mn(2)	42.2(2)	O(34)-Mn(9)-O(36)	82.4(3)

Table A-13. Continued.

O(8)-Mn(9)-O(33)	93.9(3)	O(42)-Mn(12)-O(44)	88.8(4)
O(1)-Mn(9)-O(33)	94.5(3)	O(43)-Mn(12)-O(44)	85.4(3)
O(35)-Mn(9)-O(33)	83.3(3)	O(12)-Mn(12)-O(41)	91.3(4)
O(34)-Mn(9)-O(33)	87.3(3)	O(6)-Mn(12)-O(41)	93.8(3)
O(36)-Mn(9)-O(33)	168.1(3)	O(42)-Mn(12)-O(41)	82.3(4)
O(5)-Mn(10)-O(7)	95.1(3)	O(43)-Mn(12)-O(41)	87.9(4)
O(5)-Mn(10)-O(39)	90.2(3)	O(44)-Mn(12)-O(41)	169.5(4)
O(7)-Mn(10)-O(39)	173.6(3)	Mn(2)-O(1)-Mn(9)	134.6(4)
O(5)-Mn(10)-O(38)	172.0(3)	Mn(2)-O(1)-Mn(1)	94.7(3)
O(7)-Mn(10)-O(38)	91.9(3)	Mn(9)-O(1)-Mn(1)	127.7(4)
O(39)-Mn(10)-O(38)	83.0(3)	Mn(2)-O(2)-Mn(1)	96.0(4)
O(5)-Mn(10)-O(37)	92.6(3)	Mn(2)-O(2)-Mn(11)	132.5(4)
O(7)-Mn(10)-O(37)	94.2(3)	Mn(1)-O(2)-Mn(11)	122.4(3)
O(39)-Mn(10)-O(37)	81.9(3)	Mn(6)-O(3)-Mn(2)	94.6(3)
O(38)-Mn(10)-O(37)	90.6(3)	Mn(6)-O(3)-Mn(3)	95.4(3)
O(5)-Mn(10)-O(40)	93.4(3)	Mn(2)-O(3)-Mn(3)	100.5(3)
O(7)-Mn(10)-O(40)	90.6(3)	Mn(7)-O(4)-Mn(3)	95.4(3)
O(39)-Mn(10)-O(40)	92.7(3)	Mn(7)-O(4)-Mn(2)	96.1(3)
O(38)-Mn(10)-O(40)	82.8(3)	Mn(3)-O(4)-Mn(2)	101.4(3)
O(37)-Mn(10)-O(40)	172.0(3)	Mn(4)-O(5)-Mn(3)	96.2(3)
O(11)-Mn(11)-O(46)	174.9(4)	Mn(4)-O(5)-Mn(10)	123.9(3)
O(11)-Mn(11)-O(2)	93.6(3)	Mn(3)-O(5)-Mn(10)	133.4(3)
O(46)-Mn(11)-O(2)	90.6(4)	Mn(3)-O(6)-Mn(12)	133.0(3)
O(11)-Mn(11)-O(48)	92.9(3)	Mn(3)-O(6)-Mn(4)	95.1(3)
O(46)-Mn(11)-O(48)	83.9(4)	Mn(12)-O(6)-Mn(4)	128.6(4)
O(2)-Mn(11)-O(48)	94.2(3)	Mn(5)-O(7)-Mn(6)	95.3(3)
O(11)-Mn(11)-O(45)	93.4(3)	Mn(5)-O(7)-Mn(10)	123.6(3)
O(46)-Mn(11)-O(45)	89.2(4)	Mn(6)-O(7)-Mn(10)	131.7(3)
O(2)-Mn(11)-O(45)	94.3(3)	Mn(9)-O(8)-Mn(6)	134.2(3)
O(48)-Mn(11)-O(45)	169.1(3)	Mn(9)-O(8)-Mn(5)	130.2(4)
O(11)-Mn(11)-O(47)	90.7(4)	Mn(6)-O(8)-Mn(5)	95.0(3)
O(46)-Mn(11)-O(47)	85.4(4)	Mn(6)-O(9)-Mn(3)	96.4(3)
O(2)-Mn(11)-O(47)	174.1(4)	Mn(6)-O(9)-Mn(7)	100.8(3)
O(48)-Mn(11)-O(47)	89.7(4)	Mn(3)-O(9)-Mn(7)	94.6(3)
O(45)-Mn(11)-O(47)	81.3(3)	Mn(2)-O(10)-Mn(7)	96.2(3)
O(12)-Mn(12)-O(6)	92.9(3)	Mn(2)-O(10)-Mn(6)	94.8(3)
O(12)-Mn(12)-O(42)	92.0(4)	Mn(7)-O(10)-Mn(6)	100.4(3)
O(6)-Mn(12)-O(42)	173.8(4)	Mn(7)-O(11)-Mn(11)	134.2(4)
O(12)-Mn(12)-O(43)	173.9(3)	Mn(7)-O(11)-Mn(8)	95.7(3)
O(6)-Mn(12)-O(43)	93.2(3)	Mn(11)-O(11)-Mn(8)	122.9(3)
O(42)-Mn(12)-O(43)	81.9(4)	Mn(7)-O(12)-Mn(12)	134.1(4)
O(12)-Mn(12)-O(44)	94.5(3)	Mn(7)-O(12)-Mn(8)	96.0(3)
O(6)-Mn(12)-O(44)	94.7(3)	Mn(12)-O(12)-Mn(8)	128.4(4)

Table A-14. Selected interatomic distances (Å) and angles (°) for  
 (NMe<sub>4</sub>)[Mn<sub>12</sub>O<sub>12</sub>(O<sub>2</sub>CC<sub>6</sub>F<sub>5</sub>)<sub>16</sub>(H<sub>2</sub>O)<sub>4</sub>] $\cdot$ 4.5CH<sub>2</sub>Cl<sub>2</sub> $\cdot$  $\frac{1}{2}$ H<sub>2</sub>O  
 (21 $\cdot$ 4.5CH<sub>2</sub>Cl<sub>2</sub> $\cdot$  $\frac{1}{2}$ H<sub>2</sub>O).

Mn(1)-O(1)	1.874(3)	Mn(6)-O(7)	1.915(3)
Mn(1)-O(5)	1.882(3)	Mn(6)-O(24)	1.992(4)
Mn(1)-O(6)	1.890(3)	Mn(6)-O(20)	2.031(4)
Mn(1)-O(2)	1.907(3)	Mn(6)-O(22)	2.069(4)
Mn(1)-O(4)	1.911(3)	Mn(6)-O(21)	2.072(4)
Mn(1)-O(14)	1.924(3)	Mn(7)-O(8)	1.856(3)
Mn(1)-Mn(4)	2.7972(9)	Mn(7)-O(7)	1.885(3)
Mn(1)-Mn(5)	2.8012(10)	Mn(7)-O(28)	1.947(3)
Mn(1)-Mn(2)	2.8253(10)	Mn(7)-O(25)	1.981(3)
Mn(1)-Mn(3)	2.9486(9)	Mn(7)-O(23)	2.199(3)
Mn(2)-O(8)	1.832(3)	Mn(7)-O(27)	2.236(4)
Mn(2)-O(7)	1.856(3)	Mn(8)-O(9)	2.080(3)
Mn(2)-O(2)	1.915(3)	Mn(8)-O(29)	2.135(3)
Mn(2)-O(26)	1.927(3)	Mn(8)-O(8)	2.153(3)
Mn(2)-O(3)	1.943(3)	Mn(8)-O(30)	2.164(3)
Mn(2)-O(1)	1.967(3)	Mn(8)-O(48)	2.179(4)
Mn(2)-Mn(7)	2.7454(10)	Mn(8)-O(47)	2.200(4)
Mn(2)-Mn(3)	2.8654(10)	Mn(9)-O(9)	1.842(3)
Mn(2)-Mn(4)	2.9575(9)	Mn(9)-O(10)	1.919(3)
Mn(3)-O(9)	1.818(3)	Mn(9)-O(31)	1.947(3)
Mn(3)-O(10)	1.878(3)	Mn(9)-O(36)	1.957(3)
Mn(3)-O(3)	1.903(3)	Mn(9)-O(32)	2.193(3)
Mn(3)-O(2)	1.944(3)	Mn(9)-O(34)	2.206(3)
Mn(3)-O(4)	1.945(3)	Mn(10)-O(10)	1.860(3)
Mn(3)-O(33)	1.951(3)	Mn(10)-O(11)	1.898(3)
Mn(3)-Mn(9)	2.7645(10)	Mn(10)-O(40)	1.947(3)
Mn(3)-Mn(4)	2.8284(9)	Mn(10)-O(37)	2.007(3)
Mn(4)-O(11)	1.875(3)	Mn(10)-O(38)	2.150(3)
Mn(4)-O(4)	1.884(3)	Mn(10)-O(35)	2.163(3)
Mn(4)-O(12)	1.903(3)	Mn(11)-O(11)	1.883(3)
Mn(4)-O(1)	1.905(3)	Mn(11)-O(12)	1.901(3)
Mn(4)-O(3)	1.916(3)	Mn(11)-O(42)	1.953(3)
Mn(4)-O(45)	1.945(3)	Mn(11)-O(41)	1.977(3)
Mn(4)-Mn(11)	2.7957(9)	Mn(11)-O(39)	2.164(3)
Mn(5)-O(5)	1.880(3)	Mn(11)-O(44)	2.179(3)
Mn(5)-O(6)	1.895(3)	Mn(12)-O(5)	1.868(3)
Mn(5)-O(19)	1.919(3)	Mn(12)-O(12)	1.881(3)
Mn(5)-O(16)	1.957(3)	Mn(12)-O(43)	1.948(3)
Mn(5)-O(18)	2.204(4)	Mn(12)-O(15)	1.971(3)
Mn(5)-O(13)	2.222(3)	Mn(12)-O(17)	2.207(4)
Mn(6)-O(6)	1.899(3)	Mn(12)-O(46)	2.221(4)
O(1)-Mn(1)-O(5)	89.76(13)	O(1)-Mn(1)-O(6)	92.08(13)

Table A-14. Continued.

O(5)-Mn(1)-O(6)	83.36(13)	O(7)-Mn(2)-O(2)	93.03(13)
O(1)-Mn(1)-O(2)	85.41(12)	O(8)-Mn(2)-O(26)	94.73(14)
O(5)-Mn(1)-O(2)	174.71(13)	O(7)-Mn(2)-O(26)	92.72(14)
O(6)-Mn(1)-O(2)	98.95(12)	O(2)-Mn(2)-O(26)	171.79(13)
O(1)-Mn(1)-O(4)	84.20(12)	O(8)-Mn(2)-O(3)	101.98(13)
O(5)-Mn(1)-O(4)	96.38(13)	O(7)-Mn(2)-O(3)	172.34(13)
O(6)-Mn(1)-O(4)	176.28(13)	O(2)-Mn(2)-O(3)	82.73(12)
O(2)-Mn(1)-O(4)	81.01(12)	O(26)-Mn(2)-O(3)	90.88(13)
O(1)-Mn(1)-O(14)	174.93(13)	O(8)-Mn(2)-O(1)	174.10(13)
O(5)-Mn(1)-O(14)	91.57(14)	O(7)-Mn(2)-O(1)	94.15(13)
O(6)-Mn(1)-O(14)	92.93(13)	O(2)-Mn(2)-O(1)	82.69(12)
O(2)-Mn(1)-O(14)	93.06(13)	O(26)-Mn(2)-O(1)	91.06(13)
O(4)-Mn(1)-O(14)	90.78(13)	O(3)-Mn(2)-O(1)	79.02(12)
O(1)-Mn(1)-Mn(4)	42.68(9)	O(8)-Mn(2)-Mn(7)	42.24(9)
O(5)-Mn(1)-Mn(4)	88.52(9)	O(7)-Mn(2)-Mn(7)	43.21(9)
O(6)-Mn(1)-Mn(4)	134.16(10)	O(2)-Mn(2)-Mn(7)	100.34(9)
O(2)-Mn(1)-Mn(4)	86.47(9)	O(26)-Mn(2)-Mn(7)	87.86(10)
O(4)-Mn(1)-Mn(4)	42.14(8)	O(3)-Mn(2)-Mn(7)	143.80(9)
O(14)-Mn(1)-Mn(4)	132.45(10)	O(1)-Mn(2)-Mn(7)	137.16(9)
O(1)-Mn(1)-Mn(5)	97.72(9)	O(8)-Mn(2)-Mn(1)	132.73(10)
O(5)-Mn(1)-Mn(5)	41.84(9)	O(7)-Mn(2)-Mn(1)	87.96(10)
O(6)-Mn(1)-Mn(5)	42.34(9)	O(2)-Mn(2)-Mn(1)	42.21(9)
O(2)-Mn(1)-Mn(5)	141.07(9)	O(26)-Mn(2)-Mn(1)	132.26(10)
O(4)-Mn(1)-Mn(5)	137.91(9)	O(3)-Mn(2)-Mn(1)	84.61(9)
O(14)-Mn(1)-Mn(5)	86.51(10)	O(1)-Mn(2)-Mn(1)	41.39(8)
Mn(4)-Mn(1)-Mn(5)	121.60(3)	Mn(7)-Mn(2)-Mn(1)	121.77(3)
O(1)-Mn(1)-Mn(2)	43.94(9)	O(8)-Mn(2)-Mn(3)	92.05(10)
O(5)-Mn(1)-Mn(2)	133.15(10)	O(7)-Mn(2)-Mn(3)	135.31(10)
O(6)-Mn(1)-Mn(2)	90.44(9)	O(2)-Mn(2)-Mn(3)	42.43(9)
O(2)-Mn(1)-Mn(2)	42.43(9)	O(26)-Mn(2)-Mn(3)	131.94(10)
O(4)-Mn(1)-Mn(2)	87.04(9)	O(3)-Mn(2)-Mn(3)	41.31(9)
O(14)-Mn(1)-Mn(2)	135.21(10)	O(1)-Mn(2)-Mn(3)	84.90(9)
Mn(4)-Mn(1)-Mn(2)	63.47(2)	Mn(7)-Mn(2)-Mn(3)	125.72(3)
Mn(5)-Mn(1)-Mn(2)	122.98(3)	Mn(1)-Mn(2)-Mn(3)	62.41(2)
O(1)-Mn(1)-Mn(3)	84.13(9)	O(8)-Mn(2)-Mn(4)	141.47(10)
O(5)-Mn(1)-Mn(3)	136.84(9)	O(7)-Mn(2)-Mn(4)	133.56(10)
O(6)-Mn(1)-Mn(3)	139.39(9)	O(2)-Mn(2)-Mn(4)	81.83(9)
O(2)-Mn(1)-Mn(3)	40.48(9)	O(26)-Mn(2)-Mn(4)	89.96(10)
O(4)-Mn(1)-Mn(3)	40.54(9)	O(3)-Mn(2)-Mn(4)	39.63(9)
O(14)-Mn(1)-Mn(3)	91.56(10)	O(1)-Mn(2)-Mn(4)	39.43(8)
Mn(4)-Mn(1)-Mn(3)	58.91(2)	Mn(7)-Mn(2)-Mn(4)	175.94(3)
Mn(5)-Mn(1)-Mn(3)	177.56(3)	Mn(1)-Mn(2)-Mn(4)	57.80(2)
Mn(2)-Mn(1)-Mn(3)	59.46(2)	Mn(3)-Mn(2)-Mn(4)	58.09(2)
O(8)-Mn(2)-O(7)	84.46(13)	O(9)-Mn(3)-O(10)	84.34(13)
O(8)-Mn(2)-O(2)	91.65(13)	O(9)-Mn(3)-O(3)	92.45(13)

Table A-14. Continued.

O(10)-Mn(3)-O(3)	92.47(13)	O(4)-Mn(4)-O(12)	87.99(12)
O(9)-Mn(3)-O(2)	98.30(13)	O(11)-Mn(4)-O(1)	174.91(13)
O(10)-Mn(3)-O(2)	174.84(13)	O(4)-Mn(4)-O(1)	84.13(12)
O(3)-Mn(3)-O(2)	83.01(12)	O(12)-Mn(4)-O(1)	99.56(13)
O(9)-Mn(3)-O(4)	175.06(13)	O(11)-Mn(4)-O(3)	94.66(12)
O(10)-Mn(3)-O(4)	97.78(12)	O(4)-Mn(4)-O(3)	84.32(12)
O(3)-Mn(3)-O(4)	83.02(12)	O(12)-Mn(4)-O(3)	172.16(13)
O(2)-Mn(3)-O(4)	79.25(12)	O(1)-Mn(4)-O(3)	81.25(12)
O(9)-Mn(3)-O(33)	91.97(14)	O(11)-Mn(4)-O(45)	91.87(13)
O(10)-Mn(3)-O(33)	92.62(13)	O(4)-Mn(4)-O(45)	175.36(14)
O(3)-Mn(3)-O(33)	173.57(13)	O(12)-Mn(4)-O(45)	90.85(13)
O(2)-Mn(3)-O(33)	91.72(12)	O(1)-Mn(4)-O(45)	91.64(13)
O(4)-Mn(3)-O(33)	92.39(13)	O(3)-Mn(4)-O(45)	96.93(13)
O(9)-Mn(3)-Mn(9)	41.29(9)	O(11)-Mn(4)-Mn(11)	42.05(9)
O(10)-Mn(3)-Mn(9)	43.87(9)	O(4)-Mn(4)-Mn(11)	96.14(9)
O(3)-Mn(3)-Mn(9)	99.85(9)	O(12)-Mn(4)-Mn(11)	42.68(9)
O(2)-Mn(3)-Mn(9)	139.32(9)	O(1)-Mn(4)-Mn(11)	142.00(9)
O(4)-Mn(3)-Mn(9)	141.41(9)	O(3)-Mn(4)-Mn(11)	136.70(9)
O(33)-Mn(3)-Mn(9)	86.55(9)	O(45)-Mn(4)-Mn(11)	86.02(10)
O(9)-Mn(3)-Mn(4)	134.28(10)	O(11)-Mn(4)-Mn(1)	135.21(10)
O(10)-Mn(3)-Mn(4)	90.07(9)	O(4)-Mn(4)-Mn(1)	42.91(9)
O(3)-Mn(3)-Mn(4)	42.39(9)	O(12)-Mn(4)-Mn(1)	89.56(9)
O(2)-Mn(3)-Mn(4)	84.91(9)	O(1)-Mn(4)-Mn(1)	41.84(9)
O(4)-Mn(3)-Mn(4)	41.54(8)	O(3)-Mn(4)-Mn(1)	85.89(9)
O(33)-Mn(3)-Mn(4)	133.67(10)	O(45)-Mn(4)-Mn(1)	132.62(10)
Mn(9)-Mn(3)-Mn(4)	124.16(3)	Mn(11)-Mn(4)-Mn(1)	122.95(3)
O(9)-Mn(3)-Mn(2)	90.03(10)	O(11)-Mn(4)-Mn(3)	87.86(9)
O(10)-Mn(3)-Mn(2)	134.29(10)	O(4)-Mn(4)-Mn(3)	43.21(9)
O(3)-Mn(3)-Mn(2)	42.37(9)	O(12)-Mn(4)-Mn(3)	130.11(9)
O(2)-Mn(3)-Mn(2)	41.65(9)	O(1)-Mn(4)-Mn(3)	87.07(9)
O(4)-Mn(3)-Mn(2)	85.30(9)	O(3)-Mn(4)-Mn(3)	42.05(9)
O(33)-Mn(3)-Mn(2)	132.97(9)	O(45)-Mn(4)-Mn(3)	138.67(10)
Mn(9)-Mn(3)-Mn(2)	122.51(3)	Mn(11)-Mn(4)-Mn(3)	118.71(3)
Mn(4)-Mn(3)-Mn(2)	62.58(2)	Mn(1)-Mn(4)-Mn(3)	63.22(2)
O(9)-Mn(3)-Mn(1)	137.79(10)	O(11)-Mn(4)-Mn(2)	134.95(9)
O(10)-Mn(3)-Mn(1)	137.43(9)	O(4)-Mn(4)-Mn(2)	83.73(9)
O(3)-Mn(3)-Mn(1)	81.86(9)	O(12)-Mn(4)-Mn(2)	140.25(9)
O(2)-Mn(3)-Mn(1)	39.56(9)	O(1)-Mn(4)-Mn(2)	40.98(9)
O(4)-Mn(3)-Mn(1)	39.71(8)	O(3)-Mn(4)-Mn(2)	40.30(9)
O(33)-Mn(3)-Mn(1)	91.73(9)	O(45)-Mn(4)-Mn(2)	94.33(10)
Mn(9)-Mn(3)-Mn(1)	177.95(3)	Mn(11)-Mn(4)-Mn(2)	177.00(3)
Mn(4)-Mn(3)-Mn(1)	57.88(2)	Mn(1)-Mn(4)-Mn(2)	58.73(2)
Mn(2)-Mn(3)-Mn(1)	58.13(2)	Mn(3)-Mn(4)-Mn(2)	59.32(2)
O(11)-Mn(4)-O(4)	92.48(13)	O(5)-Mn(5)-O(6)	83.27(13)
O(11)-Mn(4)-O(12)	84.08(13)	O(5)-Mn(5)-O(19)	174.88(15)

Table A-14. Continued.

O(6)-Mn(5)-O(19)	95.81(14)	O(7)-Mn(7)-O(27)	86.70(13)
O(5)-Mn(5)-O(16)	95.08(13)	O(28)-Mn(7)-O(27)	88.62(14)
O(6)-Mn(5)-O(16)	177.22(14)	O(25)-Mn(7)-O(27)	83.14(14)
O(19)-Mn(5)-O(16)	85.64(14)	O(23)-Mn(7)-O(27)	174.13(13)
O(5)-Mn(5)-O(18)	93.79(14)	O(8)-Mn(7)-Mn(2)	41.56(9)
O(6)-Mn(5)-O(18)	93.54(14)	O(7)-Mn(7)-Mn(2)	42.39(9)
O(19)-Mn(5)-O(18)	91.28(15)	O(28)-Mn(7)-Mn(2)	135.46(10)
O(16)-Mn(5)-O(18)	88.79(14)	O(25)-Mn(7)-Mn(2)	134.07(10)
O(5)-Mn(5)-O(13)	85.63(13)	O(23)-Mn(7)-Mn(2)	103.83(9)
O(6)-Mn(5)-O(13)	87.20(13)	O(27)-Mn(7)-Mn(2)	78.77(9)
O(19)-Mn(5)-O(13)	89.30(14)	O(9)-Mn(8)-O(29)	177.55(13)
O(16)-Mn(5)-O(13)	90.45(14)	O(9)-Mn(8)-O(8)	88.63(12)
O(18)-Mn(5)-O(13)	179.01(14)	O(29)-Mn(8)-O(8)	89.01(13)
O(5)-Mn(5)-Mn(1)	41.89(9)	O(9)-Mn(8)-O(30)	90.21(13)
O(6)-Mn(5)-Mn(1)	42.20(9)	O(29)-Mn(8)-O(30)	92.15(13)
O(19)-Mn(5)-Mn(1)	136.15(11)	O(8)-Mn(8)-O(30)	178.78(13)
O(16)-Mn(5)-Mn(1)	135.76(10)	O(9)-Mn(8)-O(48)	91.41(13)
O(18)-Mn(5)-Mn(1)	101.40(10)	O(29)-Mn(8)-O(48)	89.36(14)
O(13)-Mn(5)-Mn(1)	78.71(9)	O(8)-Mn(8)-O(48)	92.85(14)
O(6)-Mn(6)-O(7)	93.64(13)	O(30)-Mn(8)-O(48)	86.80(15)
O(6)-Mn(6)-O(24)	174.33(14)	O(9)-Mn(8)-O(47)	86.21(13)
O(7)-Mn(6)-O(24)	90.74(14)	O(29)-Mn(8)-O(47)	93.23(14)
O(6)-Mn(6)-O(20)	92.76(14)	O(8)-Mn(8)-O(47)	92.08(13)
O(7)-Mn(6)-O(20)	173.61(14)	O(30)-Mn(8)-O(47)	88.21(14)
O(24)-Mn(6)-O(20)	82.88(14)	O(48)-Mn(8)-O(47)	174.47(15)
O(6)-Mn(6)-O(22)	93.50(13)	O(9)-Mn(9)-O(10)	82.53(13)
O(7)-Mn(6)-O(22)	93.99(13)	O(9)-Mn(9)-O(31)	96.36(13)
O(24)-Mn(6)-O(22)	89.78(15)	O(10)-Mn(9)-O(31)	175.81(14)
O(20)-Mn(6)-O(22)	85.66(14)	O(9)-Mn(9)-O(36)	174.82(14)
O(6)-Mn(6)-O(21)	95.27(14)	O(10)-Mn(9)-O(36)	95.18(13)
O(7)-Mn(6)-O(21)	91.72(15)	O(31)-Mn(9)-O(36)	85.59(14)
O(24)-Mn(6)-O(21)	80.99(16)	O(9)-Mn(9)-O(32)	87.32(13)
O(20)-Mn(6)-O(21)	87.65(16)	O(10)-Mn(9)-O(32)	86.58(12)
O(22)-Mn(6)-O(21)	169.21(15)	O(31)-Mn(9)-O(32)	89.33(13)
O(8)-Mn(7)-O(7)	82.99(13)	O(36)-Mn(9)-O(32)	87.90(13)
O(8)-Mn(7)-O(28)	95.83(13)	O(9)-Mn(9)-O(34)	94.24(13)
O(7)-Mn(7)-O(28)	175.22(14)	O(10)-Mn(9)-O(34)	95.68(13)
O(8)-Mn(7)-O(25)	170.03(14)	O(31)-Mn(9)-O(34)	88.43(14)
O(7)-Mn(7)-O(25)	95.10(13)	O(36)-Mn(9)-O(34)	90.61(14)
O(28)-Mn(7)-O(25)	85.27(14)	O(32)-Mn(9)-O(34)	177.40(13)
O(8)-Mn(7)-O(23)	98.46(13)	O(9)-Mn(9)-Mn(3)	40.64(9)
O(7)-Mn(7)-O(23)	91.76(13)	O(10)-Mn(9)-Mn(3)	42.69(9)
O(28)-Mn(7)-O(23)	93.00(14)	O(31)-Mn(9)-Mn(3)	135.44(10)
O(25)-Mn(7)-O(23)	91.37(14)	O(36)-Mn(9)-Mn(3)	136.17(10)
O(8)-Mn(7)-O(27)	86.98(13)	O(32)-Mn(9)-Mn(3)	79.62(9)

Table A-14. Continued.

O(34)-Mn(9)-Mn(3)	102.92(9)	O(12)-Mn(12)-O(17)	95.74(14)
O(10)-Mn(10)-O(11)	94.83(13)	O(43)-Mn(12)-O(17)	84.96(15)
O(10)-Mn(10)-O(40)	174.45(14)	O(15)-Mn(12)-O(17)	86.83(16)
O(11)-Mn(10)-O(40)	89.57(13)	O(5)-Mn(12)-O(46)	89.06(14)
O(10)-Mn(10)-O(37)	92.49(13)	O(12)-Mn(12)-O(46)	93.79(13)
O(11)-Mn(10)-O(37)	170.95(13)	O(43)-Mn(12)-O(46)	91.78(15)
O(40)-Mn(10)-O(37)	83.46(14)	O(15)-Mn(12)-O(46)	83.32(15)
O(10)-Mn(10)-O(38)	94.45(13)	O(17)-Mn(12)-O(46)	169.98(15)
O(11)-Mn(10)-O(38)	93.09(13)	Mn(1)-O(1)-Mn(4)	95.48(13)
O(40)-Mn(10)-O(38)	88.67(14)	Mn(1)-O(1)-Mn(2)	94.66(13)
O(37)-Mn(10)-O(38)	81.04(14)	Mn(4)-O(1)-Mn(2)	99.59(13)
O(10)-Mn(10)-O(35)	94.98(13)	Mn(1)-O(2)-Mn(2)	95.36(13)
O(11)-Mn(10)-O(35)	97.76(14)	Mn(1)-O(2)-Mn(3)	99.96(13)
O(40)-Mn(10)-O(35)	81.06(14)	Mn(2)-O(2)-Mn(3)	95.92(12)
O(37)-Mn(10)-O(35)	86.87(14)	Mn(3)-O(3)-Mn(4)	95.57(13)
O(38)-Mn(10)-O(35)	164.96(13)	Mn(3)-O(3)-Mn(2)	96.32(13)
O(11)-Mn(11)-O(12)	83.91(13)	Mn(4)-O(3)-Mn(2)	100.07(13)
O(11)-Mn(11)-O(42)	178.84(14)	Mn(4)-O(4)-Mn(1)	94.96(13)
O(12)-Mn(11)-O(42)	95.11(13)	Mn(4)-O(4)-Mn(3)	95.25(13)
O(11)-Mn(11)-O(41)	94.39(13)	Mn(1)-O(4)-Mn(3)	99.75(13)
O(12)-Mn(11)-O(41)	171.53(14)	Mn(12)-O(5)-Mn(5)	129.49(17)
O(42)-Mn(11)-O(41)	86.48(13)	Mn(12)-O(5)-Mn(1)	132.24(16)
O(11)-Mn(11)-O(39)	94.51(13)	Mn(5)-O(5)-Mn(1)	96.27(13)
O(12)-Mn(11)-O(39)	95.77(12)	Mn(1)-O(6)-Mn(5)	95.46(13)
O(42)-Mn(11)-O(39)	86.21(13)	Mn(1)-O(6)-Mn(6)	132.03(16)
O(41)-Mn(11)-O(39)	92.64(14)	Mn(5)-O(6)-Mn(6)	123.72(16)
O(11)-Mn(11)-O(44)	87.91(13)	Mn(2)-O(7)-Mn(7)	94.40(14)
O(12)-Mn(11)-O(44)	84.64(13)	Mn(2)-O(7)-Mn(6)	135.14(17)
O(42)-Mn(11)-O(44)	91.38(13)	Mn(7)-O(7)-Mn(6)	125.39(16)
O(41)-Mn(11)-O(44)	87.00(14)	Mn(2)-O(8)-Mn(7)	96.20(14)
O(39)-Mn(11)-O(44)	177.58(13)	Mn(2)-O(8)-Mn(8)	131.32(16)
O(11)-Mn(11)-Mn(4)	41.83(9)	Mn(7)-O(8)-Mn(8)	124.25(15)
O(12)-Mn(11)-Mn(4)	42.73(9)	Mn(3)-O(9)-Mn(9)	98.07(14)
O(42)-Mn(11)-Mn(4)	137.11(10)	Mn(3)-O(9)-Mn(8)	133.29(16)
O(41)-Mn(11)-Mn(4)	133.86(10)	Mn(9)-O(9)-Mn(8)	127.81(16)
O(39)-Mn(11)-Mn(4)	102.70(9)	Mn(10)-O(10)-Mn(3)	132.66(16)
O(44)-Mn(11)-Mn(4)	79.22(9)	Mn(10)-O(10)-Mn(9)	123.74(16)
O(5)-Mn(12)-O(12)	95.31(13)	Mn(3)-O(10)-Mn(9)	93.45(12)
O(5)-Mn(12)-O(43)	173.48(14)	Mn(4)-O(11)-Mn(11)	96.11(13)
O(12)-Mn(12)-O(43)	91.09(13)	Mn(4)-O(11)-Mn(10)	133.28(16)
O(5)-Mn(12)-O(15)	91.76(14)	Mn(11)-O(11)-Mn(10)	124.60(16)
O(12)-Mn(12)-O(15)	172.32(14)	Mn(12)-O(12)-Mn(11)	129.12(16)
O(43)-Mn(12)-O(15)	81.92(14)	Mn(12)-O(12)-Mn(4)	131.00(16)
O(5)-Mn(12)-O(17)	93.12(14)	Mn(11)-O(12)-Mn(4)	94.60(13)

Table A-15. Selected interatomic distances (Å) and angles (°) for  
 (NMe<sub>4</sub>)<sub>2</sub>[Mn<sub>12</sub>O<sub>12</sub>(O<sub>2</sub>CC<sub>6</sub>F<sub>5</sub>)<sub>16</sub>(H<sub>2</sub>O)<sub>4</sub>]·6C<sub>7</sub>H<sub>8</sub> (**22**·6C<sub>7</sub>H<sub>8</sub>).

Mn(1)-O(4)	1.832(4)	Mn(3)-O(10)	1.949(4)
Mn(1)-O(3)	1.869(4)	Mn(3)-O(11)	2.197(4)
Mn(1)-O(2)	1.889(3)	Mn(3)-O(9)	2.268(4)
Mn(1)-O(1a)	1.921(3)	Mn(4)-O(6)	1.878(4)
Mn(1)-O(1)	1.945(4)	Mn(4)-O(3)	1.882(4)
Mn(1)-O(5)	1.947(3)	Mn(4)-O(14)	1.967(4)
Mn(1)-Mn(5)	2.7717(12)	Mn(4)-O(13)	1.979(4)
Mn(1)-Mn(2)	2.8206(12)	Mn(4)-O(15)	2.151(4)
Mn(1)-Mn(2a)	2.8582(12)	Mn(4)-O(12)	2.180(4)
Mn(1)-Mn(1a)	2.9588(17)	Mn(5)-O(4)	1.862(4)
Mn(2)-O(7)	1.830(4)	Mn(5)-O(3)	1.904(4)
Mn(2)-O(6)	1.877(4)	Mn(5)-O(17)	1.955(4)
Mn(2)-O(1)	1.893(3)	Mn(5)-O(18)	1.980(4)
Mn(2)-O(2a)	1.921(4)	Mn(5)-O(19)	2.171(4)
Mn(2)-O(8)	1.940(4)	Mn(5)-O(16)	2.193(4)
Mn(2)-O(2)	1.942(4)	Mn(6)-O(7a)	2.075(4)
Mn(2)-Mn(3)	2.7638(13)	Mn(6)-O(4)	2.117(4)
Mn(2)-Mn(1a)	2.8582(12)	Mn(6)-O(21)	2.126(5)
Mn(2)-Mn(2a)	2.9392(18)	Mn(6)-O(22)	2.139(5)
Mn(3)-O(7)	1.841(4)	Mn(6)-O(20)	2.219(4)
Mn(3)-O(6)	1.901(4)	Mn(6)-O(23)	2.281(4)
Mn(3)-O(24a)	1.944(5)		
O(4)-Mn(1)-O(3)	84.26(16)	O(4)-Mn(1)-Mn(2)	133.43(11)
O(4)-Mn(1)-O(2)	91.34(15)	O(3)-Mn(1)-Mn(2)	87.87(11)
O(3)-Mn(1)-O(2)	93.23(15)	O(2)-Mn(1)-Mn(2)	43.33(11)
O(4)-Mn(1)-O(1a)	100.12(15)	O(1a)-Mn(1)-Mn(2)	85.99(11)
O(3)-Mn(1)-O(1a)	173.85(16)	O(1)-Mn(1)-Mn(2)	42.00(10)
O(2)-Mn(1)-O(1a)	82.40(14)	O(5)-Mn(1)-Mn(2)	134.36(12)
O(4)-Mn(1)-O(1)	175.42(15)	Mn(5)-Mn(1)-Mn(2)	121.34(4)
O(3)-Mn(1)-O(1)	95.23(15)	O(4)-Mn(1)-Mn(2a)	92.62(11)
O(2)-Mn(1)-O(1)	84.14(15)	O(3)-Mn(1)-Mn(2a)	134.95(11)
O(1a)-Mn(1)-O(1)	80.06(16)	O(2)-Mn(1)-Mn(2a)	41.81(11)
O(4)-Mn(1)-O(5)	91.76(15)	O(1a)-Mn(1)-Mn(2a)	41.10(10)
O(3)-Mn(1)-O(5)	91.45(15)	O(1)-Mn(1)-Mn(2a)	84.52(10)
O(2)-Mn(1)-O(5)	174.62(16)	O(5)-Mn(1)-Mn(2a)	133.59(11)
O(1a)-Mn(1)-O(5)	92.72(15)	Mn(5)-Mn(1)-Mn(2a)	125.05(4)
O(1)-Mn(1)-O(5)	92.80(15)	Mn(2)-Mn(1)-Mn(2a)	62.34(4)
O(4)-Mn(1)-Mn(5)	41.78(11)	O(4)-Mn(1)-Mn(1a)	140.45(12)
O(3)-Mn(1)-Mn(5)	43.21(11)	O(3)-Mn(1)-Mn(1a)	135.00(12)
O(2)-Mn(1)-Mn(5)	99.26(11)	O(2)-Mn(1)-Mn(1a)	83.07(11)
O(1a)-Mn(1)-Mn(5)	141.68(11)	O(1a)-Mn(1)-Mn(1a)	40.36(11)
O(1)-Mn(1)-Mn(5)	138.26(11)	O(1)-Mn(1)-Mn(1a)	39.78(10)
O(5)-Mn(1)-Mn(5)	85.97(11)	O(5)-Mn(1)-Mn(1a)	91.74(11)

Table A-15. Continued.

Mn(5)-Mn(1)-Mn(1a)	176.96(4)	O(2)-Mn(2)-Mn(2a)	40.18(10)
Mn(2)-Mn(1)-Mn(1a)	59.22(3)	Mn(3)-Mn(2)-Mn(2a)	175.90(3)
Mn(2a)-Mn(1)-Mn(1a)	57.98(3)	Mn(1)-Mn(2)-Mn(2a)	59.46(3)
O(7)-Mn(2)-O(6)	84.07(16)	Mn(1a)-Mn(2)-Mn(2a)	58.21(3)
O(7)-Mn(2)-O(1)	94.19(16)	O(7)-Mn(3)-O(6)	83.09(16)
O(6)-Mn(2)-O(1)	94.06(15)	O(7)-Mn(3)-O(24a)	94.65(18)
O(7)-Mn(2)-O(2a)	97.80(16)	O(6)-Mn(3)-O(24a)	171.60(18)
O(6)-Mn(2)-O(2a)	176.02(15)	O(7)-Mn(3)-O(10)	179.34(19)
O(1)-Mn(2)-O(2a)	82.31(14)	O(6)-Mn(3)-O(10)	97.45(17)
O(7)-Mn(2)-O(8)	90.73(16)	O(24a)-Mn(3)-O(10)	84.77(19)
O(6)-Mn(2)-O(8)	92.33(16)	O(7)-Mn(3)-O(11)	90.29(15)
O(1)-Mn(2)-O(8)	172.30(17)	O(6)-Mn(3)-O(11)	93.80(15)
O(2a)-Mn(2)-O(8)	91.17(16)	O(24a)-Mn(3)-O(11)	94.30(17)
O(7)-Mn(2)-O(2)	177.92(16)	O(10)-Mn(3)-O(11)	90.06(17)
O(6)-Mn(2)-O(2)	97.21(15)	O(7)-Mn(3)-O(9)	86.53(16)
O(1)-Mn(2)-O(2)	84.09(15)	O(6)-Mn(3)-O(9)	85.64(16)
O(2a)-Mn(2)-O(2)	80.83(16)	O(24a)-Mn(3)-O(9)	86.16(17)
O(8)-Mn(2)-O(2)	90.87(15)	O(10)-Mn(3)-O(9)	93.12(17)
O(7)-Mn(2)-Mn(3)	41.30(12)	O(11)-Mn(3)-O(9)	176.82(16)
O(6)-Mn(2)-Mn(3)	43.33(11)	O(7)-Mn(3)-Mn(2)	41.00(12)
O(1)-Mn(2)-Mn(3)	100.96(11)	O(6)-Mn(3)-Mn(2)	42.64(11)
O(2a)-Mn(2)-Mn(3)	138.91(12)	O(24a)-Mn(3)-Mn(2)	133.55(14)
O(8)-Mn(2)-Mn(3)	86.64(12)	O(10)-Mn(3)-Mn(2)	139.47(14)
O(2)-Mn(2)-Mn(3)	140.18(11)	O(11)-Mn(3)-Mn(2)	97.99(11)
O(2)-Mn(2)-Mn(3)	140.18(11)	O(9)-Mn(3)-Mn(2)	79.47(12)
O(7)-Mn(2)-Mn(1)	136.67(12)	O(6)-Mn(4)-O(3)	93.88(15)
O(6)-Mn(2)-Mn(1)	89.79(11)	O(6)-Mn(4)-O(14)	173.18(18)
O(1)-Mn(2)-Mn(1)	43.41(11)	O(3)-Mn(4)-O(14)	90.99(17)
O(2a)-Mn(2)-Mn(1)	86.45(11)	O(6)-Mn(4)-O(13)	92.73(17)
O(8)-Mn(2)-Mn(1)	132.44(12)	O(3)-Mn(4)-O(13)	172.52(17)
O(2)-Mn(2)-Mn(1)	41.86(10)	O(14)-Mn(4)-O(13)	82.71(18)
Mn(3)-Mn(2)-Mn(1)	123.97(4)	O(6)-Mn(4)-O(15)	93.02(16)
O(7)-Mn(2)-Mn(1a)	92.94(12)	O(3)-Mn(4)-O(15)	96.73(16)
O(6)-Mn(2)-Mn(1a)	135.62(11)	O(14)-Mn(4)-O(15)	81.66(17)
O(1)-Mn(2)-Mn(1a)	41.85(10)	O(13)-Mn(4)-O(15)	86.38(17)
O(2a)-Mn(2)-Mn(1a)	40.96(10)	O(6)-Mn(4)-O(12)	97.24(16)
O(8)-Mn(2)-Mn(1a)	132.03(12)	O(3)-Mn(4)-O(12)	94.78(16)
O(2)-Mn(2)-Mn(1a)	84.99(10)	O(14)-Mn(4)-O(12)	87.10(16)
Mn(3)-Mn(2)-Mn(1a)	124.77(4)	O(13)-Mn(4)-O(12)	80.93(17)
Mn(1)-Mn(2)-Mn(1a)	62.80(4)	O(15)-Mn(4)-O(12)	164.02(16)
O(7)-Mn(2)-Mn(2a)	138.51(13)	O(4)-Mn(5)-O(3)	82.49(15)
O(6)-Mn(2)-Mn(2a)	137.39(12)	O(4)-Mn(5)-O(17)	173.93(16)
O(1)-Mn(2)-Mn(2a)	83.11(11)	O(3)-Mn(5)-O(17)	95.87(17)
O(2a)-Mn(2)-Mn(2a)	40.74(11)	O(4)-Mn(5)-O(18)	97.44(17)
O(8)-Mn(2)-Mn(2a)	89.28(12)	O(3)-Mn(5)-O(18)	177.46(16)

Table A-15. Continued.

O(17)-Mn(5)-O(18)	84.46(18)	O(22)-Mn(6)-O(20)	98.7(2)
O(4)-Mn(5)-O(19)	86.89(15)	O(7a)-Mn(6)-O(23)	95.29(15)
O(3)-Mn(5)-O(19)	87.04(15)	O(4)-Mn(6)-O(23)	80.15(15)
O(17)-Mn(5)-O(19)	87.18(16)	O(21)-Mn(6)-O(23)	93.98(17)
O(18)-Mn(5)-O(19)	95.49(16)	O(22)-Mn(6)-O(23)	87.9(2)
O(4)-Mn(5)-O(16)	94.64(15)	O(20)-Mn(6)-O(23)	173.26(17)
O(3)-Mn(5)-O(16)	93.13(15)	Mn(2)-O(1)-Mn(1a)	97.05(15)
O(17)-Mn(5)-O(16)	91.29(16)	Mn(2)-O(1)-Mn(1)	94.59(15)
O(18)-Mn(5)-O(16)	84.34(16)	Mn(1a)-O(1)-Mn(1)	99.87(16)
O(19)-Mn(5)-O(16)	178.47(15)	Mn(1)-O(2)-Mn(2a)	97.23(15)
O(4)-Mn(5)-Mn(1)	40.96(11)	Mn(1)-O(2)-Mn(2)	94.81(16)
O(3)-Mn(5)-Mn(1)	42.24(11)	Mn(2a)-O(2)-Mn(2)	99.08(16)
O(17)-Mn(5)-Mn(1)	136.23(13)	Mn(1)-O(3)-Mn(4)	135.0(2)
O(18)-Mn(5)-Mn(1)	138.03(13)	Mn(1)-O(3)-Mn(5)	94.55(16)
O(19)-Mn(5)-Mn(1)	79.95(11)	Mn(4)-O(3)-Mn(5)	124.08(18)
O(16)-Mn(5)-Mn(1)	101.19(11)	Mn(1)-O(4)-Mn(5)	97.25(17)
O(7a)-Mn(6)-O(4)	93.37(14)	Mn(1)-O(4)-Mn(6)	129.64(18)
O(7a)-Mn(6)-O(21)	170.29(17)	Mn(5)-O(4)-Mn(6)	125.87(18)
O(4)-Mn(6)-O(21)	91.03(16)	Mn(2)-O(6)-Mn(4)	133.0(2)
O(7a)-Mn(6)-O(22)	89.87(17)	Mn(2)-O(6)-Mn(3)	94.03(17)
O(4)-Mn(6)-O(22)	167.8(2)	Mn(4)-O(6)-Mn(3)	124.2(2)
O(21)-Mn(6)-O(22)	87.61(19)	Mn(2)-O(7)-Mn(3)	97.70(18)
O(7a)-Mn(6)-O(20)	83.05(16)	Mn(2)-O(7)-Mn(6a)	130.03(19)
O(4)-Mn(6)-O(20)	93.40(15)	Mn(3)-O(7)-Mn(6a)	127.57(19)
O(21)-Mn(6)-O(20)	88.06(18)		

---

Table A-16. Selected interatomic distances (Å) and angles (°) for  
 $[\text{Mn}_{12}\text{O}_{12}(\text{O}_2\text{CCH}_2\text{Br})_{16}(\text{H}_2\text{O})_4] \cdot 4\text{CH}_2\text{Cl}_2$  (**26**·4CH<sub>2</sub>Cl<sub>2</sub>).

Mn(1)-O(3a)	1.898(4)	Mn(2)-O(9)	2.220(5)
Mn(1)-O(2)	1.898(4)	Mn(2)-Mn(3)	2.7938(12)
Mn(1)-O(11)	1.959(4)	Mn(3)-O(3)	1.865(4)
Mn(1)-O(5)	1.970(5)	Mn(3)-O(2)	1.878(4)
Mn(1)-O(7)	2.114(5)	Mn(3)-O(4b)	1.902(4)
Mn(1)-O(1)	2.193(5)	Mn(3)-O(4c)	1.922(4)
Mn(2)-O(3)	1.871(4)	Mn(3)-O(10)	1.923(4)
Mn(2)-O(2)	1.902(4)	Mn(3)-O(4)	1.934(4)
Mn(2)-O(6)	1.932(4)	Mn(3)-Mn(3a)	2.8180(14)
Mn(2)-O(12b)	1.948(5)	Mn(3)-Mn(3b)	2.8180(14)
Mn(2)-O(8)	2.187(5)	Mn(3)-Mn(3c)	2.9851(16)
O(3a)-Mn(1)-O(2)	92.35(17)	O(6)-Mn(2)-Mn(3)	137.96(15)
O(3a)-Mn(1)-O(11)	91.35(18)	O(12b)-Mn(2)-Mn(3)	135.42(15)
O(2)-Mn(1)-O(11)	175.94(19)	O(8)-Mn(2)-Mn(3)	97.83(12)
O(3a)-Mn(1)-O(5)	172.88(18)	O(9)-Mn(2)-Mn(3)	77.67(12)
O(2)-Mn(1)-O(5)	93.06(18)	O(3)-Mn(3)-O(2)	83.75(17)
O(11)-Mn(1)-O(5)	83.4(2)	O(3)-Mn(3)-O(4b)	89.63(18)
O(3a)-Mn(1)-O(7)	89.58(18)	O(2)-Mn(3)-O(4b)	91.05(17)
O(2)-Mn(1)-O(7)	92.73(17)	O(3)-Mn(3)-O(4c)	97.33(17)
O(11)-Mn(1)-O(7)	85.63(18)	O(2)-Mn(3)-O(4c)	175.16(18)
O(5)-Mn(1)-O(7)	94.8(2)	O(4b)-Mn(3)-O(4c)	84.25(18)
O(3a)-Mn(1)-O(1)	93.34(18)	O(3)-Mn(3)-O(10)	93.56(18)
O(2)-Mn(1)-O(1)	93.8(2)	O(2)-Mn(3)-O(10)	91.64(18)
O(11)-Mn(1)-O(1)	87.7(2)	O(4b)-Mn(3)-O(10)	176.03(17)
O(5)-Mn(1)-O(1)	81.7(2)	O(4c)-Mn(3)-O(10)	92.99(17)
O(7)-Mn(1)-O(1)	172.74(19)	O(3)-Mn(3)-O(4)	172.64(17)
O(3)-Mn(2)-O(2)	82.91(17)	O(2)-Mn(3)-O(4)	99.87(17)
O(3)-Mn(2)-O(6)	176.0(2)	O(4b)-Mn(3)-O(4)	83.91(18)
O(2)-Mn(2)-O(6)	97.27(19)	O(4c)-Mn(3)-O(4)	78.54(18)
O(3)-Mn(2)-O(12b)	95.08(19)	O(10)-Mn(3)-O(4)	92.75(17)
O(2)-Mn(2)-O(12b)	175.9(2)	O(3)-Mn(3)-Mn(2)	41.67(12)
O(6)-Mn(2)-O(12b)	84.5(2)	O(2)-Mn(3)-Mn(2)	42.69(12)
O(3)-Mn(2)-O(8)	91.34(19)	O(4b)-Mn(3)-Mn(2)	96.05(12)
O(2)-Mn(2)-O(8)	92.13(17)	O(4c)-Mn(3)-Mn(2)	138.89(12)
O(6)-Mn(2)-O(8)	92.6(2)	O(10)-Mn(3)-Mn(2)	87.90(13)
O(12b)-Mn(2)-O(8)	91.46(19)	O(4)-Mn(3)-Mn(2)	142.52(12)
O(3)-Mn(2)-O(9)	85.37(17)	O(3)-Mn(3)-Mn(3a)	131.93(14)
O(2)-Mn(2)-O(9)	84.44(17)	O(2)-Mn(3)-Mn(3a)	89.65(13)
O(6)-Mn(2)-O(9)	90.70(19)	O(4b)-Mn(3)-Mn(3a)	42.80(12)
O(12b)-Mn(2)-O(9)	91.9(2)	O(4c)-Mn(3)-Mn(3a)	86.12(11)
O(8)-Mn(2)-O(9)	175.50(17)	O(10)-Mn(3)-Mn(3a)	134.29(13)
O(3)-Mn(2)-Mn(3)	41.51(12)	O(4)-Mn(3)-Mn(3a)	42.28(11)
O(2)-Mn(2)-Mn(3)	42.00(12)	Mn(2)-Mn(3)-Mn(3a)	121.28(5)

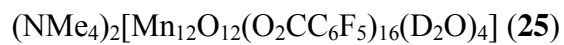
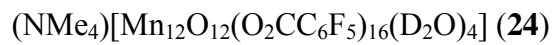
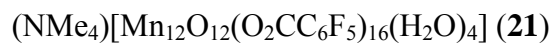
Table A-16. Continued.

O(3)-Mn(3)-Mn(3b)	86.97(13)	O(4)-Mn(3)-Mn(3c)	39.12(11)
O(2)-Mn(3)-Mn(3b)	133.35(14)	Mn(2)-Mn(3)-Mn(3c)	177.25(4)
O(4b)-Mn(3)-Mn(3b)	43.17(12)	Mn(3a)-Mn(3)-Mn(3c)	58.018(17)
O(4c)-Mn(3)-Mn(3b)	42.25(12)	Mn(3b)-Mn(3)-Mn(3c)	58.018(17)
O(10)-Mn(3)-Mn(3b)	134.60(13)	Mn(3)-O(2)-Mn(1)	132.8(2)
O(4)-Mn(3)-Mn(3b)	85.89(12)	Mn(3)-O(2)-Mn(2)	95.31(17)
Mn(2)-Mn(3)-Mn(3b)	119.24(5)	Mn(1)-O(2)-Mn(2)	122.5(2)
Mn(3a)1-Mn(3)-Mn(3b)	63.96(3)	Mn(3)-O(3)-Mn(2)	96.82(18)
O(3)-Mn(3)-Mn(3c)	136.36(13)	Mn(3)-O(3)-Mn(1b)	133.8(2)
O(2)-Mn(3)-Mn(3c)	138.73(13)	Mn(2)-O(3)-Mn(1b)	128.0(2)
O(4b)-Mn(3)-Mn(3c)	81.77(12)	Mn(3a)-O(4)-Mn(3c)	94.96(17)
O(4c)-Mn(3)-Mn(3c)	39.42(11)	Mn(3a)-O(4)-Mn(3)	94.55(17)
O(10)-Mn(3)-Mn(3c)	94.29(12)	Mn(3c)-O(4)-Mn(3)	101.46(18)

---

APPENDIX B  
LIST OF COMPOUNDS

- [Mn<sub>12</sub>O<sub>12</sub>(O<sub>2</sub>CMe)<sub>16</sub>(H<sub>2</sub>O)<sub>4</sub>]·2MeCO<sub>2</sub>H·4H<sub>2</sub>O (1)
- [Mn<sub>12</sub>O<sub>12</sub>(O<sub>2</sub>CMe)<sub>8</sub>(O<sub>3</sub>SPh)<sub>8</sub>(H<sub>2</sub>O)<sub>4</sub>] (2)
- [Mn<sub>12</sub>O<sub>12</sub>(O<sub>2</sub>CMe)<sub>12</sub>(O<sub>3</sub>SPh)<sub>4</sub>(H<sub>2</sub>O)<sub>4</sub>] (3)
- [Mn<sub>12</sub>O<sub>12</sub>(O<sub>2</sub>CMe)<sub>8</sub>(O<sub>2</sub>PPh<sub>2</sub>)<sub>8</sub>(H<sub>2</sub>O)<sub>4</sub>] (4)
- [Mn<sub>4</sub>O<sub>4</sub>(O<sub>2</sub>PPh<sub>2</sub>)<sub>6</sub>] (5)
- [Mn<sub>7</sub>O<sub>8</sub>(O<sub>2</sub>CMe)(O<sub>2</sub>SePh)<sub>8</sub>(H<sub>2</sub>O)] (6)
- [Mn<sub>7</sub>O<sub>8</sub>(O<sub>2</sub>SePh)<sub>9</sub>(H<sub>2</sub>O)] (7)
- [Mn<sub>12</sub>O<sub>12</sub>(O<sub>2</sub>CPh)<sub>16</sub>(H<sub>2</sub>O)<sub>4</sub>] (8)
- [Mn<sub>4</sub>O<sub>4</sub>(O<sub>2</sub>AsMe<sub>2</sub>)<sub>6</sub>] (9)
- {[Mn<sub>4</sub>O<sub>4</sub>(O<sub>2</sub>AsMe<sub>2</sub>)<sub>6</sub>](NO<sub>3</sub>)}<sub>2</sub> (10)
- [Mn<sub>16</sub>O<sub>8</sub>Ca<sub>4</sub>(O<sub>2</sub>CPh)<sub>8</sub>(O<sub>2</sub>AsMe<sub>2</sub>)<sub>28</sub>(NO<sub>3</sub>)<sub>4</sub>] (11)
- [Mn<sub>16</sub>O<sub>8</sub>Sr<sub>4</sub>(O<sub>2</sub>CPh)<sub>16</sub>(O<sub>2</sub>AsMe<sub>2</sub>)<sub>24</sub>] (12)
- [Mn<sub>12</sub>O<sub>12</sub>(O<sub>2</sub>CCH<sub>2</sub>Bu<sup>t</sup>)<sub>16</sub>(H<sub>2</sub>O)<sub>4</sub>] (13)
- [Mn<sub>12</sub>O<sub>12</sub>(O<sub>2</sub>CPe<sup>t</sup>)<sub>16</sub>(H<sub>2</sub>O)<sub>4</sub>] (14)
- [Mn<sub>12</sub>O<sub>12</sub>(O<sub>2</sub>CPe<sup>t</sup>)<sub>16</sub>(MeOH)<sub>4</sub>] (15)
- [Mn<sub>6</sub>O<sub>2</sub>(O<sub>2</sub>CH<sub>2</sub>)(O<sub>2</sub>CPe<sup>t</sup>)<sub>11</sub>(HO<sub>2</sub>CPe<sup>t</sup>)<sub>2</sub>(O<sub>2</sub>CMe)] (16)
- [Mn<sub>9</sub>O<sub>6</sub>(OH)(CO<sub>3</sub>)(O<sub>2</sub>CPe<sup>t</sup>)<sub>12</sub>(H<sub>2</sub>O)<sub>2</sub>] (17)
- [Mn<sub>4</sub>O<sub>2</sub>(O<sub>2</sub>CPe<sup>t</sup>)<sub>6</sub>(bpy)<sub>2</sub>] (18)
- [Mn<sub>9</sub>O<sub>7</sub>(O<sub>2</sub>CCH<sub>2</sub>Bu<sup>t</sup>)<sub>13</sub>(THF)<sub>2</sub>] (19)
- [Mn<sub>12</sub>O<sub>12</sub>(O<sub>2</sub>CC<sub>6</sub>F<sub>5</sub>)<sub>16</sub>(H<sub>2</sub>O)<sub>4</sub>] (20)



## APPENDIX C PHYSICAL MEASUREMENTS

Infrared spectra were recorded in the solid state (KBr pellets) on a Nicolet Nexus 670 FTIR spectrophotometer in the 400-4000  $\text{cm}^{-1}$  range. Elemental analyses (C, H, and N) were performed at the in-house facilities of the University of Florida Chemistry Department. Electrochemical studies were performed under argon using a BAS model CV-50W voltammetric analyzer and a standard three-electrode assembly (glassy carbon working, Pt wire auxiliary, and Ag / Ag<sub>3</sub>I<sub>4</sub> reference) with 0.1 M NBu<sup>n</sup><sub>4</sub>PF<sub>6</sub> as supporting electrolyte. No IR compensation was employed. Quoted potentials are vs the ferrocene / ferrocenium couple, used as an internal standard. The scan rates for cyclic voltammetry (CV) and differential pulse voltammetry (DPV) were 100 and 20 mV/s, respectively. Distilled solvents were employed, and the concentration of the complex was approximately 1 mM. <sup>1</sup>H NMR spectra were obtained at 300 MHz on a Varian VXR-300 spectrometer, using protio-solvent signals as internal references. <sup>19</sup>F NMR spectra were obtained at 282 MHz on a Varian VXR-300 spectrometer, using CFC<sub>3</sub> as an internal standard. Variable-temperature DC magnetic susceptibility data down to 1.80 K were collected on a Quantum Design MPMS-XL SQUID magnetometer equipped with a 70 kG (7 T) DC magnet at the University of Florida. Pascal's constants were used to estimate the diamagnetic corrections, which were subtracted from the experimental susceptibility to give the molar magnetic susceptibility ( $\chi_M$ ). AC magnetic susceptibility data were collected on the same instrument employing a 3.5 G field oscillating at frequencies up to 1500 Hz. Samples were embedded in solid eicosane, unless otherwise

stated, to prevent torquing. Magnetization vs field and temperature data were fit using the program MAGNET, and contour plots were obtained using the program GRID, both written at Indiana University by E. R. D. Low temperature ( $< 1.8$  K) hysteresis loop and DC relaxation measurements were performed at Grenoble using an array of micro-SQUIDS.<sup>65</sup> The high sensitivity of this magnetometer allows the study of single crystals of SMMs on the order of  $10$ - $500$   $\mu\text{m}$ . The field can be applied in any direction by separately driving three orthogonal coils.

INS experiments were performed on the time-of-flight spectrometer NEAT at the Hahn-Meitner Institute (HMI) in Berlin, using cold neutrons of wavelength  $\lambda = 6.0$   $\text{\AA}$ . This resulted in a resolution of about  $70$   $\mu\text{eV}$  (fwhm) at the elastic line. The polycrystalline powder samples were placed under helium into a rectangular flat aluminum container of dimensions  $43 \times 61 \times 5$   $\text{mm}^3$ , with an accessible sample volume of  $30 \times 50 \times 3$   $\text{mm}^3$  for **23** and **25** and  $30 \times 50 \times 2$   $\text{mm}^3$  for **24**. Data were collected at several temperatures between  $1.8$  and  $20$  K and corrected for the detector efficiency by means of the spectrum of vanadium metal. Data reduction was performed using the program INX. The background of each spectrum was estimated from a polynomial fit to the baseline of the low temperature spectra for each compound and then subtracted. The analysis is limited to the neutron energy loss side due to the experimental setup which was chosen to have its best resolution on the neutron energy loss side. Therefore, transitions on the neutron energy gain side could not be resolved and usefully analyzed.

<sup>55</sup>Mn NMR measurements were made using a home-built MagRes2000 Integrated Wideband NMR spectrometer with quadrature detection and a home-built probe.<sup>202</sup> The crystal samples were prepared by removing the crystal from its mother liquor and

immediately covering in 5-minute epoxy to prevent interstitial solvent loss. Immediately after the epoxy was set, the sample was mounted into the coil and cooled in a dewar of liquid helium. Aligned powder samples were made by crushing the crystals and then mixing with Stycast 1266 epoxy, which was allowed to cure overnight at room temperature in a field of 8.5 T. Data was acquired at  $\sim 2$  K, below the blocking temperature of  $\sim 3$  K as the signal deteriorates rapidly above the blocking temperature because of short  $T_2$  times. A Hahn echo pulse sequence was used while the frequency was scanned from 220-400 MHz, usually taking 0.1-0.2 MHz steps. Frequency scans were necessary because of the large peak widths ( $\sim 5$ -20 MHz). Pulse lengths were on the order of hundreds of nanoseconds giving a bandwidth of roughly  $\sim 2$  MHz. After the scan, the data was processed using a Fast Fourier Transform Sum (FFT Sum). For angular measurements of **26** in its *ab* plane, the crystal was cooled to 2 K in a field of 5 T. Crystal orientation was possible with a relative accuracy of  $0.2^\circ$ .

High frequency electron paramagnetic resonance (HFEPR) measurements were performed at various frequencies, ranging from  $\sim 50$  GHz to  $\sim 350$  GHz by sweeping the magnetic field at fixed microwave frequencies and temperatures. A millimeter-wave vector network analyzer (MVNA) was used as a microwave source and the use of a high sensitivity cavity perturbation technique<sup>203</sup> allowed the detection of the EPR signals. The measurements were performed using a commercial superconducting solenoid capable of producing fields of up to 9 T. In all cases, the temperature was stabilized ( $\pm 0.01$  K) relative to a calibrated Cernox<sup>TM</sup> resistance sensor. We have outfitted our cavities with rotatable endplates for sample orientation with  $0.18^\circ$  resolution.<sup>204</sup> The single crystal was optimally positioned and oriented in the cavity driven at the fundamental TE<sub>01n</sub> modes

( $n = \text{integer}$ ), and the DC field was aligned either along the easy-axis or in the hard plane of the sample. The field orientation relative to the easy-axis (or hard plane) is determined by performing angle-dependent HF-EPR spectra. The hard plane angle-dependent study is also done by rotating the DC field in the hard plane. In order to avoid solvent loss in the EPR measurements, the sample was removed from the mother liquor, immediately sealed in silicone grease, and quickly transferred to the cryostat (ca. 5 minutes) where it was cooled under atmospheric pressure helium gas.

## LIST OF REFERENCES

- (1) Miller, J. S.; Epstein, A. J. *MRS Bulletin* **2000**, *25*, 21.
- (2) West, A. R. *Solid State Chemistry and Its Applications*; Wiley: New York, 1984; pp 553-582.
- (3) *Magnetism: A Supramolecular Function*; Kahn, O., Ed.; Kluwer: Dordrecht, 1996; pp 357-642.
- (4) Jiles, D. *Introduction to Magnetism and Magnetic Materials*; Chapman and Hall: New York, 1991, pp 1-344.
- (5) Huheey, J. E.; Keiter, E. A.; Keiter, R. L. *Inorganic Chemistry: Principles of Structure and Reactivity*; 4<sup>th</sup> ed.; HarperCollins College: New York, 1993; pp 459-468.
- (6) Smart, L.; Moore, E. *Solid State Chemistry: An Introduction*; Chapman and Hall: New York, 1992; pp 294-320.
- (7) West, A. R. *Basic Solid State Chemistry*; Wiley: New York, 1988; pp 342-375.
- (8) Kahn, O. *Molecular Magnetism*; VCH Publishers: New York, 1993; pp 287-328.
- (9) Rittner, M. Nanomagnetism: Materials, Devices and Markets, Report GB293, Business Communications Company, Norwalk, CT, 2004.
- (10) Grochowski, E.; Halem, R. D. *IBM Systems Journal* **2003**, *42*, 338.
- (11) Aromí, G.; Aubin, S. M. J.; Bolcar, M. A.; Christou, G.; Eppley, H. J.; Folting, K.; Hendrickson, D. N.; Huffman, J. C.; Squire, R. C.; Tsai, H.-L.; Wang, S.; Wemple, M. *Polyhedron* **1998**, *17*, 3005.
- (12) Aubin, S. M. J.; Wemple, M. W.; Adams, D. M.; Tsai, H.-L.; Christou, G.; Hendrickson, D. N. *J. Am. Chem. Soc.* **1996**, *118*, 7746.
- (13) Eppley, H. J.; Tsai, H.-L.; de Vries, N.; Folting, K.; Christou, G.; Hendrickson, D. N. *J. Am. Chem. Soc.* **1995**, *117*, 301.
- (14) Miller, J. S. *Adv. Mater.* **1994**, *6*, 4.

- (15) Wickman, H. H.; Trozzolo, A. M.; Williams, H. J.; Hull, G. W.; Merritt, F. R. *Phys. Rev.* **1967**, *155*, 563.
- (16) Miller, J. S.; Calabrese, J. C.; Rommelmann, H.; Chittipeddi, S. R.; Zhang, J. H.; Reiff, W. M.; Epstein, A. J. *J. Am. Chem. Soc.* **1987**, *109*, 769.
- (17) Miller, J. S.; Epstein, A. J.; Reiff, W. M. *Chem. Rev.* **1988**, *88*, 201.
- (18) Kahn, O.; Pei, Y.; Nakatani, K.; Journaeux, Y. *Mol. Cryst. Liq. Cryst.* **1989**, *176*, 481.
- (19) Christou, G.; Gatteschi, D.; Hendrickson, D. N.; Sessoli, R. *MRS Bulletin* **2000**, *25*, 66.
- (20) Aubin, S. M. J.; Ruiz, D.; Rumberger, E.; Sun, Z.; Albela, B. Wemple, M. W.; Dilley, N. R.; Ribas, J.; Maple, M. B.; Christou, G.; Hendrickson, D. N. *Mol. Cryst. Liq. Cryst.* **1999**, *335*, 371.
- (21) Caneschi, A.; Gatteschi, D.; Sessoli, R.; Barra, A. L.; Brunel, L. C.; Guillot, M. *J. Am. Chem. Soc.* **1991**, *113*, 5873.
- (22) Sessoli, R.; Tsai, H.-L.; Schake, A. R.; Wang, S.; Vincent, J. B.; Folting, K.; Gatteschi, D.; Christou, G.; Hendrickson, D. N. *J. Am. Chem. Soc.* **1993**, *115*, 1804.
- (23) Sessoli, R.; Gatteschi, D.; Caneschi, A.; Novak, M. A. *Nature* **1993**, *365*, 141.
- (24) Regnault, N.; Jolicœur, Th.; Sessoli, R.; Gatteschi, D.; Verdaguer, M. *Phys. Rev. B* **2002**, *66*, 054409.
- (25) (a) Sessoli, R. *Mol. Cryst. Liq. Cryst.* **1995**, *274*, 145. (b) Cheesman, M. R.; Oganessian, V. S.; Sessoli, R.; Gatteschi, D.; Thomson, A. J. *Chem. Commun.* **1997**, *17*, 1677.
- (26) Takahashi, S.; Edwards, R. S.; North, J. M.; Hill, S.; Dalal, N. S. *Phys. Rev. B* **2004**, *70*, 094429.
- (27) Thomas, L.; Lioni, F.; Ballou, R.; Gatteschi, D.; Sessoli, R.; Barbara, B. *Nature* **1996**, *383*, 145.
- (28) Hendrickson, D. N.; Christou, G.; Ishimoto, H.; Yoo, J.; Brechin, E. K.; Yamaguchi, A.; Rumberger, E. M.; Aubin, S. M. J.; Sun, Z.; Aromí, G. *Polyhedron* **2001**, *20*, 1479.
- (29) Ruiz, D.; Aubin, S. M. J.; Rumberger, E.; Incarvito, C. D.; Folting, K.; Rheingold, A. L.; Christou, G.; Hendrickson, D. N. *Mol. Cryst. Liq. Cryst.* **1999**, *335*, 413.

- (30) Ruiz, D.; Sun, Z.; Albela, B.; Folting, K.; Ribas, J.; Christou, G.; Hendrickson, D. N. *Angew. Chem. Int. Ed.* **1998**, *37*, 300.
- (31) Barra, A.-L.; Debrunner, P.; Gatteschi, D.; Shulz, Ch. E.; Sessoli, R. *Europhys. Lett.* **1996**, *35*, 133.
- (32) Artus, P.; Boskovic, C.; Yoo, J.; Streib, W. E.; Brunel, L.-C.; Hendrickson, D. N.; Christou, G. *Inorg. Chem.* **2001**, *40*, 4199.
- (33) Boskovic, C.; Pink, M.; Huffman, J. C.; Hendrickson, D. N.; Christou, G. *J. Am. Chem. Soc.* **2001**, *123*, 9914.
- (34) *CRC Handbook of the Tables for Organic Compound Identification*; Rappoport, Z., Ed.; CRC Press: Cleveland, OH, 1967.
- (35) Sommer, L. H.; Gold, J. R.; Goldberg, G. M.; Marans, N. S. *J. Am. Chem. Soc.* **1949**, *71*, 1509.
- (36) *Handbook of Physical Properties of Organic Chemicals*; Howard, P. H.; Meylan, W. M., Eds.; CRC Press: New York, 1997.
- (37) Strong, L. E.; Brummel, C. L.; Lindower, P. *J. Sol. Chem.* **1987**, *16*, 105.
- (38) Eppley, H. J.; Christou, G.; Law, N. A.; Pecoraro, V. L. *Inorg. Synth.* **2002**, *33*, 61.
- (39) (a) Chakov, N. E.; Wernsdorfer, W.; Abboud, K. A.; Hendrickson, D. N.; Christou, G. *Dalton Trans.* **2003**, *11*, 2243. (b) Chakov, N. E.; Abboud, K. A.; Zakharov, L. N.; Rheingold, A. L.; Hendrickson, D. N.; Christou, G. *Polyhedron* **2003**, *22*, 1759.
- (40) Johnson, C. K.; Burnett, M. N. ORTEP-III, Report ORNL-6895, Oak Ridge National Laboratory, Tennessee, USA, 1996; Farrugia, L. J. *J. Appl. Crystallogr.* **1997**, *30*, 565.
- (41) (a) Brown, I. D.; Altermatt, D. *Acta Cryst.* **1985**, *B41*, 244. (b) Palenik, G. J. *Inorg. Chem.* **1997**, *36*, 4888. (c) Palenik, G. J. *Inorg. Chem.* **1997**, *36*, 122.
- (42) Pauling, L. *J. Am. Chem. Soc.* **1929**, *51*, 1010.
- (43) Brown, I. D.; Wu, K. K. *Acta Cryst.* **1976**, *B32*, 1957.
- (44) (a) Thorp, H. H. *Inorg. Chem.* **1998**, *37*, 5690. (b) Liu, W.; Thorp, H. H. *Inorg. Chem.* **1993**, *32*, 4102. (c) Thorp, H. H. *Inorg. Chem.* **1992**, *31*, 1585.
- (45) (a) Ramesh, S.; Wedge, M. S. *Physica C: Superconductivity* **1994**, *230*, 135. (b) Chmaisnen, O.; Eckstein, Y.; Kuper, C. G. arXiv: cond-mat/0010079.

- (46) Soler, M.; Artus, P.; Folting, K.; Huffman, J. C.; Hendrickson, D. N.; Christou, G. *Inorg. Chem.* **2001**, *40*, 4902.
- (47) Kuroda-Sowa, T.; Fukuda, S.; Miyoshi, S.; Maekawa, M.; Munakata, M.; Miyasaka, H.; Yamashita, M. *Chem. Lett.* **2002**, *31*, 682.
- (48) Ruettinger, W. F.; Campana, C.; Dismukes, G. C.; Dismukes, J. *J. Am. Chem. Soc.* **1997**, *119*, 6670.
- (49) Hendrickson, D. N.; Christou, G.; Schmitt, E. A.; Libby, E.; Bashkin, J. S.; Wang, S.; Tsai, H.-L.; Vincent, J. B.; Boyd, P. D. W.; Huffman, J. C.; Folting, K.; Li, Q.; Streib, W. E. *J. Am. Chem. Soc.* **1992**, *114*, 2455.
- (50) Lis, T. *Acta Crystallogr.* **1980**, *B36*, 2042.
- (51) Kambe, K. *J. Phys. Soc. Jpn.* **1950**, *5*, 48.
- (52) Vincent, J. B.; Christmas, C.; Chang, H.-R.; Li, Q.; Boyd, P. D. W.; Huffman, J. C.; Hendrickson, D. N.; Christou, G. *J. Am. Chem. Soc.* **1989**, *111*, 2086.
- (53) Yoo, J.; Yamaguchi, A.; Nakano, M.; Krzystek, J.; Streib, W. E.; Brunel, L.-C.; Ishimoto, H.; Christou, G.; Hendrickson, D. N. *Inorg. Chem.* **2001**, *40*, 4604.
- (54) Davidson, E. R. *MAGNET*; Indiana University: Bloomington, IN.
- (55) Davidson, E. R. *GRID*; Indiana University: Bloomington, IN.
- (56) (a) Sun, Z.; Ruiz, D.; Dilley, N. R.; Soler, M.; Ribas, J.; Folting, K.; Maple, M. B.; Christou, G.; Hendrickson, D. N. *Chem. Commun.* **1999**, *19*, 1973. (b) Soler, M.; Wernsdorfer, W.; Sun, Z.; Huffman, J. C.; Hendrickson, D. N.; Christou, G. *Chem. Commun.* **2003**, *21*, 2672.
- (57) (a) Aubin, S. M. J.; Sun, Z.; Guzei, I. A.; Rheingold, A. L.; Christou, G.; Hendrickson, D. N. *Chem. Commun.* **1997**, *22*, 2239. (b) Aubin, S. M. J.; Sun, Z.; Eppley, H. J.; Rumberger, E. M.; Guzei, I. A.; Folting, K.; Gantzel, P. K.; Rheingold, A. L.; Christou, G.; Hendrickson, D. N. *Polyhedron* **2001**, *20*, 1139. (c) Aubin, S. M. J.; Sun, Z.; Eppley, H. J.; Rumberger, E. M.; Guzei, I. A.; Folting, K.; Gantzel, P. K.; Rheingold, A. L.; Christou, G.; Hendrickson, D. N. *Inorg. Chem.* **2001**, *40*, 2127.
- (58) Brockman, J. T.; Abboud, K. A.; Hendrickson, D. N.; Christou, G. *Polyhedron* **2003**, *22*, 1765.
- (59) Zhao, H.; Berlinguette, C. P.; Basca, J.; Prosvirin, A. V.; Bera, J. K.; Tichy, S. E.; Schelter, E. J.; Dunbar, K. R. *Inorg. Chem.* **2004**, *43*, 1359.
- (60) Abragam, A.; Bleaney, B. *Electron Paramagnetic Resonance of Transition Ions*; Dover Press: Minneaola, NY, 1986.

- (61) (a) Soler, M.; Wernsdorfer, W.; Abboud, K. A.; Huffman, J. C.; Davidson, E. R.; Hendrickson, D. N.; Christou, G. *J. Am. Chem. Soc.* **2003**, *125*, 3576. (b) Soler, M.; Wernsdorfer, W.; Abboud, K. A.; Hendrickson, D. N.; Christou, G. *Polyhedron* **2003**, *22*, 1777.
- (62) (a) Brechin, E. K.; Boskovic, C.; Wernsdorfer, W.; Yoo, J.; Yamaguchi, A. Sañudo, E. C.; Concolino, T. R.; Rheingold, A. L.; Ishimoto, H.; Hendrickson, D. N.; Christou, G. *J. Am. Chem. Soc.* **2002**, *124*, 9710. (b) Sañudo, E. C.; Brechin, E. K.; Boskovic, C.; Wernsdorfer, W.; Yoo, J.; Yamaguchi, A.; Concolino, T. R.; Abboud, K. A.; Rheingold, A. L.; Ishimoto, H.; Hendrickson, D. N.; Christou, G. *Polyhedron* **2003**, *22*, 2267. (c) Brechin, E. K.; Sañudo, E. C.; Wernsdorfer, W.; Boskovic, C.; Yoo, J.; Hendrickson, D. N.; Yamaguchi, A.; Ishimoto, H.; Concolino, T. E.; Rheingold, A. L.; Christou, G. *Inorg. Chem.* **2005**, *44*, 502.
- (63) (a) Soler, M.; Wernsdorfer, W.; Folting, K.; Pink, M.; Christou, G. *J. Am. Chem. Soc.* **2004**, *126*, 2156. (b) Soler, M.; Rumberger, E.; Folting, K.; Hendrickson, D. N.; Christou, G. *Polyhedron* **2002**, *20*, 1365.
- (64) Sheldrick, G. M. *SHELXTL5*, Bruker-AXS, **1998**, Madison, WI.
- (65) (a) Friedman, J. R.; Sarachik, M. P. *Phys. Rev. Lett.* **1996**, *76*, 3830. (b) Tejada, J.; Ziolo, R. F.; Zhang, X. X. *Chem. Mater.* **1996**, *8*, 1784.
- (66) Tasiopoulos, A. J.; Vinslava, A.; Wernsdorfer, W.; Abboud, K. A.; Christou, G. *Angew. Chem. Int. Ed.* **2004**, *43*, 2117.
- (67) Libby, E.; McCusker, J. K.; Schmitt, E. A.; Folting, K.; Hendrickson, D. N.; Christou, G. *Inorg. Chem.* **1991**, *30*, 3486.
- (68) Bouwman, E.; Bolcar, M. A.; Libby, E.; Huffman, J. C.; Folting, K.; Christou, G. *Inorg. Chem.* **1992**, *31*, 5185.
- (69) Wang, S.; Huffman, J. C.; Folting, K.; Streib, W. E.; Lobkovsky, E. B.; Christou, G. *Angew. Chem. Int. Ed.* **1991**, *30*, 1672.
- (70) McCullough, J.; Gould, E. S. *J. Am. Chem. Soc.* **1949**, *71*, 674.
- (71) Jansen, J. C.; Van Koningsveld, H.; Van Ooijen, J. A. C.; Reedijk, J. *Inorg. Chem.* **1980**, *19*, 170.

- (72) (a) Law, N. A.; Kampf, J. W.; Pecoraro, V. L. *Inorg. Chim. Acta* **2000**, 297, 252. (b) Goodson, P. A.; Hodgson, D. J.; Glerup, J.; Michelsen, K.; Weihe, H. *Inorg. Chim. Acta* **1992**, 197, 141. (c) Goodson, P. A.; Glerup, J.; Hodgson, D. J.; Michelsen, K.; Weihe, H. *Inorg. Chem.* **1991**, 30, 4909. (d) Larson, E.; Lah, M. S.; Li, X.; Bonadies, J. A.; Pecoraro, V. L. *Inorg. Chem.* **1992**, 31, 373. (e) Gohdes, J. W.; Armstrong, W. H. *Inorg. Chem.* **1992**, 31, 368. (f) Libby, E.; Webb, R. J.; Streib, W. E.; Folting, K.; Huffman, J. C.; Hendrickson, D. N.; Christou, G. *Inorg. Chem.* **1989**, 28, 4037. (g) Pal, S.; Olmstead, M. M.; Armstrong, W. H. *Inorg. Chem.* **1995**, 34, 4708. (h) Torayama, H.; Asada, H.; Fujiwara, M.; Matsushita, T. *Polyhedron* **1998**, 17, 3859. (i) Oki, A. R.; Glerup, J.; Hodgson, D. J. *Inorg. Chem.* **1990**, 29, 2435.
- (73) Tasiopoulos, A. J.; Abboud, K. A.; Christou, G. *Chem. Commun.* **2003**, 5, 580.
- (74) (a) Bashkin, J. S.; Schake, A. R.; Vincent, J. B.; Chang, H.-R.; Li, Q.; Huffman, J. C.; Christou, G.; Hendrickson, D. N. *Chem. Commun.* **1988**, 11, 700. (b) Wiegardt, K.; Bossek, U.; Zsolnai, G.; Huttner, G.; Blondin, G.; Girerd, J.-J.; Babonneau, F. *Chem. Commun.* **1987**, 9, 651. (c) Osawa, M.; Fujisawa, K.; Kitajima, N.; Moro-oka, Y. *Chem. Lett.* **1997**, 9, 919. (d) Bossek, U.; Saher, M.; Weyhermuller, T.; Wiegardt, K. *Chem. Commun.* **1992**, 24, 1780. (e) Schafer, K.-O.; Bittl, R.; Zwegart, W.; Lenzian, F.; Haselhorst, G.; Weyhermuller, T.; Wiegardt, K.; Lubitz, W. *J. Am. Chem. Soc.* **1998**, 120, 13104. (f) Lal, T. K.; Mukherjee, R. *Inorg. Chem.* **1998**, 37, 2373. (g) Pal, S.; Gohdes, J. W.; Wilisch, W. C. A.; Armstrong, W. H. *Inorg. Chem.* **1992**, 31, 713.
- (75) (a) Bhaduri, S.; Tasiopoulos, A. J.; Bolcar, M. A.; Abboud, K. A.; Streib, W. E.; Christou, G. *Inorg. Chem.* **2003**, 42, 1483. (b) Mok, H. J.; Davis, J. A.; Pal, S.; Mandal, S. K.; Armstrong, W. H. *Inorg. Chim. Acta* **1997**, 263, 385. (c) Dave, B. C.; Czernuszewicz, R. S.; Bond, M. R.; Carrano, C. J. *Inorg. Chem.* **1993**, 32, 3593. (d) Reddy, K. R.; Rajasekharan, M. V.; Padhye, S.; Dahan, F.; Tuchagues, J.-P. *Inorg. Chem.* **1994**, 33, 428. (e) Pal, S.; Chan, M. K.; Armstrong, W. H. *J. Am. Chem. Soc.* **1992**, 114, 6398. (f) Pal, S.; Armstrong, W. H. *Inorg. Chem.* **1992**, 31, 5417.
- (76) Harden, N. C.; Bolcar, M. A.; Wernsdorfer, W.; Abboud, K. A.; Streib, W. E.; Christou, G. *Inorg. Chem.* **2003**, 42, 7067.
- (77) Perlepes, S. P.; Huffman, J. C.; Christou, G. *Chem. Commun.* **1991**, 23, 1657.
- (78) Chandrasekhar, V.; Muralidhara, M. G.; Justin Thomas, K. R.; Tiekink, E. R. T. *Inorg. Chem.* **1992**, 31, 4707.
- (79) Barton, D. H.; Hall, M. B.; Lin, Z.; Parekh, S. I.; Reibenspies, J. *J. Am. Chem. Soc.* **1993**, 115, 5056.
- (80) Fujihara, H.; Nakahodo, T.; Furukawa, N. *Tet. Lett.* **1995**, 36, 6275.

- (81) Goldstein, B. M.; Kennedy, S. D.; Hennen, W. J. *J. Am. Chem. Soc.* **1990**, *112*, 8265.
- (82) Abbati, G. L.; Cornia, A.; Fabretti, A. C.; Caneschi, A.; Gatteschi, D. *Inorg. Chem.* **1998**, *37*, 3759.
- (83) Bolcar, M. A.; Aubin, S. M. J.; Folting, K.; Hendrickson, D. N.; Christou, G. *Chem. Commun.* **1997**, *16*, 1485.
- (84) Pilawa, B.; Kelemen, M. T.; Wanka, S.; Giesselmann, A.; Barra, A. L. *Europhys. Lett.* **1998**, *43*, 7.
- (85) Castro, S. L.; Sun, Z.; Grant, C. M.; Bollinger, J. C.; Hendrickson, D. N.; Christou, G. *J. Am. Chem. Soc.* **1998**, *120*, 2365.
- (86) Albela, B.; El Fallah, M. S.; Ribas, J.; Folting, K.; Christou, G.; Hendrickson, D. N. *Inorg. Chem.* **2001**, *40*, 1037.
- (87) Clérac, R.; Miyasaka, H.; Yamashita, M.; Coulon, C. *J. Am. Chem. Soc.* **2002**, *124*, 12837.
- (88) Miyasaka, H.; Clérac, R.; Mizushima, K.; Sugiura, K.; Yamashita, M.; Wernsdorfer, W.; Coulon, C. *Inorg. Chem.* **2003**, *42*, 8203.
- (89) (a) Caneschi, A.; Gatteschi, D.; Lalioti, N.; Sangregorio, C.; Sessoli, R.; Venturi, G.; Vindigni, A.; Rettori, A.; Pini, M. G.; Novak, M. A. *Angew. Chem. Int. Ed.* **2001**, *40*, 1760. (b) Caneschi, A.; Gatteschi, D.; Lalioti, N.; Sessoli, R.; Sorace, L.; Tangoulis, V.; Vindigni, A. *Chem. Eur. J.* **2002**, *8*, 286. (c) Caneschi, A.; Gatteschi, D.; Lalioti, N.; Sangregorio, C.; Sessoli, R.; Venturi, G.; Vindigni, A.; Rettori, A.; Pini, M. G.; Novak, M. A. *Europhys. Lett.*, **2002**, *58*, 771.
- (90) (a) Liu, T.-F.; Fu, D.; Gao, S.; Zhang, Y.-Z.; Sun, H.-L.; Su, G.; Liu, Y.-J. *J. Am. Chem. Soc.* **2003**, *125*, 13976. (b) Shaikh, N.; Panja, A.; Goswami, S.; Banerjee, P.; Vojtišek, P.; Zhang, Y.-Z.; Su, G.; Gao, S. *Inorg. Chem.* **2004**, *43*, 849.
- (91) (a) Lescouëzec, R.; Vaissermann, J.; Ruiz-Pérez, C.; Lloret, F.; Carrasco, R.; Julve, M.; Verdaguer, M.; Dromzee, Y.; Gatteschi, D.; Wernsdorfer, W. *Angew. Chem. Int. Ed.* **2003**, *42*, 1483. (b) Toma, L. M.; Lescouëzec, R.; Lloret, F.; Julve, M.; Vaissermann, J.; Verdaguer, M. *Chem. Commun.* **2003**, *15*, 1850.
- (92) Wernsdorfer, W. *Adv. Chem. Phys.* **2001**, *118*, 99.
- (93) Glauber, R. J. *J. Math. Phys.* **1963**, *4*, 294.
- (94) Tasiopoulos, A. J.; Wernsdorfer, W.; Moulton, B.; Zaworotko, M. J.; Christou, G. *J. Am. Chem. Soc.* **2003**, *125*, 15274.

- (95) Goodwin, J. C.; Sessoli, R.; Gatteschi, D.; Wernsdorfer, W.; Powell, A. K.; Heath, S. L. *Dalton Trans.* **2000**, 12, 1835.
- (96) van der Sluis, P.; Spek, A. L. *Acta Crystallogr.* **1990**, A46, 194.
- (97) Spek, A. L. *Acta Crystallogr.* **1990**, A46, 1.
- (98) Mishra, A.; Wernsdorfer, W.; Abboud, K. A.; Christou, G. *J. Am. Chem. Soc.* **2004**, 126, 15648.
- (99) Miyasaka, H.; Clérac, R.; Wernsdorfer, W.; Lecren, L.; Bonhomme, C.; Sugiura, K.; Yamashita, M. *Angew. Chem. Int. Ed.* **2004**, 43, 2801.
- (100) (a) Aubin, S. M. J.; Sun, Z.; Pardi, L.; Krzystek, J.; Folting, K.; Brunel, L.-C.; Rheingold, A. L.; Christou, G.; Hendrickson, D. N. *Inorg. Chem.* **1999**, 38, 5329. (b) Tsai, H.-L.; Jwo, T.-Y.; Lee, G.-H.; Wang, Y. *Chem. Lett.* **2000**, 29, 346. (c) Kuroda-Sowa, T.; Lam, M.; Rheingold, A. L.; Frommen, C.; Reiff, W. M.; Nakano, M.; Yoo, J.; Maniero, A. L.; Brunel, L.-C.; Christou, G.; Hendrickson, D. N. *Inorg. Chem.* **2001**, 40, 6469. (d) Kuroda-Sowa, T.; Nogami, T.; Konaka, H.; Maekawa, M.; Munakata, M.; Miyasaka, H.; Yamashita, M. *Polyhedron* **2003**, 22, 1795.
- (101) Kuroda-Sowa, T.; Handa, T.; Kotera, T.; Maekawa, M.; Munakata, M.; Miyasaka, H.; Yamashita, M. *Chem. Lett.* **2004**, 33, 540.
- (102) Brechin, E. K.; Yoo, J.; Nakano, M.; Huffman, J. C.; Hendrickson, D. N.; Christou, G. *Chem. Commun.* **1999**, 9, 783.
- (103) Boskovic, C.; Brechin, E. K.; Streib, W. E.; Folting, K.; Bollinger, J. C.; Hendrickson, D. N.; Christou, G. *J. Am. Chem. Soc.* **2002**, 124, 3725.
- (104) Rajaraman, G.; Murugesu, M.; Sañudo, E. C.; Soler, M.; Wernsdorfer, W.; Helliwell, M.; Muryn, C.; Raftery, J.; Teat, S. J.; Christou, G.; Brechin, E. K. *J. Am. Chem. Soc.* **2004**, 126, 15445.
- (105) Murugesu, M.; Raftery, J.; Wernsdorfer, W.; Christou, G.; Brechin, E. K. *Inorg. Chem.* **2004**, 43, 4203.
- (106) Murugesu, M.; Wernsdorfer, W.; Abboud, K. A.; Christou, G. *Angew. Chem. Int. Ed.* **2005**, 44, 892.
- (107) Foguet-Albiol, D.; O'Brien, T. A.; Wernsdorfer, W.; Moulton, B.; Zaworotko, M. J.; Abboud, K. A.; Christou, G. *Angew. Chem. Int. Ed.* **2005**, 44, 897.
- (108) Brockman, J. T.; Huffman, J. C.; Christou, G. *Angew. Chem. Int. Ed.* **2002**, 114, 2616.

- (109) Bian, G.-Q.; Kuroda-Sowa, T.; Konaka, H.; Hatano, M.; Maekawa, M.; Munakata, M.; Miyasaka, H.; Yamashita, M. *Inorg. Chem.* **2004**, *43*, 4790.
- (110) Bian, G.-Q.; Kuroda-Sowa, T.; Gunjima, N.; Maekawa, M.; Munakata, M. *Inorg. Chem. Commun.* **2005**, *8*, 208.
- (111) (a) Yoo, J.; Brechin, E. K.; Yamaguchi, A.; Nakano, M.; Huffman, J. C.; Maniero, A. L.; Brunel, L.-C.; Awaga, K.; Ishimoto, H.; Christou, G.; Hendrickson, D. N. *Inorg. Chem.* **2000**, *39*, 3615. (b) Boskovic, C.; Wernsdorfer, W.; Folting, K.; Huffman, J. C.; Hendrickson, D. N.; Christou, G. *Inorg. Chem.* **2002**, *41*, 5107. (c) Brechin, E. K.; Soler, M.; Davidson, J.; Hendrickson, D. N.; Parsons, S.; Christou, G. *Chem. Commun.* **2002**, *19*, 2252. (d) Price, D. J.; Batten, S. R.; Moubaraki, B.; Murray, K. S. *Chem. Commun.* **2002**, *7*, 762. (e) Boskovic, C.; Bircher, R.; Tregenna-Piggott, P. L. W.; Güdel, H. U.; Paulsen, C.; Wernsdorfer, W.; Barra, A.-L.; Khatsko, E.; Neels, A.; Stoeckli-Evans, H. *J. Am. Chem. Soc.* **2003**, *125*, 14046. (f) Yang, E.-C.; Harden, N.; Wernsdorfer, W.; Zakharov, L.; Brechin, E. K.; Rheingold, A. L.; Christou, G.; Hendrickson, D. N. *Polyhedron* **2003**, *22*, 1857. (g) Murugesu, M.; Habrych, M.; Wernsdorfer, W.; Abboud, K. A.; Christou, G. *J. Am. Chem. Soc.* **2004**, *126*, 4766. (h) Tasiopoulos, A. J.; Wernsdorfer, W.; Abboud, K. A.; Christou, G. *Angew. Chem. Int. Ed.* **2004**, *43*, 6338. (i) King, P.; Wernsdorfer, W.; Abboud, K. A.; Christou, G. *Inorg. Chem.* **2004**, *43*, 7315. (j) Wittick, L. M.; Murray, K. S.; Moubaraki, B.; Batten, S. R.; Spiccia, L.; Berry, K. J. *Dalton Trans.* **2004**, *7*, 1003.
- (112) Chakov, N. E.; Abboud, K. A.; Zakharov, L. N.; Rheingold, A. L.; Christou, G. *Inorg. Chem.* **2005**, accepted.
- (113) Chakov, N. E.; Soler, M.; Wernsdorfer, W.; Abboud, K. A.; Christou, G. *Inorg. Chem.* **2005**, accepted.
- (114) Sañudo, E. C.; Wernsdorfer, W.; Abboud, K. A.; Christou, G. *Inorg. Chem.* **2004**, *43*, 4137.
- (115) Sun, Z.; Grant, C. M.; Castro, S. L.; Hendrickson, D. N.; Christou, G. *Chem. Commun.* **1998**, *6*, 721.
- (116) Yang, E.-C.; Hendrickson, D. N.; Wernsdorfer, W.; Nakano, M.; Zakharov, L. N.; Sommer, R. D.; Rheingold, A. L.; Ledezma-Gairaud, M.; Christou, G. *J. Appl. Phys.* **1991**, *91*, 7382.

- (117) (a) Nakano, M.; Matsubayashi, G.-E.; Muramatsu, T.; Kobayashi, T. C.; Amaya, K.; Yoo, J.; Christou, G.; Hendrickson, D. N. *Mol. Cryst. Liq. Cryst.* **2002**, *376*, 405. (b) Cadiou, C.; Murrie, M.; Paulsen, C.; Villar, V.; Wernsdorfer, W.; Winpenny, R. E. P. *Chem. Commun.* **2002**, *24*, 2666. (c) Ochsenbein, S. T.; Murrie, M.; Rusanov, E.; Stoeckli-Evans, H.; Sekine, C.; Güdel, H. U. *Inorg. Chem.* **2002**, *41*, 5133. (d) Yang, E.-C.; Wernsdorfer, W.; Hill, S.; Edwards, R. S.; Nakano, M.; Maccagnano, S.; Zakharov, L. N.; Rheingold, A. L.; Christou, G.; Hendrickson, D. N. *Polyhedron* **2003**, *22*, 1727.
- (118) (a) Sangregorio, C.; Ohm, T.; Paulsen, C.; Sessoli, R.; Gatteschi, D. *Phys. Rev. Lett.* **1997**, *78*, 4645. (b) Barra, A. L.; Caneschi, A.; Cornia, A.; Fabrizi de Biani, F.; Gatteschi, D.; Sangregorio, C.; Sessoli, R.; Sorace, L. *J. Am. Chem. Soc.* **1999**, *121*, 5302. (c) Oshio, H.; Hoshino, N.; Ito, T. *J. Am. Chem. Soc.* **2000**, *122*, 12602. (d) Benelli, C.; Cano, J.; Journaux, Y.; Sessoli, R.; Solan, G. A.; Winpenny, R. E. P. *Inorg. Chem.* **2001**, *40*, 188. (e) Jones, L. F.; Brechin, E. K.; Collison, D.; Helliwell, M.; Mallah, T.; Piligkos, S.; Rajaraman, G.; Wernsdorfer, W. *Inorg. Chem.* **2003**, *42*, 6601. (f) Boudalis, A. K.; Donnadiou, B.; Nastopoulos, V.; Clemente-Juan, J. M.; Mari, A.; Sanakis, Y.; Tuchagues, J.-P.; Perlepes, S. P. *Angew. Chem. Int. Ed.* **2004**, *43*, 2266. (g) Moragues-Cánovas, M.; Rivière, E.; Ricard, L.; Paulsen, C.; Wernsdorfer, W.; Rajaraman, G.; Brechin, E. K.; Mallah, T. *Adv. Mater.* **2004**, *16*, 1101.
- (119) Chakov, N. E.; Wernsdorfer, W.; Abboud, K. A.; Christou, G. *Inorg. Chem.* **2004**, *43*, 5919.
- (120) Gresley, N. M.; Griffith, W. P.; Parkin, B. C.; White, A. J. P.; Williams, D. J. *Dalton Trans.* **1996**, *10*, 2039.
- (121) *Dissociation Constants of Organic Acids in Aqueous Solution*; Kortüm, G.; Vogel, W.; Andrussow, K., Eds.; Butterworth: London, 1961.
- (122) Ferreira, K. N.; Iverson, T. M.; Maghlaoui, K.; Barber, J.; Iwata, S. *Science* **2004**, *303*, 1831.
- (123) (a) Eulerling, B.; Ahlers, F.; Zippel, F.; Schmidt, M.; Nolting, H.-F.; Krebs, B. *Chem. Commun.* **1995**, *12*, 1305. (b) Eulerling, B.; Schmidt, M.; Pinkernell, U.; Karst, U.; Krebs, B. *Angew. Chem. Int. Ed.* **1996**, *35*, 1973. (c) Than, R.; Schrod, A.; Westerheide, L.; van Eldik, R.; Krebs, B. *Eur. J. Inorg. Chem.* **1999**, *9*, 1537.
- (124) (a) Barkigia, K. M.; Rajković, L. M.; Pope, M. T.; Quicksall, C. O. *J. Am. Chem. Soc.* **1975**, *97*, 4146. (b) Barkigia, K. M.; Rajković-Blazer, L. M.; Pope, M. T.; Prince, E.; Quicksall, C. O. *Inorg. Chem.* **1980**, *19*, 2531.
- (125) Gresley, N. M.; Griffith, W. P.; White, A. J. P.; Williams, D. J. *Dalton Trans.* **1997**, *1*, 89.

- (126) Wu, J.-Z.; Sellitto, E.; Yap, G. P. A.; Sheats, J.; Dismukes, G. C. *Inorg. Chem.* **2004**, *43*, 5795.
- (127) Ruettinger, W. F.; Ho, D. M.; Dismukes, G. C. *Inorg. Chem.* **1999**, *38*, 1036.
- (128) (a) Wemple, M. W.; Adams, D. M.; Folting, K.; Hendrickson, D. N.; Christou, G. *J. Am. Chem. Soc.* **1995**, *117*, 7275. (b) Wemple, M. W.; Adams, D. M.; Hagen, K. S.; Folting, K.; Hendrickson, D. N.; Christou, G. *Chem. Commun.* **1995**, *15*, 1591. (c) Wang, S.; Folting, K.; Streib, W. E.; Schmitt, E. A.; McCusker, J. K.; Hendrickson, D. N.; Christou, G. *Angew. Chem. Int. Ed.* **1991**, *30*, 305. (d) Gider, S.; Awschalom, D. D.; Douglas, T.; Mann, S.; Chaparala, M. *Science* **1995**, *268*, 77. (e) Wang, S.; Tsai, H.-L.; Libby, E.; Folting, K.; Streib, W. E.; Hendrickson, D. N.; Christou, G. *Inorg. Chem.* **1996**, *35*, 7578.
- (129) Serjeant, E. P.; Dempsey, B. *Ionisation Constants of Organic Acids in Aqueous Solution*; Pergamon Press: New York, 1979.
- (130) Mishra, A.; Wernsdorfer, W.; Abboud, K. A.; Christou, G. *Chem. Commun.* **2005**, *1*, 54.
- (131) Tsai, H.-L.; Wang, S.; Folting, K.; Streib, W. E.; Hendrickson, D. N.; Christou, G. *J. Am. Chem. Soc.* **1995**, *117*, 2503.
- (132) Brockman, J. T.; Wernsdorfer, W.; Abboud, K. A.; Christou, G., unpublished results.
- (133) Mishra, A.; Wernsdorfer, W.; Abboud, K. A.; Christou, G., unpublished results.
- (134) (a) O'Connor, C. J. *Prog. Inorg. Chem.* **1982**, *29*, 203. (b) *The Theory of Electric and Magnetic Susceptibilities*; Van Vleck, J. H., Ed.; Oxford University Press: London, 1932.
- (135) Hill, S.; Edwards, R. S.; Aliaga-Alcalde, N.; Christou, G. *Science* **2003**, *302*, 1015.
- (136) Wernsdorfer, W.; Aliaga-Alcalde, N.; Hendrickson, D. N.; Christou, G. *Nature* **2002**, *416*, 406.
- (137) Schake, A. R.; Tsai, H.-L.; Webb, R. J.; Folting, K.; Christou, G.; Hendrickson, D. N. *Inorg. Chem.* **1994**, *33*, 6020.
- (138) Li, J.-Y.; Xu, H.; Zou, J.-Z.; Xu, Z.; You, X.-Z.; Yu, K.-P. *Polyhedron* **1996**, *15*, 3325.
- (139) Boskovic, C.; Huffman, J. C.; Christou, G. *Chem. Commun.* **2002**, *21*, 2502.
- (140) Scherer, O. J.; Jungmann, H.; Hussong, K. *J. Organometall. Chem.* **1983**, *247*, C1.

- (141) Kitajima, N.; Hikichi, S.; Tanaka, M.; Moro-oka, Y. *J. Am. Chem. Soc.* **1993**, *115*, 5496.
- (142) Day, V. W.; Fredrich, M. F.; Klemperer, W. G.; Liu, R.-S. *J. Am. Chem. Soc.* **1979**, *101*, 491.
- (143) Murugesu, M.; Abboud, K. A.; Christou, G. *Polyhedron* **2004**, *23*, 2779.
- (144) Tanase, T.; Inagaki, T.; Yamada, Y.; Kato, M.; Ota, E.; Yamazaki, M.; Sato, M.; Mori, W.; Yamaguchi, K.; Mikuriya, M.; Takahashi, M.; Takeda, M.; Kinoshita, I.; Yano, S. **1998**, *4*, 713.
- (145) Stibrany, R. T.; Gorun, S. M. *Angew. Chem. Int. Ed.* **1990**, *29*, 1156.
- (146) McCusker, J. K.; Christmas, C. A.; Hagen, P. M.; Chadha, R. K.; Jarvey, D. F.; Hendrickson, D. N. *J. Am. Chem. Soc.* **1991**, *113*, 6114.
- (147) Christmas, C. A.; Tsai, H.-L.; Pardi, L.; Kesselman, J. M.; Gantzel, P. K.; Chadha, R. K.; Gatteschi, D.; Jarvey, D. F.; Hendrickson, D. N. *J. Am. Chem. Soc.* **1993**, *115*, 12483.
- (148) Micklitz, W.; Lippard, S. J. *J. Inorg. Chem.* **1988**, *27*, 3067.
- (149) Micklitz, W.; Bott, S. G.; Bentsen, J. G.; Lippard, S. J. *J. Am. Chem. Soc.* **1989**, *111*, 372.
- (150) Low, D. W.; Eichhorn, D. M.; Draganescu, A.; Armstrong, W. H. *Inorg. Chem.* **1991**, *30*, 877.
- (151) Murrie, M.; Parsons, S.; Winpenny, R. E. P. *Dalton Trans.* **1998**, *9*, 1423.
- (152) (a) Kolks, G.; Lippard, S. J.; Waszczak, J. V. *J. Am. Chem. Soc.* **1980**, *102*, 4833. (b) van Albada, G. A.; Mutikainen, I.; Roubeau, O.; Turpeinen, U.; Reedijk, J. *Inorg. Chim. Acta* **2002**, *331*, 208. (c) Escuer, A.; Vicente, R.; Peñalba, E.; Solans, X.; Font-Bardía, M. *Inorg. Chem.* **1996**, *35*, 248. (d) Bazzicalupi, C.; Bencini, A.; Bencini, A.; Bianchi, A.; Corana, F.; Fusi, V.; Giorgi, C.; Paoli, P.; Paoletti, P.; Valtancoli, B.; Zanchini, C. *Inorg. Chem.* **1996**, *35*, 5540. (e) Mao, Z.-W.; Liehr, G.; van Eldik, R. *Dalton Trans.* **2001**, *10*, 1593. (f) Rodríguez, M.; Llobet, A.; Corbella, M.; Müller, P.; Usón, M. A.; Martell, A. E.; Reibenspies, J. *Dalton Trans.* **2002**, *14*, 2900. (g) van Albada, G.; Mutikainen, I.; Roubeau, O. S.; Turpeinen, U.; Reedijk, J. *Eur. J. Inorg. Chem.* **2000**, *10*, 2179.

- (153) (a) Mann, K. L. V.; Jeffery, J. C.; McCleverty, J. A.; Ward, M. D. *Dalton Trans.* **1998**, 18, 3029. (b) Schrodtr, A.; Neubrand, A.; van Eldik, R. *Inorg. Chem.* **1997**, 36, 4579. (c) Trösch, A.; Vahrenkamp, H. *Inorg. Chem.* **2001**, 40, 2305. (d) Bazzicalupi, C.; Bencini, A.; Bianchi, A.; Fusi, V.; Paoletti, P.; Valtancoli, B. *Chem. Commun.* **1995**, 15, 1555. (e) Chen, X.-M.; Deng, Q.-Y.; Wang, G.; Xu, Y.-J. *Polyhedron* **1994**, 13, 3085. (f) Murthy, N. N.; Karlin, K. D. *Chem. Commun.* **1993**, 15, 1236.
- (154) Yamase, T.; Ohtaka, K. *Dalton Trans.* **1994**, 18, 2599.
- (155) Cotton, F. A.; Lin, C.; Murillo, C. A. *J. Am. Chem. Soc.* **2001**, 123, 2670.
- (156) (a) Lee, J.; Chasteen, N. D.; Zhao, G.; Papaefthymiou, G. C.; Gorun, S. M. *J. Am. Chem. Soc.* **2002**, 124, 3024. (b) Lee, J.; Gorun, S. M. *Angew. Chem. Int. Ed.* **2003**, 42, 1512.
- (157) Novak, M. A.; Sessoli, R. In *Quantum Tunneling of Magnetization – QTM '94*; Gunther, L., Barbara, B., Eds.; Kluwer: Amsterdam, 1995; pp 171-188.
- (158) Awschalom, D. D.; DiVincenzo, D. P. *Phys. Today* **1995**, 48, 43.
- (159) Caneschi, A.; Gatteschi, D.; Sangregorio, C.; Sessoli, R.; Sorace, L.; Cornia, A.; Novak, M. A.; Paulsen, C.; Wernsdorfer, W. *J. Magn. Magn. Mat.* **1999**, 200, 182.
- (160) Wernsdorfer, W.; Soler, M.; Christou, G.; Hendrickson, D. N. *J. Appl. Phys.* **2002**, 91, 7164.
- (161) Wernsdorfer, W.; Sessoli, R. *Science* **1999**, 284, 133.
- (162) Wernsdorfer, W.; Chakov, N. E.; Christou, G. *Phys. Rev. Lett.* **2005**, accepted.
- (163) Leuenberger, M. N.; Loss, D. *Nature* **2001**, 410, 789.
- (164) Basler, R.; Sieber, A.; Chaboussant, G.; Güdel, H. U.; Chakov, N. E.; Soler, M.; Christou, G.; Desmedt, A.; Lechner, R. *Inorg. Chem.* **2005**, 44, 649.
- (165) Artus, P.; Christou, G. University of Florida, Gainesville, FL, manuscript in preparation.
- (166) Drago, R. S. *Physical Methods for Chemists*; 2<sup>nd</sup> ed.; Saunders College: New York, 1992; pp 500-556.
- (167) *NMR of Paramagnetic Molecules: Principles and Applications*; La Mar, G. N., Horrocks, W. DeW., Jr., Holm, R. H., Eds.; Academic Press: New York, 1973.
- (168) Drago, R. S.; Zink, J. I.; Perry, W. D. *J. Chem. Educ.* **1974**, 51, 464.

- (169) Castro, S. L.; Streib, W. E.; Sun, J.-S.; Christou, G. *Inorg. Chem.* **1996**, *35*, 4462.
- (170) (a) Mirebeau, I.; Hennion, M.; Casalta, H.; Andres, H.; Güdel, H. U.; Irodova, A. V.; Caneschi, A. *Phys. Rev. Lett.* **1999**, *83*, 628. (b) Hennion, M.; Pardi, L.; Mirebeau, I.; Suard, E.; Sessoli, R.; Caneschi, A. *Phys. Rev. B* **1997**, *56*, 8819. (c) Chaboussant, G.; Sieber, A.; Ochsenbein, S.; Güdel, H.-U.; Murrie, M.; Honecker, A.; Fukushima, N.; Normand, B. *Phys. Rev. B* **2004**, *70*, 104422.
- (171) (a) Andres, H.; Basler, R.; Blake, A. J.; Cadiou, C.; Chaboussant, G.; Grant, C. M.; Güdel, H.-U.; Murrie, M.; Parsons, S.; Paulsen, C.; Semadini, F.; Villar, V.; Wernsdorfer, W.; Winpenny, R. E. P. *Chem. Eur. J.* **2002**, *8*, 4867. (b) Andres, H.; Basler, R.; Güdel, H.-U.; Aromí, G.; Christou, G.; Büttner, H.; Rufflé, B. *J. Am. Chem. Soc.* **2000**, *122*, 12469. (c) Basler, R.; Chaboussant, G.; Cañada-Vilalta, C.; Christou, G.; Mutka, H.; Janssen, S.; Altorfer, F.; Güdel, H. U. *Polyhedron*, **2003**, *22*, 2471. (d) Carretta, S.; Livioti, E.; Amoretti, G.; Caciuffo, R.; Caneschi, A.; Gatteschi, D. *Phys. Rev. B* **2002**, *65*, 052411. (e) Amoretti, G.; Caciuffo, R.; Combet, J.; Murani, A.; Caneschi, A. *Phys. Rev. B* **2000**, *62*, 3022.
- (172) Cornia, A.; Sessoli, R.; Sorace, L.; Gatteschi, D.; Barra, A. L.; Daiguebonne, C. *Phys. Rev. Lett.* **2002**, *89*, 257201.
- (173) Cornia, A.; Fabretti, A. C.; Sessoli, R.; Sorace, L.; Gatteschi, D.; Barra, A.-L.; Daiguebonne, C.; Roisnel, T. *Acta Crystallogr.* **2002**, *C58*, 371.
- (174) Marshall, W.; Lovesey, S. W. *Theory of Therman Neutron Scattering*; Clarendon Press, Oxford, 1971.
- (175) Birgenau, R. J. *J. Phys. Chem. Solids* **1972**, *33*, 59.
- (176) Cole, K. S.; Cole, R. H. *J. Chem. Phys.* **1941**, *9*, 341.
- (177) Barra, A. L.; Gatteschi, D.; Sessoli, R. *Phys. Rev. B* **1997**, *56*, 8192.
- (178) Caneschi, A.; Ohm, T.; Paulsen, C.; Rovai, D.; Sangregorio, C.; Sessol, R. *J. Mag. Magn. Mat.* **1998**, *117*, 1330.
- (179) Tejada, J.; Chudnovsky, E. M.; del Barco, E.; Hernandez, J. M. *Nanotechnology* **2001**, *12*, 181.
- (180) Zhong, Y.; Sarachik, M. P.; Friedman, J. R.; Robinson, R. A.; Kelley, T. M.; Nakotte, H.; Christianson, A. C.; Trouw, F.; Aubin, S. M. J.; Hendrickson, D. N. *J. Appl. Phys.* **1999**, *85*, 5636.
- (181) (a) Chudnovsky, E. M.; Garanin, D. A. *Phys. Rev. Lett.* **2001**, *87*, 187203. (b) Garanin, D. A.; Chudnovsky, E. M. *Euro. Phys. J. B* **2002**, *29*, 3.

- (182) (a) Tsai, H.-L.; Chen, D.-M.; Yang, C.-I.; Jwo, T.-Y.; Wur, C.-S.; Lee, G.-H.; Wang, Y. *Inorg. Chem. Commun.* **2001**, *4*, 511. (b) An, J.; Chen, Z.-D.; Zhang, X.-X.; Raubenheimer, H. G.; Esterhuysen, C.; Gao, S.; Xu, G.-X. *Dalton Trans.* **2001**, *22*, 3352.
- (183) Bondi, A. *J. Phys. Chem.* **1964**, *68*, 441.
- (184) (a) Harter, A. G.; Chakov, N. E.; Roberts, B.; Achey, R.; Reyes, A.; Kuhns, P.; Christou, G.; Dalal, N. S. *Inorg. Chem.* **2005**, *44*, 2122. (b) Harter, A. G.; Chakov, N. E.; Achey, R.; Reyes, A.; Kuhns, P.; Christou, G.; Dalal, N. S. *Polyhedron* **2005**, accepted.
- (185) Kubo, T.; Goto, T.; Koshiba, T.; Takeda, K.; Awaga, K. *Phys. Rev. B* **2002**, *65*, 224425.
- (186) Furukawa, Y.; Watanabe, K.; Kumagai, K.; Borsa, F.; Gatteschi, D. *Phys. Rev. B* **2001**, *64*, 104401.
- (187) Furkawa, Y.; Watanabe, K.; Kumagai, K.; Borsa, F.; Sasaki, T.; Kobayashi, N.; Gatteschi, D. *Phys. Rev. B* **2003**, *67*, 064426.
- (188) Hill, S.; Edwards, R. S.; Jones, S. I.; Dalal, N. S.; North, J. M. *Phys. Rev. Lett.* **2003**, *90*, 217204.
- (189) del Barco, E.; Kent, A. D.; Rumberger, E. M.; Hendrickson, D. N.; Christou, G. *Phys. Rev. Lett.* **2003**, *91*, 047203.
- (190) (a) Park, K.; Novotny, M. A.; Dalal, N. S.; Hill, S.; Rikvold, P. A. *Phys. Rev. B* **2002**, *65*, 014426. (b) Hill, S.; Maccagnano, S.; Achey, R. M.; North, J. M.; Dalal, N. S. *Phys. Rev. B* **2002**, *65*, 224410.
- (191) (a) Chamberlin, R. V.; Mozurkewich, G.; Orbach, R. *Phys. Rev. Lett.* **1984**, *52*, 867. (b) Weiss, G. H.; Dishon, M.; Long, A. M.; Bendler, J. T.; Jones, A. A.; Inglefield, P. T.; Bandis, A. *Polymer* **1994**, *35*, 1880.
- (192) (a) Brunel, L.-C.; Barra, A.-L.; Martinex, G. *Physica B.* **1995**, *204*, 298. (b) Barra, A.-L.; Brunel, L.-C.; Gatteschi, D.; Pardi, L.; Sessoli, R. *Acc. Chem. Res.* **1998**, *31*, 460. (c) Barra, A.-L.; Caneschi, A.; Gatteschi, D.; Sessoli, R. *J. Am. Chem. Soc.* **1995**, *117*, 8855.
- (193) Barra, A.-L.; Caneschi, A.; Gatteschi, D.; Sessoli, R. *J. Magn. Magn. Mater.* **1998**, *177-181*, 709.
- (194) Aubin, S. M. J.; Dilley, N. R.; Pardi, L.; Krzystek, J.; Wemple, M. W.; Brunel, L.-C.; Maple, M. B.; Christou, G.; Hendrickson, D. N. *J. Am. Chem. Soc.* **1998**, *120*, 4991.

- (195) Petukhov, K.; Hill, S.; Chakov, N. E.; Abboud, K. A.; Christou, G. *Phys. Rev. B* **2004**, *70*, 054426.
- (196) Hill, S.; Perenbloom, J. A. A. J.; Dalal, N. S.; Hathaway, T.; Stalcup, T.; Brooks, J. S. *Phys. Rev. Lett.* **1998**, *80*, 2453.
- (197) (a) Hill, S.; Edwards, R. S.; North, J. M.; Maccagnano, S.; Dalal, N. S. *Polyhedron* **2003**, *22*, 1897. (b) Edwards, R. S.; Hill, S.; Maccagnano, S.; Dalal, N. S.; North, J. M., arXiv: cond-mat/0302052.
- (198) Chakov, N. E.; Hill, S.; Lee, J.; Edwards, R. S.; Wernsdorfer, W.; Abboud, K. A.; Christou, G. manuscript in preparation.
- (199) (a) Glerup, J.; Weihe, H. *Acta Chem. Scand.* **1991**, *45*, 444. (b) Jacobsen, C. J. H.; Pedersen, E.; Villadsen, J.; Weihe, H. *Inorg. Chem.* **1993**, *32*, 1216.
- (200) Park, K.; Pederson, M. R.; Hellberg, C. S. *Phys. Rev. B* **2004**, *69*, 014416.
- (201) Katsnelson, M. I.; Dobrovitski, V. V.; Harmon, B. N. *Phys. Rev. B* **1999**, *59*, 6919.
- (202) (a) Achey, R. M.; Kuhns, P. L.; Reyes, A. P.; Moulton, W. G.; Dalal, N. S. *Phys. Rev. B* **2001**, *64*, 064420. (b) Achey, R. M.; Kuhns, P. L.; Reyes, A. P.; Moulton, W. G.; Dalal, N. S. *Sol. St. Commun.* **2002**, *120*, 107.
- (203) Mola, M.; Hill, S.; Goy, P.; Gross, M. *Rev. Sci. Instrum.* **2000**, *71*, 186.
- (204) Takahashi, S.; Hill, S. *Rev. Sci. Instrum.* **2005**, *76*, 023114.

## BIOGRAPHICAL SKETCH

Born in the USA on February 24, 1978, Nicole E. Chakov received a Bachelor of Science degree from the University of Alabama in May 2000. During her undergraduate studies, she performed research in the group of Professor John B. Vincent primarily on the synthesis and characterization of a biologically relevant chromium-containing oligopeptide. In addition to her undergraduate research, she participated in a National Science Foundation Research Experiences for Undergraduates (NSF-REU) program and also completed an internship sponsored by the Howard Hughes Medical Institute. After the completion of her undergraduate degree, she joined the Department of Chemistry at Indiana University in August 2000. She joined the research group of Professor George Christou and, with her group and research advisor, transferred to the University of Florida in August 2001. Her doctoral research primarily involves the preparation and the physical and magnetic characterization of polynuclear transition metal complexes that function as single-molecule magnets.